Transactions of the ASME®

Technical Editor, T. H. OKIISHI (1998)
Associate Technical Editors
Aeromechanical Interaction
R. E. KIELB (1996)
Gas Turbine
C. J. RUSSO (1995)
Heat Transfer
M. G. DUNN (1996)
Nuclear Engineering
H. H. CHUNG (1996)
Power
P. H. GILSON (1996)
Turbomachinery
N. A. CUMPSTY (1995)

BOARD ON COMMUNICATIONS
Chairman and Vice-President
R. D. ROCKE

Members-at-Large
T. BARLOW, N. H. CHAO, A. ERDMAN, G. JOHNSON, L. KEER, W. MORGAN, E. M. PATTON, S. PATULSKI, R. E. REDER, S. ROHDE, R. SHAH, F. WHITE, J. WHITEHEAD

OFFICERS OF THE ASME
President, P. J. TORPEY
Executive Director
D. L. BELDEN
Treasurer
R. A. BENNETT

PUBLISHING STAFF
Mng. Dir., Publ.,
CHARLES W. BEARDSLEY
Managing Editor,
CORNELIA MONAHAN
Sr. Production Editor,
VALERIE WINTERS
Production Assistant,
MARISOL ANDINO

Transactions of the ASME, Journal of Turbomachinery (ISSN 0889-504X) is published quarterly (Jan., Apr., July, Oct.) for $150.00 per year by The American Society of Mechanical Engineers, 345 East 47th Street, New York, NY 10017. Second class postage paid at New York, NY and additional mailing offices. POSTMASTER: Send address change to Transactions of the ASME, Journal of Turbomachinery, c/o THE AMERICAN SOCIETY OF MECHANICAL ENGINEERS, 22 Law Drive, Box 2300, Fairfield, NJ 07007-2300.
CHANGES OF ADDRESS must be received at Society headquarters seven weeks before they are to be effective. Please send old label and new address.
PRICES: To members, $40.00, annually; to nonmembers, $150.00.
Add $24.00 for postage to countries outside the United States and Canada.
STATEMENT from By-Laws. The Society shall not be responsible for statements or opinions advanced in papers or ... printed in its publications (B7.1, Par. 3).

INDEXED by Applied Mechanics Reviews and Engineering Information, Inc.
Canadian Goods & Services Tax Registration #126148048

Journal of Turbomachinery

Published Quarterly by The American Society of Mechanical Engineers

VOLUME 116 • NUMBER 3 • JULY 1994

TECHNICAL PAPERS

(Contents Continued on p. 404)

(Contents Continued)

Predictions of Three-Dimensional Steady and Unsteady Inviscid Transonic Stator/Rotor Interaction With Inlet Radial Temperature Nonuniformity[1]

A. P. Saxer
Research Associate,
Turbomachinery Laboratory,
Institute of Energy Technology,
Swiss Federal Institute of Technology,
ETH-Zentrum,
8092 Zürich, Switzerland

M. B. Giles
Rolls-Royce Reader in
Computational Fluid Dynamics,
Oxford University Computing Laboratory,
Wolfson Building, Parks Road,
Oxford, OX1 3QD, United Kingdom

Numerical predictions of three-dimensional inviscid, transonic steady and periodic unsteady flow within an axial turbine stage are analyzed in this paper. As a first case, the unsteady effects of the stator trailing edge shock wave impinging on the downstream rotor are presented. Local static pressure fluctuations up to 60 percent of the inlet stagnation pressure are observed on the rotor suction side. The second case is an analysis of the rotor-relative radial secondary flow produced by a spanwise parabolic nonuniform temperature profile at the stator inlet. The generation of local hot spots is observed on both sides of the rotor blade behind the passing shock waves. The magnitude of the unsteady stagnation temperature fluctuations is larger than the time-averaged rotor inlet disturbance. In both cases, steady, unsteady, and time-averaged solutions are presented and compared. From these studies, it is concluded that the steady-state solution in static pressure matches well with the time-averaged periodic unsteady flow field. However, for the stagnation temperature distribution only the trend of the time-averaged solution is modeled in the steady-state solution.

1 Introduction

The demand for an increase in the cycle performance of today's gas turbines creates severe heat loads in the first turbine stage since higher operating temperatures are required. The mean flow temperature is usually well above the limit supported by the surrounding material. Cooling of both the endwalls and the blades of the first stage is thus usually necessary. Consequently, midspan streaks of hot, less dense gas pass through the first stator row and become hot jets of fluid.

This, and the inherent unsteadiness of a turbomachine flow field created by the relative motion between the stationary blades (stator) and the rotating rotor blades, requires the designer to account for three-dimensional as well as unsteady effects. For example, the thermal analysis of a turbine airfoil requires the knowledge of the local heat loads, which means that the knowledge of the average driving temperature in the blade passage is not sufficient to design the cooling system optimally. Hence, time-accurate values are required as well as deviations from the average.

In this context, this paper presents a numerical methodology for analyzing the three-dimensional inviscid, transonic, steady, and periodic unsteady flows within an axial turbine stage. In particular, the computations of steady and unsteady flow fields in a complete industrial first turbine stage under different, though realistic inlet conditions, will serve to evaluate the extent of the changes that may occur with respect to design techniques (throughflow procedures; AGARD, 1981; Turner, 1991) based on uniform inlet conditions and steady flow field.

Another motivation for analyzing and comparing the steady solution with the time-averaged periodic unsteady flow solution stems from the emergence of numerical methods that incorporate "corrections" to the baseline steady flow in order to account for deterministic periodic unsteadiness; see for instance the work of Adamczyk (1985) and Giles (1992). Adamczyk derived a set of average-passage flow equations for a multistage turbomachine by sequentially applying an ensemble-averaging, a time-averaging, and a passage-to-passage averaging operator to the governing equations. Giles proposed an asymptotic approach for multistage unsteady flow computations in which the effect of periodic unsteadiness on the steady flow is included through quadratic terms. Compared to the full nonlinear unsteady flow methods, these techniques offer potentially great savings in computer time, though still retaining the global effects of unsteadiness. However, the use of

[1]This work was carried out while the authors were at the Massachusetts Institute of Technology, Cambridge, MA, USA.

Contributed by the International Gas Turbine Institute and presented at the 38th International Gas Turbine and Aeroengine Congress and Exposition, Cincinnati, Ohio, May 24–27, 1993. Manuscript received at ASME Headquarters February 12, 1993. Paper No. 93-GT-10. Associate Technical Editor: H. Lukas.

these improved throughflow solution procedures needs to be justified by evaluating the extent of the changes resulting from unsteadiness. These are examined here for two flow cases occurring in a highly loaded transonic first turbine stage.

Finally, from a CFD point of view an underlying motivation for comparing the steady-state and the time-averaged solutions is to highlight the importance of the formulation of the numerical boundary conditions at the inlet, at the exit as well as at the stator/rotor interface.

This paper is structured as follows. After a brief description of the numerical procedure given in Section 2, the first case is presented in Section 3. It focuses on the effects resulting from the impact of the stator trailing edge shock wave off the adjacent rotor, for which a two-dimensional flow computation was previously performed by Giles (1990a). Here, the three-dimensional effects and the extent of the unsteadiness are addressed, and a comparison between steady-state and time-averaged solutions is performed. It has been experimentally observed that the periodic unsteady interaction between a shock wave and a turbine airfoil can cause considerable effects in terms of blade loading and heat transfer; see for instance Doorly and Oldfield (1985), Johnson et al. (1990), and Collie et al. (1993). Then, in Section 4, the unsteady rotor-relative secondary flow produced by a vane inlet spanwise temperature gradient is presented. The comparison between the steady-state and the time-averaged solutions allows us to extract the extent of the unsteady temperature migration. The problem of temperature redistribution in an axial flow turbine stage has been analyzed by several authors (see for instance Butler et al., 1986; Krouthén and Giles, 1988; Ni and Sharma, 1990; Harasgama, 1990; Dorney et al.,1990). In particular, the numerical studies of Ni and Sharma, and Dorney et al., tend to reproduce the migration of one midspan, circular hot streak of fluid, experimentally investigated by Butler et al. Notice that in contrast to the present analysis, all of the above-mentioned studies report on a turbine operating under subsonic flow conditions, where the level of unsteadiness is very much lower than for the transonic cases. Finally, the essential conclusions are given in Section 5.

2 Numerical Procedure

The governing relations considered here are the time-dependent three-dimensional Euler equations solved in conservation form. The numerical methodology uses a node-based, explicit Ni-Lax-Wendroff discretization scheme (Ni, 1981) implemented on an unstructured grid composed of hexahedral cells (Saxer, 1992). Relative flow variables attached to each individual blade row are used. The mesh itself is first generated in a structured fashion by iteratively solving a three-dimensional Poisson system, in which the source terms are automatically evaluated in order to provide a control of the cell size and of the skewness at the blade boundary. Then, the structured mesh is transformed into an unstructured grid. The Euler algorithm presented here requires the addition of a numerical smoothing, whose purpose is to capture shocks and to prevent unwanted high-frequency oscillations in the solution. It has the form of a combined fourth- and second-difference operator acting on the state vector. The fourth-difference smoothing exploits the advantages of a pseudo-Laplacian to ensure second-order accuracy in shock-free regions even in the presence of grid irregularities. This is an important property when comparing different solutions and when studying the effects of prescribed inlet distortions, which must not be smeared out numerically in the computational domain. It is an extension to three dimensions of the method introduced by Holmes and Connell (1989). The shocks are captured using a nonlinear second-difference operator, which includes an artificial bulk viscosity parameter tailored by the local flow divergence and the Mach number to avoid large shock overshoots, and not to alter the global accuracy of the scheme in smooth flow regions.

2.1 Boundary Conditions. For steady-state flow computations, the quasi-three-dimensional nonreflecting boundary condition formulation developed by the authors (Saxer and Giles, 1993) is used at the inlet and the outlet as well as at the stator/rotor interface, and is designed to avoid numerical reflections. In this technique, the solution at the boundary is circumferentially decomposed into Fourier modes, the zeroth mode corresponding to the average solution. This part is treated according to the standard one-dimensional characteristics theory, which allows the user to specify certain physical quantities at the boundaries by setting average changes in the incoming characteristics. Using a Lax-Wendroff type algorithm to time-march the solution to the steady state, the changes in the boundary values from time level n to time level $n+1$ are required. Thus, the characteristic variables are defined in terms of perturbations to the average inflow or outflow at the time level n. For example, at the inflow, the average characteristic changes are calculated from the requirement that the average entropy, radial and tangential flow angles, and stagnation enthalpy have certain values.

$$
\begin{aligned}
(\bar{s})^{n+1} &= \bar{s}_{\text{inl}},\\
(\bar{\alpha}_\theta)^{n+1} &= \alpha_{\theta\text{inl}},\\
(\bar{\alpha}_R)^{n+1} &= \alpha_{R\text{inl}},\\
(\bar{h}_t)^{n+1} &= \bar{h}_{t\text{inl}}.
\end{aligned}
\tag{1}
$$

$\bar{s}$ is an entropy-related function defined by

$$
\bar{s} = \overline{\log(\gamma p) - \gamma \log \rho}, \tag{2}
$$

and $\bar{h}_t$ is the mean total enthalpy. $\alpha_{\theta\text{inl}}$ and $\alpha_{R\text{inl}}$ together with $\bar{s}_{\text{inl}}$ and $\bar{h}_{t\text{inl}}$ are user-specified average inflow angles, entropy, and total enthalpy, respectively, which are usually a function of the radius. For an axially subsonic outflow, the first four characteristics are outgoing, so only the fifth characteristic

Nomenclature

c = speed of sound
h_t = stagnation enthalpy
p = static pressure
p_t = stagnation pressure
p_t^* = rotary stagnation pressure, Eq. (7)
R = radius = $\sqrt{y^2+z^2}$
s = entropy
t = time (nondimensionalized with period)
T_t = stagnation temperature
u, v, w = Cartesian velocity components in (x, y, z)
u_x, u_θ, u_R = cylindrical velocity components in (x, θ, R)
V = absolute velocity (stator)
W = relative velocity (rotor)
α_θ, α_R = tangential and radial flow angles
γ = ratio of specific heats
ρ = static density
ϕ = characteristic variable
Ω = angular speed
ω = vorticity
$(\ )^n$ = time index
$(\ )_F$ = flux-averaged quantity
$(\ )_{\text{inl}}$ = inlet
$(\ )_{\text{out}}$ = outlet
$(\ )_{r,s}$ = rotor, stator
$(\ )_{\text{rel}}$ = relative frame (rotor)
$(\ )_{s,n,b}$ = streamwise, normal, and binormal components
$\overline{(\ )}$ = circumferential arithmetic average

variable needs to be set. The average change in the characteristic is determined to achieve the user-specified average exit pressure $\bar{p}_{\text{out}}$ at a certain radius together with the requirement that the outflow is in radial equilibrium. The latter condition is expressed by

$$\left(\frac{\partial \bar{p}(R)}{\partial R} = \bar{\rho}\,\frac{\bar{u}_\theta^2}{R}\right)_{\text{out}}, \tag{3}$$

together with the specification of $\bar{p}_{\text{out}}$ at some particular radius. At the inflow and outflow, the changes in the outgoing characteristics are obtained from the changes distributed by the Lax–Wendroff algorithm. The remaining part of the solution, represented by the sum of the harmonics, is treated according to the two-dimensional nonreflecting boundary condition theory, which prevents spurious reflections at the boundaries (Giles, 1990b).

In a steady-state calculation of a stator/rotor interaction, a circumferential stream-thrust flux-averaging technique is used in order to conserve mass, momentum, and energy across the mixing plane between a stator and a rotor row. Hence, radial variations are automatically accounted for and the stator and the rotor flow fields are matched at the interface. In this technique, the average characteristic changes at the stator outflow and the rotor inflow are set to eliminate the following characteristic jumps, taking note of the direction of propagation of each characteristic:

$$\begin{pmatrix} \Delta\bar{\phi}_1 \\ \Delta\bar{\phi}_2 \\ \Delta\bar{\phi}_3 \\ \Delta\bar{\phi}_4 \\ \Delta\bar{\phi}_5 \end{pmatrix} = \begin{pmatrix} -\bar{c}^2 & 0 & 0 & 0 & 1 \\ 0 & 0 & \bar{\rho}\bar{c} & 0 & 0 \\ 0 & 0 & 0 & \bar{\rho}\bar{c} & 0 \\ 0 & \bar{\rho}\bar{c} & 0 & 0 & 1 \\ 0 & -\bar{\rho}\bar{c} & 0 & 0 & 1 \end{pmatrix} \begin{pmatrix} \rho_{Fs} - \rho_{Fr} \\ u_{xFs} - u_{xFr} \\ u_{\theta Fs} - u_{\theta Fr} - \Omega R \\ u_{RFs} - u_{RFr} \\ p_{Fs} - p_{Fr} \end{pmatrix} \tag{4}$$

where ρ_F, u_{xF}, $u_{\theta F}$, u_{RF}, and p_F represent the stream-thrust flux-averaged values of density, axial, circumferential and radial velocity components, and pressure, respectively. Note that because of the use of relative flow variables, the rotor wheel speed ΩR has to be introduced into the condition of matching circumferential velocities. Once this is done for both sides of the interface, the remainder of the boundary condition treatment (i.e., harmonics) is exactly the same as for a standard inflow and outflow boundary (Saxer, 1992).

For time-accurate calculations of stator/rotor flow fields, Eq. (4) is used on a one-dimensional local basis to calculate the changes in the incoming characteristics on both sides of the interface. The outgoing characteristics changes are calculated by the Lax–Wendroff algorithm. The combined five characteristic changes on both sides of the interface are then converted back to primitive and finally conservation variables before the flow field is updated. The importance of formulating nonreflecting boundary conditions will be highlighted later in Section 4. In addition to these boundary conditions, a no-mass-flux condition is enforced at the hub and the tip endwalls as well as on the stator and the rotor blades. Also, periodic boundary conditions along the outer boundaries of the **H**-type grid are enforced in the tangential direction.

3 Shock Interaction in an Axial Turbine Stage

In this section, the numerical procedure is applied to investigate both the steady and the unsteady flow fields occurring in a generic (i.e., the stator-to-rotor pitch ratio is 1) highly loaded transonic first turbine stage; see Fig. 1. For supersonic vane exit conditions, a system of oblique shock waves is generated at the trailing edge of the stator. For small axial gaps, the suction side trailing edge shock extends to the downstream rotor and impinges on the suction side. This produces reflected waves on both the adjacent rotor and on the upstream stator

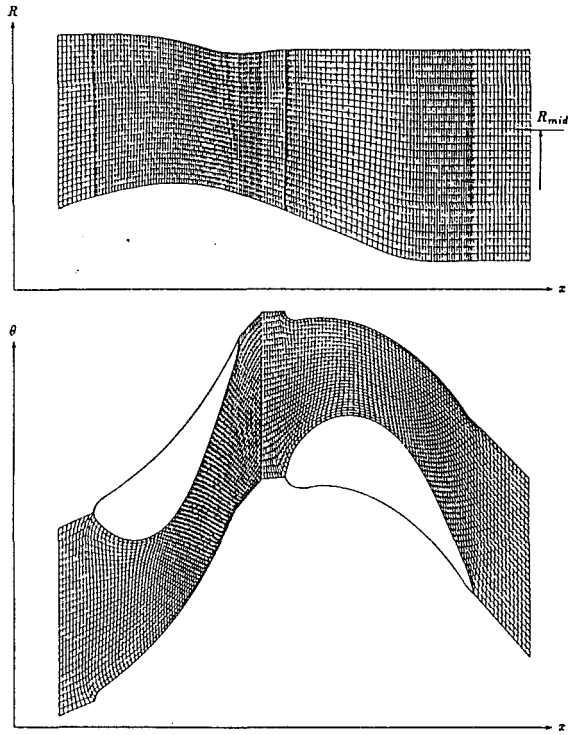

Fig. 1 (Top) side view of the scaled transonic first turbine stage with stator pressure and rotor suction sides, and (bottom) mean height blade-to-blade mesh (stator: 80 × 30 × 30, rotor: 80 × 30 × 30 nodes)

causing unsteady blade loading. For these closely spaced blades, the formulation of the boundary conditions at the stator/rotor interface becomes a keypoint in the numerical simulation.

3.1 Unsteady Shock Motion. Figure 2 shows the instantaneous static pressure contours at a constant radius $R = R_{\text{mid}}$ at eight intervals during one blade-passing period, i.e., from $t = 0$ at the beginning of the period to $t = 1$ at the end of the period, which also corresponds to $t = 0$ by periodicity. Note that the unsteady pressure contours match well across the stator/rotor boundary at any time during the period.

At $t = 0$, the stator trailing edge oblique shock has hit the crown of the rotor suction surface. As the rotor blade moves upward, the location of impingement moves forward towards the leading edge. A reflection is clearly visible at $t = 0.375$. In addition to this primary reflection, the portion of the reflected wave that moves toward the pressure surface of the adjacent rotor is reflecting a second time and is moving back toward the original rotor. At $t = 0.5$, the primary shock wave reflection has reached the rotor leading edge and the secondary reflected wave has crossed back to the original rotor. It has sufficiently intensified to be now visible on the pressure contours.

At $t = 0.625$, the stator oblique shock no longer impacts on the rotor, and from $t = 0.625$ to $t = 0.875$ the length of its straight portion is increased (due to a velocity component approximately $\sqrt{V^2 - c^2}$ along the shock front) until it refracts with the secondary reflected shock. Also at $t = 0.625$, the primary reflected wave has left the rotor and is propagating upstream toward the stator suction surface. At $t = 0.75$, the primary reflected shock has just struck the suction side of the upstream stator in a region close to the trailing edge. The secondary reflected shock wave is still moving upstream toward the crown of the rotor.

At $t = 0.875$, the primary oblique shock has almost regained its maximum strength. The primary reflected shock is reflecting from the upstream stator suction surface and moves back to the adjacent rotor. This reflection is also visible at $t = 0$, but

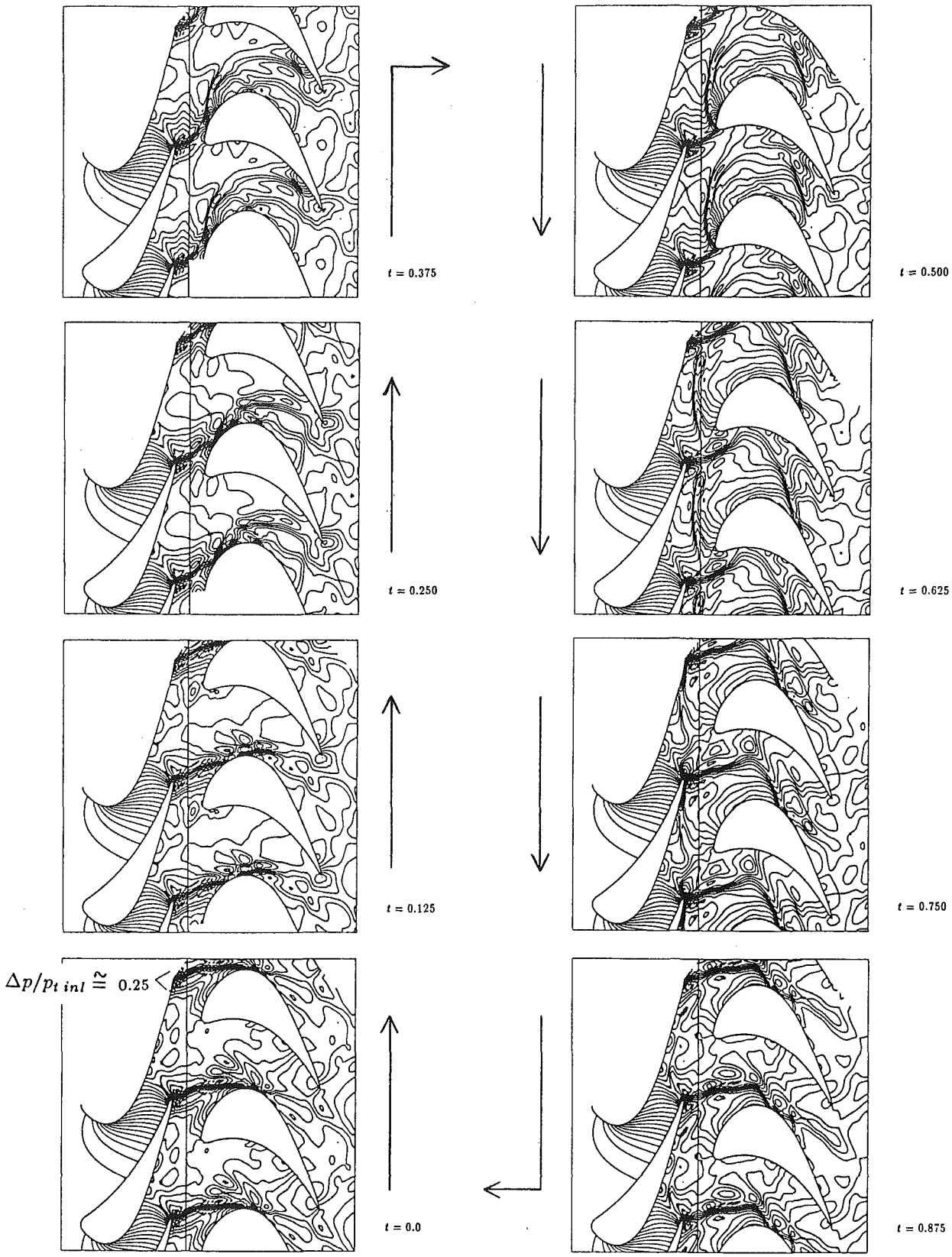

Fig. 2 Unsteady static pressure contours at $R = R_{mid}$

then it disappears as it strikes the rotor leading edge at $t = 0.125$. However, this effect is recorded in the history of the rotor leading edge pressure in Fig. 3. In addition, this figure clearly illustrates the impact of the stator oblique shock on the rotor leading edge at $t = 0.5$.

Figure 4 shows the instantaneous tuft distribution on the rotor suction surface for one blade-passing period. A secondary flow is visible in the aft part of the blade that drives fluid from hub toward midspan. Reverse flow occurs behind the secondary reflected wave as it moves forward toward the lead-

ing edge and strengthens. However, recirculation occurs only partially during the cycle.

For the case examined here, the unsteady stator/rotor shock interaction is essentially a two-dimensional process driven by the oblique shock leaving the stator trailing edge and impinging on the moving rotor blade. This unsteady shock interaction is similar in nature to the result presented by Giles (1990a) in a two-dimensional time-accurate numerical simulation, which included quasi-three-dimensional source terms. However, some differences appear in the timing of the events because Giles' computation was performed on the actual configuration with a stator-to-rotor pitch ratio of 1.69.

3.2 Steady and Time-Averaged Results. The flow conditions for the steady-state and for the time-averaged periodic unsteady computation are listed in Table 1. The Mach and angle values represent flux-averaged quantities. Starting from the steady-state solution, the unsteady computation took 12 periods to converge to a periodic solution, using 400 iterations/period. A CPU time of 385×10^{-6} s/iteration/grid point was required on a Stardent GS-2000 in vector mode.

The stator static pressure distributions around the blade root and at midspan are given in Fig. 5. Also shown are the maximum and the minimum unsteady pressures on both the suction and the pressure sides. Because the flow is choked at the throat, and since the stator inlet conditions are steady, no unsteadiness is present upstream of that area and so the mass flow is the same in both cases. Although the unsteady pressure envelope can locally account for 50 percent of the inlet stagnation pressure, the time-averaged solution almost matches the steady-state result over the entire span. It should be pointed out that the time-averaged solutions presented in this paper were computed during the blade-passing period from all the time-steps, i.e., they represent the following equation:

$$\bar{\varphi}(x, y, z) = \frac{1}{T}\int_0^T \varphi(x, y, z, t)\,dt, \qquad (5)$$

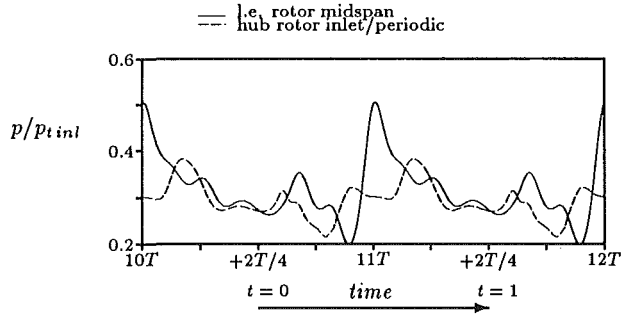

Fig. 3 Pressure history for the last two periods

with $(\bar{})$ representing a quantity that has been time-averaged over a period T. On the other hand, the maximum and minimum values were extracted from eight unsteady snapshots during the final blade-passing period. This is why a certain amount of discreteness in those quantities is observed in Figs. 5 and 6. The rotor blade pressure distributions at three spanwise locations are shown in Fig. 6. Here, the unsteadiness is much more intense, especially on the suction side of the blade due to the unsteady shock motion and shock reflection described in the previous section. At the hub, the steady-state shock located at the front part of the suction side is intensified during a portion of the period. On the suction side near the leading edge, the peak-to-peak pressure variation accounts for up to 60 percent of the (stator) inlet reference stagnation pressure. It is surprising to notice that although the variations in pressure (and Mach number) are large, the time-averaged solution is similar to the steady-state result over all but the root section of the blade. In particular, the maximum variation in the blade static pressure between the steady-state and the time-averaged unsteady solution is less than 4 percent of the stator inlet stagnation pressure. In general, the level of unsteadiness is larger on the suction side than on the pressure side, and also at the hub and at the tip compared to midspan.

In the unsteady solution, a shock-induced secondary flow creates a slight flow blockage at the lower radii (hub); see Fig. 7. This is compensated by an increase in mass flow through the outer rotor radii streamtubes. Tufts on the rotor suction

Table 1 Steady and time-averaged flow parameters for scaled transonic turbine stage

parameter		steady	time-averaged
Stator inlet tangential angle	hub	0.0^0	0.0^0
	mid	0.0^0	0.0^0
	tip	0.0^0	0.0^0
Stator outlet tangential angle	hub	72.1^0	72.6^0
	mid	74.8^0	74.6^0
	tip	73.9^0	73.8^0
Rotor-relative inlet tangential angle	hub	51.3^0	53.4^0
	mid	50.2^0	51.0^0
	tip	40.6^0	41.1^0
Rotor-relative outlet tangential angle	hub	-57.1^0	-60.6^0
	mid	-67.8^0	-67.0^0
	tip	-76.3^0	-76.8^0
Stator inlet Mach number	hub	0.15	0.15
	mid	0.13	0.13
	tip	0.13	0.13
Stator outlet Mach number	hub	1.37	1.33
	mid	1.25	1.24
	tip	1.19	1.18
Rotor-relative inlet Mach number	hub	0.69	0.67
	mid	0.52	0.52
	tip	0.44	0.44
Rotor-relative outlet Mach number	hub	1.00	0.99
	mid	0.96	0.97
	tip	0.95	0.93
Rotor Mach number	hub	0.76	0.73
	mid	0.81	0.79
	tip	0.86	0.84
Rotor wheel speed $\Omega/\sqrt{c_{t\,inl}/L_{hub}}$		0.097	0.097
Stator axial torque $T_x/\sqrt{(\rho_t c_t)_{inl} L_{hub}^3}$		-1.6926	-1.6812
Rotor axial torque $T_x/\sqrt{(\rho_t c_t)_{inl} L_{hub}^3}$		1.7678	1.7579
Ratio of specific heats γ		1.27	1.27

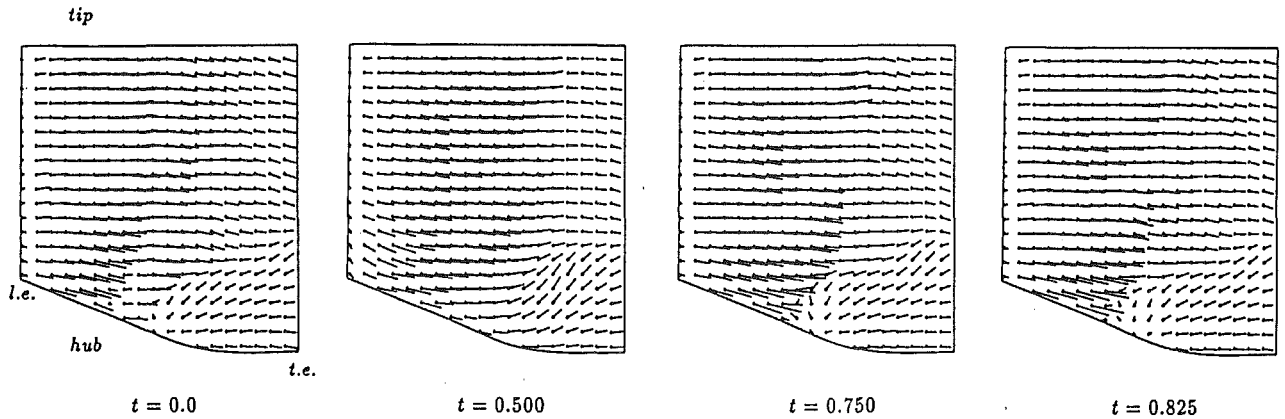

Fig. 4 Computed tufts on rotor suction side at different times

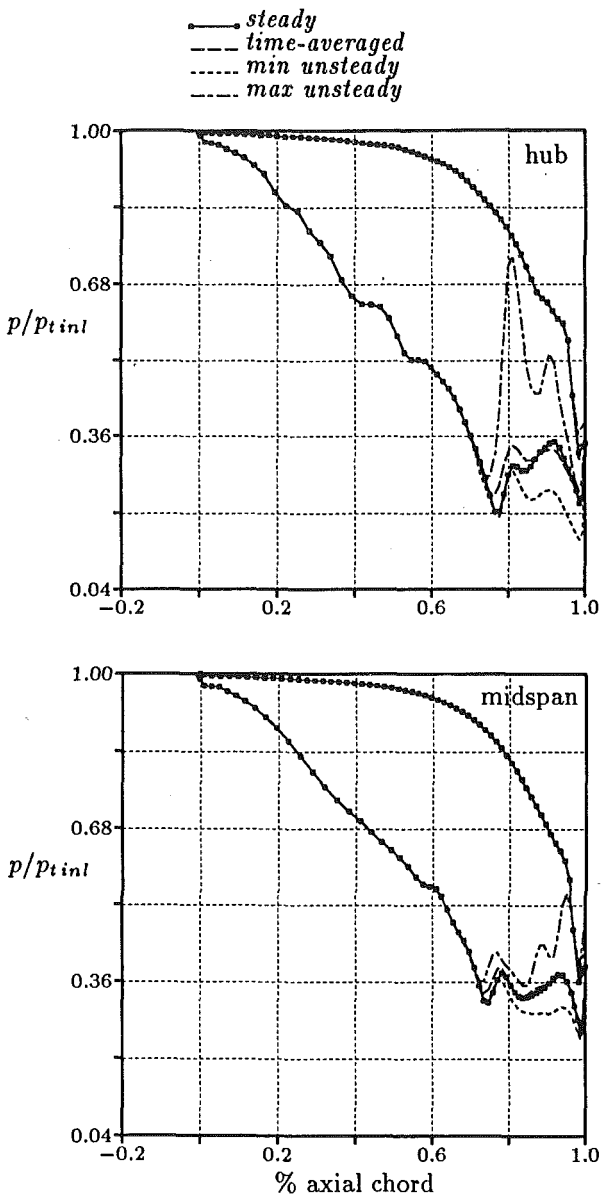

Fig. 5 Steady and unsteady stator blade static pressure

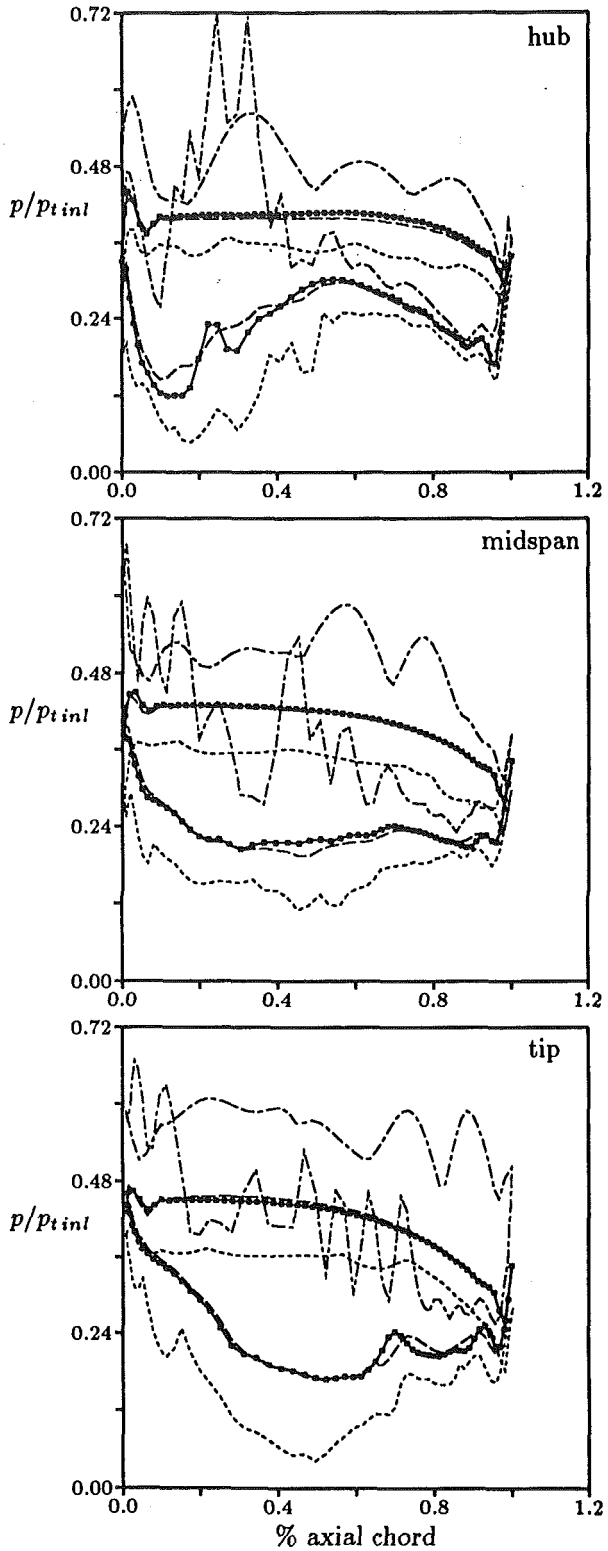

Fig. 6 Steady and unsteady rotor blade static pressure

side are plotted in Fig. 8 for the steady and the time-averaged solutions. The crossflow seen in Fig. 8(*b*) is a direct consequence of the entropy production caused by the unsteady shock interaction and can be qualitatively understood by using secondary flow theory applied on the time-averaged solution. By assuming locally incompressible flow, it can be shown that the generation of a streamwise component of vorticity can be written as a function of gradients of rotary stagnation pressure in the binormal and axial directions, respectively (Hawthorne, 1974; Johnson, 1978; Horlock and Lakshminarayana, 1973).

$$\frac{\partial}{\partial s}\left(\frac{\omega_s}{\rho W}\right)=\frac{2}{\rho W^2}\left(\underbrace{\frac{1}{\sigma}\hat{b}\cdot\nabla p_t^*}_{\text{curvature}}+\underbrace{\frac{1}{W}\Omega\cdot\nabla p_t^*}_{\text{rotation}}\right). \tag{6}$$

Equation (6) is written in intrinsic coordinates where $\hat{s}$, $\hat{n}$, $\hat{b}$ represent the unit vectors in the direction of relative streamline, inward of principal normal, and in the binormal direction, respectively. σ is the principal radius of curvature of the relative streamline and p_t^* is the rotary stagnation pressure, defined by

$$p_t^*=p+\frac{1}{2}\rho\left((u^2+v^2+w^2)_{\text{rel}}-\Omega^2R^2\right). \tag{7}$$

In the steady-state calculation p_t^* is almost constant over the entire blade except behind the hub shock; see Fig. 9(*a*). In the time-averaged solution, however, gradients of rotary stagnation pressure show up not only near the location of the steady-state shock but over the entire near-hub suction surface; see Fig. 9(*b*). The comparison clearly shows that a strong axial

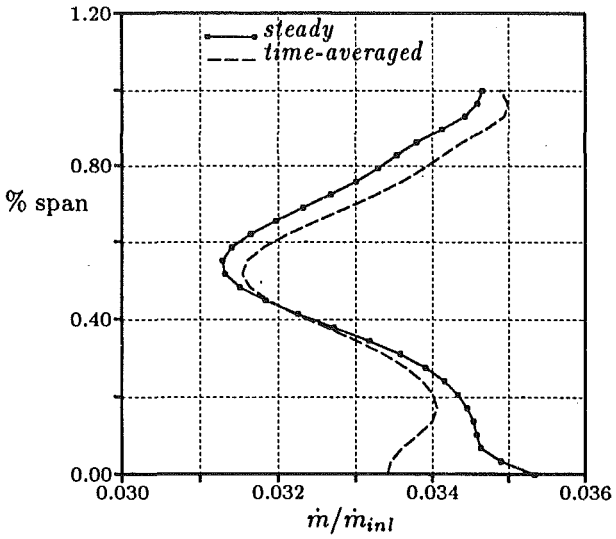

Fig. 7 Spanwise distribution of mass flow at rotor inlet

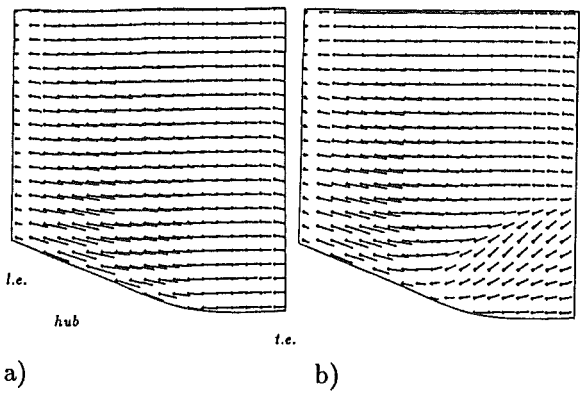

Fig. 8 Computed tufts on rotor suction side: (*a*) steady-state, (*b*) time-averaged

p_i^* gradient exists in the time-averaged solution, which, when dot-producted with the rotation vector, produces a positive component of streamwise vorticity. This tends to develop a radially outward component of velocity.

On the stator there is a 6 percent unsteady peak-to-peak variation in torque, despite the fact that the pressure field is steady on all but a small portion of the suction side near the trailing edge. This variation is essentially caused by the primary rotor-reflected shock wave moving upstream and striking the stator suction side. Notice that in the two-dimensional simulation (Giles, 1990a) the unsteady stator lift has a peak-to-peak variation of 6 percent, which compares well to the three-dimensional case. However, as opposed to a rotor unsteady peak-to-peak torque variation of 66 percent, "only" 40 percent variation in lift is experienced by the rotor in the two-dimensional case. In general the agreement between the time-averaged and the steady-state axial torque is excellent with differences less than 0.5 percent of the time-averaged value.

4 Radial Temperature Migration

The objective of this section is to analyze the migration of a spanwise nonuniform inlet temperature distribution in an axial flow turbine stage (similar to the one discussed in the previous section). The design of this stage was performed by Rolls-Royce and is representative of a high pressure (4:1 stage pressure ratio), cooled aircraft turbine operating in the transonic regime. The flow simulation uses a 3-to-5 stator-to-rotor

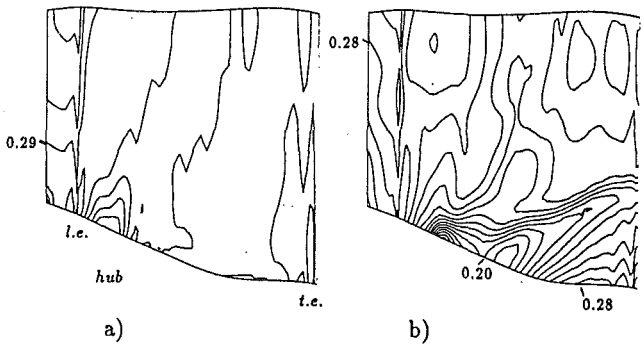

Fig. 9 Rotary stagnation pressure (p_i^*/p_{tinl}) on rotor suction side: (*a*) steady-state, (*b*) time-averaged (inc. = 0.01)

blade count ratio, which corresponds closely to the actual configuration of (36 stators)/(61 rotors); see Figs. 10 and 11. 56 × 36 × 21 nodes are used in each of the three stator channels, and 56 × 22 × 21 in each of the five rotor passages.

The stator inlet conditions are set by two flow angles and by assuming a uniform stagnation pressure. A radially parabolic stagnation temperature profile is set in which the temperature is 21 percent higher at midspan than at the hub and the tip endwalls. Notice that these conditions produce a radially sheared velocity field, hence vorticity. However, under the invariance of the inlet stagnation pressure and by using the Munk and Prim substitution principle (Munk and Prim, 1947), it can be shown that no three-dimensional secondary flow associated with the temperature gradient occurs in the vane (Saxer, 1992). This is because the Munk and Prim principle states that if a steady isentropic flow field without body forces is determined for a specific geometry and a total pressure distribution, then the streamline pattern, the Mach number, and the static pressure fields remain unchanged for any stagnation temperature distribution. Another way of checking this statement is again to use secondary flow theory (Hawthorne, 1974; Johnson, 1978; Horlock and Lakshminarayana, 1973). Rewriting Eq. (6) in the absolute frame of reference would show that the growth of the absolute streamwise vorticity is dependent upon the gradient of stagnation pressure, which is set to zero at the inlet, i.e., the vortex lines introduced at the inlet have to remain perpendicular to the flow in the vane. In fact, the secondary flow developed by the turning of the inlet normal vorticity is exactly balanced by the secondary flow introduced by the temperature gradient.

These arguments are not valid in the rotor frame of reference where a radial secondary flow occurs. It can be qualitatively explained by using vorticity and velocity triangle arguments and simple dynamics (Butler et al., 1986; Saxer, 1992). Figure 12 is a schematic of the vorticity and the velocity triangles at the stator/rotor interface. In the relative frame, the stator vorticity (normal to the flow) can be decomposed into a normal and a streamwise component, which will strengthen as the normal component turns into the rotor passage producing a three-dimensional secondary flow. From the velocity triangle it can be inferred that in the rotor frame the hot midspan fluid is streaming with a relative higher velocity than the cold endwall fluid, and with an incidence angle oriented more toward the pressure side of the rotor. This implies that relative to a uniform inlet condition solution, the temperature distortion calculation exhibits an excess of rotary stagnation pressure (or rotor-relative inlet stagnation pressure) at midspan and a deficit at the hub and the tip of about 12 percent of the rotor-relative inlet dynamic head, which contributes to the generation of secondary flow. The overall effect is the collection of hotter gas on the rotor pressure side than on the suction side. On the pressure side, the hot fluid is spreading from midspan toward the hub and the tip endwalls, resulting in the heating of the upper and

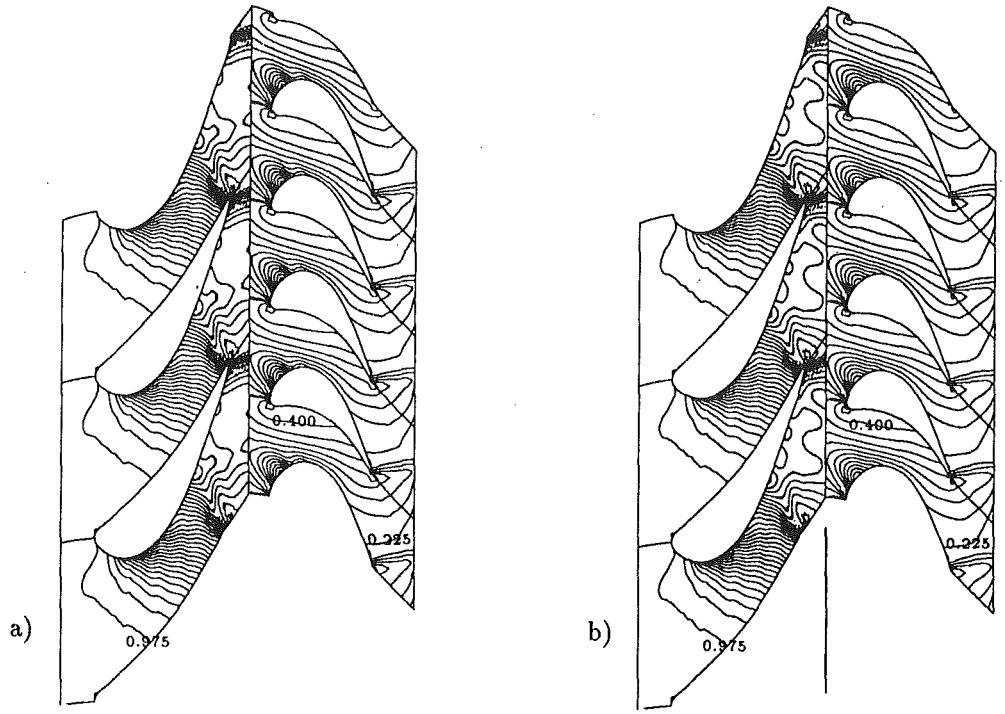

Fig. 10 Static pressure field at the hub: (*a*) steady-state, (*b*) time-averaged (increment $\Delta p/p_{tinl} = 0.025$)

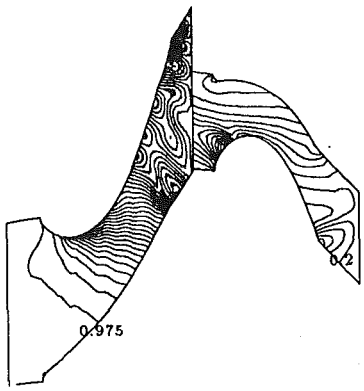

Fig. 11 Steady-state static pressure at the hub using reflecting boundary conditions

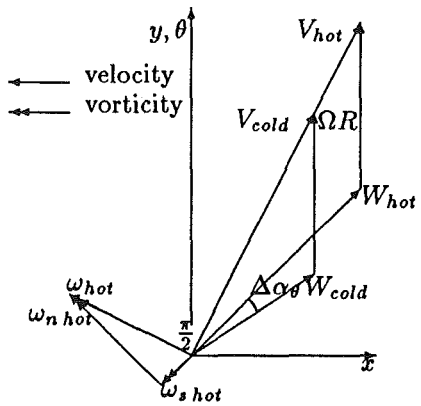

Fig. 12 Velocity and vorticity triangles at stator/rotor interface

lower walls. On the suction side, cool endwall gas flows toward midspan. Also a comparison between steady-state flow solutions without and with inlet radial temperature distortion shows that the rotor-relative secondary flow affects the vane flow field by reducing the stator/rotor interface pressure (about 17 percent of the rotor inlet dynamic head for the case examined); see Saxer and Giles (1990). In turn this produces an increase in both the stator exit and the rotor inlet Mach numbers and also the rotor inlet angle. This is sufficient to trigger a shock at the rotor root; see Fig. 10(*a*).

4.1 Unsteady Rotor-Relative Temperature. Instantaneous rotor-relative stagnation temperature contours and static pressure contours on the suction side (of the lower rotor blade) are plotted in Fig. 13 for four snapshots during one period. Notice that for the case examined here, the period, starting at $t = 0$ in the configuration shown in Fig. 10, is defined as the time for one rotor passage to rotate by an amount of five rotor pitches to $t = 1$, which also corresponds to $t = 0$. The suction side radial migration of the cooler gas at the hub and the tip toward midspan is small at any time during the period. However, under the shock interaction, the local instantaneous surface stagnation temperature can exceed the time-averaged midspan rotor inlet value by about 10 percent, which corresponds to half of the stator inlet distortion. This shows up as local hot spots of elliptical shape created behind the passing shock waves. Notice that in the rotating frame of reference the time-averaged parabolic inlet distortion is reduced from 21 to 17 percent. The local envelope of these temperature fluctuations has a magnitude of the order of the absolute distortion, hence larger than the rotor-relative inlet variation. The rotor-relative pressure surface stagnation temperature distribution together with the static pressure contours during one period are illustrated in Fig. 14. As explained in Section 3, the rotor pressure side is less affected by the shock interaction, thus the local unsteady temperature fluctuations are smaller than on the suction side. However, under the influence of the radial secondary flow, which is stronger on the pressure side than on the suction side, the hot spots cover a broader portion of the blade.

4.2 Steady and Time-Averaged Results. Steady-state and time-averaged periodic unsteady static pressure contours at the hub are represented in Fig. 10. Clearly, the results are very

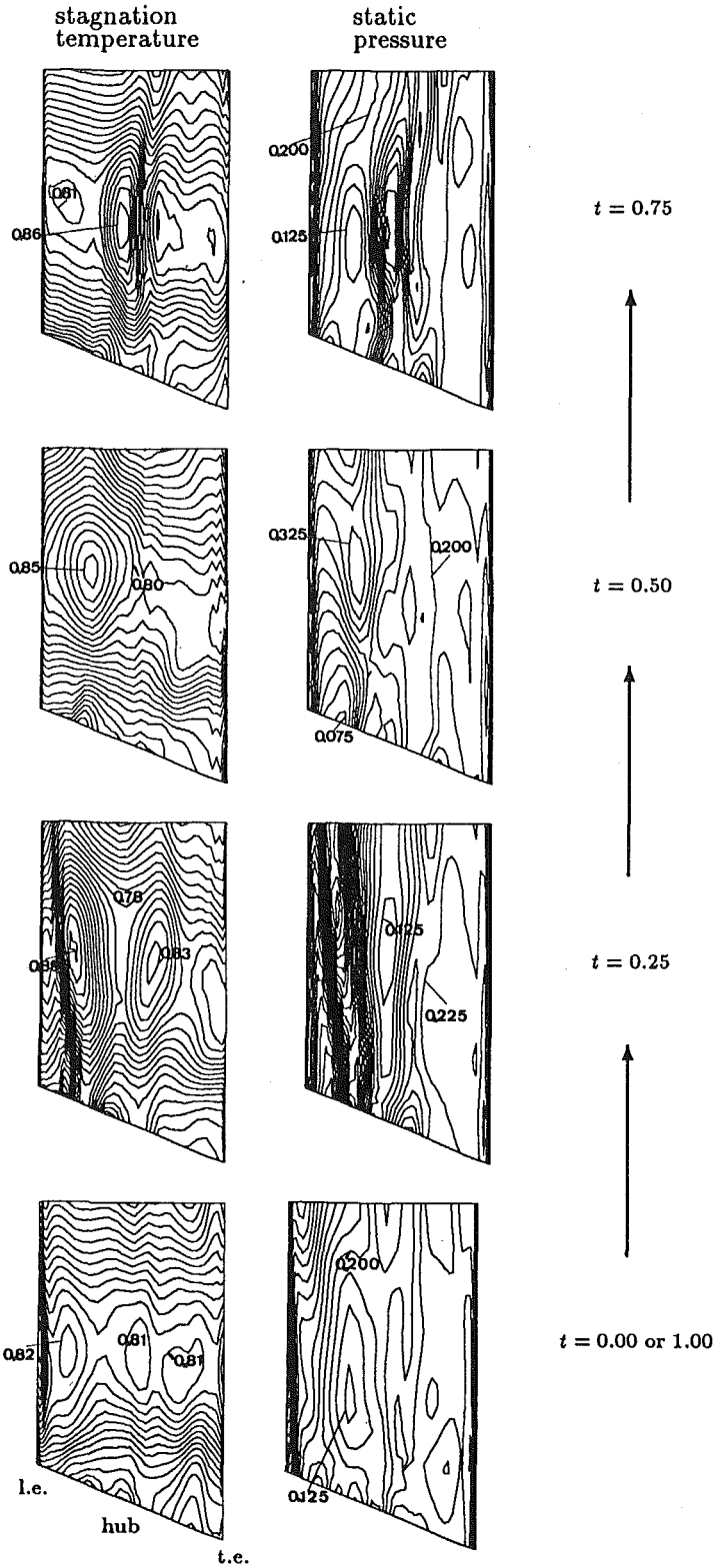

Fig. 13 Rotor-relative stagnation temperature contours and static pressure contours on the suction side at different times. $\Delta T_t/\gamma T_{tinl} = 0.01$, $\Delta p/p_{tinl} = 0.025$

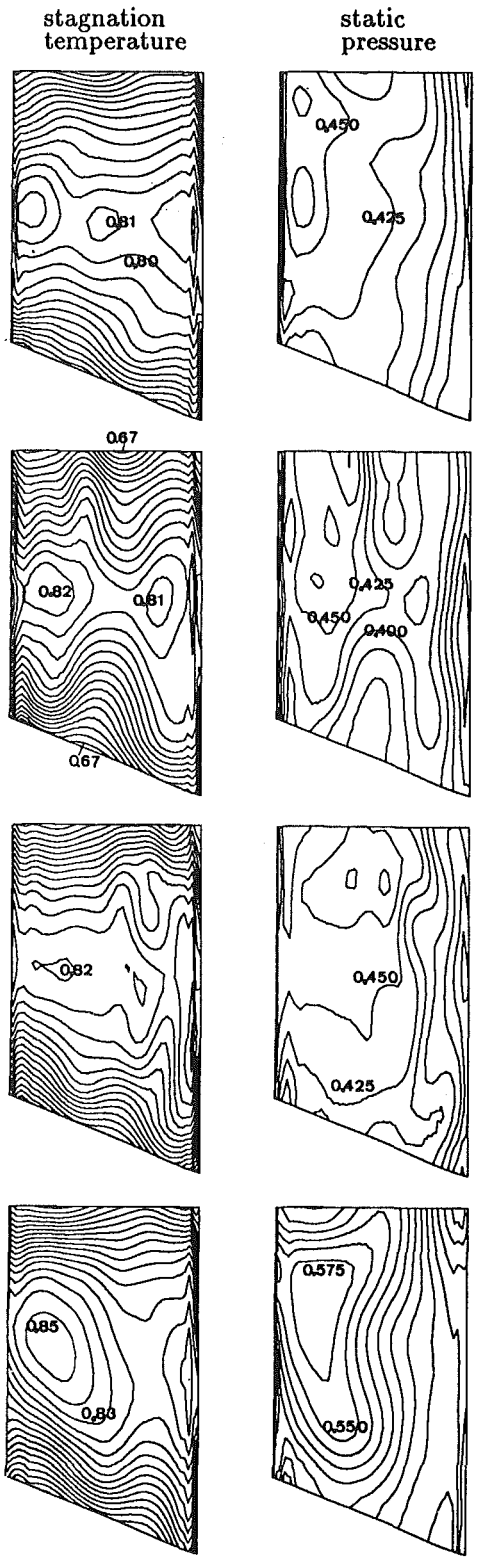

Fig. 14 Same as Fig. 13 but for rotor pressure side

similar, with a discrepancy less than 2.5 percent of p_{tinl} between the two solutions. This is small when compared to the level of unsteady pressure fluctuations that can be ten times larger during the cycle. To show the importance of the formulation of the boundary conditions in the calculation of this type of transonic flow, Fig. 11 presents a result for which the standard one-dimensional boundary conditions have been used at the inlet, the exit, and the stator/rotor interface. Notice the spurious reflections at the stator/rotor interface and at the rotor exit where a uniform pressure has been set. In particular, the trailing edge oblique shock waves of both the stator and the rotor are reflected back into the computational domain as expansion waves. The use of the improved (nonreflecting) boundary conditions in the calculation of the steady-state sta-

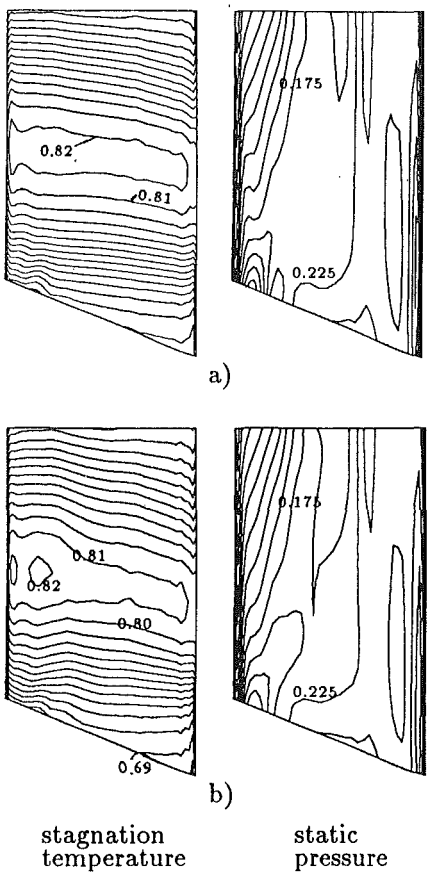

Fig. 15 Rotor-relative stagnation temperature contours ($T_t/\gamma T_{tinl}$) and static pressure contours (p/p_{tinl}) on the suction side: (*a*) steady-state, (*b*) time-averaged

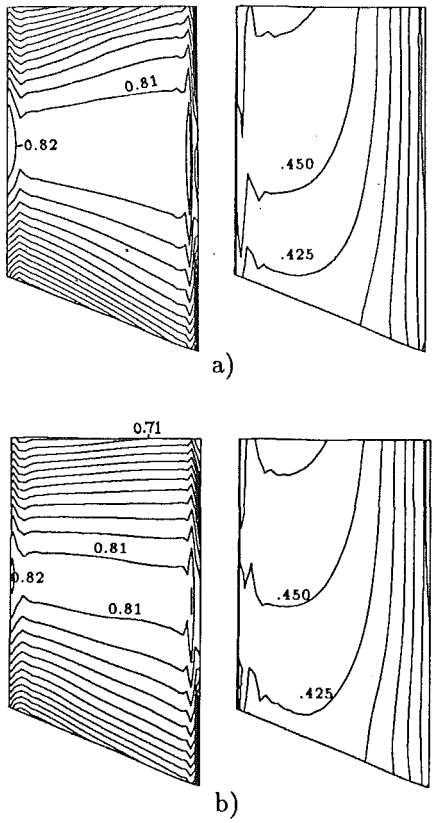

Fig. 16 Rotor-relative stagnation temperature contours ($T_t/\gamma T_{tinl}$) and static pressure contours (p/p_{tinl}) on the pressure side: (*a*) steady-state, (*b*) time-averaged

tor/rotor interaction avoids these numerical reflections, and thus allows for a fair comparison between steady-state and time-averaged solutions.

Steady-state and time-averaged periodic unsteady rotor-relative stagnation temperature contours are compared in Fig. 15 for the suction side. Clearly the pattern is the same, with a slightly stronger secondary flow in the time-averaged solution. The local difference of one contour between the two solutions corresponds approximately to 6 percent of the (stator) inlet temperature variation (i.e., radial distortion). At midspan, the time-averaged surface temperature downstream of the leading edge on the suction side is higher than the time-averaged inlet temperature. This is not really predicted by the steady-state code. A similar conclusion was found by Takahashi and Ni (1990) for the migration of a hot spot in a subsonic turbine stage. Also shown on Fig. 15 are the corresponding static pressure distributions. Except for some minor differences at the root near the weak shock, the agreement is excellent. On the rotor pressure side, see Fig. 16, the differences are larger with steady-state temperature contours showing a stronger radial flow in the tip region. For instance, at the tip near the trailing edge, the steady-state heating reaches 9 percent of the inlet stagnation temperature reference taken at the hub, which corresponds to 42 percent of the inlet distortion. On the other hand, the time-averaged tip heating corresponds only to 2.5 percent of $T_{tinl,hub}$, i.e., 12 percent of the inlet radial temperature variation. This means that compared to the time-averaged solution, the steady-state result locally overpredicts the temperature migration by about one third of the inlet distortion. However, the static pressure contours plots of Fig. 16 show a nearly perfect agreement for this quantity on the pressure side. Hence the steady-state code is adequate for blade loading information, a conclusion similar to the one found by Takahashi and Ni. The close agreement between the steady-state and the time-averaged flow solutions is a consequence of the similar distributions of rotor-relative inlet stagnation enthalpy (a local difference less than 0.5 percent of the stator inlet distortion) and flow angles (less than 1.5 deg). Moreover, the difference in rotary stagnation pressure between the steady-state solution and the time-averaged result, which could explain a different secondary flow behavior, is less than 2 percent of the rotor inlet dynamic head.

Finally, the steady-state rotor-relative stagnation temperature contours on the pressure side are compared in Fig. 17 with Pappas's results (Pappas, 1990) using Denton's inviscid solver. Although some differences exist in the definition of the blading (discussed by Saxer, 1992), the agreement is good.

5 Summary and Conclusions

This study has demonstrated the importance of three-dimensional inviscid periodic unsteady flow in a generic transonic axial turbine. A periodic stator/rotor shock wave interaction has been described for uniform vane inlet conditions. The unsteady static pressure envelope can exceed the level of the time-averaged local value. This leads to three-dimensional shock-induced unsteady secondary flow, not present in the steady-state solution. Although the computed level of unsteadiness is higher at the hub and at the tip compared to midspan, the behavior in time of the stator/rotor shock wave interaction is similar in nature across the span. The integrated blade surface pressure coefficient fluctuates as much as 2/3 of the time-averaged value. This is 60 percent larger than in the two-dimensional case.

The steady-state solution agrees extremely well with the time-averaged result (especially for the static pressure distribution),

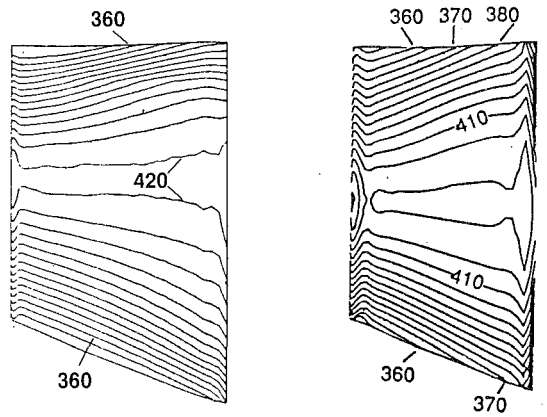

Fig. 17 Rotor-relative stagnation temperature contours on the pressure side with $(T_{t\text{mid}}/T_{t\text{hub}})_{\text{inl}} = 1.30$

which is a surprising result considering the fact that for the cases examined here the unsteady fluctuations can be one order of magnitude larger than the ones occurring in standard designed subsonic axial flow turbines. It is believed that such good agreement between the two solutions is greatly due to the use of the nonreflecting boundary conditions in the steady-state calculation of the stator/rotor interaction. By avoiding spurious reflections and by providing a relieving effect for the flow to account for the presence of the leading and the trailing edge of neighboring blades, these steady-state conditions represent, to a good approximation, the time-averaged physical phenomena. However, in terms of the blade stagnation temperature distribution, while the steady-state solution retains the same trend as the time-averaged flow field, differences appear in the local values. This has been examined in the second flow case by looking at the rotor-relative secondary flow caused by the introduction of a spanwise temperature distortion at the stator inlet (21 percent over-temperature at midspan compared to the endwalls, with a parabolic variation). The time-averaged rotor surface temperature radial migration on the pressure side of the blade near the tip is reduced compared to the steady-state solution. This may be due to the essentially two-dimensional pattern of the shock interaction mentioned in the first case. The unsteady temperature field is very different from the steady-state solution. Unsteady hot spots of elliptical shape, whose strength corresponds to half of the inlet temperature distortion, are periodically created behind the passing shock waves on both the blade suction and pressure sides. The magnitude of the local unsteady rotor-relative stagnation temperature envelope reaches the level of the stator inlet distortion. This is larger than the time-averaged rotor inlet distortion.

Acknowledgments

This work has been partially funded through a research grant from Rolls-Royce PLC, Dr. P. Stow technical supervisor. Additional funding was provided by the Air Force Office of Scientific Research, Major D. Fant technical monitor.

References

Adamczyk, J. J., 1985, "Model Equation for Simulating Flows in Multistage Turbomachinery," ASME Paper No. 85-GT-226.

AGARD Working Group 12, 1981, "Through Flow Calculations in Axial Turbomachines," AGARD Rept. AR-175.

Butler, T. L., Sharma, O. P., Joslyn, H. D., and Dring, R. P., 1986, "Redistribution of an Inlet Temperature Distortion in an Axial Flow Turbine Stage," AIAA Paper No. 86-1468.

Collie, J. C., Moses, H. L., Schetz, J. A., and Gregory, B. A., 1993, "Recent Advances in Simulating Unsteady Flow Phenomena Brought About by Passage Shock Waves in a Linear Turbine Cascade," ASME JOURNAL OF TURBOMACHINERY, Vol. 115, pp. 687–698.

Doorly, D. J., and Oldfield, M. L. G., 1985, "Simulation of the Effects of Shock Wave Passing on a Turbine Rotor Blade," ASME *Journal of Engineering for Gas Turbines and Power*, Vol. 107, pp. 998–1006.

Dorney, D. J., Roger, L. D., Edwards, D. E., and Madavan, N. K., 1990, "Unsteady Analysis of Hot Streak Migration in a Turbine Stage," AIAA Paper No. 90-2354.

Giles, M. B., 1990a, "Stator/Rotor Interaction in a Transonic Turbine," *AIAA Journal of Propulsion and Power*, Vol. 6, No. 5.

Giles, M. B., 1990b, "Non-reflecting Boundary Conditions for Euler Equation Calculations," *AIAA Journal*, Vol. 28, No. 12, pp. 2050–2058.

Giles, M. B., 1992, "An Approach for Multi-stage Calculations Incorporating Unsteadiness," ASME Paper No. 92-GT-282.

Harasgama, S. P., 1990, "Combustor Exit Temperature Distortion Effects on Heat Transfer Aerodynamics Within a Rotating Turbine Blade Passage," ASME Paper 90-GT-174.

Hawthorne, W. R., 1974, "Secondary Vorticity in Stratified Compressible Fluids in Rotating Systems," Technical Rept. CUED/A-Turbo/TR 63, Cambridge University, United Kingdom.

Holmes, D. G., and Connell, S. D., 1989, "Solution of the 2-D Navier–Stokes Equations on Unstructured Adaptive Grids," AIAA Paper No. 89-1932-CP.

Horlock, J. H., and Lakshminarayana, B., 1973, "Secondary Flows: Theory, Experiment, and Application in Turbomachinery Aerodynamics," *Annual Review of Fluid Mechanics*, Vol. 5.

Johnson, A. B., Rigby, M. J., Oldfield, M. L. G., and Giles, M. B., 1990, "Nozzle Guide Vane Shock Wave Propagation and Bifurcation in a Transonic Turbine Rotor," ASME Paper No. 90-GT-310.

Johnson, M. W., 1978, "Secondary Flow in Rotating Bends," Technical Rept. CUED/A-Turbo/TR 92, Cambridge University, United Kingdom.

Krouthén, B., and Giles, M. B., 1988, "Numerical Investigation of Hot Streaks in Turbines," AIAA paper No. 88-3015.

Munk, M., and Prim, R. C., 1947, "On the Multiplicity of Steady Gas Flows Having the Same Streamline Pattern," *Proceedings of the National Academy of Sciences*, Vol. 33, pp. 137–141.

Ni, R.-H., 1981, "A Multiple Grid Scheme for Solving the Euler Equations," *AIAA Journal*, Vol. 20, No. 11, pp. 1565–1571.

Ni, R.-H., and Sharma, O. P., 1990, "Using 3-D Euler Flow Simulations to Assess Effects of Periodic Unsteady Flow Through Turbines," AIAA Paper No. 90-2357.

Pappas, G., 1990, "Influence of Inlet Radial Temperature Distribution on Turbine Rotor Heat Transfer," M.S. Thesis, Massachusetts Institute of Technology, Cambridge, MA, Aug.

Saxer, A. P., and Giles, M. B., 1990, "Inlet Radial Temperature Redistribution in a Transonic Turbine Stage," AIAA Paper No. 90-1543.

Saxer, A. P., 1992, "A Numerical Analysis of 3-D Inviscid Stator/Rotor Interactions Using Non-reflecting Boundary Conditions," Ph.D. Thesis, Massachusetts Institute of Technology, Cambridge, MA, June.

Saxer, A. P., and Giles, M. B., 1993, "Quasi-Three-Dimensional Nonreflecting Boundary Conditions for Euler Equations Calculations," *AIAA Journal of Propulsion and Power*, Vol. 9, No. 2, pp. 263–271.

Takahashi, R. K., and Ni, R.-H., 1990, "Unsteady Euler Analysis of the Redistribution of an Inlet Temperature Distortion in a Turbine," AIAA Paper No. 90-2262.

Turner, M. G., 1991, "Design and Analysis of Internal Flowfields Using a Two Stream Function Formulation," Ph.D. Thesis, Massachusetts Institute of Technology, MA, Jan.

Discrete-Jet Film Cooling: A Comparison of Computational Results With Experiments

J. H. Leylek[1]

R. D. Zerkle

General Electric Company—Aircraft Engines,
Mail Drop A-331; P. O. Box 156301,
One Neumann Way,
Cincinnati, OH 45215-6301

Large-scale computational analyses have been conducted and results compared with experiments to understand coolant jet and crossflow interaction in discrete-jet film cooling. Detailed three-dimensional elliptic Navier–Stokes solutions, with high-order turbuence modeling, are presented for film cooling using a new model enabling simultaneous solution of fully coupled flow in plenum, film-hole, and cross-stream regions. Computations are carried out for the following range of film cooling parameters typically found in gas turbine airfoil applications: single row of jets with a film-hole length-to-diameter ratio of 1.75 and 3.5; blowing ratio from 0.5 up to 2; coolant-to-crossflow density ratio of 2; streamwise injection angle of 35 deg; and pitch-to-diameter ratio of 3. Comparison of computational solutions with experimental data give good agreement. Moreover, the current results complement experiments and support previous interpretations of measured data and flow visualization. The results also explain important aspects of film cooling, such as the development of complex flow within the film-hole in addition to the well-known counterrotating vortex structure in the cross-stream.

1.0 Introduction

Modern aircraft gas turbine hot section components operate in extremely harsh environments where ambient temperatures routinely exceed the melting point of available alloys. Reliable operation and prolonged useful life of components require controlling both temperature level and gradient. Discrete-jet film cooling, often used in conjunction with internal convective cooling, is a popular method available to designers of such components. Although there are many configurations of film cooling, one common feature is the highly complex nature of the flowfield created by a coolant jet interacting with a hot cross-stream.

Current flowpath heat transfer design practice is mostly empirical in nature and relies heavily on a large experimental data base. However, it is inconceivable to have a large enough data base for all possible combinations of geometric and flow parameters. Yet, recent design trends toward even higher cycle pressure and temperature with drastically reduced coolant supply have rapidly moved present day designs away from existing data bases. In addition, design cycle time is being compressed in order to beat the competition to the market. Thus, there is an urgent need to reduce the level of empiricism in heat transfer design practice and to develop a truly predictive capability for film cooling.

There have been significant advances in all facets of computational fluid dynamics methods for complex fluid flow problems in the last two decades. Concurrently, storage capacity and computation speed of computers have increased by many orders of magnitude with accompanying decreases in the cost of computation. Proliferation of supercomputers has made these machines readily available for many. In light of these advances, a real predictive capability for film cooling heat transfer is now feasible.

2.0 Literature Review

For the purpose of the following discussion, the large body of film cooling papers in the open literature is divided into the broad categories of experiment and computation. Experimental works, in turn, are split into two groups. The first group includes studies that generate "surface" measurement data for use in design activities. These data are presented most commonly in the form of adiabatic film cooling effectiveness (η). Other studies that support computational model development activities and provide detailed "field" measurements are discussed in the second group. Computational works are also split into two groups. Two-dimensional boundary layer models, relatively simple and fast-running codes that provide circumferentially averaged results when calibrated against a suitable data base, are presented in one group. The final group includes three-dimensional Navier–Stokes models, which generate detailed results and have the greatest potential for true predictive capability.

2.1 Experimental Studies

2.1.1 Surface Measurements. There are an abundance of surface measurement data in the open literature for design use

[1] Present address: Department of Mechanical Engineering, Clemson University, Clemson, SC 29634-0921.

Contributed by the International Gas Turbine Institute and presented at the 38th International Gas Turbine and Aeroengine Congress and Exposition, Cincinnati, Ohio, May 24–27, 1993. Manuscript received at ASME Headquarters March 3, 1993. Paper No. 93-GT-207. Associate Technical Editor: H. Lukas.

especially for slot, transpiration, and single hole injection configurations. Most of these and the early single row of discrete-jet experiments were conducted with coolant jet-to-crossflow density ratio (DR) close to unity. High-DR cases are more relevant for gas turbine applications and such studies have been carried out at many institutions. A short list of representative investigations in this category includes the works of: (*i*) Petersen et al. (1977), (*ii*) Foster and Lampard (1980), and (*iii*) Forth and Jones (1988). Although these and other studies have covered a wide range of density and blowing ratios, one feature they all had in common was their use of large film-hole length-to-diameter ratio (L/D ranging from about 10 to 40), configurations atypical of gas turbine airfoils.

Sinha et al. (1991) reported adiabatic effectiveness for a large number of density ratio (DR = 1.2, 1.6, and 2) and blowing ratio (M = 0.25 to 1.0) combinations for a single row of 35 deg holes with PD of 3. A unique feature of this study is its use of short film holes resulting in a small film-hole length-to-diameter ratio of L/D = 1.75. The configuration used in these experiments was replicated exactly in one of the two computational models reported in the present study.

2.1.2. Field Measurements. The number of studies available in the open literature on field measurements is far less then those for surface data. The instrumentation used to survey the field is critically important in these types of measurement and they were found to range from pitot probes in early studies, to single, X-sensor, and triple-sensor hot-wire anemometry, and finally to three-beam laser-Doppler velocimetry (LDV) used in the latest publications. A brief review of the most significant papers for our purposes is provided next.

Crabb et al. (1981) studied the hydrodynamics of a normal jet interacting with a crossflow using an X-sensor hot-wire probe in the far field and LDV in the near field. In these tests the density ratio was kept at unity with a blowing ratio of 1.15 and 2.3. Results indicate a highly distorted velocity profile at the jet exit plane. The jet supply pipe was long, as commonly found in almost all early studies, with L/D = 30.

The present authors benefited greatly from a series of papers published by a group headed by Prof. Rodi at the University of Karlsruhe in Germany. Andreopoulos and Rodi (1984) documented what was then the most detailed study of the turbulence field for a normal jet in a crossflow. Density ratio was kept at unity and blowing ratio at 0.5. The measurements clearly showed the presence of a massive blockage occupying the upstream portion of the jet exit area. The jet was forced to leave mostly from the downstream half of the exit plane. Consequently, the velocity profile taken at the centerline of the jet exit plane was highly skewed with its maximum point shifted downstream from the center. Disturbances created by the interaction of jet and crossflow were found to penetrate into the supply pipe and influence the flow upstream of the exit plane. This configuration, too, had a long supply pipe with L/D = 12.

A row of inclined jets at a number of injection angle, density ratio, and blowing ratio parameter combinations were studied by Kadotani and Goldstein (1979), Yoshida and Goldstein (1984), Le Brocq et al. (1973), Launder and York (1974), Foster and Lampard (1980), and others. Again, a common feature of all these studies was their use of long coolant supply tubes with L/D ranging from about 11 to 62.

Studies conducted by the University of Texas group represent to our knowledge the most comprehensive survey of inclined jets-in-crossflow. Pietrzyk et al. (1989) documented jets with density ratio of unity and in a companion paper the same authors (1990) published results for density ratio of 2. Both studies were done on the same film configuration with a single row of jets inclined at 35 deg and spaced 3 diameters in the lateral direction The blowing ratios were 0.25, 0.5, and 1 in the first paper and 0.5 in the second. Aside from a cryogenically cooled jet, this particular facility is set apart from all others because of its ability to accommodate models with a small film-hole length-to-diameter ratio of 3.5. The low L/D makes this study very relevant to gas turbine airfoil applications. Detailed measurements were reported of the distributions of streamwise and normal components of the mean and fluctuating velocity along with the dominant Reynolds stress from one diameter upstream to 30 diameters downstream of the hole. A two-axis, five-beam laser-Doppler velocimetry system enabled simultaneous measurements of all three velocity components for accurate turbulence data. Two observations were made that are most interesting and unique in the open literature. First, as the blowing ratio varied from 0.25 to 1.0, the location of the maximum in the centerline velocity profile at jet exit shifted from downstream to upstream of the center. Second, at increased blowing ratio a high level of turbulence was measured in the downstream half of the jet exit plane. The authors explained these two observations by hypothesizing the presence of a possible separation region within the film hole. One of the two three-dimensional Navier–Stokes models presented in the present study is a detailed replica of the configuration described in these papers.

2.2 Computational Studies

2.2.1 Two-Dimensional Layer Models. A number of two-dimensional boundary layer type computer programs that predict laterally averaged behavior of film cooling are described in the literature by Crawford et al. (1980), Tafti and Yavuzkurt (1990), Norton et al. (1990), and Haas et al. (1992). These codes are intended for parametric runs in preliminary design-type settings. By nature they are relatively simple, fast-running, and very economical. A suitable data base, either experimental or computational, is needed in order to calibrate these models.

Nomenclature

D = diameter of coolant jet injection hole
DR = density ratio = ρ_j/ρ_∞
I = momentum flux ratio = $(\rho V^2)_j/(\rho V^2)_\infty = DR(VR)^2$
k = turbulent kinetic energy
L = length of film-hole
L/D = length-to-diameter ratio of film-hole
M = blowing (or mass flux) ratio = $(\rho V)_j/(\rho V)_\infty$
PD = pitch-to-diameter ratio of adjacent jets
T = local temperature
T_{aw} = adiabatic wall temperature
T_∞ = mainstream temperature
T_j = coolant jet temperature
TL = turbulence intensity level
u, v, w = lateral, vertical, and streamwise components of velocity vector
V = magnitude of velocity vector
VR = velocity ratio = V_j/V_∞
x, y, z = lateral, vertical, and streamwise directions in Cartesian coordinates
α = injection angle of coolant jet
ϵ = dissipation rate of turbulent kinetic energy
η = adiabatic film effectiveness = $(T_{aw} - T_\infty)/(T_j - T_\infty)$

Subscripts

aw = conditions at adiabatic wall
j = conditions at exit plane of film-hole
p = conditions in coolant supply plenum
∞ = mainstream conditions at crossflow inlet plane

It is then hoped that the calibrated model will not only reproduce the entire data base faithfully but, in fact, successfuly interpolate to fill in the gaps in the data base and perhaps even extrapolate beyond it. Clearly, two-dimensional boundary layer models cannot predict film cooling in a totally new configuration or an existing geometry placed in a substantially different flow regime.

2.2.2 Three-Dimensional Navier–Stokes Models. There are a limited number of entries in the open literature on Three-Dimensional Navier–Stokes models to predict film cooling. As stated above, these models have the greatest potential to reduce the level of empiricism and provide a true predictive capability in design tools. However, along with the increased level of sophistication comes an order of magnitude increase in the required computational resources.

The original "fully parabolic" scheme applied to jet-boundary-layer interaction region by Tatchell (1975) resulted in physically unrealistic solutions, thus providing an early indication of strong deviation from boundary-layer-like flows.

Bergeles et al. (1978) documented a "semi-elliptic" (or "partially parabolic") scheme used in conjunction with an anisotropic turbulence model for an isolated jet injected into a crossflow at 90 and 30 deg. Their results indicated reasonably good agreement with measurements as long as blowing ratio remained extremely low. For example, for the case with a 90 deg injection angle, it proved to be impossible to obtain fully converged solution at blowing ratio of 0.2. Similarly, the results deteriorated rapidly beyond $M = 0.5$ in 30 deg jet simulations. These authors discovered that the relative insensitivity of the results to the details of the injectant profiles at the exit plane did not apply at higher M when the jet was on the verge of lift-off. The predicted flow character just downstream of the jet was poor even after altering the jet exit plane treatment, thus leading to a conclusion that "evidently there were more important factors involved." In closing, the authors indicated that this situation could perhaps be remedied by extending the numerical computations some distance into the injection hole itself.

A total of 27 test cases were computed for a single row of holes by Demuren et al. (1986) using the "locally elliptic" procedure of Rodi and Srivatsa (1980). In this model, the fully elliptic treatment was applied only to a small region containing flow reversal; however, in the near and far fields the model reverted to partially parabolic and fully parabolic schemes, respectively. Also included in the model was the extension of Bergeles et al. (1978) to account for anisotropic eddy viscosity and diffusivity. The authors acknowledged the significant influence of the crossflow on the jet exit profiles. However, indicating a lack of sufficient experimental information, they assumed uniform velocity at the jet exit plane.

White (1980) presented a fully elliptic treatment for an isolated normal jet injected into a crossflow. The novel feature of this model was its use of separately computed flowfields in the pipe and cross-stream regions, which were linked via constant total pressure assumption across the jet exit plane. Comparison of jet exit profiles with measurements showed good agreement; however, the method was found in that study of be restricted to normal jets supplied from tubes with large length-to-diameter ratios. An encouraging observation from that study and another one by Patankar et al. (1977) for a dilution jet involves the ability of a fully elliptic scheme to handle strong jets that are far beyond lift-off.

2.2.3 Remarks. The three-dimensional models cited above suffer from a number of serious deficiencies. For example, the flow simulations are confined to the crossflow region only. This region is represented using a simple Cartesian grid where the jet exit geometry, typically round or elliptic depending upon jet injection angle, is approximated as an "equivalent area" in a stair-step manner. More critically, various assumptions used to obtain boundary conditions at the jet exit plane in the form of exit profiles are, at best, poor approximations for those cases with large length-to-diameter ratios. They would be even worse when L/D is small. According to measurements made in recent experiments by Pietrzyk (1989), the use of such profiles in configurations more representative of gas turbine airfoil applications cannot be justified.

3.0 The Present Contribution

There were two primary objectives of this work. The first was to develop a three-dimensional Navier–Stokes model to predict film cooling in configurations relevant to gas turbine airfoils. The second was to compare the results from these predictions to experiments in order to explain measured data and flow visualization observations. The notable features of the present study, which have not been considered in any previous investigation, are:

(*a*) Fully coupled and elliptic computation of flow in plenum, film-hole, and cross-stream regions of a film cooling situation.
(*b*) Detailed description of the complex nature of flow within a small length-to-diameter ratio film-hole and mechanisms responsible for unusual profiles at the jet exit plane.
(*c*) Exact representation of an inclined, round film-hole geometry using a highly orthogonalized grid mesh obtained from a state-of-the-art solid modeler integrated with a generalized, nonorthogonal curvilinear coordinate system grid generator.
(*d*) Description of a computational strategy to obtain fully converged results for blowing ratios as high as 2.0 in a multizone film cooling domain.

4.0 Technical Approach

The overall approach used to achieve the above objectives is as follows: (*i*) The computational effort made full use of data obtained in a test program set up at the University of Texas at Austin by Profs. Bogard and Crawford and their students to conduct fundamental studies of jets-in-crossflow in large-scale film cooling configurations relevant to gas turbine airfoils. (*ii*) A three-dimensional, elliptic Navier–Stokes model was developed to compute the flowfield in a single row film cooling situation in a fully coupled manner. Two relatively fine computational grid meshes were generated on two different film cooling geometries which resulted in large-scale simulations of film cooling flowfields for a single density and a number of blowing ratios. (*iii*) The results were used to understand important aspects of flow in film cooling.

5.0 Three-Dimensional Navier–Stokes System

The Navier–Stokes system used to obtain the computational results presented in this paper is described briefly. This system was created by modifying, extending, and then integrating together a number of readily available, suitable codes into a computational film cooling prediction tool for use in gas turbine applications. It is comprised of the following major modules: geometry generator, grid generator, preprocessor, CRAY JCL generator, solver, and postprocessor. The geometry and grid generator modules represent a breakthrough in our ability to capture a complex film cooling configuration and generate a high-quality computational grid. This capability is critically important because the quality of a computational solution is strongly linked to the quality of the grid mesh.

5.1 Computational Elements. A state-of-the-art solid modeler, I-DEAS, available commercially from Structural Dynamics Research Corporation (SDRC), was integrated into the

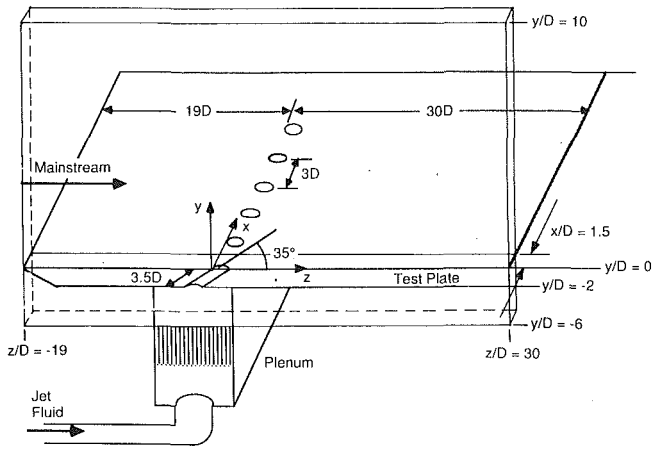

Fig. 1 Essential features of experimental film cooling configuration showing overall extent of computation domain and coordinate system

computational system as a geometry generator. This approach was selected because it appears to be most promising especially in film cooling applications employing shaped holes on gas turbine airfoils.

The grid generator creates a grid mesh within each subvolume of the entire computation domain passed to it by the geometry modeler. All subvolumes are then combined and grid nodes renumbered so as to form a single consistent cluster for a structured grid solver.

The preprocessor, solver, and postprocessor modules employed in the present system were essentially the PHOENICS system of codes described by Ludwig et al. (1989) with suitable modifications and a JCL generator to run it on a CRAY Y/MP supercomputer. The solver is based on a finite-volume discretization scheme and uses a staggered grid as described by Patankar (1980).

Turbulence closure is attained by the use of the standard k–ϵ model employing the generalized wall function treatment described by Launder and Spalding (1974). It is important to note that absolutely no special handling, tuning, or adjustment of any kind was made to the turbulence model, or any other part of the code, to "match" experimental data in the present study. Our intent is to determine how well the standard k–ϵ model can perform in an elliptic, fully coupled simulation of film cooling jets and to remedy its shortcomings in future studies.

5.2 Validation of Computational System. The three-dimensional Navier–Stokes system has undergone extensive in-house testing by applying it to relatively simple two-dimensional to more demanding three-dimensional problems for which code validation quality data exist. The battery of validation test cases includes the following: (*i*) heat transfer on smooth surfaces, (*ii*) flow over a backward-facing step, (*iii*) two-dimensional normal slot-jet injection, and (*iv*) three-dimensional channel flow heat transfer. Overall, the results obtained in these test cases were found to be satisfactory.

6.0 Experimental Test Facility

A complete description of the experimental facility, including the test section, cryogenic cooling system, and instrumentation used, is given by Pietrzyk (1989). The facility was used to make detailed measurements of mean and turbulence characteristics of jets-in-crossflow along with adiabatic film cooling effectiveness for injection from a single row of 35 deg holes, laterally spaced 3 diameters apart, on a flat test surface as shown in Fig. 1. The row of holes are placed 19 diameters downstream of the leading edge of the test plate and data are obtained from 1 diameter upstream to 30 diameters downstream of the holes.

Two separate series of tests were run. In one of the series, Pietrzyk et al. (1989, 1990) documented the hydrodynamics of jet/crossflow interaction using a test plate with a hole length-to-diameter ratio of 3.5. In these tests density ratio was set at either 1 or 2, and blowing ratio varied from 0.25 to 1. In the other series, Sinha et al. (1991) acquired adiabatic effectiveness data on a test plate with L/D of 1.75 where density and blowing ratios were varied from 1.2 to 2 and from 0.25 to 1, respectively.

The boundary layer growing on the bottom surface of the wind tunnel was sucked out and a uniform starting velocity profile created at the leading edge of the test plate. Measured data indicate that a turbulent boundary layer commenced immediately downstream of the test plate leading edge, due perhaps to the presence of a small separation bubble there (Crawford, 1992). This is believed to be the main reason for the excellent agreement between the predicted and measured boundary layer thickness at 1 diameter upstream of the film holes.

7.0 Details of Computational Model

Details of the computational model, corresponding to its experimental counterpart described above, are presented here. All dimensions are measured in a Cartesian coordinate system with its origin placed at the upstream edge of the film hole on the top surface of the test plate and its x, y, and z axes aligned with the lateral, vertical, and streamwise directions as seen in Fig. 1.

7.1 Geometry. Two exact replica solid models of the test facility including the plenum, film-hole, and cross-stream regions were constructed using I-DEAS. The only difference between the two models was the film-hole length-to-diameter ratio L/D. The first model had an L/D of 3.5 and the second 1.75, just as in the experiments. Details of the plenum construction not found in Pietrzyk (1989) were obtained from Crawford (1991) and incorporated into these models. Also, edges of the film hole at the top and bottom surfaces of the test plate were made sharp as indicated in the description of the experimental test facility. As shown in Fig. 1, overall extent of the computational domain in the lateral, vertical, and streamwise directions was $1.5D$, $16D$, and $49D$, respectively.

7.2 Grid Mesh. A highly orthogonalized, nonuniform, single-block fine grid mesh was generated with grid nodes clustered in the immediate vicinity of the discrete film cooling jet. A total of 200,090 grid nodes were used with 22 nodes in the lateral, 85 nodes in the vertical, and 107 nodes in the streamwise directions. The most difficult to grid and yet the most critical portion of the entire mesh is the region within the film hole itself. A highly enlarged view of the grid mesh in this region on the hole centerline plane is shown in Fig. 2(*a*). The film hole was divided into four subvolumes stacked in the vertical direction in such a way that the center two volumes naturally contained an orthogonal grid as seen in this figure. Grid nodes in the other two subvolumes at the inlet and exit regions of the film hole were individually orthogonalized with the use of surface and volume optimizers. Figure 2(*b*) shows the top view of the orthogonalized grid at the exit plane of the round film-hole with a semi-elliptic break-out. The semi-elliptic cross section was transformed into a purely orthogonal rectangle within a short distance above and below the test plate.

Other important grid parameters were conservatively set and tightly controlled. For example, the stretching ratio used in all three directions in the whole domain was kept well within 20 percent. Similarly, the grid aspect ratio, especially near the coolant jet, was kept well under 10. Finally, proximity of nodes near metal surfaces was carefully adjusted so that average $y+$ was about 30 inside the plenum, ranged from 30 to 100 within the film hole, and 50 in the crossflow as M varied from 0.5 to 2.

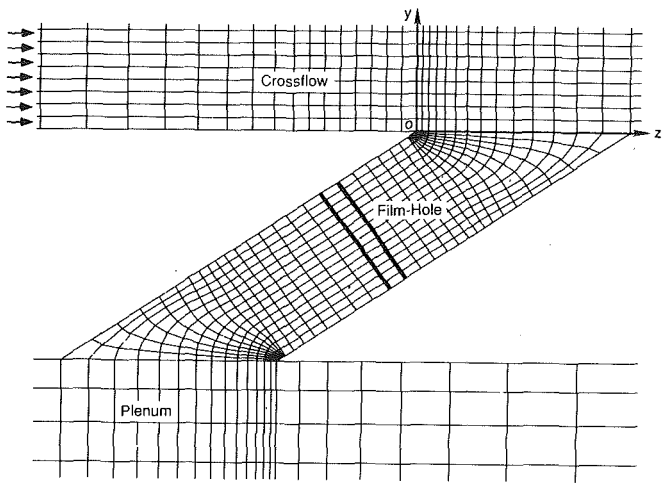

(a) Within Film-Hole

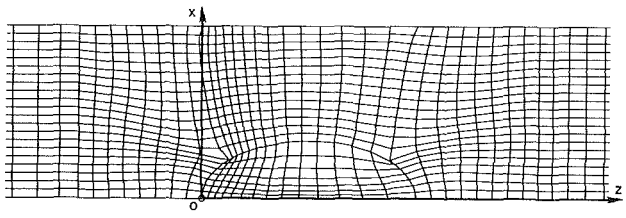

(b) Jet Exit Plane

Fig. 2 Computational grid for three-dimensional discrete jet film cooling: 200,090 total grid nodes with 22 lateral, 85 vertical, and 107 streamwise nodes

7.3 Boundary Conditions. Boundary conditions are prescribed at all six boundary surfaces of the computation domain by imposing exactly the measurements made in experiments. Mainstream conditions were kept the same in all cases and the coolant flow rate was altered to change the blowing ratio in a way fully consistent with the procedure described by Pietrzyk (1989). In the lateral (x) direction, both bounding surfaces are symmetry planes; therefore, the x-direction component (u) of the velocity vector and normal gradients of all other dependent variables are prescribed as zero.

In the vertical (y) direction, at the bottom surface, which sits on the flow straighteners, coolant mass flux, enthalpy, and the y-direction component (v) of the velocity are fixed to produce the desired blowing ratio at the known plenum temperature (T_p) of 153 K. The remaining two components of velocity were set to zero. Similarly, assuming a condition of local equilibrium, a uniform distribution of k and epsilon was computed from velocity, turbulence intensity of 0.2 percent, and length scale equal to 1/10 of plenum width. All parameters affected by pressure were adjusted during the computation cycle as the correct plenum pressure emerged while iterations continued and the solution proceeded toward convergence. At the top surface, measured data indicate that a "slip-wall" type boundary condition should work properly due to sufficiently far placement of this surface from the test plate. Therefore, a slip condition was imposed by setting the v component of velocity and normal gradients of all other dependent variables to zero.

In the streamwise (z) direction, at the inlet plane, crossstream mass flux, uniform enthalpy, and z-direction component (w) of 20 m/s were specified to produce the desired mainstream Reynolds number at the measured crossflow temperature (T_∞) of 302 K. The remaining two components of the inlet velocity vector were set to zero. It was possible to prescribe a "plug-flow" velocity profile because the inlet plane was placed at the leading edge of the test plate where a new boundary layer was triggered. Also, a uniform inlet k and epsilon profiles were imposed following a procedure similar to that described for the boundary conditions at the plenum inlet plane except that turbulence length scale was 1/10 of computational passage height. At the exit plane, pressure level was specified along with zero streamwise gradient for all other dependent variables.

7.4 Initialization Strategy. Initialization of all the dependent variables in the entire field turned out to be a critical item especially at high M, in securing converged solutions in the fully elliptic and fully coupled computation of the complex film cooling situations presented in this paper. First, the three regions, namely, plenum, film-hole, and cross-stream, were separately initialized as accurately as possible for the lowest blowing ratio ($M = 0.5$) case. Next, the fully converged solution obtained from this run was used as the initial field for the next case with a slightly higher M, and so on. This strategy made it possible to successfully converge the computational solution for the highest blowing ratio ($M = 2$) attempted in this study.

7.5 Convergence. Starting from a suitable initial distribution for all field variables, iterations were continued until each transport equation satisfied a built-in convergence criterion. The computational solution was declared "fully converged" when the normalized residual of each governing equation was at or below 1 percent level. The normalized residual was computed by adding the absolute values of the residuals for all the finite volumes in the whole domain and dividing this sum by the total inlet flux (crossflow and plenum combined) of a relevant quantity for each equation (e.g., enthalpy flux for the energy equation).

8.0 Computed Three-Dimensional Flowfield

Simulation details and comparisons of computed flowfield with experiment are presented in this section. Unless otherwise noted, all results presented here, except for those for adiabatic effectiveness, are for the case with $L/D = 3.5$.

8.1 Details of Flow in Film Hole. The complex nature of flow within the film-hole itself is described in this subsection. This, to our knowledge, is the first time that any information, either experimental or computational, regarding the nature of flow in a film-hole with a small L/D is documented in the film cooling literature.

Computed velocity vectors on the centerline plane of the film-hole are presented in Figs. 3(a, b) for $M = 0.5$ and $M = 2.0$, respectively. Clearly, no part of this flow resembles a fully developed pipe flow as would be the case in a long coolant supply tube. Instead, a low-momentum region appears near the inlet and downstream wall of the film-hole at $M = 0.5$, Fig. 3(a). The coolant flow appears to be showing a slight jetting effect near the upstream wall. At the highest blowing ratio of $M = 2$, shown in Fig. 3(b) a strong jetting effect is seen near the upstream wall with the coolant hugging this surface as it rides over the low momentum region near the downstream wall.

A view of the velocity vectors on a plane perpendicular to the general direction of the throughflow in the film-hole reveals the exact nature of the coolant flow in this region, Figs. 4(a,b). The exact location of this plane within the film-hole is indicated by the two bold lines in Fig. 2(a). In this view, the crossflow direction above the jet exit plane is from left to right. Two counterrotating vortices are present in the film-hole at both blowing ratios with their cores close to the downstream wall of the coolant supply tube. The vortex strength is directly related to blowing ratio as it is much higher in the high M situation shown in Fig. 4(b) than the low M case seen in Fig. 4(a). The vortex structure seen here is due to the secondary flow created by a large change in the direction of the coolant flow as it enters the inclined supply tube from the plenum.

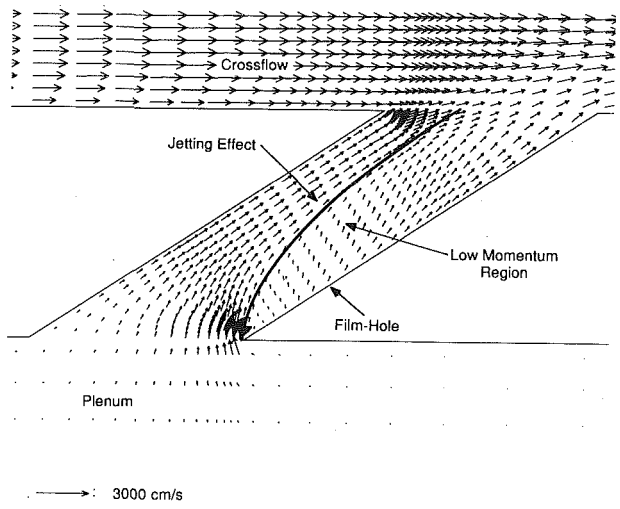

(a) $M = 0.5$, $DR = 2.0$

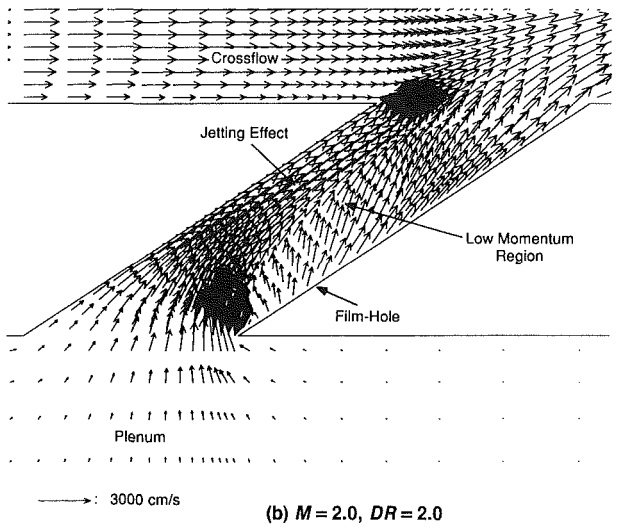

(b) $M = 2.0$, $DR = 2.0$

Fig. 3 Computed velocity vectors on centerline plane show complex nature of flow within film hole

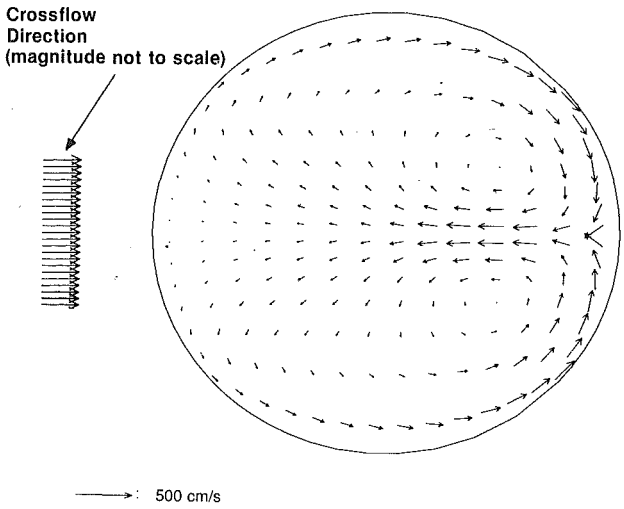

(a) $M = 0.5$, $DR = 2.0$

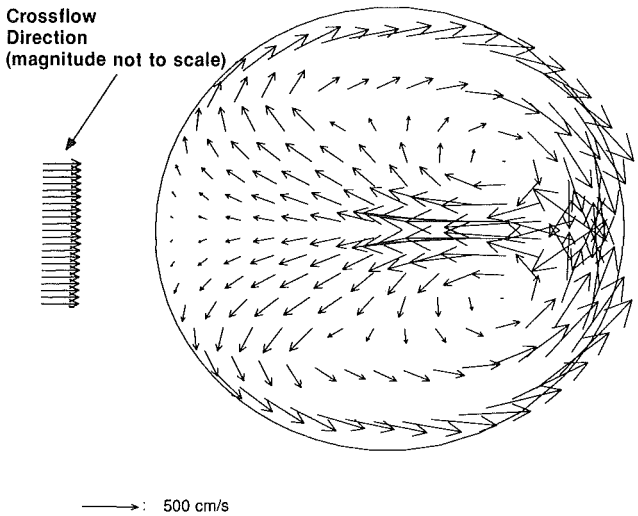

(b) $M = 2.0$, $DR = 2.0$

Fig. 4 Computed velocity vectors show counterrotating vortex structure within film-hole on a plane perpendicular to general flow direction and halfway between inlet and exit surfaces of the coolant jet

The same mechanism that induces secondary flow in curved tubes is responsible for the creation of vortices within the film-hole. The sense of rotation of the vortices is the same as a similar counterrotating vortex structure in the cross-stream to be discussed shortly. Flow visualization experiments conducted at the University of Texas confirm the existence of the counterrotating vortex structure shown here (Crawford, 1992).

The final observation, which is important for our discussion in Section 8.3.1 below, involves the production of turbulence inside the film-hole. Computational results indicate that as the blowing ratio increases, the coolant supply tube becomes the major source of turbulence. The centerline turbulent kinetic energy contours for $M = 2$ presented in Fig. 5 reveal that the location of the peak level is indeed within the film-hole. Previous results, presented in Figs. 3 and 4, are helpful in explaining this observation. As M increases, the counterrotating vortex strength increases and is accompanied by strong jetting of coolant over the vortices. The highest velocity gradients are found in the interface region between the jet and the vortex structure. It is precisely at this interface that high turbulence is generated.

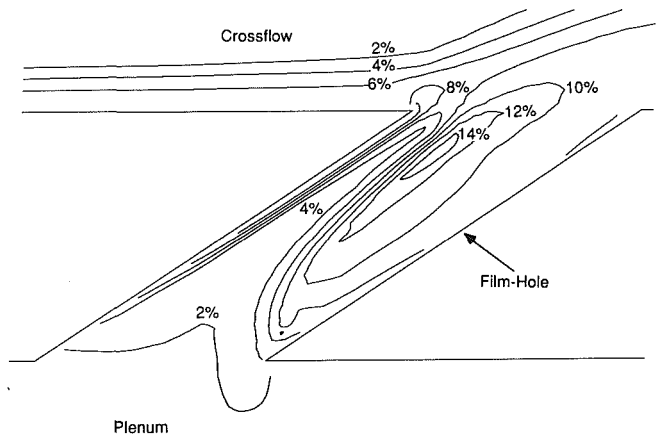

Fig. 5 Computed turbulence intensity contours on centerline plane show high levels of turbulence created in film-hole at $M = 2$, $DR = 2$

8.2 Details of Flow at Exit Plane of Coolant Jet. In this subsection we focus our attention on the distribution of dependent variables at the coolant jet exit plane because other numerical studies published in the open literature have concluded that downstream results are very sensitive to the profile assumptions made there.

High L/D. The previously accepted view of exit profiles of coolant jets was based on either film cooling or jets-in-

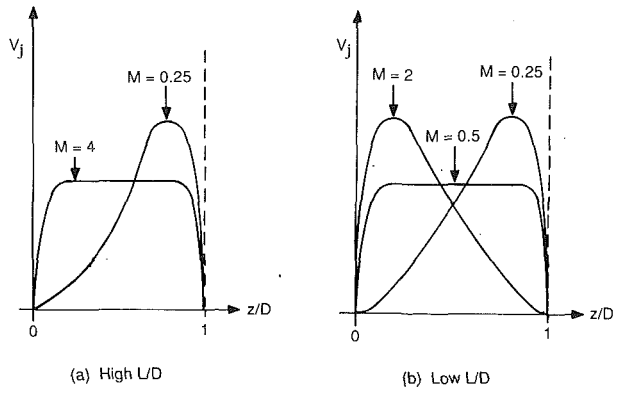

Fig. 6 Exit plane velocity profiles of film cooling jets at various blowing ratios

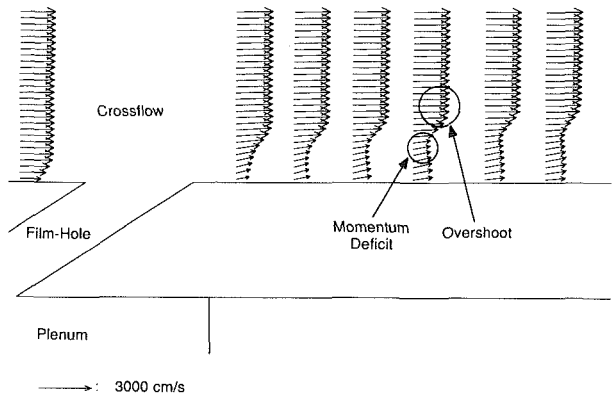

Fig. 7 Computed centerline velocity profiles near jet exit for $DR = 2$ and $M = 1$ show momentum deficit away from wall and slight overshoot above coolant jet

crossflow experiments conducted with unrealistically long supply tubes. Here, a single mechanism, namely the relative magnitudes of crossflow and coolant jet momentum, is thought to be the final arbiter of the profiles at the exit plane. According to this view, at low blowing ratios, say $M = 0.25$, the coolant jet exits mostly through the downstream half of the exit plane due to blockage caused by the crossflow carrying much higher momentum. The result is a skewed velocity profile with its peak shifted downstream of the center as depicted in Fig. 6(*a*). At much higher blowing ratios, say $M = 4$, the coolant jet exits as though the crossflow does not exist. This time, the exit velocity profile is very much like a fully developed turbulent pipe flow profile shown in Fig. 6(*a*). Of course, no variation is prescribed in the lateral direction.

This view, and hence the profiles resulting from it, when applied in a typical gas turbine film cooling configuration with a small L/D, may be highly misleading and is perhaps one of the prime causes of anomalous results (Jubran, 1989; Amer et al., 1992).

Low L/D. The current computational results point to three mechanisms competing to control the profiles of coolant jets at exit plane. These are: (*i*) relative magnitudes of crossflow and coolant jet momentum, (*ii*) strength of jetting effect near upstream wall of film-hole, and (*iii*) strength of counterrotating vortex structure. These mechanisms explain experimental measurements of Pietrzyk et al. (1989, 1990) and the current computational results at the exit plane are fully consistent with their data.

Velocity profiles measured by Pietrzyk (1989) along the centerline at the exit plane at $M = 0.25$ show some crossflow blockage induced skewness. However, unlike previous measurements, the blockage is not excessive because it is offset by a relatively weak jetting effect present even at such low M, Fig. 3(*a*). Experiments indicate a fully developed profile at a blowing ratio of only 0.5. This means that the crossflow blockage is fully offset by the presence of coolant jet at the upstream wall of the film-hole. At higher blowing ratio, such as presented in Fig. 3(*b*) for $M = 2$, the jetting effect overpowers the crossflow blockage and results in a velocity profile skewed upstream, Fig. 6(*b*). The role of the experimentally confirmed vortex structure is to create lateral variation and impart swirl to the coolant jet.

The same authors report data showing high turbulence levels spewing out of the exit plane at high blowing ratios. They hypothesized the existence of a separation bubble and a reattachment region within the film hole to explain their data (Pietrzyk et al., 1989). This too is explained by the present simulations as turbulent kinetic energy contours shown in Fig. 5 indicate the true source of turbulence (see discussion at the end of Section 8.1).

8.3 Details of Flowfield Within Cross-Stream. There are many consequences when a coolant jet interacts with a hot crossflow. In this subsection, it is our aim to document the details of this interaction and the resulting flowfield in the cross-stream using data from computations and experiments.

8.3.1. Crossflow Results on Centerline Plane. Computed velocity vectors on the hole centerline plane near the jet exit are presented in Fig. 7. These profiles are remarkably similar to those measured by Pietrzyk et al. (1989) and have two important features that are noteworthy. First, the profile at $z/D = 5$ indicates that the greatest streamwise momentum deficit is away from the test surface at about y/D of 0.5. Second, right above the momentum deficit zone there is a small region with a slight velocity overshoot created by the crossflow accelerating over the coolant jet.

One of the important indicators of the effectiveness of a film cooling jet is its trajectory. A low trajectory results in a high film effectiveness when a coolant jet is attached to the surface to be protected. A high trajectory, on the other hand, implies penetration of the jet into the crossflow and away from the injection surface, therefore, low film effectiveness. A scalar field, such as temperature, can be used as a tracer to determine the trajectory of a coolant jet.

Figures 8(*a,b*) show temperature contours for a jet with $DR = 2$ and $M = 0.5$ and 2, respectively, to demonstrate the effect of blowing ratio on jet trajectory. The coolant hugs the test surface at the low blowing ratio case presented in Fig. 8(*a*). A strong jet penetration, therefore, a high trajectory results as the blowing ratio increases to $M = 2$, as seen in Fig. 8(*b*).

Experiments also indicate that blowing ratio influences the source of turbulence in film cooling situations such as the one considered here (Pietrzyk, 1989). At low M, centerline turbulent kinetic energy contours in Fig 9(*a*) indicate that the shear layer between the crossflow and coolant jet is the main source of turbulence. This can be explained by noting that the difference in the streamwise momentum content of the jet and crossflow is highest at low M. At high M situations, Fig. 9(*b*), especially at small injection angles, this difference diminishes and the film-hole becomes the main source of turbulence for the reasons presented in Section 8.1.

8.3.2. Crossflow Results on Planes Normal to Cross-Stream. More details of the complex nature of flow structure in the cross-stream are revealed by results plotted on planes perpendicular to crossflow. All views in the series of plots presented in this section are aft-looking-forward.

Two of the most important features in the cross-stream, namely, the counterrotating vortex structure and kidney-shaped cross-section of coolant, are captured in Figs. 10(*a, b*) by superimposing velocity vectors on temperature contours on a

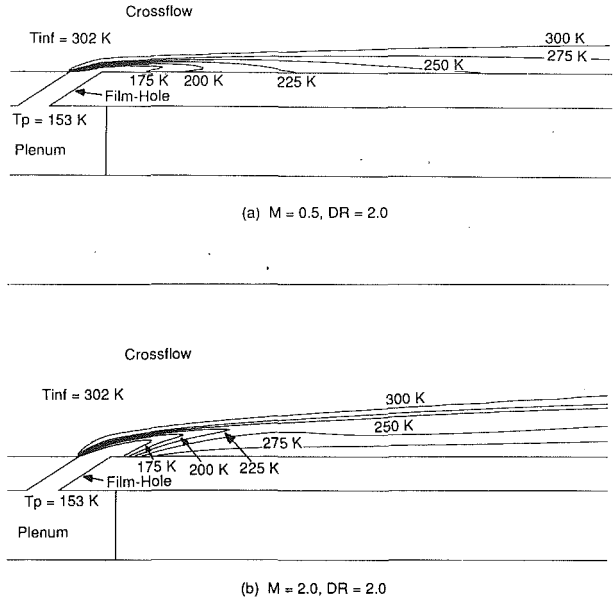

Fig. 8 Computed centerline temperature contours demonstrating effect of blowing ratio on trajectory of coolant jet

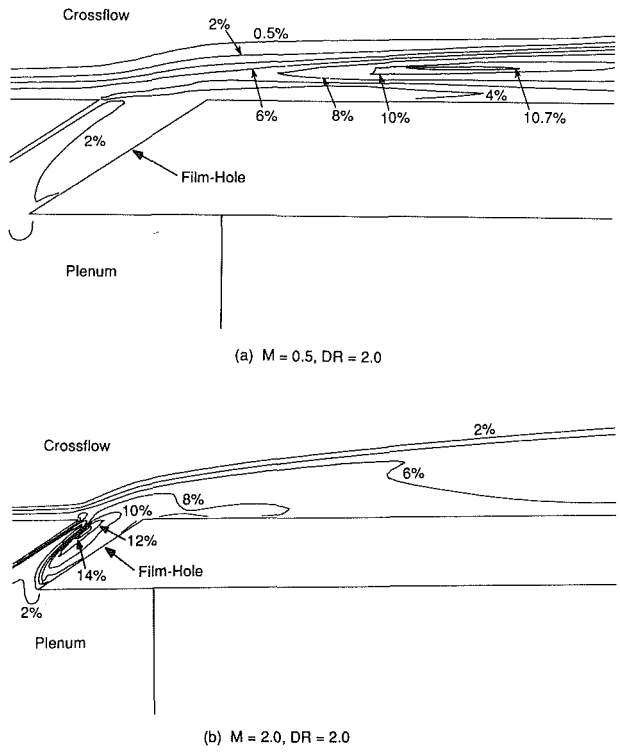

Fig. 9 Computed centerline turbulence intensity contours showing change in turbulence source with blowing ratio

plane located 5 diameters downstream of film-hole leading edge. Apparently, the strength of secondary flow is again directly related to blowing ratio as was the case within the film-hole. This is evidenced by the low magnitudes of secondary flow velocity vectors in Fig. 10(*a*) for $M=0.5$, and high ones in Fig. 10(*b*) for $M=2.0$. The vertical and lateral location of the core center in Fig. 10(*a*) agrees well with experimental data presented in Fig. 10(*c*) for the same case. The net aerodynamic effect of the vortices interacting in such close proximity is to bring the individual cores laterally closer together and to lift the entire coolant film vertically away from the surface at high M. Another action of the vortex motion is the very undesirable

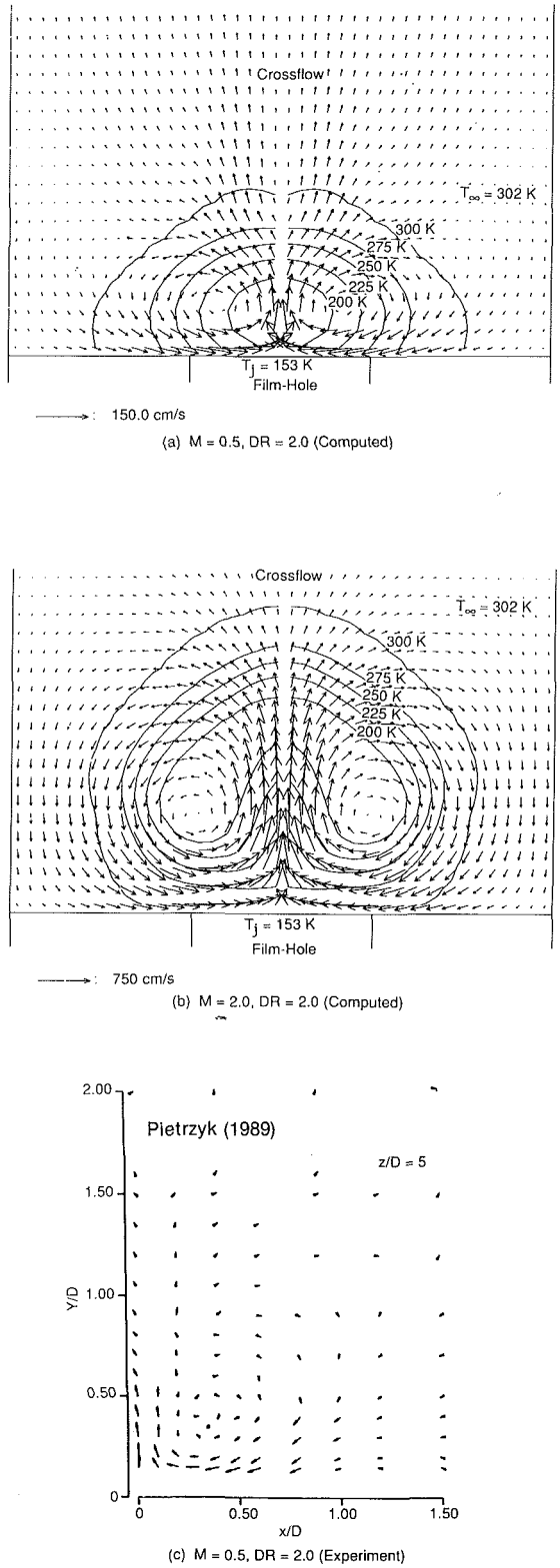

Fig. 10 Velocity vectors superimposed on temperature contours showing counterrotating vortices and kidney-shaped crosssection of coolant jet at $z/D=5$ (aft-looking-forward)

outcome that hot crossflow is forced down and under the film layer. A kidney-shaped cross-section of the coolant jet is the final consequence of all the interactions reported here.

An isometric view of temperature contours on many crossflow planes is presented in Figs. 11(*a*, *b*) for $M=0.5$ and $M=2.0$. These figures show clearly the differences in the tra-

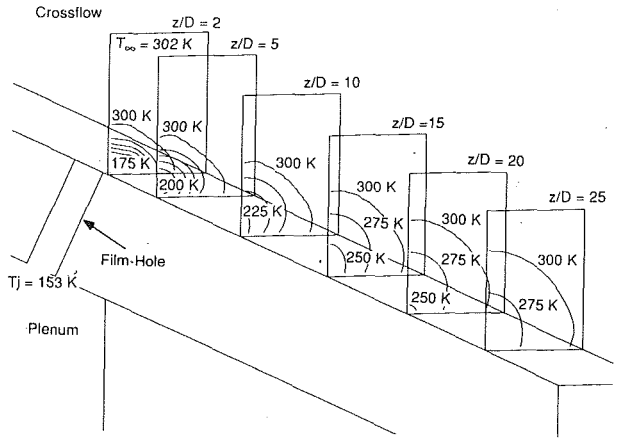

(a) M = 0.5, DR = 2.0

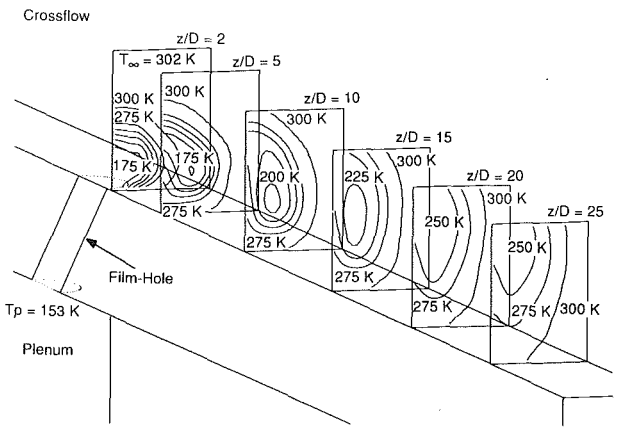

(b) M = 2.0, DR = 2.0

Fig. 11 Isometric view of computed temperature contours on many crossflow planes shows coolant jet trajectories and lateral diffusion

jectories of these two jets as they diffuse laterally and convect in the streamwise direction. It appears that computed jets do not seem to be diffusing as much as they should. This assessment is based on the observation that the limiting contours shown on the last plane at $z/D=25$ do not extend to the symmetry plane. However, contour plots of various parameters presented by Pietrzyk (1989) indicate merging of adjacent jets further upstream of this location. More on this later.

A similar isometric view of computed turbulence level contours for $M=0.5$ and $M=2.0$ is presented in Figs. 12(a, b) along with experimentally measured data for $M=0.5$ shown in Fig. 12(c). There is a striking similarity between the shapes of computed and measured contours for $M=0.5$ shown in Figs. 12(a) and 12(c). Furthermore, quantitative agreement is also quite good. As discussed in previous sections, the shear layer between crossflow and coolant jet is the main source of turbulence at $M=0.5$, but the film-hole becomes the dominant source of this quantity at $M=2$.

8.4 Adiabatic Film Cooling Effectiveness. In this section we document the streamwise and lateral variation of film cooling effectiveness for the case with $L/D=1.75$ because experimental data are available on this configuration only. Note also that all streamwise distances are measured from the trailing edge ($z/D=0$) of the film-hole at the exit plane.

Computed and measured distribution of η along the jet centerline for three blowing ratios (M = 0.5, 0.8, and 1.0) are presented in Figs. 13(a-c). Although the overall streamwise trend is correct, the predicted values are consistently high at $M=0.5$, Fig. 13(a). This situation is improved downstream of

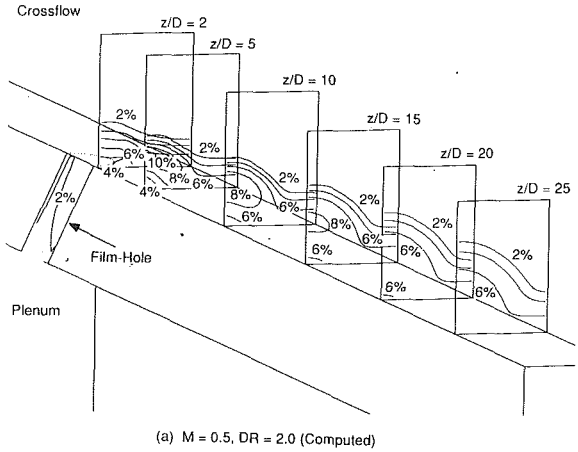

(a) M = 0.5, DR = 2.0 (Computed)

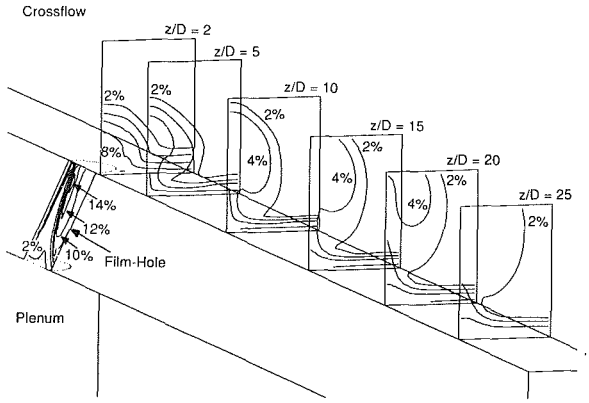

(b) M = 2.0, DR = 2.0 (Computed)

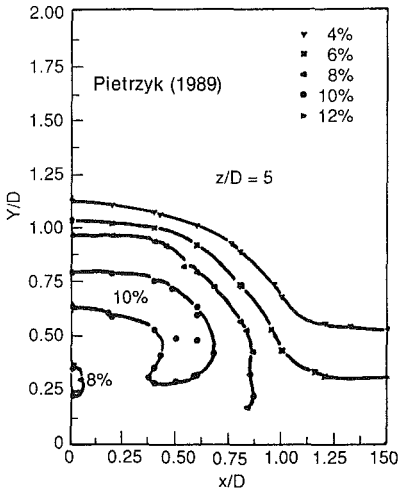

(c) M = 0.5, DR = 2.0 (Experiment)

Fig. 12 Isometric view of computed and measured turbulence intensity contours on crossflow planes shows remarkable similarities

$z/D=5$ for $M=0.8$ and much improved for $M=1.0$ predictions shown in Figs. 13(b) and 13(c), respectively. It appears that the computed film jet stays attached even at the highest blowing ratio shown as η is always 1 near $z/D=0$. It is for this reason that bumps in the measured η curves related to jet detachment-reattachment are missed by predictions.

Comparison of computed lateral variation of η with that of experiments at five streamwise stations, shown in Fig. 14, reveals one serious consequence of the insufficient rate of spreading noted in Section 8.3.2 above. Measured data indicates nonzero η at the midpitch location (x/D = 1.5) for all lateral profiles except the one for z/D = 1. Computed η curves,

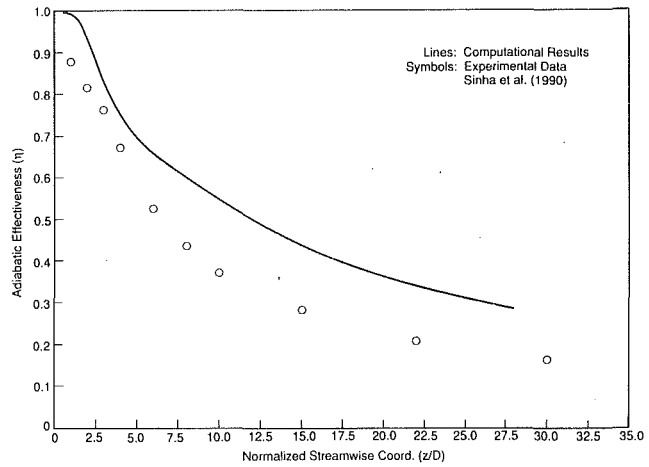

(a) M = 0.5, DR = 2.0

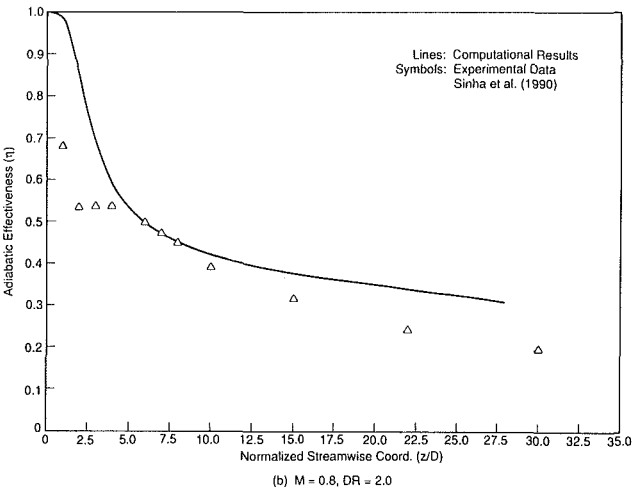

(b) M = 0.8, DR = 2.0

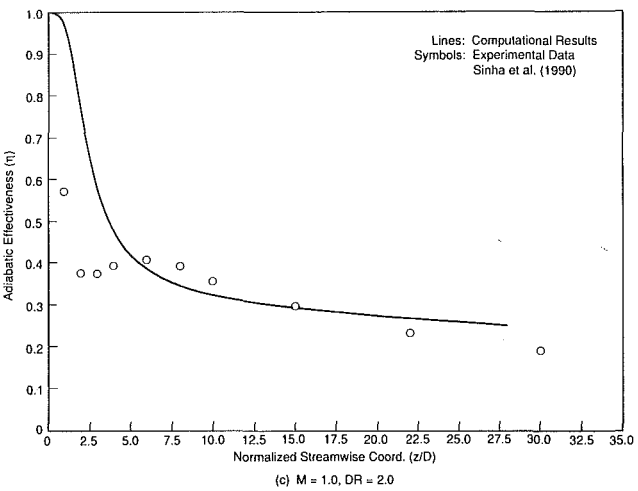

(c) M = 1.0, DR = 2.0

Fig. 13 Streamwise variation of adiabatic effectiveness from computations and experiments along jet centerline

on the other hand, show almost zero effectiveness beyond about $x/D = 1.2$ at all streamwise stations. Also, note that predicted centerline ($x/D = 0$) η is higher at every station than measurements. This is consistent with our earlier observations on centerline effectiveness data for $M = 0.5$.

9.0 Discussion

This discussion focuses on the strongly coupled and fully

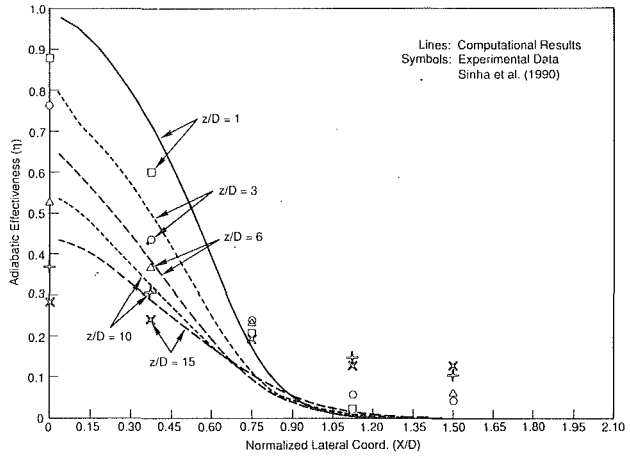

Fig. 14 Lateral variation of adiabatic effectiveness from computations and experiments for $M = 0.5$, $DR = 2.0$ at five streamwise stations

elliptic nature of film cooling flows in gas turbine configurations with small L/D, the complexity of flow within both the film-hole and the cross-stream, and the anisotropic behavior of turbulence created by jets-in-crossflow.

Flow in the film cooling configurations considered in this paper is strongly coupled and fully elliptic. Previous studies have concluded that film cooling results downstream of the coolant injection location are very sensitive to the distribution of dependent variables at the jet exit plane. However, due to the close proximity of the inlet and exit planes, these exit plane conditions, in turn, are dependent upon conditions at the inlet plane of the film-hole. Therefore, the coupling is, by nature, three-way as it involves interaction of flow between the plenum, film-hole, and cross-stream regions. The strength of coupling increases as injection angle and L/D decrease and M increases. Also, flow both within and outside the film cooling hole is fully elliptic as seen in our results. This observation establishes the need for fully elliptic treatment of such flows and signals that it is about time to abandon both fully and partially parabolic approaches.

There is a surprisingly complex flow within the film-hole itself. A counterrotating vortex structure is generated in the hole, which imparts swirl to the coolant jet as it is discharged into the hot crossflow. This vortex structure, together with the jetting effect created as the coolant is forced to accelerate over it, generates complex conditions at the jet exit plane. In fact, some of the measured and computed profiles have exactly the opposite trends of those obtained in experiments with large L/D.

Jets-in-crossflow create one of the prime examples of an anisotropic turbulence field. We are fully aware of the inadequacies of eddy-viscosity type turbulence closure models to deal with these types of flows. We believe, however, that even if a perfect turbulence model existed, one could not obtain film cooling solutions with high accuracy the way that such flows have historically been modeled in the open literature. The improved three-dimensional Navier–Stokes model presented in this paper eliminates the need to specify boundary conditions at the jet exit plane, thus removing one of the main obstacles in the successful simulation of jet-crossflow interactions in film cooling. Our results show that using a computational model with a fully elliptic solution procedure to compute, simultaneously, the strongly coupled flow in the plenum, film-hole, and cross-stream regions can enable one to capture and explain much of the flow physics in discrete-jet film cooling at high blowing ratios. Thus, the stage is set for more accurate film cooling predictions with the use of a turbulence model that is capable of dealing with an anisotropic field. The lack of lateral spreading of the coolant in our results

is caused by the inability of the k–ϵ model to cope with non-uniform rates of diffusion in different directions. It is to this task that we plan to turn next.

10.0 Conclusions

The following key conclusions about discrete-jet film cooling with a film-hole length-to-diameter ratio typical of gas turbine airfoils are drawn from three-dimensional Navier–Stokes analyses and experiments.

- The entire flowfield was dominated by a strong threeway coupling caused by interaction between the plenum, film-hole, and cross-stream regions. However, fully coupled and elliptic simulation of this flowfield captured much of the flow physics since predictions effectively supplement, support, and help explain experimental data and observations from flow visualization tests.
- Distribution of dependent variables at the jet exit plane was highly two-dimensional and fundamentally different from those observed in large L/D situations. The final distribution resulted from the interaction of three competing mechanisms, namely, counterrotating structure and local jetting effects within the film-hole, and crossflow blockage.
- Flow within the film-hole was shown to be extremely complex. It contains counterrotating vortices and local jetting effects, which make the flowfield in this region highly elliptic. Strength of these structures was found to be controlled mainly by a combination of three parameters, namely, film-hole length-to-diameter ratio, blowing ratio, and injection angle.
- The main source of turbulence shifted from the shear layer above the coolant jet in the cross-stream at low blowing ratios to the layer between the vortices and jetting regions within the film-hole at high blowing ratios.
- With proper care and an effective solution strategy, full convergence was attained for this strongly coupled and elliptic film cooling flowfield in a multizone domain at a blowing ratio as high as 2.0.

Acknowledgments

The authors are indebted to Dr. Mikio Suo for his support and encouragement, and for his genuine interest in film cooling heat transfer. We would like to thank Profs. M. E. Crawford and D. G. Bogard for providing feedback on our predictions. We also appreciate fruitful discussions with our colleagues Drs. B. K. Sultanian and C. Prakash. Another colleague, Dr. R. K. Rout, provided expert advice on the use of I-DEAS. Last but not least, the authors wish to thank GE Aircraft Engines for permission to publish this paper.

References

Amer, A. A., Jubran, B. A., and Hamdan, M. A., 1992, "Comparison of Different Two-Equation Turbulence Models for Prediction of Film Cooling From Two Rows of Holes," *Numerical Heat Transfer, Part A*, Vol. 21, Hemisphere Publishing Corporation, pp. 143–162.

Andreopoulos, J., and Rodi, W., 1984, "Experimental Investigation of Jets in a Crossflow," *Journal of Fluid Mechanics*, Vol. 138, pp. 93–127.

Bergeles, G., Gosman, A. D., and Launder, B. E., 1978, "The Turbulent Jet in a Cross Stream at Low Injection Rates: A Three-Dimensional Numerical Treatment," *Numerical Heat Transfer*, Vol. 1, Hemisphere Publishing Corporation, pp. 217–242.

Crabb, D., Durao, D. F. G., and Whitelaw, J. H., 1981, "A Round Jet Normal to a Crossflow," ASME *Journal of Fluids Engineering*, Vol. 103, pp. 142–152.

Crawford, M. E., Kays, W. M., and Moffat, R. J., 1980, "Full-Coverage Film Cooling, Part II: Heat Transfer Data and Numerical Simulation," ASME *Journal of Engineering for Power*, Vol. 102, pp. 1006–1012.

Crawford, M. E., 1991, Private Communications.

Crawford, M. E., 1992, Private Communications.

Dermuren, A. O., Rodi, W., and Schönung, B., 1986, "Systematic Study of Film Cooling With a Three-Dimensional Calculation Procedure," ASME JOURNAL OF TURBOMACHINERY, Vol. 108, pp. 124–130.

Forth, C. J. P., and Jones, T. V., 1988, "Scaling Parameters in Film Cooling," *Proc. 8th International Heat Transfer Conference*, Vol. 3, pp. 1271–1276.

Foster, N. W., and Lampard, D., 1980, "The Flow and Film Cooling Effectiveness Following Injection Through a Row of Holes," ASME *Journal of Engineering for Power*, Vol. 102, pp. 584–588.

Haas, W., Rodi, W., and Schonung, B., 1992, "The Influence of Density Difference Between Hot and Coolant Gas on Film Cooling by a Row of Holes: Predictions and Experiments," ASME JOURNAL OF TURBOMACHINERY, Vol. 114, pp. 747–755.

Jubran, B. A., 1989, "Correlation and Prediction of Film Cooling From Two Rows of Holes," ASME JOURNAL OF TURBOMACHINERY, Vol. 111, pp. 502–509.

Kadotani, K., and Goldstein, R. J., 1979, "On the Nature of Jets Entering a Turbulent Flow, Part A. Jet-Mainstream Interaction," ASME *Journal of Engineering for Power*, Vol. 101, pp. 459–465.

Launder, B. E., and Spalding, D. B., 1974, "The Numerical Computation of Turbulent Flows," *Computer Methods in Applied Mechanics and Engineering*, Vol. 3, pp. 269–289.

Launder, B. E., and York, J., 1974, "Discrete-Hole Cooling in the Presence of Free Stream Turbulence and Strong Favorable Pressure Gradient," *International Journal of Heat and Mass Transfer*, Vol. 17, pp. 1403–1409.

Le Brocq, P. V., Launder, B. E., and Priddin, C. H., 1973, "Discrete Hole Injection as a Means of Transpiration Cooling; An Experimental Study," *Proc. Instn. Mech. Engrs.*, Vol. 187, pp. 149–157.

Ludwig, J. C., Qin, H. Q., and Spalding, D. B., 1989, "The PHOENICS Reference Manual," CHAM Limited, Report No. TR/200.

Norton, R. J. G., Forest, A. E., White, A. J., Henshaw, D. G., Epstein, A. H., Schultz, D. L., and Oldfield, M. L. G., 1990, "Turbine Cooling System Design—Vol. I—Technical Report," Wright Research and Development Center Report No. WRDC-TR-89-2109, Vol. 1.

Patankar, S. V., Basu, D. K., and Alpay, S. A., 1977, "Prediction of the Three-Dimensional Velocity Field of a Deflected Turbulent Jet," ASME *Journal of Fluids Engineering*, Vol. 99, pp. 758–762.

Patankar, S. V., 1980, *Numerical Heat Transfer and Fluid Flow*, Hemisphere Publishing Corporation, New York.

Petersen, D. R., Eckert, E. R. G., and Goldstein, R. J., 1977, "Film Cooling With Large Density Differences Between the Mainstream and Secondary Fluid Measured by Heat-Mass Transfer Analogy," ASME *Journal of Heat Transfer*, Vol. 99, pp. 620–627.

Pietrzyk, J. R., 1989, "Experimental Study of the Interaction of Dense Jets With a Crossflow for Gas Turbine Applications," Ph.D. Dissertation, University of Texas at Austin.

Pietrzyk, J. R., Bogard, D. G., and Crawford, M. E., 1989, "Hydrodynamic Measurements of Jets in Crossflow for Gas Turbine Film Cooling Applications," ASME JOURNAL OF TURBOMACHINERY, Vol. 111, pp. 139–145.

Pietrzyk, J. R., Bogard, D. G., and Crawford, M. E., 1990, "Effects of Density Ratio on the Hydrodynamics of Film Cooling," ASME JOURNAL OF TURBOMACHINERY, Vol. 112, pp. 437–443.

Rodi, W., and Srivatsa, S. K., 1980, "A Locally Elliptic Calculation Procedure for Three-Dimensional Flows and Its Application to a Jet in a Cross Flow," *Comp. Meth. Appl. Mech. Engg.*, Vol. 23, pp. 67–83.

Sinha, A. K., Bogard, D. G., and Crawford, M. E., 1991, "Film-Cooling Effectiveness Downstream of a Single Row of Holes With Variable Density Ratio," ASME JOURNAL OF TURBOMACHINERY, Vol. 113, pp. 442–449.

Tafti, D. K., and Yavuzkurt, S., 1990, "Prediction of Heat Transfer Characteristics for Discrete Hole Cooling for Turbine Blade Applications," ASME JOURNAL OF TURBOMACHINERY, Vol. 112, pp. 504–511.

Tatchell, D. G., 1975, "Convection Process in Confined Three-Dimensional Boundary Layers," Ph.D. Dissertation, University of London, United Kingdom.

White, A. J., 1980, "The Prediction of the Flow and Heat Transfer in the Vicinity of a Jet in Crossflow," presented at the ASME Winter Annual Meeting, Chicago, IL.

Yoshida, T., and Goldstein, R. J., 1984, "On the Nature of Jets Issuing From a Row of Holes Into a Low Reynolds Number Mainstream Flow," ASME *Journal of Engineering for Gas Turbines and Power*, Vol. 106, pp. 612–618.

K. W. Van Treuren

Z. Wang

P. T. Ireland

T. V. Jones

Department of Engineering Science,
University of Oxford,
Oxford, United Kingdom

Detailed Measurements of Local Heat Transfer Coefficient and Adiabatic Wall Temperature Beneath an Array of Impinging Jets

A transient method of measuring the local heat transfer under an array of impinging jets has been developed. The use of a temperature-sensitive coating consisting of three encapsulated thermochromic liquid crystal materials has allowed the calculation of both the local adiabatic wall temperature and the local heat transfer coefficient over the complete surface of the target plate. The influence of the temperature of the plate through which the impingement gas flows on the target plate heat transfer has been quantified. Results are presented for a single in-line array configuration over a range of jet Reynolds numbers.

Introduction

Impinging jets are frequently used to cool both the leading edge and midspan regions of gas turbine vanes and blades. Analytic means of accurately predicting the heat transfer to vanes are not available and consequently many experiments have been performed on different impingement cooling geometries. The only application of a transient heat transfer method was reported by Bunker and Metzger (1990a) who measured local heat transfer coefficients over the curved surface of a model of the inside of a blade leading edge. Increasing the target surface curvature was shown to reduce the heat transfer levels, and the effect of Reynolds number on average Nusselt numbers was reported. A very comprehensive study of many different arrays of jets was reported by Florschuetz and his co-authors (1980, 1981, 1982, 1985) who correlated heat transfer levels on geometric parameters of the array. The heat transfer level predicted by their correlation is dependent on local jet Reynolds number, crossflow to jet mass velocity ratio, and array geometry. A steady-state experimental method was used that produced row resolved Nusselt numbers. The same technique but with narrower heaters was used by Saad et al. (1980) and Hollworth and Cole (1987). The spatial resolution achieved by these workers was sufficient to measure the peak in spanwise average h, which occurs beneath the jets, and to observe the downstream shift in peak h as local crossflow increases. Liquid crystals have been employed by Goldstein and Franchett (1988), Baughn and Shimizu (1989), and Lucas et al. (1992) to measure detailed local heat transfer coefficient distributions beneath a single impinging jet. The high-resolution results obtained by these more advanced techniques have provided significant insight into the fluid dynamic processes responsible for the large heat transfer coefficients that occur directly beneath the jet. No detailed heat transfer information has been obtained, however, on jet interaction within an array or the effect of crossflow on cooling performance. Only Hippensteele et al. (1983) have previously applied liquid crsytals to an array of jets, though the results presented were not quantitative.

Florschuetz et al. (1982), Andrews and Mkpadi (1983), and Andrews et al. (1985) concluded that the influence of the plate temperature on target plate heat transfer levels needed to be quantified. In the current work, attention was paid to the careful control of the impingement plate temperature. The contribution of this thermal boundary condition to the overall heat transfer coefficient at the target plate was recently measured by Lucas et al. (1992). They concluded that beneath a single confined jet at large hole to target plate spacing and high Reynolds numbers, the impingement plate heat transfer coefficient can locally exceed the plenum temperature heat transfer coefficient. The effect is caused by a large recirculation vortex that encircles the jet and draws air back to the jet flow along the impingement plate. Significant heat transfer between the plate and the recirculation gas is responsible for the impingement plate temperature influence on target plate heat transfer. The present work has succeeded in measuring the impingement plate effect in an engine representative array of impinging jets.

Experimental Apparatus

A sharp-edged circular hole was chosen to represent the engine impingement hole geometries after studying several tur-

Contributed by the International Gas Turbine Institute and presented at the 38th International Gas Turbine and Aeroengine Congress and Exposition, Cincinnati, Ohio, May 24-27, 1993. Manuscript received at ASME Headquarters March 3, 1993. Paper No. 93-GT-205. Associate Technical Editor: H. Lukas.

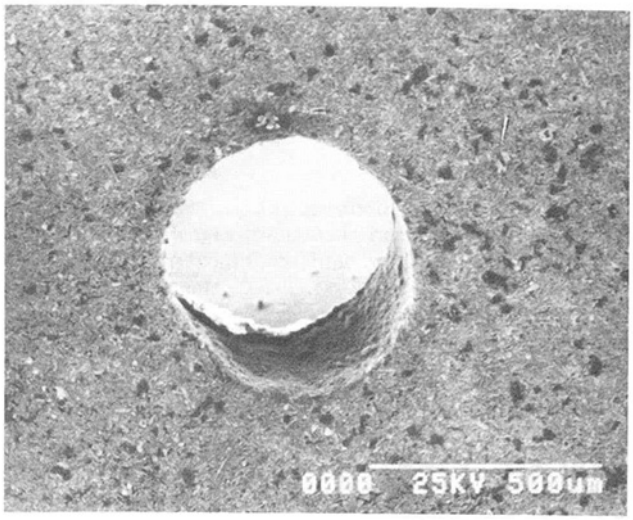

Fig. 1 Image of engine impingement hole produced by a scanning electron microscope

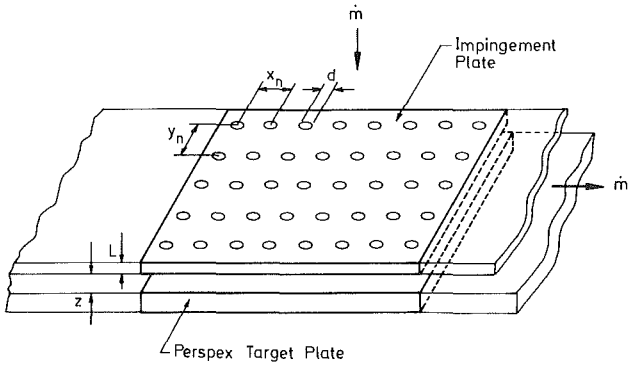

Fig. 2 Inline array geometry

bine blades employing impingement cooling under a scanning electron microscope, Fig. 1. In the large-scale model used in these experiments, the impingement plate thickness to hole diameter ratio, L/d, is 1.2 and the target plate is one hole diameter from the impingement plate. The hole spacing is $8d$ in both the streamwise and spanwise directions. The array plate was manufactured from brass sheet and includes a water channel used to hold the plate temperature constant throughout the transient experiments. Eight rows of 5-mm-dia holes are included in the streamwise direction and five rows span the channel in an in-line configuration, as shown in Fig. 2. The air velocity on the channel centerline is measured with a pitot tube 0.21 m downstream of the last row of holes. Measurements of the temperature and static pressure at this site permit the mass flow from the array of jets to be calculated and compared to that measured at an orifice plate upstream of the jet plenum.

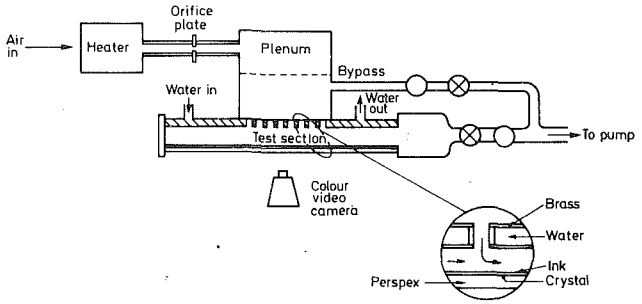

Fig. 3 Experimental apparatus

A 0.1 ms response semiconductor pressure transducer was used to measure the time for the flow to be established. Otherwise the instrumentation and data acquisition system remained as described by Byerley (1989). Figure 3 is a diagram of the experimental setup. A coating that combined three different encapsulated liquid crystals was used to measure the surface temperature of the perspex. The liquid crystal response was recorded using CCD video cameras positioned outside the tunnel that viewed through the 12-mm-thick perspex wall. Light transmitted through the crystal was eliminated by a coating of thermally thin black ink. The liquid crystal color play was calibrated in place using thin surface-mounted thermocouples fixed to the perspex beneath the temperature-sensitive coating. The coating was illuminated by fluorescent tubes positioned above and beneath the test section. A frame grabber and software written by Wang et al. (1993) were used to determine the peak signal times for the intensity averaged over 5×5 squares of pixels.

Experimental Method

The transient method has been applied to other internal cooling geometries by Wang (1991) and Byerley (1989) to measure heat transfer coefficients. With known adiabatic wall temperature, the method yields local values of h to an uncertainty of within 7 percent. The experiment starts with the perspex model and brass impingement plate at room temperature. The required jet array Reynolds number is achieved with air at ambient temperature. The valves are switched to take the same flow through the bypass and the heaters are then switched on. This phase continues until the plenum temperature is constant. A small amount of air is bled back through the impingement plate from atmosphere. This air bleed together with water cooling of the impingement plate are sufficient to hold the perspex target plate temperature constant during the bypass phase. Heat transfer to the liquid crystal coated surface begins when the fast-acting valves are actuated and hot gas is pulled through the cooled brass plate to impinge on the target plate. A flow establishment time of 0.16 seconds was achieved by using digital timers to sequence the fast-acting valves so that they finished their travel at precisely the same instant. During

Nomenclature

c = specific heat capacity, J/kgK
d = jet hole diameter, m
G_c = crossflow mass velocity, kg/m^{2}s
G_j = jet mass velocity, kg/m^{2}s
h = heat transfer coefficient, W/m^{2}K
k = thermal conductivity, W/mk
L = impingement plate thickness, m
$\dot{m}$ = mass flow, kg/s
Nu = Nusselt number
Nu_{tot} = $\mathrm{Nu}_j + \mathrm{Nu}_p$
P = pressure, N/m^2
$\dot{q}$ = heat flux, W/m^2
Re = Reynolds number
T = temperature, °C
t = time, s
x = streamwise distance, m
y = spanwise distance, m
z = impingement plate to target plate separation, m
η = dimensionless adiabatic wall temperature
ρ = density, kg/m^3

Subscripts

avg = average
aw = adiabatic wall
c = liquid crystal, crossflow
chan = channel
g = gas
j = jet
o = initial
p = plate
plen = plenum
w = wall

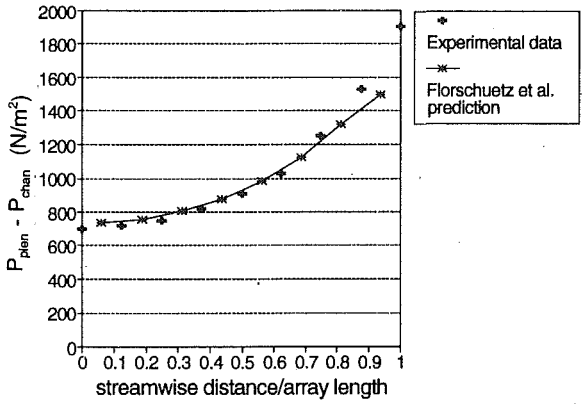

Fig. 4 Channel pressure distribution as a function of position

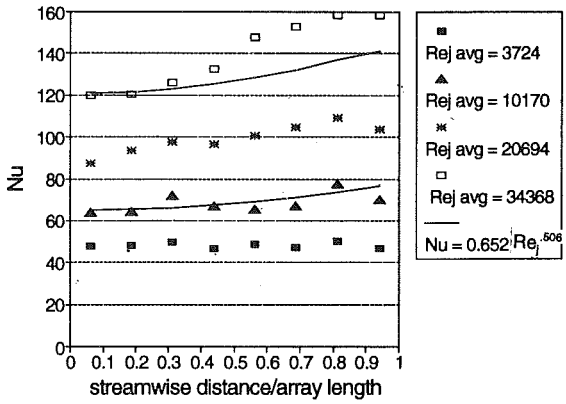

Fig. 5 Peak total Nusselt number as a function of position

the heat transfer experiment, air from the impingement array leaves from one side of the channel and hence the local crossflow increases with row number (1–8) through the array.

The pipework between the heaters and plenum was well insulated to avoid the potential effect of heat loss on plenum gas temperature uniformity. The plenum box had dimensions $0.5 \times 0.5 \times 0.2$ m and was fabricated from steel insulated with 25-mm-thick expanded polystrene. At the end of the by-pass phase, the temperature inside the plenum upstream of the flow straightener was measured as being within 0.4°C of the air temperature on the centerline of the pipe connecting to the plenum. The small amount of atmospheric air that was allowed to bleed into the test channel kept the pressure in the channel slightly higher than that in the plenum. This prevented the higher temperature plenum air from entering the test section and preheating the target surface during the bypass phase but had little effect on plenum heating. No significant effect on the plenum temperature profile was noted once the flow was switched. A temperature survey with a thermocouple revealed that, once steady testing conditions had been achieved, the gas temperature was uniform to within 0.5°C across all the holes on the plenum centerline. Furthermore, the double crystal analysis applied to more than one pair of the crystal color change times was used to prove that the driving gas temperature changed as a step over all of the impinging jets.

Data Analysis

The surface temperature rise is related to the local heat transfer coefficient and gas temperature by the solution to the one-dimensional Fourier equation. Both h and T_{aw} are found by numerically solving two implicit equations, which arise from the use of a double crystal method:

$$\frac{T_{ci} - T_o}{T_{aw} - T_o} = 1 - \exp\left(\frac{h\sqrt{t_i}}{\sqrt{\rho ck}}\right)^2 \operatorname{erfc}\left(\frac{h\sqrt{t_i}}{\sqrt{\rho ck}}\right)$$

Here $i = 1$ or 2 since at least two event times are obtained at each location. Vedula and Metzger (1991) applied a similar technique to determine heat transfer results for a film cooling situation. Three narrow color play liquid crystals with calibrated temperatures of 26.1°C, 30.6°C, and 35.1°C were used in the current series of experiments. At the locations of the highest heat transfer coefficient, directly under the jet, the second and third crystals were used in the analysis, while at regions of lower heat transfer, the first and second crystals were used. The 12 mm perspex wall was thick enough to ensure that the semi-infinite assumption could be used in all data analysis. The perturbation method of Moffat (1988) was used to calculate the experimental uncertainty in h and effectiveness. Ireland and Jones (1987) showed that the double crystal technique is sensitive to measured uncertainties. An extensive rig validation exercise together with careful selection of plenum and crystal temperatures enabled an experimental uncertainty below 10 percent to be achieved.

Superposition can be used to show that the local heat flux at the target plate can be described in terms of two heat transfer coefficients:

$$\dot{q} = h_j\ (T_j - T_w) + h_p\ (T_p - T_w)$$

The analysis is very similar to that detailed by Lucas et al. (1992). The double crystal method yields the local heat transfer coefficient, h, defined as

$$h = \frac{\dot{q}}{T_{aw} - T_w}$$

and the adiabatic wall temperature, T_{aw}. In the present work, the results are presented in terms of the Nusselt number, hd/k, and the effectiveness defined as

$$\eta = \frac{T_{aw} - T_p}{T_j - T_p}$$

It is easily shown that the effectiveness is the jet heat transfer coefficient, h_j, divided by the total heat transfer coefficient, $h_j + h_p$. In regions where the effectiveness is one, the adiabatic wall temperature is the same as the jet temperature.

Results

Static Pressure. The measure static pressure distribution along a line midway between two rows of jets is shown as a function of streamwise distance in Fig. 4. The experimental data are compared to values predicted using the approach of Florschuetz et al. (1982). The best agreement to the experimental pressure data is achieved by choosing a uniform discharge coefficient of 0.83. This discharge coefficient compares to a value of 0.76–0.83 used by the latter authors in an array with a similar geometry with widely spaced holes. The overall discharge coefficient for this experimental array, measured after completing the analysis, was found to be 0.82. The flow uniformity between holes with the target plate removed was assessed with a total pressure probe. Variation between holes was found to be insignificant. Allowance was made in the analytic model for pressure drop caused by shear stress acting at the target wall. The agreement with the measured data is seen to be excellent and the analysis was later used to predict the variation of local jet Reynolds numbers throughout the array.

Stagnation Point Nu. Nu levels were calculated by the double crystal technique using mostly the second and third crystals. The values of the peak local Nusselt number that occurs beneath each jet are plotted as a function of position in Fig. 5. At the beginning of the array, where the crossflow is small, the peak is located on the hole centerline. As the crossflow develops, the peak position can be seen to shift slightly down-

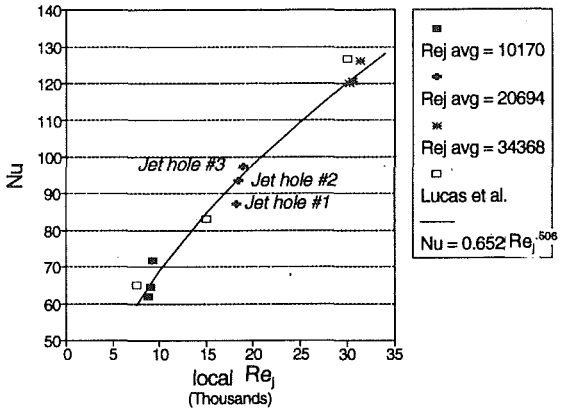

Fig. 6 Stagnation point total Nusselt number as a function of jet Reynolds number

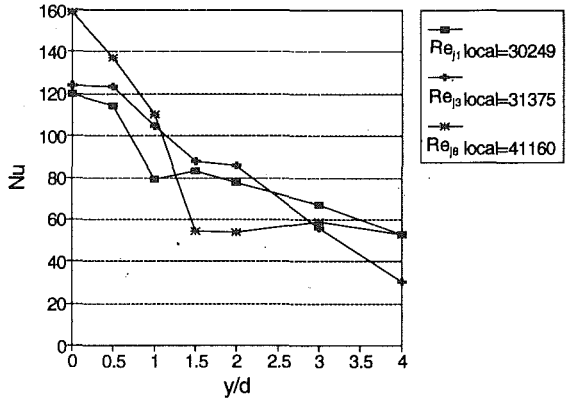

Fig. 8 Spanwise variation of total Nusselt number at successive holes

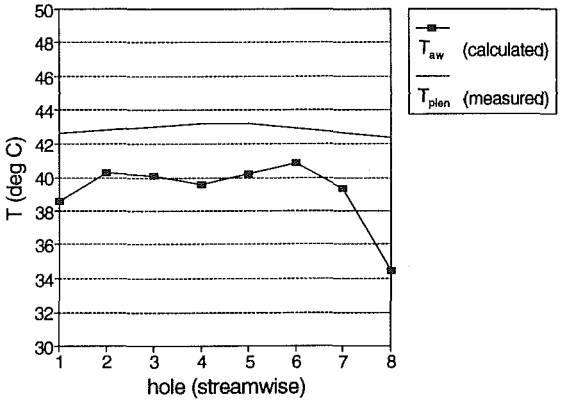

Fig. 7 Adiabatic wall temperature as a function of position

stream as the increased crossflow displaces the jets. The same effect was reported by Saad et al. (1980). The analysis showed that, moving through the array, the increased pressure difference between the plenum and the channel caused the jet massflow through each jet hole to increase. The increase in the peak level through the array is explained by the increasing local jet Reynolds number.

The crossflow is seen to have little effect on the position of the peak heat transfer for the first three rows. The peak Nusselt number here is compared to a least-squares fit to Reynolds number in Fig. 6. The data of Lucas et al. (1992) for an isolated, confined jet in the absence of crossflow are also included. The value of the exponent to which the Reynolds number is raised in the correlation is very close to 0.5. This is the theoretical exponent for Nusselt number beneath a laminar boundary layer at a stagnation point and is evidence that the jet potential core extends to the target plate surface. Yan et al. (1992) showed that, for a free jet, this exponent remained at 0.5 up to a hole to plate spacing of $6d$ after which it increased. The increase was associated with the end of the potential core and the influence of the turbulent shear layer on the stagnation point heat transfer.

The double crystal method yields values of the local adiabatic gas temperature as well as the local heat transfer coefficient. The calculated adiabatic wall temperature at the location of the peak Nu throughout the array for an average Re_j of 3724 is shown in Fig. 7. The impingement plate was held at a constant 20°C during this experiment. It is interesting to note that the adiabatic wall temperature is slightly below the measured plenum temperature. Lucas et al. (1992) measured heat transfer beneath a confined jet and reported that the adiabatic wall temperature was between the plenum and impingement plate temperature for plate separations of $2.0d$ and $3.0d$. At a separation of $1.0d$, however, the adiabatic temperature at the stagnation point was the same as the plenum temperature since the potential core of the jet extended to the plate surface. The influence of the impingement plate was observed farther out from the stagnation point. Their impingement plate was of a composite construction, which was thermally insulated on the plenum side. The current work has used an impingement plate manufactured from two water-cooled brass sheets, Fig. 3. The water flow rate is such that both brass sheets are at sensibly the same temperature as the water. It is thought that there is significant heat transfer from the air at the impingement plate as it is drawn along the plate inner surface before entering the hole. This cooling of the jet gas would account for the difference between the adiabatic wall temperature at the stagnation point and the plenum temperature. An extended flow path along the inside of the plate at the first and last rows is probably responsible for the additional reduction in the stagnation point driving gas temperature at the ends of the array, Fig. 7.

Variation of Nu Along a Radial Line. At the first row of jets, the liquid crystal color change contours advance in a circular manner up to about $3.0d$ from the stagnation point. This indicates that the heat transfer and hence flow field local to the stagnation point should be comparable to that of a single jet. Figure 8 shows the variation in total Nusselt number ($Nu_j + Nu_p$) in the spanwise direction for the first, third, and eighth rows at the highest mass flow tested. This plot is of interest since previous measurements of array heat transfer have only been able to resolve data in a streamwise sense. It can be seen that the heat transfer drops off rapidly up to one diameter from the centerline but a second peak exists at approximately 1.5 diameters. This peak has been observed at high Reynolds numbers under a confined jet (Lucas et al. 1992) and under a free jet (Yan et al., 1983; den Ouden and Hoggerdoorm, 1974; Obot et al., 1979). It is thought to be close to the point of transition from laminar to turbulent flow. Outward from this secondary peak, the heat transfer decreases much more rapidly than for the single jet (Lucas et al., 1992) due to the spent flow from the first jet exiting downstream between the jets. Row three has a slightly higher stagnation Nu but the second peak has been smoothed and noticeably shifted in the spanwise direction. Also noticeable is a 45 percent reduction in Nu at the four diameter point compared with hole number one. The data for row eight clearly show the effect of crossflow on the local Nu. From the centerline the heat transfer decreases steadily to the 1.5 diameter point and then remains relatively constant with spanwise direction at the level of the channel Nu measured for row one. At this location in the array, the jet is no longer acting purely as an impinging jet but also appears to present a significant obstacle to the spent flow from upstream holes.

Figures 9, 10, and 11 show the separate contributions of the

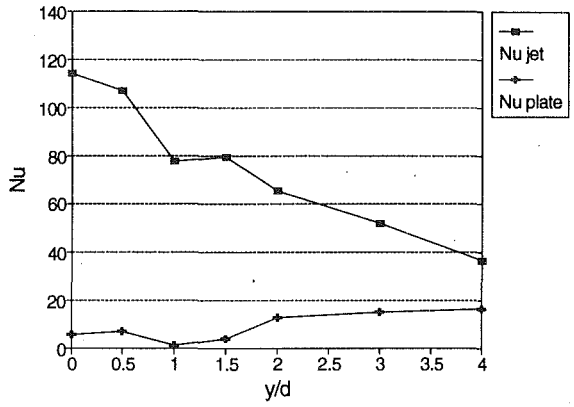

Fig. 9 Spanwise variation of plate and jet Nusselt number at row one

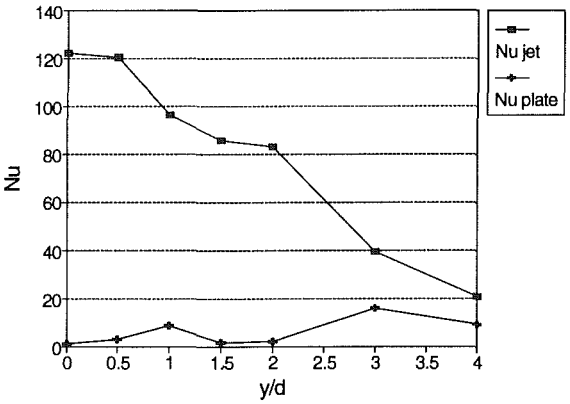

Fig. 10 Spanwise variation of plate and jet Nusselt number at row three

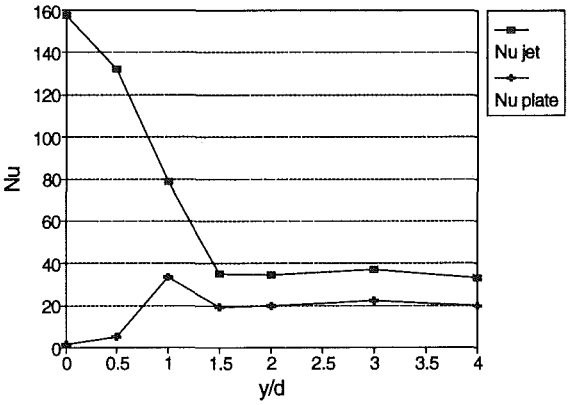

Fig. 11 Spanwise variation of plate and jet Nusselt number at row eight

jet and the impingement plate to the target plate and heat transfer. Again, the second peak in Nu_j is apparent for holes one and three. Through the array the plate heat transfer coefficient becomes increasingly significant. Inspection of the row eight data shows that the plate heat transfer accounts for as much as 40 percent of the overall value in the region of exhausting flow between the jets.

Contours of Heat Transfer. High resolution local surface heat transfer contours were obtained using the image processing technique developed by Wang et al. (1993). Total Nu distributions at three different streamwise row locations are given in Figs. 12, 13, and 14. The corresponding effectiveness plots are given in Figs. 15, 16, and 17. In Figs. 12–17, the jet hole is aligned with the position (0, 0) and the flow is from negative to positive on the "Flow Direction" axis. Figure 12 shows Nu_{tot} beneath the jets in row one.The second peak in Nu_{tot} discussed previously is apparent as the ring that encircles

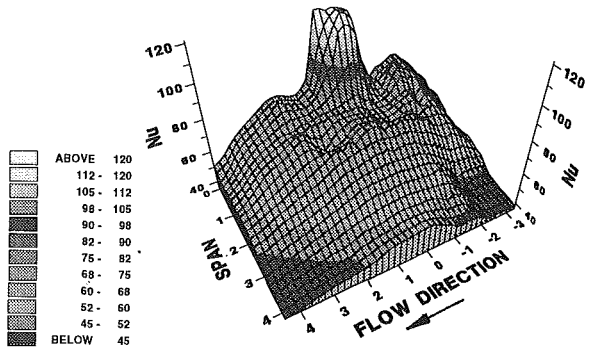

Fig. 12 Total Nusselt number distribution at the first row of jets

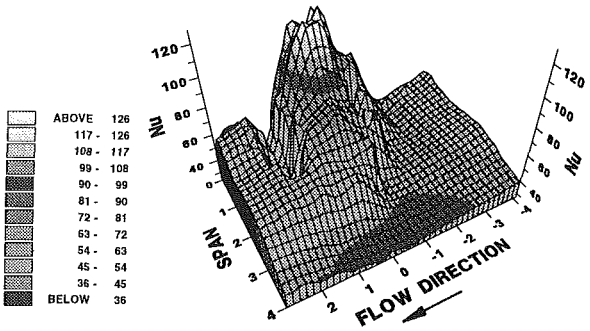

Fig. 13 Total Nusselt number distribution at the third row of jets

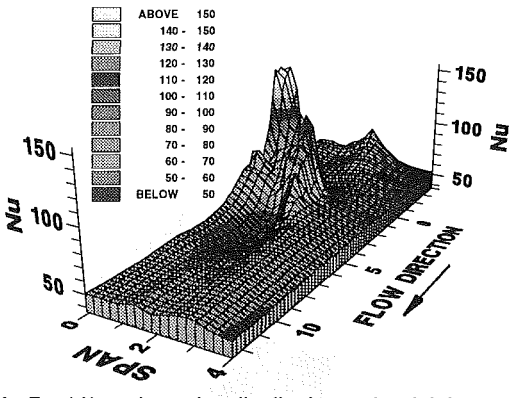

Fig. 14 Total Nusselt number distribution at the eighth row of jets

the central peak. The circular nature of the heat transfer patterns shows that crossflow has little effect on the heat transfer distribution in the vicinity of the stagnation point. The plate heat transfer coefficient, shown in Fig. 9, is seen to increase with distance from the stagnation point. Andrews et al. (1992) and Lucas et al. (1992) identified a large recirculating region that surrounds the jet and that thermally couples the target plate to the impingement plate. This recirculation vortex contributes to the significant plate heat transfer coefficient.

The heat transfer distribution beneath the eighth row, Fig. 14, shows a markedly different structure. The enhancement brought about by the jet is narrower as a result of the crossflow (the crossflow mass velocity was calculated as 0.557 times the jet mass velocity). There also is an enhancement due to the flow directly upstream of the jet being deflected between the jets. This shows a localized peak in Nu, which starts at the jet and angles off between the jets. This value in the channel is not as high as the value directly under the jet. The jet effectiveness, Fig. 17, indicates that the flow is very well mixed except under the jet. Immediately downstream of the jet is another region of enhanced heat transfer though not as the region that extends into the channel. This downstream region also includes a circular peak, which occurs approximately one diameter downstream.

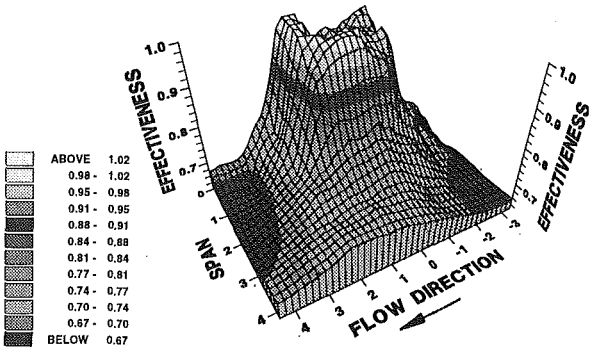

Fig. 15 Jet effectiveness at the first row of jets

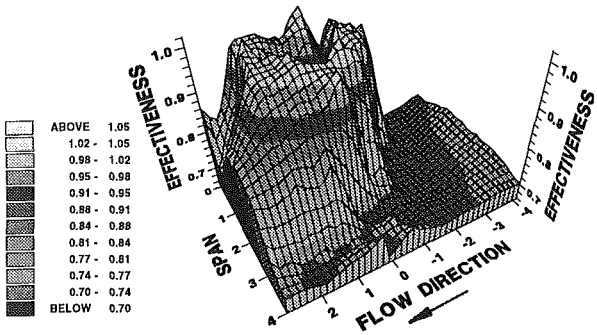

Fig. 16 Jet effectiveness at the third row of jets

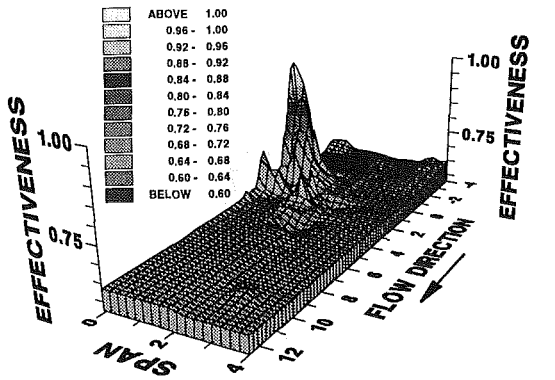

Fig. 17 Jet effectiveness at the eighth row of jets

Conclusions

A new method of obtaining local heat transfer coefficients under an engine representative array of impinging jets has been reported. The double crystal analysis has allowed the influence of the plate temperature to be quantified. The results show that this thermal boundary condition can significantly affect the average cooling performance of an impingement array.

Acknowledgments

This work has been carried out with the support of the UK Ministry of Defence and Rolls-Royce Plc. The lead author thanks the Air Force Institute of Technology for the opportunity to study at the University of Oxford. The authors are also very grateful to Dr. P. Wilshaw who produced the S.E.M. images of the engine impingement holes and Mr. P. Timms who manufactured the experimental apparatus. Liquid crystals were supplied by Hallcrest LCT Ltd.

References

Andrews, G. E., and Mkpadi, M. C., 1983, "Full Coverage Discrete Hole Wall Cooling: Discharge Coefficients," ASME *Journal of Engineering for Gas Turbines and Power*, Vol. 106, pp. 183–192.

Andrews, G. E., Asere, A. A., Hussain, C. I., and Mkpadi, M. C., 1985, "Full Coverage Impingement Heat Transfer: The Variation in Pitch to Diameter Ratio at a Constant Gap," AGARD Conference on Heat Transfer and Cooling in Gas Turbines, CP390 Paper No. 26.

Andrews, G. E., Al Dabagh, A. M., Asere, A. A., Bazdidi-Tehrani, F., Mkpadi, M. C., and Nazari, A., 1992, "Impingement/Effusion Cooling," AGARD 80th PEP Symposium, Paper No. 30.

Baughn, J. W., and Shimizu, S., 1989, "Heat Transfer Measurements From a Surface With Uniform Heat Flux and an Impinging Jet," ASME *Journal of Heat Transfer*, Vol. 111, pp. 1096–1098.

Bunker, R. S., and Metzger, D. E., 1990, "Local Heat Transfer in Internally Cooled Turbine Airfoil Leading Edge Regions: Part I—Impingement Cooling Without Film Coolant Extraction," ASME JOURNAL OF TURBOMACHINERY, Vol. 112, pp. 451–458.

Bunker, R. S., and Metzger, D. E., 1990, "Local Heat Transfer in Internally Cooled Turbine Airfoil Leading Edge Regions: Pat II—Impingement Cooling With Film Coolant Extraction," ASME JOURNAL OF TURBOMACHINERY, Vol. 112, pp. 459–466.

Byerley, A. R., 1989, "Heat Transfer Near the Entrance to a Film Cooling Hole in a Gas Turbine Blade," D. Phil. Thesis, Department of Engineering Science, University of Oxford, United Kingdom.

den Ouden, C., and Hoggerdoorm, C. J., 1974, "Local Convective-Heat-Transfer Coefficients for Jets Impinging on a Plate: Experiments Using Liquid Crystal," presented at the 5th International Heat Transfer Conference.

Florschuetz, L. W., Metzger, D. E., Takeuichi, D. I., and Berry, R. A., 1980, "Multiple Jet Impingement Heat Transfer Characteristic—Experimental Investigation of In-Line and Staggered Arrays With Crossflow," NASA Contractor Report 3217.

Florschuetz, L. W., Metzger, D. E., and Truman, C. R., 1981, "Jet Array Impingement With Crossflow—Correlation of Streamwise Resolved Flow and Heat Transfer Distributions," NASA Contractor Report 3373.

Florschuetz, L. W., Metzger, D. E., Su, C. C., Isoda, Y., and Tseng, H. H., 1982, "Jet Array Impingement Flow Distributions and Heat Transfer Characteristics—Effects of Initial Crossflow and Nonuniform Array Geometry," NASA Contractor Report 3630.

Florschuetz, L. W., and Su, C. C., 1985, "Heat Transfer Characteristics Within an Array of Impinging Jets—Effects of Crossflow Temperature Relative to Jet Temperature," NASA Contractor Report 3936.

Goldstein, R. J., and Franchett, M. E., 1988, "Heat Transfer From a Flat Surface to an Oblique Impinging Jet," ASME *Journal of Heat Transfer*, Vol. 110, pp. 84–90.

Hippensteele, S. A., Russsell, L. M., and Stepka, F. S., 1983, "Evaluation of a Method for Heat Transfer Measurements and Thermal Visualization Using Composite of a Heater Element and Liquid Crystals," ASME *Journal of Heat Transfer*, Vol. 105, pp. 184–189.

Hollworth, B. R., and Cole, G. H., 1987, "Heat Transfer to Arrays of Impinging Jets in a Crossflow," ASME JOURNAL OF TURBOMACHINERY, Vol. 109, pp. 564–571.

Ireland, P. T., and Jones, T. V., 1987, "Note on the Double Crystal Method of Measuring Heat Transfer Coefficient," Oxford University Department of Engineering Science Report No. 1710/87.

Lucas, M. L., Ireland, P. T., Wang, Z., and Jones, T. V., 1992, "Fundamental Studies of Impingement Cooling Thermal Boundary Conditions, AGARD 80th PEP Symposium, Paper No. 14.

Moffat, R. J., 1988, "Describing Uncertainties in Experimental Results," *Experimental Thermal and Fluid Science*, Vol. 1, pp. 3–17.

Obot, N. T., Majumdar, A. A., and Douglas, W. J. M., 1979, "The Effects of Nozzle Geometry on Impingement Heat Transfer Under a Round Turbulent Jet," ASME Paper No. 79-WA/HT-53.

Saad, N. R., Majumdar, A. S., Abdel Messeh, W., and Douglas, W. J. M., 1980, "Local Heat Transfer Characteristics for Staggered Arrays of Circular Impinging Jets With Cross Flow of Spent Air," ASME Paper No. 80-HT-23.

Vedula, R. J. and Metzger, D. E., 1991, "A Method for the Simultaneous Determination of Local Effectiveness and Heat Transfer Distributions in Three-Temperature Convection Situations," ASME Paper No. 91-GT-345.

Wang, Z., 1991, "The Application of Thermochromic Liquid Crystals to Detailed Turbine Blade Cooling Measurements," D. Phil Thesis, Department of Engineering Science, University of Oxford, United Kingdom.

Wang, Z., Ireland, P. T., and Jones, T. V., 1993, "An Advanced Method of Processing Liquid Crystal Color Change Images From Transient Heat Transfer Experiments Using an Intensity History Method," ASME Paper No. 93-GT-282; ASME JOURNAL OF TURBOMACHINERY, in press.

Yan, X., Baughn, J. W., and Mesbah, M., 1992, "The Effect of Reynolds Number on the Heat Transfer Distribution From a Flat Plate to an Impinging Jet," ASME HTD-Vol. 226, pp. 1–8.

An Investigation of Boundary Layer Development in a Multistage LP Turbine

H. P. Hodson

I. Huntsman

Whittle Laboratory,
Cambridge University,
Cambridge, United Kingdom

A. B. Steele

Rolls-Royce plc,
Derby, United Kingdom

This paper describes an investigation of the behavior of suction surface boundary layers in a modern multistage Low-Pressure turbine. An array of 18 surface-mounted hot-film anemometers was mounted on a stator blade of the third stage of a four-stage machine. Data were obtained at Reynolds numbers between 0.9×10^5 and 1.8×10^5. At the majority of the test conditions, wakes from upstream rotors periodically initiated transition at about 40 percent surface length. In between these events, laminar separation occurred at about 75 percent surface length. Because the wake-affected part of the flow appeared to be only intermittently turbulent, laminar separation also occurred at about 75 percent surface length while this flow was instantaneously laminar. At all but the lowest Reynolds numbers, the time-mean boundary layer appeared to have re-attached by the trailing edge even though it was not fully turbulent. It is inferred that the effect of the wakes on the performance of the blade row is limited and that steady flow design methods should provide an adequate assessment of LP turbine performance during design.

Introduction

The emerging generation of civil transport aircraft requires fewer engines, each with a larger thrust. New families of turbofan engines have been designed to meet these requirements. They feature fans of a larger diameter, which demand more power from the Low-Pressure (LP) turbine at a lower rotational speed. The resulting increase in the duty of the LP turbine must be accompanied by reductions in weight, cost of manufacture, overall size, and specific fuel consumption. Since present-day LP turbines already operate with aerodynamic efficiencies above 90 percent, the quest for further increases in efficiency and performance has become progressively more difficult. This paper describes an investigation of a four-stage LP turbine that will enter service in the Rolls-Royce Trent 700 turbofan engine.

The aspect ratios in the new generation of LP turbines are such that an accurate prediction of the development of the blade-surface boundary layer is vital if performance targets are to be met. When the boundary layers are either laminar or turbulent, the prediction process is relatively straightforward. Unfortunately, the prediction of transitional boundary layers is much more difficult. This is particularly important in the context of LP turbines because the location and nature of the transition zone affect the existence, the location, and the nature of laminar separation. The research described here was conducted to verify the design of the present LP turbine and to enable the further development of techniques capable of predicting boundary layer transition in the complex environment of turbomachines.

One of the issues confronting the designer of LP turbines is the relative impact of unsteady flow on the transition process. In the present context, there are two possible sources of unsteadiness. The potential influence of a blade extends both upstream and downstream and decays exponentially with a length scale typically of the order of the chord or pitch. In contrast, the wakes are convected downstream from the blade row and their rate of decay is much less than that of the potential influence. Consequently, the disturbances associated with the wakes are usually more significant at entry to the next blade row. It is an objective of the current work to quantify the significance of the effects of wake-generated unsteadiness on the development of the blade surface boundary layers.

When wakes from upstream blade rows impinge on a laminar boundary layer, transition occurs nearer to the leading edge than would otherwise be the case. As turbulent boundary layers usually produce more loss than laminar ones, the profile loss is usually increased. The level of increase depends on how far transition is moved upstream and how often the wakes arrive. At low Reynolds numbers, it is possible that the wakes may reduce the profile loss to below the steady level, just as promoting transition can reduce the drag on bodies where laminar separation is not followed by re-attachment. This effect is of particular interest in the present study since laminar flow is more likely to exist in LP turbines.

In recent years, the problem of wake-boundary layer interactions has received much attention. The investigations carried out by Hourmouziadis et al. (1987), Binder et al. (1989), and Schröder (1991) in cold-flow LP turbines are especially relevant

Contributed by the International Gas Turbine Institute and presented at the 38th International Gas Turbine and Aeroengine Congress and Exposition, Cincinnati, Ohio, May 24-27, 1993. Manuscript received at ASME Headquarters March 12, 1993. Paper No. 93-GT-310. Associate Technical Editor: H. Lukas.

to the present work. On the basis of data obtained using flow visualization, surface-mounted hot-film anemometers and blade surface pressure tappings, this work has shown that separation bubbles exist on the rear part of the suction surfaces of many of the blade rows and that the behavior of these bubbles is affected by the presence of upstream wakes. In a complementary study, Arndt (1993) observed the strength of the wakes issuing from each rotor row in a four-stage LP turbine and concluded that wake-induced rotor–rotor interactions may be as significant as rotor–stator and stator–rotor interactions.

Wake-Induced Transition

In this section, only a brief introduction to the main features of wake-induced transition is provided. Mayle (1991) and Hodson et al. (1992) provide further details.

As the wakes are convected over the surface of the blade at the free-stream velocity, the laminar boundary layer is simply disturbed by the wake. However, at some point (typically, when Re_θ = 90–150), the boundary layer is sufficiently receptive to disturbances that the wakes cause the onset of transition. In both steady and unsteady cases, boundary layer transition is understood to occur through the formation of turbulent spots in an otherwise laminar flow. The spots have delta-like shape when viewed normal to the surface. As a spot moves downstream, it spreads longitudinally and laterally. Eventually, the leading edges of some will catch up with the trailing edges of others, while others merge in the spanwise direction (see Narasimha, 1985).

In wake-induced transition, the spots are formed in the boundary layer underneath the wake. In cases where the wake turbulence is very high, the rate of spot formation may be so great that the spots merge almost immediately to form a spanwise turbulent strip. In these cases, the flow periodically changes between laminar and turbulent states (Doorly, 1987). In other cases the formation rate is lower, individual spots may be seen in the wake-affected region (Hodson and Addison, 1989) and the flow oscillates between laminar and intermittently turbulent states. In either case, the trailing edge of the transition strip propagates at the speed of the rear of the individual spots, i.e., a half of free-stream velocity, while the leading edge propagates at approximately the free-stream velocity. For this reason the transitional/turbulent strips may eventually merge unless natural transition intervenes.

The relative significance of wake-induced and natural transition may be estimated using a distance–time diagram such as that of Fig. 1. The hatched area represents the transitional/turbulent flow. Wake-induced transition begins at a distance s_t from the leading edge. Assuming that the wakes induce the formation of fully turbulent strips, the time-mean intermittency $\bar{\gamma}$ at a distance s from the leading edge is equal to the ratio of the time it takes for the turbulent zones to pass over the location in question to the period time T. The time taken to pass over the location in question is governed by the distance $(s - s_t)$ and by the propagation rates of the leading and trailing edges of the turbulent strip. If these are assumed to be equal to the free-stream velocity and one half of the free-stream velocity U, respectively, then the maximum intermittency that

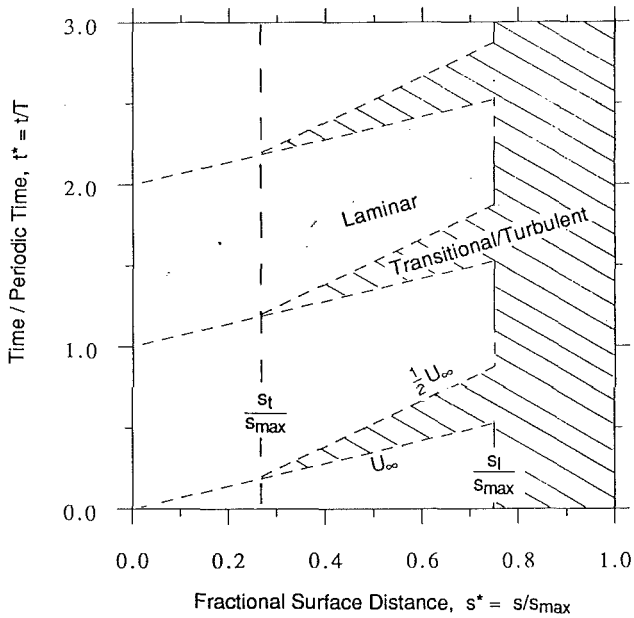

Fig. 1 Schematic distance–time diagram of boundary layer states assuming constant free-stream velocity (Hodson, 1989)

can be reached prior to natural transition at s_l is given by the value of the reduced frequency parameter $\bar{f}$, i.e.,

$$\bar{\gamma}(s_l) = \frac{1}{T}\int_{s_t}^{s_l}\left(\frac{1}{U_{te}} - \frac{1}{U_{le}}\right)ds = \bar{f} \approx f\frac{s_l - s_t}{U} \qquad (1)$$

Hodson (1989) showed that this parameter could be used to correlate the effects of waked-induced transition on profile loss if the loss data were expressed in a suitable form. When $\bar{f}$ is less than unity, natural transition should occur between wake-passing events.

Using typical values of the important parameters, it is possible to show that in LP turbines, the values of $\bar{f}$ rarely exceed 0.3. Thus, wake-induced transition is unlikely to be complete before natural transition occurs. This is the situation depicted in Fig. 1. It is for this reason that investigations have revealed the presence of laminar separation bubbles in LP turbines. For the same reason, the work reported by Dong and Cumpsty (1990) and Addison and Dong (1989) on the effect of wakes on compressor blades revealed that separation bubbles exist in LP compressors. They also observed that the wakes had very little effect on the profile loss of the compressor blades. This was because the value of $\bar{f}$ was small. This is an encouraging result. The present study was instigated, in part, to confirm the extent of the wake-affected regions of the boundary layer flow in LP turbines. The behavior of the boundary layers is explained through a detailed examination of data obtained using surface-mounted hot-film anemometers.

Test Facility and Instrumentation

Test Facility. A new facility has recently been commissioned at Rolls-Royce for the testing of the new generation of

Nomenclature

A = calibration constant
E = anemometer voltage
E_0 = anemometer voltage under zero-flow conditions
f = wake-passing frequency
$\bar{f}$ = reduced frequency (see Eq. (1))
k = calibration constant
Re = Reynolds number based on axial chord and exit velocity
s = surface distance
s^* = fractional surface distance = s/s_{max}
s_l = start of natural transition
s_t = start of wake-induced transition
T = periodic time
t = time measured from once-per-revolution trigger
t^* = fractional time = t/T
U = free-stream velocity
γ = intermittency
τ_w = wall shear stress = $(E^2/E_0^2 - 1)^3$, arbitrary units

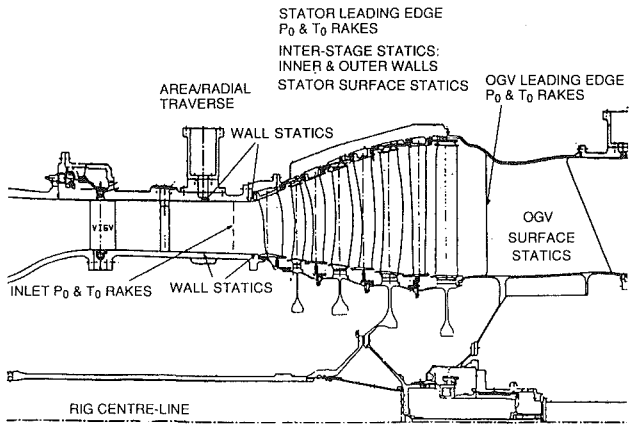

Fig. 2 Schematic of Trent 700 LP turbine parts rig as configured for present investigation

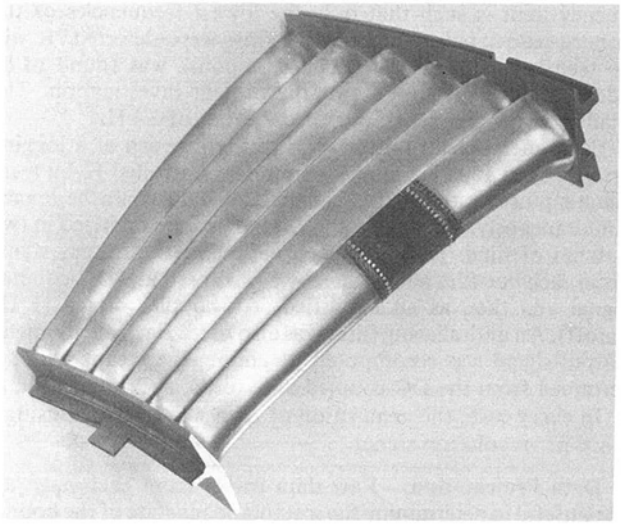

Fig. 3 Instrumented stator segment

LP turbines. It is a cold-flow facility that accommodates engine-size rigs. The facility uses a pressurized air supply in conjunction with an exhaust extraction system and a variable speed brake. The full range of operating conditions can be obtained. Figure 2 illustrates the LP turbine.

The design of the LP turbine has been described in a previous publication (Scrivener et al., 1991). The new aerofoils were intended to control the development of the boundary layers on the suction and pressure surfaces and to provide an improved tolerance to changes in incidence. Three-dimensional design methods were used to determine the stacking of the aerofoils and the vortex distributions in order to limit the spanwise migration of the viscous flows.

Surface Mounted Hot-Film Anemometers. The present paper is specifically concerned with the development of the suction-side boundary layer on the stator of the third stage of the LP turbine. It was investigated using a multi-sensor array of surface mounted constant-temperature hot-film anemometers.

The array consisted of 18 individual sensors, each 1 × 0.1 mm in size, spaced at intervals of 3 mm in the direction of the flow. It was similar to those used in the Transonic Cascade Facility at the Whittle Laboratory (Hodson, 1983, 1985a). The array covered the entire surface length of the blade. It was bonded directly to the original surface of a blade. Calculations had shown that the effect on the pressure distribution of increasing the blade thickness, by an amount equal to the thickness of the array and adhesive (72 μm), was minimal. The array was placed at approximately 60 percent of span. The line of the sensors was aligned with the predicted streamwise direction. Figure 3 shows the instrumented blade. With a height-axial chord ratio of 7.5, the array is far from the regions of secondary flow.

The similarity between the velocity profile adjacent to the wall and the temperature profile of the thermal boundary layer, generated by the heated sensor, leads to a relationship between the rate of heat transfer to the fluid and the wall shear stress of the form (e.g., Bellhouse and Schultz, 1968)

$$\tau_w = k\left(\frac{E^2 - A^2}{\Delta T}\right)^3 \tag{2}$$

where k is a constant, ΔT is the temperature difference between the air and the heated sensor, E is the instantaneous output voltage from the anemometer bridge, and the constant A represents the heat lost to the substrate. The constants A and k in Eq.(2) may be determined by calibration. In the present investigation, this was not possible since the array was permanently fixed to the blade. However, uncalibrated hot films can provide qualitative or semiquantitative data about the state of the boundary layers.

Semiquantitative data can be obtained because the rate of heat lost to the substrate, which is proportional to A^2 (Eq. (2)), is approximately proportional to the square of the voltage E_0 measured under zero-flow conditions (Hodson, 1983, and 1985b). In practice, the heat transfer under zero-flow conditions is a result of conduction to the substrate and natural convection and radiation to the air from the sensor and from the plated leads, which form part of the electrical circuit on the substrate. However, the major component is due to the conduction to the substrate from the sensor.

If the approximations above are valid and if the bulk temperature of the blade is equal to the air temperature, which will normally be the case, then the temperature difference ΔT is proportional to E_0^2 and so the data may be presented in the form

$$\tau_w \propto \left(\frac{E^2 - E_0^2}{E_0^2}\right)^3 \tag{3}$$

This form also reduces the effects of the small differences in sensor area, sensor and lead resistance, etc., upon the calibrations of the various sensors so that the output from different sensors can be compared. It allows us to attach significance to the *relative* magnitude of the hot-film output signals. Of course, the units associated with the quantity τ_w are arbitrary. In practice, the effects of changes in air density should also be considered, but this is usually unnecessary.

The quantity $(E^2 - E_0^2)$ is of the same order as E_0^2. Thus, the accuracy of the measurement of τ_w is very dependent upon an accurate knowledge of the zero-flow voltage at the temperature of the air encountered during the rig tests. It is possible to obtain this value by setting the overheat temperature ΔT of each gage so that it is equal to that when E_0 is measured under, say, cooler ambient conditions (Schröder, 1991). This can be time consuming. In the experiments described below, a different procedure was adopted. The anemometer circuits were operated at constant resistance. The required E_0–temperature characteristics of each sensor were obtained in an oven. Operation at constant resistance does mean that the overheat temperature ΔT varies as the air temperature changes. This affects the quality of the data obtained if the overheat temperature becomes too small. In obtaining the results described here, the sensor temperatures were approximately 230–275°C. The air temperature varied between 96 and 98°C but ranged from 66 to 109°C for all of the test points.

Signal Processing and Data Acquisition. The upper frequency limit of the sensors, as indicated by "square-wave" tests, was of the order of 20 kHz to 30 kHz. The upper fre-

quency limit is such that only the lowest frequencies of the spectra associated with turbulent flow were detected. It will be seen below that the frequency response was found to be adequate for the purposes of the present investigation. The blade passing frequency was of the order of 3 kHz.

Each anemometer output signal was recorded at a logging frequency of 100 kHz using a computer-controlled 12-bit transient-capture system. Nine channels of data could be logged simultaneously. Therefore, the 18 signals were digitized in two batches of nine. During each experiment, the output signal from each hot-film anemometer was acquired as a DC-coupled signal and then as an amplified, AC-coupled signal (1 Hz cutoff). An anti-aliasing filter was also used. Each anemometer output signal was recomposed by adding the mean value determined from the DC-coupled data to the AC-coupled data.

In every case, the acquisition of data was triggered using a once-per-revolution signal.

Data Presentation. Raw data traces from each gage are very useful in determining the instantaneous state of the boundary layer. The raw data are presented in the form given by Eq. (3). When following the development of individual events through successive raw data signals, it should be recalled that data obtained using the sensors located between the leading edge and 0.48 s^* were obtained at a different time to data from the remainder of the sensors.

The use of phase-locked averaging to process data that has been obtained in rotating machinery is a well-established technique. All the measured voltages were converted according to Eq. (3) prior to the determination of the statistical quantities. The ensemble-mean of N realizations of τ_w (t, n) is then defined by

$$\langle \tau_w(t) \rangle \equiv \frac{1}{N} \sum_{n=1}^{N} \tau_w(t, n) \tag{4}$$

where t is measured from a once-per-cycle datum point for a periodic process. The time-mean of $\tau_w(t, n)$ is denoted by $\bar{\tau}$.

The ensemble-root-mean-square is defined as

$$\text{rms}(t) \equiv \sqrt{\langle\langle \tau_w(t)^2 \rangle\rangle} = \sqrt{\frac{1}{N} \sum_{n=1}^{N} (\tau_w(t, n) - \langle \tau_w(t) \rangle)^2} \tag{5}$$

It represents the amount of deviation, positive or negative, from the average value of the signal at that phase.

The ensemble-skew is defined as

$$\frac{\frac{1}{N} \sum_{n=1}^{N} (\tau_w(t, n) - \langle \tau_w(t) \rangle)^3}{\langle\langle \tau_w(t)^2 \rangle\rangle^{3/2}} \tag{6}$$

It is a characteristic of surface-mounted hot-film output signals that high positive skew is found in flows with low intermittency where turbulent "spikes" interrupt the lower laminar signal. Conversely, negative values of skew are expected toward the end of transition. The skew is almost zero at about 50 percent intermittency. However, the positive skew early in transition is usually more obvious than the later negative skew in investigations of this type.

For presentation of the unsteady measurements, the time t is nondimensionalized with respect to the wake passing period T. The surface distance coordinate s has been measured from the geometric leading edge. It is usually expressed as a fraction of the maximum surface distance s_{max}.

Results and Discussion

The data obtained at an intermediate Reynolds number of 1.3×10^5 will be examined in detail in the following paragraphs. At an incidence angle of -5 deg, the blade is operating close to its design point at this condition.

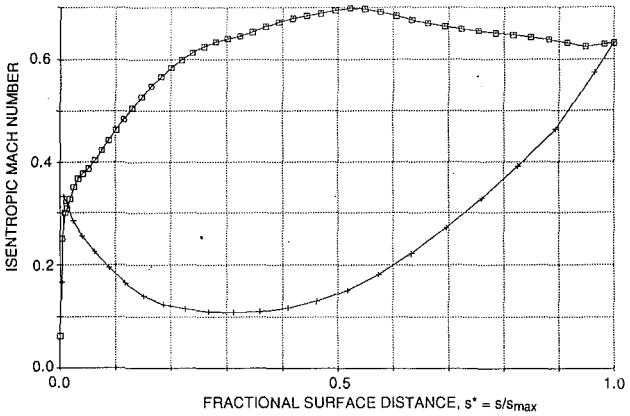

Fig. 4 Predicted blade-surface Mach number distributions for the stream surface corresponding to hot-film gage location

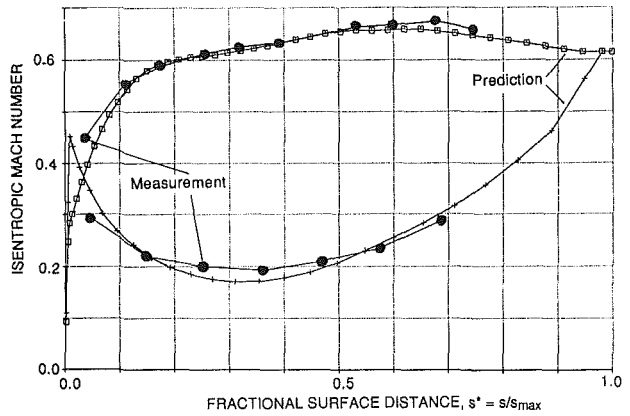

Fig. 5 Measured and predicted blade-surface Mach number distributions for midheight stream surface of stator 4 at the design condition

Mach Number Distribution: Re = 1.3 × 10^5. The array of hot-film sensors was located at approximately 60 percent of span. The predicted Mach number distribution corresponding to this location is presented in Fig. 4. It shows that the maximum velocity on the suction surface is located near 0.52 s^* and that there is approximately a 10 percent reduction in velocity over the rear half of the suction surface. Predictions of the boundary layer development indicate that should laminar separation occur, the separation point would be located at 0.62 s^* on the suction surface.

The accuracy of the predicted Mach number distribution may be determined from Fig. 5. This provides a comparison between measured and predicted values on the fourth-stage stator at 50 percent span.

Raw and Ensemble-Mean Hot-Film Data: Re = 1.3 × 10^5. Figure 6 presents a selection of the raw hot-film data traces. The most important aspect of these data is provided by the trace at 0.75 s^*. The form of this trace is typical of those observed in an intermittently separated flow. The baseline of the signal is almost equal to zero, which indicates a very low level of shear stress. The positive value of the wall shear stress during these intervals of apparent separation probably arises because the quantitative value of the data is limited by the approximations implied when using Eq. (2) to process the data. Upstream, at 0.64 s^*, the minimum level of the signal is greater than at 0.75 s^*, suggesting that separation occurs between 0.64 s^* and 0.75 s^*. Steady flow predictions indicate that separation might occur at 0.62 s^*. This discrepancy is not

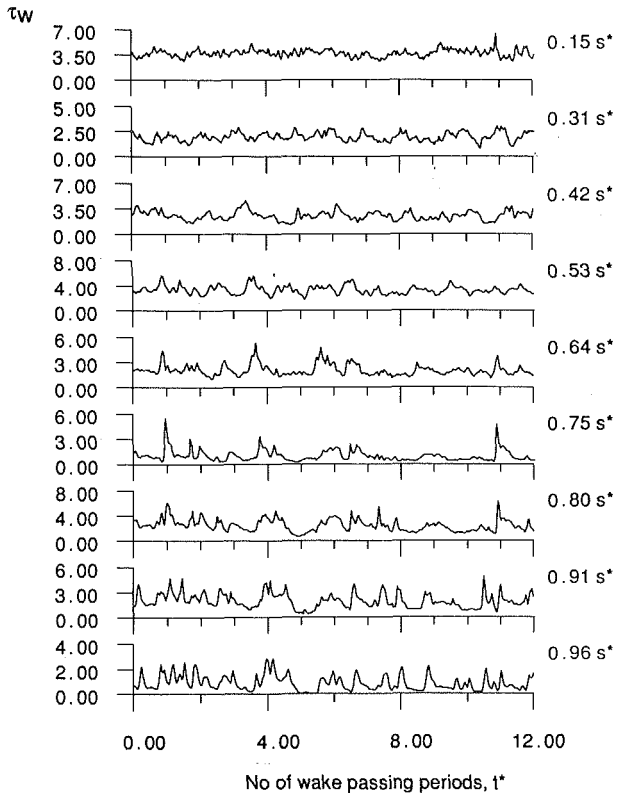

Fig. 6 Raw hot-film traces, Re = 1.3 × 10^5

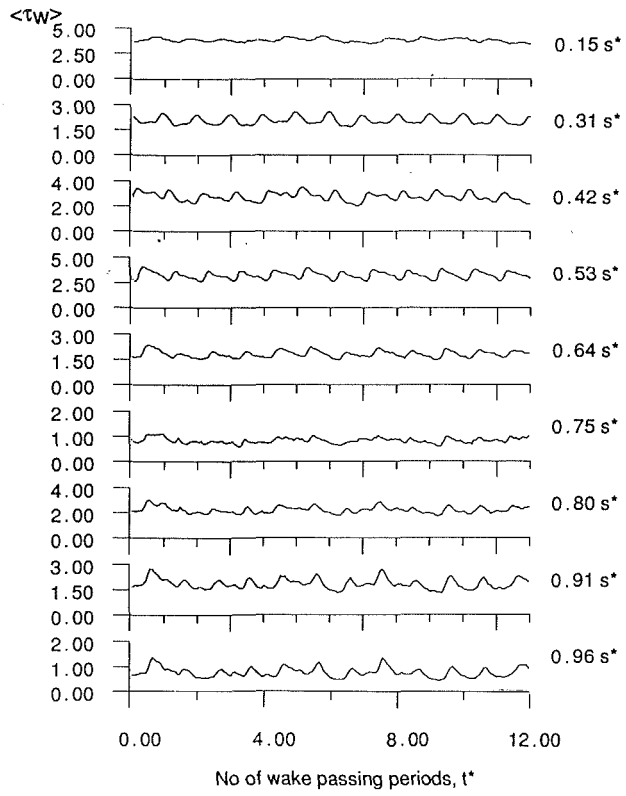

Fig. 7 Ensemble-mean hot-film traces, Re = 1.3 × 10^5

unreasonable. It is unfortunate that one of the few gages to fail was located between 0.64 s^* and 0.75 s^*.

In the signal at 0.75 s^*, the intervals of laminar separated flow are punctuated by upward spikes and longer duration events of an intermediate height. Gostelow et al. (1992) provide a correlation for the rate of production of turbulent spots when bypass transition occurs in attached decelerating flows. This correlation indicates that if transition occurred at, say, the predicted separation point (0.62 s^*), of the order of 20 spots would be produced during one wake-passing cycle over the width of the hot-film sensors (i.e., per millimeter of span). The correlation is not valid for separated flows but the value may be taken as an indication of the level of spot production that might be expected in the vicinity of the separation zone.

The raw traces of Fig. 6 suggest that individual spots or, at least, small collections of coalesced spots may have been detected by the sensor at 0.75 s^*. The spots are believed to be represented by the spikes of relatively high shear stress. This conclusion is supported by the observation that the spikes tend to occur just after a period when the level of the shear stress indicates that separation has occurred, though not exclusively so. Transition is more likely to occur in a separated flow. Hodson (1983) used similar gages to study transition in steady-flow cascades where the length scales and time scales were similar to those found in the present experiment. Spikes of a similar duration were observed underneath laminar separation bubbles during laminar–turbulent transition.

The longer duration events noted above tend to appear at preferred parts of the wake-passing cycle. However, they do not appear every wake-passing cycle. Indeed, a comparison of the ensemble-mean traces of Fig. 7 with the raw data of Fig. 6 shows that there are considerable differences between the passing of individual wakes. The longer duration events are thought to be associated with wake-induced transition. At 0.75 s^*, Fig. 6 shows that these have a time scale that is typically of the order of 0.5–1.0 t^*. At the mean convection speed of a turbulent spot, this corresponds to a length-scale of the order of 0.5–1.0 s^*. Thus, the longer duration events must originate upstream of the region of separated flow. In fact, their origin can be seen to be considerably upstream of 0.75 s^*.

It will be argued below that wake-induced transition begins near 0.42 s^*. Indeed, Fig. 6 contains evidence to support this view. At this position, the Reynolds number (Re_θ) based on the momentum thickness of the laminar boundary layer is predicted to be approximately 130. This is not untypical (Hodson et al., 1992) of the values encountered at the start of wake-induced transition. At this location, the correlation of Narasimha (1985), which is strictly valid only for bypass transition in steady zero pressure gradient flows, would suggest that approximately one turbulent spot should be produced during one wake-passing cycle over the width of the hot-film sensors (i.e., per millimeter of span). Therefore, it is unlikely that many individual spots would be detected. This will be discussed further below.

Downstream of 0.75 s^*, Fig. 6 reveals that the spikes that first appeared in the trace at 0.75 s^* have increased in duration. Also, apparently new, shorter duration spikes appear for the first time. Since data were only obtained at one spanwise location, it is impossible to determine if the shorter duration spikes have formed between adjacent measurement locations or if they are associated with the spanwise spreading of spots that originated upstream at a different spanwise location. Whatever the case, it is clear from Fig. 6 that the rate of transition is such that laminar flow persists as far as 0.96 s^*.

Supporting evidence that the flow remains intermittent at the trailing edge is provided by the ensemble-mean traces, which are presented in Fig. 7. These show that there is considerable variation in the height of the ensemble-mean traces. This is unlikely to be the case if the flow were fully turbulent because a turbulent boundary layer is much less affected by the presence of the wakes or the effects of its history than an intermittent boundary layer (Addison and Hodson, 1990).

Even though laminar flow exists at 0.96 s^*, this should not be regarded as indicating that time-mean re-attachment has

Table 1 LP turbine blade numbers and beating frequencies

Bladerow	Number of Blades	Beats/Rotor Rev. in Inlet Flow
Stator 1	102	-
Rotor 1	140	-
Stator 2	130	-
Rotor 2	84	14
Stator 3	120	28
Rotor 3	84	5
Stator 4	120	-
Rotor 4	84	-
OGV	12	-

not occurred. At the trailing edge, the minimum level of shear stress is usually approached in the raw traces only when the period between elevated levels of shear stress is greater than the wake-passing interval. This indicates that although the flow may be laminar at times, it is usually attached when in that state. In addition, Fig. 7 indicates that the minimum ensemble-mean value is greater than that indicated in the raw traces at 0.96 s^*. If the description above of the flow is correct, then it would seem that the wakes play a part in the re-attachment of the separated flow.

Blade Row Interactions: Re = 1.3 × 10^5. The discussion above has suggested that transition to turbulent flow occurs as a result of the wake-passing and as a result of laminar separation. As explained in the introduction, this was expected since the value of f is much less than unity in most LP turbines. Binder et al. (1989), Arndt (1993), and Schröder (1991) have also demonstrated that separation bubbles can exist on the suction surfaces of LP turbine blades. In addition, they found that the behavior of these bubbles was affected by the presence of upstream wakes and that rotor–rotor interactions may be as significant as rotor–stator and stator–rotor interactions. Rotor–rotor interactions were detected due to the occurrence of bearing in the anemometer output signals.

In the present experiment, the frequency of the beats is determined by the difference in the number of rotor blades in the preceding two rotor blade rows. The blade numbers and resulting frequencies of beating are listed in Table 1. For stator blades of the third stage, the bearing frequency of the inlet flow is one third of the passing frequency of the rotor blades immediately upstream. The ensemble-mean traces of Fig. 7 contain no evidence of rotor–rotor interactions. Frequency spectra also confirm that there are no significant rotor–rotor interactions.

In the present turbine, the wakes are likely to be weaker than in the LP turbines reported by Binder et al. (1989), Arndt (1993), and Schröder (1991). This is mainly because the level of suction surface deceleration is much lower in the present turbine. The Reynolds numbers are also greater. These differences suggest that the observation of beats by these authors may be associated with the periodic separation, without re-attachment, of the laminar boundary layers on the downstream of the two interaction rotors. The separation would be prevented when the wakes from the upstream rotor are in a favorable position with respect to the downstream rotor. However, as Schröder (1991) indicates, there is insufficient evidence to draw any definite conclusions.

Distance-Time Diagrams: Re = 1.3 × 10^5. After the experiments had been performed, it became apparent that an insufficient number of ensembles (200) had been obtained, particularly with regard to the accurate determination of the higher statistical moments. Therefore, it was decided to average the data from ten successive wake-passing cycles, before presentation of the remaining data. Since only rotor–stator interactions appear to be significant in the anemometer output signals obtained in the present turbine, very little information has been lost during this process.

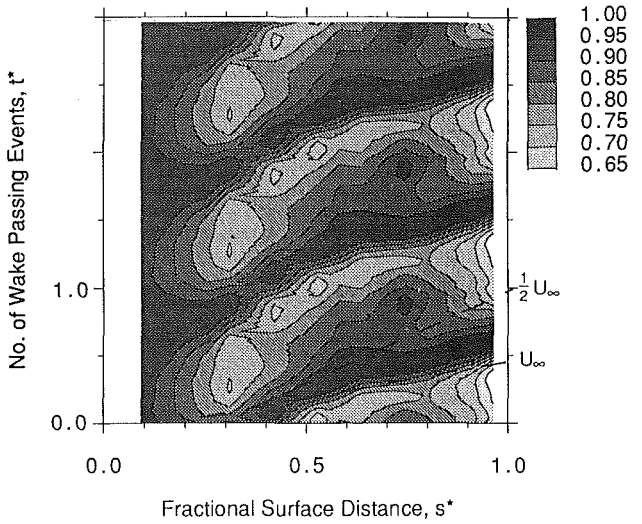

Fig. 8 Distance–time diagram of "average" ensemble-mean expressed as a fraction of its maximum value at the same surface location, Re = 1.3 × 10^5

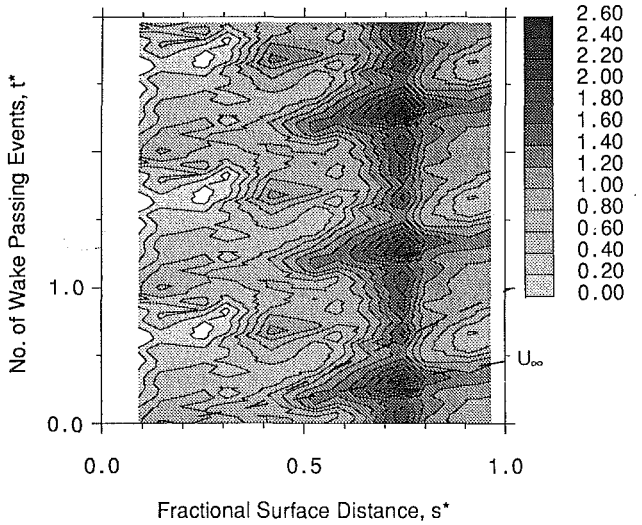

Fig. 9 Distance–time diagram of "average" ensemble-skew, Re = 1.3 × 10^5

Figure 8 presents a distance–time diagram of the "averaged" ensemble-mean shear stress. Three wake-passing intervals are shown. The contours denote the ratio of the ensemble-mean $\langle \tau_w(s, t) \rangle$ to its maximum value at the same location. This form of presentation emphasizes the periodic fluctuations at the expense of providing data on the changes in the mean level. Over much of the blade surface, there are large periodic variations in the ensemble-mean shear stress. This usually indicates the presence of wake-induced transition. Figure 9 presents the ensemble-skew for the same case. Figure 10 shows the ensemble-rms, also expressed as a fraction of its maximum value at the same location. Trajectories corresponding to the free-stream velocity and one half of the free-stream velocity are shown in each of the figures. The wake is expected to convect at approximately the free-stream velocity. The rear portions of turbulent spots are expected to travel at about one half of the free-stream velocity.

Like Fig. 8, Fig. 9 contains evidence of periodic, wake-induced transition. Ridges of positive ensemble-skew run almost parallel to the trajectory, which corresponds to the free-stream velocity (U_∞) as indicated by the broken line. It would seem that these ridges begin at the first measurement location,

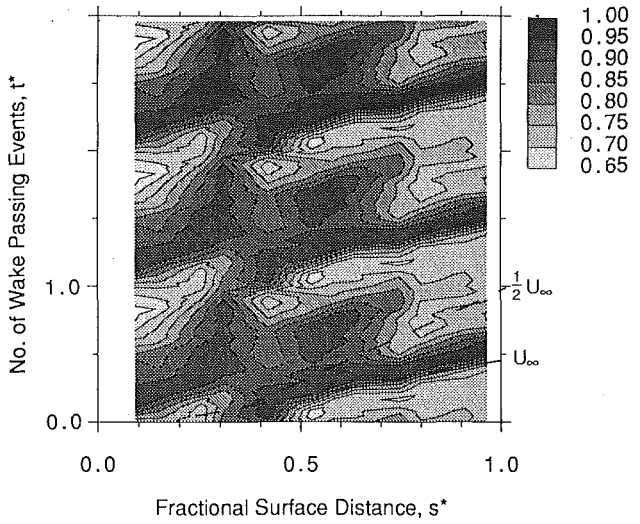

Fig. 10 Distance-time diagram of "average" ensemble-rms expressed as a fraction of its maximum value at the same surface location, Re = 1.3 × 10^5

but this is thought to indicate no more than the effect of the turbulence on the laminar boundary layer. However, near 0.4 s^*, the leading edge and the trailing edge of these ridges diverge as the ridges begin to rise significantly. The slowing of the trailing edge is consistent with the onset of transition under the wake. This rise in the value of the ensemble-skew, particularly near the leading edge of the wake-affected region, and the appearance of relatively high values of the ensemble-rms (Fig. 10), also indicate the start of transition. Thus, the data suggest that wake-induced transition begins near 0.4 s^*. Indeed, examination of the raw data presented in Fig. 6 reveals some evidence of turbulent events downstream of this location.

If the wakes were to initiate the formation of turbulent spots, then the trailing edge of the wake-affected transition region would propagate at a rate of about one half of the free-stream velocity (i.e., at the speed of the trailing edge of a turbulent spot) rather than the free-stream velocity (the speed of the trailing edge of the wake). In Fig. 9, it can be seen that the rate of propagation of the rear of the wake-affected transitional flow is approximately equal to this value except, perhaps, downstream of peak suction (0.52 s^*). However, it also appears that the leading edge of the wake-affected flow moves faster than the wake. Again this is more pronounced downstream of peak suction. Doorly and Oldfield (1985) and Addison and Hodson (1990), in very different turbines, have also observed similar features in distance-time diagrams.

An explanation of the shape of the outline of the ridges of positive ensemble-skew is provided by Addison and Hodson (1990). In the general case of a narrow wake, the first spots are most likely to occur near to the centerline of the wake where the turbulence is greatest. However, there is an undisturbed (i.e., laminar) boundary layer downstream, which, as it develops, becomes capable of undergoing transition at the lower levels of free-stream turbulence, which are to be found away from the centerline of the wakes. Therefore, further spots can form downstream of the origin of those formed nearer the front of the blade. Since the data are ensemble averaged, the loci of the leading edges in Fig. 9 will tend to indicate the leading boundary of spot formation and not those of individual spots. Even so, the present data seem to indicate that the majority of spot production takes place near the centerline of the wake and that the spots that develop ahead of the wake are unlikely to be significant in the development of the boundary layer.

A closer examination of the ridges of positive ensemble-skew, which have been noted in Fig. 9, reveals that the ridges resemble a rising escarpment with the steep side occurring first in time. This is to be expected during wake-induced transition. Toward the rear of the wake-affected transitional flow, the boundary layer is generally more turbulent (see Hodson et al., 1992). If it were turbulent, negative ensemble-skew would be expected in the current environment. In this case, the ensemble-skew remains positive toward the rear of the zone. This suggests that the wake-affected flow is transitional rather than turbulent.

Wake-induced transition would seem to begin near 0.4 s^*. If steady flow bypass transition commenced at the same position, the correlation of Narashima (1985) suggests that the intermittency would be approximately 50 percent just before separation. The maximum intermittency in the wake-affected flow should be close to this value (Hodson et al., 1992) if the correlation is valid. In fact, the flow is accelerating at 0.4 s^*. This would give rise to a lower rate of spot formation and a lower maximum value of intermittency. Nevertheless, the correlation and the data seem to suggest that the wake-affected flow is transitional as it approaches the separation zone.

When the wake-induced transitional flow reaches the neighborhood of the separation zone (i.e., 0.75 s^*), it appears to occupy approximately 40 percent of the wake-passing interval. The simple analysis (Eq. (1)), which is based on Fig. 1, would suggest that the wake-affected zone should occupy approximately 25 percent of the wake-passing period. This difference may be explained by reference to the arguments presented above regarding the apparent propagation rates of the leading and trailing edges of the wake-induced transitional flow.

The ridges of ensemble-skew, which have been described in detail, reach a maximum value near 0.75 s^*. At this location they intersect another ridge of positive ensemble-skew. The position of this ridge is shown by the broken vertical line. The ridge appears to be stationary but its height varies with a period equal to the wake passing interval. The presence of this ridge indicates the formation of turbulent flow within the separated laminar flow region. It is significant that the ridge of positive ensemble-skew, which denotes transition within the separated flow, persists for the entire wake passing cycle. This is because it suggests that separated flow persists even within that part of the flow that, on average, is affected by the wake-induced transition. Turbulent flow will not separate from this blade. This supports the hypothesis that the part of the flow that, on average, is affected by the wake-induced transition must be intermittently laminar as it approaches the separation zone near 0.75 s^*.

In practice, it would seem most appropriate to visualize the transition process on this blade as proceeding by way of one of two mechanisms. Either, the passing of a given wake creates a turbulent spot or series of spots at or near the spanwise location in question or it does not. If it does not, the persisting laminar flow probably separates and undergoes transition as a result. The probability that the flow is not turbulent as it approaches the separation zone depends on the level of intermittency associated with the wake induced transition. The ensemble-skew associated with transition in the separated flow is lowest toward the rear of the region of influence of the wake where the intermittency is highest. The regions of relatively low ensemble-skew downstream of 0.9 s^* arise for the same reason. They indicate that the most turbulent flow is to be found downstream of the separation zone within the flow affected by the wake.

To predict the intermittency of the type of flow described above, one must define the shape of the so-called "dependence volume" and the spot formation rate within that volume. As noted by Narasimha (1985), the approach required for unsteady flow is essentially the same as it is for steady flow. As yet, the definition does not exist for unsteady flow. It is not sufficient to assume that the two forms of transition are distinct.

The outline of the wake-induced transition zone, as deduced from the distance–time diagram of the ensemble-skew, is also shown in the distance–time diagram of the ensemble-mean (Fig. 8) and the ensemble-rms (Fig. 10). At any given surface distance between 0.5 and 0.75 s^*, the highest values of ensemble-mean shear stress occur after the highest values of ensemble-skew have been reached. The highest values of the ensemble-rms also occur after the highest values of ensemble-skew have been reached. These observations are to be expected if transition proceeds by way of the formation of turbulent spots. The highest values of the ensemble-mean and ensemble-rms lie between the lines identifying the free-stream velocity and one half of that rate. This is to be expected if wake-induced transition begins near the centerline of the wake as noted above. Upstream of 0.5 s^*, Fig. 8 shows that the phase of the ensemble-mean shear-stress varies more rapidly than would be expected from a simple convective argument. The reasons for this are not properly understood but they are believed to be associated with the nature of the wake distortion, which generally takes place over the leading part of an aerofoil. Similar changes also take place in the phase of the ensemble-rms upstream of 0.5 s^* (Fig.10).

Between 0.65 s^* and 0.75 s^*, Fig. 8, Fig. 9, and Fig. 10 reveal that the phase of the ensemble-mean shear stress, the ensemble-skew, and the ensemble-rms advances relative to that of the free-stream. This change of phase occurs as the wake enters the region of laminar separation. It is believed that this phase change is associated with the production of turbulent flow. If this is so, then it may be argued that the change in relative phase may simply arise because, as the flow approaches separation or separates, it becomes more receptive to free-stream disturbances. Therefore, it becomes susceptible to influences of a lower intensity, which lie farther downstream of the centerline of the wake than those that are responsible for transition upstream. This change of phase may be similar to the much larger change in phase (type. 180 deg), which is visible in the results presented by Schröder (1991). Similar, unpublished observations have been made by the author in cascade tests where LP turbine blades were subjected to incoming wakes. However, both of the above-mentioned investigations were carried out at a lower Reynolds number using higher-lift blades. Consequently, the phase shift observed in these investigations is more likely to be associated with the appearance of the more dominant transition in the separated shear layer in between the wake-passing events.

One interesting feature of Fig. 8, Fig. 9, and Fig. 10 remains to be described. This is the existence of regions of the flow that appear to be less susceptible to transition. They are identified by the relatively low levels of ensemble-mean, ensemble-rms, and ensemble-skew that lie just downstream of the wake-induced transition zones. Their presence is also suggested by the traces in Fig. 6 and Fig. 7. The reasons for these "quiet zones" of laminar flow are not understood. It is possible that they are associated with the negative-jet effect of the wakes (see Hodson, 1985a), which would lead to an acceleration of the flow toward the downstream side of the wake. This may encourage the boundary layer to remain attached and, therefore, laminar.

The observation above may be compared with that of Dong and Cumpsty. They reported "becalmed" regions toward the rear of the wake-induced suction-side transitional flow in their compressor cascade experiments. On the suction surface of a compressor blade, the acceleration takes place toward the upstream side of the wake. Thus, while the wakes seem to promote transition during some parts of the wake-passing cycle, it is also possible that they discourage transition during others. This aspect of the flow clearly requires further investigation before the overall impact of the wakes may be fully understood.

Off-Design Conditions: Re = 0.9 and 1.8 × 10^5. Figure 11 presents a selection of the raw data traces, which were obtained at a Reynolds number of 0.9 × 10^5. The Reynolds number was varied by altering the inlet pressure to the turbine while maintaining the same pressure ratio, inlet temperature, and rotational speed. Thus, these data can be compared directly with those presented in Fig. 6.

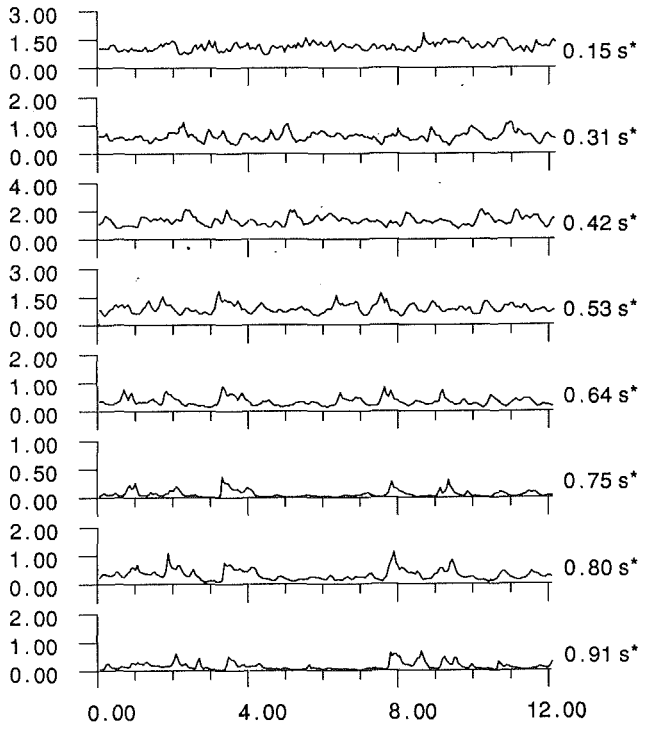

Fig. 11 Raw hot-film traces, Re = 0.9 × 10^5

At the lowest Reynolds number, the traces at 0.75 s^* and beyond indicate that there are very few turbulent events. Consequently, the most common state of the boundary layer appears to be that of separated laminar flow. Unfortunately, the instrumentation associated with the gage at 0.96 s^* temporarily malfunctioned during the acquisition of this data so that the DC-coupled values were unavailable. However, the character of the data at 0.96 s^* was very similar to that at 0.91 s^*. This indicates that re-attachment of the flow was unlikely. In all other respects, the nature of the flow at the lowest Reynolds number was found to be similar to that described above for the Reynolds number of 1.3 × 10^5. In particular, transition began as a result of wake-boundary layer interactions and separation of the laminar flow. The most turbulent flow was found to be associated with the passing of the wakes.

The raw data plotted in Fig. 12 were obtained at a Reynolds number of 1.8 × 10^5. This figure may be compared with Fig. 6 and Fig. 11. Again, the flow has the character associated with separated flow at 0.75 s^*. As expected, the flow appears to be much more intermittent at the highest Reynolds number. Many more turbulent spikes appear to have formed within the separation zone. More may also be seen upstream of this region. The locations of some of the turbulent spikes coincide with wake-passing while others do not. In addition, the number of spikes present in the trace at 0.96 s^* is much greater than the number of wake-passing events. Again, it would seem that two modes of transition are present. Even so, periods of low shear stress persist up to the trailing edge though the laminar flow with which they are associated is unlikely to be separated at this location.

Conclusions

The development of the boundary layer on the suction sur-

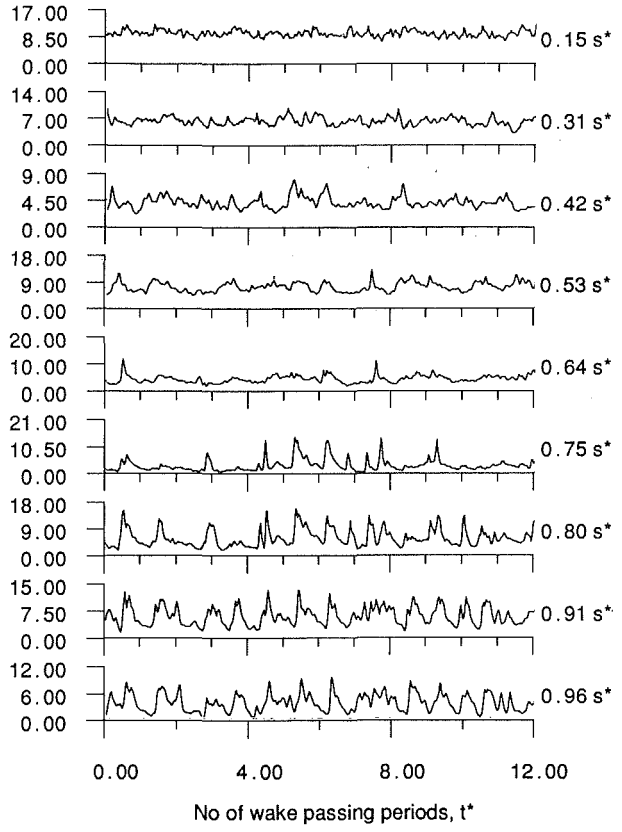

Fig. 12 Raw hot-film traces, Re = 1.8 × 10^5

face of an embedded LP turbine stator blade has been investigated using surface-mounted hot-film anemometers. The tests have confirmed the effectiveness of the methods used to design the LP turbine aerofoils insofar as attached flow is obtained at the trailing edge of the suction surface at the design condition.

Transition occurs as a result of laminar separation both inside and outside the wake-affected transitional flow. Thus, the use of steady-flow predictions methods might be sufficient to enable the production of acceptable aerofoils for use in LP turbines. However, there is evidence to suggest that the process of transition in the separated flow region is influenced by the presence of the wakes. Consequently, a design produced by the application of steady flow methods may not represent the optimum that can be achieved and improved prediction methods may be required.

Acknowledgments

The authors wish to thank M. Underwood of the Whittle Laboratory for his help in the development of the hot-film technique. The contribution to the acquisition and processing of the data by C. A. Shepherdson, formerly of the Whittle Laboratory and Rolls-Royce, is also acknowledged.

References

Addison, J. S., and Dong, Y., 1989, "Unsteady Wake-Boundary Layer Interaction in a Compressor Cascade," *Proc. 5th Int. Symp. on Unsteady Aerodynamics and Aeroelasticity of Turbomachines and Propellers*, Beijing, Sept. 18–21, pub. IAP.

Addison, J. S., and Hodson, H. P., 1990, "Unsteady Transition in an Axial Flow Turbine, Part 1: Measurements on the Turbine Rotor," ASME JOURNAL OF TURBOMACHINERY, Vol. 112, pp. 206–214.

Addison, J. S., and Hodson, H. P., 1992, "Modeling of Unsteady Transitional Boundary Layers," ASME JOURNAL OF TURBOMACHINERY, Vol. 114, pp. 580–589.

Arndt, N., 1993, "Blade Row Interaction in a Multistage Low-Pressure Turbine," ASME JOURNAL OF TURBOMACHINERY, Vol. 115, pp. 137–146.

Bellhouse, B. J., and Schultz, D. L., 1968, "The Measurement of Fluctuating Skin Friction in Air With Heated Thin-Film Gauges," *Journal of Fluid Mechanics*, Vol. 32, No. 4.

Binder, A., Schröder, Th., and Hourmouziadis, J., 1989, "Turbulence Measurements in a Multistage Low-Pressure Turbine," ASME JOURNAL OF TURBOMACHINERY, Vol. 117, pp. 153–161.

Dong, Y., and Cumpsty, N. A., 1990, "Compressor Blade Boundary Layers: Part I—Test Facility and Measurements With No Incident Wakes," JOURNAL OF TURBOMACHINERY, Vol. 112, pp. 222–230; "Part II—Measurements With Incident Wakes," ASME JOURNAL OF TURBOMACHINERY, Vol. 112, pp. 231–240.

Doorly, D. J., and Oldfield, M. L. G., 1985, "Simulation of the Effects of Shock Wave Passing on a Turbine Rotor Blade," ASME *Journal of Engineering for Gas Turbines and Power*, Vol. 107, pp. 998–1006.

Doorly, D. J., 1988, "Modeling the Unsteady Flow in a Turbine Rotor Passage," ASME JOURNAL OF TURBOMACHINERY, Vol. 110, pp. 27–37.

Gostelow, J. P., Blunden, A. R., and Walker, G. J., 1992, "Effects of Free-Stream Turbulence and Adverse Pressure Gradient on Boundary Layer Transition," ASME Paper No. 92-GT-380; ASME JOURNAL OF TURBOMACHINERY, in press.

Hodson, H. P., 1983, "The Detection of Boundary Layer Transition and Separation in High Speed Turbine Cascades," presented at 8th Int. Symp. on Measurement Techniques in Transonic and Supersonic Flows, Aachen, Sept.

Hodson, H. P., 1985a, "Boundary-Layer Transition and Separation Near the Leading Edge of a High-Speed Turbine Blade," ASME *Journal of Engineering for Gas Turbines and Power*, Vol. 107, pp. 127–134.

Hodson, H. P., 1985b, "Measurements of Wake-Generated Unsteadiness in the Rotor Passages of Axial Flow Turbines," ASME *Journal of Engineering for Gas Turbines and Power*, Vol. 107, pp. 467–476.

Hodson, H. P., 1989, "Modelling Unsteady Transition and Its Effects on Profile Loss," *Proceedings, AGARD Conf. PEP 74a on Unsteady Flows in Turbomachines*, AGARD CP 468.

Hodson, H. P., and Addison, J. S., 1989, "Wake-Boundary Layer Interactions in an Axial-Flow Turbine at Off-Design Conditions," ASME JOURNAL OF TURBOMACHINERY, Vol. 111, pp. 181–192.

Hodson, H. P., Addison, J. S., and Shepherdson, C. A., 1992, "Models for Unsteady Wake Induced Transition in Axial Turbomachines," *Jnl. Phys. III*, France 2, pp. 545–574.

Hourmouziadis, J., Buckl, F., and Bergmann, P., 1987, "The Development of the Profile Boundary Layer in a Turbine Environment," ASME JOURNAL OF TURBOMACHINERY, Vol. 109, pp. 286–295.

Mayle, R. E., 1991, "The Role of Laminar–Turbulent Transition in Gas Turbine Engines," ASME JOURNAL OF TURBOMACHINERY, Vol.113, pp. 509–537.

Mayle, R. E., and Dullenkopf, K., 1991, "More on the Turbulent-Strip Theory for Wake-Induced Transition," ASME JOURNAL OF TURBOMACHINERY, Vol. 113, pp. 428–432.

Narasimha, R., 1985, "The Laminar-Turbulent Transition Zone in the Boundary Layer," *Progress in Aerospace Science*, Vol. 22, pp. 29–80.

Schröder, T., 1991, "Investigations of Blade Row Interaction and Boundary Layer Transition in a Multistage Aero Engine Low Pressure Turbine by Measurements With Hot-Film Probes and Surface Mounted Hot-Film Gauges," VKI Lecture Series 1991-06, Sept. 2–6.

Scrivener, C. T. J., Connolly, C. F., Cox, J. C., and Dailey, G. M., 1991, "Use of CFD in the Design of a Modern Multistage Aero Engine LP Turbine Design," IMechE Paper No. C423/056.

The Effect of Wake-Passing and Free-Stream Turbulence on Laminar Gas Turbine Blade Boundary Layers

D. Greenblatt
Division of Aeronautical Systems Technology (Aerotek), Council for Scientific and Industrial Research, Pretoria, Republic of South Africa

A computational procedure has been developed that accounts for the combined time-mean effect of wake-passing and free-stream turbulence on laminar turbine blade boundary layers. The procedure has the advantage of being computationally efficient as well as providing a realistic model of the unsteady nature of the flow. The procedure yielded the parameter $Tu\sqrt{Re_D}/\sqrt{\sigma_D/2}$ *for characterizing the time-mean flow in the leading edge region and the parameter* $\Gamma\ (\equiv 2\tilde{T}u^2\sigma_x/\gamma)$ *for describing the flow downstream of the stagnation point. A provisional comparison with stagnation flow experimental data showed that the procedure may be more general than initially expected.*

Introduction

Accurate estimation of heat loading on the external surfaces of gas turbine blades and vanes has become vital for the effective design of modern gas turbine engines. Satisfactory prediction of the heat transfer to these surfaces still eludes the gas turbine designer due to the highly complex and interactive external flow-field environment. Among the many factors influencing heat transfer, the time-unsteady condition of the flow as it enters the blade or vane row is one of the most important (Graham, 1979). In recent years much effort has been invested in experimentally investigating the unsteady flow phenomena where actual engine operating conditions were closely simulated (e.g., Dunn et al., 1986; Dring et al., 1986; Guenette et al., 1989). In the engine, combustion processes are responsible for the generation of high-energy turbulence while periodic unsteadiness of the flow arises from the relative motion of the alternatively stationary and rotating vane and blade rows that comprise each turbine stage. Of the factors that contribute to the overall flow unsteadiness (see Schultz, 1986; Doorly, 1988), wake-passing and free-stream turbulence may be considered to dominate.

The role of wake-passing on heat transfer to turbine blades has recently received much attention (e.g., Mayle, 1991; Paxson and Mayle, 1991). Particularly, the phenomenon of laminar-turbulent transition in the presence of wakes plays a pivotal role in controlling local heat transfer rates. A new theory, which shows exceptional agreement with experiment, has recently been developed (Mayle and Dullenkopf, 1990, 1991). Despite these advances, uncertainty still remains with regard to predicting wake-induced transition onset.[1] It is envisaged that, much like flows where wakes are absent, a wake-induced transition onset parameter will be correlated with local time-mean boundary layer quantities such as momentum thickness Reynolds number and turbulence level, in addition to other wake-associated parameters. It is important to note that, even if well-validated experimental data are available, the designer will not be in a position to implement experimental data effectively without accurate modeling of the wake-perturbed laminar boundary layer. Therefore, the development of a method for accurately representing the laminar boundary layer is critical from the viewpoint of transition prediction.

Quite apart from problems related to boundary layer transition, the unsteady nature of the flow in laminar boundary layers can have a substantial effect on local heat transfer rates. These effects are apparent in, and just downstream of, the stagnation region where the laminar boundary layers are highly perturbed. The effect of a turbulent stream on these boundary layers under idealized conditions has received considerable attention over the last thirty years from experimental (e.g., Smith and Kuethe, 1966), computational (e.g., Traci and Wilcox, 1975), and theoretical (e.g., Sutera, 1965) perspectives. Traditionally, velocity fluctuations have been considered to be the primary mechanism affecting heat transfer, but recent studies indicate that density as well as stagnation enthalpy fluctuations may play a role (see Kurosaka et al., 1987; Bogucz et al., 1988; and Rigby and Rae, 1989). In recent years, simulated engine conditions have been employed to gage the effect of realistic turbulence levels on heat transfer augmentation within laminar

Contributed by the International Gas Turbine Institute and presented at the 38th International Gas Turbine and Aeroengine Congress and Exposition, Cincinnati, Ohio, May 24–27, 1993. Manuscript received at ASME Headquarters March 3, 1993. Paper No. 93-GT-204. Associate Technical Editor: H. Lukas.

[1]Currently, even in cases where wakes are absent, there is no widely accepted method for relating transition onset to local conditions within the boundary layer (Mayle, 1991).

boundary layers (e.g., Krishnamoorthy et al., 1988). The effect of a pure sinusoidal perturbation of the free stream on laminar boundary layers has also been extensively studied, but mainly from a theoretical and computational point of view (e.g., Ishigaki, 1970; Phillips and Ackerberg, 1973) while the combined effect of free-stream turbulence and a standing wave perturbation were studied computationally by Greenbiatt (1991). The effect of traveling wave disturbances, representing an idealized model of the wake-passing over turbomachinery blades, was studied both experimentally and theoretically by Patel (1975) and has received revived attention in recent times (Evans, 1989; Paxson and Mayle, 1991; Greenblatt and Damelin, 1992).

To date, no computational procedure has been developed to account simultaneously for the combined effect of high levels of free-stream turbulence and wake-passing on laminar turbine blade boundary layers. In this paper, such a procedure is presented and its advantages over other methods proposed in the literature are illustrated. Results of the numerical scheme are presented and a provisional comparison has been carried out with stagnation flow experimental data.

Free-Stream Considerations

Paxson and Mayle (1991) analyzed the effect of the wake perturbed mean velocity field and turbulence contained in the wake on the boundary layer. They argued that both wake and turbulence perturbations may be considered inviscid relative to the boundary layer, imposing upon it a complex unsteady flow. Using these arguments the free-stream edge velocity that the gas turbine boundary layer is subjected to can be considered the sum of a mean component (U_0), a wake component (U_w), and a turbulent component (u'). This so-called triple decomposition is presented schematically in Fig. 1.

The edge velocity in Fig. 1 may be mathematically expressed as

$$U_e(x, t) = U_0(x) + U_w(x, t) + u'(x, t). \quad (1)$$

Here we adopt Evans' (1989) characterization of the wake:

$$U_w(x, t) = U_1(x) \sin \omega(t - x/Q), \quad (2)$$

where $U_1(x)$ is the amplitude of the wake disturbance, Q is the wake velocity, x is the spatial coordinate in the flow direction, and t represents time. In order to distinguish between the magnitudes of the various forms of unsteadiness it is convenient to define the overall disturbance levels as

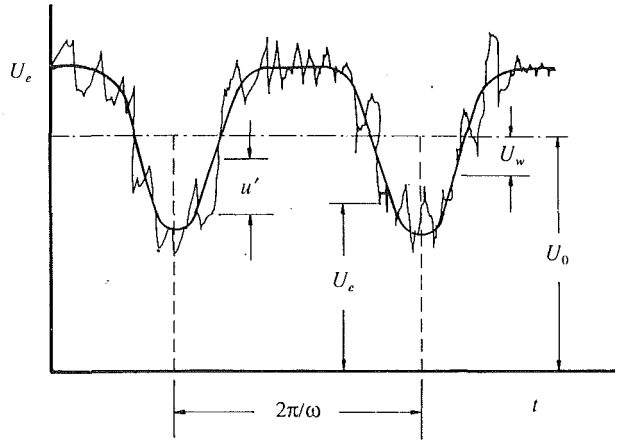

Fig. 1 Triple decomposition of an unsteady free-stream flow; adapted from Dullenkopf et al. (1991)

$$Tu_o^2 = \tilde{T}u^2 + Tu^2,$$

where $\tilde{T}u$ is the wake disturbance $U_1/\sqrt{2}U_0$ and Tu is the ensemble-averaged turbulence level $\sqrt{\langle u'^2 \rangle}/U_0$ (see Evans, 1975). Substituting Eqs. (1) and (2) into the unsteady Bernoulli equation for the free-stream, viz:

$$-\frac{1}{\rho}\frac{\partial p}{\partial x} = \frac{\partial U_e}{\partial t} + U_e \frac{\partial U_e}{\partial x}, \quad (3)$$

renders a complicated expression for the time-dependent pressure gradient $\partial p/\partial x$. Fortunately, for most design-related problems we are only interested in the time-mean flow behavior and, if the free-stream turbulence is considered to be spatially, but not temporally, frozen (see, e.g., McDonald and Fish, 1973), the expression reduces to

$$-\overline{\frac{1}{\rho}\frac{dp}{dx}} = \overline{U_0 \frac{dU_0}{dx}} + \overline{\frac{U_1}{2}\frac{dU_1}{dx}}, \quad (4)$$

where the overbars denote time-mean quantities. It should be noted that while $U_0(x)$ is readily determined from the Euler equations (e.g., Denton, 1983), $U_1(x)$ represents the wake amplitude variation as it passes through the blade row. The calculation of its magnitude for general turbomachinery flow is not considered to be within the scope of this paper.

Nomenclature

c_p = specific heat
D = cylinder diameter
F = time-mean wake contributions
f' = dimensionless velocity
k = thermal conductivity
Nu = Nusselt number
p = pressure
Q = wake velocity
Re = Reynolds number
T = temperature
t = time
Tu = turbulence level
$\tilde{T}u$ = wake disturbance level
Tu_o = overall disturbance level
U = free-stream velocity
u = velocity in x direction
v = velocity in the y direction
x = streamwise spatial coordinate
y = cross-stream spatial coordinate
Γ = wave parameter = $2\tilde{T}u^2\sigma_x/\gamma$
γ = traveling-wave convection velocity = Q/U_0
δ = boundary layer thickness
δ_0 = oscillatory flow boundary layer thickness
δ^* = boundary layer displacement thickness
η = dimensionless spatial coordinate
λ = skin friction coefficient
ν = kinematic viscosity
ρ = fluid density
σ = Strouhal number
ω = frequency

Subscripts

D = cylinder diameter
e = edge condition
s = solid boundary
w = wake quantity
$w1$ = momentum wake quantity
$w2$ = thermal wake quantity
x = streamwise spatial coordinate
0 = mean condition
1 = unsteady quantity
∞ = condition far from the solid wall(s)

Superscripts and Other Symbols

$'$ = fluctuating quantity, differentiation with respect to η
$\bar{\cdot}$ = time-mean quantity
* = dimensionless quantities
$\tilde{\cdot}$ = wake-induced disturbance
$\langle \cdot \rangle$ = ensemble-averaged quantities

Modeling Overview

The time-mean boundary layer equations incorporating the triple decomposition may be derived in a similar fashion to the time-mean pressure gradient of the previous section (Norris and Reynolds, 1975). The derivation, however, gives rise to an additional Reynolds stress term, which represents the nonlinear contribution from the wake interactions and is difficult to quantify. An alternative approach, based on the small perturbation assumption, has been developed by Telionis (1977) and more recently by Paxson and Mayle (1991). In certain turbomachinery applications, combustor turbulence can introduce gross disturbances of the order $0.5U_0$ (Graham, 1979), and the small perturbation assumption does not enjoy general validity. In order to obtain badly needed engineering information relatively quickly, many investigators have extended steady boundary layer procedures to unsteady flow problems by simply adding the unsteady terms to the equations (e.g., Gorla, 1986; Cebeci et al., 1990). While these methods have achieved moderate success, computational problems arise due to unsteady boundary layer separation, and more importantly, modeling boundary layer transition in an inherently unsteady environment is poorly understood. These methods are also computationally expensive when compared to typical two-dimensional steady flow boundary layer code performance.

General Method

The approach adopted in this paper is based upon generalizing a method first proposed by Lin (1957). Whereas Lin considered the laminar flow equations subjected to a standing wave perturbation, this procedure includes the turbulent stresses in much the same manner as the extended steady flow equations mentioned above and considers a traveling wave perturbation. An attractive feature of Lin's method is that no restriction is imposed on the magnitude of the wake perturbation. For the application of this method, however, the condition $(\delta_0/\delta)^2 \ll 1$ must be satisified, where δ_0 $(\equiv\sqrt{2\nu/\omega})$ is the oscillatory flow boundry layer thickness and δ is the mean flow boundary layer thickness. Apart from the region very close to the stagnation point, where a second-order approximation may be warranted, this condition is satisfied to various degrees of approximation along the gas turbine blade boundary layer. When using this method the computational problems inherent in unsteady boundary layer separation are avoided and the much simplified time-mean transition, as opposed to unsteady transition, must be modeled.

In order to eliminate unnecessary complications at this stage the incompressible boundary layer equations are considered, where viscous heating is neglected. Here, we commence with the extended steady flow boundary layer equations for two-dimensional unsteady flow, viz:

$$\frac{\partial u}{\partial x}+\frac{\partial v}{\partial y}=0, \tag{5a}$$

$$\frac{\partial u}{\partial t}+u\frac{\partial u}{\partial x}+v\frac{\partial u}{\partial y}=-\frac{1}{\rho}\frac{\partial p}{\partial x}+\frac{\partial}{\partial y}\left(\nu\frac{\partial u}{\partial y}-\langle u'v'\rangle\right), \tag{5b}$$

$$\frac{\partial T}{\partial t}+u\frac{\partial T}{\partial x}+v\frac{\partial T}{\partial y}=\frac{\partial}{\partial y}\left(\frac{k}{\rho c_p}\frac{\partial T}{\partial y}-\langle v'T'\rangle\right), \tag{5c}$$

where u and v represent ensemble-averaged velocities in the x and y directions and the primed quantities with $\langle\,\rangle$'s denote ensemble-averaged fluctuating quantities. The quantities p and T refer to pressure and temperature while ν, ρ, k, and c_p are the kinematic viscosity, density, thermal conductivity, and specific heat, respectively. Applying the method of Lin, we substitute

$$u(x, y, t)=u_0(x, y)+u_w(x, y, t), \tag{6a}$$

$$v(x, y, t)=v_0(x, y)+v_w(x, y, t), \tag{6b}$$

$$T(x, y, t)=T_0(x, y)+T_w(x, y, t), \tag{6c}$$

$$p(x, t)=p_0(x)+p_w(x, t), \tag{6d}$$

into equations (5*a*, *b*, *c*). As in the case of the free-stream quantities, subscripts 0 and w refer to time-mean and wake components of the ensemble-averaged quantities, respectively. Upon time-averaging, making use of Eq. (4) and dropping the 0's and mean quantity overbars, the mean flow equations

$$\frac{\partial u}{\partial x}+\frac{\partial v}{\partial y}=0, \tag{7a}$$

$$u\frac{\partial u}{\partial x}+v\frac{\partial u}{\partial y}=U_0\frac{dU_0}{dx}+\frac{\partial}{\partial y}\left(\nu\frac{\partial u}{\partial y}-\overline{\langle u'v'\rangle}\right)+F_{w1}(x, y), \tag{7b}$$

$$u\frac{\partial T}{\partial x}+v\frac{\partial T}{\partial y}=\frac{\partial}{\partial y}\left(\frac{k}{\rho c_p}\frac{\partial T}{\partial y}-\overline{\langle v'T'\rangle}\right)+F_{w2}(x, y), \tag{7c}$$

are obtained, where the time-mean wake contributions F_{w1} and F_{w2}, which are expressed as

$$F_{w1}(x, y)=\overline{\frac{U_1}{2}\frac{\partial U_1}{\partial x}}-\left(\overline{u_w\frac{\partial u_w}{\partial x}}+\overline{v_w\frac{\partial u_w}{\partial y}}\right) \tag{8a}$$

and

$$F_{w2}(x, y)=-\overline{u_w\frac{\partial T_w}{\partial x}}-\overline{v_w\frac{\partial T_w}{\partial y}}, \tag{8b}$$

are determined from the linearized unsteady equations

$$\frac{\partial u_w}{\partial x}+\frac{\partial v_w}{\partial y}=0, \tag{9a}$$

$$\frac{\partial u_w}{\partial t}=\frac{\partial U_w}{\partial t}+\frac{\partial}{\partial y}\left(\nu\frac{\partial u_w}{\partial y}\right)+\phi_1(x, y)+\epsilon_u, \tag{9b}$$

$$\frac{\partial T_w}{\partial t}=\frac{\partial}{\partial y}\left(\frac{k}{\rho c_p}\frac{\partial T_w}{\partial y}\right)+\phi_2\ (x, y)+\epsilon_T. \tag{9c}$$

The form of the terms ϕ_1 and ϕ_2 depends on the assumptions that are made regarding the Reynolds stress modeling in Eq. (5*b*, *c*) while ϵ_u and ϵ_T represent the contribution of the nonlinear terms, which are ignored here. The boundary conditions for Eqs. (7) and (9) are:

$$u=0, \quad v=0, \quad T=T_s \quad \text{at } y=0,$$

$$u\to U_e, \quad v\to 0, \quad T\to T_e \quad \text{as } y\to\infty,$$

and

$$u_w=0, \qquad T_w=T_s, \qquad \text{at } y=0,$$

$$\partial u_w/\partial y\to 0, \quad \partial T_w/\partial y\to 0, \quad \text{as } y\to\infty,$$

respectively, where the subscript s refers to the solid wall boundary. For the application of this method the wake effects are first ascertained by means of Eqs. (9*a*) to (9*c*). These effects are then incorporated into the steady flow Eqs. (7*b*) and (7*c*) via the F_w terms, which are ascertained from Eqs. (8*a*) and (8*b*).

The advantages of this method over other methods published in the literature are clear: First, the unsteady Eqs. (9*a*) to (9*c*) are readily solved with relatively modest computational effort. Second, the time-mean terms F_{w1} and F_{w2} appearing in Eqs. (7*b*) and (7*c*) need only to be computed once for a particular turbulence model and thereafter either stored in a data base or be represented by means of best-fit correlations. Third, the resulting time-mean equations can be solved by one of the many available space-marching methods resulting in computational times that are comparable to those currently used in turbine design practice where wake effects are ignored (e.g., Crawford and Kays, 1976). Fourth, this method is not restricted to sinusoidal-type periodic disturbances. Indeed, Dul-

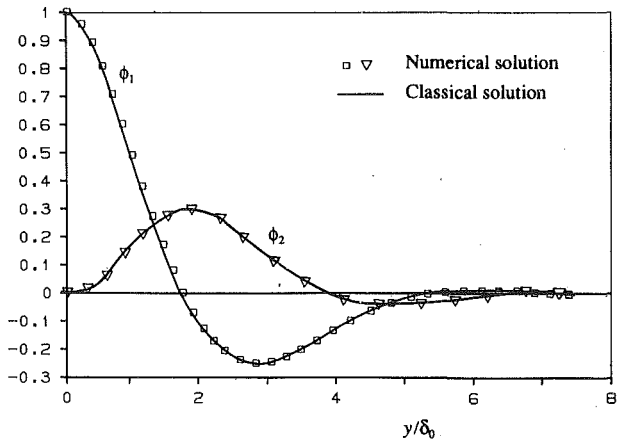

Fig. 2 Comparison of the numerical and analytical solutions to Eqs. (9*a*), (9*b*) and (8*a*) for purely laminar flow

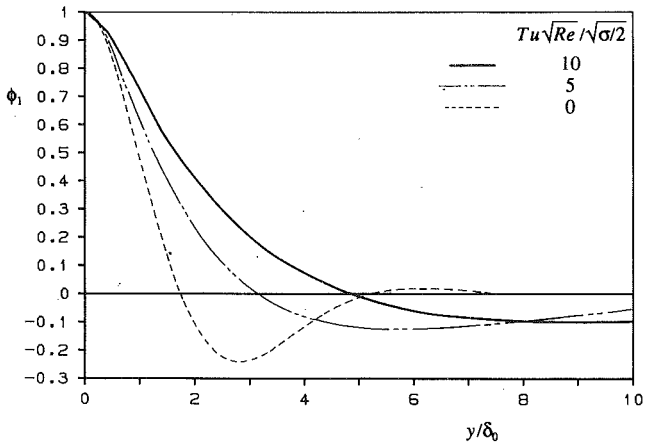

Fig. 3 Numerical solutions to Eqs. (9*a*), (9*b*) and (8*a*) for increasing $Tu\sqrt{\mathrm{Re}}/\sqrt{\sigma/2}$

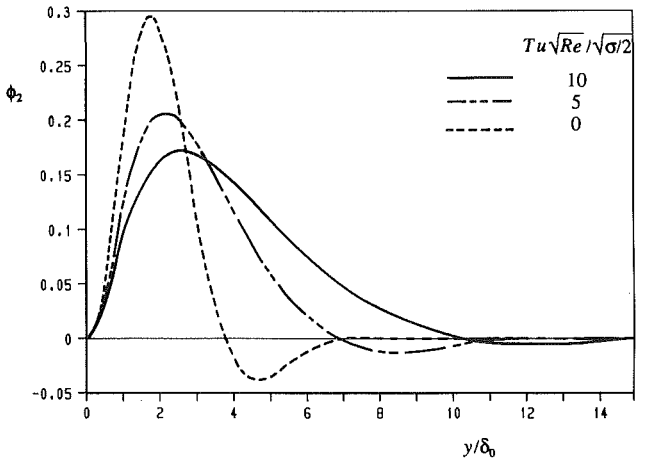

Fig. 4 Numerical solutions to Eqs. (9*a*), (9*b*) and (8*a*) for increasing $Tu\sqrt{\mathrm{Re}}/\sqrt{\sigma/2}$

lenkopf et al. (1991) and others have shown that, while the wake is periodic, it deviates significantly from a sinusoidal shape. Fifth, the method takes the "traveling" nature of the wake into account. Sixth, the time dependence of the turbulence level Tu can be accounted for via the Reynolds stress terms in Eqs. (9*b*, *c*), and finally, only time-mean phenomena such as, for example, wake-induced transition need be modeled. This last item is particularly advantageous in the light of recent developments by Mayle and Dullenkopf (1990, 1991).

Numerical Results

In this section, the numerical results of the wake and time-mean equations are presented in three stages. First, the solution to the wake Eqs. (9*a*, *b*) are presented where turbulence effects are ignored. Second, the effect of turbulence on the solution is examined, and finally, the effect of the wake behavior on the resulting time-mean flow is illustrated. Only the mass and momentum equations are considered because their solution is sufficient to illustrate the salient failures of the method.

Turbulence-Free Oscillations

In the absence of turbulence, the F_{wl} term appearing in Eq. (8*a*) is obtained from the classical solution to Eqs. (9*a*) and (9*b*):

$$F_{wl}(x, y) = \frac{U_1}{2}\frac{dU_1}{dx}\left[(2+y/\delta_0)\cos(y/\delta_0) + (y/\delta_0 - 1)\sin(y/\delta_0) - e^{-y/\delta_0}\right]e^{-y/\delta_0} + \frac{U_1^2\omega}{2Q}\left[(1-y/\delta_0)\cos(y/\delta_0) + y/\delta_0 \sin(y/\delta_0) - e^{-y/\delta_0}\right]e^{-y/\delta_0}, \quad (10)$$

where the first term in the expression $0.5\ U_1 dU_1/dx\phi_1(y/\delta_0)$ is that derived by Lin (1957) and the second term $0.5U_1^2\ \omega/Q$ $\phi_2(y/\delta_0)$ represents the traveling-wave contribution, derived by Greenblatt and Damelin (1992). These functions are plotted in Fig. 2. In order to test the computational scheme (see appendix), the equations were solved numerically and the results are plotted on the same system of axes. It is evident from the figure that the computation yields an acceptable solution to the equations, thereby validating their use for cases where no classical solution is possible due to inclusion of eddy viscosity or thermal conductivity in the momentum and energy equations, respectively.

Combined Wake and Turbulence Effects

As a means of introducing the effects of turbulence into the equations, the Reynolds stress term in Eq. (5*b*) was modeled by means of the *turbulence* viscosity relationship (see Hylton et al., 1983):

$$\langle u'v' \rangle = \nu_{Tu}\frac{\partial u}{\partial y}, \quad (11)$$

and the eddy viscosity model of Smith and Kuethe (1966):

$$\nu_{Tu} = 0.164\sqrt{\langle u'^2 \rangle}\, y.$$

For simplicity it was assumed that $\langle u'^2 \rangle$ remains "frozen" i.e., independent of time throughout the cycle. It should be noted, however, that this is not a necessary constraint but proved to be convenient. Suitable nondimensionalization of the equations (see appendix) yielded the controlling parameter $Tu\sqrt{\mathrm{Re}}/\sqrt{\sigma/2}$, where Re and σ are the Reynolds and Strouhal numbers, respectively, and the results of computations performed for increasing values of this parameter are presented in Figs. 3 and 4. It is evident from the figures that the effect of increasing $Tu\sqrt{\mathrm{Re}}/\sqrt{\sigma/2}$ is manifested by a larger penetration into the laminar boundary layer of the functions ϕ_1 and ϕ_2.

Time-Mean Flow

The effect of the above-mentioned factors on the time-mean boundary layer development was ascertained by considering a stagnation flow over an infinite cylinder and the flow over a flat plate. By considering the ratio of the two terms in Eq. (10) it can be shown that $U_1 dU_1/dx$ dominates over $U_1^2\omega/Q$

in the stagnation region, whereas the opposite is true when little or no pressure gradient is present such as in the case of flow over a flat plate. Consequently, for the remainder of the results presented in this section, traveling wake effects are ignored in the stagnation region while these effects are considered exclusively for the flat plate problem.

Stagnation Flow. In keeping with previous stagnation point investigations, the substitution $U_0(x)=Ax$ was made where $A=4U_\infty/D$. The quantities U_∞ and D represent the free-stream velocity and cylinder diameter, respectively. Making the substitutions for U_0 and F_{w1}, the mass and momentum Eqs. (7*a*, *b*) took the form

$$\frac{\partial u}{\partial x}+\frac{\partial v}{\partial y}=0, \tag{12}$$

$$u\frac{\partial u}{\partial x}+v\frac{\partial u}{\partial y}=A^2x\,[1+\tilde{T}u^2\phi_1(y/\delta_0)]+\frac{\partial}{\partial y}\left(\nu-\nu_{Tu}\frac{\partial u}{\partial y}\right), \tag{13}$$

and bringing about the substitutions

$$u=U_e f'(\eta),\ v=-(\nu A)^{1/2}f(\eta),\ \eta=(A/\nu)^{1/2}y,$$
$$a=0.082Tu\sqrt{\mathrm{Re}_D},\ b=1+\tilde{T}u\phi_1(1/2\sqrt{\sigma_D/2}\eta),$$

Eq. (12) was automatically satisfied and Eq. (13) was reduced to the ordinary differential equation

$$f'^2-f''(f+a)=(1+a\eta)f'''+b$$

where the primes refer to differentiation with respect to η. The equation above was subject to the boundary conditions

$$f=f'=0 \quad \text{at } \eta=0$$
$$f'=1 \qquad \text{as } \eta\to\infty.$$

Following Smith and Kuethe (1966), $\eta=6.0$ was taken as the boundary layer edge and a Runge–Kutta integration procedure was used to obtain the solutions.

The results for normalized time-mean displacement thickness ($\delta^*/\delta^*_{\tilde{T}u,\ Tu=0}$) and skin friction coefficient ($\lambda/\lambda_{Tu,\ \tilde{T}u=0}$) are plotted in Figs. 5 and 6, respectively, where the Strouhal number σ_D was set equal to 2. It is evident from the figures that the effect of both the turbulence and the time-mean wake unsteadiness is fully characterized by this method. In addition, for this particular case, the method yields the much sought-after controlling parameter $Tu\sqrt{\mathrm{Re}_D}/\sqrt{\sigma_D/2}$ by suitable nondimensionalization of the governing equations.

With regard to Fig. 5 it is evident that δ^* increases with increasing Tu but unexpectedly decreases with increasing $\tilde{T}u$. This is an important result since in many boundary layer codes the transition onset Reynolds number is based on either displacement or momentum thickness. Consequently, it is important that the starting upstream conditions are accurate otherwise a valid estimation of the onset Reynolds number will not necessarily predict an accurate transition location on the blade surface. This in turn, could lead to erroneous estimates of the local heat transfer coefficient.

The results for skin friction, which are plotted in Fig. 6, indicate that increases in both Tu and $\tilde{T}u$ bring about an increase in the time-mean skin friction coefficient. It is evident, however, that the effect of the wake is not as significant as the free-stream turbulence effect with $\tilde{T}u=50$ percent bringing about a skin friction augmentation of only 15 percent. On the basis of the findings of Ishigaki (1970) and using the Reynolds analogy it can be inferred that similar trends will be apparent for time-mean heat transfer. This result can be used to explain qualitatively the widely varying results in gas turbine heat transfer augmentation when novel turbulence generators are used (see Bayley and Priddy, 1981, and Krishnamoorthy et al., 1988). For example, while the measured overall disturbance level Tu_o is large, the actual turbulent component Tu may be much smaller—giving rise to only a slight increase in heat transfer and consequently misleading results.

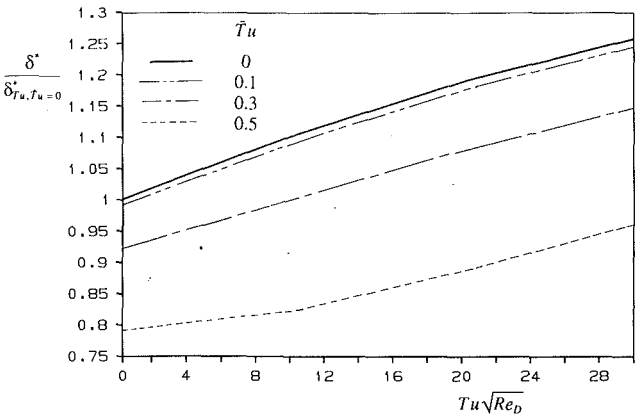

Fig. 5 Time-mean normalized displacement thickness variation when subjected to the combined effect of wake-passing and free-stream turbulence for $\sigma_D = 2$

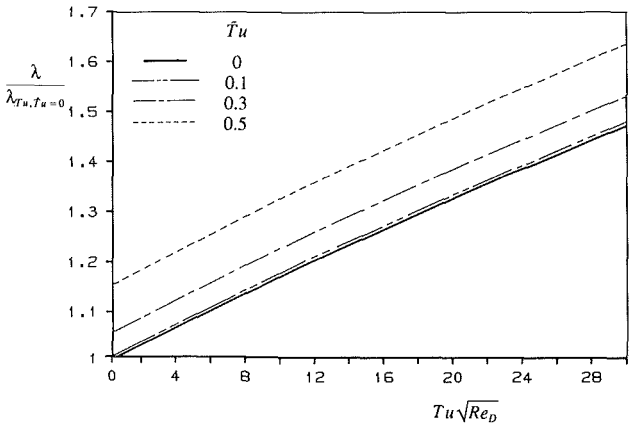

Fig. 6 Time-mean normalized skin friction coefficient variation when subjected to the combined effect of wake-passing and free-stream turbulence for $\sigma_D = 2$

The computations above were performed with σ_D equal to 0.5 and 4.0 respectively, and it was ascertained that the results for both δ^* and λ were only slightly affected when compared to the $\sigma_D=2.0$ case.

Flat Plate Flow. In order to illustrate the time-mean effect of the traveling wave on the laminar boundary layer in the absence of free-stream turbulence, the classical flat plate problem was considered here. The external fluid stream was assumed to be free of pressure gradient and the amplitude and velocity of the traveling-wave were assumed constant. For this problem, the outer edge of the boundary layer was defined at the point $u=0.99U$, and consequently $(\delta_0/\delta)^2=2/25\sigma_x$, where the subscript x refers to the distance measured from the leading edge of the plate. This relation can be derived from the definition contained in the section entitled "General Method" and the well-known flat plate formula for δ. It can be seen by inspection that the condition $(\delta_0/\delta)^2 \ll 1$ holds for typical gas turbine blade Strouhal numbers with the exception of the region very close to the leading edge. Introducing the well-known Blasius substitutions (see Schlichting, 1979), once again the mass equation is automatically satisfied and the momentum equation reduces to the ordinary differential form:

$$ff''+2f'''+(2\tilde{T}u^2\sigma_x/\gamma)\phi(\sqrt{\sigma_x/2}\eta)=0. \tag{14}$$

The term γ represents the traveling-wave convection velocity ratio Q/U_0 and for convenience we define the wave parameter $\Gamma=2\tilde{T}u^2\sigma_x/\gamma$. The equation above was subject to the same

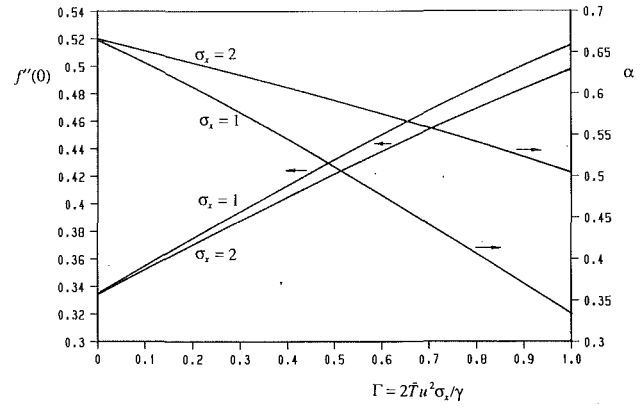

Fig. 7 Effect of the wave parameter on skin friction and momentum thickness

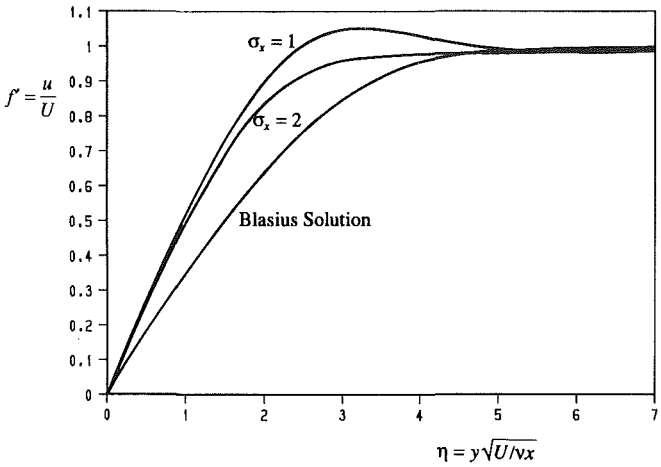

Fig. 8 Effect of the wave parameter and Strouhal number on time-mean velocity profiles

boundary conditions as in the stagnation flow case and the same integration scheme was used.

Making use of the principle of similarity, the local skin friction and momentum thickness Reynolds number may be expressed as

$$c_f/2 = f''(0)/\sqrt{\mathrm{Re}_x} \text{ and } \mathrm{Re}_\theta = \alpha\sqrt{\mathrm{Re}_x}$$

respectively. The quantities $f''(0)$ and α are plotted in Fig.7 as a function of the wave parameter Γ, for σ_x values of 1 and 2. In general, the local skin friction coefficient increases with the wave parameter while the momentum thickness decreases. All curves exhibit a very small negative second derivative type curvature but can be adequately represented by linear functions for the range of Γ presented here. The skin friction increases by approximately 50 percent as the wave parameter increases from 0 to 1. This quantity also exhibits a very small dependence on σ_x with the difference between the two results typically around 3 percent. Using the Reynolds analogy once again it is evident that traveling-wave fluctuations can have a pronounced effect on the local heat transfer coefficient within the laminar boundary layer of gas turbine blades.

In contrast to the skin friction coefficient, the momentum thickness Reynolds number is strongly affected by *both* the wave parameter and the Strouhal number. For the condition $\sigma_x = 2$, α decreases by approximately one quarter of its original value at maximum Γ,while for $\sigma_x = 1$ it decreases to half its value. Thus, it is conceivable that the traveling wave effect may have an influence over the point of transition onset.

Due consideration should also be given to the stability characteristics of these boundary layers as their mean profiles are

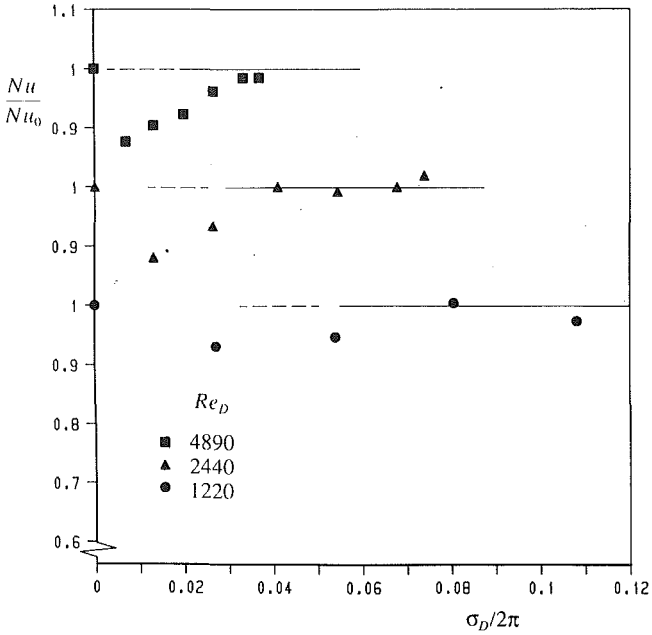

Fig. 9 Comparison of the numerical heat transfer predictions with the experimental data of Base et al. (1981)

markedly different to that of the Blasius profile. This feature is evident from Fig. 8 where profiles for $\Gamma = 1$ are compared with the Blasius profile. These curves qualitatively reflect the results of the previous figure.

Provisional Experimental Validation

The numerical results attained here were compared with the experimental data of Base et al. (1981) and Marziale and Mayle (1983). The Base et al. experiment consisted of a low-speed blow-down wind tunnel in which the turbulence level, unsteadiness level, and frequency could be set. Overall disturbance levels as high as 20 percent were examined. All experiments were performed on a heated cylinder, which was located in the working section of the tunnel. Traveling wave effects were absent from the free-stream and the temperature in the free stream was constant.

The numerical technique described in the previous section was used and, in addition, the energy equation was solved. For the solution of the energy equation, laminar and turbulent Prandtl numbers of 0.7 and 1.0, respectively, were employed. Since free-stream fluctuations in temperature were absent, the wake term in the energy equation F_{w2} was equal to zero.

Figure 9 contains the experimental data as well as the numerical results of the method described in the paper, where comparisons are presented for Nusselt number, normalized with respect to its value in a nonoscillatory flow, as a function of Strouhal number. Incident flow Reynolds numbers of 1220, 2440, and 4890 were considered. The experimental data for all three Reynolds numbers show similar trends, namely that the heat transfer drops at low frequency, but recovers to approximately its original value at higher frequencies. The numerical results, on the other hand, show an insensitivity to σ_D as was discovered in the previous section and as a consequence of this, the experimental data tend asymptotically to the computed results. This was expected since the theory was developed specifically for high-frequency oscillations. It is surprising to note, however, that these data are outside the valid range of the numerical model. This is evident from Table 1 where representative σ_D values are compared with their corresponding $(\delta_0/\delta)^2$ values. In the section entitled "General Method" it was pointed out that the numerical scheme is only valid for $(\delta_0/\delta)^2$

Table 1 Boundary layer thickness ratio as a function of Strouhal number

$\sigma_D/2\pi$	$(\delta_0/\delta)^2$
0.02	11
0.06	3.7
0.1	2.2

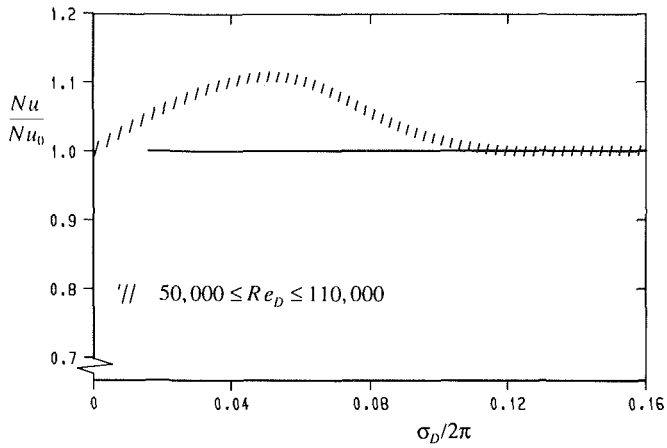

Fig. 10 Comparison of the numerical heat transfer predictions with the experimental data of Marziale and Mayle (1983)

$\ll 1$ and this is clearly not the case here. Thus the theory may enjoy greater generality than was originally believed, but definite conclusions in this regard cannot be drawn until further validation has been carried out.

In the experiment of Marziale and Mayle (1983) the effect of periodic variation in the angle of attack on heat transfer at the leading edge of a turbine blade was examined. As in the previous investigation a circular cylinder was employed, but in this investigation it was oscillated rotationally about its axis. The incident flow Reynolds numbers and Strouhal numbers were chosen to be representative of those found in turbomachinery while turbulence levels up to approximately 5 percent were generated. A mass transfer technique was used to infer heat transfer results.

For the computational results, the external free-stream velocity was represented by

$$U_e = Ax \pm |Ax' \sin \omega t|,$$

where the sign between the two terms is dependent upon the stagnation region location under consideration and x' is the amplitude of the oscillation measured from the stagnation point.

It is evident from Eqs. (9*a*, *b*) that the flow will be unsteady in nature since $U_w = \pm |Ax' \sin \omega t|$. However, the time-mean effect will be equal to zero since U_w is not a function of x. Consequently with F_{w1} and F_{w2} equal to zero, neither frequency nor amplitude should have any effect on time-mean heat transfer. It is also important to note that this result is independent of the high-frequency assumption $(\delta_0/\delta)^2 \ll 1$ and therefore valid for all σ_D.

The experimental data as well as the results of the above-mentioned conclusion are presented in Fig. 10. The experimental data show a 10 percent increase in inferred Nusselt number at intermediate values of Strouhal number and then decrease to the value that was measured in the absence of angle of attack oscillation. Contrary to this, the method developed here shows no variation with Strouhal number. It is believed that the small discrepancy between the data and prediction can be attributed to the fact that U_w is weakly dependent on x due to interaction of the boundary layer and free stream during the oscillation. However, for the prediction presented here, this was not taken into account as the free-stream and boundary layer regimes were assumed to be independent of one another.

Concluding Remarks

A computational procedure has been developed that accounts for the time-mean effect of wake-passing and free-stream turbulence on laminar turbine blade boundary layers. Among the advantages of the procedure over many others currently found in the literature are rapid computation of the time-mean unsteady effects and realistic modeling of the turbulent wake. The procedure also yielded useful parameters such as $Tu\sqrt{\mathrm{Re}_D}/\sqrt{\sigma_D/2}$ and $\Gamma\ (\equiv 2\bar{T}u^2\sigma_x/\gamma)$ for describing the time-mean effects of unsteadiness on the laminar boundary layer. A provisional comparison with experimental data showed that the procedure, may be more general than initially expected. On the basis of this encouraging preliminary comparison with experimental data it is envisaged that, in the near future, the results of this procedure will undergo extensive experimental validation.

Acknowledgments

The author of this paper would like to thank the members of the Computational Fluid Dynamics Facility and the Turbomachinery Program at Aerotek for their many useful comments and constructive criticisms. In addition, the typesetting effort of Mrs. G. Proudfoot is greatly appreciated.

References

Bayley, F. J., and Priddy, W. J., 1981, "Effects of Free-Stream Turbulence Intensity and Frequency on Heat Transfer to Turbine Blading," ASME *Journal of Engineering for Power*, Vol. 103, pp. 60–64.

Base, T. E., Patel, J. M., and Vilaitis, G. C., 1981, "Heat Transfer From Cylinders in Unsteady Flow," *The Canadian Journal of Chemical Engineering*, Vol. 59, pp. 247–250.

Bogucz, E. A., Dirik, E. A., and Lyman, F. A., 1988, "Unsteady Stagnation-Point Heat Transfer Due to the Motion of Free-Stream Vortices," *Proceedings of the AIAA/ASME/SIAM/APS, 1st National Fluid Dynamics Congress*, Cincinnati, OH.

Cebeci, T., Simoneau, R. J., and Platzer, M. F., 1990, "Unsteady Heat Transfer on Turbine Blades," *Journal of Thermophysics*, Vol. 4, No. 1, pp. 47–52.

Crawford, M. E., and Kays, W. M., 1976, "STAN5—A Program for Numerical Computation of Two-Dimensional Internal and External Boundary Layer Flows," NASA CR-2742.

Denton, J. D., 1982, "An Improved Time-Marching Method for Turbomachinery Flow Calculation," ASME *Journal of Engineering for Power*, Vol. 105, pp. 514–524.

Doorly, D. J., 1988, "Modeling the Unsteady Flow in a Turbine Rotor Passage," ASME JOURNAL OF TURBOMACHINERY, Vol. 110, pp. 27–37.

Dring, R. P., Blair, M. F., Josyln, H. D. Power, G. D., and Verdon, J. M., 1986, "The Effects of Inlet Turbulence and Rotor–Stator Interactions on the Aerodynamics and Heat Transfer of a Large-Scale Rotating Turbine Model: I—Final Report," NASA Contractor Report No. 4079.

Dullenkopf, K., Schulz, A., and Wittig, S. 1991, "The Effect of Incident Wake Conditions on the Mean Heat Transfer of an Airfoil," ASME JOURNAL OF TURBOMACHINERY, Vol. 113, pp. 412–418.

Dunn, M. G., Martin, H. L., and Stanek, M. J., 1986, "Heat Flux and Pressure Measurements and Comparison With Prediction for a Low Aspect Ratio Turbine Stage," ASME JOURNAL OF TURBOMACHINERY, Vol. 108, pp. 108–115.

Evans, R. L., 1975, "Turbulence and Unsteadiness Measurements Downstream of a Moving Blade Row," ASME *Journal of Engineering for Power*, Vol. 97, pp. 131–139.

Evans, R. L., 1989, "Computation of Unsteady Laminar Boundary Layers Subject to Travelling-Wave Free-Stream Fluctuations," *AIAA Journal*, Vol. 27, No. 11, pp. 1644–1646.

Gorla, R. S. R., 1986, "Combined Influence of Unsteady Free Stream Velocity and Free Stream Turbulence on Stagnation Point Heat Transfer International," *Journal of Turbo and Jet Engines*, Vol. 3, pp. 117–123.

Graham, R. W., 1979, "Fundamental Mechanisms That Influence the Estimate of Heat Transfer to Gas Turbine Blades," ASME Paper No. 79-HT-43.

Greenblatt, D., 1991, "The Combined Effect of Unsteady Free-Stream Velocity and Free-Stream Turbulence on Heat Transfer to Gas Turbine Blades," *Tenth International Symposium on Air Breathing Engines*, Nottingham, United Kingdom, F. S. Billig, ed., Vol. 2, pp. 1285–1290.

Greenblatt, D., and Damelin, S. B., 1992, "Laminar Boundary Layers Sub-

jected to High-Frequency Travelling-Wave Fluctuations," *AIAA Journal*, Vol. 31, No. 5, pp. 957–959.

Guenette, G. R., Epstein, A. H., Giles, M. B., Haimes, R., and Norton, R. J. G., 1989, "Fully Scaled Transonic Turbine Rotor Heat Transfer Measurements," ASME JOURNAL OF TURBOMACHINERY, Vol. 111, pp. 1–7.

Hylton, L. D., Mihelc, M. S., Turner, E. R., Nealy, D. A., and York, R. E., 1983, "Analytical and Experimental Evaluation of the Heat Transfer Distribution Over the Surfaces of Turbine Vanes," NASA-CR-168015.

Ishigaki, H., 1970, "Periodic Boundary Layer Near a Two Dimensional Stagnation Point," *Journal of Fluid Mechanics*, Vol. 43, Part 3, pp. 477–486.

Krishnamoorthy, V., Pai, B. R., and Sukhatme, S. P., 1988, "Influence of Upstream Flow Conditions on the Heat Transfer to Nozzle Guide Vanes," ASME JOURNAL OF TURBOMACHINERY, Vol. 110, pp. 412–416.

Kurosaka, M., Gertz, J. B., Graham, J. E., Goodman, J. R., Sundaram, P., Riner, W. C., Kuroda, H., and Hankey, W. L., 1987, "Energy Separation in a Vortex Sheet," *Journal of Fluid Mechanics*, Vol. 178, pp. 1–29.

Lin, C. C., 1957, "Motion in the Boundary Layer With a Rapidly Oscillating External Flow," *Ninth International Conference for Applied Mechanics*, Brussels.

Marziale, M. L., and Mayle, R. E., 1983, "Effect of an Oscillating Flow-Direction on Leading Edge Heat Transfer," *Proceedings of the Tokyo IGTC*, pp. 37–44.

Mayle, R. E., and Dullenkopf, K., 1990, "A Theory for Wake-Induced Transition," ASME JOURNAL OF TURBOMACHINERY, Vol. 112, pp. 188–195.

Mayle, R. E., and Dullenkopf, K., 1991, "More on the Turbulent-Strip Theory for Wake-Induced Transition," ASME JOURNAL OF TURBOMACHINERY, Vol. 113, pp. 428–432.

Mayle, R. E., 1991, The 1991 IGTI Scholar Lecture, "The Role of Laminar-Turbulent Transition in Gas Turbine Engines," ASME JOURNAL OF TURBOMACHINERY, Vol. 113, pp. 509–537.

McDonald, H., and Fish, R. W., 1973, "Practical Calculation of Transitional Boundary Layers," *International Journal of Heat and Mass Transfer*, Vol. 16, pp. 1729–1744.

Norris, H. L., III, and Reynolds, W. C., 1975, "Turbulent Channel Flow With a Moving Wavy Boundary," Stanford University Technical Report No. TF-7.

Patel, M. H., 1975, "On Laminar Boundary Layers in Oscillatory Flow," *Proc. Royal Society, London*, Vol. A 347, pp. 99–123.

Paxson, D. E., and Mayle, R. E., 1991, "Laminar Boundary Layer Interaction With an Unsteady Wake," ASME JOURNAL OF TURBOMACHINERY, Vol. 113, pp. 419–427.

Phillips, J. H., and Ackerberg, R. C., 1973, "A Numerical Method for Integrating the Unsteady Boundary-Layer Equations When There Are Regions of Backflow," *Journal of Fluid Mechanics*, Vol. 58, part 3, pp. 561–579.

Rigby, D. L., and Rae, W. J., 1989, "Unsteady Stagnation-Point Heat Transfer During Passage of a Concentrated Vortex," AIAA Paper 89-1690, 24th Thermophysics Conference.

Schlichting, H., 1979, *Boundary Layer Theory*, McGraw-Hill, New York.

Schultz, D. L., 1986, "The Effect of Wake-Passing on Turbine Blades," von Karman Lecture Series 1986-06.

Smith, M. C., and Kuethe, A. M., 1966, "Effects of Turbulence on Laminar Skin Friction and Heat Transfer," *The Physics of Fluids*, Vol. 9, No. 12, pp. 2337–2344.

Sutera, S. P., 1965, "Vorticity Amplification in Stagnation-Point Flow and Its Effect on Heat Transfer," *Journal of Fluid Mechanics*, Vol. 21, Part 3, pp. 513–534.

Telionis, D. P., 1977, "Unsteady Boundary Layers, Separated and Attached," *AGARD Conference Proceedings*, No. 227, Paper No. 16.

Traci, R. M., and Wilcox, D. C., 1975, "Freestream Turbulence Effects on Stagnation Point Heat Transfer," *AIAA Journal*, Vol. 13, No. 7, pp. 890–896.

APPENDIX

Numerical Solution

On substituting Eqs. (2), (11), and the turbulence model into Eq. (9*b*), Eqs. (9*a*) and (9*b*) become

$$\frac{\partial u_w}{\partial x}+\frac{\partial v_w}{\partial y}=0, \tag{A1}$$

$$\frac{\partial u_w}{\partial t}=\omega U_1 \cos\,\omega(t-x/Q)+\frac{\partial}{\partial y}\left(\nu+\nu_{Tu}\frac{\partial u_w}{\partial y}\right), \tag{A2}$$

subject to the boundary conditions

$$u_w=0 \qquad \text{at } y=0,$$

$$\partial u_w/\partial y=0 \quad \text{as } y\to\infty.$$

The equations above were rendered dimensionless by making the substitutions

$$u^*=u_w/U_1, \quad v^*=v_w/U_1,$$

$$x^*=x/\delta_0, \qquad y^*=y/\delta_0,$$

$$t^*=\omega t, \qquad \sigma_Q=-\omega x/Q.$$

The resulting dimensionless equations to be solved were

$$\frac{\partial u^*}{\partial x^*}+\frac{\partial v^*}{\partial y^*}=0, \tag{A3}$$

$$\frac{\partial u^*}{\partial t^*}=\cos\,(t^*+\sigma_Q)+0.5\,\frac{\partial}{\partial y^*}\,(1+r)\,\frac{\partial u^*}{\partial y^*}, \tag{A4}$$

where $r=0.164y^*Tu\sqrt{\mathrm{Re}}/\sqrt{\sigma/2}$. The quantities Re and σ refer to the Reynolds number ($U_\infty L/\nu$) and the Strouhal number ($\omega L/U_\infty$) based on the free-stream conditions and some characteristic length scale L, which is typically cylinder diameter D or distance from the leading edge x. Equation (A4) was discretized by replacing the derivative terms with the simple mean of the finite difference approximations at the jth and $(j+1)$th time steps, i.e., an implicit Crank-Nicolson-type formulation. Dropping the *'s for convenience the discretized equations took the form:

$$\frac{\partial u}{\partial t}=\frac{u_{i,j+1}-u_{i,j}}{k} \tag{A5}$$

$$\frac{\partial u}{\partial y}=\frac{\epsilon}{2}\left(\frac{u_{i+1,j+1}-u_{i,j+1}}{h}+\frac{u_{i+1,j}-u_{i,j}}{h}\right) \tag{A6}$$

$$\frac{\partial^2 u}{\partial y^2}=\frac{1}{2}\left[\frac{\epsilon}{h}\left(\frac{u_{i+1,\,j+1}-u_{i,j+1}}{h}\right)+\left(\frac{u_{i-1,j+1}-u_{i,j+1}}{h^2}\right)+\frac{\epsilon}{h}\left(\frac{u_{i+1,j}-u_{i,j}}{h}\right)+\left(\frac{u_{i-1,j}-u_{i,j}}{h^2}\right)\right], \tag{A7}$$

where $\epsilon=0$ at the free-stream boundary and $\epsilon=1$ elsewhere. Substituting Eq. (A5) to (A7) into Eq. (A4) yielded the linear system of equations:

$$-k_1u_{i-1,j+1}+k_2u_{i,j+1}-k_3u_{i+1,j+1}=k_1u_{i-1,j}+k_4u_{i,j}+k_5u_{i+1,j}+k\,\cos\,kj,$$

where

$$k_1=k(1+r)/4h^2$$

$$k_2=1+rk/4hy+k(1+r)/2h^2$$

$$k_3=rk/4hy+k(1+r)/4h^2$$

$$k_4=1-\epsilon rk/4hy-(\epsilon+1)k(1+r)/4h^2$$

$$k_5=\epsilon(rk/4hy+k(1+r)/4h^2).$$

Since the $u_w(y,\,t=0)$ boundary condition was not known, an array of zeros was used as the starting vector and the solution procedure was marched in time. It was discovered that after 2 to 3 cycles the solution was found to be independent of the starting condition. Fifty spatial increments were used with 250 time steps per cycle. It was ascertained that doubling the spatial grid density and time steps per cycle resulted in neglible difference to the solution. Once u had been calculated the dimensionless continuity equation (A3) was integrated to yield

$$v=-\int_0^y\frac{\partial u}{\partial x}\,dy,$$

and consequently F_{w1} could be computed by time integration over one cycle.

Effects of Free-Stream Turbulence and Adverse Pressure Gradients on Boundary Layer Transition

J. P. Gostelow

A. R. Blunden

University of Technology, Sydney,
Sydney, Australia

G. J. Walker
University of Tasmania,
Hobart, Tasmania, Australia

Boundary layer measurements are presented through transition for six different free-stream turbulence levels and a complete range of adverse pressure gradients for attached laminar flow. Measured intermittency distributions provide an excellent similarity basis for characterizing the transition process under all conditions tested when the Narasimha procedure for determining transition inception is used. This inception location procedure brings consistency to the data. Velocity profiles and integral parameters are influenced by turbulence level and pressure gradient and do not provide a consistent basis. Under strong adverse pressure gradients transition occurs rapidly and the velocity profile has not fully responded before the completion of transition. The starting turbulent layer does not attain an equilibrium velocity profile. A change in pressure gradient from zero to even a modest adverse level is accompanied by a severe reduction in transition length. Under diffusing conditions the physics of the transition process changes and the spot formation rate increases rapidly; instead of the "breakdown in sets" regime experienced in the absence of a pressure gradient, transition under strong adverse pressure gradients is more related to the amplification and subsequent instability of the Tollmien–Schlichting waves. Measurements reveal an exponential decrease in transition length with increasing adverse pressure gradient; a less severe exponential decrease is experienced with increasing turbulence level. Correlations of transition length are provided that facilitate its prediction in the form of suitable length parameters including spot formation rate.

Introduction

The computational fluid dynamics approach to the aerodynamic design of compressor and turbine blading is critically dependent on the accurate prediction of boundary layer transition. Substantial regions of the blade surfaces can be transitional, especially at the low Reynolds numbers encountered in high-altitude flight or in the last stages of steam turbines. The phenomenon of transition is not fully understood and attempts to predict it theoretically have not hitherto been successful. Excellent reviews of the problems and progress in this area have recently been published by Mayle (1991) and Narasimha and Dey (1989).

Information is required on transition inception and completion for a wide range of pressure gradients and under the conditions of high free-stream turbulence encountered in turbomachinery. Designers have tended to rely on correlations of experimental data for this purpose. These correlations are generally valid for zero streamwise pressure gradient, reflecting the considerable body of experimental data available for this condition. The scarcity for information on flows under streamwise pressure gradients is emphasized by a recent critical survey of transition data performed by Dey and Narasimha (1988). They were able to identify only six data sets for which turbulent spot formation rates for transition in accelerating flows could be evaluated. No suitable data could be identified for decelerating flow cases and a correlation of spot formation rates in this regime was not attempted. The paucity of available experimental data for diffusing conditions has made existing correlations unreliable when significant adverse pressure gradients are present. Correlations have predicted excessive transition lengths for both attached flows under adverse pressure gradients and separated shear layers. In the latter case the use of existing transition length correlations has led to the prediction of a completely separated shear layer where experience would indicate the existence of a laminar separation bubble (Walker et al., 1988). Prediction of a fully separated shear layer usually results in a termination of the run due to the failure of the inviscid–viscous interaction blade design program to converge.

Under these circumstances compressor designers have often resorted to drastic assumptions to force convergence. The most common approach is to postulate a point transition at either the leading edge or the suction peak. Although it is usually

Contributed by the International Gas Turbine Institute and presented at the 37th International Gas Turbine and Aeroengine Congress and Exposition, Cologne, Germany, June 1–4, 1992. Manuscript received by the International Gas Turbine Institute February 24, 1992. Paper No. 92-GT-380. Associate Technical Editor: L. S. Langston.

acknowledged that this is physically unrealistic, the assumption is considered to be conservative, and therefore satisfactory. There are, however, many situations, especially under off-design conditions, in which point transition is not a conservative assumption. Stall resulting from a laminar separation is such a case. If point transition is assumed then rapid reattachment will be predicted, whereas the actual flow might exhibit a bubble that lengthens or bursts.

Widely used criteria for transition and laminar separation are based on plots of the Crabtree (1958) type extended to account for variations in turbulence level. Crabtree proposed a correlation of available low turbulence level data in the form of Re_θ against λ_θ. To use such a correlation one plots the locus of the developing laminar boundary layer in the coordinates above. Laminar separation would be indicated by λ_θ reaching the Thwaites (1949) limit of -0.082, or the Curle and Skan (1955) limit of -0.09. Assuming this limit is not encountered first, then transition is predicted where the locus crosses the Crabtree curve. The difficulty with this approach occurs in extending it to the high turbulence levels encountered in turbomachines. Turbulence levels vary between 2 and 14 percent axial flow compressors and can reach 18 percent in axial flow turbines (Wood, 1973), thus constituting an important independent variable.

Interpretation of transition data is complicated by the variety of different criteria used to define the inception and completion of the transition process. The most consistent definition of the state of transition has proved to be the observation of turbulent intermittency. Measurements of transition in a streamwise pressure gradient, in which observations of intermittency have been reported in addition to the other boundary layer properties, have been made by Narasimha (1957), Abu-Ghannam and Shaw (1980), Fraser et al. (1988), Ashworth et al. (1989), Gostelow and Blunden (1988), and others.

The work by Gostelow and Blunden, on transitional flows over a wide range of adverse pressure gradients, used intermittency measurements for locating transition inception, and for defining transition length, by plotting $F(\gamma) = [-\ln(1-\gamma)]^{1/2}$. This technique, originally suggested by Narasimha, was instrumental in identifying a universal distribution of intermittency in the transition zone.

The previous papers had examined the effects of turbulence level and adverse pressure gradients in isolation. An extensive series of boundary layer transition measurements has been undertaken at the University of Technology, Sydney, over a wide range of levels of free-stream turbulence and adverse pressure gradient, and in this paper the combined effects of both variables are documented.

The approach has been to test a range of adverse pressure gradients for each of the six turbulence levels. Since the adverse pressure gradients are produced by angle variation of a hinged flap, they are basically of the form of a constant diffusion in the region of the flat plate under test.

Since the range of turbulence levels and pressure gradients tested is wide it is pertinent to consider whether the data revealed any degree of similarity over the whole range. In introducing his universal intermittency distribution for transitional boundary layers Narasimha had raised questions about its validity under strong pressure gradients. It was therefore planned to scrutinize the current data for any discrepancies in intermittency distribution; it was additionally proposed to investigate streamwise variations in velocity profiles and the associated integral properties from a similar perspective.

It has been demonstrated (Walker and Gostelow, 1989) that adverse pressure gradients have a major impact on the physics of the transition process. In the absence of a streamwise pressure gradient the appearance of turbulent spots is random in nature (Gostelow, 1991). In conditions of moderate to strong adverse pressure gradient, typical of the suction surfaces of turbomachinery blading, the process is more evolutionary with turbulent spots appearing regularly in a manner akin to forced transition.

The breakdown of instability waves in sets was an observed characteristic of the zero pressure gradient condition. Continuous breakdown every cycle of the Tollmien–Schlichting wave was thought to be characteristic of the adverse pressure gradient case. It was predicted that the transition length for an adverse pressure gradient would be several times shorter than that for zero pressure gradient.

Walker (1987) advanced a model for predicting the minimum length of the transition region, which explained the qualitative differences in transition under zero and adverse pressure gradient conditions in terms of the influence of pressure gradient on the breakdown mechanism for turbulent spots. A continuous breakdown of turbulent spots on an equispaced spanwise array was hypothesized. These idealized spots, based on each Tollmien–Schlichting wave cycle, eventually coalesced by streamwise spreading, resulting in the completion of transition. The corresponding transition length was given by

$$Re_{Lt} = 2.3 Re_{\delta_t^*}^{3/2}. \quad (1)$$

Nomenclature

b = turbulence grid bar diameter
Cp = static pressure coefficient
c_f = skin-friction coefficient
$F(\gamma) = [-\ln(1-\gamma)]^{1/2}$
H = form factor $= \delta^*/\theta$
H' = normalized form factor $= (H-H_e)/(H_t-H_e)$
L_T = transition length
m = mesh spacing in turbulence grids
N = dimensionless spot formation rate $= n\sigma\theta_t^3/\nu$
n = spot formation rate
q = turbulent level, percent
Re_{δ^*} = displacement thickness Reynolds number
Re_ϑ = momentum thickness Reynolds number
Re_x = distance Reynolds number
s = distance downstream of turbulence grid
U = free-stream velocity
u = local velocity
u^+ = dimensionless velocity $= u/u^*$
u^* = friction velocity $= \sqrt{\tau_w/\rho}$
x = streamwise distance from leading edge
y = normal distance from wall
y^+ = dimensionless distance from wall $= yu^*/\nu$
γ = intermittency factor
δ = absolute thickness (based on $u/U = 0.99$)
δ^* = displacement thickness
η = dimensionless distance $= (x-x_s)/(x_e-x_s)$
θ = momentum thickness
θ' = momentum thickness ratio $= (\theta-\theta_s)/(\theta_e-\theta_s)$
λ = distance from $\gamma = 0.25$ to $\gamma = 0.75$
λ_ϑ = pressure gradient parameter $= (\theta^2/\nu)\cdot(dU/dx)$
ν = kinematic viscosity
ξ = dimensionless distance $= (x-x_t)/\lambda$
ρ = density
σ = turbulent spot dependence area parameter
τ_w = wall shear stress

Subscripts

e = end of transition ($\gamma = 0.99$)
lam = laminar value
min = minimum value
s = start of transition ($\gamma = 0.01$)
t = start of transition (Narasimha definition)
turb = turbulent value

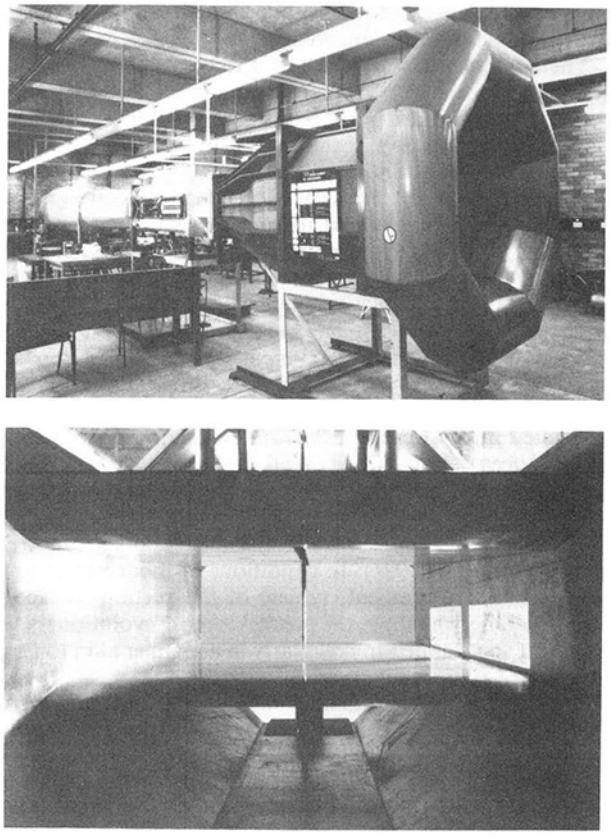

Fig. 1 Wind tunnel and its working section

The above expression was taken to represent the minimum transition length corresponding to the maximum pressure gradient parameter for an attached laminar boundary layer at transition inception, $\lambda_{\vartheta_t} = -0.082$.

Transition lengths corresponding to zero pressure gradient flows are reasonably well established. A representative correlation would be that of Narasimha (1978):

$$\mathrm{Re}_\lambda = 9\mathrm{Re}_t^{3/4}. \quad (2)$$

Experiments described by Walker and Gostelow (1989) tended to confirm the theoretical predictions. Measurements at a moderate turbulence level by Gostelow and Blunden (1988) had indicated a similar trend for transition length, as had measurements under a high turbulence level (Gostelow, 1989).

One consequence of the accelerated nature of transition in adverse pressure gradients is that failure of the incipient turbulent layer velocity profiles to reach equilibrium upon completion of the transition process. Gostelow and Walker (1991) have shown that in adverse pressure gradients the distance required for the velocity profile to reach equilibrium after transition may be considerably greater than the transition length. This raised questions concerning the use of form factor as an indicator of the state of transition and about computational approaches, which presumed a linear combination of laminar and turbulent properties in proportion to the intermittency.

If transitional flow modeling in adverse pressure gradients is to be improved a more complete understanding of transition is needed. This specifically relates to the physics of turbulent spots, their formation rate and distribution, and their mutual interaction, especially when they occur at spacings comparable to the wavelength of the preceding laminar instability.

In computational methods currently used for predicting transitional behavior, it is desirable to move to a more advanced state of semi-empiricism in which improved physical models or statistical distributions of measured data are used to represent the intermittency process. The latter route was charted by Emmons (1951) but has subsequently been inadequately exploited. Narasimha (1985) has rendered a valuable service in attending to the outer region scaling of the bursting phenomena by identifying amplitude functions and distributions that would be needed to adequately represent the transition process. He has provided a correlation of experimental data to represent his spot formation rate parameter, N.

In this paper the data obtained in the current investigation are summarized and presented in the form of correlations for transition length as normalized by boundary layer thickness at inception and by predicted minimum transition length; they are also presented on the basis of spot formation rate parameter.

Establishment of Independent Variables

The experiments were performed in the 608 mm × 608 mm octagonal section open circuit tunnel described by Gostelow and Blunden (1980). Views of the tunnel and its working section containing the flat plate and fairing are given in Fig. 1. Air enters through a bellmouth to the settling chamber, which contains a honeycomb and a set of screens for reducing swirl and turbulence, respectively. A contraction, of area ratio 3.88, precedes the working section, which has a maximum velocity of 40 m/s. The free-stream turbulence level is usually around 0.3 percent.

Boundary layer measurements are made on the top surface of a flat aluminum plate of 1500 × 608 × 25 mm having a high-quality surface finish. The upper surface leading edge has a slender elliptical arc form to avoid leading edge separation and is located 1200 mm from the working section entrance. The exception to this is testing without a turbulence grid installed; in this case the distance between entrance and leading edge is reduced to 600 mm. Static pressure taps are installed on the plate centerline. A negative incidence of 0.25 deg is imparted to the plate to avoid any occurrence of leading edge separation.

Transition regions are identified using hot-wire measurements of intermittency. A single Dantec 5 μm platinum hot wire is used for this purpose with a Dantec 55M10 anemometer. A key element in the test program was the development of an on-line intermittency meter (Alt, 1987). A comparator stage and two series of mono-stable amplifiers produced a digital pulse, which triggered a counter-timer, giving an on-line intermittency reading. This removed any practical upper limit to sampling time, 100 seconds being used routinely.

The reference velocity is set using a pitot tube. Boundary layer traverses are performed using a 1.2 × 0.72 mm flattened head pitot tube in conjunction with plate static pressures.

A traverse carries the probes longitudinally over one meter from the leading edge and a lead-screw system is mounted on the carriage for vertical traverse. A dial gage having a least count of 0.01 mm is used for close-interval measurements of vertical movement. A concentrated beam of light is focused on the probe tip, its reflection being used for accurate positioning close to the wall.

Streamwise Pressure Distributions. In tests involving adverse pressure gradients a fairing is used having a rounded leading edge followed by a straight diffusing section. The fairing was fabricated from perspex formed over a rigid aluminum frame. The leading edge of the fairing extends 300 mm upstream of that of the flat plate. The fairing can be rotated about an axis in the throat region, permitting the application of a range of diffusing static pressure gradients.

Representative streamwise distributions of static pressure coefficient for two turbulence levels are presented in Fig. 2. It is difficult to impose a diffusion of constant gradient using a simple linear fairing but the pressure distributions show that

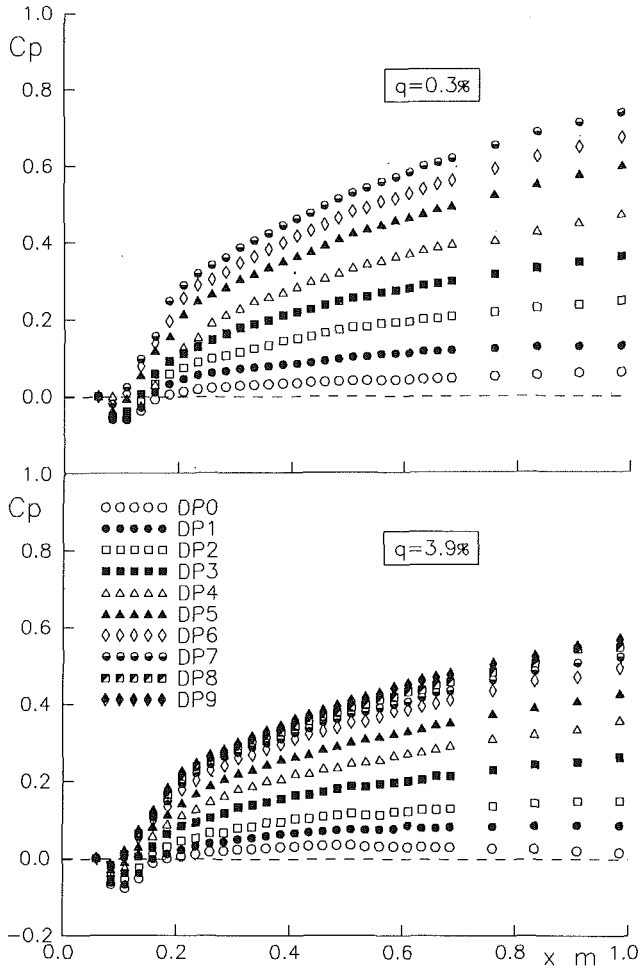

Fig. 2 Representative static pressure distributions

there are no serious irregularities or departures from the desired pattern in the region downstream of the throat.

Turbulence Levels. The high turbulence levels required for this study were generated by inserting square array biplanar grids, constructed from circular steel bars, at a fixed location 1200 mm from the plate leading edge. Five grids were designed, using the relation

$$q = 112(s/b)^{-5/7} \tag{3}$$

given by Frenkiel (1948), to produce homogeneous, well-mixed turbulence over the plate.

Some difficulties were experienced with the spatial variability of measured turbulence levels. This has been especially the case in regions of varying free-stream velocity where there are known to be strong nonistropic influences on the components of turbulent fluctuation. Accordingly a separate test was commissioned in which the turbulence level was measured at a distance of 20 mm upstream of the plate leading edge for each of the grid configurations tested. The results of this test are given in Table 1 and are considered to be representative. The observed turbulence levels are compared with levels predicted by Eq. (3); the discrepancies are considered to result from the turbulence grids having cylindrical, rather than square-edged, bars and from the effects of pressure gradient on isotropy. The observed upstream turbulence levels have been adopted as reference values for correlating the results of the various grids.

Results

Intermittency Distributions. Figure 3 presents intermittency distributions from all six turbulence levels. A consistent representation of the transition region was obtained by adopting the Narasimha procedure for determining inception. Intermittency data were plotted on the basis of $F(\gamma)$ as a function of η, where $F(\gamma)$ is given by

$$F(\gamma) = [-\ln(1-\gamma)]^{1/2}. \tag{4}$$

A best straight line fit was established on the plot of $F(\gamma)$ against η between the intermittency levels of 25 and 75 percent. The intercept of this line with the $\gamma = 0$ axis gave a value of η_t, the effective start of transition under the Narasimha procedure.

This procedure also provided characteristic length scales for transition, λ. As can be seen from Fig. 3, incorporation of the values of η_t and λ obtained from the $F(\gamma)$ curves into a new dimensionless distance, ξ, resulted in distributions giving good agreement with the universal intermittency distribution of Narasimha,

$$\gamma = 1 - \exp(-0.412\xi^2) \tag{5}$$

which is also plotted as a solid line. That this applies to the entire range of turbulence levels between 0.3 and 5.4 percent, over a wide range of pressure gradients, is demonstrated in Fig. 3.

The effective transition inception location, t, was used to define the pressure gradient parameter at transition inception, λ_{ϑ_t}, which is the independent variable used to represent the strength of the adverse pressure gradient. Transition completion, e, was represented by the 99 percent intermittency value.

Table 2 lists the values of pressure gradient parameter at transition inception, λ_{ϑ_t}, corresponding to the designated pressure gradients DP0–DP9 for all six turbulence levels tested.

Testing without a grid present was less comprehensive than with turbulence grids in place, fewer intermittency values being established, and this is reflected in the relatively sparse data set at the 0.3 percent turbulence level. In the Grid 4 tests measurement difficulties were experienced for the higher intermittency levels of the DP0 and DP1 tests; these resulted in the highest recorded intermittency levels being a little lower than the usual 99 percent completion value. This affected the quality of results for transition completion for these two cases.

If no pressure gradient is present the $F(\gamma)$ plot may be expected to be approximately linear. Narasimha (1985), however, has shown that when a pressure gradient is applied the $F(\gamma)$ plot may experience a sudden change in slope from a subcritical level to a supercritical level at a "subtransition" point. The subtransition can have the effect of providing an ambiguous and erroneous transition inception location if this is based on a 1 percent intermittency definition.

Subtransition behavior is significantly influenced by both free-stream turbulence and streamwise pressure gradient. Observations suggest a steady increase in the length of the subtransition region of low intermittency flow upstream of x_t as the turbulence level is increased. Increasing the adverse pressure gradient has a similar effect and subtransition effects are particularly evident for a combination of high turbulence levels

Table 1 Representative turbulence levels for different grid configurations

Grid	m mm	b mm	s/b	Pred. q %	Obs. q %
0	-	-	-	-	0.3
1	18.6	3.2	371.1	1.6	1.2
2	36.1	6.4	185.8	2.7	2.1
3	68.1	12.7	92.9	4.4	3.1
5	87.6	19.1	61.9	5.9	3.9
4	122.6	25.4	46.5	7.2	5.4

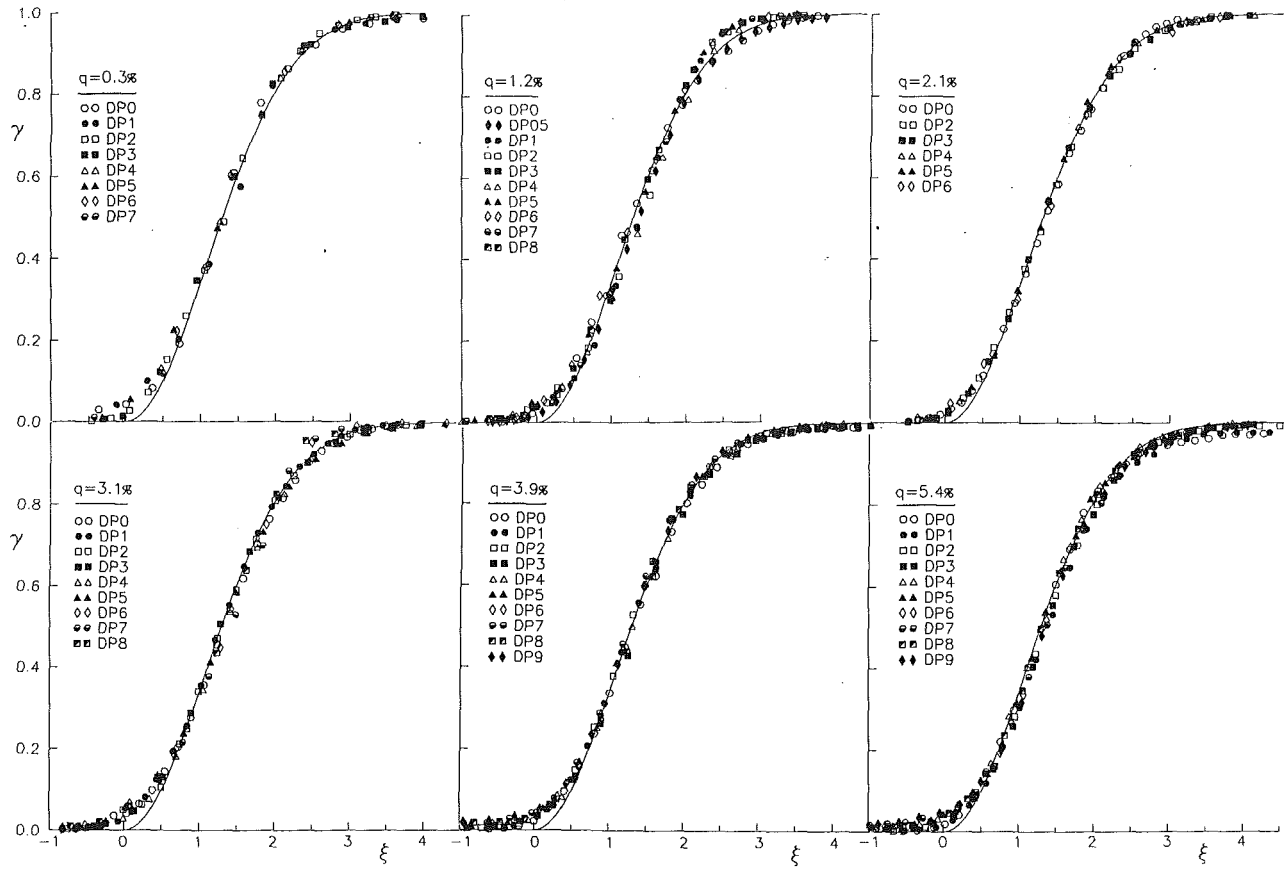

Fig. 3 Intermittency data for the six turbulence levels compared with Narasimha's universal intermittency distribution

Table 2 Values of pressure gradient parameter, λ_{ϑ_t}, for each nominal trubulence level and for designated pressure gradient settings DP0-DP9

Grid	0	1	2	3	5	4
q %	0.3	1.2	2.1	3.1	3.9	5.4
DP0	-0.005	-0.000	-0.000	-0.000	-0.002	-0.003
DP1	-0.012	-0.022	-	-0.012	-0.005	-0.011
DP2	-0.024	-0.033	-0.012	-0.021	-0.009	-0.019
DP3	-0.034	-0.035	-0.013	-0.020	-0.016	-0.030
DP4	-0.043	-0.043	-0.020	-0.024	-0.022	-0.031
DP5	-0.055	-0.067	-0.055	-0.028	-0.028	-0.046
DP6	-0.069	-0.061	-0.071	-0.041	-0.030	-0.047
DP7	-0.079	-0.068	-	-0.075	-0.040	-0.052
DP8	-	-0.064	-	-0.083	-0.044	-0.050
DP9	-	-	-	-	-0.048	-0.063
DP05	-	-0.017	-	-	-	-

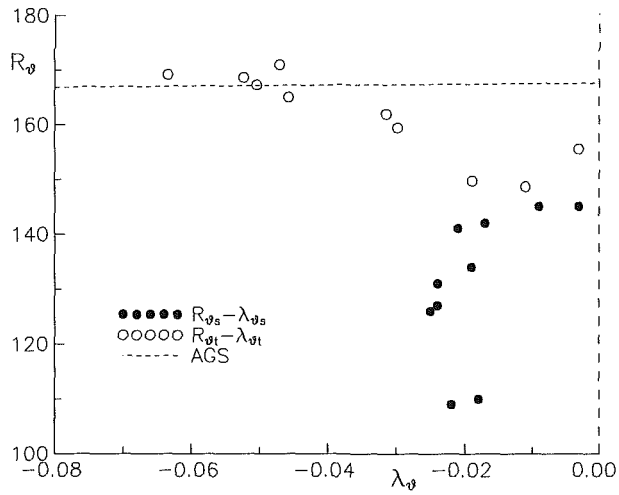

Fig. 4 Reynolds number based on momentum thickness as a function of pressure gradient parameter, at transition inception locations "s" and "t," for 5.4 percent turbulence level

and adverse pressure gradients. These difficulties are avoided if the procedure is adopted of extrapolating the $F(\gamma)$ line back from 25 percent intermittency since this avoids the subcritical region entirely.

By adopting γ_{ϑ_t} to define inception the previously ambiguous Grid 5 results were rendered single valued; this also extended the available range of pressure gradient parameter (Gostelow, 1989).

Figure 4 demonstrates that this behavior is even more pronounced for the Grid 4 results. If transition inception is assumed to occur at 1 percent intermittency a double-valued inception curve is obtained with λ_ϑ limited to -0.025. Using the "t" basis removes this problem giving access to a complete range of values. Data based on the alternative definitions are compared in Fig. 4. The superimposed curve is the 5.4 percent turbulence level prediction from the Abu-Ghannam and Shaw (1980) correlation, which is in reasonable agreement with the $\mathrm{Re}_{\vartheta_t}$ values.

Intermittency traverses were carried out across the boundary layer for the extremes of 0.3 and 5.4 percent free-stream turbulence level; the results were presented by Gostelow and Walker (1991). An intermittency plateau, observed at y/δ between 0.15 and 0.25, is a consistent feature of the traverses and corresponds with the most active region of the turbulent spots. Another significant feature is that under high free-stream turbulence levels the intermittency continues to rise out to the

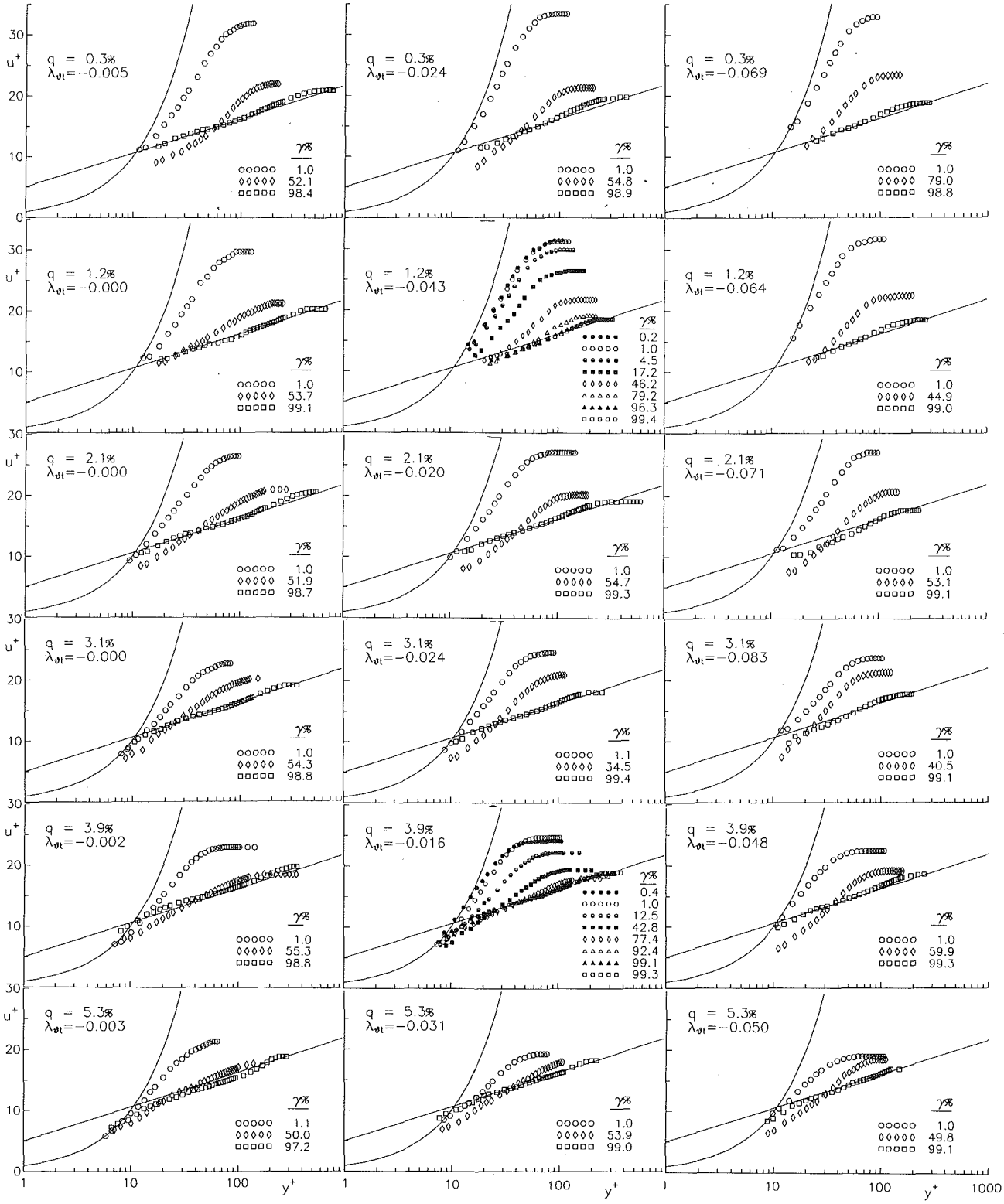

Fig. 5 Dimensionless velocity profiles for the six turbulence levels under zero, moderate, and strong adverse pressure gradients

edge of the boundary layer. The difference in behavior between the two sets of results is especially marked at low intermittencies and the effect contributes substantially to the subtransition.

The intermittency was measured at a distance from the surface for which the local velocity was 80 percent of the free-stream velocity. For the early stages of transition this corresponded to a y/δ range of 0.4 to 0.6. This represented free-stream turbulence effects well but made the readings susceptible to subtransition effects. For the later stages of transition y/δ was between 0.1 and 0.25 corresponding to the intermittency plateau region and therefore representing well the development of turbulent spots.

Velocity Profiles. Following boundary layer traverses throughout the transition region, velocity profiles were obtained and presented in the dimensionless form of plots of u^+

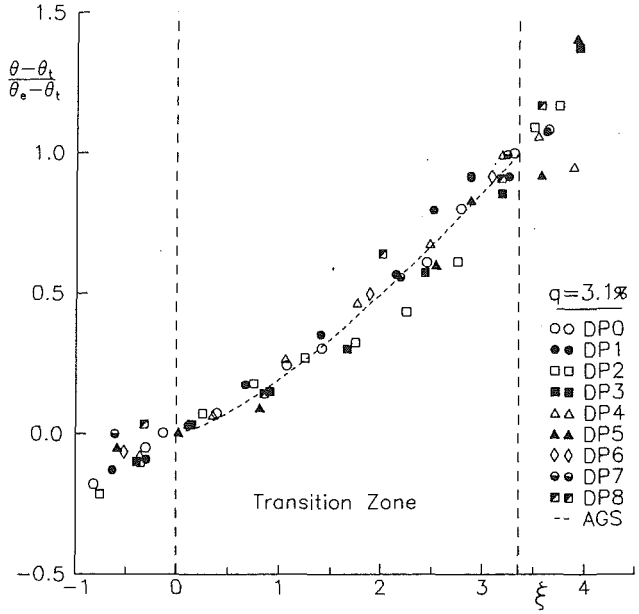

Fig. 6 Momentum thickness development through transition for 3.1 percent turbulence level

against y^+ in Fig. 5. The results are given for each of the six turbulence levels. Although results are available for all pressure gradients tested, they are represented in this paper by the zero, moderate, and strong adverse pressure gradients listed. Traverses were taken for at least eight intermittency readings for all testing with grids present. For clarity velocity profiles are presented for low, moderate, and high intermittencies only, other than for two sample cases for which eight traverses are given.

Different methods were adopted for deriving the laminar and turbulent values of skin friction coefficient. The value at transition inception was determined by linear extrapolation of readings closest to the wall on the basis of $u^+ = y^+$.

The value at transition completion was obtained using the power law formulation

$$\tau_w/\rho = 0.0464(\nu/U\delta)^{1/4}U^2/2. \tag{6}$$

Skin friction values at intermediate intermittencies were obtained using the Emmons (1951) superposition formulations of

$$c_f = (1-\gamma)c_{f\text{lam}} + \gamma c_{f\text{turb}} \tag{7}$$

and

$$u^{*2} = (1-\gamma)u^{*2}_{\text{lam}} + \gamma u^{*2}_{\text{turb}}. \tag{8}$$

Values of u^*_{lam} and u^{*2}_{turb} were evaluated for each set of traverses and combined in Eq. (8) to give a local value of u^*; this was then used to produce the dimensionless velocity profiles.

The shape of the dimensionless velocity profile is a sensitive indicator of the state of transition. For 1 percent intermittency and low turbulence levels the profiles lie close to the laminar viscous flow asymptote, $u^+ = y^+$.

Although the $F(\gamma)$ procedure provides a consistent basis for defining the physical extent of transition there remain, under high turbulence levels and at low intermittencies, significant deviations from the usual laminar profiles.

Free-stream turbulence has a strong effect on the laminar layer; results show a consistent trend toward lower values of u^+ in the outer region of the boundary layer as q is increased. This may result from an increase in wall shear stress throughout the layer associated with the higher levels of free-stream turbulence. The entire velocity profile is affected and hence both the form factor and skin friction.

For 99 percent intermittency the profiles follow the law of the wall asymptote

$$u^+ = 2.439 \ln y^+ + 5.0 \tag{9}$$

quite well in the turbulent layer region $y^+ > 30$. The obvious exception is the wake region in the outer part of the layer.

The velocity profiles at transition completion show a more extensive region of wall similarity as turbulence level is increased. These observations are consistent with the reduced lag in adjustment of form factor, H, during transition under high free-stream turbulence conditions. The influence of pressure gradient on these velocity profiles is only slight. Strong adverse pressure gradients, which would tend to produce laminar separation at transition inception, are relatively mild for the ensuing turbulent layer.

The most significant effect of pressure gradient is to cause an increasing undershoot of the turbulent wall layer asymptote in the intermediate part of the layer as the pressure gradient becomes more adverse. This is thought to be associated with a rapid increase in shear stress achieved by the low inertia fluid at the wall and a slower adjustment of velocity profile farther out, causing reductions in the level of dimensionless velocity. Errors in evaluating the transitional skin friction values using Eq. (7) could be an additional factor.

Variation of Integral Parameters. The determination of similarity of intermittency distributions, on the basis of the Narasimha universal distribution, for all levels of adverse pressure gradient and free-stream turbulence has resulted in a consistent definition of transition inception. On this basis it was possible to investigate the variation of other properties through the transition region. All velocity traverses were integrated to give information on the variation of integral parameters through transition.

Abu-Ghannam and Shaw (1980) investigated the variation through the transition region of the momentum thickness ratio

$$\theta' = (\theta-\theta_s)/(\theta_e-\theta_s). \tag{10}$$

The curve fitted to the data presented in that paper was

$$\theta' = \eta^{1.35}. \tag{11}$$

Similar evaluations were performed for the test data but replacing "s" by "t" as an inception criterion and plotting against ξ. The nature of the results was similar across the turbulence level range and those for Grid 3 are given in Fig. 6 as an example. The data were represented quite well by Eq. (11), in which η has been replaced by $\xi/3.36$. Departures from the trend tended to be random rather than systematic and the scatter was of the same order as that of Abu-Ghannam and Shaw despite coverage of a wider range of pressure gradients and turbulence levels. This probably reflects the relatively consistent definition of inception and completion obtained by using the $F(\gamma)$ procedure for defining the extent of transition. It is concluded that no strong departure from similarity is revealed in momentum thickness data. The situation is different, however, with regard to form factor.

Variations of form factor were plotted in order to establish whether similarity in H was obtained through the transition region. The resulting streamwise distributions exhibited scatter and, in some cases, a pronounced lag effect. The scatter was due to the differing influences of preceding pressure gradient, turbulence level and Reynolds number. The data were therefore normalized to present $H' = (H-H_e)/(H_t-H_e)$. This eliminates differences in starting conditions and in the fall in H through transition and allows the similarity of the form factor distributions between transition inception and completion to be examined. The resulting distributions are presented in Fig. 7 for testing with no grid present and with Grid 5 installed. The results for the DP3 and DP6 conditions without a grid present are corrected versions of the data given by Gostelow and Walker (1991).

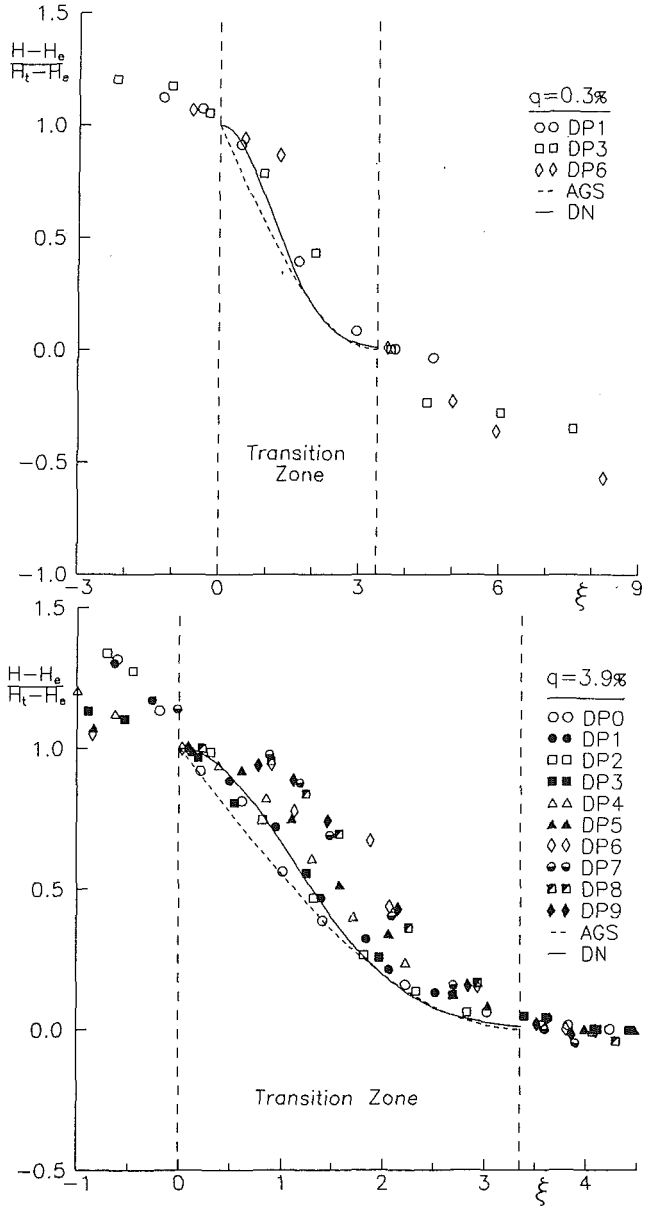

Fig. 7 Streamwise variation of normalized form factor for 0.3 and 3.9 percent turbulence levels

Under zero pressure gradient conditions transition occurs sufficiently gradually that, for low free-stream turbulence levels, local equilibrium of the velocity profile is reached upon transition completion. This is not the case under adverse pressure gradients where transition occurs relatively rapidly and H is not able to reach the equilibrium value prior to transition completion. With respect to the transition process there is, therefore, an effective lag in H, which is a strong function of pressure gradient and turbulence level. This emphasizes and reflects the inherently dynamic and nonlinear nature of the transition process.

The results for 0.3 percent turbulence level in Fig. 7 show that, under a strong adverse pressure gradient, H continues to fall after transition completion. The streamwise distance required for the velocity profile to stabilize is more than double the transition length. It is considered that this increased lag effect results from the transition length, under strong adverse pressure gradients, becoming comparable with the distance of 25δ needed for the velocity profile to re-adjust from a laminar to a turbulent state. This criterion was established from work on turbulent spots under the same turbulence level of 0.3 percent (Gostelow et al., 1992). For weak adverse pressure gradients, however, the transition length is typically an order of magnitude greater and the distance needed to achieve local equilibrium is not a consideration.

The results from testing at 3.9 percent turbulence level in Fig. 7 also exhibit lag effects. Because the turbulence level is higher the transition region in this case extends for more than 25 absolute thicknesses. The lag effects are therefore seen as a delay in the adjustment of H within the transition region under strong adverse pressure gradients.

The form factor has only reached its minimum value by transition completion for low adverse pressure gradients. There is a systematic trend for dH/dx to become increasingly negative at transition completion as the pressure gradient becomes more adverse. This effect becomes more pronounced as the free-stream turbulence level is reduced.

Another reason for increased lag effects in strong adverse pressure gradient boundary layers is the greater change in form factor through the transition region in this case. This arises because the laminar boundary layer form factor prior to transition increases much more rapidly than that of the ensuing turbulent layer as the pressure gradient becomes stronger. The reduced lag effects for high free-stream turbulence conditions can be partly explained by the associated lower values of H prior to transition reducing the change in H to be effected over the transition region; another factor could be the possible modification of turbulent mixing in the boundary layer as a result of disturbances in the free stream.

Two commonly used relationships that describe the variation of form factor through transition have been superimposed on Fig. 7 to permit a comparison with the normalized form factor variation observed in the present investigation. The relationship of Dhawan and Narasimha (1958) is

$$H' = \exp(-0.412\xi^2) \tag{12}$$

whereas Abu-Ghannam and Shaw (1980) proposed the relation

$$H' = 1 - \sin(\pi\eta/2); \tag{13}$$

where $\eta = \xi/3.36$.

Equation (12) gives a better representation of the data in the early stages of transition whereas toward transition completion the two equations are in close agreement. In general, results from zero pressure gradient testing are best represented by Eq. (13); data taken under a mild adverse pressure gradient are best represented by Eq. (12) and data taken under strong adverse pressure gradients, where lag effects are important, are not well represented by either equation. There is scope for a new relationship, which would be a function of pressure gradient and would permit variations in dH/dx at transition inception and completion.

Use of the normalized plot of H' through transition significantly reduces the spread noted previously in connection with the raw distributions of shape factor. A single universal curve giving the variation of H' with ξ cannot be expected because of the subtransition effects on the preceding laminar layer and the lag effects on the developing turbulent layer.

Nevertheless the lag effects have implications for both future experimentation and for code development. Experimentalists have often used the variation in H as a guide to transition length. This practice will inevitably result in erratic predictions and is not recommended. Integral codes have assumed local equilibrium of the velocity profile and this assumption has been shown to be incorrect. Boundary layer codes need to be improved to take into account the transition mode and its varying speed of development, especially in regions of rapid changes in pressure gradient.

Correlations for Transition Length

In this section the results are first presented in the basic form

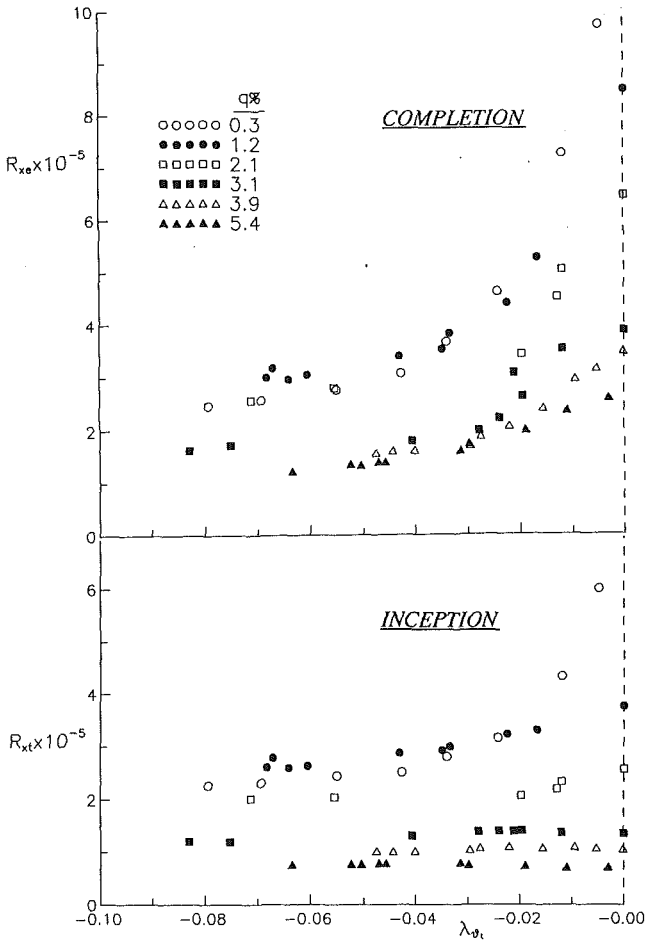

Fig. 8 Reynolds number based on distance as a function of pressure gradient parameter at transition inception

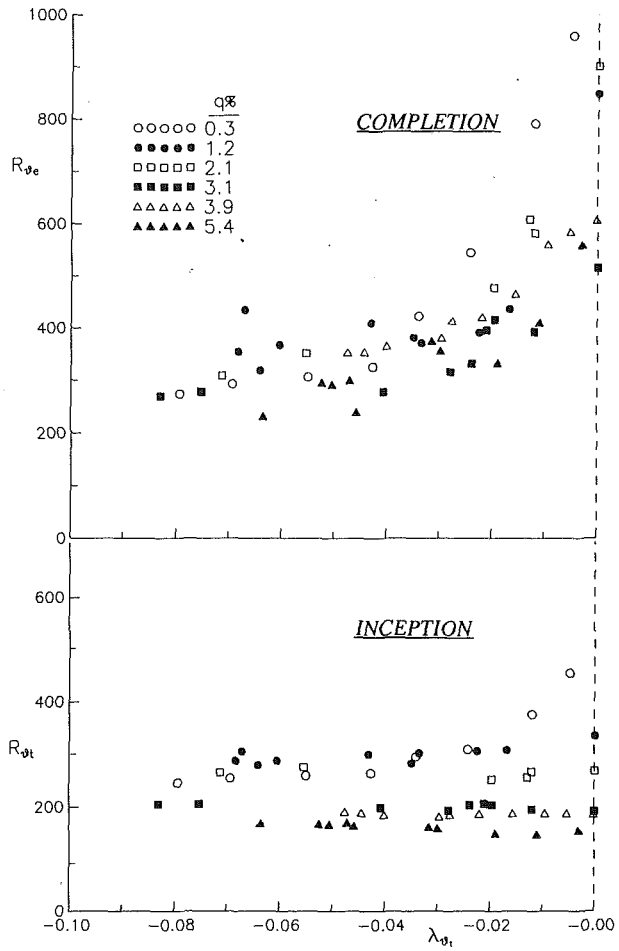

Fig. 9 Reynolds number based on momentum thickness as a function of pressure gradient parameter at transition inception

of Reynolds number at transition inception and completion. Transition length is then evaluated for all of the results and presented in correlations of three different transition length parameters.

Reynolds Numbers at Inception and Completion. Figure 8 presents Re_x at transition inception and completion as a function of $\lambda_{\theta t}$. Corresponding information for Re_θ is presented in Fig. 9.

Transition inception occurs at a higher Reynolds number under zero pressure gradient conditions, the value falling and then tending to a constant level under strong adverse pressure gradients. For the end of transition, however, the corresponding values fall much more rapidly with increasing adverse pressure gradient. Transition length under a strong adverse pressure gradient is an order of magnitude shorter than in the absence of a pressure gradient.

Under conditions of high free-stream turbulence level the transition inception Reynolds number is essentially independent of pressure gradient. This is not the case for lower turbulence levels where transition inception occurs much sooner under an adverse pressure gradient than under a zero pressure gradient.

Reynolds numbers for transition completion, whether based on streamwise distance or boundary layer thickness, exhibit a significant decrease with increasing adverse pressure gradient under all turbulence levels. This behavior is in accordance with the Walker model and is quantified in the correlations for transition length to be provided.

The transition inception and completion data of Figs. 8 and 9 seem to be anomalous. Under zero pressure gradient conditions the Reynolds numbers for transition inception and completion vary monotonically with turbulence level. Under adverse pressure gradients, however, the variation is less consistent. Figures 8 and 9 show that under strong adverse pressure gradients transition inception and completion both occur earlier for the 0.3 percent turbulence level than for the 1.2 percent level. At higher turbulence levels than 1.2 percent the inception and completion Reynolds numbers drop consistently with increasing turbulence level.

Two systematic differences could have a bearing on this discrepancy. The working section ahead of the plate is 600 mm shorter with no grid present and this could influence the flow in various ways, including the thickness of the side-wall boundary layers. The 0.3 percent turbulence level range is also thought to be equivalent to typical tunnel acoustic and vibration effects and this tunnel is by no means "clean," especially at low frequencies.

It was suspected that experimental error could cause such a discrepancy and accordingly repeat sets of readings were taken for both turbulence levels. These essentially confirmed the previous readings, although under strong adverse pressure gradients at low turbulence levels, different intermittency readings caused a slight upward revision of the Reynolds number for transition completion. As a result of this process the data presented in Figs. 8 and 9 are believed to be essentially correct.

Predictions of transition inception Reynolds numbers are available from other authors. No attempts has been made to produce a transition inception correlation from the present data but at turbulence levels above 2 percent the data are in good agreement with the correlation of Abu-Ghannam and Shaw (1980). At lower turbulence levels the agreement is poor,

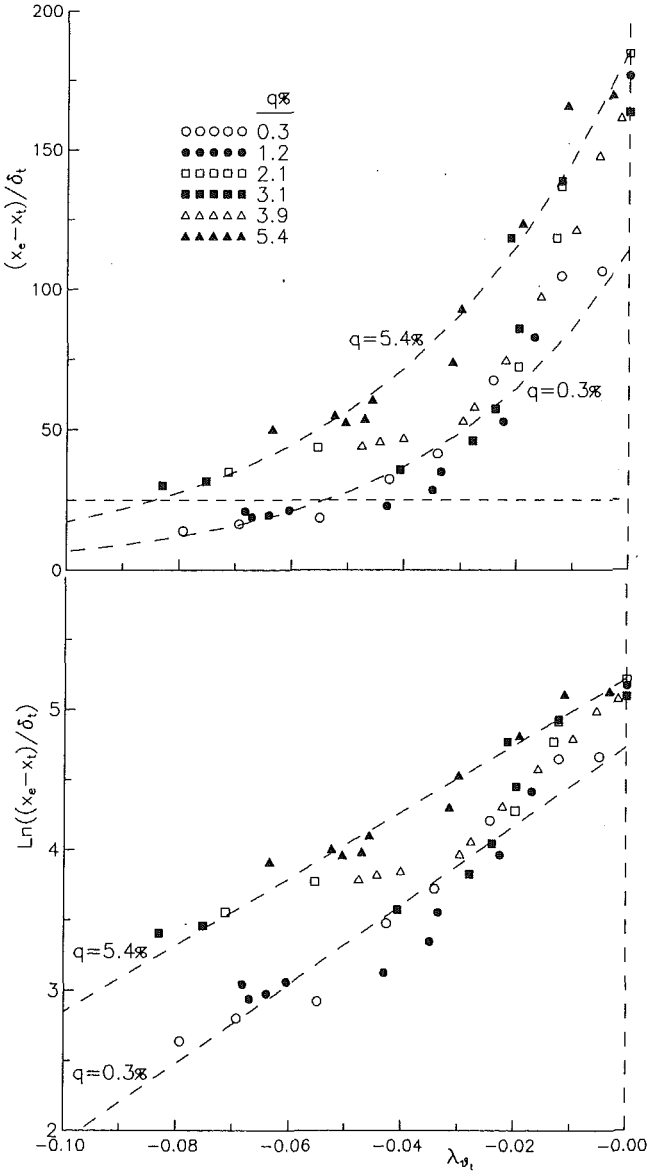

Fig. 10 Normalized transition length as a function of inception pressure gradient parameter

transition in these experiments occurring much earlier than predicted by the Abu-Ghannam and Shaw correlation.

Considerable subsequent work has been performed at the 0.3 percent turbulence level especially with regard to the mode of transition and the nature of the turbulent spots. Under higher turbulence levels it is quite clear that transition occurs through a bypass mechanism, as discussed by Morkovin (1991), the triggering influence being that of free-stream turbulence. For a turbulence level of 0.3 percent a plurality of mechanisms exists.

The changes in the physics of transition as the adverse pressure gradient is increased have been discussed by Walker and Gostelow (1989). Under a zero pressure gradient, breakdown occurs in sets, the behavior being quite random (Gostelow, 1991). Under an adverse pressure gradient the amplification of Tollmien-Schlichting waves is a dominant feature of the flow, the wave amplitude and frequency being comparable with those of the ensuing turbulent spots. This is a mechanism that does not predominate under other conditions. Such a transition is observed to begin and end at a lower Reynolds number than would be expected for bypass transition. This is because the amplification of subharmonics is a common precursor to the establishment of turbulent spots.

A tendency to subharmonic behavior under adverse pressure gradients was noted by Walker and Gostelow. Research on clean wind tunnels often results in a very rapid transition by amplification and "filling in" of subharmonic modes rather than by the occurrence of spots. The most usual mode is the progressive increase in the amplitude of subharmonics and transition occurring principally by a downward cascading of the spectrum below the Tollmien-Schlichting frequency. Such behavior has been observed in the present investigations under strong adverse pressure gradients and at a turbulence level of 0.3 percent; it appears that this condition is on the boundary between the spot scenario and the subharmonic scenario. Which of these occurs may depend on several factors including the Reynolds number. Subharmonic transition may present itself as a competing scenario, which results in earlier inception and completion than the spot mechanism and this is thought to be the most likely explanation of the anomalies at low turbulence levels.

Length as a Function of Boundary Layer Thickness. In considering the variation of shape factor through transition it was found that, under conditions of adverse pressure gradient and low turbulence level, transition occurred sufficiently rapidly that the velocity profile was unable to regain equilibrium.

Indications from experiments on turbulent spots (Gostelow et al., 1992) have suggested that a streamwise distance of about 25 absolute thicknesses is required for the change from a laminar velocity profile to a turbulent velocity profile to become established. This criterion provides a useful basis for evaluating such dynamic effects and accordingly the distance between transition inception and completion has been normalized by the absolute thickness at transition inception in Fig. 10. The results have been plotted on both a logarithmic and a linear basis. The linear plot demonstrates that the effect of pressure gradient is strong and that there is a weaker effect of free-stream turbulence, within the range tested. It also shows that all results from strong adverse pressure gradients, at free-stream turbulence levels below 2 percent, have a transition length of less than 25δ and are therefore likely to be influenced by lag effects. The linear plot also provides an alternative (and possibly more accessible) approach to that of the Walker model, avoiding the need for evaluating the theoretical minimum transition length. It should, however, be noted that there exists little physical justification for a correlation based simply on inception boundary layer thicknesses.

The logarithmic plot provides a viable basis for a correlation. The representation for each turbulence level on the logarithmic plot is reasonably well approximated by a straight line, although there is, understandably, some scatter. The results for the extreme turbulence levels of 0.3 and 5.4 percent have been represented by fitting a straight line in the logarithmic plot. The linear fits were then used to derive exponential expressions for the variation of $(x_e-x_t)/\delta_t$, which have been added to the linear plot for that expression. The derived equation is

$$(x_e-x_t)/\delta_t = 139.143\exp(-1.523\lambda_{\theta_t}\ln(q) + 26.278\lambda_{\theta_t} + 0.169\ln(q)). \quad (14)$$

Length as a Function of Predicted Minimum Length. The transition length predicted by Eq. (1) for a strong adverse pressure gradient is considerably shorter than that for a zero pressure gradient. Experimental investigations over a wide range of pressure gradients and turbulence levels have suggested that the change from the long transition lengths of zero pressure gradient flows to the short transition lengths under adverse pressure gradients is rapid at first, the zero pressure gradient case being sensitive to the imposition of even mild

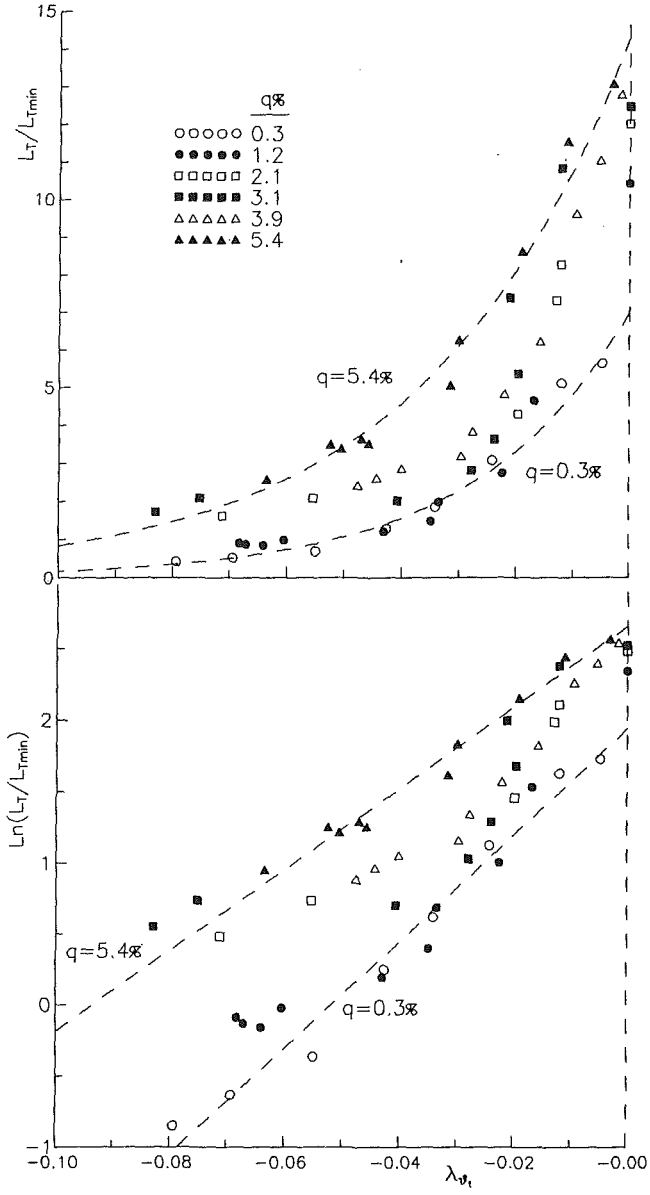

Fig. 11 Length normalized by minimum predicted length as a function of pressure gradient parameter at inception

diffusion. The adjustments to the rather different physics under diffusing conditions are progressive and under strong adverse pressure gradients the new physical regime, in which the strong amplification of Tollmien–Schlichting waves predominates, is firmly established. Accordingly it is reasonable to expect an exponential truncation in transition length between the zero pressure gradient and the strong adverse levels.

The minimum transition length predicted by the Walker model has been evaluated for the present data set and then used to normalize the measured transition length. The results for all six turbulence levels are presented in Fig. 11. These are given on both a logarithmic and a linear basis.

By fitting the data sets for the two extreme turbulence levels with a best straight line on the logarithmic plot and interpolating a reasonable fit for the data is obtained. The curve fitting and interpolation procedures have resulted in a correlation for L_T/L_{Tmin} in the form of exponential variations of this parameter with pressure gradient and turbulence level. The correlation is

$$L_T/L_{Tmin} = 9.412 \exp(-3.121\lambda_{\theta_t} \ln(q) + 33.692\lambda_{\theta_t} + 0.248 \ln(q)). \quad (15)$$

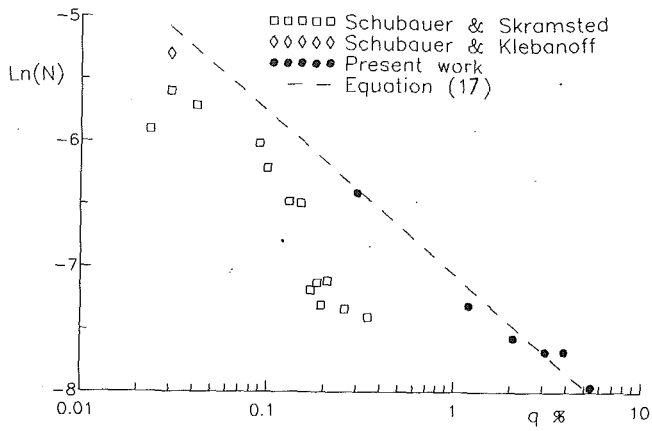

Fig. 12 Spot formation rate parameter as a function of turbulence level for zero pressure gradient

While there is an exponential dependence of transition length, as normalized by predicted minimum transition length, on the levels of both adverse pressure gradient and free-stream turbulence, the dependence on pressure gradient is much the strongest.

In passing it may be observed that the data set for 0.3 percent turbulence level is identical with that presented by Walker and Gostelow (1989). A difference expression was presented for the correlation in that paper, based on the results of that data set alone. When presented in the context of all six turbulence levels, a simple exponential fit for each data set seems justifiable and such an approach has been adopted in this paper.

Spot Formation Rate. The nondimensional spot formation rate parameter N, as defined by Narasimha (1985), has been obtained for all conditions tested. Values of N were evaluated using the relation

$$N = 0.412\ \mathrm{Re}_{\theta_t}^3/\mathrm{Re}_\lambda^2 \quad (16)$$

which is derived from the defined relationship for N in conjunction with Narasimha's universal intermittency distribution.

Data for the variation of N with free-stream turbulence level under zero pressure gradient conditions, originally compiled by Narasimha and Dey (1984), are presented on a logarithmic basis in Fig. 12. The data of Abu-Ghannam and Shaw (1980), for which the zero pressure gradient condition was not clearly identified, are omitted. Data from the current investigation are superimposed as solid symbols. The points at 0.3, 3.9, and 5.4 percent turbulence levels are extrapolated slightly from data taken over a range of pressure gradients since no readings corresponded precisely with zero pressure gradient in those cases. The data show that in the absence of a streamwise pressure gradient the spot formation rate parameter decreases monotonically with increasing free-stream turbulence. The value of N recorded agrees with the level of 0.7×10^{-3}, quoted by Narasimha (1985), at a turbulence level, q, of 1.44 percent an reaches asymptotically a level of somewhat less than half of that value. In view of the paucity of confirming data this degree of agreement is considered to be reasonable.

The new data are represented well by the equation

$$N = 0.86 \times 10^{-3} \exp(-0.564 \ln(q)) \quad (17)$$

and this is superimposed as a dashed line in Fig. 12.

The correlation line is also close to the Schubauer and Klebanoff (1955) result, thereby covering a turbulence level range of over two decades. Equation (17) indicates a higher spot formation rate than the data of Schubauer and Skramstad (1948), thus emphasizing their observation that acoustical and other disturbances are at least as influential as low turbulence levels.

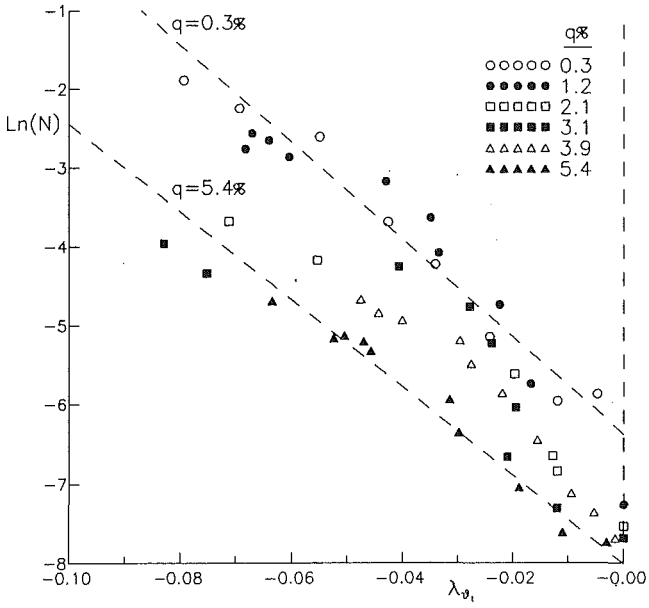

Fig. 13 Spot formation rate parameter as a function of pressure gradient parameter at inception

In order to provide designers with a more reliable basis for representation of the transition zone in boundary layer predictions, the results of the investigation are summarized in a correlation of the experimental data under adverse pressure gradients.

The demonstrated exponential variation of spot rate with turbulence level and pressure gradient makes it possible to relate these parameters in a family of curves. The complete data set is presented in Fig. 13 on a logarithmic basis with an indication of the trend and limits of the derived correlation. Although there is some scatter and the data fit is relatively loose, in general the data are adequately represented for correlation purposes.

It is clear from Fig. 13 that any significant departure from zero pressure gradient conditions causes a rapid increase in nondimensional spot formation rate. As the laminar separation limit is approached, the value of N has increased by two orders of magnitude. Clearly there is a direct connection (the inverse square law relationship of Eq. (16)) between the increased spot formation rate and the reduction in transition length indicated in Figs. 10 and 11, as the pressure gradient changes from zero to moderate adverse values.

The equation derived is

$$N = 0.86 \times 10^{-3} \exp(2.134 \lambda_{\theta_t} \ln(q) - 59.23 \lambda_{\theta_t} - 0.564 \ln(q). \quad (18)$$

The transition length for zero and mild adverse pressure gradients has been shown to be much longer than that for the more severe pressure gradients often encountered in turbomachines. Although no attempt has been made to extract from the data an explanation for this behavior, some clues are readily forthcoming. The high spot formation rates, for example, and the correspondingly reduced transition lengths, are entirely consistent with the prediction of Walker (1987) that length correlations developed for constant pressure flows would seriously overestimate the length under an adverse pressure gradient.

Walker attributed this discrepancy to the tendency for natural transition in a zero pressure gradient to evolve from the breakdown of instability waves in "sets" and argued that under adverse pressure gradients transition tended to be a forced process with a continuous breakdown of instability waves into turbulence and hence a much shorter transition zone.

This explanation is fundamental for axial flow compressors. Were the transition length not considerably shorter than indicated by flat plate correlations, the boundary layer would be transitional over most of the blade surface. The blade would be quite incapable of sustaining the required aerodynamic loadings. The strong increases in spot formation rate as laminar separation is approached are also thought to be a determinant of the bubble mode of separation. If these increases in spot formation rate did not occur, any laminar separation would result in the more severe mode of complete breakaway from the surface.

It is important to be able to model the local spot formation rate and to treat this as a variable throughout the transition region. The most promising approach is the identification of an appropriate representation of the spot formation rate for incorporation locally into boundary layer prediction codes.

Conclusions

Measurements of boundary layer transition have covered six different turbulence levels and a wide range of adverse pressure gradients. The development of an on-line intermittency meter was an essential feature of the reported program in which extensive intermittency and velocity profile data were generated. Use of the Narasimha procedure for determining transition inception revealed strong similarity in the observed streamwise variation of intermittency for all conditions.

Effects of free-stream turbulence on the velocity profiles in the early stages of transition were particularly strong. Under high levels of free-stream turbulence and adverse pressure gradient the data had exhibited a pronounced subtransition. In this situation the entire velocity profile appears to be affected; the influence of free-stream turbulence on laminar boundary layers is a matter that needs further attention.

Under the adverse pressure gradients typical of axial flow compressors transition occurs much more rapidly than had been appreciated. Whereas the momentum thickness obeys the distribution through transition presented by Abu-Ghannam and Shaw, lag effects on the velocity profile are strong. The velocity profile responds sufficiently slowly to the perturbation imposed by transition that, in the short transition regions prevailing, much of the expected reduction in form factor has not occurred prior to the end of transition.

This raises questions about the use of form factor as an indicator of the extent of transition in experimental work. For boundary layer calculations of the integral type a lag formulation appears to be necessary; the incorporation of the Narasimha intermittency distribution is a logical starting point since it provides a universal basis for describing the transition process.

In the absence of an imposed pressure gradient the transition region is long, in keeping with established results from flat plate testing. Any departure into the adverse region results in a strong reduction in transition length. For quite a modest adverse pressure gradient the transition length becomes severely reduced.

Associated with the shortening of transition is a dramatic increase in turbulent spot formation rate. This is consistent with Walker's model, in which transition in the absence of a streamwise pressure gradient occurs in sets of instability waves interspersed with periods of stable laminar flow. In contrast, transition under an adverse pressure gradient is a forced transition with a continuous breakdown of individual waves. The observed strong reduction in transition length under adverse pressure gradients, with the associated rapid increase in turbulence spot formation rate, is fundamental for the loading capability of the axial flow compressor and also an important prerequisite for laminar separation bubble formation.

Data for spot formation rates under conditions of zero pressure gradient have been compared with the compilation of

Narasimha and Dey. The trend and levels recorded are in reasonable agreement with existing data. As adverse pressure gradients are applied the spot formation rate increases rapidly in accordance with the differences in the physics of the transition process under those conditions.

It has been possible to obtain a reasonable fit to the transition length data, resulting in serviceable correlations for its variations as a function of both turbulence level and adverse pressure gradient. This was achieved for transition length, as normalized by inception boundary layer thickness, for predicted minimum transition length, and also for spot formation rate.

Acknowledgments

The authors wish to express their appreciation to the Australian Research Council and to Rolls-Royce plc for their financial support and encouragement.

References

Abu-Ghannam, B. J., and Shaw, R., 1980, "Natural Transition of Boundary Layers—the Effects of Turbulence, Pressure Gradient, and Flow History," *Journal of Mech. Eng. Sci.*, Vol. 22, No. 5.

Alt, P., 1987, "An Intermittency Meter for Investigating Boundary Layer Transition," University of Technology, Sydney, Technical Report No. NSWT/ME17.

Ashworth, D. A., LaGraff, J. E., and Schultz, D. L., 1989, "Unsteady Interaction Effects on a Transitional Turbine Blade Boundary Layer," ASME JOURNAL OF TURBOMACHINERY, Vol. 111, pp. 162–168.

Crabtree, L. F., 1958, "Prediction of Transition in the Boundary Layer on an Aerofoil," *J. Roy. Aer. Soc.*, Vol. 62.

Curle, N., and Skan, S. W., 1955, "Approximate Method for Predicting Separation of Laminar Boundary Layers," *Aero. Quart.*, Vol. 8.

Dey, J., and Narasimha, R., 1988, "An Integral Method for the Calculation of 2-D Transition Boundary Layers," Dept. of Aerospace Eng., Indian Institute of Science, Report No. 88FM7.

Dhawan, S., and Narasimha, R., 1958, "Some Properties of Boundary-Layer Flow During the Transition From Laminar to Turbulent Motion," *Journal of Fluid Mech.*, Vol. 8, pp. 418–436.

Emmons, H. W., 1951, "The Laminar-Turbulent Transition in a Boundary Layer—Part 1," *Journal of Aero. Sci.*, Vol. 8.

Fraser, C. J., Milne, J. S., and Gardiner, I. D., 1988, "The Effect of Pressure Gradient and Freestream Turbulence Intensity on the Length of Transitional Boundary Layers," *Proc. Instn. Mech. Engrs.*, Vol. 202, No. C3, pp. 195–203.

Frenkiel, F. N., 1948, "The Decay of Isotropic Turbulence," *Trans. ASME*, Vol. 70, p. 311.

Gostelow, J. P., and Blunden, A. R., 1988, "Investigations of Boundary Layer Transition in an Adverse Pressure Gradient," ASME JOURNAL OF TURBOMACHINERY, Vol. 111, pp. 366–375.

Gostelow, J. P., 1989, "Adverse Pressure Gradient Effects on Boundary Layer Transition in a Turbulent Free Stream," *Proceedings 9th International Symposium on Air Breathing Engines*, Athens.

Gostelow, J. P., and Walker, G. J., 1991, "Similarity Behavior in Transitional Boundary Layers Over a Range of Adverse Pressure Gradients and Turbulence Levels," ASME JOURNAL OF TURBOMACHINERY, Vol. 113, pp. 617–625.

Gostelow, J. P., 1991, "Influence of Adverse Pressure Gradients on Chaotic Regimes Encountered During Transition," *Proceedings, First Joint ASME-JSME Fluids Engineering Conference*, Portland, OR.

Gostelow, J. P., Hong, G., and Sheppeard, M. A., 1992, "Investigations of a By-pass Spot With Reference to Boundary Layers on Turbomachinery Blading," *Proc. Fourth International Symposium on Rotating Machinery*, Honolulu, HI.

Mayle, R. E., 1991, "The Role of Laminar-Turbulence Transition in Gas Turbine Engines," ASME JOURNAL OF TURBOMACHINERY, Vol. 113, pp. 509–537.

Morkovin, M. V., 1991, "Bypass-Transition Research: Issues and Philosophy," *Proceedings, Symposium on 60th Birthday of E. Reshotko*, Newport News, VA.

Narasimha, R., 1957, "On the Distribution of Intermittency in the Transition Region of the Boundary Layer," *J. Aero. Sci.*, Vol. 24, p. 711.

Narasimha, R., 1978, "A Note on Certain Turbulent Spot and Burst Frequencies," Indian Institute of Science Report No. 78FM10.

Narasimha, R., and Dey, J., 1984, "Spot Formation Rate in Incompressible Constant-Pressure Boundary Layer," Indian Institute of Science Report No. 84FM11.

Narasimha, R., 1985, "The Laminar-Turbulent Transition Zone in the Boundary Layer," *Progress in Aerospace Sci.*, Vol. 22, pp. 29–80.

Narasimha, R., and Dey, J., 1989, "Transition-Zone Models for 2-Dimensional Boundary Layers: A Review," *Sadhana*, Vol. 14, pp. 518–523.

Schubauer, G. B., and Skramstad, H. K., 1948, "Laminar-Boundary-Layer Oscillations and Transition on a Flat Plate," NACA Rep. 909.

Schubauer, G. B., and Klebanoff, P. S., 1955, "Contributions on the Mechanics of Boundary-Layer Transition," NACA TN-3489.

Thwaites, B., 1949, "Approximate Calculation of the Laminar Boundary Layer," *Aero. Quart.*, Vol. 1, p. 245.

Walker, G. J., 1987, "Transitional Flow on Axial Turbomachine Blading," *AIAA Journal*, Vol. 27, No. 5, pp. 595–602.

Walker, G. J., Subroto, P. H., and Platzer, M. F., 1988, "Transition Modeling Effects on Viscous/Inviscid Interaction Analysis of Low Reynolds Number Airfoil Flows Involving Laminar Separation Bubbles," ASME Paper No. 88-GT-32.

Walker, G. L., and Gostelow, J. P., 1989, "Effects of Adverse Pressure Gradients on the Nature and Length of Boundary Layer Transition," ASME JOURNAL OF TURBOMACHINERY, Vol. 112, pp. 196–205.

Wood, N. B., 1973, "Flow Unsteadiness and Turbulence Measurements in the Low-Pressure Cylinder of a 500 MW Steam Turbine," *I.Mech.E. Conf. Publ.*, Vol. 3, p. 115.

Fluid Mechanics and Heat Transfer Measurements in Transitional Boundary Layers Conditionally Sampled on Intermittency

J. Kim
Assistant Professor,
Department of Engineering,
University of Denver,
Denver, CO 80208

T. W. Simon
Professor,
Department of Mechanical Engineering,
University of Minnesota,
Minneapolis, MN 55455

M. Kestoras
Assistant Professor,
ISITEM, Laboratory de Thermocinetique,
University of Nantes,
Nantes, France

An experimental investigation of transition on a flat-plate boundary layer was performed. Mean and turbulence quantities, including turbulent heat flux, were sampled according to the intermittency function. Such sampling allows segregation of the signal into two types of behavior—laminarlike and turbulentlike. Results show that during transition these two types of behavior cannot be thought of as separate Blasius and fully turbulent profiles, respectively. Thus, simple transition models in which the desired quantity is assumed to be an average, weighted on intermittency, of the laminar and fully turbulent values may not be entirely successful. Deviation of the flow identified as laminarlike from theoretical laminar behavior is due to a slow recovery after the passage of a turbulent spot, while deviation of the flow identified as turbulentlike from fully turbulent characteristics is possibly due to an incomplete establishment of the fully turbulent power spectral distribution. Measurements were taken for two levels of free-stream disturbance—0.32 and 1.79 percent. Turbulent Prandtl numbers for the transitional flow, computed from measured shear stress, turbulent heat flux, and mean velocity and temperature profiles, were less than unity.

Introduction

Despite the attention of many investigators, an understanding of boundary layer transition remains elusive. The sensitivity of transition to many factors (free-stream acceleration, the level of free-stream disturbance and its characteristics, surface roughness, surface curvature, surface heating, wall suction, compressibility, and unsteadiness, to name a few) makes prediction of transition in complex machines such as gas turbines difficult. Direct numerical simulation, though quite useful where applied, has thus far been restricted to a few, simple geometry cases. The transition process is sufficiently complex that experimental observations must first be made under conditions where only a few effects are allowed. Later, as understanding builds, more effects can be added and more realistic geometries can be investigated. The following discusses results from a program that has been underway at the University of Minnesota in which measurements are made to support a fundamental understanding of transition.

The program began with a study of the effects of free-stream disturbance level (Wang et al., 1985) and streamwise convex-curvature (Wang and Simon, 1987). The purpose of the present portion of the program is to document flat-plate transitional boundary layer flow further by applying some new measurement capabilities. The present experiments provide further evidence of the effect of free-stream turbulence, lending support for the testing and development of transition prediction models. Specifically, these results allow one to test the applicability of intermittency-based transition models, the first of which was proposed by Dhawan and Narasimha (1958), in which a Blasius-type flow for the laminar portion and a fully turbulent flow for the turbulent portion were employed. Although many researchers have studied flat-plate transition (see Wang and Simon, 1987, for a review), only a few have used conditional sampling on intermittency to look at the laminar and turbulent portions of the transitional boundary layer separately. No researchers, to the authors' knowledge, have directly done so with turbulent heat flux and turbulent Prandtl number measurements.

In the tests, a boundary layer was allowed to undergo transition naturally, becoming a fully turbulent boundary layer by the end of the test section. The effects of two levels of free-stream disturbance (0.32 and 1.79 percent) were investigated. The measurements included local Stanton number, intermittency, turbulent heat flux ($\overline{v't'}$), turbulent shear stress ($\overline{u'v'}$), and profiles of velocity and temperature. Turbulent Prandtl

Contributed by the International Gas Turbine Institute for publication in the JOURNAL OF TURBOMACHINERY. Manuscript received at ASME Headquarters September 1993. Associate Technical Editor: T. H. Okiishi.

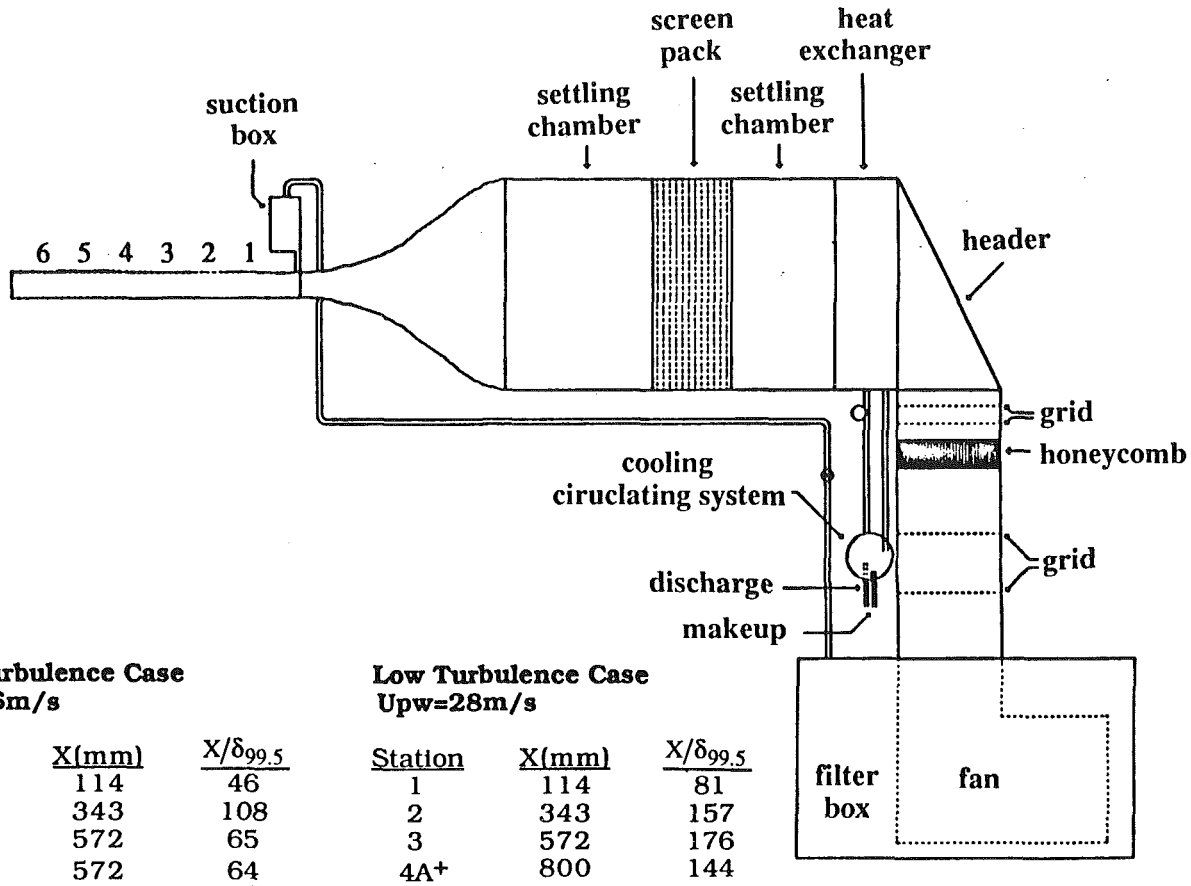

High Turbulence Case
Upw=16m/s

Station	X(mm)	$X/\delta_{99.5}$
1	114	46
2	343	108
3A++	572	65
3	572	64
4	800	60
5	1029	59

++Upw=12m/s

Low Turbulence Case
Upw=28m/s

Station	X(mm)	$X/\delta_{99.5}$
1	114	81
2	343	157
3	572	176
4A+	800	144
5	1029	102
6	1257	114

+Upw =26 m/s

Fig. 1 Schematic of test facility

number profiles were computed from the last four quantities. A special circuit was employed for generating an analog intermittency function from a hot-wire signal.

Test Facility Description and Qualification

The experiment was conducted in an open-circuit, blown-type wind tunnel. Details of this tunnel are described by Wang and Simon (1987) (Fig. 1). The test channel was rectangular, 68 cm wide, 11.4 cm deep, and 137 cm long. Higher free-stream turbulence levels were obtained by inserting a coarse grid constructed of 2.5 cm wide by 0.32 cm thick aluminum strips in a square array of 10 cm center-to-center distance at the entrance of the nozzle.

Mean velocity measurements within the potential core at the nozzle exit showed a peak-to-peak variation of 0.2 percent about a nominal velocity of 27 m/s. The free-stream turbulence intensity values at the nozzle exit were measured using a cross-wire probe oriented with the stem first in the y direction, then in the z direction. This allowed measurement of the three velocity components. Values of turbulence intensity were 1.79 and 0.32 percent with and without the turbulence generating grid, respectively. Details of the turbulence data taken with the grid in place will be presented in the results section. Measurements of mean temperature within the flow exiting the nozzle showed a peak-to-peak variation of 0.2°C. The outer wall was adjusted such that the static pressure coefficient, C_{pr}, was zero, within 1.5 percent, along the test wall for each case.

The test wall was heated with a uniform heat flux (within 1 percent) over the test surface, as measured by Wang (1984). Except for small unheated starting length effects (the unheated

Nomenclature

C_f = skin friction coefficient
C_p = specific heat
C_{pr} = static pressure coefficient = $(P - P_{ref})/(0.5\ \rho u_\infty^2)$
H = shape factor
Re = Reynolds number
Q = wall heat flux
St = Stanton number
t = temperature
u = streamwise velocity
v = cross-stream velocity
w = cross-span velocity
x = streamwise distance
y = cross-stream distance
γ = intermittency
ρ = density

Superscripts

\+ = wall coordinates
′ = rms value or fluctuation, depending on context
— = time-averaged quantity

Subscripts

max = maximum value of the profile
w = wall value
∞ = free-stream value

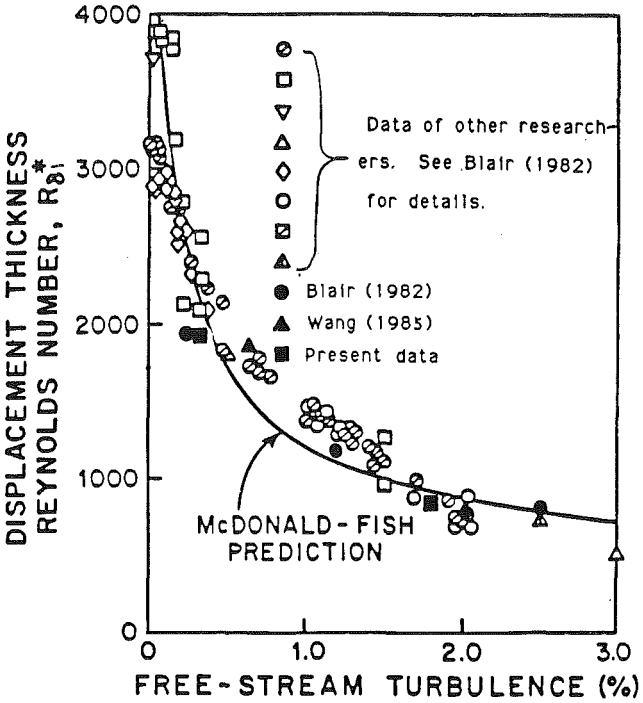

Fig. 2 Comparison of transition start location with that of other researchers and with the McDonald-Fish prediction (1973)

starting length was ~ 1.5 cm), Stanton numbers for the laminar boundary layer were in excellent agreement with the accepted correlation (for constant wall heat flux in terms of Re_x, Kays and Crawford, 1980). A slight dip in Stanton number below the laminar correlation was noted, which is caused by a decrease in wall heat flux, with streamwise distance, due to increasing radiant heat loss. A STAN5 (Crawford and Kays, 1976) simulation, using the measured wall convective heat flux as the boundary condition, yielded Stanton numbers at the start of transition that were 4 percent lower than the values given by the constant-wall-heat-flux correlation—in agreement with the data.

For the lower-turbulence baseline case, the measured Reynolds numbers based on streamwise distance, displacement, and momentum thicknesses at the beginning of transition (unheated flow) were 1×10^6, 1920, and 737, respectively. A plot of the transition start Reynolds number versus the free-stream turbulence intensity is shown on Fig. 2. The start of transition is taken to be the point at which the near-wall ($y^+ < 20$) intermittency becomes 5 percent. This measurement was performed in the unheated flow to avoid the known effects of wall heating on transition (Schlichting, 1979). The present data are comparable to those of other researchers. An energy balance, performed by integrating the wall heat flux along the centerline of the test wall and comparing with the increase in energy carried in the boundary layer flow, showed closure to within 3 percent. Measurements of mean velocity profiles, shape factor (H), and intermittency were consistent with other researchers' results (e.g., Wang et al., 1985; Blair, 1982; Kuan and Wang, 1988).

For the heat transfer data, the nominal heat flux was 160 W/m^2, which yielded a minimum temperature difference of about 4°C for the TI = 0.32 percent case. Because of the effect of heating, heated and unheated data cannot be compared within the transition zone for the low TI case. For this reason, the only heat transfer data presented for the low TI case will be profiles of the turbulent heat flux and turbulent Prandtl number. Positions within transition are indicated by their respective intermittency values. Transition for the high TI case (TI = 1.79 percent) was not affected by heating; thus heat transfer data and unheated flow hydrodynamic data can be compared in the transition region for the TI = 1.79 percent case.

The shear velocity is found by curve fitting near-wall data obtained using a single-element, hot-wire probe to expected near-wall relationships. In turbulent flows, the viscous sublayer relationship, $u^+ = y^+$, the van Driest relationship (Kays and Crawford, 1980) and the law-of-the-wall given as:

$$u^+ = 2.44 \ln y^+ + 5.0$$

where

$$u^+ = \frac{\bar{u}/u_\infty}{\sqrt{C_f/2}} \text{ and } y^+ = \frac{y u_\infty \sqrt{C_f/2}}{\nu}$$

were used to find the local skin friction coefficient (C_f). In laminar and transitional flows the data were fit to the equation $u^+ = y^+$ to find C_f. They were segregated into laminar and turbulent flows according to the intermittency function, then processed to determine the laminar C_f and turbulent C_f, separately.

Intermittency Circuit

A circuit for determining when the flow is laminarlike or turbulentlike was constructed. This circuit, based on a design by Kim et al. (1978), provides a bimodal signal (the intermittency function) that identifies the flow as either laminar or turbulent. The intermittency is the time-averaged value of the intermittency function. The intermittency function is used to conditionally sample the laminarlike flow and the turbulentlike flow.

The circuit takes advantage of the much larger time derivative of the turbulentlike signal as compared to that of the laminarlike signal. To do this, the hot-wire-anemometer signal is processed by a series of filters, differentiators, and rectifiers. At a level detector, the signal is compared to an adjustable threshold value. If it is higher than the threshold, the output signal of the level detector is high (turbulentlike). It is low (laminarlike) otherwise. Comparison with the threshold is performed in two channels. In the first channel, the rectified derivative of the hot-wire signal is compared with a threshold value. In the second channel, the rectified second derivative of the hot-wire signal is compared with another threshold value. The two channels are used to avoid the problem of zero crossing: a fully turbulent signal has derivative values, which unavoidably fall below the threshold value as they change sign and cross the zero-volt axis. Thus, the flow will at times falsely be declared laminar. The zero-crossing problem can be eliminated if both channels are monitored: Both channels have crossing drop-outs, however the zero crossings of the two channels do not coincide; the reason is that the second derivative is zero when the rectified first derivative is maximum. An "OR" gate is used to declare the flow turbulent if either channel output is high. The flow is declared laminar otherwise.

The choice of the threshold value of the intermittency circuit can be important. However, a range of values of the threshold produces intermittencies that are independent of the value of the threshold. The circuit is tuned at each station. The hot wire is placed in a transitional flow and the first derivative of the signal along with the output of the channel's level detector are observed on an oscilloscope. The threshold of the first derivative channel is then raised until the laminar flow, as shown by the hot-wire signal derivative, is truly declared laminar. The threshold of the second derivative channel is then lowered until the zero-crossing drop-outs are mostly eliminated from the signal available at the "OR" gate output. Since the drop-outs that still persist occur at high frequencies, they are eliminated by using a low-pass filter and a level detector at the "OR" gate output.

An example of the circuit performance in a transitional boundary layer flow is shown on Fig. 3.

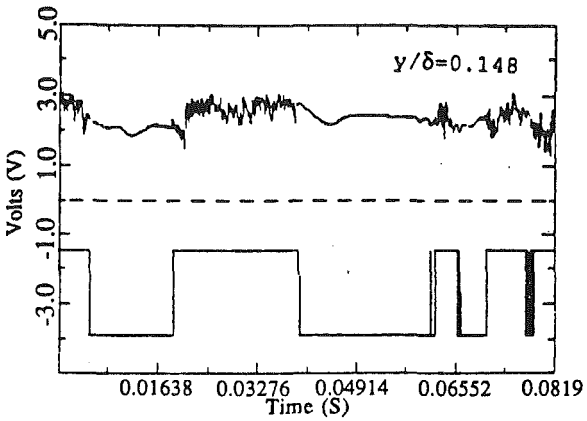

Fig. 3 Intermittency circuit performance in a transitional boundary layer, position in the boundary layer is as noted

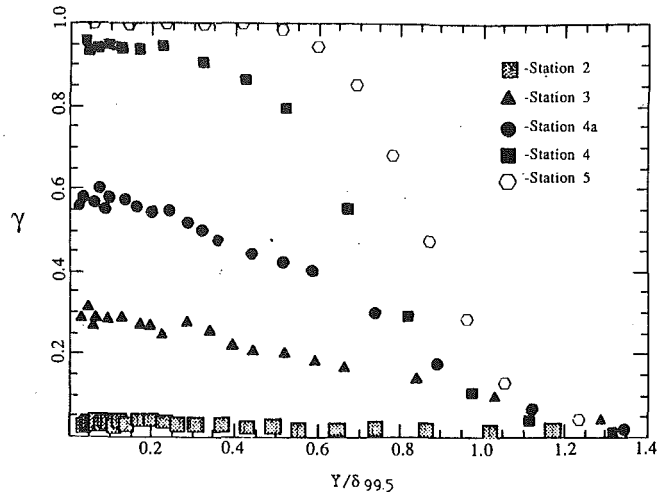

Fig. 4 Intermittency profile variation through transition ($TI = 0.32$ percent)

Triple-Wire Probe for Turbulent Heat Flux Measurements

A probe to measure $\overline{v't'}$ in turbulent boundary layers was implemented by Kim and Simon (1988) and used to take measurements in a turbulent boundary layer passing over a convex surface, followed by a flat wall. The probe geometry was based on a design by Blair and Bennett (1984). As used in the present study, one wire was operated in the constant-current mode as a resistance thermometer to measure the instantaneous flow temperature, the other two wires being operated as standard constant-temperature wires. The method of Hishida and Nagano (1978) was chosen to compensate for the low-frequency response of the constant-current cold wire. The heat transfer coefficient over the constant-current cold wire, which is required in this method, is estimated from the parallel hot-wire signal. The cold-wire signal and its time derivative were used in the signal processing. The temperature sensing wire was 1.25 μm in diameter. The frequency response of the probe was measured to be 4 kHz. This was determined from a square-wave test in which the probe was placed in a flow and the cold-wire current was stepped down from 30 mA (wire is heated) to 1 mA (wire cools to room temperature). The voltage drop across the wire and its derivative were recorded on a digital oscilloscope as the wire cooled in a characteristic exponential fashion. A compensated voltage trace was then calculated as discussed by Hishida and Nagano (1978). The inverse of the compensated voltage drop time was taken as the probe frequency response. A circuit built for this purpose is described by Kim (1990). The data taken with the compensated probe in a heated, flat-wall, turbulent boundary layer were in excellent agreement with the data of Gibson and Verriopoulos (1984).

Results

The Low TI Case—TI = 0.32 Percent

Free-Stream Turbulence Intensity and Spectra. A power spectral density (PSD) distribution of the streamwise velocity component using a horizontal wire revealed a spectrum with a relatively strong peak corresponding to 29 Hz. This peak was traced (using an accelerometer and a vibration analyzer) to a slight rocking motion of the blower. All reasonable effort has been applied to reduce this fan motion. This frequency is not expected to influence the transition process as the minimum critical frequency for amplification of disturbances, estimated from linear stability theory, is 1600 Hz. The spectrum was relatively clean otherwise.

Measurements of the free-stream turbulence intensity versus streamwise distance using a cross-wire probe revealed that u' was roughly twice the value of either v' or w'. The u', v', and w' values did not decay appreciably along the streamwise length of the test section. It should be noted that this anisotropy would improve if the fan rocking frequency were removed. Specifically, the free-stream turbulence intensity based on the streamwise fluctuating component was 0.45 percent, of which 0.03 percent was due to the fan rocking frequency. The free-stream velocity was nominally 26.5 m/s.

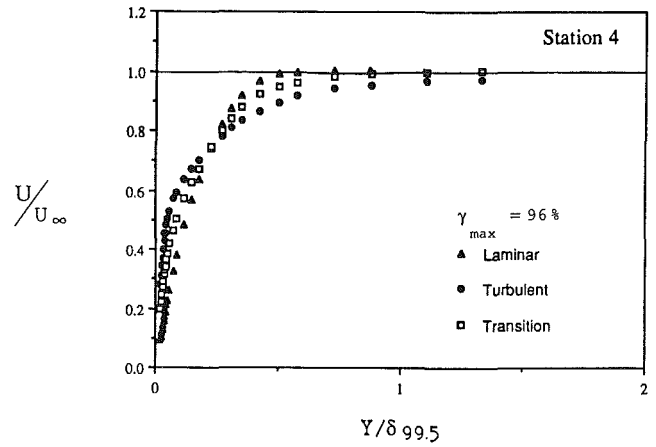

Fig. 5 Mean velocity profile sampled on intermittency (TI = 0.32 percent); the profile is normalized on the transitional profile thickness

Intermittency Profiles. Intermittency profiles, Fig. 4, show the same qualitative behavior from one station to the next, a relatively flat value in the near-wall region followed by, with increasing y values, a decay to zero at the edge of the boundary layer. The near-wall intermittency of the turbulent boundary layer is nearly 1.0. The decay at the edge of the boundary layer describes the intermittency presence of free-stream flow being entrained into the boundary layer in the wake region. In transitional flow, the near-wall intermittency is below 1.0 because only a portion of the surface is covered by turbulent spots. A profile, 4a, has been added to this figure. This profile was taken at the same position as that of station 4 but with a lower velocity so that transition was less complete. Adding this station allows better characterization of the evolution of intermittency profiles through transition. In the laminar boundary layer, the intermittency is nearly zero throughout the boundary layer. In the following, quantities are discussed in terms of the degree of completion of transition. This is expressed in terms

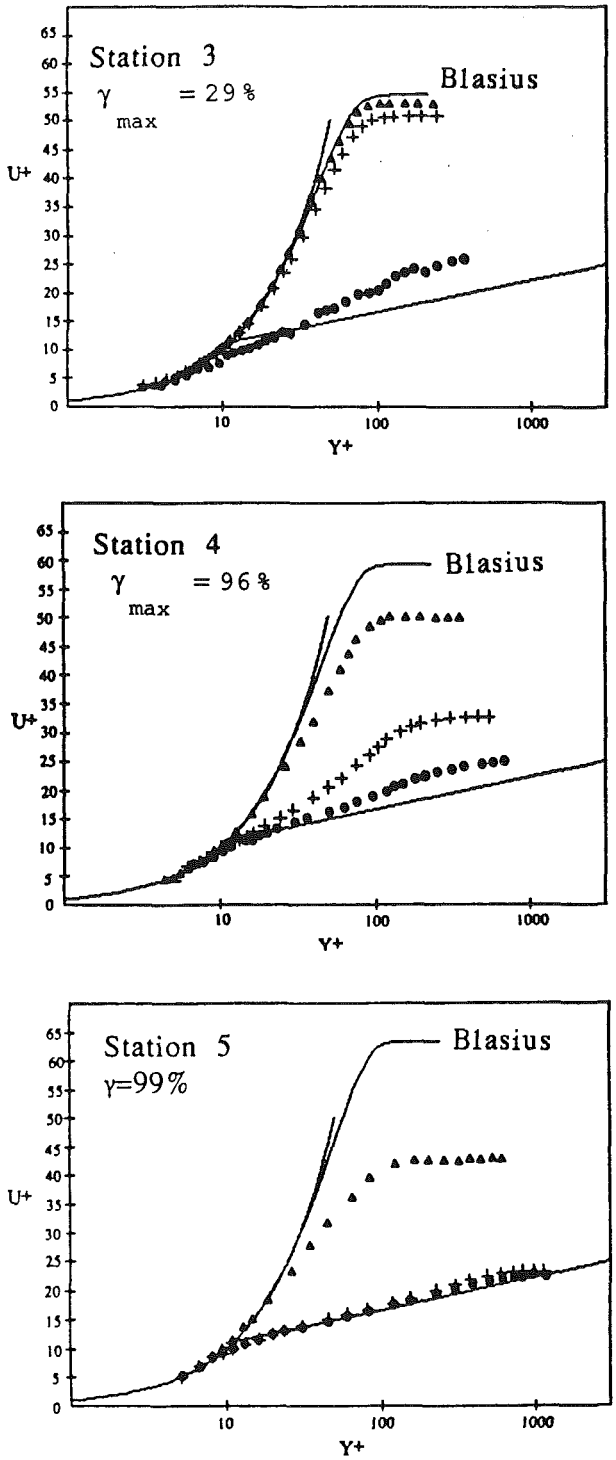

Fig. 6 Mean velocity profiles sampled on intermittency in wall coordinates; ▲—laminar; ●—turbulent; +—transition

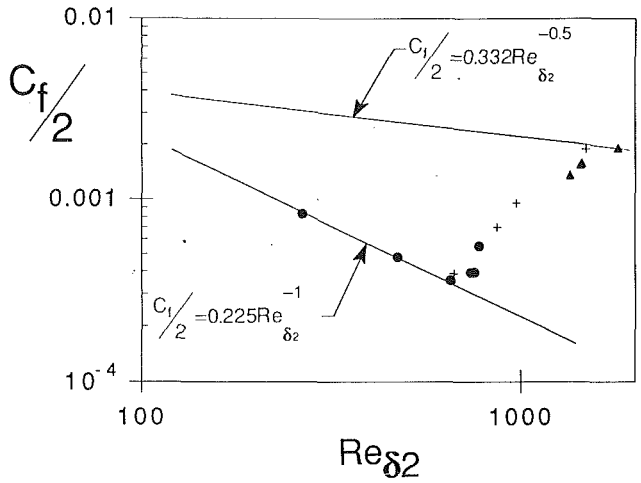

Fig. 7 Skin friction sampled on intermittency (*TI* = 0.32 percent): ● — laminar; ▲ turbulent; + —transition

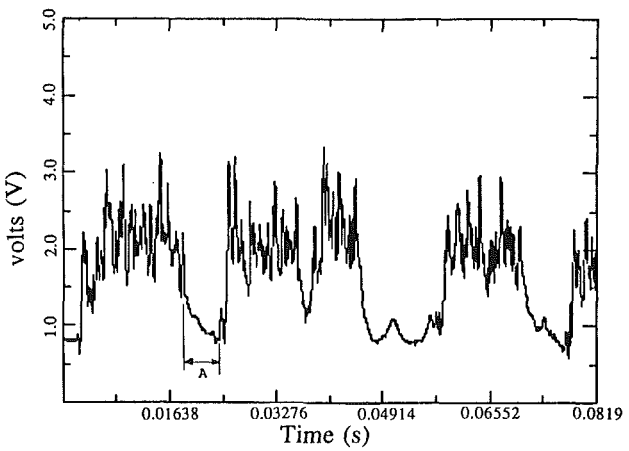

Fig. 8 Near-wall hot-wire voltage trace in transition illustrating the different mean velocities between the two regimes and the relaxation of the boundary layer after turbulent spot passage

of the intermittency value, which corresponds to the maximum intermittency, γ_{max}, in the near-wall region ($y/\delta_{995} < 0.1$).

Mean Velocity Profiles. An example of a mean velocity profile sampled within the transitional boundary layer and segregated according to laminar and turbulent behavior is shown in Fig. 5. The distance away from the wall has been normalized on the boundary layer thickness taken from the time-averaged profile. This time-averaged profile, called the transition profile, includes both laminarlike and turbulentlike portions. It is also the algebraic average of the laminarlike and turbulentlike measurements weighted according to the intermittency. The turbulent boundary layer is thicker than the corresponding laminar boundary layer, as expected, due to turbulent transport generated by the turbulent spots. The turbulent boundary layer profile is flatter than the corresponding laminar profile, resulting in a crossover between the two. The transition profile, being an average of the turbulent and laminar profiles, must lie between the two.

Plots of the mean velocity, sampled on intermittency and normalized on wall coordinates at various locations, are presented in Fig. 6. The Blasius profile, shown, is the theoretical profile of a laminar flow having the wall shear stress computed from the laminar flow data. The composite flow profiles evolve from Blasius-like profiles (upstream of the first station) to fully turbulent, log-law profiles. Velocity profiles within the transitional flow, sampled on intermittency, do not agree with either the Blasius or log-law profiles, however.

A plot of the local skin friction, C_f, values deduced from the profiles is shown on Fig. 7. Skin friction values in the laminarlike flow increasingly deviate from the laminar correlation as transition proceeds. The higher laminar stress as the transition region is entered may be a result of slow recovery of the laminar flow after passage of turbulent spots. A near-wall, hot-wire trace in the intermittent region (Fig. 8) illustrates this. Although transition from laminar to turbulent flow is quite sharp at the leading interface (end of interval A), the laminar flow signal is slow to relax to a nominally laminar state (slow relaxation of velocity within interval A). When the

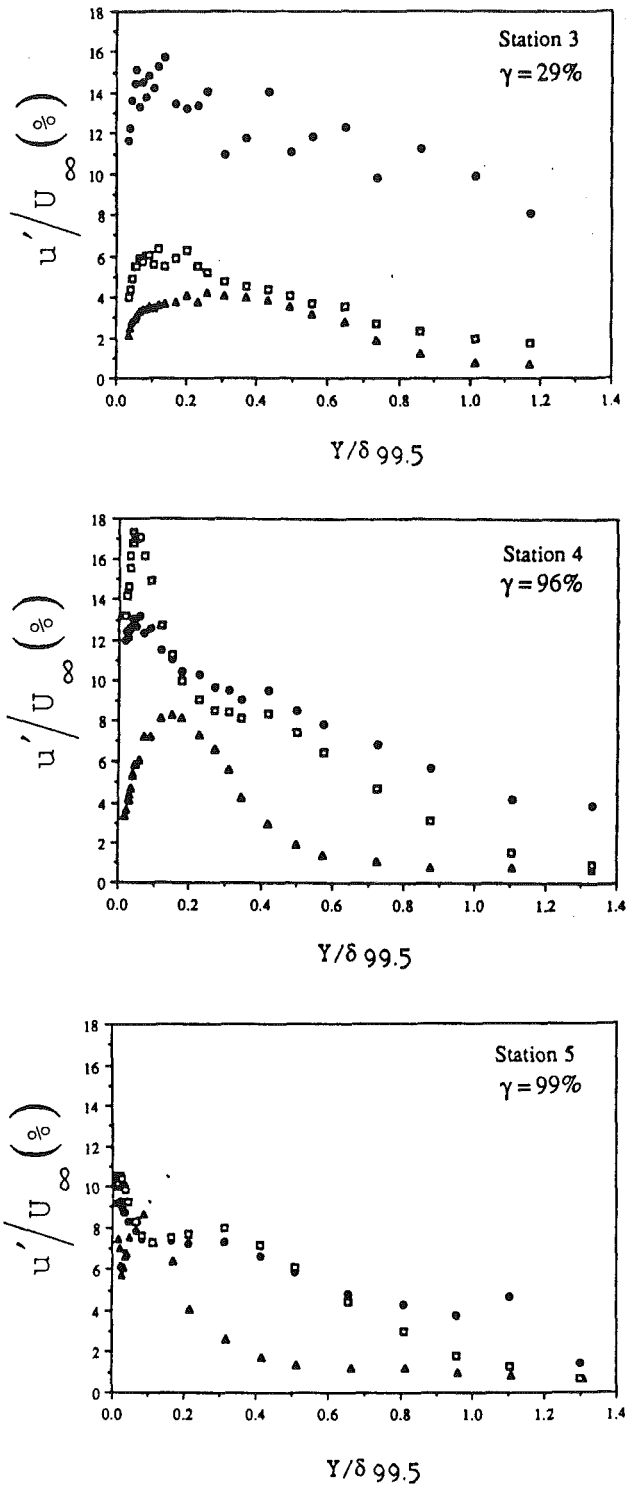

Fig. 9 Streamwise turbulence intensity sampled on intermittency (TI = 0.32 percent): ▲—laminar; ●—turbulent; □—transition

intermittency is high, i.e., spots pass frequently, the laminar portion of the boundary layer is continually disturbed, resulting in higher velocities near the wall and, consequently, higher-than-laminar C_f values.

Skin friction coefficients in the turbulentlike flow, at the end of transition (Fig. 7), are essentially the same as given by the fully turbulent correlation. A similar variation was seen in the shape factor, H. As transition proceeded, H for the laminarlike flow increasingly deviated from the laminar value of 2.6, indicating an increasingly non-Blasius behavior. Similar to the behavior of skin friction coefficient, H within the turbulentlike flow quickly reached the high-Reynolds-number turbulent value of 1.4. Based upon both H and C_f measurements, the laminarlike and turbulentlike portions of the transitional flows cannot be thought of as simply Blasius or turbulent flows, respectively. Although this conclusion seems to conflict with the results of Wygnanski et al. (1976) and Blair and Anderson (1987), who found that the turbulent zone mean velocity profile conformed to the standard law-of-the-wall, it is in agreement with the results of Antonia et al. (1981) who found that unreasonably high values of skin friction were necessary to make the velocity profiles agree with the log-law (as measured along the centerline of the turbulent spot). Results of Cantwell et al. (1978) agree with those of Antonia et al. (1981). The results of a flow-visualization study by Gad-El-Hak et al. (1981) also support the results of the present study. They found that the flow in the overhang of the turbulent spot was relatively passive, being cut off from the regeneration mechanism (bursting) in the near-wall region. It should therefore not be surprising that in the present study, where turbulentlike flow is accepted for processing regardless of whether it came from the overhang, the wings, or within the core of the turbulent spot, the parameters measured within the turbulentlike transitional flow do not agree with those of a standard turbulent boundary layer.

Velocity Fluctuation. Figure 9 shows the rms values of the streamwise velocity fluctuation at stations 3, 4, and 5 (station locations are shown on Fig. 1). The rms values of the laminar profiles increase with axial distance, and reach a peak value of 8 percent at station 4. Peaks in the laminar profiles occur at roughly 30 percent of the laminar boundary layer thickness for all stations. The laminarlike data at station 5 (γ = 99 percent) are not used in this discussion since there are few data points used in their processing. Initially, high rms values (16 percent at station 3) in the turbulent profiles indicate a high production of turbulence. These values decay to a peak value of 8 percent as dissipation in the boundary layer increases. The composite flow transition profile initially follows the laminar profile, but then jumps to a peak value of 17.5 percent at station 4, a value larger than the peak in the corresponding turbulent profile. Much of this behavior is due to intermittent "switching" of the flow from a laminarlike to a turbulentlike profile, then back to a laminar profile as each turbulent spot passes the probe (visible in Fig. 8). The rms fluctuation value associated with this switching appears in the composite profile. This was first shown by Arnal et al. (1978). Fluctuations of this type may be greater than the respective unsteadiness values in either the laminarlike or turbulentlike regime. In fact, the various contributions to u' can be computed by the expression (Hedley and Keffer, 1974):

$$u_c'^2 = g u_t'^2 + (1-g) u_l'^2 + g(1-g)(u_t - u_l)^2 \qquad (1)$$

where the subscripts c, t and l represent composite, turbulentlike, and laminarlike characteristics, respectively. The level of turbulence, as indicated by the transition profile, is thus not a good measure of the turbulent activity (turbulent transport) in a transitioning boundary layer.

Shear Stress Profiles. Shear stress profiles, $\overline{u'v'}$, in transitional flow are shown in Fig. 10. The laminar contribution is quite small for all stations and the peak moves progressively toward the wall as transition proceeds, realizing a fully turbulent profile at station 5. Although the composite flow profile is between the turbulent and laminar profiles for all stations, it also is affected by the intermittent "switching" from laminar to turbulent flow. Note that, for all the stations, the composite value is less than the product of the intermittency and the corresponding turbulent value. Thus, the effect of switching from a laminar profile to a turbulent profile, for instance, is a rise in both u' and v' creating an artificial value of "shear-

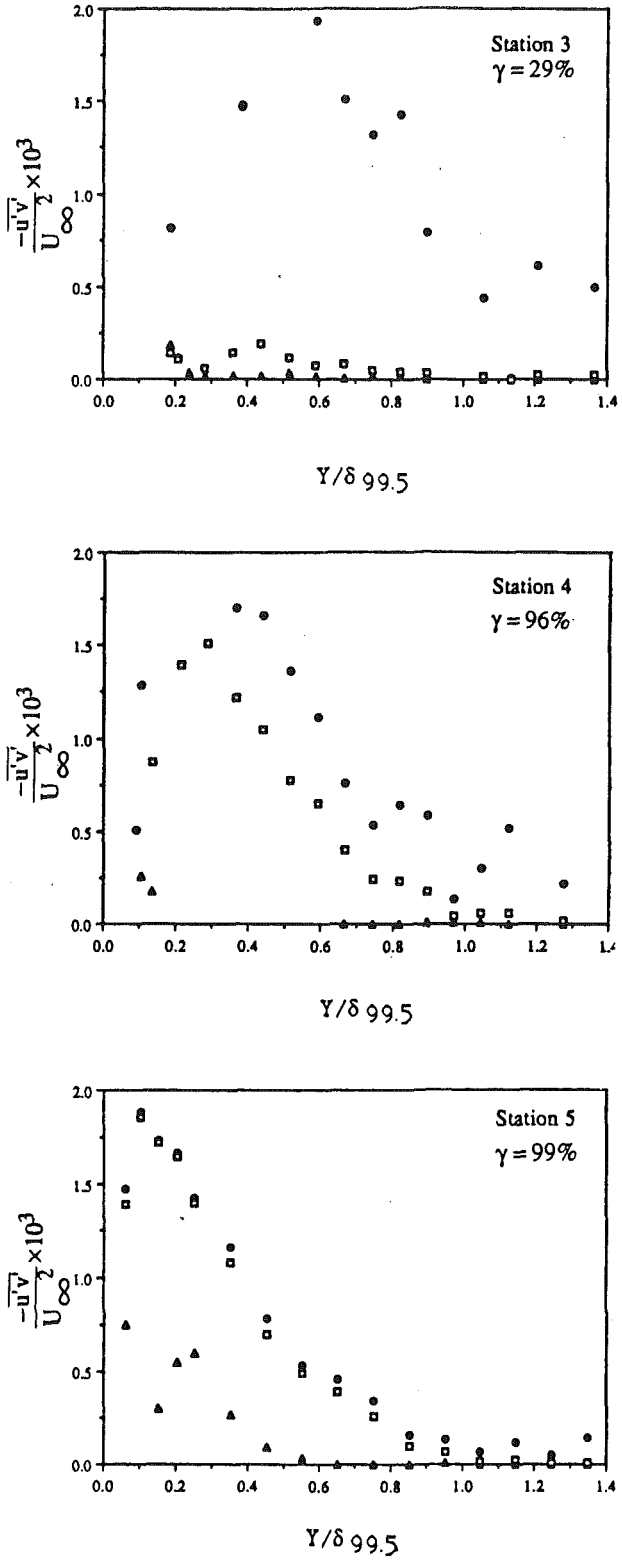

Fig. 10 Shear stress sampled on intermittency through transition (*TI* = 0.32 percent): ▲—laminar; ●—turbulent; □—transition

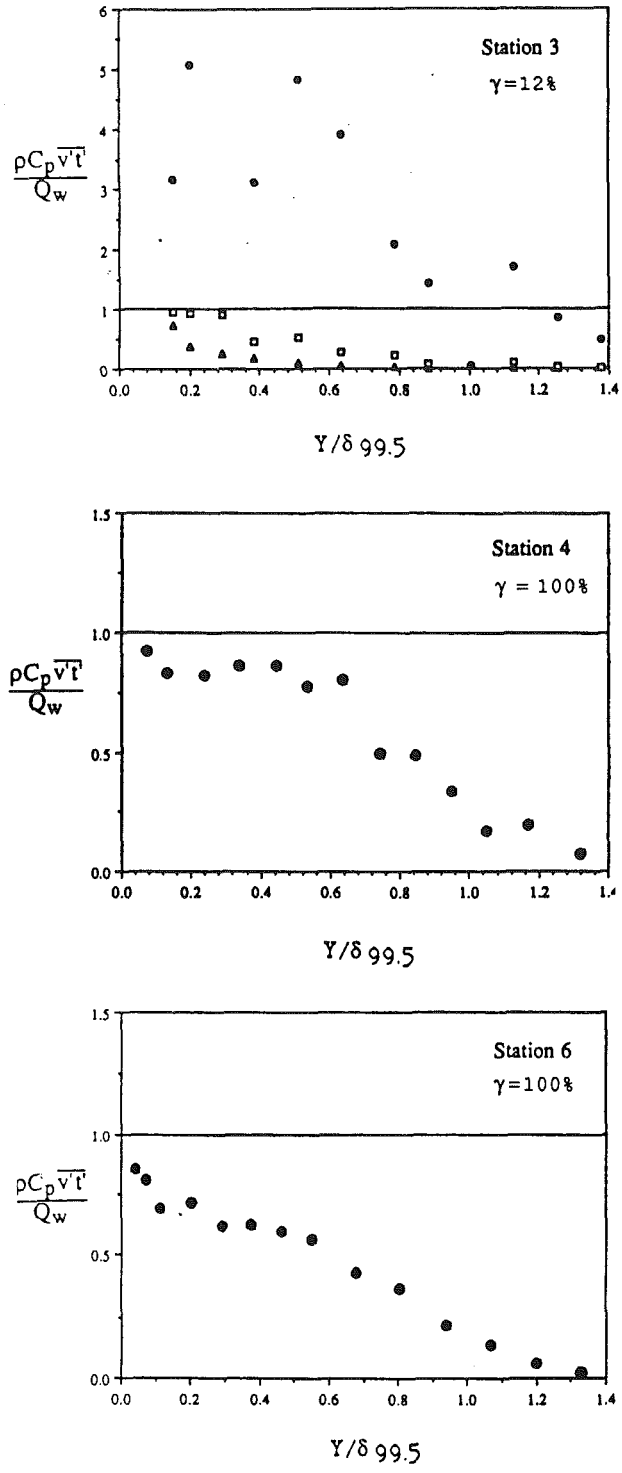

Fig. 11 Turbulent heat fluxes sampled on intermittency (*TI* = 0.32 percent). Station 3 is within transition (γ = 12 percent), stations 4 and 6 are fully turbulent. ▲—laminar; ●—turbulent; □—transition.

stress," $\overline{u'v'}$. As with the fluctuation plots of Fig. 9, the composite flow profile is, therefore, not indicative of the true turbulent shear stress in the transitional boundary layer. A more accurate shear stress is found by a weighted (on intermittency) average of the laminarlike and turbulentlike contributions. Similar turbulent shear stress measurements were taken in the heated flow.

Turbulent Heat Flux Measurements. Turbulent heat flux normalized on the wall heat flux and sampled on intermittency are shown on Fig. 11. As discussed above, heating of the boundary layer is destabilizing, resulting in an earlier and more rapid transition. Consequently, station 3 is in early transition and subsequent stations are post-transitional. Within the turbulent portion of a transitional flow (station 3), one can observe a large increase in turbulent heat flux above the time-averaged wall heat flux value. A simple heat balance on an element in the flow will show that, since there is no energy production within the flow, the cross-stream heat flux ($\overline{v't'}$)

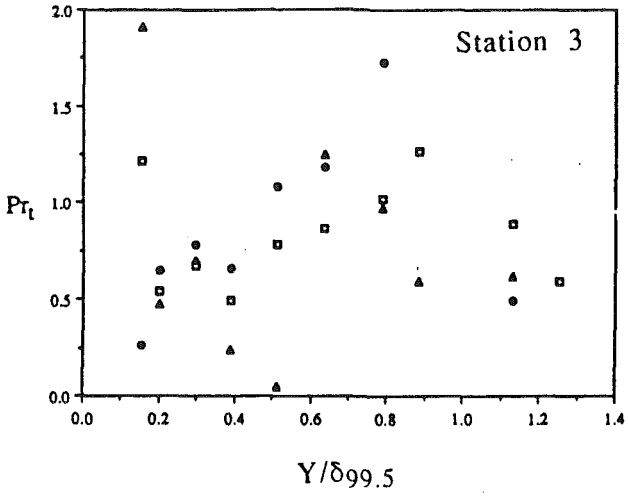

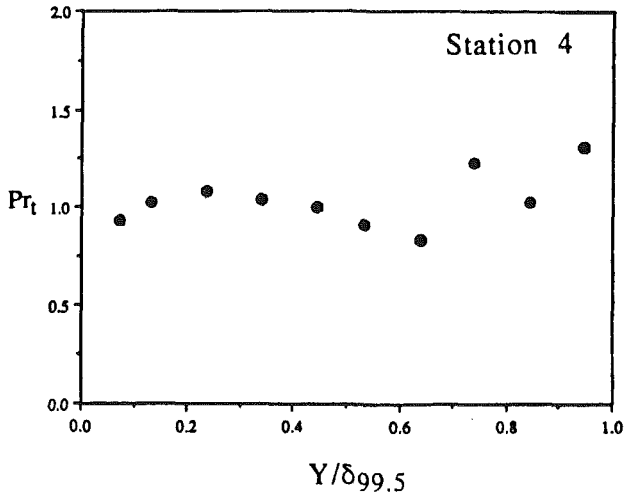

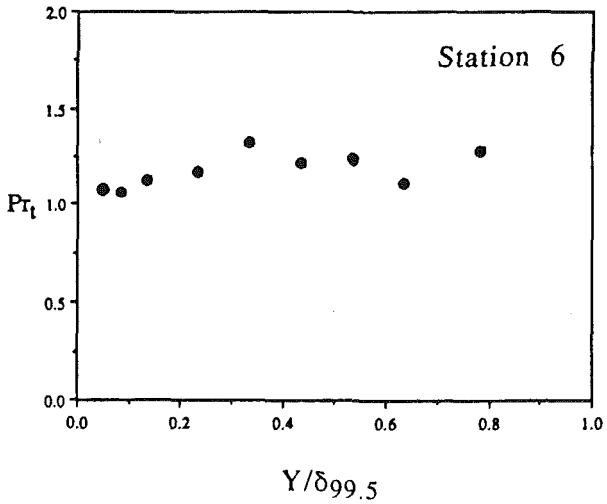

Fig. 12 *Turbulent Prandtl number sampled on intermittency (TI = 0.32 percent). Station 3 is within transition (γ = 12 percent), stations 4 and 6 are fully turbulent.* ▲ —laminar; ● —turbulent; □ —transition.

can increase in the y direction if the streamwise heat flux ($\overline{u't'}$) decreases in the streamwise direction. The triple-wire measurements indicate that such a streamwise decrease exists. The streamwise heat flux $\overline{u't'}$ was found to decrease almost an order of magnitude between Stations 3 and 4 in the near-wall region, and remain relatively constant thereafter. Whether the

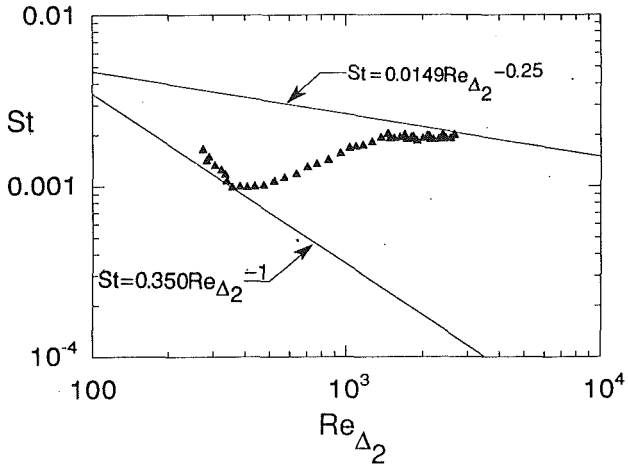

Fig. 13 *Stanton number variation through transition (TI = 1.79 percent)*

measurements sampled on turbulentlike flow for station 3 approach unity as the wall is approached is not known. It is possible that the wall transfers more energy to the flow during the passage of a turbulent spot than during the times the adjacent flow is laminarlike. The time-averaged energy transfer must, of course, be equal to the time-average wall heat flux. It is also seen that $\overline{v't'}$ in the laminarlike portion of the boundary layer is not zero. This does not mean that a true turbulent eddy transport of heat is present in this flow, but simply that v' and t' are correlated as fluid velocity and temperature and the wall temperature fluctuate. Note that this unsteadiness is limited to the near-wall region where the fluid would be influenced by the fluctuating wall temperature. Because $\overline{v't'}$ in the laminarlike regime is not negligible (station 3 of Fig. 11), the value of $\overline{v't'}$ near the wall for the composite flow profile is not precisely equal to the near-wall intermittency times the turbulent flow contribution, as was anticipated.

Turbulent Prandtl Number Measurements. The variation of turbulent Prandtl number, Pr_t, sampled on intermittency, is shown on Fig. 12. These values were computed from:

$$Pr_t = \frac{\overline{u'v'}\,(\partial\bar{t}/\partial y)}{\overline{v't'}\,(\partial\bar{u}/\partial y)}$$

where the entries, turbulent shear stress, turbulent heat flux, and mean temperature and velocity profiles were all taken in the heated flow by the triple-wire probe. The single-sample uncertainty value of these data is typically 20 percent. Uncertainties in turbulent Prandtl numbers in the early transitional boundary layer are higher than 20 percent. This higher uncertainty is mainly due to three reasons: (1) The boundary layer, especially early in transition, is thin relative to the triple-wire probe; thus, spatial resolution is inadequate in early-transition measurements. (2) The early-transitional boundary layer is mostly laminarlike; therefore, the shear stresses and turbulent heat fluxes used to calculate turbulent Prandtl numbers are small and hence difficult to measure accurately. (3) Since the flow is mostly laminarlike, few samples for processing are available of the turbulentlike flow. The data at post-transitional stations 4 and 6 show Pr_t values consistently close to unity in the inner half of the boundary layer, as would be expected of fully turbulent boundary layers. The data in the outer half of the boundary layer are not reliable due to the very shallow gradients of velocity and temperature. The data for station 3, however, show a drop in Pr_t (sampled on the intermittency function) substantially below unity in the near-wall region. This implies that the eddy diffusivity of heat increases during transition more rapidly than does the eddy diffusivity of momentum. This contradicts the conclusions of

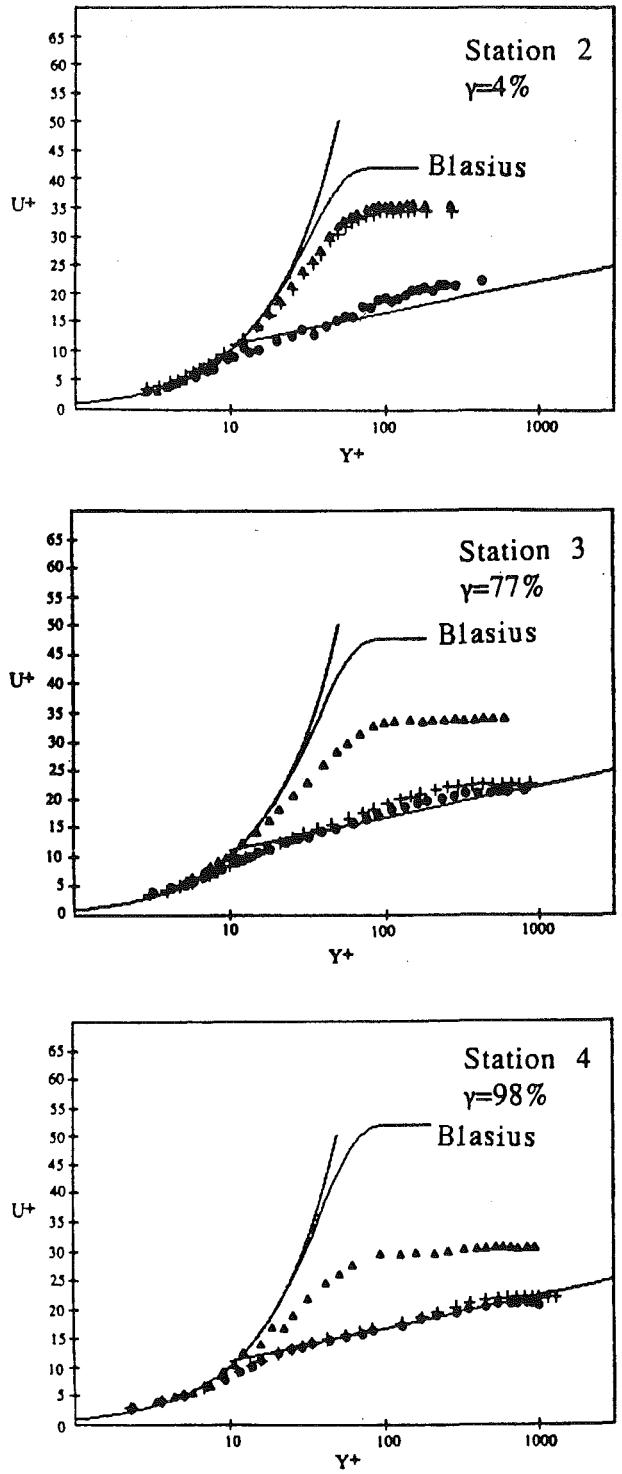

Fig. 14 Mean velocity profiles sampled on intermittency in wall coordinates (*TI* = 1.79 percent): ▲—laminar; ●—turbulent; +—transition

other researchers (Blair and Anderson, 1987; Sohn et al., 1989; Wang et al., 1985). To the authors' knowledge, these are the first direct measurements of Pr_t in transitional flows. Previous conclusions were inferred from mean profile data. The transition region may be more sensitive to molecular diffusion than is the fully turbulent boundary layer since the eddies there tend to be relatively large, and the small-scale structure (the full turbulence spectrum) has not been established. If so, one would expect a subunity turbulent Prandtl number when the molecular Prandtl number is less than one.

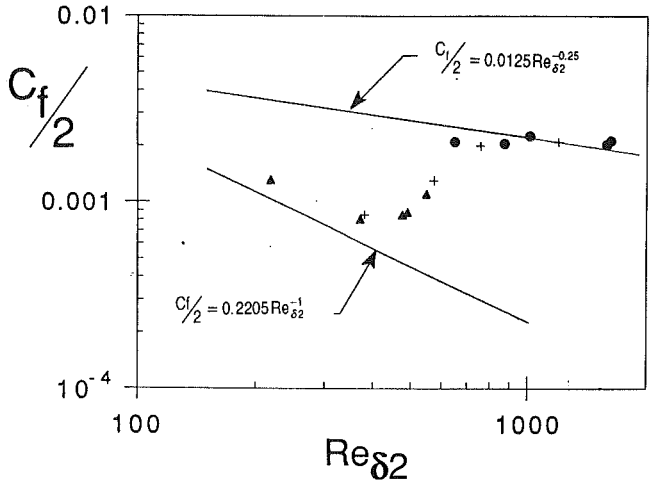

Fig. 15 Skin friction sampled on intermittency (*TI* = 1.79 percent): ▲—laminar; ●—turbulent; +—transition

The High *TI* Case—*TI* = 1.79 Percent

Free-Stream Turbulence Intensity and Spectra. The Power Spectral Density (PSD) for this case was generally similar in shape to that for the low *TI* case. The peak, due to fan rocking, again present, was a much smaller fraction of the total turbulence kinetic energy in this case.

The average free-stream turbulence intensity at the entry to the test section was about 1.8 percent, with u' values increasing from 0.9 to 1.00 percent and v' decreasing from 2.3 to 2.1 percent between station 1 and station 6. The measured value of w' was 2.0 percent at station 2. The free-stream velocity was nominally 16.7 m/s.

Stanton Number. The Stanton number variation through transition is shown on Fig. 13. The points in the laminar regime agree with the uniform heat flux correlation in Kays and Crawford (1980) when Stanton numbers are plotted against Re_x (not shown). In Fig. 13 Stanton numbers are plotted against the local coordinate, enthalpy thickness Reynolds number, $Re_{\Delta 2}$. The value of $Re_{\Delta 2}$ measured at station 4 is used as a boundary condition to the integral energy equation. Then, forward and backward integrations are performed, using measured wall temperatures to determine $Re_{\Delta 2}$ values downstream and upstream of station 4. In these coordinates, the data follow the laminar and turbulent correlations at the extremes of transition and smoothly pass from one to the other during transition. Increasing the free-stream turbulence intensity has a strong effect on the transition onset location, causing it to move from the low-turbulence-case value of $Re_x = 1 \times 10^6$ to $Re_x = 3 \times 10^5$, and from $Re_{\Delta 2} = 500$ to $Re_{\Delta 2} = 400$. Good agreement of the onset location with other researchers was observed (see Fig. 3). These data are consistent with those of Blair (1982).

Mean Velocity Profiles. Profiles of the mean velocity sampled on intermittency are shown on Fig. 14. The laminar profile deviates quite strongly from the Blasius profile throughout transition (much more than in the lower *TI* case). The turbulent profile, in contrast, agrees with the log-law profile from very early in transition. The trends above are reflected in the skin friction values (Fig. 15). The C_f values computed from the laminarlike portion of the transitional flow deviate strongly from the laminar correlation while those in the turbulentlike portion are near fully turbulent values (essentially equal to an extension of the turbulent data to low Reynolds numbers).

Velocity Fluctuation. The rms values of streamwise velocity fluctuation are shown on Fig. 16. The most striking feature

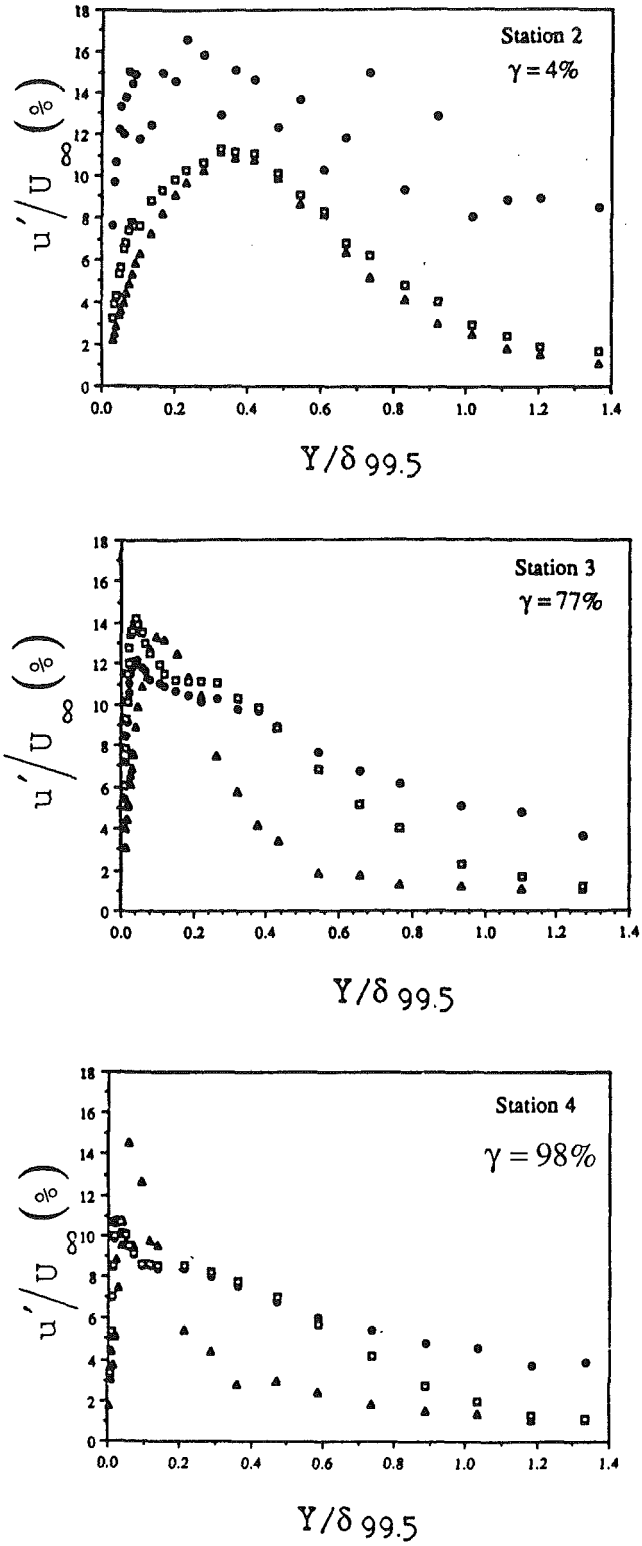

Fig. 16 Streamwise turbulence intensity sampled on intermittency (*TI* = 1.79 percent): ▲—laminar; ●—turbulent; □—transition

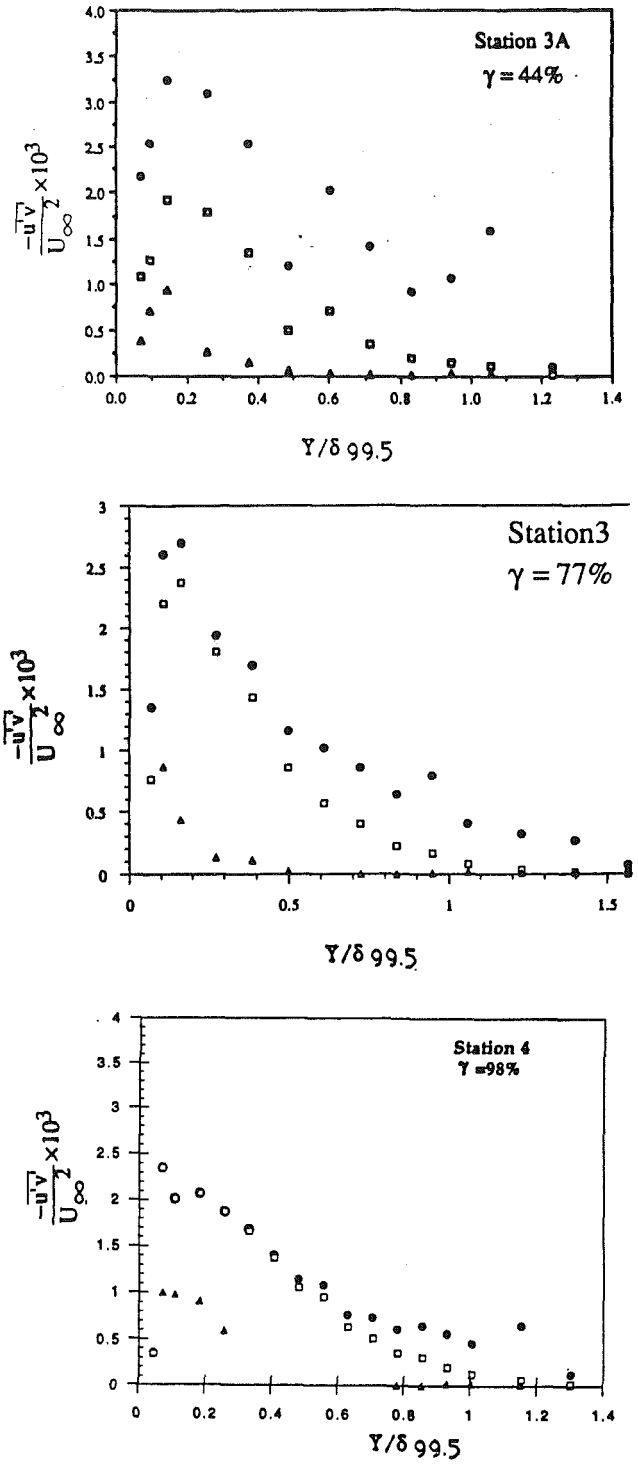

Fig. 17 Shear stress sampled on intermittency through transition (*TI* = 1.79 percent). Station 3*a* refers to data taken at station 3, but at a reduced free-stream velocity. This was done to obtain a more reasonable intermittency value. ▲—laminar; ●—turbulent; □—transition

of these profiles, in comparison with those of the low *TI* case, is the large increase in laminar unsteadiness, which even exceeds some parts of the turbulent profile at station 3. The high values are consistent with the elevated C_f values within the laminar regime. The turbulence intensity profiles evolve as in the low *TI* case. In both cases, the peak values of the turbulence intensity drop monotonically with increasing values of near-wall intermittency.

Shear Stress Profiles. The variation in shear stress, $\overline{u'v'}$, profiles through transition is shown on Fig. 17. As in the low *TI* case, the laminar contribution to the shear stress is small everywhere except very near the wall. With successive downstream positions, the peaks in the turbulent profiles decrease in amplitude while moving toward the wall.

Turbulent Heat Flux. Profiles of the turbulent heat flux, $\overline{v't'}$, are shown in Fig. 18. As in the lower *TI* case, a strong

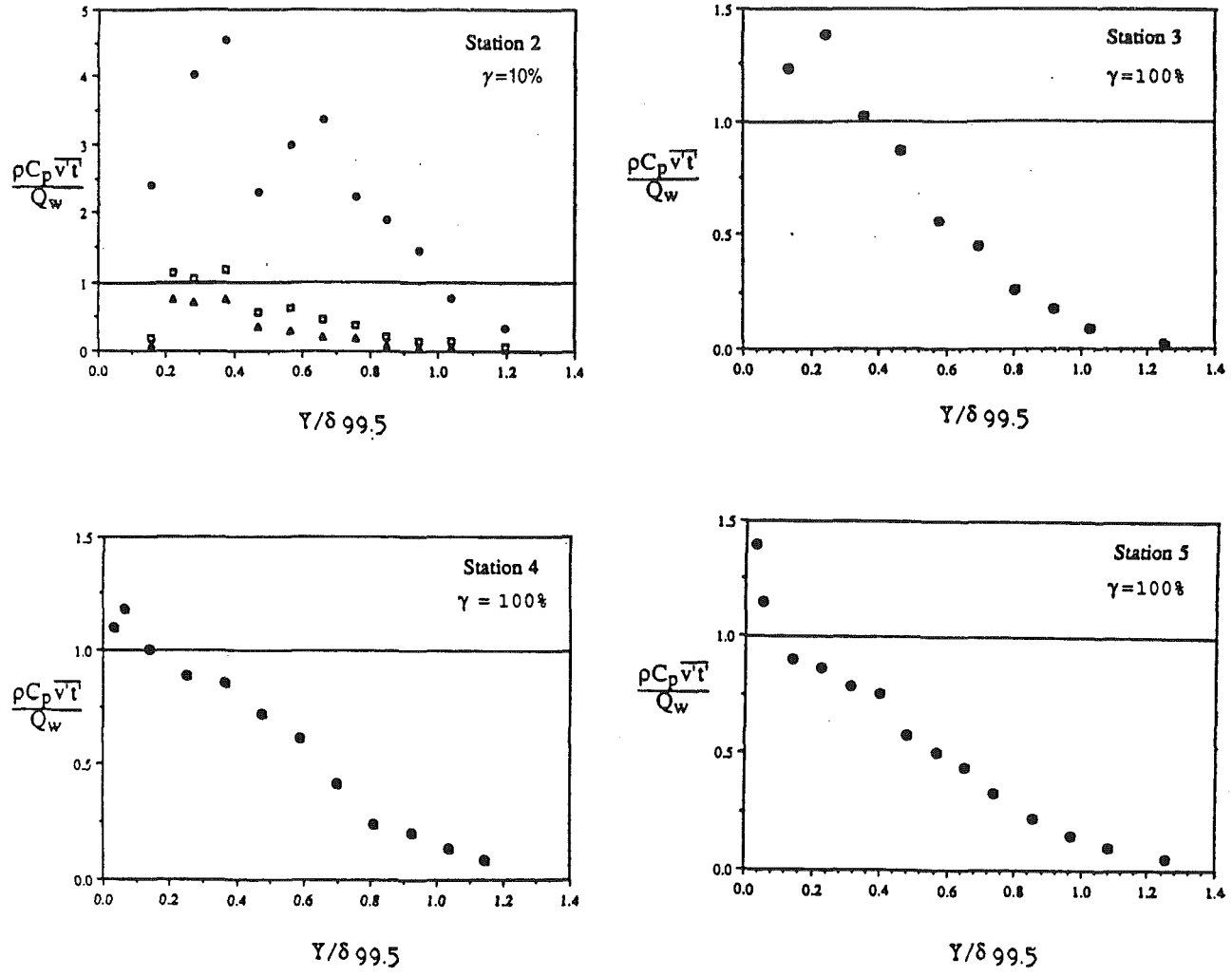

Fig. 18 Turbulent heat flux sampled on intermittency through transition (*TI* = 1.79 percent). The intermittency at station 2 is 9.5 percent. The other profiles are fully turbulent. ▲—laminar; ●—turbulent; □—transition.

increase in the turbulent heat flux above the wall heat flux is seen. This peak decays rapidly. The profiles appear to assume a turbulentlike shape (as described by Kim, 1986, and Gibson and Verripoulos, 1984) by station 5.

Turbulent Prandtl numbers were all in the vicinity of unity, dipping slightly below unity in the transitional flow (0.8–0.9 at Station 2).

Conclusions

The main conclusions of this study are:

1 It appears that the transitional boundary layers should not be thought of as simple composites of Blasius and fully turbulent flows. Transition modeling based on the intermittency function weighting of pure laminar and turbulent flows may be in error.

2 Conditional sampling of turbulence quantities on the intermittency function must be made during transition to obtain an accurate view of the transition process.

3 The turbulent Prandtl numbers in the turbulent core region of the transitional flow are somewhat smaller than unity when free-stream turbulence levels are low, increasing toward unity with increasing disturbance levels.

Acknowledgments

This study was supported by the NASA Lewis Research Center under grant number NASA/NAG3-881. The grant monitor was Dr. James O'Brien. The intermittency technique was developed under AFOSR Grant #F49620-85-C-0049. Further support was provided by the Graduate School of the University of Minnesota and the AMOCO Foundation.

References

Antonia, R. A., Chambers, A. J., Sokolov, M., and van Atta, C. W., 1981, "Simultaneous Temperature and Velocity Measurements in the Plane of Symmetry of a Transitional Turbulent Spot," *J. Fluid Mechanics*, Vol. 108, pp. 317–343.

Arnal, D., Juillen, J. C., and Michel R., 1978, "Experimental Analysis and Computation of the Onset and Development of the Boundary Layer Transition," NASA TM-75325.

Blair, M. F., 1982, "Influence of Free-Stream Turbulence on Boundary Layer Transition in Favorable Pressure Gradients," ASME *Journal of Engineering for Power*, Vol. 104, pp. 743–750.

Blair, M. F., and Anderson, O. L., 1987, "Study of the Structure of Turbulence in Accelerating Transitional Boundary Layers," United Technologies Research Center Report No. E87-956900-1.

Blair, M. F., and Bennett, J. C., 1984, "Hot Wire Measurements of Velocity and Temperature Fluctuations in a Heated Layer," *Phys. E.*, Vol. 20, No. 2, pp. 209–216.

Cantwell, B., Coles, D., and Dimotakis, P., 1978, "Structure and Entrainment in the Plane of Symmetry of a Turbulent Spot," *J. Fluid Mechanics*, Vol. 87, pp. 641–672.

Crawford, M. E., and Kays, W. M., 1976, "STAN5—A Program for Numerical Computation of Two-Dimensional Internal and External Boundary Layer Flows," NASA CR-2742.

Dhawan, S., and Narasimha, R., 1958, "Some Properties of Boundary Layer Flow During the Transition From Laminar to Turbulent Motion," *J. Fluid Mechanics*, Vol. 3, pp. 418–436.

Gad-El-Hak, M., Blackwelder, R. F., and Riley, J. J., 1981, "On the Growth of Turbulent Regions in Laminar Boundary Layers," *J. Fluid Mechanics*, Vol. 110, pp. 73–95.

Gibson, M. M., and Verriopoulos, C. A., 1984, "Turbulent Boundary Layer on a Mildly Curved Convex Surface. Part 2: Temperature Field Measurements," *Experiments in Fluids*, Springer-Verlag, Vol. 2, pp. 73–80.

Hedley, T. B., and Keffer, J. F., 1974, "Turbulent/Non-turbulent Decisions in an Intermittent Flow," *J. Fluid Mechanics*, Vol. 64, pp. 625–644.

Hishida, M., and Nagano, Y., 1978, "Simultaneous Measurements of Velocity and Temperature in Non-isothermal Flows," *ASME Journal of Heat Transfer*, Vol. 100, pp. 340–345.

Kays, W. M., and Crawford, M. E., 1980, *Convective Heat and Mass Transfer*, 2nd ed., McGraw-Hill.

Kim, J., Kline, S. J., and Johnston, J. P., 1978, "Investigation of Separation and Reattachment of a Turbulent Shear Layer Flow Over a Backward-Facing Step," Report MD-37, Thermosciences Division, Dept. of Mechanical Engineering, Stanford University, Stanford, CA.

Kim, J., 1986, "The Development of a Turbulent Heat Flux Probe and Its Use in a 2-D Boundary Layer Over a Convex Surface," MSME Thesis, Dept. of Mech. Engrg., University of Minnesota, Minneapolis, MN.

Kim, J., and Simon, T. W., 1988, "Measurements of the Turbulent Transport of Heat and Momentum in Convexly Curved Boundary Layers: Effects of Curvature, Recovery, and Free-Stream Turbulence," ASME JOURNAL OF TURBOMACHINERY, Vol. 110, pp. 80–87.

Kim, J., 1990, "Free-Stream Turbulence and Concave Curvature Effects on Heated, Transitional Boundary Layers," PhD Thesis, University of Minnesota, Minneapolis, MN.

Kuan, C. L., and Wang, T., 1988, "Some Intermittent Behavior of Transitional Boundary Layers," Paper No. AIAA-89-1890, pp. 1–15.

McDonald, H., and Fish, R. W., 1973, "Practical Calculations of Transitional Boundary Layers," *Int. J. Heat Mass Transfer*, Vol. 16, No. 9, pp. 1729–1944.

Schlichting, H., 1979, *Boundary Layer Theory*, 7th ed., McGraw-Hill, New York.

Sohn, K. H., O'Brien, J. E., and Reshotko, E., 1989, "Some Characteristics of Bypass Transition in a Heated Boundary Layer," *Proceedings of the 7th Symposium on Turbulent Shear Flows*, Aug., Stanford University, Stanford CA.

Wang, T., 1984, "An Experimental Investigation of Curvature and Freestream Turbulence Effect on Heat Transfer and Fluid Mechanics in Transition Boundary Layer Flows," PhD Thesis, University of Minnesota, Minneapolis, MN.

Wang, T., Simon, T. W., and Buddhavarapu, J., 1985, "Heat Transfer and Fluid Mechanics Measurements in Transitional Boundary Layer Flows," ASME *Journal of Engineering for Gas Turbines and Power*, Vol. 107, pp. 1007–1015.

Wang, T., and Simon, T. W., 1987, "Heat Transfer and Fluid Mechanics Measurements in Transitional Boundary Layers on Convex-Curved Surfaces," ASME JOURNAL OF TURBOMACHINERY, Vol. 109, pp. 443–452.

Wygnanski, I., Sokolov, M., and Friedman, D., 1976, "On a Turbulent 'Spot' in a Laminar Boundary Layer," *J. Fluid Mechanics*, Vol. 78, pp. 785–819.

Effects of Leaning and Curving of Blades With High Turning Angles on the Aerodynamic Characteristics of Turbine Rectangular Cascades

Han Wanjin

Wang Zhongqi

Tan Chunqing

Shi Hong

Zhou Mochun

Power Engineering Department,
Harbin Institute of Technology,
Harbon, People's Republic of China

To understand the effects of the origination and development of centralized vortices on the aerodynamic characteristics of turbine rectangular cascades with high turning angles, experiments with five-hole microspherical probes, accompanied by color helium bubble flow displays, were carried out. The measurement planes are arranged as three before, six in, and one after the cascade. The experiments reveal that the origination and development of horseshoe vortices and passage vortices as well as the interaction of the latters almost dominate the whole flow field of traditional linear cascades. Lean linear cascades favor the horseshoe vortices and passage vortices in the acute angle zone, and impede those in the obtuse angle zone. So it is a logical result to adopt the negatively curved blades, whose pressure surfaces and both endwalls compose both obtuse angles, respectively, to improve the cascade aerodynamic characteristics.

Introduction

Blades with low aspect ratio and high turning angle are widely used in guide cascades of adjustable stage, rotor cascades with low reaction of high pressure stages of a steam turbine, and in a gas turbine with high pressure ratio. Even though this kind of blade has obvious advantages in mechanical property and cost, the following problems usually exist: centralized vortices of high intensity and large scale produced by big airflow turning angles, especially the leading edge vortices composed most of horseshoe vortices, and the upper and lower passage vortices almost govern the whole flow field, as shown by Langston et al. (1977). These vortices not only cause three-dimensional separation of the endwall boundary layer, dissipating the airflow energy and raising secondary flow losses noticeably, but also change the airflow outlet angles and hence the incidences on the next cascade (Sieverding, 1985). A good design should ensure that for equal turbine work, the unfavorable effect of secondary flows is reduced to the minimum, and the secondary flow losses and outlet angles are predicted accurately (Harrison, 1990). So it is necessary to study the model of flow through the cascade with blades with low aspect ratio and high turning angle, and methods to reduce the secondary flow losses.

Using curved blades can reduce the secondary flow losses efficiently. In cascades with low turning angle, the transverse secondary flow losses in the end parts of blades take the main portion of the total losses. When lean linear blades are used in this type of cascade, the flows in the acute angle zone between pressure surfaces and endwalls are improved (Wang, 1988). The positively curved blade, where the pressure surface forms acute angles with both endwalls, introduces improvement in the acute angle zone into a cascade (Han et al., 1990). The present paper discusses the loss mechanism in the cascades with high turning angles and effects of blade leaning on the flows in the acute and obtuse angle zones, trying to find the curving method of blades with high turning angle to reduce the losses.

Experimental Models

The experiment was finished in a low-speed plane cascade wind tunnel. The tested cascades are: (*a*) traditional linear blade cascade; (*b*) lean linear one ($\epsilon = 20$ deg); (*c*) positively curved one ($\epsilon = 15$ deg); (*d*) negatively curved one ($\epsilon = 15$ deg). Ten measurement planes shown in Fig. 2 cover the space before and after the cascades. The flow parameters along the directions of pitch and blade height are measured by five-hole spherical probes. The other geometry and aerodynamic parameters of tested cascades are: chord, $b = 120$ mm; axial chord, $B = 105$ mm; blade height, $h = 110$ mm; aspect ratio, $h/b = 0.917$; pitch-chord ratio, $t/b = 0.667$; inlet airflow angle, $\alpha_o = 64$ deg; geometry outlet angle, $\alpha_{1p} = 64.5$ deg; inlet total pressure, $P_o = 5773\ p_a$, Reynolds number and Mach number at the mid-span of outlet plane, $\mathrm{Re} = 6.4 \times 10^5$ and $\mathrm{M} = 0.26$, respectively.

Contributed by the International Gas Turbine Institute and presented at the 38th International Gas Turbine and Aeroengine Congress and Exposition, Cincinnati, Ohio, May 24-27, 1993. Manuscript received at ASME Headquarters March 10, 1993. Paper No. 93-GT-296. Associate Technical Editor: H. Lukas.

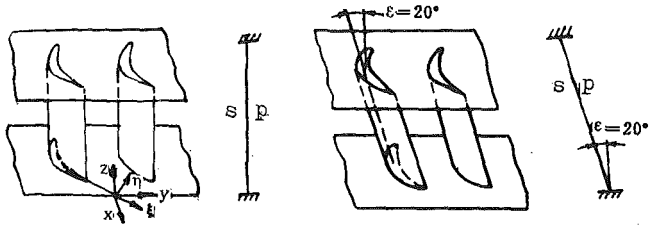

(a) Traditional linear blade cascade (b) Lean linear blade cascade

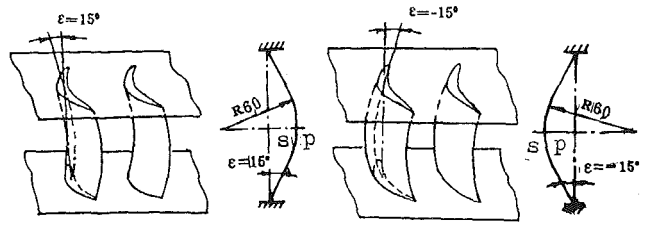

(c) Positively curved blade cascade (d) Negatively curved blade cascade

Fig. 1 Tested cascades and shapes of profile stacked lines

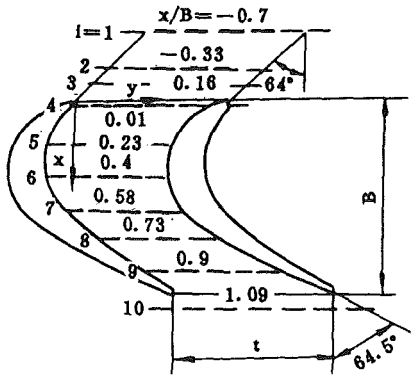

Fig. 2 Measurement planes

The coordinate systems used are x, y, z and ξ, η, z. Here x is for axial, y pitchwise, and z blade height direction, while ξ is in the streamwise direction at midspan midpitch, and η is perpendicular to both ξ and z, respectively (Fig. 1*a*). The velocity components, v, w in the η and z directions then represent the secondary velocities, $v = c \cos \sigma \sin (\alpha_{1p} - \alpha_1)$, $w = c \sin \sigma$, where c is the outlet airflow velocity, σ is the angle between c and the plane parallel to the endwall, α_{1p} is the cascade geometry outlet angle, α_1 is the outlet airflow angle. Velocity vectors in the plane perpendicular to flow direction in Fig. 4 are the vectorial sums of v and w, and streamwise vorticity contours are obtained by finite differentiations of v and w.

Experimental Results and Discussion

Flows in Upstream and at Leading Edge. To study the influence of types of cascades on the inlet boundary layers, the parameters in the boundary layer are measured without cascades and with different cascades. The measurement results are shown in Table 1. From the table it is seen that the parameters in the upper inlet boundary layer are equal to those in the lower inlet boundary layer whenever cascade is not present, or traditional linear blade, positively curved blade, negatively curved blade cascade is present, meaning the inlet flow field is rather even. When different cascades are mounted, or no cascades, the parameters of the boundary layers in the table are different, which results from different axial pressure decrease produced by using different cascades.

Inlet boundary layers develop into leading edge vortices, mainly composed of horseshoe vortices, in terms of three-dimensional separation at the saddle points ahead of cascade leading edges. Some references concerned proposed that it is difficult to measure the leading edge vortices by five-hole probe. But from our measured result one can see the slight rotation of velocity components in the plane perpendicular to the main flow, and the deformation of inlet boundary layers, which agree with the color helium bubble flow display of the geometry similarity amplified traditional linear blade cascade in a large scale wind tunnel. Figure 3 shows leading edge vortices include two zones, zone 1 consisting of horseshoe vortices (1) and corner vortices (2) and zone 2 of countervortices (3) separation vortices (4) and separation points (5) which agrees with the vortical structure of Ishii (1986). When leading edge vortices run through the leading edges of a blade, the horseshoe vortex is split into two legs called the pressure side leg and the suction side leg, respectively, and continue going into the passage. The other vortices are dissipated by the viscosity.

Flows in Passages. Downstream of a cascade, one can see the pressure side leg of a horseshoe vortex near the lower endwalls, while going into its passage in the counterclockwise direction, and the other leg in the clockwise direction. Measurement plane 4 in Fig. 4 shows clearly that the scale and intensity of horseshoe vortices in the acute angle zones of the lean blade cascade and positively curved blade cascade are bigger than those of the traditional cascade. In the obtuse angle zones of the lean blade cascade and negatively curved cascade the opposite cases hold.

Three factors determine the origination and development of

Nomenclature

h = blade height
z = distance of measuring point from lower endwall
$\bar{h}$ = relative blade height $= z/h$
p = static pressure
i = number of measuring stations
α_1 = airflow angle measured from the axial direction
α_{1p} = cascade geometric outlet angle
p = pressure surface of a blade
s = suction surface of a blade
c_u = pitchwise-averaged tangential velocity
$(c_u)_{\epsilon=0°}$ = mass-flux-averaged total tangential velocity of traditional cascade
$\bar{c}_u$ = tangential velocity coefficient $= c_u/(c_u)_{\epsilon=0°}$
t_y = distance of measuring point from suction surface in pitch direction
t = distance between suction surface and pressure surface in pitch direction
$\bar{t}_y$ = relative distance in pitch direction $= t_y/t$
$\bar{p}$ = static pressure coefficient $= (p_i - p_1)/(p_o^* - p_1)$
ξ = energy loss coefficient $= [(p_i/p_1^*)\ k - 1/k - (p_i/p_o^*)\ k - 1/k]/[1 - (p_i/p_o^*)\ k - 1/k]$
k = specific heat ratio

Subscripts and Superscripts

0 = inlet parameter of a cascade
1 = parameter behind a cascade
* = stagnation parameter
i = parameter at a measuring station
m = pitchwise-averaged parameter
t = mass-flux-averaged total parameter

Table 1 Measurement results of boundary layers on inlet endwalls

	Without cascade	Traditional cascade	Acute angle zone of lean blade cascade	Obtuse angle zone of lean blade cascade	Positively curve blade cascade	Negatively curved blade cascade
Thickness δ (mm)	23.6	26.9	34	25.8	33.2	24.6
Displacement thickness δ^*(mm)	2.5	2.9	3.6	2.8	3.5	2.7
Shape factor H	1.47	1.45	1.47	1.52	1.5	

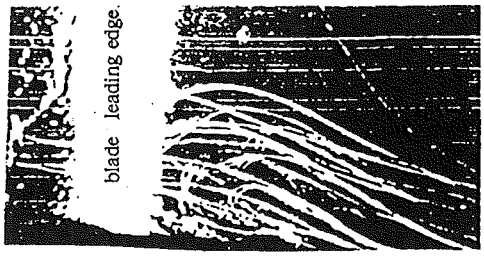

Fig. 3(*a*) Color helium flow display

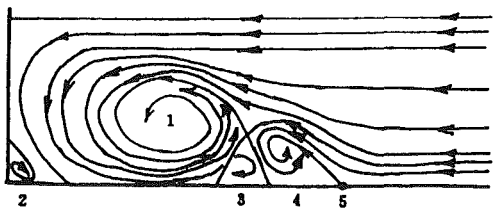

Fig. 3(*b*) Flow model near leading edge: (1) horseshoe vortices; (2) corner vortices; (3) countervortices; (4) separation vortices; (5) separation points

Fig. 3 Flow model near leading edge of cascade

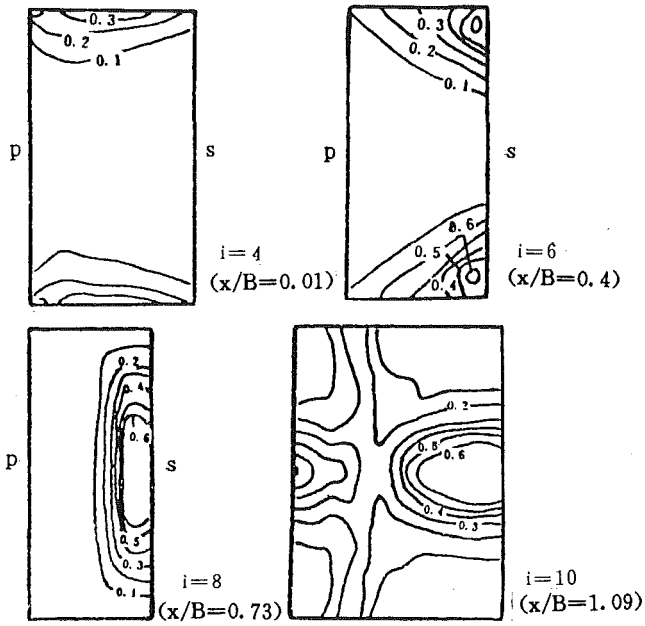

Fig. 4(*a*) Loss coefficient contours of traditional linear blades

horseshoe vortices: inlet boundary layer thickness, streamwise adverse pressure gradient, and the stagnation pressure gradient in the normal direction of endwalls. Any one of the three, if intensified will favor the separation of boundary layers and the development of horseshoe vortices, and move the separation saddle point A and the separation line S to upstream (Fig. 5). Because the inlet boundary layers in the acute angle zones of lean blades and positively curved blades are thicker, and the inlet adverse pressure segment is longer and adverse pressure gradients are greater (Fig. 6), the boundary layer saddle points are farther from the leading edges, and the scale and intensity of the horseshoe vortices in the same measurement plane are bigger, compared with those of the traditional cascade. The opposite case holds for the obtuse angle zones of lean blade cascade and negatively curved cascade.

The pressure side leg of the horseshoe vortex accompanies the suction side leg of the adjacent blade going into the same passage. Both of them roll toward the suction side by the transverse pressure gradient. As the pressure side leg rolls up the main portion of the lower energy airflows in inlet boundary layers, new boundary layers are formed behind the separation line. When horseshoe vortices reach the suction side corner, the lower energy air-flow in new boundary layers, driven by the transverse pressure gradient to here, joins them and rolls toward the middle of the passage and pressure side of the blade, developing into high-intensity and large-scale passage vortices (Figs. 4*b*, *c*, measurement plane 6). Because the pressure side leg coincides with the core of the passage vortex, the passage vortex, when is formed, has high rotation velocity such that a low pressure point and a peak of energy loss appear

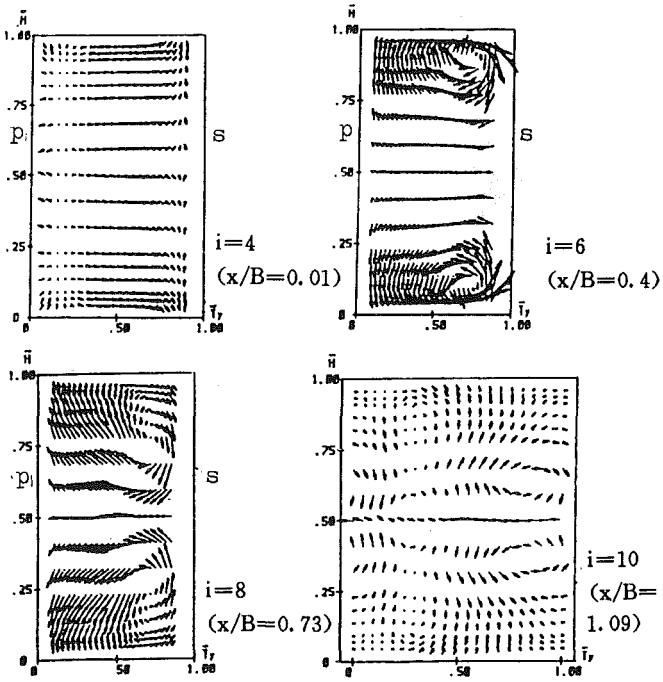

Fig. 4(*b*) Velocity vectors in planes perpendicular to flow direction of traditional blades

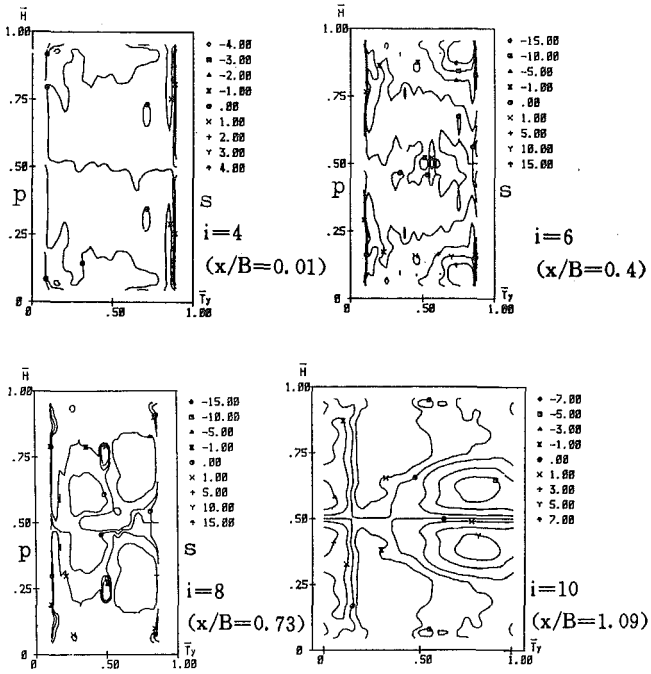

Fig. 4(*c*) Streamwise vorticity contours of traditional blades (the vorticities in the clockwise direction are negative, the ones in the counterclockwise direction are positive)

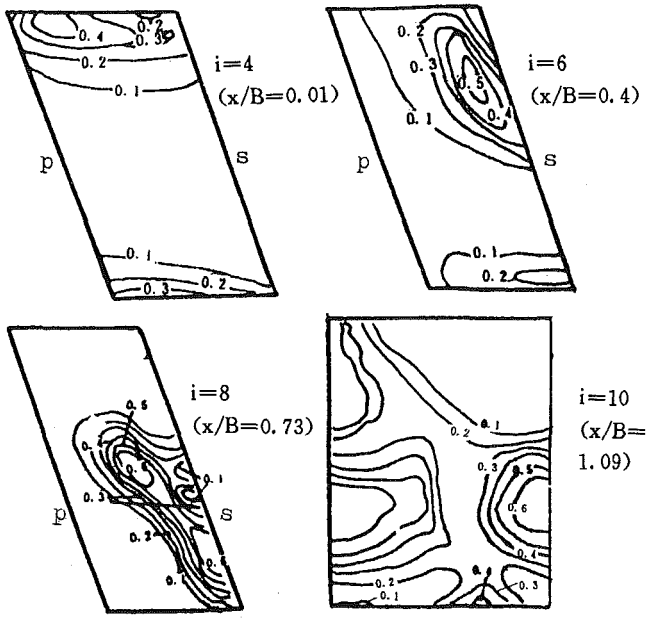

Fig. 4(*d*) Loss coefficient contours of lean linear blades

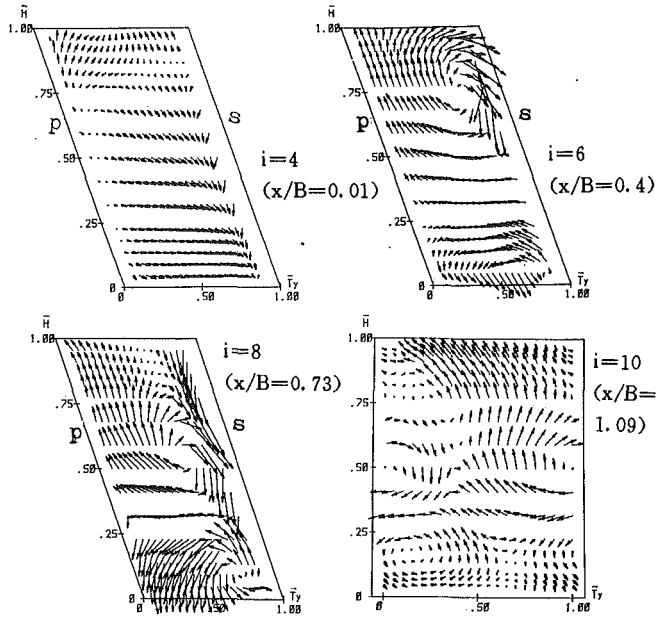

Fig. 4(*e*) Velocity vectors in planes perpendicular to flow direction of lean linear blades

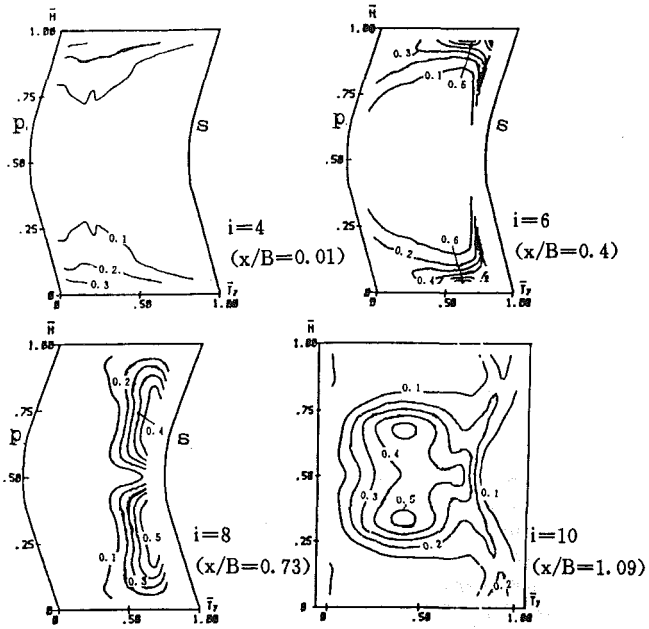

Fig. 4(*f*) Loss coefficient contours of negatively curved blades

near the core. The suction side leg, as it rotates in the opposite direction of the passage vortex, gradually dissolves by the shear force when meeting with the passage vortex.

Four parameters decide the origination and development of passage vortices. They are the intensity of horseshoe vortices, transverse pressure gradient in the passage, pressure distribution along blade height, and the streamwise adverse pressure gradient. In cascades with high turning angle, the transverse pressure gradient, being large, is almost not affected by the leaning or curving of blades. Therefore, it becomes the key factor to produce passage vortices of high intensity. The other factors only affect the intensity, scale, and position of passage vortices. The static pressure distribution along the blade height is the second role for the scale and intensity is the first one for the location of the passage vortices in the direction of the blade height. In traditional cascades the static pressure distribution along blade height is derived by passage vortices. The static pressure gradient from endwalls to the core of vortices is negative, and from the core to midspan of blades is positive as shown in Fig. 4(*l*). In curved blade cascades there is another static pressure gradient along the blade height produced by the blade force component along the blade height, except the one by the passage vortices. Positively curved blades produce a negative pressure gradient starting from both endwalls, i.e., shape, "C" static pressure distribution along blade height, while negatively curved blades produce a positive one, i.e., opposite shape "C" static pressure distribution. In both curved blade cascades the static pressure gradient is the summation

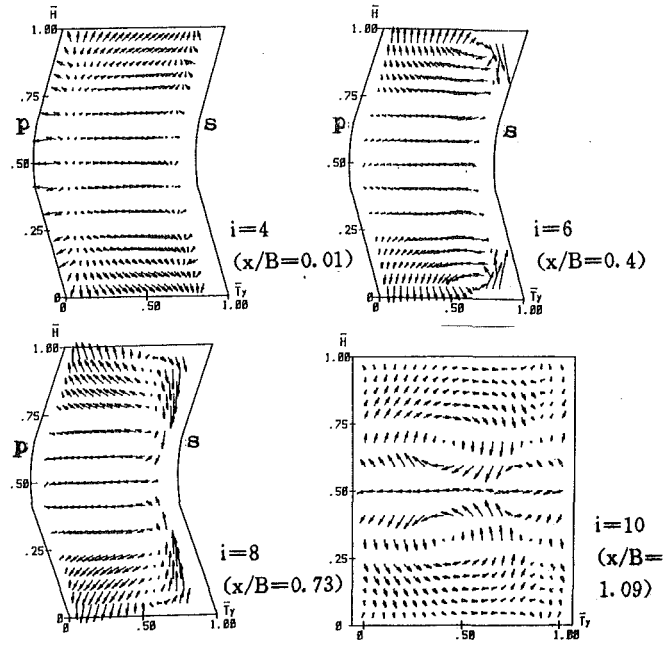

Fig. 4(*g*) Velocity vectors in planes perpendicular to flow direction of negatively curved blades

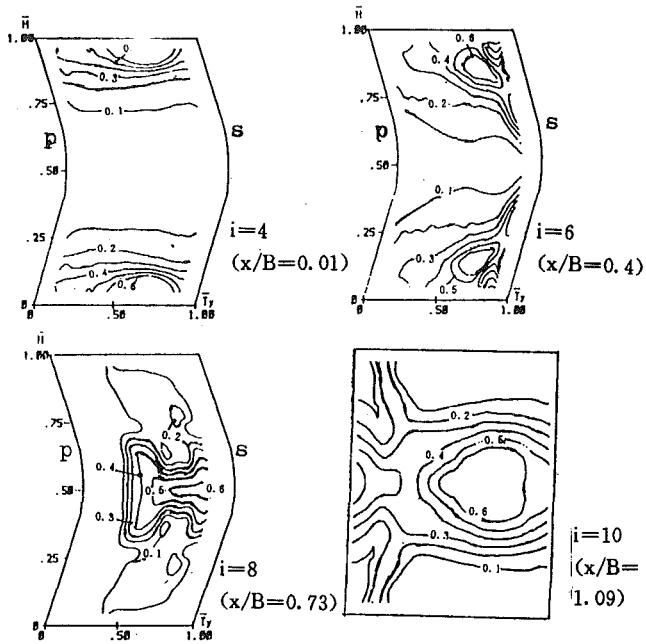

Fig. 4(*i*) Loss coefficient contours of positively curved blades

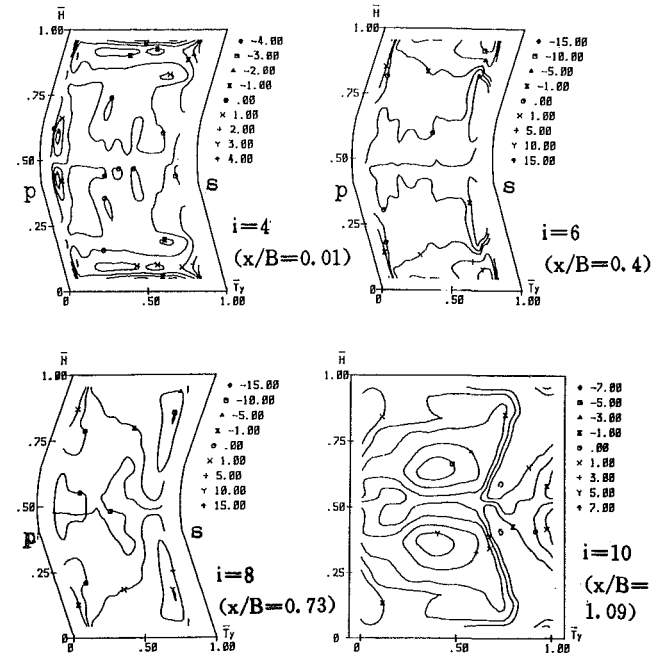

Fig. 4(*h*) Streamwise vorticity contours of negatively curved blades

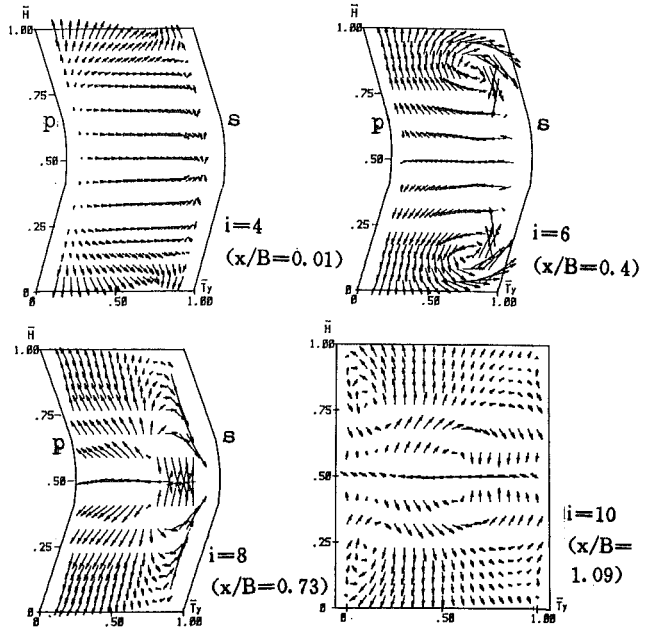

Fig. 4(*j*) Velocity vectors in planes perpendicular to flow direction of positively curved blades

of the one from passage vortices and the other from blade force components along blade height (Fig. 4*l*). Experimental results indicate that the static pressure gradient produced by the blade force has a considerable effect on the origination and development of passage vortices, and shape "C" static pressure distribution favors the passage vortices, while the opposite shape "C" one hinders them.

Compared with that of the traditional cascade in the same measurement plane, the intensity of horseshoe vortices in the acute angle zones of lean blade cascade and positively curved blade cascade is greater. Besides, there is a negative pressure gradient starting from the endwall and a shape "C" static pressure distribution. So the passage vortices in those two cases are formed in the more upstream plane and have a higher intensity and larger scale in the same measurement plane, and are located nearer the midspan and pressure side. The passage vortices in the obtuse angle zones and negatively curved blade cascade are the opposite cases. From measurement planes 5 to 8 in Fig. 4, one finds that the passage vortices in the acute angle zone and positively curved blade cascade have formed in plane 5; in the traditional cascade in plane 6; and in obtuse angle zones and the negatively curved blade cascade in plane 7. Moreover, for the two latter cases the passage vortices are weaker, nearer the endwalls, so produce smaller losses.

From the plane in which the passage vertices are formed to the blade outlet edge plane it is a process that the passage vortices develop toward the cascade middle and pressure side. Passage vortices, as centralized ones, are the only form to accumulate large kinetic energy in a narrow space, and their

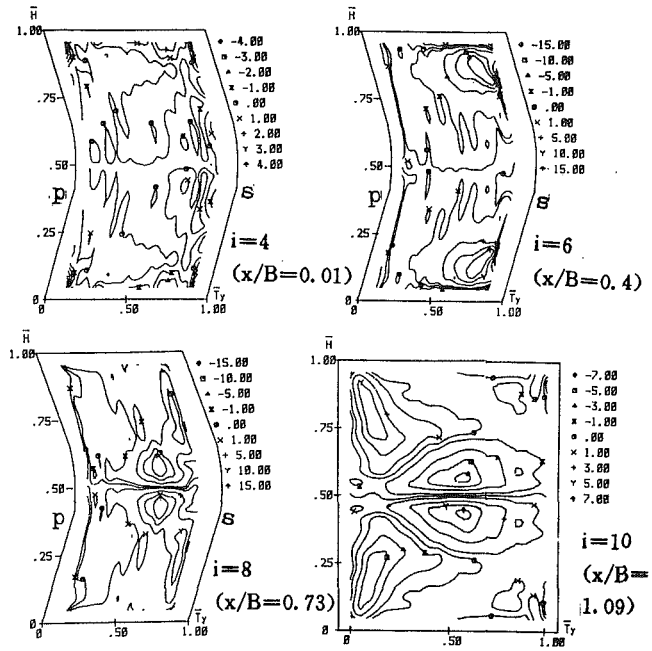

Fig. 4(*k*) Streamwise vorticity contours of positively curved blades

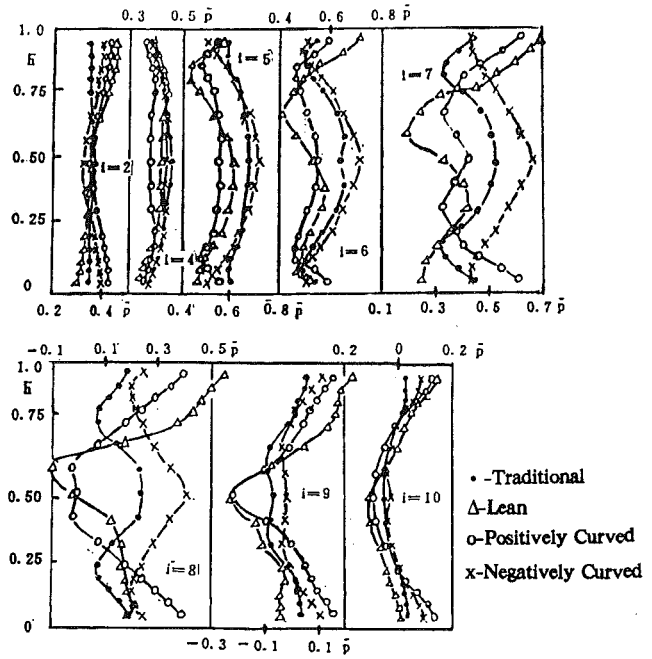

Fig. 4(*l*) Pitch-averaged static pressure coefficient distribution along blade height in the passage

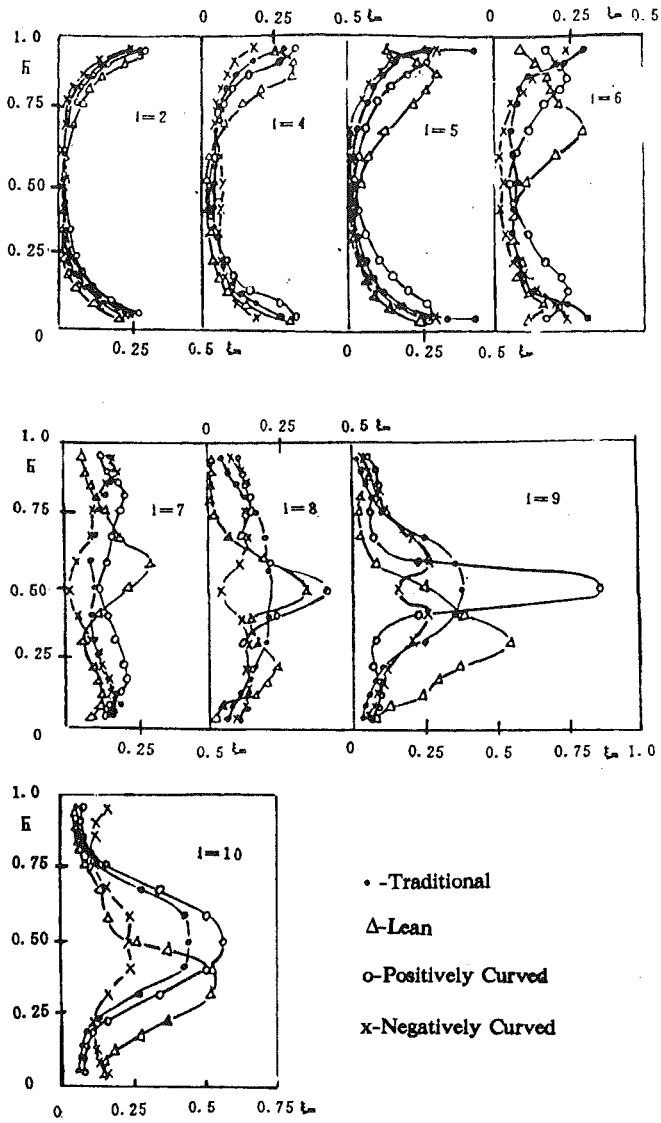

Fig. 4(*m*) Loss coefficient distribution along blade height

Fig. 4 Aerodynamic parameter distribution in measurement planes

energy is provided by average flows. In turn, they have an intensive effect on the average flows. In cascades with high turning angle, most of the mass momentum, and energy is transported by passage vortices. The low-energy airflow in new boundary layers is transported to suction surface corner by the transverse pressure gradient, and then is entrained along the suction surface by passage vortices; meanwhile on the pressure surface high energy airflows are convected from midspan to endwalls, reducing the flow losses near the endwalls greatly. By convection passage vortices roll up most of the low-energy airflow in the passage increasing in the intensity and scale themselves.

With passage vortices moving toward the middle of the cascades, the upper and lower passage vortices with the same intensity and the opposite rotation directions approach each other and meet in the midspan at last, which happens earliest in the positively curved blade cascade. When the two vortices meet, due to the strong interaction between them, a transverse flow with high velocity in the pitch direction is produced in the meeting plane, which usually leads to the breaking of the vortices and dissipating of their energy. So the losses in the midspan suddenly increase and a big zone of high losses appears. Figure 4 shows the upper and lower passage vortices of positively curved blades have completely met in measurement plane 9, and the loss peak in the midspan reach up to 86.5 percent. The two vortices of traditional cascade start meeting in plane 9. As for the lean blade cascade, the static pressure in acute angle zones, higher than that in obtuse angle zones, not only favors the passage vortices in acute angle zones and hinders them in the other zones, but also moves the passage vortices in the acute angle zone to the obtuse angle zone (Fig. 4*e*, measurement plane 6–9). In plane 9 the two vortices meet at 31 percent blade height and a loss peak of 56 percent appears. For a negatively curved blade cascade the upper and lower vortices, being controlled in their corresponding zones by the opposite shape "C" static pressure distribution, are still 0.38 blade height away from each other in measurement plane 9.

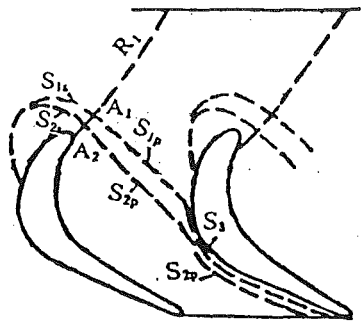

Fig. 5 Three-dimensional separation model of inlet boundary layers

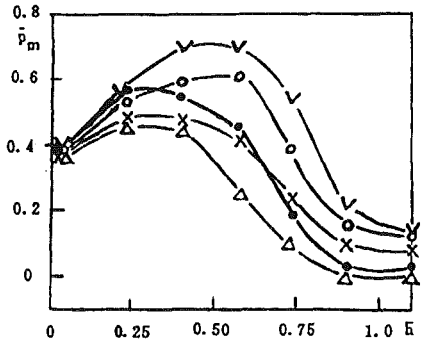

Fig. 6 Variations of static pressure coefficient averaged by pitch along axial direction: •—traditional Δ—obtuse zone; v—acute zone; o—positively curved; x—negatively curved

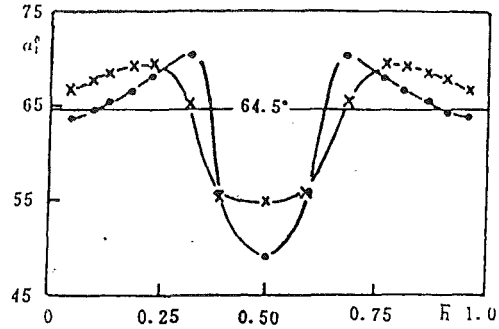

• -Traditional; x-Negatively Curved

Fig. 7 Distribution of outlet airflow angle along blade height

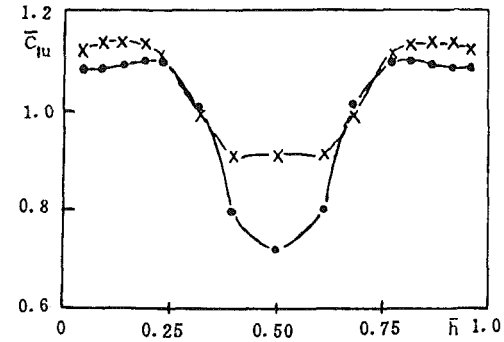

Fig. 8 Distribution of outlet tangential velocity coefficient along blade height

Flows Downstream. The experimental results from measurement plane 10 (in Fig. 4) show that in a traditional cascade the complete meeting of passage vortices at the midspan dominates the whole outlet flowfield, and high loss area occupied the large part of the cascade middle with a loss core in the center of the passage. The loss core corresponds to the low-pressure area and the lowest turning angle of airflows. In a lean blade cascade the loss peak from the meeting is dissipated by mixing, which results in loss value decreasing and high loss area expanding and loss peak position moving up to 35 percent blade height. In a negatively curved blade cascade the two vortices have not completely met in plane 10. The distance between the two vortex cores is 0.2 blade height. Compared with those of traditional cascade, the wake and high loss area are reduced enormously; the loss values in these areas also are lower. In positively curved blade cascade the loss peak in the midspan goes down to 57 percent because of the dissipating of the vortex energy; the high loss area and loss value are obviously greater than those of a traditional cascade. The growth of downstream loss is due to mixing caused by flow nonuniformity. A nonuniform flow will generally contain primary velocity in wake and secondary velocities in vortices. Both will contribute to mixing loss but the later will be much more serious since it is reasonable to assume that all of the secondary kinetic energy is lost (Moore and Adhye, 1985). For a large turning angle cascade the mixing loss mainly depends on the intensity, scale of upper and lower passage vortex, and distance between their cores. The greater the intensity and scale, the smaller the distance, the greater the mixing loss. The mass flux-averaged total loss coefficients of traditional, lean, positively curved, and negatively curved blade cascade are 0. 1948, 0.1883, 0. 2255, and 0. 1572, respectively, which indicates the losses of lean blade cascade are almost equal to those of the traditional one, so using lean blades in rectangular cascades does not reduce losses, sometimes even increases them. A negatively curved blade cascade reduces losses by 19.3 percent and a positively curved blade one increases losses by 15.6 percent over the traditional one.

It can be derived by reviewing the whole flow field that the origination and development of horseshoe vortices and passage vortices take a predominant role in the flow field a traditional cascade, especially the meeting of upper and lower vortex in midspan results in high losses, airflow underturning, and decreasing of work done ability; in lean blade cascade the improvement of exit flows in the acute zone does not result from the decrease of secondary flow losses produced in the zone. On the contrary the secondary flow losses in the acute angle zone are much bigger than those in the obtuse angle zone, and fortunately, the acute angle zone losses are transported to the obtuse angle zone by passage vortices, which further reveal that passage vortices entrain most part of low-energy airflows in the passage, where the passage vortex moves is a low-pressure, high-loss area. Analyzing Fig. 4 in detail one can find although the passage vortices core does not agee with the loss peak and the lowest pressure point exactly, they are rather close to each other. The passage vortices have an intensive three-dimensional nature. Their vorticities can be divided into two components: the spanwise and streamwise vorticities. The spanwise vorticities equal to the circulations around blades decide the aerodynamic loads of blades. The greater the streamwise vorticities producing secondary flows, the greater is the total loss of a cascade. Controlling the vortices means controlling the streamwise vorticities and keeping the spanwise vorticities, which makes the total loss of the cascade reduce to the minimum under the condition of higher aerodynamic loads of blades. From the above-mentioned we propose that in cascades with low aspect ratio and high turning angle the secondary vortical losses take the main part of the total losses. So the key to reducing the losses in this kind of cascade is to control the origination and development of horseshoe and passage vortices, especially to avoid the meeting of the passage ones. The obtuse angle zone hinders the two kinds of vortices

efficiently, so using negatively curved blades (the dihedral between pressure surface and both endwalls are obtuse) is the logical development of using leaned blades. Negatively curved blades introduce the improvement in obtuse angle zones to the same cascade.

Using negatively curved blades not only raises the cascade efficiency, but also makes the outlet airflow angles approach the geometry ones, increasing the working ability of airflows. From Fig. 7 one sees in a traditional cascade the meeting of the two passage vortices produces a 16.5 deg largest underturning angle in midspan, and approximate 6 deg overturning angles at 30 and 70 percent of relative blade height, respectively. Negatively curving blades reduce the largest underturning angle by about 7 deg, and move the position of the largest overturning angle (2 deg smaller than that of traditional cascade) to endwalls. Experiment data indicate the averaged outlet angle along the blade height is 1.5 deg larger than that of the traditional cascade, which means negatively curving blades not only decrease the secondary vortical losses, but also slightly raise the aerodynamic loading of the blades. According to Euler equations the outlet tangential velocity of rectangular cascades, C_{lu}, represents the working ability of airflows. The variation of outlet tangential velocity along blade height in negatively curved blade cascade is similar to that in traditional cascades (Fig. 8). For traditional cascades the lowest working ability point is located at midspan from which the working ability grows sharply in both directions to the endwalls, and almost holds constant from both 0.25 and 0.75 blade height to the corresponding endwalls, respectively. For a negatively curved blade cascade the working ability in the zone from 0.31 to 0.69 of blade height is raised enormously, resulting from the avoidance of the meeting of passage vortices. In the zone near endwalls the overturning of airflows increase the working ability too. In the other zone the working ability of traditional and negatively curved blade cascades is approximately equal. An obvious conclusion is that negatively curved blades increase working ability of airflows greatly.

4 Conclusions

1 In cascades with low aspect ratio and high turning angle, the secondary vortical losses from horseshoe and passage vortices take the main part of the total losses. The key to reducing the losses, therefore to improving the aerodynamic performance, of the cascades is to control the origination and development of horseshoe and passage vortices, especially to avoid the meeting of the passage vortices.

2 The leaning of blades intensities the passage vortices in the acute angle zones, and moves them to the obtuse angle zones, and at the same time controls those in the obtuse angle zones, which leads to the meeting position of both angle zone passage vortices located in the obtuse angle zones. The lower energy airflows produced in the acute angle zones are entrained by these zone passage vortices and move to the obtuse angle zones; as a result the aerodynamic performance is degraded in the obtuse angle zone and improved in the acute angle zone.

3 Use of a negatively curved blade can control the origination and development of horseshoe vortices and passage vortices and confine the upper and lower passage vortices in their own sides, avoiding their meeting. Therefore, the secondary vortical losses of cascade are greatly reduced, and the efficiency is raised.

4 As both the biggest underturning and overturning of airflows are caused by passage vortices, controlling the origination and development of passage vortices can redistribute the outlet airflow angle along the blade height, decrease the incidence on the next blade row, and intensify the working ability by slightly increasing the load of blades.

References

Han Wanjin, et al., 1990, "The Influence of Blade Curving on End Secondary Flow at Different Incidence," *Journal of Engineering Thermophysics*, Vol. 11, No. 3 [in Chinese].

Harrison, S., 1990, "Secondary Loss Generation in a Linear Cascade of High-Turning Turbine Blades," ASME JOURNAL OF TURBOMACHINERY, Vol. 112, pp. 618–624.

Ishii, et al., 1986, "A Three-Dimensional Turbulent Detached Flow With a Horseshoe Vortex," ASME *Journal of Engineering for Gas Turbines and Power*, Vol. 108, pp. 125–130.

Langston, L. S., et al., 1977, "Three-Dimensional Flow Within a Turbine Cascade Passage," ASME *Journal of Engineering for Power*, Vol. 99, pp. 21–28.

Moore, J., and Adhye, R. Y., 1985, "Secondary Flows and Losses Downstream of a Turbine Cascade," ASME *Journal of Engineering for Gas Turbines and Power*, Vol. 107, pp. 961–968.

Sieverding, C. H., 1985, "Recent Progress in the Understanding of Basic Aspects of Secondary Flows in Turbine Blade Passages," ASME *Journal of Engineering for Gas Turbines and Power*, Vol. 107, pp. 248–257.

Wang Zhongqi, et al., 1988, "The Effect of Blade Leaning on Cascade Aerodynamic Characteristics and the Experimental Study of Mechanism of Reducing Secondary Flow Losses by Leaned Blade," *Journal of Engineering Thermophysics*, Vol. 9, No. 2 [in Chinese].

An Analytical Model of Axial Compressor Off-Design Performance

T. R. Camp

J. H. Horlock

Department of Engineering,
Whittle Laboratory,
Cambridge University,
Cambridge, United Kingdom

An analysis is presented of the off-design performance of multistage axial-flow compressors. It is based on an analytical solution, valid for small perturbations in operating conditions from the design point, and provides an insight into the effects of choices made during the compressor design process on performance and off-design stage matching. It is shown that the mean design value of stage loading coefficient ($\psi = \Delta h_0/U^2$) has a dominant effect on off-design performance, whereas the stage-wise distribution of stage loading coefficient and the design value of flow coefficient have little influence. The powerful effects of variable stator vanes on stage-matching are also demonstrated and these results are shown to agree well with previous work. The slope of the working line of a gas turbine engine, overlaid on overall compressor characteristics, is shown to have a strong effect on the off-design stage-matching through the compressor. The model is also used to analyze design changes to the compressor geometry and to show how errors in estimates of annulus blockage, decided during the design process, have less effect on compressor performance than has previously been thought.

Introduction

The off-design performance of axial-flow compressors is critical for the efficient and stable operation of aircraft gas turbine engines and industrial compressors. While modern computational methods can give predictions of compressor off-design performance, there remains some lack of understanding of how various features of the original design (e.g., the magnitude of the stage loading coefficient and its distribution through the compressor) affect the off-design performance. The purpose of this paper is to advance that understanding.

A one-dimensional approach is developed here, similar in this respect to many that have proved useful in the past (e.g., Robbins and Dugan, 1956; Stone, 1958; Howell and Calvert, 1978; Wright and Miller, 1991). Critically, however, we make an assumption that allows the stage-stacking equations to be solved analytically. Our assumption is that changes in gas properties occur continuously with axial distance through the compressor and not in discrete jumps between blade rows, an assumption that is similar to an original idea of Mellor (1957). Horlock (1958) developed Mellor's concept to obtain and solve a differential equation for the temperature change through a turbomachine when it operated off-design. More recently, Goede and Casey (1988) have adopted a somewhat similar approach to the Mellor/Horlock solutions. They solved the basic stage-stacking equations, assuming that each stage deviates only slightly from its design operating point. The resulting equations are solved numerically and the authors trace out how each stage moves away from its design point when an off-design stage loading distribution is specified. Particularly enlightening in the Goede/Casey analysis is the effect of varying the stagger of stators through the compressor, and how this feature can be used to keep compressor pressure ratio and efficiency near design values.

Here we bring together the Mellor/Horlock analysis (obtaining a differential equation for the temperature rise through the equivalent compressor) and the Goede/Casey method of solution (assuming small perturbations of all the independent and dependent parameters). We obtain analytical solutions for the temperature, density, and axial-velocity variations through the machine, which enable use to deduce how the choice of design parameters affects the off-design performance of individual stages and of the overall compressor.

Inherent in the method are two further assumptions, namely that the temperature rise coefficient–flow coefficient characteristic for each stage is linear and that the stage efficiencies are constant between design and off-design conditions. These assumptions limit our solutions to operating points close to the compressor design point. However, comparisons of our solutions with a numerical method (Hynes, 1992), which takes a fuller account of the performance changes of blade rows with incidence, shows that our approximations are good. Comparisons with the results of Goede and Casey show similar predictions of compressor behavior with variable stator movement.

It is considered that the analytical solutions obtained give an improved understanding of the nature of off-design performance. Among several applications of the solutions, equa-

Contributed by the International Gas Turbine Institute and presented at the 38th International Gas Turbine and Aeroengine Congress and Exposition, Cincinnati, Ohio, May 24–27, 1993. Manuscript received at ASME Headquarters February 9, 1993. Paper No. 93-GT-96. Associate Technical Editor: H. Lukas.

tions are developed that predict the slope and spacing of constant speed characteristics and that show the effects of errors in annulus blockage estimates and the slope of the engine working line on the matching of individual stages.

Method

In this section the basis of the analysis is outlined. After a description of the necessary assumptions, the method of solution is presented using a limited set of variables. Finally the solution for a fuller set of variables is given.

It is first necessary to make five assumptions, which are described below:

1 Only small changes from the compressor design point are considered (the change in any stage flow coefficient is limited to a maximum of 4 percent from its design value).

2 The stage loading-flow coefficient characteristics for each stage of the compressor are assumed to be linear. For the unstalled operating range, the stator exit flow angle, α_1, and the rotor exit relative flow angle, β_2 (both measured from the axial direction), are assumed to be constant with changing flow coefficient. Hence

$$\psi = \frac{Cp\Delta T}{U^2} = 1 - \frac{V_X}{U}(\tan\alpha_1 + \tan\beta_2) = 1 - \phi K \qquad (1)$$

where ψ is the stage loading coefficient, ϕ is the flow coefficient and $K = \tan\alpha_1 + \tan\beta_2$, the negative slope of the characteristic, which is assumed to be constant. In practice the outlet flow angles will increase slightly with incidence and the ψ–ϕ characteristic will "droop" a little as the stall point is approached.

3 The efficiencies of each stage are assumed to be equal and, for the small off-design perturbations considered, they are assumed not to change between the design and off-design conditions. This implies that a constant polytropic efficiency (η_p) can be used. In practice, for small changes in ϕ from design, the stage efficiency changes relatively little (less than 1 percent for a 10 percent change in flow coefficient from design in an example given by Howell, 1945).

4 To obtain analytical solutions to the off-design equations given below it is necessary to assume that the design value of stage loading coefficient (ψ^*) is the same for every stage in the compressor. A study of several modern compressors showed this assumption to be close to common design choices. In a later section we compare the effects of other distributions of design stage loading through the compressor by solving the governing equations numerically.

5 The changes in gas properties are assumed to occur continuously with axial distance through the compressor, as discussed in the introduction.

Off-Design Performance of a "Baseline" Compressor. Consider first the performance of a "baseline" compressor using the following variables: ψ, ϕ, ρ (density), T (temperature), U (speed), and M (mass flow rate). We denote design values by the superscript "*". For simplicity in this first case we take U and M to be the same at every axial position through the compressor. Consider small perturbations, $k(x)$, in the design value of each parameter, where x is the axial distance through the compressor. (We choose the scale of x such that one unit of axial distance is occupied by one stage. Thus an axial compressor of N stages has a length $x = N$.)

$$\frac{\psi(x)}{\psi^*(x)} = 1 + k_\psi(x) \qquad \frac{\phi(x)}{\phi^*(x)} = 1 + k_\phi(x)$$

$$\frac{\rho(x)}{\rho^*(x)} = 1 + k_\rho(x) \qquad \frac{T(x)}{T^*(x)} = 1 + k_T(x)$$

$$\frac{U}{U^*} = 1 + k_U \qquad \frac{M}{M^*} = 1 + k_M \qquad (2)$$

where each of the perturbation terms k has a magnitude much less than unity. Note that for this baseline case, k_U and k_M are constants and are independent of x. These parameters are related by four equations, as follows.

Since the polytropic efficiency of each stage is assumed to remain constant

$$\frac{\rho(x)}{\rho^*(x)} = \left[\frac{T(x)}{T^*(x)}\right]^n \qquad (3)$$

where $n = \eta_p \dfrac{\gamma}{(\gamma - 1)} - 1$. For small perturbations this becomes

$$k_\rho(x) = n k_T(x) \qquad (4)$$

Consideration of mass continuity at design and off-design gives

$$\frac{M}{M^*} = \frac{\phi}{\phi^*}\frac{\rho}{\rho^*}\frac{U}{U^*} \qquad (5)$$

and for small changes from the design point it follows that

$$k_M = k_\phi(x) + k_\rho(x) + k_U \qquad (6)$$

Equation (1), the relation between ψ and ϕ, may be written, for small perturbations,

$$k_\psi(x) = \left(1 - \frac{1}{\psi^*}\right) k_\phi(x) \qquad (7)$$

Finally, for small movements from the design point and for ψ^* constant through the compressor, we assume that the ratio of the finite change of temperature across the stage to the finite

Nomenclature

$a, b, n, P, Q, R, S, W, \delta, \epsilon, \zeta, \iota, \kappa, \lambda, \mu, \nu, \sigma, \chi$ = constants
A = annulus area
Cp = specific heat at constant pressure
K = slope of stage characteristic
M = mass flow rate
N = number of stages
T = static temperature
U = mean blade speed
V_X = axial velocity
h = enthalpy
k = small perturbation
r_T = temperature ratio
x = axial distance
α = absolute flow angle
β = relative flow angle
γ = ratio of specific heats
η = efficiency
θ = nondimensional exit temperature
ρ = density
ϕ = flow coefficient = V_X/U
ψ = stage loading coefficient = $\Delta h_o/U^2$
ω = nondimensional temperature

Subscripts

I = compressor inlet
II = compressor exit
o = stagnation condition

Superscripts

* = design condition
· = off-design condition
′ = first derivative
″ = second derivative

design change may be represented by small (differential) quantities, so that

$$\frac{dT}{dx}=\frac{dT^*}{dx}\frac{\Delta T}{\Delta T^*} \tag{8}$$

If ψ^* is constant through the compressor then

$$T^*(x)=T_1+\frac{\psi^* U^{*2} x}{Cp} \tag{9}$$

and

$$\frac{dT^*}{dx}=\frac{\psi^* U^{*2}}{Cp} \tag{10}$$

Now

$$\frac{\Delta T}{\Delta T^*}=\frac{\psi}{\psi^*}\left(\frac{U}{U^*}\right)^2$$

which becomes

$$\frac{\Delta T}{\Delta T^*}=1+k_\psi(x)+2k_U \tag{11}$$

Thus a differential equation for the temperature variation from design (k_T) may be obtained from Eqs. (8), (9), (10), and (11)

$$k_T'(x)\left(\frac{CpT_1}{\psi^* U^{*2}}+x\right)+k_T(x)=k_\psi(x)+2k_U \tag{12}$$

We now have four equations (4), (6), (7) and (12) linking six parameters. Two of the parameters, however, are inputs to the problem: k_U (a change in speed) and k_M (a change in flow rate). The equations are combined to give

$$k_T'(x)+k_T(x)\frac{P}{(R+x)}=\frac{Q}{(R+x)} \tag{13}$$

where

$$P=1+n\left(1-\frac{1}{\psi^*}\right)$$

$$Q=\left(1-\frac{1}{\psi^*}\right)(k_M-k_U)+2k_U$$

$$R=\frac{CpT_1}{\psi^* U^{*2}}$$

This linear, first-order differential equation is solved using an integrating factor and the boundary condition that $k_T(0)=0$ (the inlet temperature remains constant at $T=T_1$).

We then obtain the solution

$$k_T(x)=\frac{Q}{P}\left[1-\left(1+\frac{x}{R}\right)^{-P}\right] \tag{14}$$

Expressions for $k_\rho(x)$, $k_\phi(x)$, and $k_\psi(x)$ follow by back-substitution into Eqs. (4), (6), and (7).

At the exit from the compressor, where $T=T_{II}$ at $x=N$,

$$(R+x)=R\left[1+\frac{N\psi^* U^{*2}}{C_pT_1}\right]=Rr_T^* \tag{15}$$

where $r_T^*=T_{II}^*/T_I$, the ratio of compressor exit to inlet temperatures at design.

Hence

$$k_{TII}=k_T(N)=\frac{Q}{P}\left[1-\frac{1}{(r_T^*)^P}\right] \tag{16}$$

This solution for the baseline compressor may be shown to be similar to a logarithmic solution obtained by Horlock (1958) if the design temperature ratio r_T^* is not much greater than unity.

A More General Solution. We next derive a more general solution in which the compressor design is allowed to change slightly from the baseline design. We follow a procedure similar to that described above, but now include the effects of other input variables. These include

1 Varying the slopes of the stage characteristics (possibly as a result of movement of variable stator vanes),

$$\frac{K(x)}{K^*(x)}=1+k_K(x) \tag{17}$$

2 Allowing annulus areas to change from design to off-design (as a function of x), either as a design modification from the baseline compressor or due to boundary layer growth,

$$\frac{A(x)}{A^*(x)}=1+k_A(x) \tag{18}$$

3 Taking account of changes in blade speed due to changes in both rotational speed off-design and changes of mean radius with x, so that $U=U(x)$,

$$\frac{U(x)}{U^*(x)}=1+k_U(x) \tag{19}$$

4 Allowing small changes in mass flow due to changes in both entry mass flow and to bleed or injection of air along the compressor, so that $M=M(x)$,

$$\frac{M(x)}{M^*(x)}=1+k_M(x) \tag{20}$$

It is possible to obtain an analytical solution if these variables take any polynomial function of x, but the solution quickly becomes very complicated with the increasing order of the polynomials. Here we consider only linear distributions of: $k_U(x)=\chi+\delta x$, $k_M(x)=\epsilon+\iota x$, $k_K(x)=\kappa+\lambda x$, and $k_A(x)=\mu+\nu x$.

For this case Eq. (13) becomes

$$k_T(x)=\frac{S}{P}\left[1-\frac{R^P}{(R+x)^P}\right]-\frac{W(R+x)}{P(P+1)}\left[1-\frac{R^{P+1}}{(R+x)^{P+1}}\right]+\frac{Wx}{P} \tag{21}$$

where

$$S=\left(1-\frac{1}{\psi^*}\right)(\epsilon-\chi-\mu+\kappa)+2\chi$$

and

$$W=\left(1-\frac{1}{\psi^*}\right)(\iota-\delta-\nu+\lambda)+2\delta$$

At compressor exit ($x=N$),

$$k_{TII}=\frac{S}{P}\left[1-\frac{1}{(r_T^*)^P}\right]-\frac{WRr_T^*}{P(P+1)}\left[1-\frac{1}{(r_T^*)^{P+1}}\right]+\frac{WN}{P} \tag{22}$$

which reduces to Eq. (16) if $W=0$ and if $S\equiv Q$.

Equations 21 and 22 can be used to consider the response of a compressor not only to changes in speed and flow rate but also to geometric "design" changes in annulus area, mean radius, stator stagger angle (which changes the slope of the stage characteristics), and/or bleed flows.

Validity of the Solution

Two exercises to check the validity of the analytical solution were undertaken. First, the results for changes in speed and flow (Eq. (14)) were compared with a numerical mean-line performance prediction code; and second, the effects of changing stator stagger angles through the compressor were compared with results by Goede and Casey (1988).

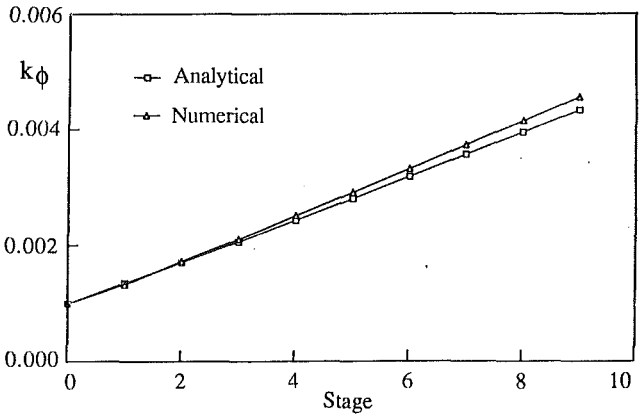

Fig. 1 Comparison between analytical and numerical solutions

Comparison of the Solution With Mean-Line Code Results. To check the accuracy of Eq. (14), several test cases were compared with the output from a mean-line compressor performance code. This code, which was developed by Dr. T. P. Hynes at the Whittle Laboratory, is not limited to small perturbations from the design point as deviation angles and efficiencies are calculated from empirical correlations.

For a hypothetical ten-stage, high-speed compressor with a constant design stage loading (ψ^*) of 0.5 for each stage, two cases were examined: first a small flow increase above the design mass flow rate ($k_M M^*$), the speed being held constant, and second a small speed increase ($k_U U^*$) at a constant mass flow rate. Figure 1 compares the changes in flow coefficient (k_ϕ) calculated with each method for the first test case. Similarly good agreement was found for all parameters for each of the two cases.

To investigate the sensitivity of the solution to the "small perturbation" approximation, the second case was investigated with several different positive values of k_U (0.001, 0.005, 0.01, and 0.05). From these calculations it was decided that, for accuracy, the size of the perturbations of the input variables (k_U and k_M) should be such that the size of the flow coefficient perturbation (k_ϕ) should nowhere exceed 4 percent.

Comparison of the Solution With the Results of Goede and Casey. As another exercise to validate our method, comparisons were made with the results of Goede and Casey (1988). They assumed that compressor speed and flow rate were fixed at the design values and they evaluated the distribution of flow coefficient after specifying the off-design stage loading distribution through the compressor. Variable stator vanes allowed the shapes of the stage characteristics to differ one from another. The equations they derived for single stages were solved numerically to obtain the distribution of flow coefficient through the whole compressor.

The method of Goede and Casey can be thought of as a special case of our analysis. Instead of specifying changes in speed, flow and stage characteristic slope (k_U, k_M, and $k_K(x)$) as input variables, they specified speed, flow, and off-design stage loading (k_U, k_M, and $k_\psi(x)$). They observed that the distribution of changes in stage loading from design was approximately linear with stage number for several industrial compressors. Consequently they specified linear distributions of stage loading as an input to their model. Below we show how our new model can provide analytical solutions for the same problem.

After Goede and Casey, assume *a priori* that

$$k_\psi(x) = a + bx \tag{23}$$

where a and b are constants and are both much less than unity. Substitution into Eq. (11) yields

$$k_T'(x)(R+x) + k_T(x) = a + bx + 2k_U \tag{24}$$

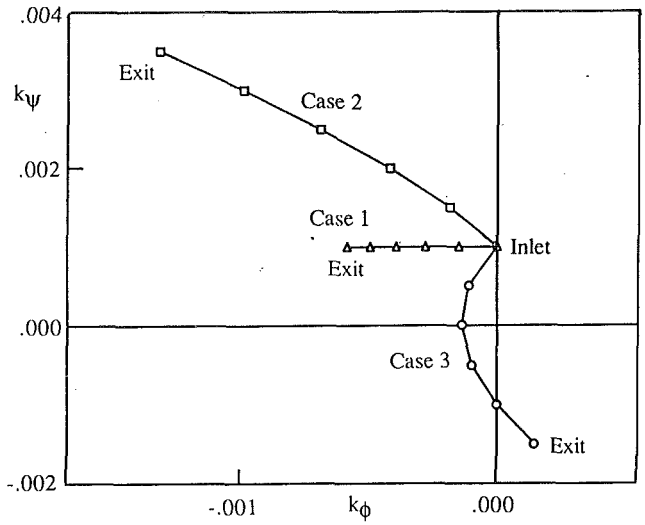

Fig. 2(a) Loci of stage operating points for three distributions of stage loading coefficient

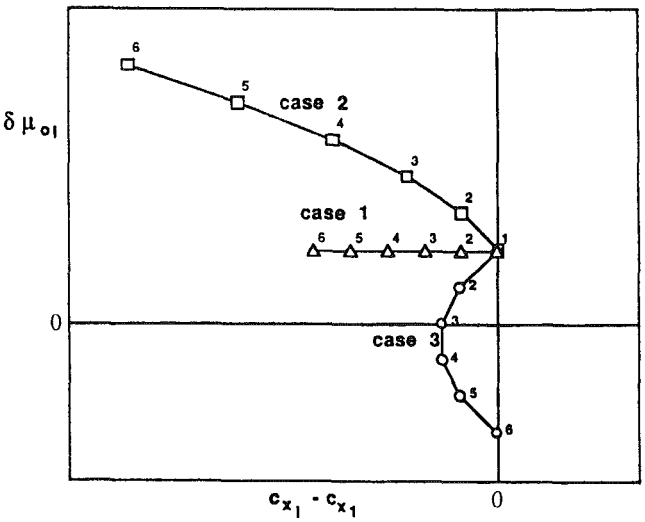

Fig. 2(b) Loci of stage operating points reproduced from Goede and Casey (1988)

We solve this equation using an integrating factor and the same boundary condition as before, namely that $k_T(0) = 0$, and obtain

$$k_T(x) = \frac{1}{(R+x)}\left[(2k_U + a)x + \frac{bx^2}{2}\right] \tag{25}$$

The Goede and Casey analysis assumes that the compressor speed and flow rate are fixed at their design values; therefore we set $k_U = k_M = 0$. Back substitution for $k_\phi(x)$ gives

$$k_\phi(x) = \frac{-n}{(R+x)}\left(ax + \frac{bx^2}{2}\right) \tag{26}$$

Goede and Casey plotted the change in stage loading against the change in flow coefficient for each stage in the compressor on one graph, creating a locus of stage operating points. In our notation this is equivalent to plotting $k_\psi(x)$ against $k_\phi(x)$. If we eliminate x between Eqs. (23) and (25) we obtain

$$k_\phi = \frac{-n(k_\psi^2 - a^2)}{2(Rb - a + k_\psi)} \tag{27}$$

This relation is plotted in Fig. 2(*a*) for a six-stage compressor for the three different distributions of off-design stage loading given in Table 1. The origin of this graph corresponds to the

Table 1 Three distributions of k_ψ as plotted in Fig. 2(a)

Case	a	b
1	+0.001	0
2	+0.001	+0.0005
3	+0.001	-0.0005

Table 2 The four cases of Fig. 3

Case	ψ^*	Remarks
1	$\psi^* < \frac{n}{(n+2)}$	$k_T''(x)$ is positive. Stages get rapidly further from their design point with increasing axial distance through the compressor.
2	$\psi^* = \frac{n}{(n+2)}$	$k_T''(x) = 0$. The distribution of $k_T(x)$ is a straight line.
3	$\frac{n}{(n+2)} < \psi^* < \frac{n}{(n+1)}$	$k_T''(x)$ is negative although $k_T(x)$ does not tend toward an upper limit as x increases.
4	$\psi^* > \frac{n}{(n+1)}$	$k_T''(x)$ is negative. As x increases, $k_T(x)$ asymptotes toward $\frac{Q}{P} = \frac{2k_U\psi^*-(1-\psi^*)(k_M-k_U)}{\psi^*-n(1-\psi^*)}$

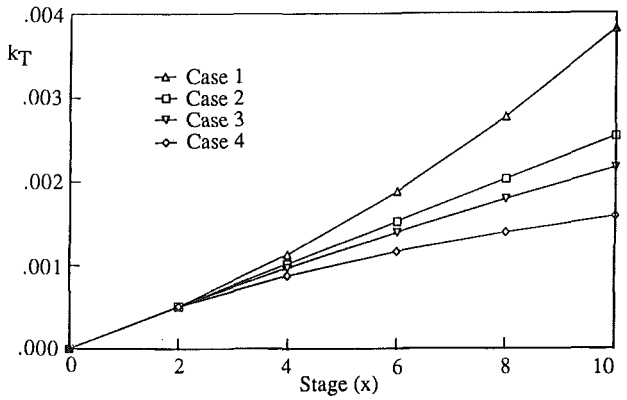

Fig. 3 k_T plotted against x for four values of ψ^*

compressor design point where, but for any perturbing influence of variable stators, all stage operating points would normally lie. If the stage loading of all stages is increased by 0.1 percent (case 1) then k_ϕ becomes negative as the flow decelerates from its design axial velocity as it passes through the compressor. If we exacerbate the situation by reducing the slope of the stage characteristics with stage number (case 2) then the stage operating points can be seen to move more rapidly from the origin. The third case illustrates a situation where the slopes of the stage characteristics are progressively increased through the machine (negative b). The effect of this is to limit the off-design movement of the front stages by counteracting the original increase in stage loading (positive a). Figure 2(b) is reproduced from Goede and Casey (1988). It shows numerical solutions for the same three test cases as above. The agreement between the analytical and numerical solutions is good.

The distribution of change in stage characteristic slope (which could be caused by variable stators) that is required to obtain the specified distribution of $k_\psi(x)$ can be found by back substitution to obtain $k_K(x)$. We find

$$k_K(x) = \frac{(a+bx)}{(1-1/\psi^*)} + \frac{nx(2a+bx)}{2(R+x)} \tag{28}$$

This relation then gives the stage geometry distribution (the variation in $K(x)$, possibly due to changes in stator outlet angles $\alpha_2(x)$) that would exactly create the linear distributions of $k_\psi(x)$ assumed *a priori* by Goede and Casey.

Similar comparisons were made with the Goede and Casey model using results for small changes in compressor speed (Casey, 1992). Again good agreement between the numerical and analytical solutions was obtained.

The Off-Design Performance of the Baseline Compressor

In this section we examine three aspects of the off-design performance of the "baseline" compressor, described by Eqs. (14) and (16). We begin by considering the importance of the choice of the design conditions (ψ^*, ϕ^*) and then use the equations to derive expressions for the slope and spacing of "overall" characteristics (compressor inlet to exit). Finally we consider the effects of the slope of the compressor working line on stage-matching.

The Choice of Design Conditions (ψ^*, ϕ^*)

The Effect of the Magnitude of ψ^*. The magnitudes of the stage loading coefficient (ψ^*) and the overall temperature ratio (r_T*) at the design point are the factors that most strongly influence how a compressor operates under off-design conditions. In this section we study how the magnitude of ψ^* affects how quickly stage operating points move away from their design points. Equation (14) gives the solution for the temperature distribution when we consider changes in rotational speed and flow rate only. Differentiating this equation twice with respect to x we obtain

$$k_T''(x) = -\frac{Q}{R^2}(P+1)\left(1+\frac{x}{R}\right)^{-(P+2)} \tag{29}$$

For this example let us consider $k_U > k_M(1-\psi^*)/(1+\psi^*)$ so that Q is positive and that $k_T(x)$ is positive for all x. (Similar conclusions to those drawn below apply to cases where Q is negative but some sign reversal is necessary in the arguments.) From Eq. (29) we see that $k_T''(x) = 0$ if $P = -1$, and hence if $\psi^* = n/(n+2)$. For $\psi^* < n/(n+2)$ the curvature of $k_T(x)$ is positive whereas for $\psi^* > n/(n+2)$ the curvature is negative. From Eq. (14) we see that if P is positive then $k_T(x)$ will tend to Q/P at large values of x. This is the case if $\psi^* > n/(n+1)$. We summarize these results in Fig. 3, which shows k_T plotted against x for four different values of ψ^* (for these examples $k_U = 0.001$ and $k_M = 0$). Table 2 provides the key to this figure.

If we assume that $\eta_p = 0.9$ and $\gamma = 1.4$ then the critical values of ψ^* are

$$\frac{n}{(n+2)} = 0.518 \quad \frac{n}{(n+1)} = 0.683$$

which are greater than typical design values.

The asymptotic behavior of case 4 in Fig. 3 represents an "off-design repeating stage" condition in which $k_\psi(x)$, $k_\phi(x)$, $k_\rho(x)$, and $k_T(x)$ converge to unique values with increasing x. In practice this effect can be observed at much lower values of ψ^* than 0.683 because the "droop" of the ψ-ϕ stage characteristic with decreasing flow coefficient reduces the slope of the characteristic.

The effect of this "repeating" phenomenon is to limit the movement of stage operating points from their design points: No matter how many stages in the compressor, the magnitudes of k_ψ, k_ϕ, k_ρ, and k_T never exceed certain fixed values.

The Effect of the Magnitude of ϕ^*. It is important to note that the analysis given above shows that $\phi^*(x)$, the design distribution of flow coefficient, has no effect on the off-design performance of a compressor in the region of the design point. For straight-line ψ-ϕ characteristics, as long as ψ^* is the same, a fixed percentage change in ϕ from ϕ^* will result in the same change in ψ from ψ^* and so the temperature and density distributions will change in the same way through the compressor, no matter what the original choice of $\phi^*(x)$ at design. In

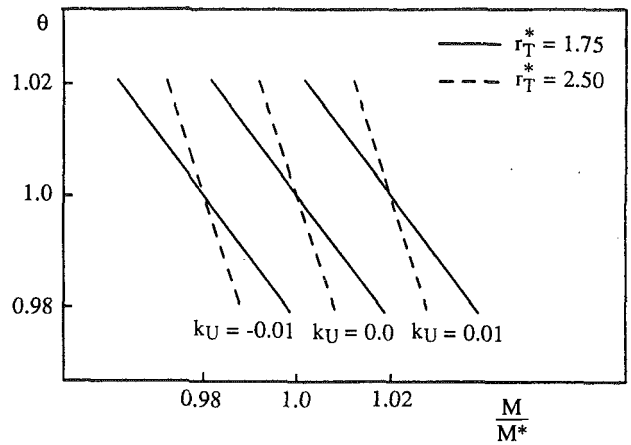

Fig. 4 A plot of overall compressor characteristics for two values of design temperature ratio

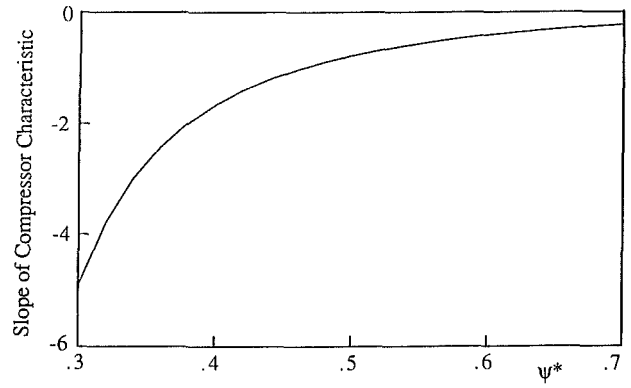

Fig. 5 Plot of characteristic slope against the design level of stage loading

practice of course, the value of ϕ^* may influence our ability to attain a certain value of ψ^*.

The Form of the Overall Characteristics. Here we discuss the form of overall characteristics of the baseline compressor (considering only changes in speed and/or flow for a baseline compressor of constant design stage loading). We use the expression for the overall temperature rise (Eq. (16)), rewriting it as follows for location II at exit from the compressor:

$$\theta = \frac{(T_{II}/T_I)}{(T^*_{II}/T_I)} = 1 + k_{TII} = 1 + \frac{Q}{P}\left[1 - \frac{1}{(r_T^*)^P}\right] \qquad (30)$$

We wish to determine how the form of the overall characteristics (the constant speed lines on a plot of nondimensional exit temperature, θ, against nondimensional flow rate, M/M^*) varies with the two important parameters in Eq. (16)—the design stage loading coefficient (ψ^*) and the design overall temperature ratio (r_T^*) (and therefore pressure ratio).

The Slope of a Constant Speed Characteristic. Differentiation of Eq. (30) at constant speed yields the slope of the nondimensional constant speed line

$$\theta' = \left[\frac{\partial\theta}{\partial(M/M^*)}\right]_U = \left(\frac{\partial\theta}{\partial k_M}\right)_{k_U}$$

$$= \frac{1}{P}\left(1 - \frac{1}{\psi^*}\right)\left[1 - \frac{1}{(r_T^*)^P}\right] \qquad (31)$$

which shows how the slope depends on ψ^* and r_T^*. This result would be modified if efficiency variations were taken into account. The slope of the characteristic is independent of the rotational speed (i.e., all constant speed lines have the same slope) for small perturbations in rotational speed about U^*.

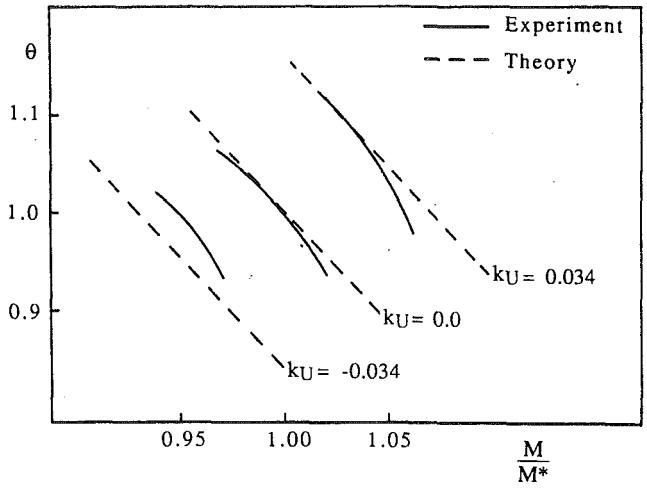

Fig. 6 Comparison between theory and Rolls-Royce Mamba characteristics

Horizontal Spacing of Constant Speed Characteristics. The horizontal spacing of the constant speed lines on the overall characteristic plot is given by

$$M' = \left[\frac{\partial(M/M^*)}{\partial(U/U^*)}\right]_\theta = \left(\frac{\partial k_M}{\partial k_U}\right)_\theta = \left(\frac{1+\psi^*}{1-\psi^*}\right) \qquad (32)$$

which is a function of the stage loading only.

The two parameters that we have considered, the design stage loading (ψ^*) and the design temperature ratio (r_T^*) are linked by the number of stages in the compressor. A given duty may be achieved by a few stages of high loading or many stages of light loading. This relationship is expressed in the following equation:

$$r_T^* = 1 + N\frac{\psi^* U^{*2}}{CpT_I} = 1 + \frac{N}{R} \qquad (33)$$

Figure 4 shows a typical set of "small perturbation" temperature–mass flow characteristics, for $r_T^* = 1.75$ and $\psi^* = 0.45$. They form a set of straight lines of slope determined by r_T^* and ψ^*, and horizontal spacing determined by ψ^*. If the overall temperature rise ratio is increased to 2.5 by keeping ψ^* unchanged and increasing the number of stages, the slope of the lines increases but their spacing is unchanged. The constant speed lines pivot about points with constant spacing as the overall temperature rise (and the number of stages of constant ψ^*) is increased, as shown in the figure. However, if we consider the characteristics of a compressor of a given duty (a fixed design temperature rise), then the slope of the constant speed lines depends on the value of the stage loading coefficient only. Figure 5 shows an example in which $r_T^* = 1.75$; the magnitude of the slope can be seen to decrease rapidly with increasing ψ^*. This figure illustrates a series of possible design choices; each value of ψ^* implies a value for the number of stages (or the speed of rotation) in accordance with Eq. (33).

Equations (31) and (32) were used to predict the shape of the overall characteristics for the Rolls-Royce Mamba compressor. Experimental characteristics together with the prediction are shown in Fig. 6. It can be seen that both the slope and spacing of the predicted characteristics agree reasonably well with the experimental results despite the simplifying assumptions used in the model.

Working Line Considerations. Figure 7 (*a–d*) shows overall characteristics and stage characteristics for the front, middle, and rear stages of a nine-stage compressor ($\psi^* = 0.45$,

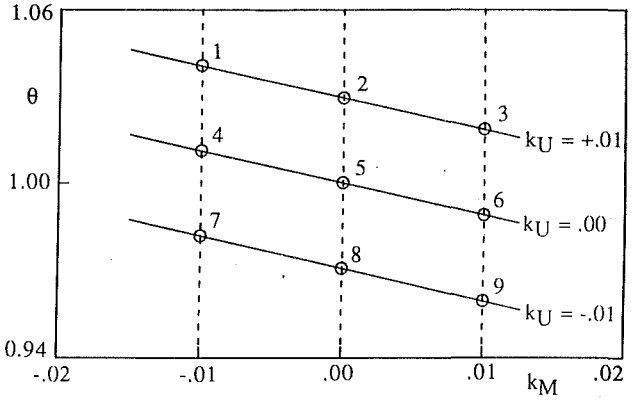

Fig. 7(a) Overall (inlet to exit) compressor characteristics

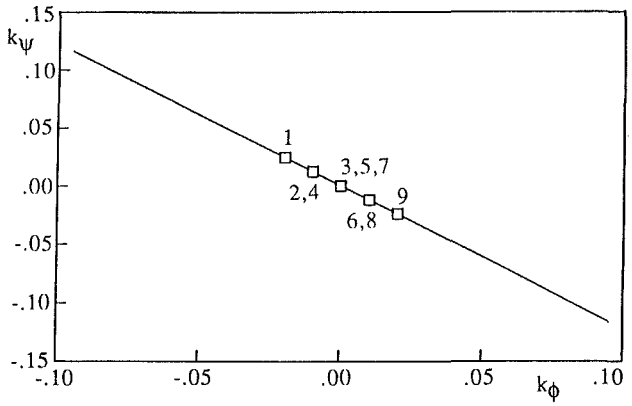

Fig. 7(b) First-stage characteristic

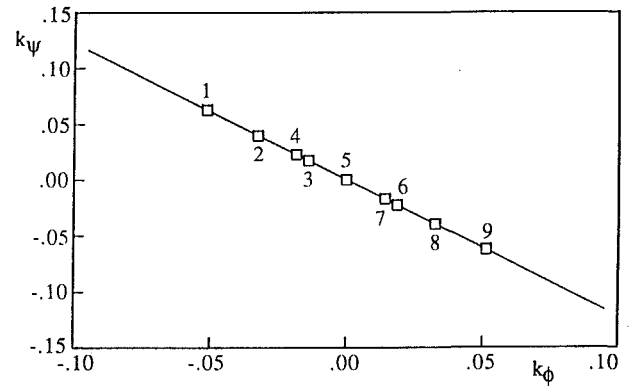

Fig. 7(c) Middle-stage characteristic

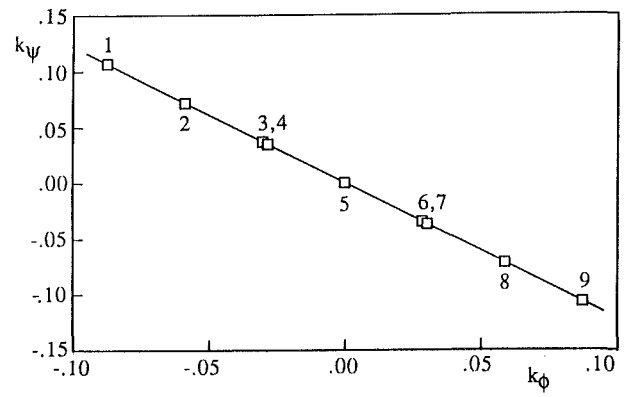

Fig. 7(d) Last-stage characteristic

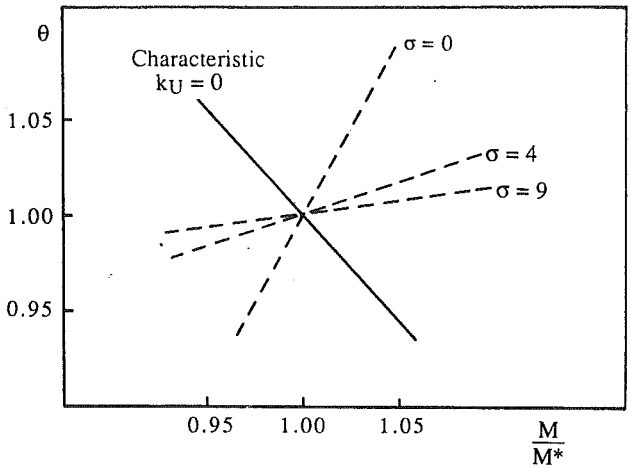

Fig. 8 Lines of no movement from design

Table 3 The effect of changing design temperature ration, for $\psi^* = 0.45$, on slope of "no movement" lines

N	r_T*	Slope
4	1.30	0.314
6	1.45	0.383
8	1.60	0.432

$r_T^* = 1.67$). The locations of nine operating points are shown on each characteristic and indicate how operating conditions on the overall characteristics are related to stage operating points. For the range of operating conditions considered it can be seen that the front stage operating point moves little from its design point, but the rear stage is subjected to a wide range of flow coefficient.

This study of the stage off-design performance may be supplemented by an inverse approach. Can we determine a locus of operating points on the overall characteristics on which a chosen stage does not move from its design operating condition? The solution for k_ϕ (the change in flow coefficient) is

$$k_\phi(x) = k_M - k_U - \frac{nQ}{P}\left[1 - \left(1 + \frac{x}{R}\right)^{-P}\right] \tag{34}$$

For k_ϕ to be zero at an axial location $x = \sigma$, $k_M = k_U/\zeta(\sigma)$, where $\zeta(\sigma)$ is readily determined from Eq. (34) for any given P, Q, R, ψ^*, and n. Using this relationship, a line of "no movement from design" may be drawn, for any axial location $x = \sigma$, on the overall characteristics. An expression for the slope of such a line may be readily derived and is a function of P, ζ, ψ^*, and r_T. For the example quoted earlier ($r_T^* = 1.75$, $\psi^* = 0.45$) Fig. 8 shows such lines of "no movement" for the first, fifth, and tenth stages of a ten-stage compressor ($\sigma = 0$, 4, 9).

Most engine working lines will be quite close to the line shown as $\sigma = 4$, i.e., the middle stages will move relatively little from their design points—a phenomenon well known to compressor engineers. The additional point that we make here is that the slopes of the "no movement" lines for the entry and middle stages are relatively insensitive to the value of stage loading (ψ^*). However, the slopes of these "no movement" lines increase with the overall design temperature ratio (or with the number of stages for a given loading), particularly at low values of temperature ratio. Thus for a compressor with $\psi^* = 0.45$ and N stages, the slope of the line for the middle stage varies with different numbers of stages (and r_T^*) as shown in Table 3.

The Effect of the Distribution of ψ^* Through the Compressor

The discussion of the previous section has shown that the

magnitude of the stage loading coefficient (ψ^*) dominates the off-design performance of a compressor. We proceeded to investigate whether varying ψ^* through the compressor, stage by stage, has a similarly powerful effect on the off-design performance.

In theory the axial flow compressor designer has a degree of flexibility in choosing the distribution of stage loading coefficient through the machine. In practice this flexibility is limited for three reasons. First, to reduce weight and cost, there is usually a requirement to design a compressor with as few stages as possible, which, for a given duty, implies high stage loading. Second, it may be necessary to "off-load" certain stages if constraints on the annulus shape or features of the working line lead to certain stages being particularly susceptible to stall. Thirdly, the rotor speed in a stage is dependent on the radius of rotation of the rotor, which itself may be constrained by the overall engine geometry.

If we remove the assumption that the design stage loading is constant through the compressor, and allow it to be a function of x, Eq. (13) for the temperature perturbation, $k_T(x)$, must be rewritten in a more general form such as:

$$\frac{d(\omega^* k_T)}{dx} = [\psi^*(x) - 1](k_M - k_U) + 2k_U\psi^*(x) - nk_T[\psi^*(x) - 1] \quad (35)$$

where

$$\omega^*(x) = \frac{CpT^*(x)}{U^{*2}} = \frac{CpT_1}{U^{*2}} + \int_0^x \psi^*(x)dx$$

assuming that U^* is constant for convenience. No exact solution to Eq. (35) has been obtained, even for a linear distribution of $\psi^*(x)$ and so in this case the equations were solved numerically. Solutions of Eq. (35) for $k_T(x)$ were calculated for three distributions of $\psi^*(x)$. The first was for a constant value of 0.4 through the machine, the second was for a linear increase from 0.3 at inlet to 0.5 at exit, and the third was for a linear decrease from 0.5 at inlet to 0.3 at exit (note that each distribution has a mean value of 0.4). In each case a small change in speed ($k_U = 0.001$) was used to put the compressors off-design. Surprisingly perhaps, the distributions of $k_T(x)$ were very similar for each of the three cases.

From this and other studies it was concluded that, for small changes from design, whereas the mean stage loading has a significant effect on off-design performance, the distribution of the stage loading coefficient through the compressor has little effect. However, for large changes in compressor operating point from design, the distribution of $\psi^*(x)$ through the compressor will be important in regard to the approach of individual stages toward stall and therefore to overall surge margin.

The Effects of Design Changes on Off-Design Performance

In this section we consider the effects of other changes to the baseline compressor involving changes to the compressor geometry. Such changes we regard as "redesign" changes. We begin by showing how Eqs. (21) and (22) can be used to model a variety of geometric changes to the baseline compressor and how the off-design performance of the redesigned compressor can be calculated. We then show a specific example of how this approach can be used to evaluate the effects of errors in blockage estimates, decided during the design process, on the final compressor performance.

The Modeling of Design Changes to the Compressor. Equation (21), the most general solution for $k_T(x)$, enables us to consider the effects of small changes to the design of the compressor on its off-design performance. Linear distributions were specified for the independent variables k_U, k_M, k_K, and k_A: $k_U = \chi + \delta_x$, $k_M = \epsilon + \iota x$, $k_K = \kappa + \lambda x$, and $k_A = \mu + \nu x$. We therefore have eight parameters as inputs to the problem: χ, δ, ϵ, ι, κ, λ, μ, and ν. Let us divide these parameters into two groups; in the first we put the "bulk" changes in speed and flow rate (χ and ϵ) and in the second we put those parameters that require a redesign of the compressor for them to be implemented (δ, ι, κ, λ, μ, and ν). We include in this second group ι, κ, and λ, which describe changes in air injection/abstraction and stator stagger angle despite the fact that these adjustments are sometimes made to a compressor in service. The changes in a compressor brought about by "bulk" changes in speed and flow (χ and ϵ) we refer to as "off-design" changes whereas changes in the other six parameters we refer to as "redesign" changes.

The design performance of the baseline compressor is denoted by state "B", a redesigned compressor by state "D," and a superscript "$\cdot$" indicates a change off-design. Then the change from B to $B^\cdot$ is caused by non-zero values for χ and/or ϵ only (the first group of parameters) and the change from B to D involves nonzero values for δ, ι, κ, λ, μ, and/or ν only (the second group of parameters). The change from B to $D^\cdot$ involves a nonzero value for at least one of the parameters from each of the two groups.

Because our analysis is based on a linearized model, the effects of moving from D to $D^\cdot$ can be expressed as the effects of moving from B to $D^\cdot$ minus the effects of moving from B to D (provided that the final state $D^\cdot$ is itself a small perturbation from B), i.e., $d_{(D\to D^\cdot)} = d_{(B\to D^\cdot)} - d_{(B-D)}$. We can therefore use Eq. (21) to investigate how changes to the design of a compressor can improve its off-design performance. By way of illustration we consider the effects of varying mean radius, using the expression for blade speed: $k_U = \chi + \delta x$, and a "bulk" change in flow: $k_M = \epsilon$. We consider a nonzero value for χ to be an off-design change as it could be facilitated by a simple change in rotational speed, but we consider a nonzero value for δ as being a redesign change as it clearly implies a different compressor geometry (a positive value for δ describes the mean radius increasing with axial distance through the compressor).

These effects are illustrated on an overall performance plot of k_{TII} against k_M, in Fig. 9.

1 Consider first the design performance of the baseline compressor for which $k_{TII} = k_U = k_M = 0$. This is shown as point B on Fig. 9.

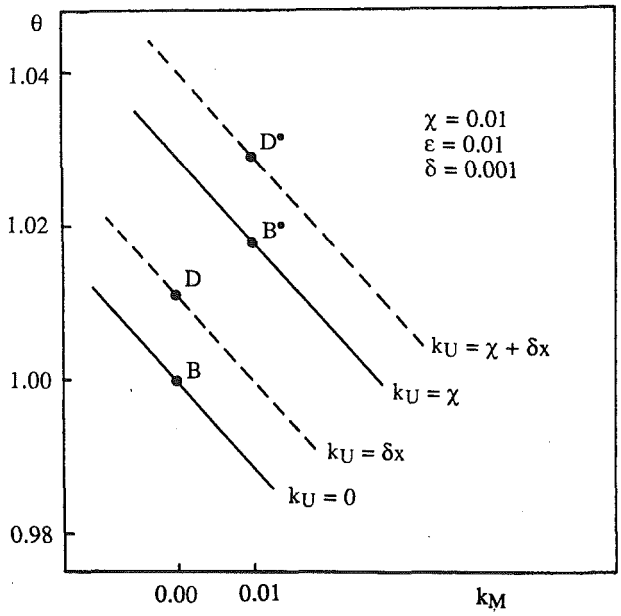

Fig. 9 Redesign changes to the baseline compressor

2 We now move the basic compressor off-design, from B to B^*, by specifying $k_U = \chi = 0.01$ and $k_M = \epsilon = 0.01$.
3 Consider next redesigning compressor B to have an increasing mean radius with axial distance. We substitute $k_U = \delta x$ (where $\delta = 0.001$) into Eq. (22) and calculate $(k_{TII})_D$. Compressor D operates at point D on Fig. 9.
4 We now move compressor D off-design by specifying $k_U = \chi + \delta x$ and $k_M = \epsilon$. We arrive at point D^*.

We could specify the magnitude and sign of δ in accordance with a particular design objective, e.g., to improve the position of an operating point from B^* to D^* under a particular off-design condition ($k_U = \chi$ and $k_M = \epsilon$). Similar changes in both design and off-design performance may be initiated by changes in k_M, k_K, and/or k_A instead of k_U.

Note that there is a multitude of ways of selecting values for the input parameters to ensure that there is any desired change, or no change, in compressor exit conditions from the design point. If we are free to select only one of the parameters k_U, k_M, k_K, k_A (and therefore two of the parameters χ, δ, ϵ, ι, κ, λ, μ, ν), then we are free to set the constants S and W in Eq. (21) to any desired value. We can therefore influence the distributions of k_ψ, k_ϕ, k_ρ, and k_T. To take a simple example, consider "bulk" changes in speed and flow (χ and ϵ) imposed on a compressor, but with a change in variable stator setting for all stages in the machine being possible (κ = the same change for each stage). We assume all other input parameters to be zero (and therefore $W = 0$). If we choose the stator stagger setting according to

$$\kappa = \chi \frac{(1+\psi^*)}{(1-\psi^*)} - \epsilon$$

then S will be zero and therefore $k_T(x) = 0$ for all x. With this strategy for varying κ, the compressor exit pressure could be held constant despite changes in speed (χ) and flow rate (ϵ) (over a limited range).

To take another example, suppose that it is necessary to change the distribution of mean radius with axial distance through the compressor. This is reflected in a change in mean blade speed and so is described by $k_U = \chi + \delta x$. How would we need to change the annulus area distribution to maintain the original pressure ratio at the design point? To set S and W to zero in Eq. (21) we must choose

$$k_A = \mu + \nu x$$

where

$$\mu = -\chi \frac{(1+\psi^*)}{(1-\psi^*)} \quad \nu = -\delta \frac{(1+\psi^*)}{(1-\psi^*)}$$

With this change in area distribution $S = W = 0$ and so k_{TII}, the change in compressor exit temperature, is zero; therefore our objective is met.

The Effects of Errors in Blockage Estimates. The purposes of including area variation in the more general solution were twofold: first, to enable the effects of changing the annulus area during the design process to be studied (as in the example above), and second, to investigate the consequences of errors in annulus blockage estimates or changes in blockage between design and off-design conditions. By "blockage" we mean here the annulus area seemingly lost due to the displacement thicknesses of the endwall boundary layers.

Thus we first postulate a compressor, having been designed with an incorrect estimate of blockage, somehow running with this incorrect design level of blockage; in this condition all parameters are at their design values, denoted by an asterisk. We now imagine the blockage to change to its correct (actual) value and as a result the other parameters change to what we have previously referred to as "off-design" values.

The calculations outlined below were made for a ten-stage compressor with the following design parameters: $\psi^* = 0.4$;

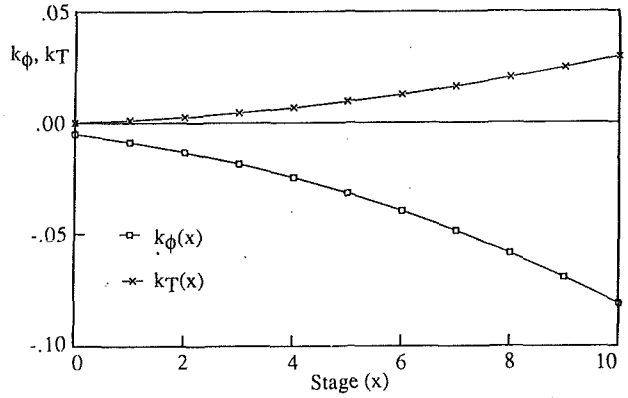

Fig. 10(a) Effect of blockage errors for a compressor on a test bed

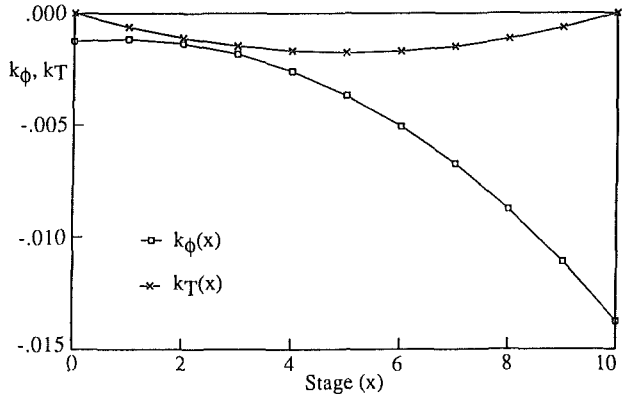

Fig. 10(b) Effect of blockage errors for a compressor in an engine (note change of scale)

$T_1 = 288$ K; $U^* = 300$ m/s; $\eta_p = 0.9$. Typical blockage estimates for such a compressor might be 2 percent of annulus area at inlet, growing linearly to 7 percent at compressor exit. Let us assume that this compressor was designed with the values above but that the real levels of blockage encountered are only three-quarters of these values. The area perturbation is therefore

$$k_A = 0.005 + 0.00125x \quad (\mu = 0.005,\ \nu = 0.00125)$$

The conditions under which the compressor operates will have an important effect on its response to this change in annulus area. If we consider the compressor to be running on a test bed where rotational speed and mass flow rate are held constant at their design values as the blockage is supposed to change, then $k_U = k_M = 0$. Figure 10(a) shows the solutions for k_T (the temperature change) and k_ϕ (the flow coefficient change) plotted against x (i.e., the conditions that actually occur). It can be seen that the effect of overestimating the blockage in this case has led to the exit temperature being 3.0 percent greater that its intended design value and the exit flow coefficient being 8.1 percent below its intended design value. These are quite sizable changes from the intended design and, considering the reduction in flow coefficient in the last stage, one could expect the compressor to have a surge margin considerably less than it was expected to achieve.

Consider now the compressor operating in a simple aero-engine with choked turbine and propelling nozzles, at a constant ratio of turbine entry temperature to compressor entry temperature (an approximately fixed fuel throttle setting). As the blockage is hypothetically reduced from its incorrect design level to its correct level, the turbine temperature and pressure ratios and hence the compressor temperature and pressure ratios will remain unchanged. As the blockage is reduced, the engine speed will "automatically" fall slightly to maintain the

compressor pressure ratio. The nondimensional flow function at compressor inlet is unchanged and, as the compressor inlet pressure and temperature remain constant, the inlet mass-flow must remain the same; we therefore set $k_M = 0$. In this case, then, to obtain the solution we simply choose a value of k_U (a change in speed) such that the temperature at compressor exit equals its design value (i.e., $k_T(10) = 0$). Figure 10(b) shows the solutions for k_T and k_ϕ plotted against x. In this case the maximum change in flow coefficient from design is only -1.4 percent and the small change in engine speed is -0.4 percent. These are small values and are unlikely to cause serious problems to the compressor's off-design operation. As a guideline, the change in flow coefficient is similar to the magnitude of the error in blockage, in percentage points. This analysis suggests that accurate estimation of blockage for the design of aero-engine compressors is less critical than has been previously thought.

Conclusions

1 An analysis of the off-design performance of multistage axial-flow compressors, based on an analytical solution, has been presented. This analytical solution is found to agree well with previous numerical solutions and provides more insight and understanding than current computer methods.

2 It is shown that, by changing the slopes of stage characteristics, variable stagger stator vanes have a major influence on the way that stage operating points move from their design points. The results of Goede and Casey (1988) have been obtained with an analytic solution.

3 It is shown that the mean design value of stage loading coefficient, ψ^*, has a dominant influence on the off-design performance. It controls the spacing of constant-speed overall characteristics and, together with the design temperature ratio, determines the slope of overall characteristics. The distribution of stage loading through the machine, $\psi^*(x)$, was seen to have little effect. In the region of the design point, the magnitude and distribution of flow coefficient at design, ϕ^*, is seen to have little or no effect on compressor off-design performance.

4 For large values of ψ^* (and for compressors approaching stall), the stage operating points approach a "repeating stage" condition. At this condition, all stages operate at the same fixed percentages of design flow coefficient and loading.

5 The slope of the engine working line, overlaid on overall compressor characteristics, has a strong influence on the distribution of off-design movement through the compressor. For a typical working line it is shown that the middle stages of a compressor move little from their design operating points.

6 A method is presented for analyzing the effects of design changes on an existing compressor. It is shown how judicious redesign can, within the limitations of small perturbations, counteract potential problems in off-design performance.

7 In the context of compressors for gas turbine engines, small errors in blockage estimates made during the design process do not have serious consequences for the installed compressor. This is due to the "self-adjusting" nature of the engine working line.

Acknowledgments

The authors would like to thank Dr. M. V. Casey for his encouragement and for the data that he supplied for comparison purposes. We would also like to thank Professor N. A. Cumpsty for his suggestions, and Dr. T. P. Hynes for the use of his mean-line performance prediction code. We would like to thank Rolls-Royce plc for permission to publish the Mamba compressor characteristics and for the financial support of one of the authors.

References

Casey, M. V., 1992, Private Communication.

Goede, E., and Casey, M. V., 1988, "Stage Matching in Multistage Industrial Axial Compressors With Variable Stagger Stator Vanes," *VDI Berichte*, No. 706, pp. 229–243.

Horlock, J. H., 1958, "A Rapid Method for Calculating the "Off-Design" Performance of Compressors and Turbines," *The Aeronautical Quarterly*, Vol. IX, Nov.

Howell, A. R., 1945, "Fluid Dynamics of Axial Compressors," *Proc. Instn. Mech. Engrs.*, London, p. 153.

Howell, A. R., and Calvert, W. J., 1978, "A New Stage Stacking Technique for Axial-Flow Compressor Performance Prediction," ASME *Journal of Engineering for Power*, Vol. 100, pp. 698–703.

Hynes, T. P., 1992, Private Communication.

Mellor, G. L., Jr., 1957, "The Aerodynamic Performance of Axial Compressor Cascades With Application to Machine Design," Sc.D. Thesis, Rep. No. 38, Massachusetts Institute of Technology, Feb.

Robbins, W. H., and Dugan, J. F., 1956, "Prediction of Off-Design Performance of Multistage Compressors," in: *Aerodynamic Design of Axial-Flow Compressors*, NASA SP-36, pp. 297–310.

Stone, A., 1958, "Effects of Stage Characteristics and Matching on Axial-Flow-Compressor Performance," *Transactions of the ASME*, Aug., pp. 1273–1293.

Wright, P. I., and Miller, D. C., 1991, "An Improved Compressor Performance Prediction Model," Paper No. C423/028, European Conference on "Turbomachinery: Latest Developments in a Changing Scene," London, Mar. 19–20.

Viscous Analysis of Three-Dimensional Rotor Flow Using a Multigrid Method

A. Arnone
Department of Energy Engineering,
University of Florence,
Florence, Italy

A three-dimensional code for rotating blade-row flow analysis has been developed. The space discretization uses a cell-centered scheme with eigenvalue scaling for the artificial dissipation. The computational efficiency of a four-stage Runge–Kutta scheme is enhanced by using variable coefficients, implicit residual smoothing, and a full-multigrid method. An application is presented for the NASA rotor 67 transonic fan. Due to the blade stagger and twist, a zonal, nonperiodic H-type grid is used to minimize the mesh skewness. The calculation is validated by comparing it with experiments in the range from the maximum flow rate to a near-stall condition. A detailed study of the flow structure near peak efficiency and near stall is presented by means of pressure distribution and particle traces inside boundary layers.

Introduction

In the last decade Fluid Dynamics has undergone impressive evolution both in the understanding and in the simulation of flow features. In this process, Computational Fluid Dynamics (CFD) is playing a more and more important role. Modern turbomachinery operates under very complex three-dimensional flow conditions, and further improvement requires detailed knowledge of the flow structure. Particularly, the need to estimate off-design conditions, secondary flows, and heat transfer forces us to look at viscous models. The real flow inside a turbomachine is unsteady and strongly influenced by rotor–stator interactions, wake, and clearance effects. Even if some important steps have been made in the time-accurate and time-averaged simulation of entire stages (e.g., Rai, 1987; Rao and Delaney, 1990; Adamczyk et al., 1990), a steady blade-row analysis should still be considered a basic tool for modern design. The works of Subramanian and Bozzola (1987), Chima and Yokota (1988), Choi and Knight (1988), Davis et al. (1988), Hah (1989), Nakahashi et al. (1989), Weber and Delaney (1991), and Dawes (1992) are some important steps in the prediction of three-dimensional viscous cascade flows.

In 1988, the University of Florence started a joint project with NASA (ICASE and ICOMP) on viscous cascade flow simulation. During this research project, the TRAF2D and TRAF3D codes (TRAnsonic Flow 2D/3D) were developed (Arnone and Swanson, 1988; Arnone et al., 1991, 1992). Those codes are capable of solving viscous cascade flows using **H**-type or **C**-type grids and of predicting heat transfer effects. In the present work, the procedure was extended to the case of rotating blade passages. Particular attention has been dedicated to important aspects such as minimization of the grid skewness, accuracy, and computational cost.

Contributed by the International Gas Turbine Institute and presented at the 38th International Gas Turbine and Aeroengine Congress and Exposition, Cincinnati, Ohio, May 24–27, 1993. Manuscript received at ASME Headquarters February 12, 1993. Paper No. 93-GT-19. Associate Technical Editor: H. Lukas.

As for accuracy, nonperiodic **C**- or **H**-type grids are stacked in three dimensions. The removal of periodicity allows the grid to be only slightly distorted even for cascades having a large camber or a high stagger angle and twist. This allows us to pick up details of the throat flow with a reasonable number of grid points. A very low level of artificial dissipation is guaranteed by eigenvalue scaling, which is a three-dimensional extension of the one proposed by Swanson and Turkel (1987), and Martinelli and Jameson (1988).

The two-layer eddy-viscosity model of Baldwin and Lomax (1978) is used for the turbulence closure.

As for efficiency, the Reynolds-averaged Navier–Stokes equations are solved using a Runge–Kutta scheme in conjunction with accelerating techniques. Variable-coefficient implicit residual smoothing, as well as the Full-Approximation-Storage multigrid scheme of Brandt (1979) and Jameson (1983) are used in the TRAF3D code. Those accelerating strategies are implemented in conjunction with grid refinement to get a Full Multigrid Method.

The code is validated by studying the NASA rotor 67 transonic fan. This fan has important viscous and three-dimensional effects and experiments are available in a wide range of flow rates from the maximum one to near stall. Moreover, this geometry was recently proposed as an AGARD test case for code validation (Fottner, 1990) and calculations from several authors are available for discussion.

By using the accelerating strategies, accurate, viscous three-dimensional solutions can be obtained in about half an hour on a modern supercomputer such as a Cray Y-MP.

Governing Equations

Let ρ, u, v, w, p, T, E, and H denote, respectively, density, the absolute velocity components in the x, y, and z Cartesian directions, pressure, temperature, specific total energy, and specific total enthalpy. The three-dimensional, unsteady,

Reynolds-averaged Navier–Stokes equations can be written for a rotating blade passage in conservative form in a curvilinear coordinate system ξ, η, ζ as

$$\frac{\partial (J^{-1}Q)}{\partial t}+\frac{\partial F}{\partial \xi}+\frac{\partial G}{\partial \eta}+\frac{\partial H}{\partial \zeta}=\frac{\partial F_v}{\partial \xi}+\frac{\partial G_v}{\partial \eta}+\frac{\partial H_v}{\partial \zeta}+I \tag{1}$$

where the Cartesian system x, y, z is rotating with angular velocity Ω around the x axis,

$$Q=\begin{Bmatrix}\rho\\ \rho u\\ \rho v\\ \rho w\\ \rho E\end{Bmatrix},\quad F=J^{-1}\begin{Bmatrix}\rho U\\ \rho uU+\xi_x p\\ \rho vU+\xi_y p\\ \rho wU+\xi_z p\\ \rho HU-\xi_t p\end{Bmatrix},\quad G=J^{-1}\begin{Bmatrix}\rho V\\ \rho uV+\eta_x p\\ \rho vV+\eta_y p\\ \rho wV+\eta_z p\\ \rho HV-\eta_t p\end{Bmatrix} \tag{2a}$$

$$H=J^{-1}\begin{Bmatrix}\rho W\\ \rho uW+\zeta_x p\\ \rho vW+\zeta_y p\\ \rho wW+\zeta_z p\\ \rho HW-\zeta_t p\end{Bmatrix},\quad I=\begin{Bmatrix}0\\ 0\\ \rho\Omega w\\ -\rho\Omega v\\ 0\end{Bmatrix} \tag{2b}$$

The contravariant velocity components of Eqs. (2) are written as

$$\begin{aligned}U&=\xi_t+\xi_x u+\xi_y v+\xi_z w\\ V&=\eta_t+\eta_x u+\eta_y v+\eta_z w\\ W&=\zeta_t+\zeta_x u+\zeta_y v+\zeta_z w\end{aligned} \tag{3}$$

and the transformation metrics are defined by

$$\begin{aligned}\xi_x&=J(y_\eta z_\zeta-y_\zeta z_\eta),\quad \xi_y=J(z_\eta x_\zeta-z_\zeta x_\eta)\\ \xi_z&=J(x_\eta y_\zeta-x_\zeta y_\eta),\quad \eta_x=J(y_\zeta z_\xi-y_\xi z_\zeta)\\ \eta_y&=J(z_\zeta x_\xi-z_\xi x_\zeta),\quad \eta_x=J(x_\zeta y_\xi-x_\xi y_\zeta)\\ \zeta_x&=J(y_\xi z_\eta-z_\xi y_\eta),\quad \zeta_y=J(z_\xi x_\eta-x_\xi z_\eta)\\ \zeta_z&=J(x_\xi y_\eta-y_\xi x_\eta),\quad \xi_t=-x_t\xi_x-y_t\xi_y-z_t\xi_z\\ \eta_t&=-x_t\eta_x-y_t\eta_y-z_t\eta_z,\quad \zeta_t=-x_t\zeta_x-y_t\zeta_y-z_t\zeta_z\\ x_t&=0,\quad y_t=-\Omega z,\quad z_t=\Omega y\end{aligned} \tag{4}$$

where the Jacobian of the transformation J is

$$J^{-1}=x_\xi y_\eta z_\zeta+x_\eta y_\zeta z_\xi+x_\zeta y_\xi z_\eta-x_\xi y_\zeta z_\eta-x_\eta y_\xi z_\zeta-x_\zeta y_\eta z_\xi \tag{5}$$

The viscous flux terms are assembled in the form

$$F_v=J^{-1}\begin{Bmatrix}0\\ \xi_x\tau_{xx}+\xi_y\tau_{xy}+\xi_z\tau_{xz}\\ \xi_x\tau_{yx}+\xi_y\tau_{yy}+\xi_z\tau_{yz}\\ \xi_x\tau_{zx}+\xi_y\tau_{zy}+\xi_z\tau_{zz}\\ \xi_x\beta_x+\xi_y\beta_y+\xi_z\beta_z\end{Bmatrix}$$

$$G_v=J^{-1}\begin{Bmatrix}0\\ \eta_x\tau_{xx}+\eta_y\tau_{xy}+\eta_z\tau_{xz}\\ \eta_x\tau_{yx}+\eta_y\tau_{yy}+\eta_z\tau_{yz}\\ \eta_x\tau_{zx}+\eta_y\tau_{zy}+\eta_z\tau_{zz}\\ \eta_x\beta_x+\eta_y\beta_y+\eta_z\beta_z\end{Bmatrix}$$

$$H_v=J^{-1}\begin{Bmatrix}0\\ \zeta_x\tau_{xx}+\zeta_y\tau_{xy}+\zeta_z\tau_{xz}\\ \zeta_x\tau_{yx}+\zeta_y\tau_{yy}+\zeta_z\tau_{yz}\\ \zeta_x\tau_{zx}+\zeta_y\tau_{zy}+\zeta_z\tau_{zz}\\ \zeta_x\beta_x+\zeta_y\beta_y+\zeta_z\beta_z\end{Bmatrix} \tag{6}$$

where

$$\begin{aligned}\tau_{xx}&=2\mu u_x+\lambda(u_x+v_y+w_z)\\ \tau_{yy}&=2\mu v_y+\lambda(u_x+v_y+w_z)\\ \tau_{zz}&=2\mu w_z+\lambda(u_x+v_y+w_z)\\ \tau_{xy}&=\tau_{yx}=\mu(u_y+v_x)\\ \tau_{xz}&=\tau_{zx}=\mu(u_z+w_x)\\ \tau_{yz}&=\tau_{zy}=\mu(v_z+w_y)\\ \beta_x&=u\tau_{xx}+v\tau_{xy}+w\tau_{xz}+kT_x\\ \beta_y&=u\tau_{yx}+v\tau_{yy}+w\tau_{yz}+kT_y\\ \beta_z&=u\tau_{zx}+v\tau_{zy}+w\tau_{zz}+kT_z\end{aligned} \tag{7}$$

and the Cartesian derivatives of Eq. (7) are expressed in terms of ξ, η, and ζ derivatives using the chain rule, i.e.,

$$u_x=\xi_x u_\xi+\eta_x u_\eta+\zeta_x u_\zeta \tag{8}$$

The pressure is obtained from the equation of state,

$$p=\rho RT \tag{9}$$

According to the Stokes hypothesis, λ is taken to be $-2\mu/3$ and a power law is used to determine the molecular coefficient of viscosity μ as function of temperature. The eddy-viscosity hypothesis is used to account for the effect of turbulence. The molecular viscosity μ and the molecular thermal conductivity k are replaced with

$$\mu=\mu_l+\mu_t \tag{10}$$

$$k=c_p\left[\left(\frac{\mu}{\mathrm{Pr}}\right)_l+\left(\frac{\mu}{\mathrm{Pr}}\right)_t\right] \tag{11}$$

where c_p is the specific heat at constant pressure, Pr is the Prandtl number, and the subscripts l and t refer to laminar and turbulent, respectively. The turbulent quantities μ_t and Pr_t are computed using the two-layer mixing length model of Baldwin and Lomax (1978). The contribution of the eddy viscosity is computed separately in the blade-to-blade direction η and in the spanwise direction ζ. The inverse of the square of the wall distances d is then used to compute the resulting eddy viscosity,

$$f=\frac{\dfrac{1}{d_\eta^2}}{\left(\dfrac{1}{d_\eta^2}+\dfrac{1}{d_\zeta^2}\right)} \tag{12}$$

$$\mu_t=f(\mu_t)_\eta+(1-f)(\mu_t)_\zeta \tag{13}$$

The transitional criteria of Baldwin and Lomax are adopted on the airfoil surface while on the end walls, the shear layer is assumed to be fully turbulent from the inlet boundary.

Spatial Discretization

Traditionally, using a finite-volume approach, the governing equations are discretized in space starting from an integral formulation and without any intermediate mapping (e.g., Jameson et al., 1981; Ni, 1981; Holmes and Tong, 1985). The transformation metrics of Eq. (4) can then be associated with the projections of the face areas as the contravariant components of Eq. (3) can be related to the normal components of the relative velocity. In the present work, due to the large use of eigenvalues and curvilinear quantities, we found it more convenient to map the Cartesian space (x, y, z) in a generalized curvilinear one (ξ, η, ζ). In the curvilinear system, the equation of motion, Eq. (1), can be easily rewritten in integral form by means of Green's theorem and the metric terms are handled following the standard finite-volume formulation. The computational domain is divided into hexahedrons and the transformation metrics are evaluated so that the projected areas of

the cell faces are given by the ratio of the appropriate metric derivatives to the Jacobian ones, i.e., ξ_x/J is the projection onto the x axis of a cell face at a fixed ξ location. A cell-centered scheme is used to store the flow variables. On each cell face the convective and diffusive fluxes are calculated after computing the necessary flow quantities at the face center. Those quantities are obtained by a simple averaging of adjacent cell-center values of the dependent variables.

Boundary Conditions

In cascade calculations we have four different types of boundaries: inlet, outlet, solid walls, and periodicity. At the inlet, the presence of boundary layers, on hub and tip end walls, is accounted for by giving a total pressure and a total temperature profile whose distribution simulates the experimental one. According to the theory of characteristics, the flow angles, total pressure, total temperature, and isentropic relations are used at the subsonic-axial inlet, while the outgoing Riemann invariant is taken from the interior. At the subsonic-axial outlet, the average value of the static pressure at the hub is prescribed and the density and components of velocity are extrapolated together with the circumferential distribution of pressure. The radial equilibrium equation is used to determine the spanwise distribution of the static pressure. On the solid walls, the pressure is extrapolated from the interior points, and the no-slip condition and the temperature condition are used to compute density and total energy. For the calculations presented in this paper, all the walls have been assumed to be at a constant temperature equal to the total inlet one.

Cell-centered schemes are generally implemented using phantom cells to handle the boundaries. The periodicity from blade passage to blade passage is, therefore, easily superimposed by setting periodic phantom cell values. On the boundaries where the grid is not periodic, the phantom cells overlap the real ones. Linear interpolations are then used to compute the value of the dependent variables in phantom cells. Even if this approach does not guarantee conservation of mass, momentum, and energy, no accuracy losses have been experienced unless strong flow gradients occur along nonperiodic grid boundaries with strong differences in mesh size. In the present work, the number of fine cells to be used for interpolation on a coarse cell never exceeded three.

The clearance region is handled by imposing periodicity conditions across the airfoil without any modelization of the blade cross section.

Artificial Dissipation

In viscous calculations, dissipating properties are present due to diffusive terms. Away from the shear layer regions, the physical diffusion is generally not sufficient to prevent the odd-even point decoupling of centered schemes. Thus, to maintain stability and to prevent oscillations near shocks or stagnation points, artificial dissipation terms are also included in the viscous calculations. Equation (1) is written in semidiscrete form as

$$\frac{\partial Q}{\partial t} + C(Q) - D(Q) = 0 \tag{14}$$

where the discrete operator C accounts for the physical convective and diffusive terms, while D is the operator for the artificial dissipation. The artificial dissipation model used in this paper is basically the one originally introduced by Jameson et al. (1981). In order to minimize the amount of artificial diffusion inside the shear layer, the eigenvalue scaling of Martinelli and Jameson (1988), and Swanson and Turkel (1987) have been used to weight these terms. The quantity $D(Q)$ in Eq. (14) is defined as

$$D(Q) = (D_\xi^2 - D_\xi^4 + D_\eta^2 - D_\eta^4 + D_\zeta^2 - D_\zeta^4)Q \tag{15}$$

where, for example, in the ξ curvilinear coordinates we have,

$$D_\xi^2 Q = \nabla_\xi(\Lambda_{i+1/2,j,k}\epsilon^{(2)}_{i+1/2,j,k})\Delta_\xi Q_{i,j,k}$$

$$D_\xi^4 Q = \nabla_\xi(\Lambda_{i+1/2,j,k}\epsilon^{(4)}_{i+1/2,j,k})\Delta_\xi \nabla_\xi \Delta_\xi Q_{i,j,k} \tag{16}$$

i, j, k are indices associated with the ξ, η, ζ directions and ∇_ξ, Δ_ξ are forward and backward difference operators in the ξ direction. The variable scaling factor Λ is defined for the three-dimensional case as

$$\Lambda_{i+1/2,j,k} = \frac{1}{2}\left[(\Lambda_\xi)_{i,j,k} + (\Lambda_\xi)_{i+1,j,k}\right] \tag{17}$$

where

$$\Lambda_\xi = \Phi_\xi \lambda_\xi \tag{18}$$

The definition of the coefficient Φ has been extended to the three-dimensional case as follows:

$$\Phi_\xi = 1 + \left(\frac{\lambda_\eta}{\lambda_\xi}\right)^\sigma + \left(\frac{\lambda_\zeta}{\lambda_\xi}\right)^\sigma$$

$$\Phi_\eta = 1 + \left(\frac{\lambda_\xi}{\lambda_\eta}\right)^\sigma + \left(\frac{\lambda_\zeta}{\lambda_\eta}\right)^\sigma$$

$$\Phi_\zeta = 1 + \left(\frac{\lambda_\xi}{\lambda_\zeta}\right)^\sigma + \left(\frac{\lambda_\eta}{\lambda_\zeta}\right)^\sigma \tag{19}$$

where λ_ξ, λ_η, and λ_ζ are the scaled spectral radii of the flux Jacobian matrices for the convective terms,

$$\lambda_\xi = |U| + a\sqrt{\xi_x^2 + \xi_y^2 + \xi_z^2}$$

$$\lambda_\eta = |V| + a\sqrt{\eta_x^2 + \eta_y^2 + \eta_z^2}$$

$$\lambda_\zeta = |W| + a\sqrt{\zeta_x^2 + \zeta_y^2 + \zeta_z^2} \tag{20}$$

and a is the speed of sound. Note that the effect of grid rotation is accounted for in Eq. (20) through the definition of the contravariant components of velocities of Eq. (3). The exponent σ is generally defined by $0 < \sigma \leq 1$, and for two-dimensional applications, a value of 2/3 gives satisfactory results. In three-dimensional cascade flow calculations, we generally have highly stretched meshes in two directions near corners. We found that $\sigma = 0.4$ introduces enough scaling without compromising the robustness. The coefficients $\epsilon^{(2)}$ and $\epsilon^{(4)}$ use the pressure as a sensor for shocks and stagnation points, and are defined as follows:

$$\epsilon^{(2)}_{i+1/2,j,k} = k^{(2)}\mathrm{MAX}(\nu_{i-1,j,k}, \nu_{i,j,k}, \nu_{i+1,j,k}, \nu_{i+2,j,k}) \tag{21}$$

$$\nu_{i,j,k} = \left|\frac{p_{i-1,j,k} - 2p_{i,j,k} + p_{i+1,j,k}}{p_{i-1,j,k} + 2p_{i,j,k} + i+1,j,k}\right| \tag{22}$$

$$\epsilon^{(4)}_{i+1/2,j,k} = \mathrm{MAX}[0,\ (K^{(4)} - \epsilon^{(2)}_{i+1/2,j,k})] \tag{23}$$

where typical values for the constants $K^{(2)}$ and $K^{(4)}$ are 1/2 and 1/64, respectively. For the remaining directions η and ζ, the contribution of dissipation is defined in a similar way. The computation of the dissipating terms is carried out in each coordinate direction as the difference between first and third difference operators. Those operators are set to zero on solid walls in order to reduce the global error on the conservation property and to prevent the presence of undamped modes (Pulliam, 1986; Swanson and Turkel, 1988).

It is important to anticipate now that from the definition of residual of Eq. (25), variable scaling, and time steps of Eqs. (26), (27), (28), the artificial dissipation is scaled with a factor proportional to the ratio between the global time step and the inviscid time step. Close to solid walls, the grid volume is very small and viscous time step limitation is dominant. The ratio of the time step over the inviscid one becomes very small and most of the artificial dissipation is removed.

Time-Stepping Scheme

The system of the differential Eq. (14) is advanced in time using an explicit four-stage Runge–Kutta scheme until the steady-state solution is reached. A hybrid scheme is implemented, where, for economy, the viscous terms are evaluated only at the first stage and then frozen for the remaining stages. If n is the index associated with time we will write it in the form

$$
\begin{aligned}
Q^{(0)} &= Q^n \\
Q^{(1)} &= Q^{(0)} + \alpha_1 R(Q^{(0)}) \\
Q^{(2)} &= Q^{(0)} + \alpha_2 R(Q^{(1)}) \\
Q^{(3)} &= Q^{(0)} + \alpha_3 R(Q^{(2)}) \\
Q^{(4)} &= Q^{(0)} + \alpha_4 R(Q^{(3)}) \\
Q^{n+1} &= Q^{(4)}
\end{aligned}
$$

$$
\alpha_1 = \frac{1}{4}, \quad \alpha_2 = \frac{1}{3}, \quad \alpha_3 = \frac{1}{2}, \quad \alpha_4 = 1 \tag{24}
$$

where the residual $R(Q)$ is defined by,

$$
R(Q) = \Delta t J[C(Q) - D(Q)] \tag{25}
$$

Good, high-frequency damping properties, important for the multigrid process, have been obtained by performing two evaluations of the artificial dissipating terms, at the first and second stages. It is worthwhile to notice that, in the Runge–Kutta time-stepping schemes, the steady-state solution is independent of the time step; therefore, this stepping is particularly amenable to convergence acceleration techniques.

Acceleration Techniques

In order to reduce the computational cost, four techniques are employed to speed up convergence to the steady-state solution. These techniques: (1) local time-stepping; (2) residual smoothing; (3) multigrid; (4) grid refinement; are separately described in the following.

Local Time-Stepping. For steady-state calculations with a time-marching approach, a faster expulsion of disturbances can be achieved by locally using the maximum available time step. In the present work the local time step limit Δt is computed accounting for both the convective (Δt_c) and diffusive (Δt_d) contributions as follows:

$$
\Delta t = c_0 \left(\frac{\Delta t_c \Delta t_d}{\Delta t_c + \Delta t_d} \right) \tag{26}
$$

where c_0 is a constant usually taken to be the Courant–Friedrichs–Lewy (CFL) number. Specifically, for the inviscid and viscous time step we used,

$$
\Delta t_c = \frac{1}{\lambda_\xi + \lambda_\eta + \lambda_\zeta} \tag{27}
$$

$$
\Delta t_d = \frac{1}{K_t \dfrac{\gamma \mu}{\rho \mathrm{Pr}} J^2 (S_\eta^2 S_\zeta^2 + S_\xi^2 S_\zeta^2 + S_\xi^2 S_\eta^2)} \tag{28}
$$

where γ is the specific heat ratio and

$$
S_\xi^2 = x_\xi^2 + y_\xi^2 + z_\xi^2, \quad S_\eta^2 = x_\eta^2 + y_\eta^2 + z_\eta^2, \quad S_\zeta^2 = x_\zeta^2 + y_\zeta^2 + z_\zeta^2, \tag{29}
$$

K_t being a constant whose value has been set equal to 2.5 based on numerical experiments.

Residual Smoothing. An implicit smoothing of residuals is used to extend the stability limit and the robustness of the basic scheme. This technique was first introduced by Lerat in 1979 in conjunction with Lax–Wendroff type schemes. Later, in 1983, Jameson implemented it on the Runge–Kutta stepping scheme. In three dimensions we carried out the residual smoothing in the form

$$
(1 - \beta_\xi \nabla_\xi \Delta_\xi)(1 - \beta_\eta \nabla_\eta \Delta_\eta)(1 - \beta_\zeta \nabla_\zeta \Delta_\zeta) \bar{R} = R \tag{30}
$$

where the residual R includes the contribution of the variable time step and is defined by Eq. (25) and $\bar{R}$ is the residual after a sequence of smoothing in the ξ, η, and ζ directions with coefficients β_ξ, β_η, and β_ζ. For viscous calculations on highly stretched meshes the variable coefficient formulations of Martinelli and Jameson (1988) and Swanson and Turkel (1987) have proven to be robust and reliable. In the present paper, the expression for the variable coefficients β of Eq. (30) has been modified to be used in three dimensions as follows:

$$
\begin{aligned}
\beta_\xi &= \mathrm{MAX}\left\{0, \ \frac{1}{4}\left[\left(\frac{\mathrm{CFL}}{\mathrm{CFL}^*} \frac{\lambda_\xi}{\lambda_\xi + \lambda_\eta + \lambda_\zeta} \Phi_\xi \right)^2 - 1 \right] \right\} \\
\beta_\eta &= \mathrm{MAX}\left\{0, \ \frac{1}{4}\left[\left(\frac{\mathrm{CFL}}{\mathrm{CFL}^*} \frac{\lambda_\eta}{\lambda_\xi + \lambda_\eta + \lambda_\zeta} \Phi_\eta \right)^2 - 1 \right] \right\} \\
\beta_\zeta &= \mathrm{MAX}\left\{0, \ \frac{1}{4}\left[\left(\frac{\mathrm{CFL}}{\mathrm{CFL}^*} \frac{\lambda_\zeta}{\lambda_\xi + \lambda_\eta + \lambda_\zeta} \Phi_\zeta \right)^2 - 1 \right] \right\}
\end{aligned} \tag{31}
$$

where the coefficients Φ_x, Φ_y, and Φ_z are the ones defined in Eqs. (19), and CFL, and CFL* are the Courant numbers of the smoothed and unsmoothed scheme, respectively. For the hybrid four-stage scheme we used CFL = 5 and CFL* = 2.5.

Multigrid. This technique was developed in the beginning of the 1970s for the solution of elliptic problems (Brandt, 1979) and later was extended to time-dependent formulations (Ni, 1981; Jameson, 1983). The basic idea is to introduce a sequence of coarser grids and to use them to speed up the propagation of the fine grid corrections, resulting in a faster expulsion of disturbances. In this work we used the Full Approximation Storage (FAS) schemes of Brandt (1979) and Jameson (1983).

Coarser auxiliary meshes are obtained by doubling the mesh spacing and the solution is defined on them using a rule that conserves mass, momentum, and energy,

$$
(J^{-1} Q^{(0)})_{2h} = \Sigma (J^{-1} Q)_h \tag{32}
$$

where the subscripts refer to the grid spacing, and the sum is over the eight cells that compose the $2h$ grid cell. Note that this definition coincides with the one used by Jameson when the reciprocal of the Jacobians are replaced with the cell volumes. To respect the fine grid approximation, forcing functions P are defined on the coarser grids and added to the governing equations. So, after the initialization of Q_{2h} using Eq. (32), forcing functions P_{2h} are defined as,

$$
P_{2h} = \Sigma R_h(Q_h) - R_{2h}(Q_{2h}^{(0)}) \tag{33}
$$

and added to the residuals R_{2h} to obtain the value R_{2h}^*, which is then used for the stepping scheme:

$$
R_{2h}^* = R_{2h}(Q_{2h}) + P_{2h} \tag{34}
$$

This procedure is repeated on a succession of coarser grids and the corrections computed on each coarse grid are transferred back to the finer one by bilinear interpolations.

A **V**-type cycle with subiterations is used as a multigrid strategy. The process is advanced from the fine grid to the coarser one without any intermediate interpolation, and when the coarser grid is reached, corrections are passed back. One Runge–Kutta step is performed on the h grid, two on the $2h$ grid, and three on all the coarser grids. It is our experience in cascade flow calculations that subiterations increase the robustness of the multigrid.

For viscous flows with very low Reynolds number or strong separation, it is important to compute the viscous terms on the coarse grids, too. The turbulent viscosity is evaluated only on the finest grid level and then interpolated on coarse grids.

On each grid, the boundary conditions are treated in the same way and updated at every Runge–Kutta stage. For econ-

omy, the artificial dissipation model is replaced on the coarse grids with constant coefficient second-order differences.

The interpolations of the corrections introduce high-frequency errors. In order to prevent those errors from being reflected in the eddy viscosity, turbulent quantities are updated after performing the stepping on the fine grid. On coarse grids, the turbulent viscosity is evaluated by averaging the surrounding fine grid values.

Grid Refinement. A grid refinement strategy is used to provide a cost-effective initialization of the fine grid solution. This strategy is implemented in conjunction with multigrid to obtain a Full Multigrid (FMG) procedure. With the FMG method, the solution is initialized on a coarser grid of the basic grid sequence and iterated a prescribed number of cycles of the FAS scheme. The solution is then passed, by bilinear interpolations, onto the next, finer grid and the process is repeated until the finest grid level is reached. In the present paper we have introduced three levels of refinement with respectively two, three, and four grids.

Computational Grid

The three-dimensional grids are obtained by stacking two-dimensional grids generated on blade-to-blade surfaces at constant radii (ξ, η plane). In order to minimize the grid skewness, in the blade-to-blade projection, the grid structure can be chosen on the basis of the blade geometry and flow conditions. Turbine blades are generally characterized by blunt leading edge and high turn with a subsonic incoming flow in the relative plane. For these geometries, nonperiodic **C**-type grids have proven to be effective (e.g., Arnone et al., 1991, 1992). In the case of a compressor, and particularly for a fan, the leading aspect of the geometry is the high stagger and twist, while the leading edge is often quite sharp (Fig. 1). In addition, the incoming flow in the relative plane can be supersonic for a large part of the blade span. As a consequence, a **C**-type structure of the grid may smear too much of the bow shock away from the leading edge (i.e., Weber and Delaney, 1991). In the present work, a nonperiodic **H**-type grid was implemented. The removal of mesh periodicity allows the grid to accommodate highly staggered airfoils with a low level of skewness. To minimize the undesired interaction between strong flow gradients and nonperiodic boundaries the mesh correspondence is broken before the leading edge and on the wake, but not inside the blade channel. The inviscid grids are elliptically generated, controlling the grid spacing and orientation at the wall. Viscous blade-to-blade grids are then obtained from inviscid grids by adding lines near the wall with the desired spacing distribution.

For highly twisted blades, a low grid skewness in the various spanwise sections can also be maintained by adjusting the grid-point distributions on the suction and pressure sides of the blade.

In the spanwise direction (ζ) a standard **H**-type structure is used. Near the hub and tip endwalls, geometric stretching is used for a specified number of grid points, after which the spanwise spacing remains constant.

Application and Discussions

As validation of the procedure that has been described above, the TRAF3D code was used to study the NASA rotor 67 transonic fan. This first-stage rotor of a two-stage transonic fan was designed and tested with laser anemometer measurements at NASA Lewis (Pierzga and Wood, 1985). The rotor has 22 low aspect ratio (1.56) blades and was designed for a rotational speed of 16,043 rpm, with a total pressure ratio of 1.63 and a mass flow of 33.25 kg/s. Experiments for simple blade-row code validation are available for the rotor without inlet guide vanes or downstream stators, and include detailed data near the peak efficiency and stall conditions. This rotor geometry has been recently proposed as an AGARD test case (Fottner, 1990) and several authors (Adamczyk et al., 1993; Chima, 1991; Hah and Reid, 1992; Jennions and Turner, 1993) have computed this geometry trying to understand the complex nature of transonic rotor flows. Therefore theoretical predictions from different codes are also available in the bibliography for comparisons and discussions.

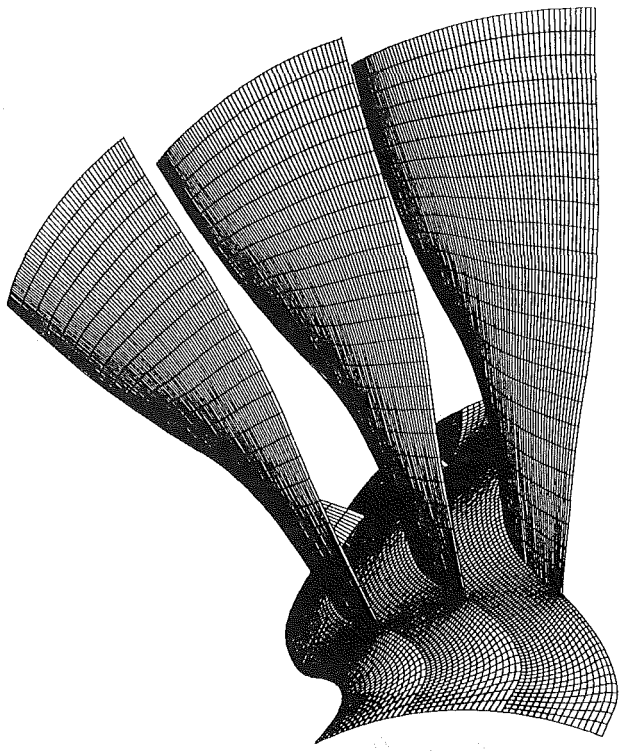

Fig. 1 Three-dimensional inviscid grid for the NASA rotor 67 transonic fan

A three-dimensional view of an inviscid grid for the rotor is given in Fig. 1. In previous works by the author (Arnone et al., 1991, 1992), a two- and three-dimensional grid dependency study was carried out in order to figure out the mesh requirements necessary to obtain a space-converged calculation, especially for viscous details such as losses, skin friction, and heat transfer. Those results can be extrapolated to the case of rotating blade passages. Using the algebraic turbulence model of Baldwin and Lomax (1978), a y^+ at the wall of about four, with a Reynolds number of about one million, gives satisfactory results unless heat transfer details are needed. This y^+ value was achieved with a mesh spacing at the wall in the blade-to-blade direction of 2×10^{-4} times the hub axial chord. In the spanwise direction, due to the relatively thick inlet boundary layer, the mesh spacing at the wall was fixed at 1×10^{-3} times the hub axial chord. One hundred thirty-seven points were used in the streamwise direction and 49 in the blade-to-blade and hub-to-tip directions. Sixty-five points were located on the suction and pressure side of the airfoil. In the spanwise direction, four cells lie inside the clearance region. Three grid sections at 70, 30, and 10 percent of the span from the shroud, are shown in Figs. 2(b), (c), and (d), respectively. Figure 2(a) gives a meridional view of the grid.

Following the approach suggested by Pierzga and Wood (1985) the comparison between calculations and experiments is carried out using the mass flow rate nondimensionalized with the choke flow rate as equivalence criteria. However, good agreement was also found in terms of absolute quantities. The TRAF3D predicts 34.5 kg/s while 34.96 ks/s was the measured one. This underestimation of the choke flow rate of about 1.3

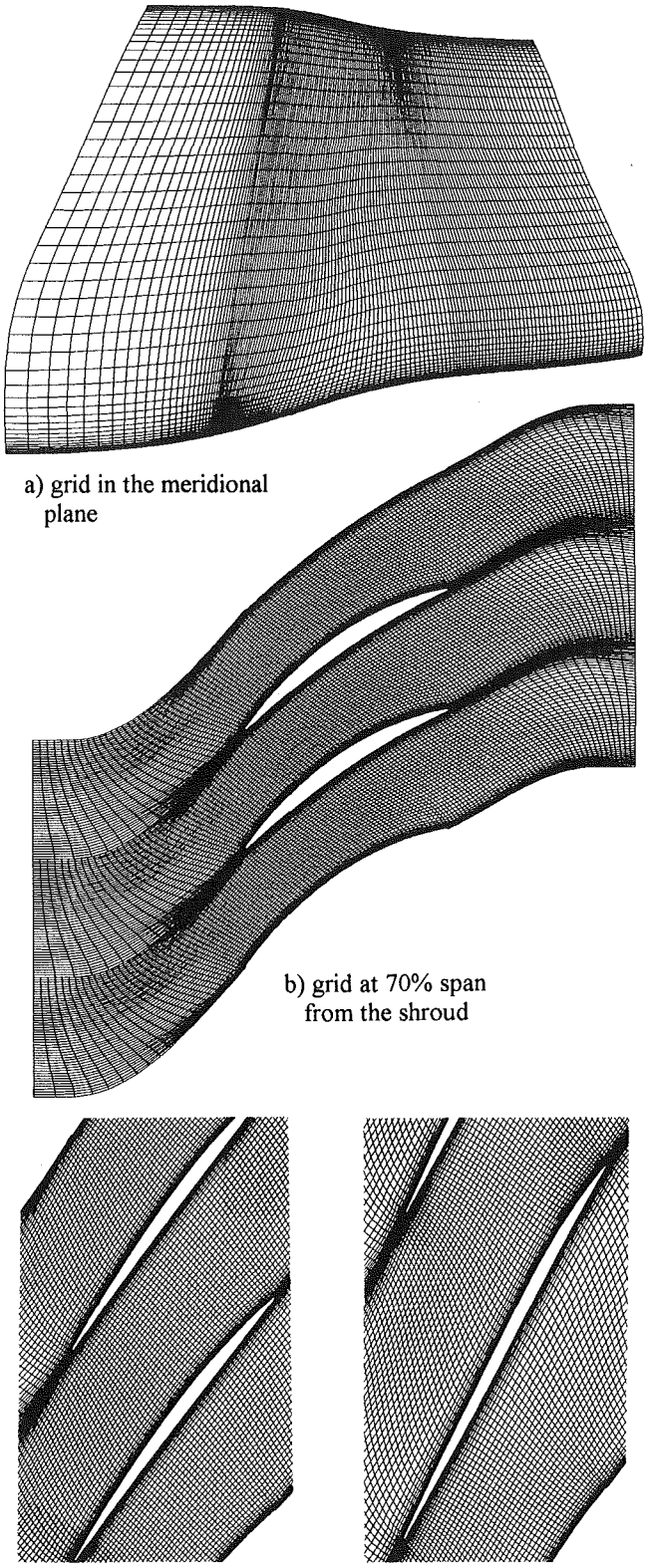

Fig. 2 137 × 49 × 49 viscous grid for the NASA rotor 67 transonic fan

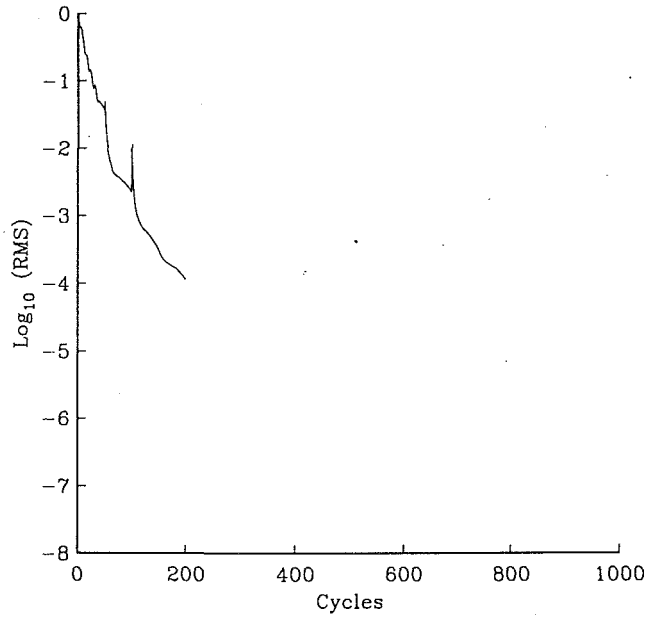

Fig. 3 Convergence history for the near-peak efficiency condition (NASA rotor 67 transonic fan)

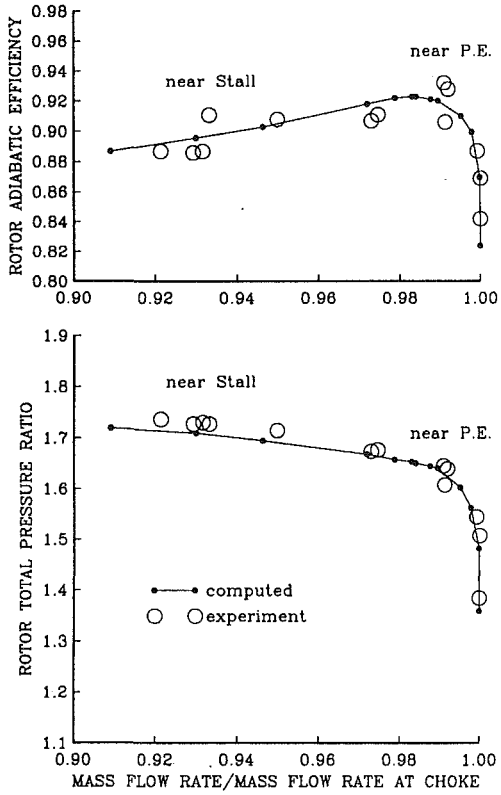

Fig. 4 NASA rotor 67 performance at design speed

percent agrees with the viscous prediction of Chima (1991) and Jennions and Turner (1993). The peak efficiency and near-stall conditions correspond to a nondimensional flow rate of 0.989 and 0.924, respectively.

The inlet boundary layer in the endwall region is accounted for by giving a total pressure profile. The thickness of the boundary layer is taken from experiments and the 1/7 power law velocity profile is used to estimate the distribution of total pressure. The core flow is assumed uniform.

The convergence of the root mean square of the norm of residuals is given in Fig. 3. This calculation refers to the near-peak efficiency condition, and requires about 35 minutes on the NASA Lewis Cray Y-MP to achieve a four decades' reduction in the residuals and corresponds to 100 multigrid cycles on the finest grid level using four grids. More than 35 minutes

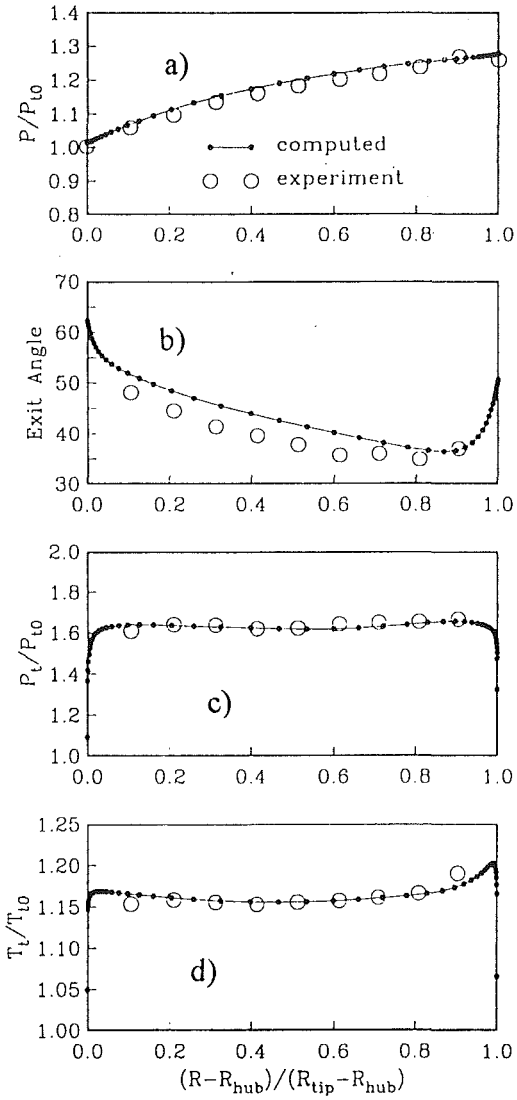

Fig. 5 Predicted and measured exit survey data near peak efficiency (NASA rotor 67)

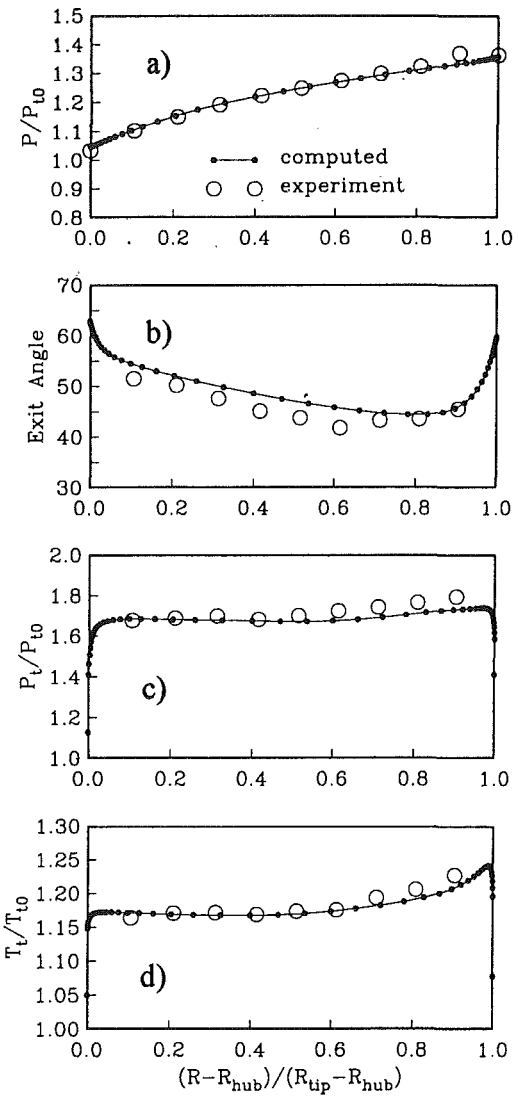

Fig. 6 Predicted and measured exit survey data near stall (NASA Rotor 67)

were needed only for solutions close to the stall condition. The global mass flow error has always been found to be less than 10^{-3}

Calculations were performed for 13 different values of the nondimensional flow rate in order to reproduce the operating characteristics of the rotor at the design speed. Results are summarized in Fig. 4 in terms of rotor adiabatic efficiency and rotor total pressure ratio. A nondimensional value of the mass flow rate equal to about 0.91 was the smaller value for which a steady solution was obtained. Further increase in the exit pressure would produce tip stall. The prediction of the rotor efficiency is quite good and agrees with the indication of Jennions and Turner (1993) in the fact that the abrupt decrease going from peak efficiency to stall conditions is smoothed out in the calculations. The peak efficiency is predicted at a slightly lower mass flow rate. Some underestimation in the total pressure ratio across the rotor should be noticed, but it seems to be evident only when approaching the stall condition. It is believed that the following aspects could be investigated in order to understand and/or address this problem:

- The distribution of the inlet boundary layer has been modeled only in terms of boundary layer thickness while experiments also show some gradients in the inviscid core of the inlet flow.
- The Baldwin–Lomax turbulence model is not very effective for transonic flow with strong adverse pressure gradients (Dawes, 1990).
- Measurements of the machine geometry while running have shown some deformation not included in the present calculations (Fottner, 1990).
- The tip clearance model that has been used is quite simple and clearance flow becomes important when the stall condition is approached (Adamczyk et al., 1993; Jennions and Turner, 1993).

The quality of the computed solutions is evaluated by comparing the spanwise distribution of circumferential energy-averaged thermodynamic quantities downstream of the rotor to experiments. The predicted distribution of static pressure, flow angle, total pressure, and total temperature at the rotor exit is compared to experiments in Figs. 5 and 6 for conditions near peak efficiency and stall, respectively. The agreement is good on the whole. The radial distribution of the static pressure is well reproduced (see Figs. 5(*a*) and 6(*a*)), which indicates a good estimation of the global losses. The exit angle is up to 5 deg off in the central part of the blade span (Figs. 5(*b*) and 6(*b*)), but this agrees with the calculations of Chima (1991) and Jennions and Turner (1992). From the plots of total pressure and total temperature of Figs. 5, 6(*c*), and 6(*d*) we can

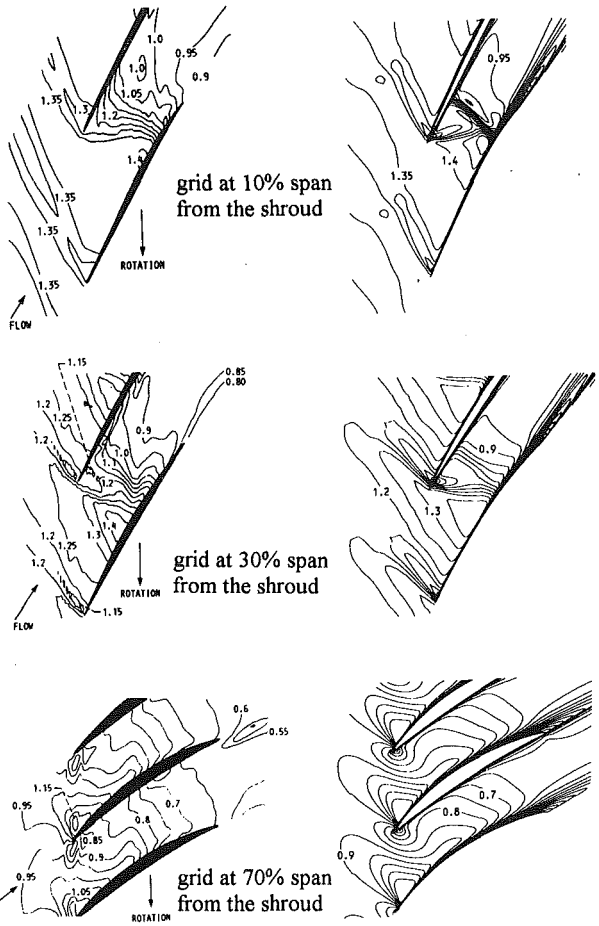

Fig. 7 Measured (left) and predicted (right) relative Mach number contours near peak efficiency (NASA rotor 67)

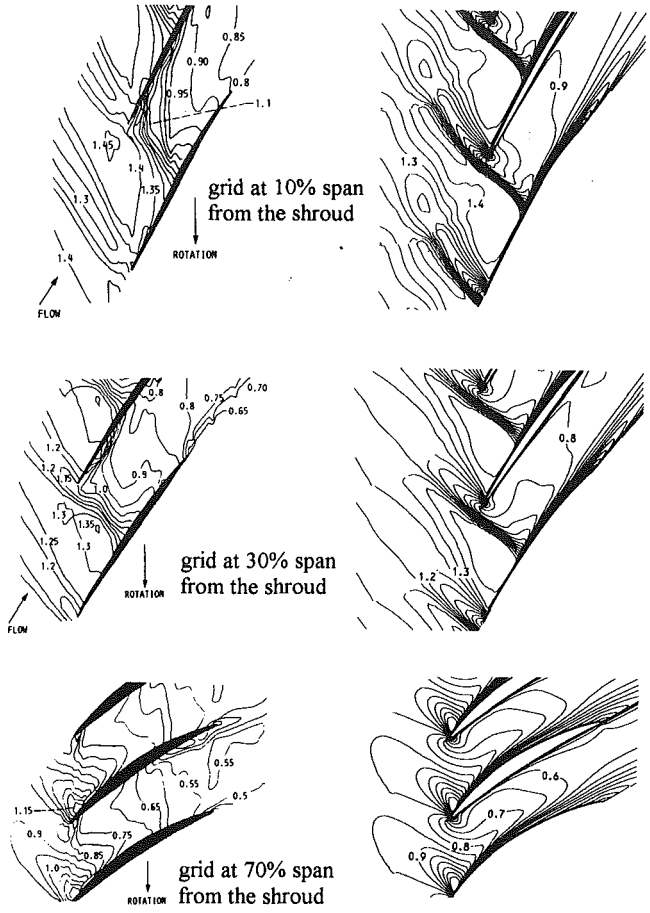

Fig. 8 Measured (left) and predicted (right) relative Mach number contours near stall (NASA rotor 67)

see that the overall prediction of the rotor characteristic is well reproduced.

As is well known, the flow pattern inside a rotor like the NASA 67 transonic fan is very complicated and characterized by effects such as shock–boundary layer interaction, clearance flow, and three-dimensional separation with vortex rollup. One attempt at interpreting the structure of the computed flow field can be analyzing the relative flow on blade-to-blade and meridional surfaces. Pictures of the limiting streamlines inside the boundary layer can be obtained by means of particle traces.

Blade-to-Blade Flow. Figures 7 and 8 report the computed and measured relative Mach number contours at three different locations of the blade span. The agreement with experiments is qualitatively good and the bow shock is not too smeared away from the leading edge. It is also interesting to notice that those contours agree very well with the ones obtained by Jennions and Turner (1993) using a two-equation model for the turbulence closure.

Near peak efficiency, the shock system has a lambda structure with a bow shock. The passage shock crosses the blade channel and involves about 30 percent of the upper part of the airfoil (see Figs. 7, and also 10 and 11). Approaching the stall condition (Fig. 8) the passage shock moves upstream and stands in front of the blade so that the airfoil pressure side is no longer intercepted (see also Figs. 12 and 13).

Blade Surface Flow Pattern. Pressure distribution and a restriction of the particle traces close to the airfoil surface are used to interpret the flow pattern inside the blade boundary layer. A schematic of this structure for the peak efficiency

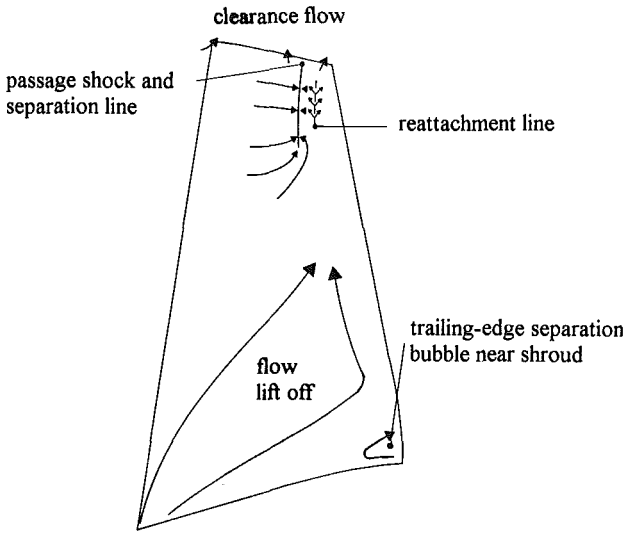

Fig. 9 Schematic of the suction side boundary-layer flow structure near peak efficiency (NASA rotor 67)

condition is depicted in Fig. 9. As discussed by Weber and Delaney (1991) and Hah and Reid (1992), most of the separation and outward flow is observed on the suction side of the blade. The passage shock is quite strong in the upper part of the rotor and the losses in axial momentum result in a rapid turn toward the shroud. The separation due to shock–boundary layer interaction is evident in Figs. 10 and 11. Separation lines are characterized by flows going toward the line, while where

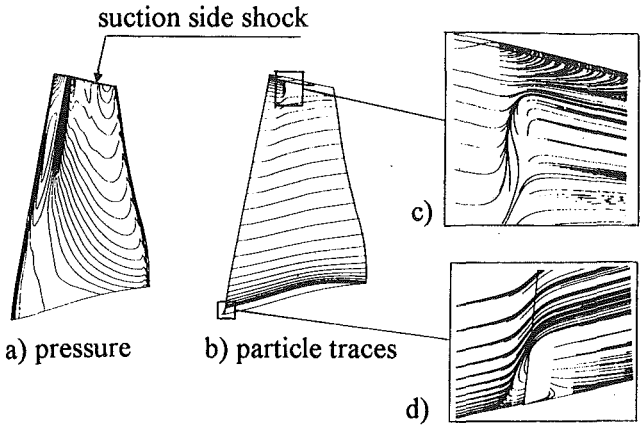

Fig. 10 Pressure contours and particle traces close to the blade pressure side near peak efficiency (NASA Rotor 67)

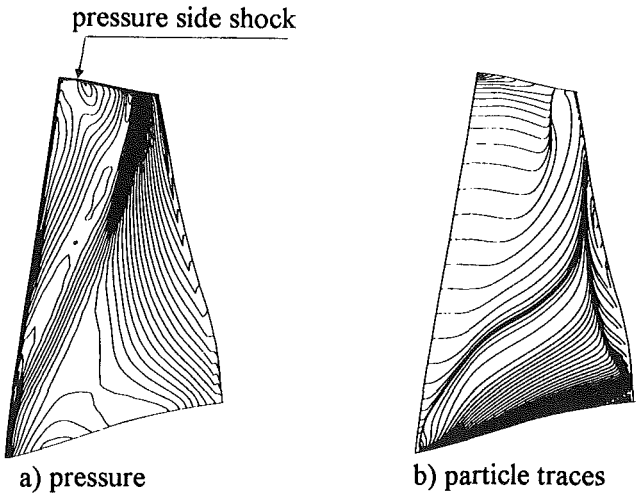

Fig. 11 Pressure contours and particle traces close to the blade suction side near peak efficiency (NASA rotor 67)

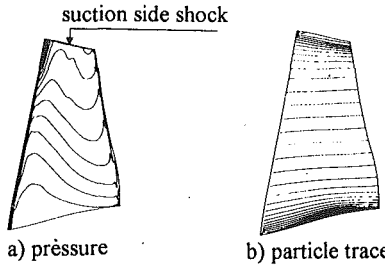

Fig. 12 Pressure contours and particle traces close to the blade pressure side near stall (NASA rotor 67)

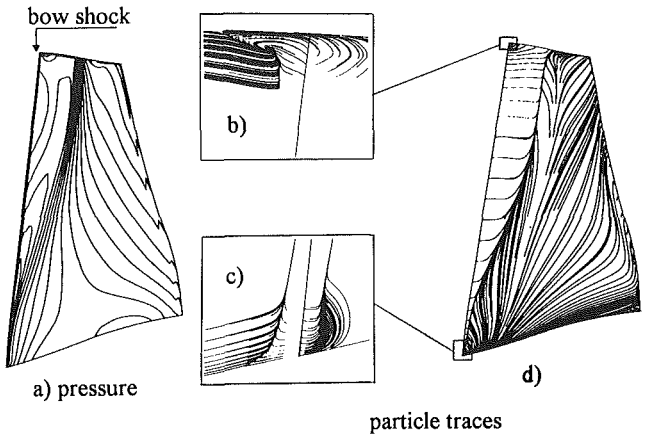

Fig. 13 Pressure contours and particle traces close to the blade suction side near stall (NASA rotor 67)

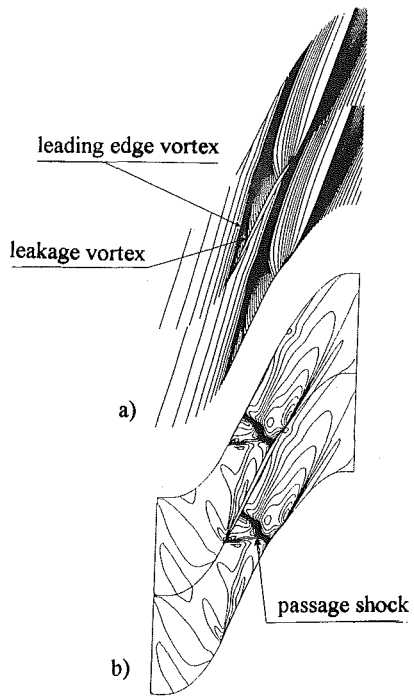

Fig. 14 Particle traces and relative Mach number contours in the clearance region near peak efficiency (NASA rotor 67)

the flow reattaches, the particle traces look like they are going away from the line (see Fig. 9). Such a situation is very clear in Figs. 10(*c*) and 13(*d*). The passage shock also induces separation on the blade pressure side but only in the very upper part of the airfoil. The blowup of Fig. 10(*c*) shows the abrupt radial migration with separation and reattachment.

In the central part of the blade span, the passage shock loses intensity and the flow lift-off is mostly related to the adverse pressure gradient in the axial direction. Eventually, near the trailing edge, the flow separates on the suction side (see Fig. 11(*b*)).

Close to the blade root, the flow is strongly influenced by a vortex rollup on the leading edge. As also pointed out by Chima (1991), particles undergo a high relative incidence close to the hub, which causes the low-momentum fluid to separate and migrate radially outward (see Figs. 10(*b*) and 11(*b*)).

In accordance with the calculations of Weber and Delaney (1991), Chima (1991), and Jennions and Turner (1993), a separation bubble is observed on the blade suction side near the hub (Figs. 9, 11(*b*), and 13(*d*)).

The flow structure of the near-stall operating condition is qualitatively similar to the peak efficiency previously discussed. Now the passage shock has moved upstream and the pressure side is shock free (Fig. 12(*a*)) with basically no radial flow mixing (Fig. 12(*b*)). On the contrary, on the suction side, the shock involves most of the blade span (Fig. 13(*a*)) and induces a strong outward flow with very clear separation and reattachment lines (Fig. 13(*d*)). The vortex rollup on the pressure side of Fig. 10(*d*) has now moved upstream and stands in front of the blade leading edge (Fig. 13(*c*)). The separation bubble on the suction side near the hub looks slightly smaller. On the shroud, the bow shock interacts with the casing boundary layer and the flow separates as depicted in Fig. 13(*b*).

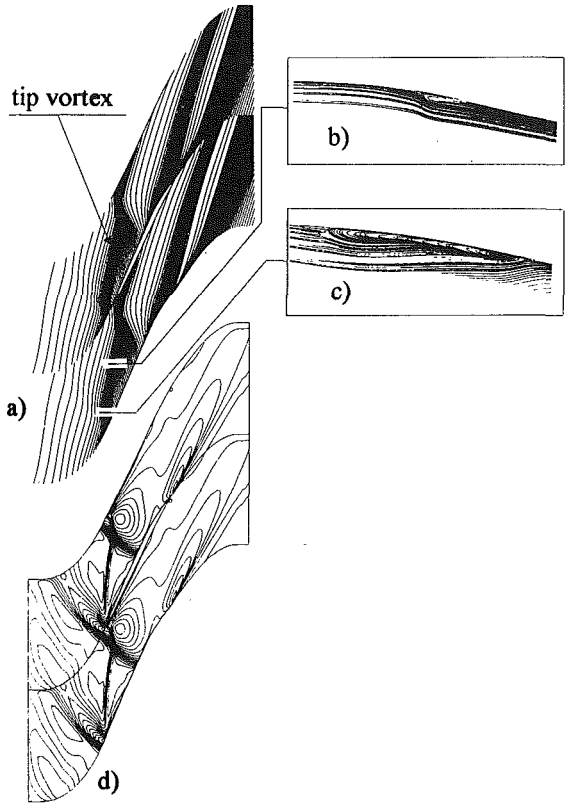

Fig. 15 Particle traces and relative Mach number contours in the clearance region near stall (NASA Rotor 67)

Clearance Flow Pattern. A picture of the clearance flow pattern is obtained by plotting the relative Mach number contours and a restriction of the particle traces on a blade-to-blade surface midway between the blade tip and the casing. Once again the flow structure looks very similar to the one computed by Jennions and Turner (1993).

The TRAF3D code predicts two tip vortices, which intersect before midchannel. At peak efficiency (Figs. 14(*a*) and 14(*b*)), the shock system still shows a lambda structure and interacts with the tip vortices. A first vortex is observed close to the leading edge and a second leakage vortex forms at an axial location just after the pressure side shock. The two vortices sum up before crossing the passage shock as shown in Fig. 14. When approaching the stall condition there is interaction between the leading edge shock separation and the leading edge vortex (Adamczyk et al., 1991; Jennions and Turner, 1993). The leading edge vortex is now associated with the casing separation of the bow shock, while the leakage vortex has moved upstream. The two vortices interact very soon while going toward the pressure side of the next consecutive blade (Figs. 15(*b*) and 15(*c*)). Figure 15(*d*) indicates a strong link between the shock system and the tip vortices for this flow condition.

Hub Endwall Flow Pattern. Particle traces in the hub boundary layer are reported for completeness in Figs. 16 and 17. The high angle of attack experienced by the flow in this region and previously discussed is evident. The separation bubble close to the trailing edge causes an easily visible lack of particles, which, when injected close to the blade, roll up radially.

Conclusions

The central-difference, finite-volume scheme with eigenvalues scaling for artificial dissipation terms, variable-coefficient implicit smoothing, and full multigrid has been extended to predict three-dimensional rotating blade passages. The procedure has been validated by comparing it with experiment for the NASA rotor 67 in a wide range of mass flow rate. With these accelerating strategies, detailed three-dimensional viscous solutions can be obtained for a reasonable fine grid in about half an hour on a modern supercomputer.

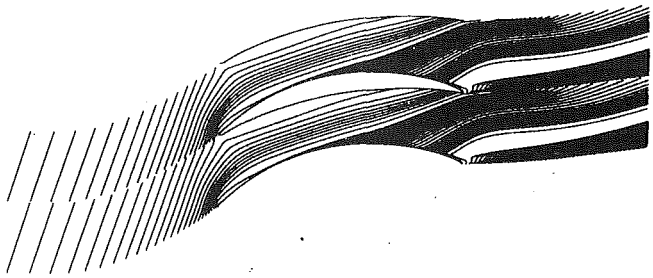

Fig. 16 Particle traces close to the hub endwall near peak efficiency (NASA rotor 67)

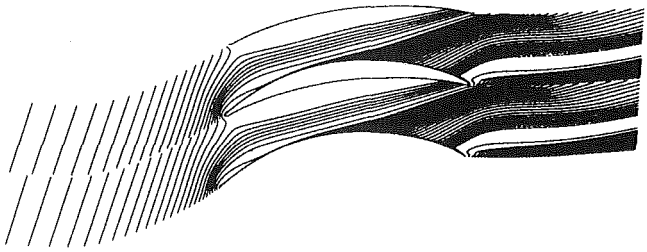

Fig. 17 Particle traces close to the hub endwall near stall (NASA rotor 67)

Acknowledgments

Gratitude is expressed to ICOMP and NASA for providing computer time for this work.

The development of the TRAF codes has been a long-term project, which was started at the University of Florence in 1985 under the supervision of Prof. Sergio S. Stecco, who unexpectedly passed away in May 1993. The author would like to dedicate this technical paper to his memory.

References

Adamczyk, J. J., Celestina, M. L., Beach, T. A., and Barnett, M., 1990, "Simulation of Three-Dimensional Viscous Flow Within a Multistage Turbine," ASME JOURNAL OF TURBOMACHINERY, Vol. 112, pp. 370–376.

Adamczyk, J. J., Celestina, M. L., and Greitzer, E. M., 1993, "The Rule of Tip Clearance in High-Speed Fan Stall," ASME JOURNAL OF TURBOMACHINERY, Vol. 115, pp. 28–39.

Arnone, A., and Swanson, R. C., 1988, "A Navier-Stokes Solver for Cascade Flows," NASA CR No. 181682.

Arnone, A., Liou, M.-S., and Povinelli, L. A., 1991, "Multigrid Calculation of Three-Dimensional Viscous Cascade Flows," AIAA Paper No. 91-3238.

Arnone, A., Liou, M.-S., and Povinelli, L. A., 1992, "Navier-Stokes Solution of Transonic Cascade Flow Using Non-periodic C-Type Grids," *Journal of Propulsion and Power*, Vol. 8, No. 2, pp. 410–417.

Baldwin, B. S., and Lomax, H., 1978, "Thin Layer Approximation and Algebraic Model for Separated Turbulent Flows," AIAA Paper No. 78-257.

Brandt, A., 1979, "Multi-level Adaptive Computations in Fluid Dynamics," AIAA Paper No. 79-1455.

Chima, R. V., and Yokota, J. W., 1988, "Numerical Analysis of Three-Dimensional Viscous Internal Flows," NASA TM 100878.

Chima, R. V., 1991, "Viscous Three-Dimensional Calculations of Transonic Fan Performance," AGARD 77th Symposium on CFD Techniques for Propulsion Applications, Paper No. 21.

Choi, D., and Knight, C. J., 1988, "Computation of Three-Dimensional Viscous Linear Cascade Flows," *AIAA Journal*, Vol. 26, No. 12, pp. 1477–1482.

Davis, R. L., Hobbs, D. E., and Weingold, H. D., 1988, "Prediction of Compressor Cascade Performance Using a Navier-Stokes Technique," ASME JOURNAL OF TURBOMACHINERY, Vol. 110, pp. 520–531.

Dawes, W. N., 1990, "A Comparison of Zero and One Equation Turbulence Modelling for Turbomachinery Calculations," ASME Paper No. 90-GT-303.

Dawes, N. W., 1992, "The Simulation of Three-Dimensional Viscous Flow

in Turbomachinery Geometries Using a Solution-Adaptive Unstructured Mesh Methodology," ASME JOURNAL OF TURBOMACHINERY, Vol. 114, pp. 528–537.

Fottner, L., 1990, "Test Case for Computation of Internal Flows in Aero Engine Components," Propulsion and Energetic Panel Working Group 18, AGARD-AR-275.

Hah, C., 1989, "Numerical Study of Three-Dimensional Flow and Heat Transfer Near the Endwall of a Turbine Blade Row," AIAA Paper No. 89-1689.

Hah, C., and Reid, L., 1992, "A Viscous Flow Study of Shock–Boundary Layer Interaction, Radial Transport, and Wake Development in a Transonic Compressor," ASME JOURNAL OF TURBOMACHINERY, Vol. 114, pp. 538–547.

Holmes, D. G., and Tong, S. S., 1985, "A Three-Dimensional Euler Solver for Turbomachinery Blade Rows," ASME *Journal of Engineering for Gas Turbines and Power*, Vol. 107, pp. 258–264.

Jameson, A., Schmidt, W., and Turkel, E., 1981, "Numerical Solutions of the Euler Equations by Finite Volume Methods Using Runge–Kutta Time-Stepping Schemes," AIAA Paper No. 81-1259.

Jameson, A., 1983, "The Evolution of Computational Methods in Aerodynamics," ASME *Journal of Applied Mechanics*, Vol. 50, pp. xx–00.

Jameson, A., 1983, "Transonic Flow Calculations," MAE Report 1651, MAE Department, Princeton University, Princeton, NJ.

Jennions, I. K., and Turner, M. G., 1993, "Three-Dimensional Navier–Stokes Computations of Transonic Fan Flow Using an Explicit Flow Solver and an Implicit k–ϵ Solver," ASME JOURNAL OF TURBOMACHINERY, Vol. 115, pp. 261–272.

Lerat, A., 1979, "Une Classe de Schemas aux Differences Implicites Pour les Systemes Hyperboliques de Lois de Conservation," *Comptes Rendus Acad. Sciences Paris*, Vol. 228A, pp. xx–00.

Martinelli, L., and Jameson, A., 1988, "Validation of a Multigrid Method for the Reynolds Averaged Equations," AIAA Paper No. 88-0414.

Nakahashi, K., Nozaki, O., Kikuchi, K., and Tamura, A., 1989, "Navier–Stokes Computations of Two- and Three-Dimensional Cascade Flowfields," *AIAA Journal of Propulsion and Power*, Vol. 5, No. 3, pp. 320–326.

Ni, R.-H., 1981, "A Multiple-Grid Scheme for Solving the Euler Equations," AIAA Paper No. 81-1025.

Pierzga, M. J., and Wood, J. R., 1985, "Investigation of the Three-Dimensional Flow Field Within a Transonic Fan Rotor: Experiment and Analysis," ASME *Journal of Engineering for Gas Turbines and Power*, Vol. 107, pp. 436–449.

Pulliam, T. H., 1986, "Artificial Dissipation Models for the Euler Equations," *AIAA Journal*, Vol. 24, No. 12, pp. 1931–1940.

Rai, M. M., 1987, "Unsteady Three-Dimensional Navier–Stokes Simulations of Rotor Stator Interactions," AIAA Paper No. 87-2058.

Rao, K. V., and Delaney, R. A., 1990, "Investigation of Unsteady Flow Through a Transonic Turbine Stage, Part I, Analysis," AIAA Paper No. 90-2408.

Subramanian, S. V., and Bozzola, R., 1987, "Numerical Simulation of Three-Dimensional Flow Fields in Turbomachinery Blade Rows Using the Compressible Navier–Stokes Equations," AIAA Paper No. 87-1314.

Swanson, R. C., and Turkel, E., 1987, "Artificial Dissipation and Central Difference Schemes for the Euler and Navier–Stokes Equations," AIAA Paper No. 87-1107.

Weber, K. F., and Delaney, R. A., 1991, "Viscous Analysis of Three-Dimensional Turbomachinery Flows on Body Conforming Grids Using an Implicit Solver," ASME Paper No. 91-GT-205.

Behavior of Three-Dimensional Boundary Layers in a Radial Inflow Turbine Scroll

K. Hara

M. Furukawa

M. Inoue

Department of Energy and Mechanical Engineering, Kyushu University, Fukuoka, Japan

A detailed experimental investigation was carried out to examine the three-dimensional boundary layer characteristics in a radial inflow turbine scroll. Some basic flow phenomena and growth of secondary flow were also investigated. In the inlet region of the scroll, the incoming boundary layer begins to have a skewed nature, namely the radially inward secondary flow caused by the radial pressure gradient. From the inlet region to one third of the scroll circumference, the secondary flow grows so strongly that most of the low-momentum fluid in the incoming boundary layer is transported to the nozzle region. The succeeding elimination of the low-momentum fluid in the boundary layer suppresses growth of the boundary layer farther downstream, where the boundary layer shows a similar velocity profile. The distributions of the boundary layer properties in the scroll correspond well to those of the flow properties at the nozzle. The behavior of the boundary layer in the scroll is found to affect the circumferential nonuniformity of the nozzle flow field.

Introduction

Vaneless scroll nozzles are widely used in small turbochargers because of their easy manufacture, low production cost, and wide range of operation. Unlike the vaned scroll nozzle,the peripheral velocity in the vaneless scroll should be high so that a turbine can be operated satisfactorily. Although the nozzle flow field seems to suppress the development of the boundary layer, the unavoidable high peripheral velocity generates the strong secondary flow in the scroll passage. The flow is distorted in the axial and peripheral directions (Miller et al., 1988; Inoue et al., 1987). It is well known that the distortion in the axial direction is due to the secondary flow generated in the scroll passage. The flow is so skewed axially that the reverse flow can be seen at the central part of the scroll nozzle for small outlet flow angle conditions. Moreover, there exists a circumferential nonuniformity, which has been considered to be due to the wake of the tongue and potential effects of the three-dimensional scroll configuration.

Measurements of the scroll flow field were conducted, for example, by Miller et al. (1988), Malak et al. (1987) and Tabakoff et al. (1984), but they were limited to the nozzle region and the mainstream of the scroll passage hindered by the complicated three dimensionality of the scroll configuration. The investigation on the three-dimensional boundary layer of the scroll is considered to be insufficient. In the present investigation, the detailed measurement of the scroll flow field and the side wall boundary layer have been conducted to study the development of the secondary flow and the three-dimensional boundary layer, and then, the formation process of the peripheral nonuniformity in the nozzle flow field has been clarified. Similar phenomena are considered to be seen in the flow field of a hydraulic turbine (Vu and Shyy, 1990) and an inlet scroll of a industrial compressor.

The vibration of the rotor blade is excited periodically by the nonuniform nozzle flow and the blade fatigue destruction breaks out especially for modern high specific speed turbine. The uniformity of the nozzle flow field improves, not only decreasing the unsteady loss of the turbine rotor but also reducing the moment of inertia of the rotor. The small inertia contributes to improve the response of turbocharged engines, which have desirable characteristics on exhaust emission, fuel consumption, and engine weight.

Experimental Apparatus and Experimental Method

The experimental apparatus is shown in Fig. 1. The front wall of the scroll was composed of a large disk 1 and a small eccentric disk 2 on which a traverse mechanism was equipped. The disks were rotated by microstep stepping motors to position radius and azimuth angle of the traverse mechanism. A three or five-hole probe was driven by two small-sized stepping motors to measure the flow direction, pressure, and velocity at an arbitrary point in the scroll.

The plane view of the scroll is shown in Fig. 2(*a*). The scroll outer wall is composed of a logarithmic spiral, the radius of which is represented as

$$r_s = 100 \exp\left(\left(\frac{7\pi}{3} - \theta\right) \tan \alpha_s\right) \quad (1)$$

where θ is an azimuth angle measured from the tongue edge. A tongue of $\theta_t = 30$ deg is installed at the end of the convergent inlet duct. The cross-sectional configuration of the scroll passage is rectangular and a cylindrical inner wall with a diameter

Contributed by the International Gas Turbine Institute and presented at the 38th International Gas Turbine and Aeroengine Congress and Exposition, Cincinnati, Ohio, May 24-27, 1993. Manuscript at ASME Headquarters March 1, 1993. Paper No. 93-GT-138. Associate Technical Editor: H. Lukas.

of 180 mm is installed at the center of the scroll. The simple cross-sectional shape allows a precise measurement of the front and rear wall boundary layers. Figure 2(*a*) shows an arrangement of the measuring sections in which measurement points of the boundary layer investigation are distributed as Fig. 2(*b*).

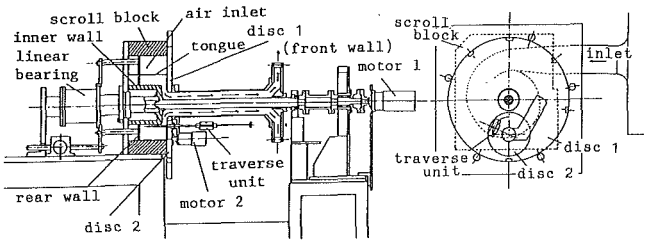

Fig. 1 Schematic of experimental apparatus

The rear wall can be moved axially to vary the outlet flow angle by changing the scroll and nozzle passage height ratio b_s/b_e with the principle of mass and angular momentum conservation. For our scroll, the outlet flow angle is simply given by

$$\tan \alpha = \frac{b_s}{b_e} \tan \alpha_s \tag{2}$$

Variations of the cross-sectional shapes of the scroll for measured b_s/b_e ratio are shown in Fig. 2(*c*). The clearance between outer and rear wall was sealed by silicone foam rubber to prevent air leakage. Experiments were performed at normal temperature and constant plenum pressure of 4.9×10^3 Pa gage for which the inlet mean velocities c_i are 25.7 to 23.4 m/s. The development of the secondary flow was investigated by measuring the three-dimensional velocity field with the five-hole

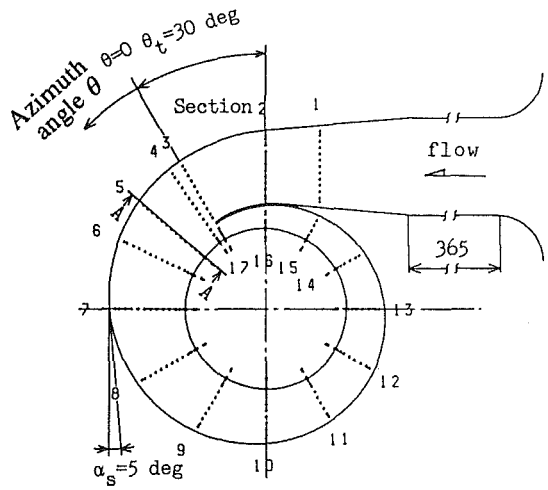

(a) Plane view and measuring section

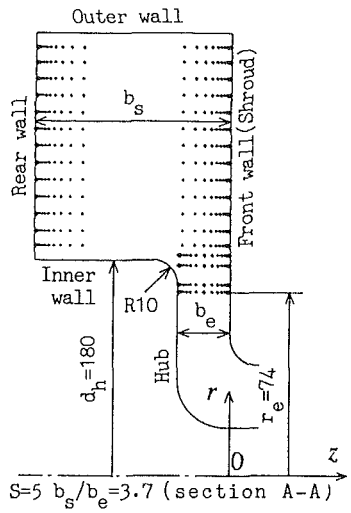

(b) Cross section and measuring point distribution

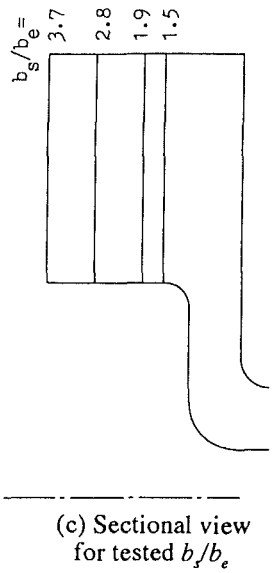

(c) Sectional view for tested b_s/b_e

Fig. 2 Scroll configuration and measuring point

Nomenclature

A_i = $b_s(r_s(0) - r_s(2\pi))$ = scroll inlet area
B = blockage factor
b_s, b_e = passage height of scroll and nozzle
c_i = scroll inlet mean velocity
$\underline{c}(c_r, c_\theta, c_z)$ = measured velocity vector
KE = kinetic energy of meridional flow
K_i = $r_i c_i$ = mean inlet angular momentum
r, θ, z = cylindrical coordinates
r_h = inner wall radius
r_i = $(r_s(0) + r_s(2\pi))/2$ = scroll mean inlet radius
r_s = scroll outer wall radius defined in Eq. (1)
$s(s_r, s_\theta, s_z)$ = secondary flow velocity vector
SE = kinetic energy of secondary flow
U = streamwise velocity at the boundary layer edge
u, w = streamwise and cross-flow velocity in the boundary layer
u^+, y^+ = universal velocity and universal distance
$\mathbf{V}(v_r, v_\theta, v_z)$ = velocity vector of axisymmetric potential flow
y = distance from wall
α = flow angle measured from peripheral direction
α_s = spiral angle of scroll outer wall
δ = boundary layer thickness
δ_u, δ_w = streamwise and cross-flow displacement thickness
δ_r, δ_θ = radial and peripheral displacement thickness
θ = azimuth angle measured from the tongue edge
θ_u, θ_w = streamwise and cross-flow momentum thickness
ρ = density
ξ = vorticity normal to meridional plane
ζ_p = total pressure loss coefficient (defined in Eq. (A1))

Subscripts

f = front wall
MR = measured region in the meridional cross section
r = rear wall
$-$ = peripheral average at the nozzle (defined in Eq. (A2))
$\sim$ = axial average at the nozzle (defined in Eq. (A3))
$=$ = total average at the nozzle (defined in Eq. (A4))

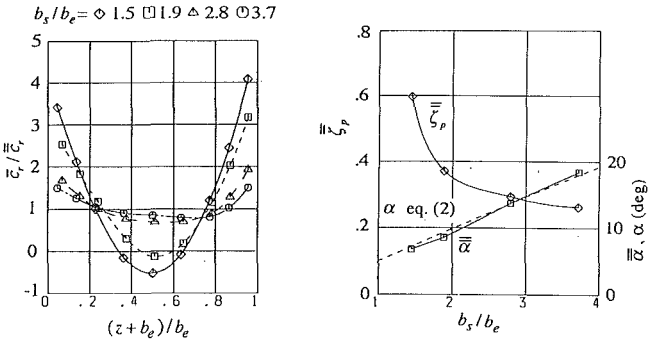

Fig. 3(*a*) Axial distribution of radial velocity; (*b*) performance of the nozzle

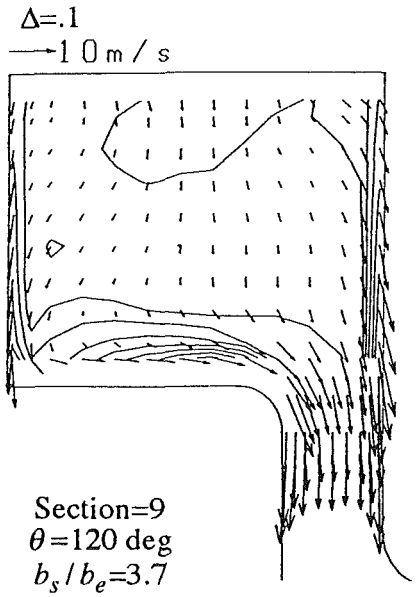

Fig. 4 Meridional velocity vector and total pressure loss contour

probe up to distance of 1 mm from the front and rear walls and up to 6 mm from the outer and inner walls. The nozzle performance was evaluated at the cylindrical region with a radius of 74 mm. The boundary layer investigation was conducted by measuring the velocity component within the plane parallel to the wall up to distance of 0.2 mm from the front and rear walls using the three-hole probe. The boundary layer edge was determined at the location where a total pressure was 99.5 percent of the local mainstream value. As shown in Fig. A1, the boundary layer velocity profile were resolved into a streamline coordinate system with "streamwise" and "cross-flow" components in which the displacement and momentum thicknesses were defined. They are listed in the appendix.

Results and Discussion

Nozzle Performance and Scroll Flow Field. The nozzle performance is evaluated by mass-flow weighted average, the definitions of which are listed in the appendix for peripheral, axial, and total average. In Fig. 3, basic characteristics of the scroll nozzle are represented. Figure 3(*a*) displays an axial distribution of inward radial velocity averaged in the peripheral direction normalized by the total averaged radial velocity. The smaller the b_s/b_e ratio becomes, the more flow field skews, so that the fluid hardly flows at the center of the nozzle for b_s/b_e = 1.9 and the flow reverses for b_s/b_e = 1.5. In Fig. 3(*b*), total pressure loss normalized by the dynamic pressure of the scroll inlet mean velocity becomes large with b_s/b_e ratio decreasing because of the flatter cross-sectional scroll configuration and reverse flow phenomena at the nozzle. Figure 3(*b*) also shows theoretical flow angle defined by Eq. (2) and mean outlet flow angle determined as $\bar{\bar{\alpha}} = \tan^{-1}(\bar{\bar{c}}_r/\bar{\bar{c}}_\theta)$.

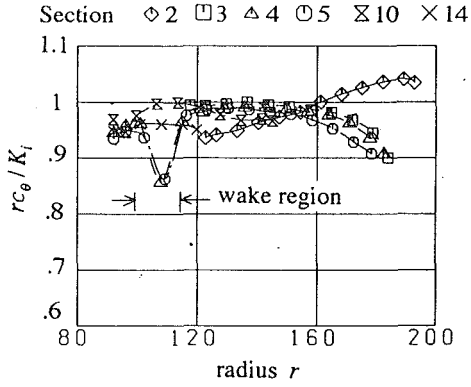

Fig. 5 Average angular momentum distribution

Figure 4 shows meridional velocity vector and contour of total pressure loss coefficient for section 9. The velocity vectors, which represent secondary flow characteristics, show larger inward radial component near the side walls where total pressure loss increases. A corner secondary flow, which convects a main flow toward a corner, is observed at the rear wall and the inner wall intersection. A high loss region can be seen near the inner wall where the velocity vectors toward the nozzle are also large. Since the tendency of high meridional velocity near the both side wall continues, the nozzle flow field is skewed in axial direction. The nozzle flow field is not uniform in the peripheral direction as well as in the axial direction. This will be discussed later in detail.

Supposing conservation of angular momentum, the scroll flow field is considered to be fundamentally free vortex. Figure 5 shows the distribution of axially averaged angular momentum in the scroll passage normalized by the inlet mean angular momentum *Ki*. At the end of the convergent duct, section 2, the angular momentum varies with radius; therefore, the flow is not completely of free vortex type. Below section 3, however, the distribution is uniform, showing the formation of free vortex flow except for a wake region and near the outer wall where outer wall boundary layer begins to be observed. It is found that the formation of free vortex flow is completed for the tongue angle of 30 deg, over which the total pressure loss increases (Inoue et al., 1987).

Development of Secondary Flow. In order to investigate the development of secondary flow in the scroll passage, the following values are defined at each measuring section. A sectional mean kinetic energy is defined by using the measured meridional velocity as

$$KE = \frac{1}{c_i^2}\int_{MR}(c_r^2 + + c_z^2)c_\theta dA / \int_{MR} c_\theta dA \qquad (3)$$

where integration is performed over the measured region by the five-hole probe. A secondary flow vector s was defined as a projection of measured velocity vector **C** to the plane normal to reference velocity vector **V** whose meridional component was determined for each cross section by the solution of the axisymmetric potential flow equation described by stream function with the boundary condition of constant inflow velocity $c_r = (K_i/r_s)\tan\alpha_s$ at the outer wall (Hara et al., 1991):

$$\mathbf{S} = \mathbf{C} - \frac{\mathbf{C}\cdot\mathbf{V}}{|\mathbf{V}|^2}\mathbf{V}$$

Radial and axial components of the secondary vector are used to evaluate the kinetic energy of the secondary flow.

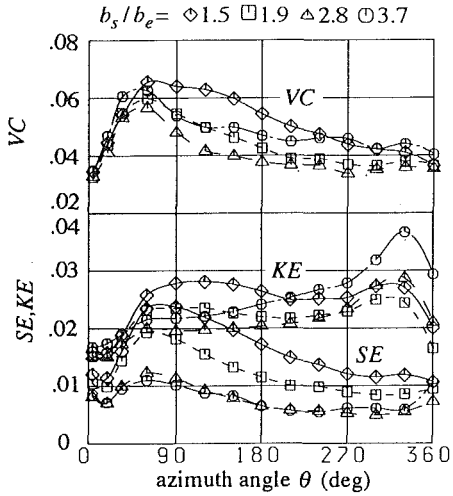

Fig. 6 Vorticity, meridional kinetic energy, and secondary kinetic energy

$$SE=\frac{1}{c_i^2}\int_{MR}(s_r^2+s_z^2)c_\theta dA/\int_{MR}c_\theta\, dA \tag{4}$$

A peripheral vorticity ξ normal to the measuring section is calculated by a numerical differentiation of the meridional velocity field as

$$\xi=\frac{\partial c_r}{\partial z}-\frac{\partial c_z}{\partial r} \tag{5}$$

and its sectional mean is defined by

$$VC=\frac{\int_{MR}|\xi|dA}{2\pi c_i/(A_i/r_i)\int_{MR}dA} \tag{6}$$

The kinetic energies of the meridional flow and the secondary flow are represented in Fig. 6. The kinetic energy of the secondary flow, which represents a viscous effect on the scroll flow field, increases in the inlet region of the scroll, because the incoming boundary layer begins to skew and is carried inward radially and because the outer wall boundary layer, which is not measured in this investigation but an evidence is mentioned later, is joined to the side wall boundary layer. However, this energy decreases gradually for more than 60 deg azimuth angle representing the elimination of low-momentum fluid to the nozzle. For b_s/b_e = 2.8 and 3.7, secondary flow changes little downstream from section 9, because the production and elimination of the secondary flow tend to balance. For b_s/b_e = 1.5 and 1.9, secondary flow does not saturate immediately because of greater production of loss in the scroll passage owing to flatter cross-sectional shape (see Fig. 2(*c*)) and reverse flow phenomena.

The difference between meridional and secondary kinetic energy represents an inviscid or potential effect of the nozzle to the meridional flow field. Since the cross-sectional area of the scroll passage decreases, the difference increases downstream. Although the secondary flow energy decreases in the azimuthal direction as mentioned above, the meridional kinetic energy tend to saturate in azimuth direction on the whole. For b_s/b_e = 3.7 and 2.8, however, the kinetic energy increases slightly from θ = 60 deg to 270 deg, because the z component of the meridional velocity vector becomes large with the scroll cross section being flattened for large azimuth angle.

The sectional mean vorticity increases at the scroll inlet region but gradually decreases downstream like the secondary flow distribution. This also represents the elimination of the boundary layer.

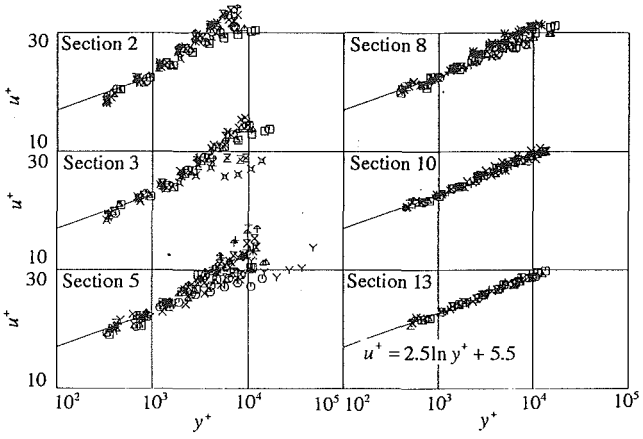

Fig. 7 Streamwise velocity profile of boundary layer

Table 1 Radii of velocity profile measurement

Section=		2	3	5	8	10	13
1	◇	122.7	117.6	76.8	77.3	77.2	77.1
2	□	126.3	122.7	80.0	80.0	80.0	80.0
3	△	133.3	129.7	88.0	88.0	88.0	88.0
4	○	140.3	136.7	92.0	92.0	92.0	92.0
5	⧖	147.3	143.7	96.0	96.0	96.0	96.0
6	×	154.3	150.7	102.2	99.8	99.5	100.3
7	+	161.3	157.7	109.2	106.8	106.5	107.3
8	Y	168.3	164.7	116.2	113.8	113.5	114.3
9	↑	175.3	171.7	123.2	120.8	120.5	121.3
10	⧖	182.3	178.7	130.2	127.8	127.5	125.6
11	⧖	189.3	183.9	137.2	134.8	134.5	-
12	⌘	192.8	-	144.2	141.8	141.5	-
13	✳	-	-	151.2	148.8	145.0	-
14	✡	-	-	158.2	155.8	-	-
15	◇	-	-	165.2	159.5	-	-
16	□	-	-	172.2	-	-	-
17	△	-	-	178.4	-	-	-

Boundary Layer Profile. Measurement of boundary layer is made by using the three-hole probe at the measuring point shown in Fig. 2. Semilogarithmic plots of the streamwise velocity profiles are presented in Fig. 7 for six cross sections of the front wall boundary layer. For each cross section, all the data from outer wall to nozzle are plotted in one frame with different symbols, which correspond to the measuring radii shown in Table 1. A solid line represents the velocity profile based on the usual law of the wall ($u^+ = 2.5 \ln y^+ + 5.5$). Deviation from logarithmic law at several cross sections indicates the following phenomena: beginning of skew of the incoming boundary layer in the turning duct of the scroll inlet (section 2), an accumulation of low-energy fluid on the tongue (section 3) and an interaction of the tongue wake with boundary layer (section 5). In the second half of the scroll passage, logarithmic velocity profiles are observed.

Figure 8 displays polar diagrams of the boundary layer profile, which represent skewed nature near the outer region of the boundary layer. The boundary layer hardly skews in section 2. In section 5, some data are seen to skew contrary due to the interaction of boundary layer and the tongue wake. The value of w/U becomes larger as the radius is smaller in section 3 and in the downstream passages (sections 8–13). Although the tendency is similar for these sections, skew reduces downstream, slightly suggesting the decrease of secondary flow and sectional mean vorticity (see Fig. 6).

Development of Side Wall Boundary Layer. Figure 9 represents the contour maps of the main stream velocity and some boundary layer characters of the front wall for b_s/b_e = 3.7. In Fig. 9(*a*), the streamwise velocity at the boundary layer edge displays a transition from straight flow to free vortex flow in

the inlet turning duct region and shows the almost axisymmetric nature in the scroll passage. In Fig. 9(*b*), the streamwise displacement thickness increases slightly in the inlet region of the scroll and decreases gradually downstream. A region of very thick boundary layer is seen below the tongue. It should be noted that the crossflow displacement thickness and the crossflow momentum thickness have negative values. This means that the transportation and the force acting on the boundary layer fluid in inward radial direction is greater than the main stream value. In Figs. 9(*b*) and 9(*c*), it is observed that absolute value of the crossflow displacement thickness increases systematically from the inlet turning duct to the inlet region, and some considerably high streaks of boundary layer come from outer wall of the wall of the scroll. These correspond to the development of secondary flow in the inlet region shown in Fig. 6. The absolute values of both distributions decreases downstream.

Figures 10(*a*) and (*b*) are contour maps of the crossflow momentum thicknesses for b_s/b_e = 3.7 and 1.9, which represent the skewed nature of the boundary layer. Both figures represent developments in the turning duct and the inlet region of the scroll. However, these developed boundary layers have been convected to the nozzle region as far as section 8 especially for b_s/b_e = 3.7. It seems that a region of large crossflow momentum thickness in Fig. 10(*a*) is generated by the region of a thick streamwise momentum thickness after the tongue in Fig. 9(*d*). Near the inner wall represented by a broken line, however, a rapid increase, which is not caused by the wake of the tongue, is observed for b_s/b_e = 1.9 indicating the strong secondary flow phenomena. Below section 9 or 10, the distributions of the boundary layer show axisymmetric nature, which indicates that generation and transportation of the boundary layer are balanced downstream in the scroll. One can analyze scroll boundary layer by simple axisymmetric theory for this region (Hara et al., 1991); however, it is found that three-dimensional boundary layer treatment or Navier–Stokes analysis is required to estimate the whole flow field of the scroll.

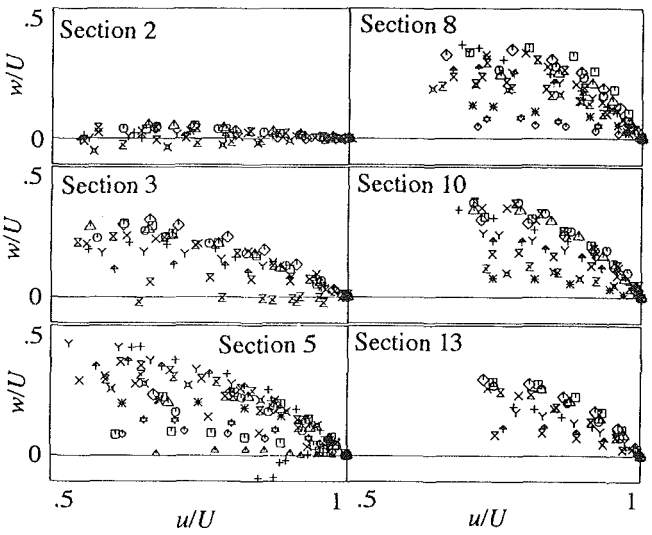

Fig. 8 Polar diagram of boundary layer

Streamlines were drawn to express the path of the transportation of boundary layer fluid on the front wall in Fig. 11. We used the flow angles of the closest measuring points to the wall, which had been found to be almost equivalent to the limiting streamline by applying the experimental data to Mager's (1952) velocity profile of the skewed boundary layer. All the streamlines inside the side wall boundary layer at section 1 reach to the nozzle as far as section 6 indicating a strong inward radial transportation of the boundary layer fluid. Although there is displayed a streamline pattern only for b_s/b_e = 3.7, they are surprisingly similar for other b_s/b_e ratios regardless of the difference of secondary flow energy of Fig. 6 and the crossflow momentum thickness distributions of Fig. 10. This looks like a contradiction; however, the main flow direction for small b_s/b_e ratio is near peripheral or negative to make the skew angle large.

The blockage factor of the scroll passage originating in the front and rear wall boundary layer can be evaluated from

$$B = \int_{r_h}^{r_s} (U_f\delta_{\theta f} + U_r\delta_{\theta r})dr \Big/ \frac{b_s}{2}\int_{r_h}^{r_s} (c_{\theta f} + c_{\theta r})dr \qquad (7)$$

where $\delta_{\theta f}$ and $\delta_{\theta r}$ are the front and rear wall peripheral displacement thickness given by coordinate transformation of Eq. (A9). $c_{\theta f}$ and $c_{\theta r}$ are front and rear wall peripheral velocity at the boundary layer edge. The denominator of the equation represents the sectional flow rate of the scroll passage without the boundary layer. The result is shown in Fig. 12 for all b_s/b_e ratios. Owing to the accelerating flow, the value of the blockage factor is so small that correction of the flow area of the scroll passage is hardly needed. Although the blockage factors in the inlet region depend on the incoming boundary layer, the factor decreases gradually below section 8 caused by the inward radial transportation of the boundary layer.

Boundary Layer and Flow Properties at the Nozzle. Figure 13 represents the distribution of peripheral and radial displacement thicknesses at the nozzle, which are also given by coordinate transformation from the streamline coordinate val-

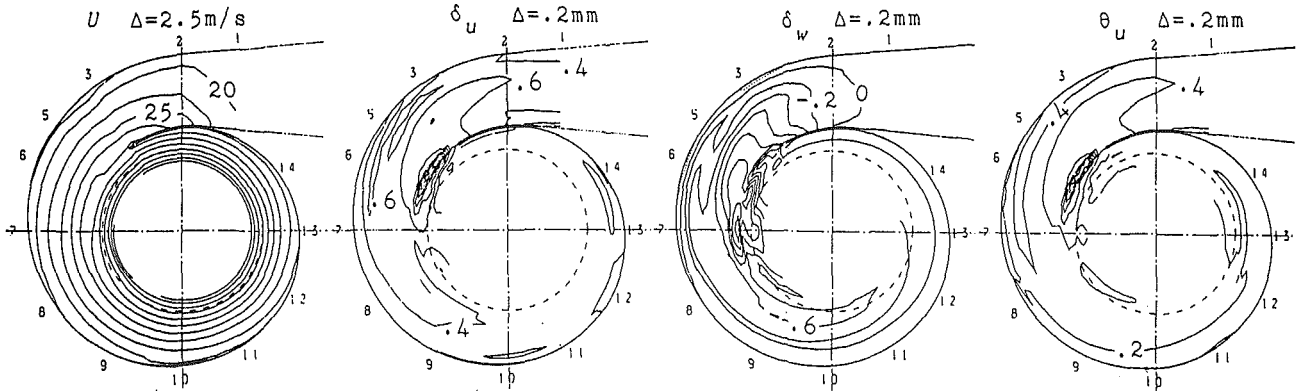

(a) Streamwise velocity at boundary layer edge
(b) Streamwise displacement thickness
(c) Cross-flow displacement thickness
(d) Streamwise momentum thickness

Fig. 9 Contours of boundary layer parameters

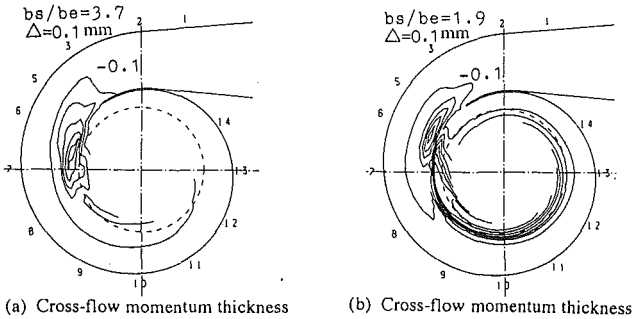

(a) Cross-flow momentum thickness (b) Cross-flow momentum thickness

Fig. 10 Contour of crossflow momentum thicknesses

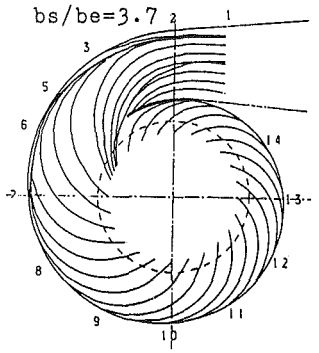

Fig. 11 Front wall streamline

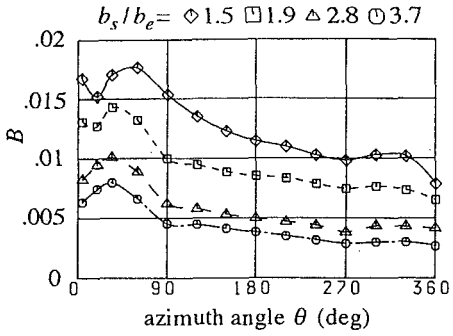

Fig. 12 Blockage distribution

ues. Since the inward radial velocity in the boundary layer is greater than that of the mainstream, the value of radial displacement thickness is negative. The radial boundary layer thickness distributions of the front and rear wall are shown separately in Fig. 13(*a*). For b_s/b_e = 3.7, we can see clearly the locations at which the incoming boundary layers issue. For front wall, the location coincides with the result of streamline observation in Fig. 11. Although all the streamlines inside the incoming boundary layer of the front wall seem to issue at near θ = 45 deg, the location can not be seen clearly for b_s/b_e = 1.5 and 1.9, and they are hidden by the development of boundary layer itself. For rear wall and b_s/b_e = 3.7, the location is considered to be θ = 120 deg. This difference is based on the asymmetric scroll cross-sectional configuration, because the incoming boundary layer on the rear wall must be carried over the inner wall surface. As the geometric asymmetry becomes small, the difference decreases for small b_s/b_e ratio.

Figure 14 represents the peripheral distribution of nozzle flow properties, which are obtained by mass flow weighted average of the nozzle flow field. The definitions should be referred to the appendix. One can find that the nozzle flow fields for every flow condition are nonuniform in the peripheral direction and are influenced by the boundary layer. The high loss region and the peripheral velocity defect are seen where

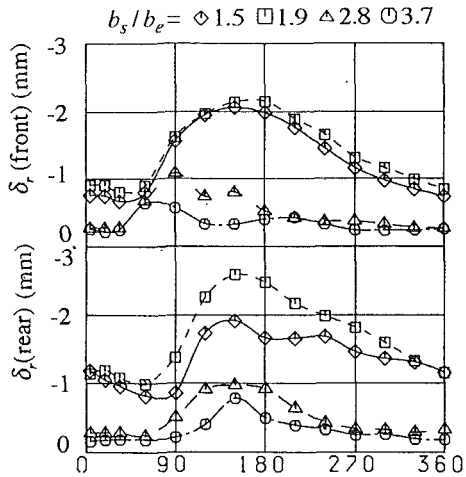

(a) Radial displacement thickness of front and rear wall

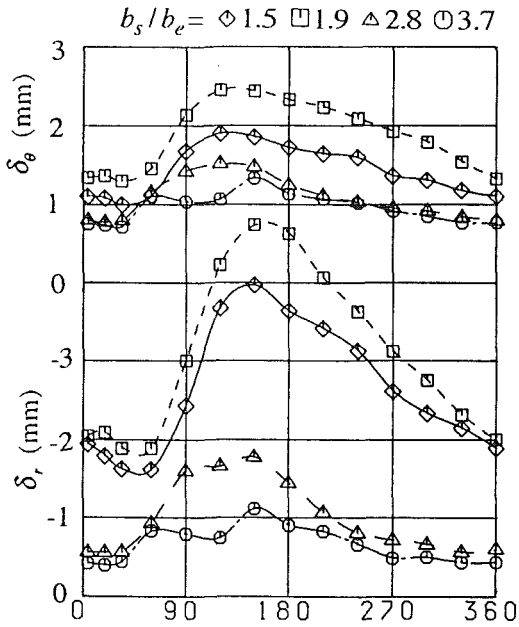

(b) Radial and peripheral displacement thickness distribution

Fig. 13 Distribution of displacement thickness at the nozzle

boundary layers are thick. Comparing the distributions of peripheral velocity and peripheral displacement thickness in Fig. 13(*b*) for b_s/b_e = 3.7, it is found that the nozzle flow field is influenced by the incoming boundary layer.

The radial velocity distribution nondimensionalized by mean radial velocity is shown in Fig. 14. It may be easy to understand the flow phenomena, if the radial velocity increases to satisfy the radial equilibrium condition at the position where peripheral velocity decreases. However, the position of maximum radial velocity does not coincide with the minimum peripheral velocity and is not extremely influenced by the b_s/b_e ratio. According to an inviscid calculation by the authors (Furukawa et al., 1991), the nozzle flow property fairly varies in peripheral direction. The present scroll, which is designed by the condition of linear decrement of sectional flow rate, may inherently have a nonuniform velocity distribution.

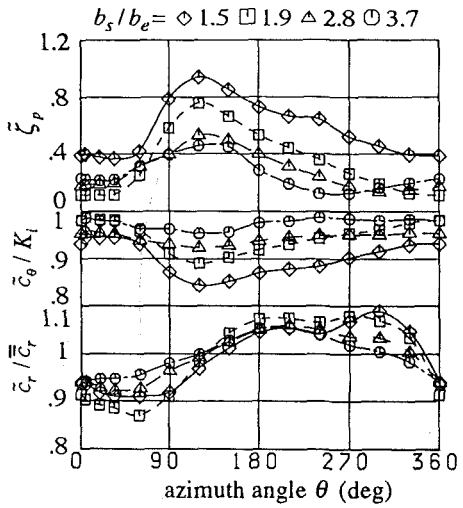

Fig. 14 Flow property at the nozzle

Conclusion Remarks

In this experimental study, the most characteristic behavior of the three-dimensional boundary layer in a radial inflow turbine scroll has been clarified by analyzing the secondary flow kinetic energy distribution, the blockage factor distribution, the contour maps of the boundary layer integral parameters, and the streamlines in the boundary layer. In the inlet region of the scroll where the free vortex flow field is already formed, the incoming boundary layer begins to have a skewed nature, namely, radially inward secondary flow caused by the radial pressure gradient. The radial mass flux in the boundary layer is larger than that in the mainstream because of the radially inward secondary flow. From the inlet region to one third of the scroll circumference, the secondary flow grows so strongly that the most of the low-momentum fluids in the incoming boundary layer are transported to the nozzle region. The successive transportation of the low-momentum fluids in the boundary layer suppresses growth of the boundary layer farther downstream, where the boundary layer shows a similarity of velocity profile. The distributions of the boundary layer properties in the scroll correspond well to those of the flow properties at the nozzle. This implies that the circumferential nonuniformity of the nozzle flow field is strongly affected by the behavior of the boundary layer in the scroll.

References

Furukawa, M., Fukui, K., Hara, K., and Inoue, M., 1991, "Outflow Boundary Conditions for Euler Analysis of Flow in Turbine Scroll," *Proceedings of the First ASME-JSME Fluids Engineering Conf.*, FED-Vol. 120.

Hara, K., Furukawa, M., Shimada, M., Abe, H., Matsuo, E., and Inoue, M., 1991, "Development of Three-Dimensional Boundary Layers in a Turbine Scroll," *Proceedings of the 91-YOKOHAMA-IGTC*, Vol. 2.

Inoue, M., Hara, K., and Furukawa, M., 1987, "Experimental Study on the Three-Dimensional Flow Field in a Turbine Scroll," *Proceedings of the 87-TOKYO-IGTC*, Vol. 2.

Mager, A., 1992, "Generalization of Boundary-Layer Momentum Integral Equations to Three-Dimensional Flows Including Those of Rotating Systems," NACA Report 1067.

Malak, M. F., Hamed, A., and Tabakoff, W., 1987, "Three-Dimensional Flow Field Measurements in a Radial Inflow Turbine Scroll Using LDV," ASME JOURNAL OF TURBOMACHINERY, Vol. 109, pp. 163–169.

Miller, E. C., L'Ecuyer, M. R., and Benisek, E. F., 1988, "Flow Field Surveys at the Rotor Inlet of a Radial Inflow Turbine," ASME *Journal Engineering for Gas Turbines and Power*, Vol. 110, pp. 552–561.

Tabakoff, W., Vittal, B. V. R., and Wood, B., 1984, "Three-Dimensional Flow Measurements in a Turbine Scroll," ASME *Journal Engineering for Gas Turbines and Power*, Vol. 106, pp. 516–522.

Vu, T., and Shyy, W., 1990, "Viscous Flow Analysis as a Design Tool for Hydraulic Turbine Components," ASME *Journal of Fluids Engineering*, Vol. 112, pp. 5–11.

APPENDIX

Total pressure loss coefficient is nondimensionalized by dynamic pressure of mean inlet velocity as

$$\zeta_p = 2(P_0 - P_t)/\rho c_i^2 \tag{A1}$$

where P_0 is plenum total pressure, P_t is local total pressure.

Weighting average of physical property q is calculated by using weight g for which ρ is selected for radial velocity c_r and ρc_r is selected for others. Axial distribution averaged in the peripheral direction is

$$\overline{q} = \int_0^{2\pi} gqd\theta / \int_0^{2\pi} gd\theta \tag{A2}$$

Peripheral distribution averaged in the axial direction is

$$\overline{q} \int_0^{b_e} gqd\theta / \int_0^{b_e} gd\theta \tag{A3}$$

Total average is defined by

$$\overline{\overline{q}} = \int_0^{2\pi} \int_0^{b_e} gqdzd\theta / \int_0^{2\pi} \int_0^{b_e} gdzd\theta \tag{A4}$$

Streamwise displacement thickness is

$$\delta_u = (1/U) \int_0^{\delta} (U-u)dy \tag{A5}$$

Crossflow displacement thickness is

$$\delta_w = (1/U) \int_0^{\delta} wdy \tag{A6}$$

Streamwise momentum thickness is

$$\theta_u = (1/U^2) \int_0^{\delta} u(U-u)dy \tag{A7}$$

Crossflow momentum thickness is

$$\theta_w = (-1/U^2) \int_0^{\delta} w^2 dy \tag{A8}$$

Peripheral displacement thickness is related to streamwise and crossflow displacement thickness, by referring to Fig. A1, as

$$\delta_\theta = \delta_u \cos\alpha - \delta_w \sin\alpha \tag{A9}$$

Radial displacement thickness is

$$\delta_r = \delta_u \sin\alpha + \delta_w \cos\alpha \tag{A10}$$

where α is a flow angle at the boundary layer edge.

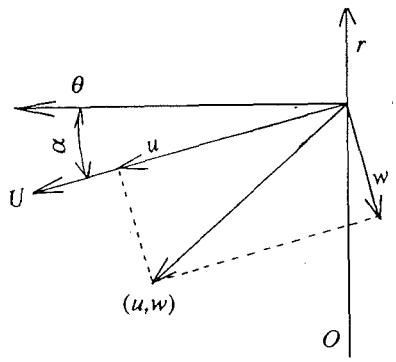

Fig. A1 Relationship between streamline and cylindrical coordinate

Detailed Flow Measurements in a Centrifugal Compressor Vaneless Diffuser

A. Pinarbasi
Department of Mechanical Engineering,
University of Cumhuriyet,
Sivas, Turkey

M. W. Johnson
Department of Mechanical Engineering,
University of Liverpool,
Liverpool, United Kingdom

Hot-wire anemometer measurements have been made in the vaneless diffuser of a 1-m-dia low-speed backswept centrifugal compressor using a phase lock loop technique. Radial, tangential, and axial velocity measurements have been made on eight measurement planes through the diffuser. The flow field at the diffuser entry clearly shows the impeller jet-wake flow pattern and the blade wakes. The passage wake is located on the shroud side of the diffuser and mixes out slowly as the flow moves through the diffuser. The blade wakes, on the other hand, distort and mix out rapidly in the diffuser. Contours of turbulent kinetic energy are also presented on each of the measurement stations, from which the regions of turbulent mixing can be deduced.

Introduction

The overall efficiency of a centrifugal compressor is equally dependent on the good design of both impeller and diffuser. In the case of an impeller, the inlet flow is uniform; however, the diffuser must accept the outlet flow from the impeller, which is usually highly nonuniform with significant three-dimensional velocity components. The diffuser must remove these nonuniformities in velocity and flow direction while reducing the overall kinetic energy of the flow to produce a pressure recovery.

The flow at the exit of a centrifugal impeller has been measured by many authors (e.g., Eckardt, 1975; Johnson and Moore, 1983a, b; Krain, 1988). The flow invariably exhibits a jet-wake flow pattern, although the location of the wake position may be on the suction surface or the shroud depending on the impeller geometry and flow rate. The flow within vaneless diffusers has also been studied by many researchers (e.g., Inoue and Cumpsty, 1984; Maksoud and Johnson, 1987; Mounts and Brasz, 1992). These studies have shown how nonuniformities in the circumferential direction mix out rapidly, but those in the axial direction persist through the diffuser.

The objective of the current work was to repeat the work of Maksoud and Johnson (1987) but with a backswept impeller in place of their radial impeller. The resolution capability of the instrumentation system was also improved such that the number of points used on each measurement plane could be increased from less than 100 to around 700.

Experimental Procedure

Test Rig and Operating Condition. Experiments were carried out on the low-speed centrifugal compressor rig at the University of Liverpool. A schematic of the facility is shown in Fig. 1. The De Havilland Ghost impeller has been modified by replacing the original radial exit section of the blading by 30 deg backswept blading. The geometry of the original impeller is given by Johnson and Moore (1980) and that of the backswept blading in Fig. 2. The vaneless diffuser has straight walls and a constant cross-sectional area. The major geometric parameters, operating conditions, and measurement locations are given in Table 1.

Instrumentation and Measurement Technique

A constant-temperature hot-wire anemometer was used to measure the instantaneous velocity within the diffuser. Three wire orientations were used on three separate test runs to pro-

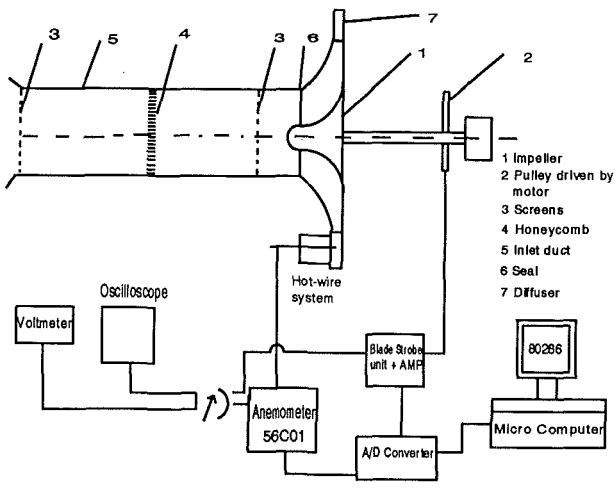

Fig. 1 Schematic of the test rig

Contributed by the International Gas Turbine Institute and presented at the 38th International Gas Turbine and Aeroengine Congress and Exposition, Cincinnati, Ohio, May 24–27, 1993. Manuscript received at ASME Headquarters February 19, 1993. Paper No. 93-GT-95. Associate Technical Editor: H. Lukas.

vide data from which the radial, axial, and tangential velocity components could be computed. A normal wire (Dantec 55P11) oriented in the circumferential direction was used during the first run and then a second wire set at 45 deg (Dantec 55P12) was used in its two possible orientations in the axial/radial plane, in the second and third runs. This choice of mutually perpendicular wire orientations ensured that the sign of the axial velocity component could be determined, which would not have been possible if the simplest orientation of wires in the circumferential, radial, and axial direction had been utilized. It was however necessary to assume that the radial velocity component was always positive and that the tangential velocity component was always in the direction of impeller rotation. The results showed that these assumptions were justified in that both velocity components maintained significant magnitudes at all measurement positions.

Hot-wire calibration was performed in two stages in a wind tunnel. First, a velocity/voltage calibration was performed for each wire with the wire perpendicular to the flow direction. A least rms error curve fitting technique to the King's law equation

$$E^2 = A + B \cdot U_e^c \tag{1}$$

was then employed to determine the calibration coefficients A, B, and C.

The second stage of calibration was necessary to determine the directional coefficients K and H to tangential and binormal velocity components. This was achieved by varying the wire

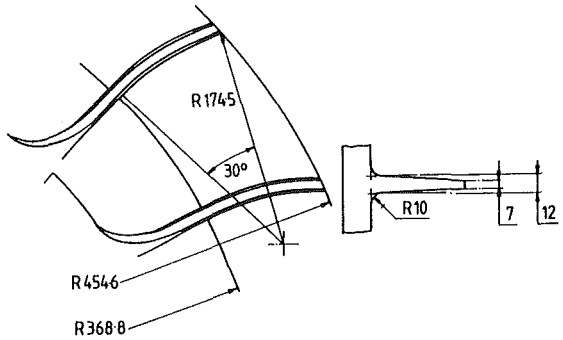

Fig. 2 Backswept blade geometry

Table 1 Geometry, operating condition, and measurement locations

Impeller Geometry and Operating Condition:

Inlet blade radius at the hub	R_h = 88.75 mm
Inlet blade radius at the shroud	R_s = 283.75 mm
Outlet radius	R_o = 454.6 mm
Backswept blade angle	β = 30°
Number of the blades	N = 19
Outlet blade span	b = 72.3 mm
Rotating speed	n = 500 rpm
Flowrate	Q = 0.142 kg/s

Measurement Locations:

Station	1	2	3	4	5	6	7	8
L/R_o	0.02	0.08	0.15	0.21	0.27	0.33	0.39	0.45

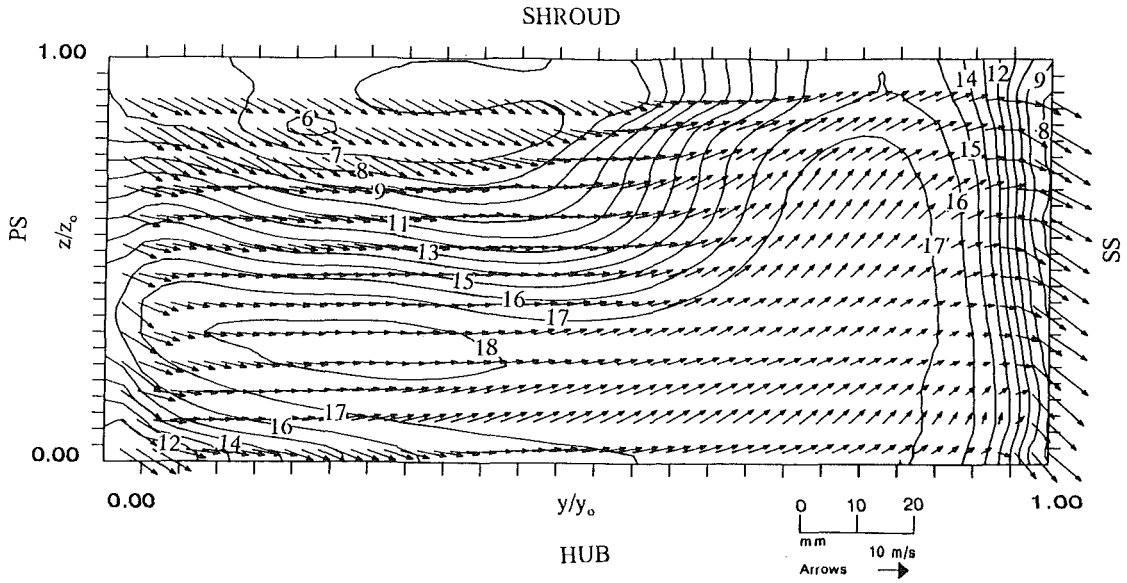

Fig. 3 Mean velocities at station 1 ($L/R_o = 0.02$)

Nomenclature

A, B, C = King's law calibration coefficients
E = hot-wire anemometer voltage
H, K = directional coefficients for hot wire
L = radial distance from impeller outlet
R_o = impeller outlet radius
U_e = effective cooling velocity
u_θ, u_r, u_z = tangential, radial, and axial mean velocity components
u_θ', u_r', u_z' = tangential, radial, and axial rms fluctuating velocity components
U_T = peripheral blade velocity at the impeller outlet
y/y_o = circumferential coordinate
z/z_o = axial coordinate

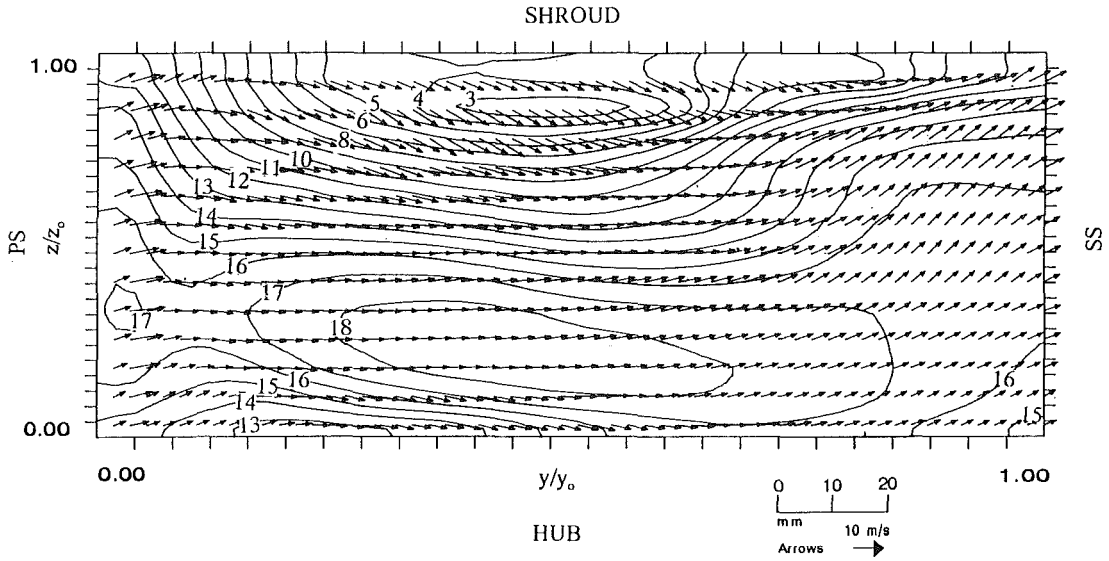

Fig. 4 Mean velocities at station 2 ($L/R_o = 0.08$)

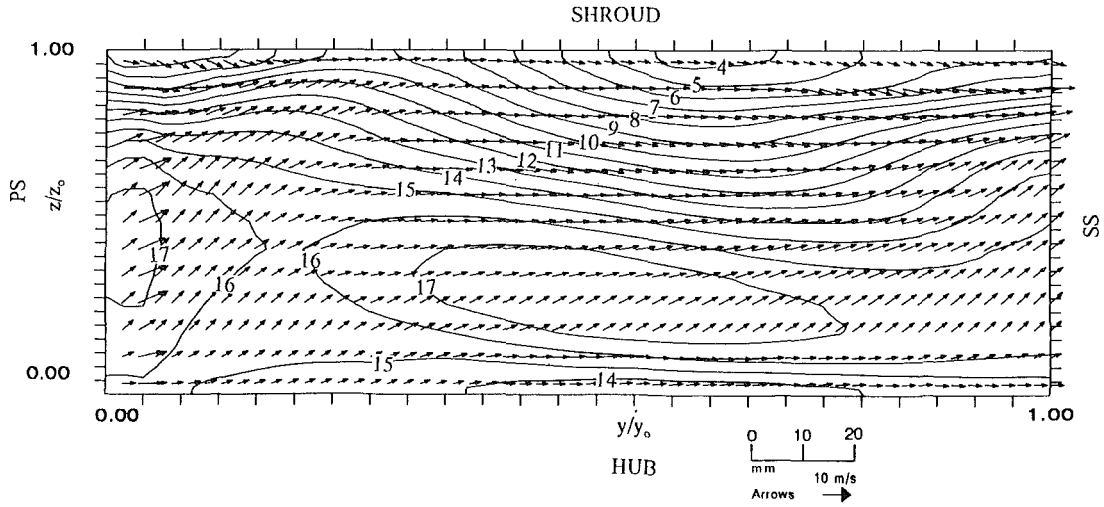

Fig. 5 Mean velocities at station 3 ($L/R_o = 0.15$)

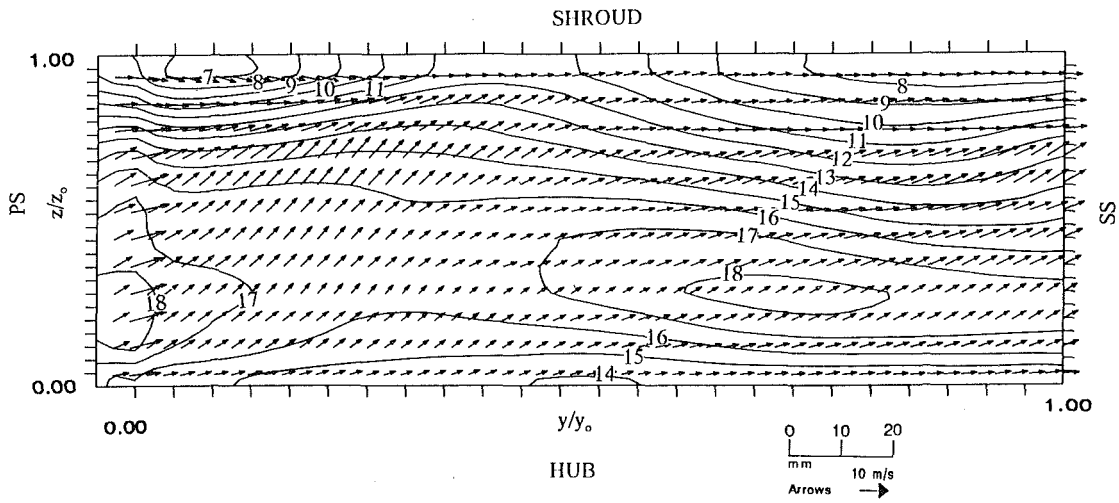

Fig. 6 Mean velocities at station 4 ($L/R_{oi} = 0.21$)

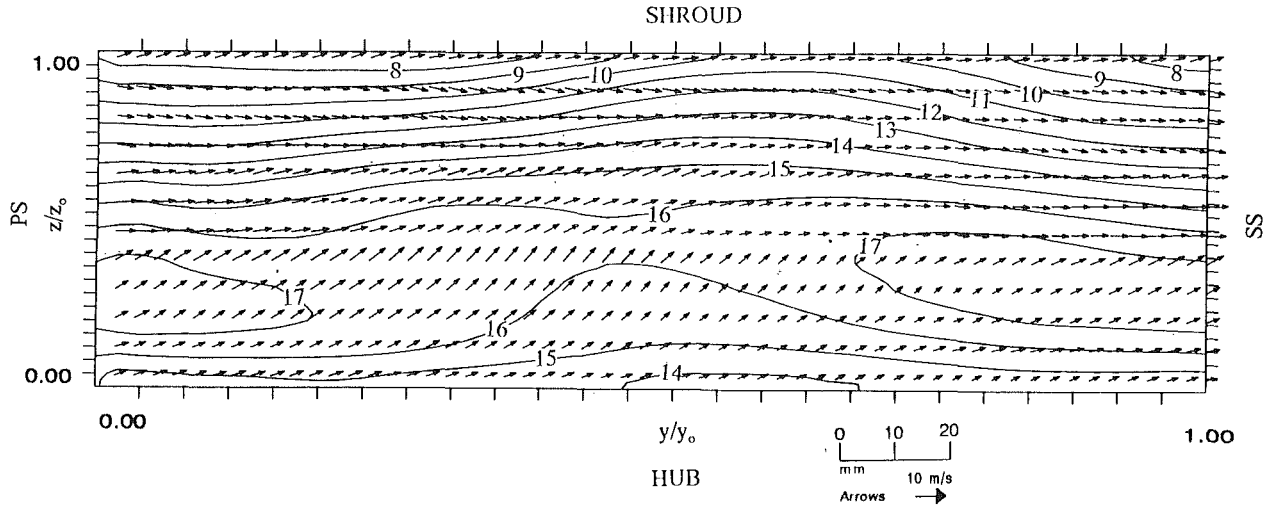

Fig. 7 Mean velocities at station 5 ($L/R_o = 0.27$)

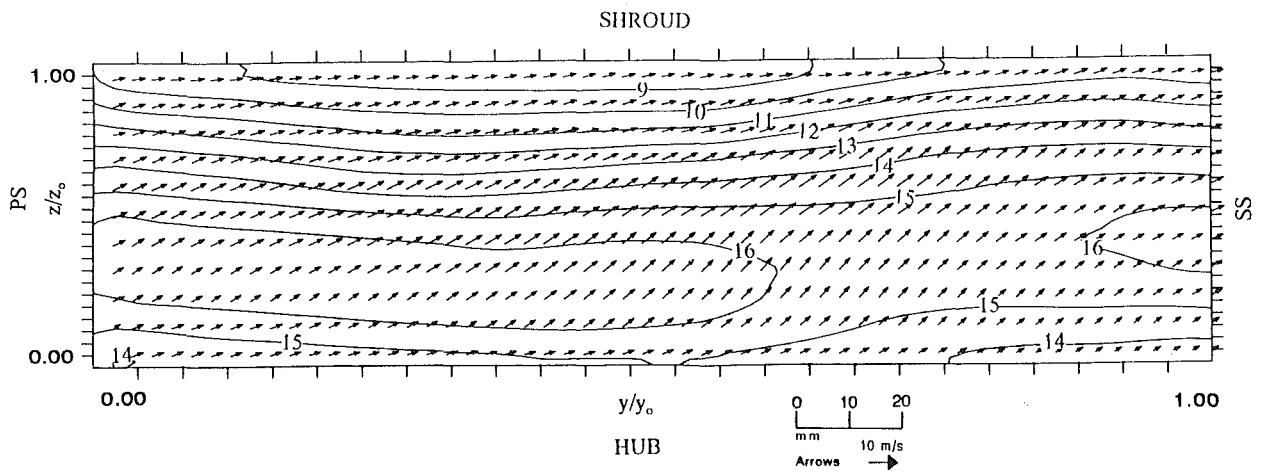

Fig. 8 Mean velocities at station 6 ($L/R_o = 0.33$)

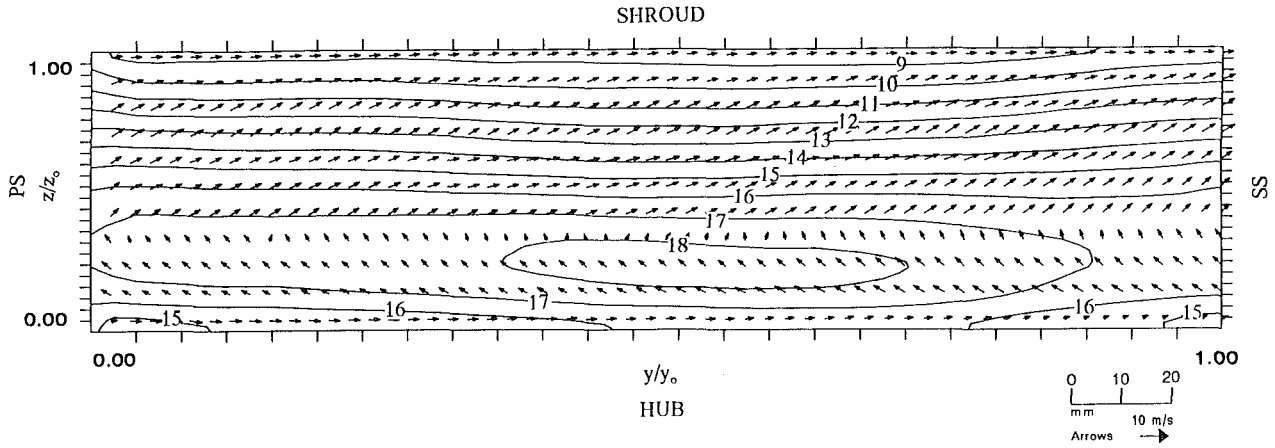

Fig. 9 Mean velocities at station 7 ($L/R_o = 0.39$)

orientation at fixed wind tunnel speed. The coefficients K and H were also obtained through a least rms error technique. The calibration procedure is similar to that detailed by Jøngensen (1971).

Phase lock loop circuitry was employed on the rig to generate a pulse every one third of a degree of rotation of the impeller to trigger the collection of the instantaneous hot-wire anemometer voltage through a 12 bit A/D converter connected to an 80286 microcomputer. On each revolution 57 readings were taken at 1/3 deg intervals to span the chosen impeller passage. These readings were recorded on each of 250 consecutive revolutions. This required a peak data acquisition rate of 9 kHz, which was achieved by means of 80286 machine code software. Between 11 and 13 axial measurement positions were used to complete the mesh of data points covering each measurement plane.

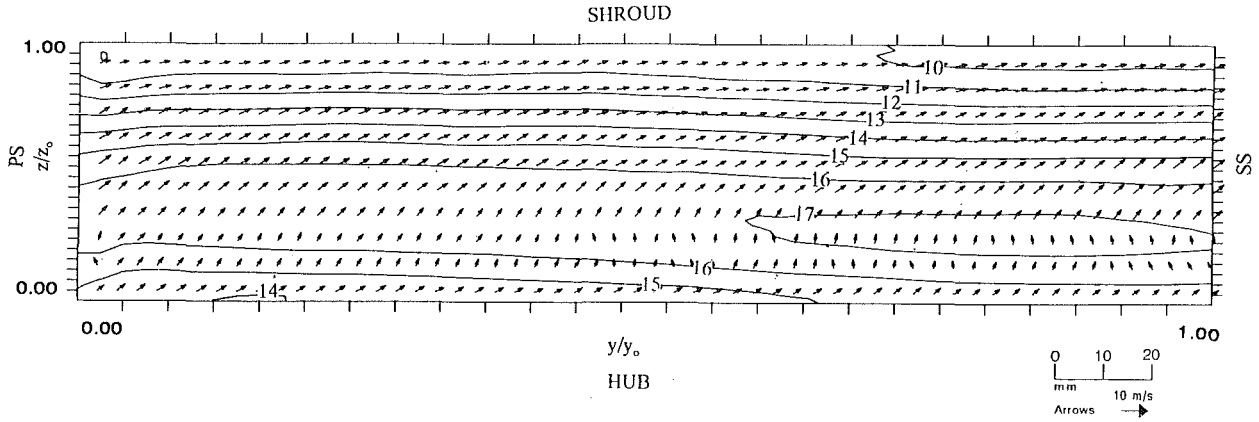

Fig. 10 Mean velocities at station 8 ($L/R_o = 0.45$)

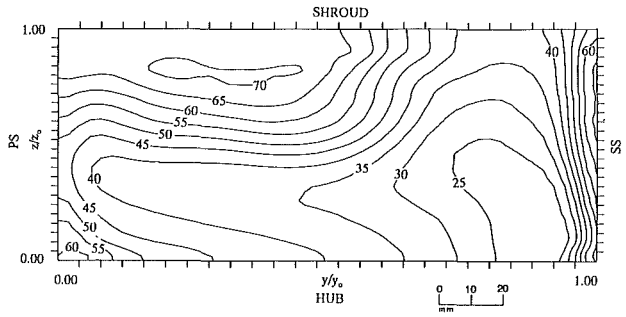

Fig. 11 Flow angle at station 1 ($L/R_o = 0.02$)

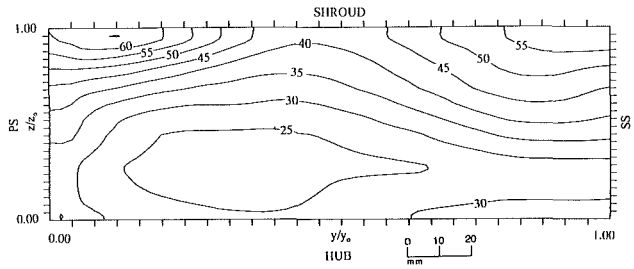

Fig. 14 Flow angle at station 4 ($L/R_o = 0.21$)

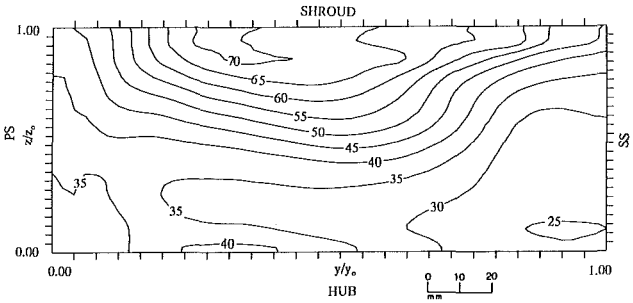

Fig. 12 Flow angle at station 2 ($L/R_o = 0.08$)

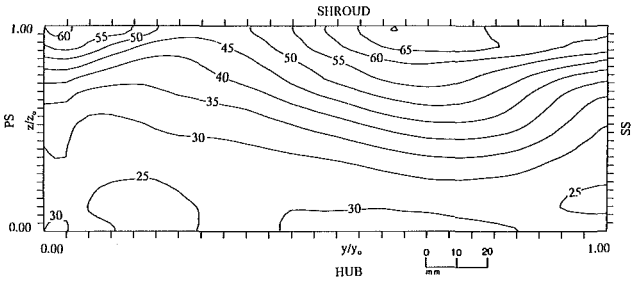

Fig. 13 Flow angle at station 3 ($L/R_o = 0.15$)

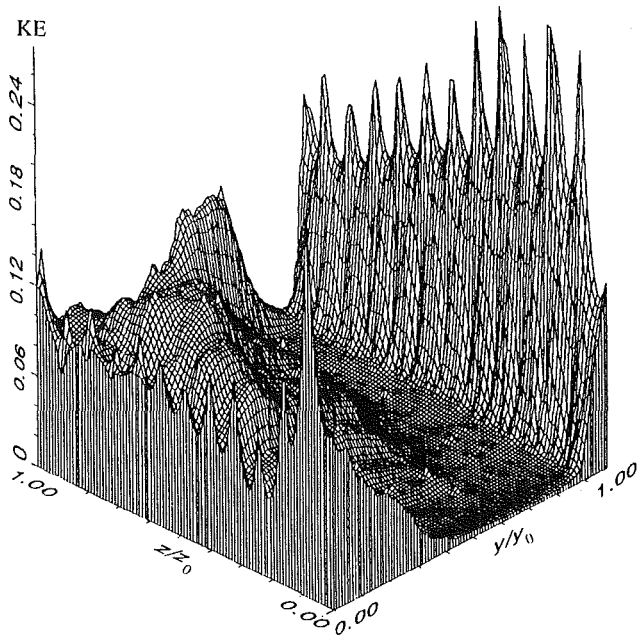

Fig. 15 Turbulent kinetic energy at station 1 ($L/R_o = 0.02$)

Analysis of Results. The 250 readings obtained for each measurement point on each of the three test runs were used to compute the tangential, radial, and axial velocity components and the turbulent kinetic energy using the King's law calibrations and the directional coefficients K and H.

As a check on the accuracy of the results, the flow rate was determined through numerical integration of the radial velocity component. The maximum deviation in flow rate between stations was found to be 4.8 percent from the mean.

Experimental Results

Mean Velocities. The mean velocities on the eight measurement planes in the diffuser are presented in Figs. 3–10. The radial velocity component is presented as a contour and the remaining velocity component in the measurement plane is shown as an arrow.

The flow pattern at Station 1 (Fig. 3), which is 12 mm downstream of the impeller, is similar to that observed at the last station within the impeller as reported by Farge and John-

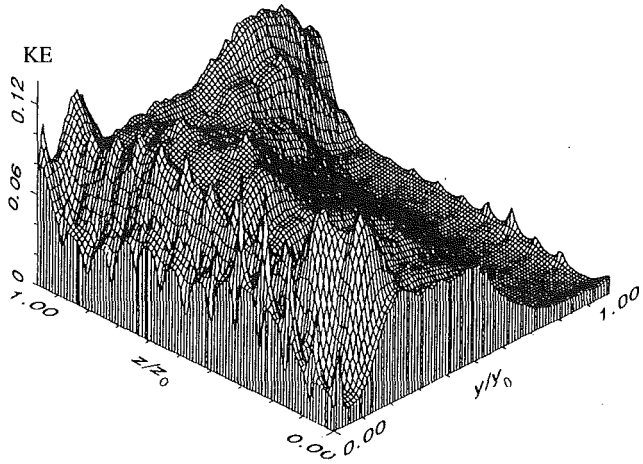

Fig. 16 Turbulent kinetic energy at station 2 ($L/R_o = 0.08$)

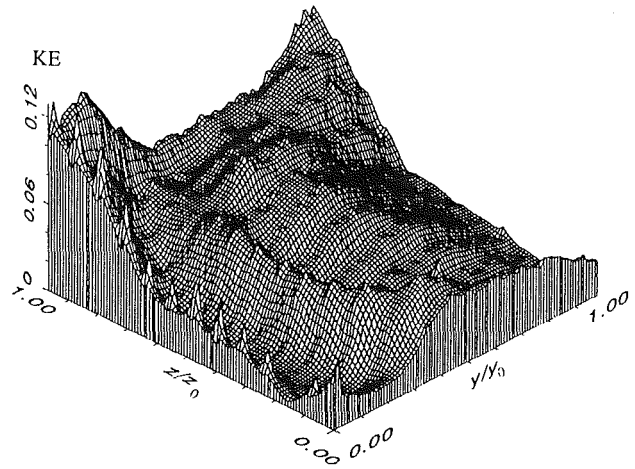

Fig. 17 Turbulent kinetic energy at station 3 ($L/R_o = 0.15$)

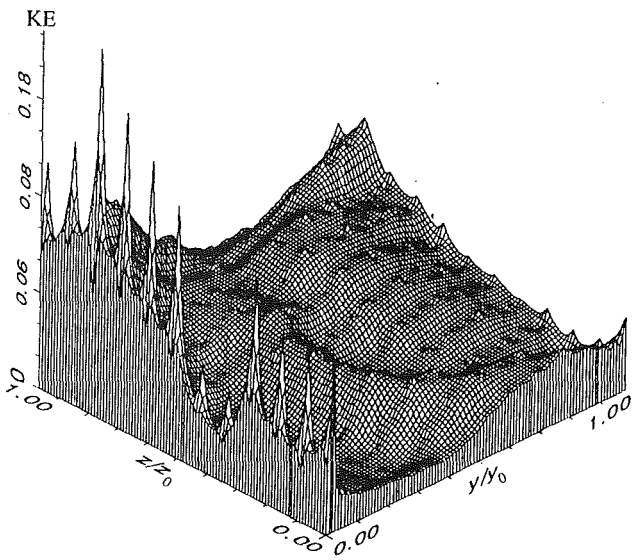

Fig. 18 Turbulent kinetic energy at station 4 ($L/R_o = 0.21$)

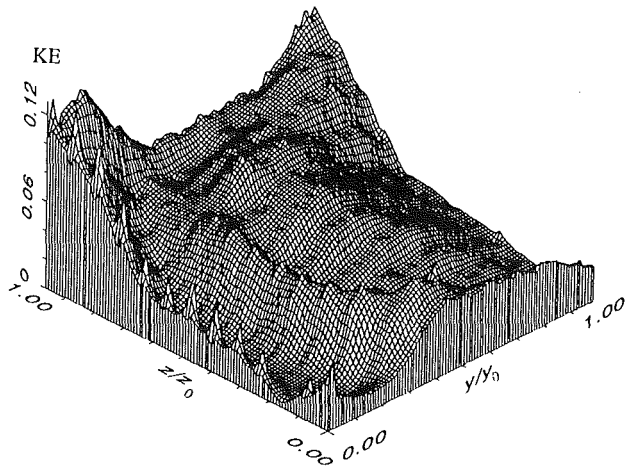

Fig. 19 Turbulent kinetic energy at station 5 ($L/R_o = 0.27$)

son (1990). Strong secondary flows in the impeller strip boundary layer fluid from the walls and carry it to the suction side shroud corner region where it accumulates in a passage wake. At the exit of the impeller this passage wake is located close to the center of the shroud wall and is moving toward the pressure side wall. In Fig. 3, the passage wake is on the shroud wall, and has moved close to the pressure side of the passage. Another feature of the impeller flow reported by Farge and Johnson (1990) and also by Krain (1988) in his backswept impeller is the presence of a strong anticlockwise passage vortex. This feature is also depicted in Fig. 3 as opposing axial flow vectors in the pressure side and suction side halves of the passage. The axial flow in the shroud to hub direction is particularly strong within the blade wake ($0.95 < y/y_o < 1$). In addition to these features observed in the impeller, a blade wake can also be seen on the right-hand side of the diagram. The velocity decreases by up to 53 percent within this wake. When the flow at station 2 (Fig. 4) is considered, it can be seen that the blade wake has been swept to the right by the strong tangential velocity component, such that the blade wake observed in Fig. 3 leaves the right-hand side of the diagram while the blade wake from the adjacent blade enters on the left-hand side. The deficit in velocity in the blade wake is also greatly diminished, indicating rapid mixing out in this region. This can be attributed to the strong opposed secondary velocity components that exist either side of the blade wake, which will greatly increase the shearing of the wake flow. The passage wake has been carried along the shroud by the tangential velocity, while altering little in size. However, the wake's shape has been modified as the low-energy fluid has spread farther along the shroud surface. Mixing out of the passage wake has not been significantly enhanced here by the interaction between the flow from neighboring passages; however, this is probably not the case in radial impellers running at below design flow rates where the passage wake is on the suction side blade surface at the impeller exit (see Johnson and Moore, 1983b). The strength of the passage vortex has diminished, which is primarily because the driving forces that produce secondary flow cease on exit from the impeller such that the passage vortex decays rapidly due to viscous dissipation.

At station 3 (Fig. 5), the blade wake is barely discernible at $y/y_o \cong 0.2$, but has continued to migrate in the pressure side to suction side direction. The passage wake has also continued to move in this same direction across the shroud. It is interesting to note that the wake moves in this direction more rapidly than the high-velocity jet (located at $y/y_o = 0.5$, $z/z_o = 0.3$). This is because the jet had a much higher relative tangential velocity than the wake in the impeller, which led to a lower absolute tangential velocity in the diffuser. The associated difference in flow angle ($\tan^{-1}(u_\theta/u_r)$) between jet and wake is marked (Figs. 11–14) and is of particular significance in the design of vaned diffusers where a compensatory variation in the vane angle across the span would be beneficial in minimizing flow separation. As the flow progresses through stations 4 to 8, variations in the blade to blade direction are gradually mixed out, and the passage wake eventually spreads out to cover the

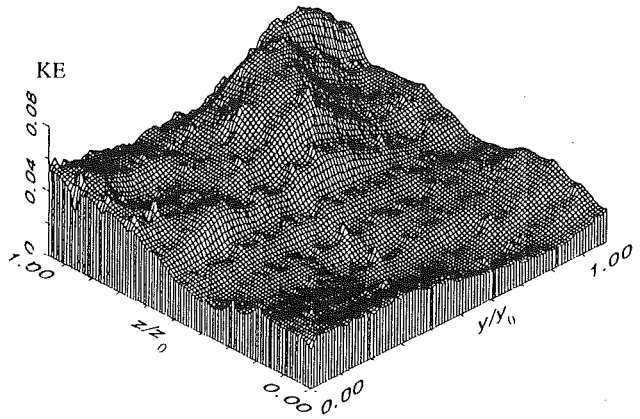

Fig. 20 Turbulent kinetic energy at station 6 ($L/R_o = 0.33$)

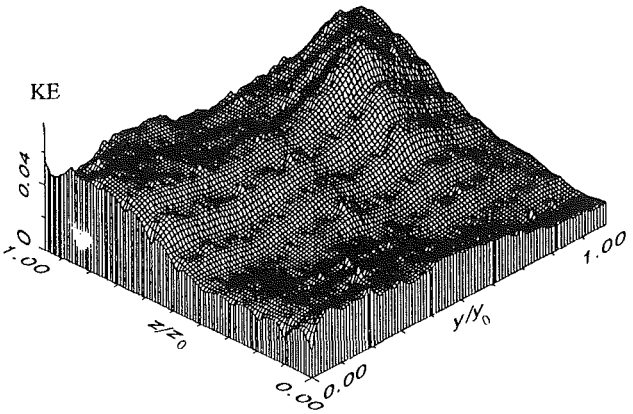

Fig. 21 Turbulent kinetic energy at station 7 ($L/R_o = 0.39$)

whole of the shroud surface fairly evenly. The hub wall boundary layer also develops slowly and although it is still thinner than the shroud boundary layer at station 8 (Fig. 10), the flow is tending toward a fully developed Couette flow between the two walls of the diffuser. A significant tangential velocity component still exists at station 8, but its magnitude is only some 30 percent of the value at station 1.

Turbulent Kinetic Energy. Distributions of turbulent kinetic energy are given in Figs. 15–22. The turbulent kinetic energy is defined as

$$\frac{\sqrt{u_\theta'^2 + u_r'^2 + u_z'^2}}{2.U_T} \tag{2}$$

where u_θ', u_r', u_z' are the tangential, radial, and axial rms fluctuating velocity components and U_T is the peripheral blade velocity at the impeller outlet.

High levels of turbulent kinetic energy occur not only in regions of mixing, but also in regions of unsteady flow where the fluctuations are of low frequency and do not result in significant Reynolds stresses. At station 1 (Fig. 15), similarly high levels of turbulent kinetic energy are observed in the blade and passage wakes. The rapid mixing out of the blade wake suggests that high Reynolds stresses are associated with the kinetic energy in the blade wake. However, in the passage wake the relatively slow mixing out rate suggests that only low Reynolds stress levels are present and the high levels of kinetic energy are due to low-frequency meandering of the wake position. This type of behavior has also been suggested by Hathaway et al. (1993) and is most likely due to low-frequency variations in flow rate, which will cause significant variations in wake position (Farge and Johnson, 1992). At station 2 (Fig. 16) the levels of kinetic energy are significantly decreased in the blade

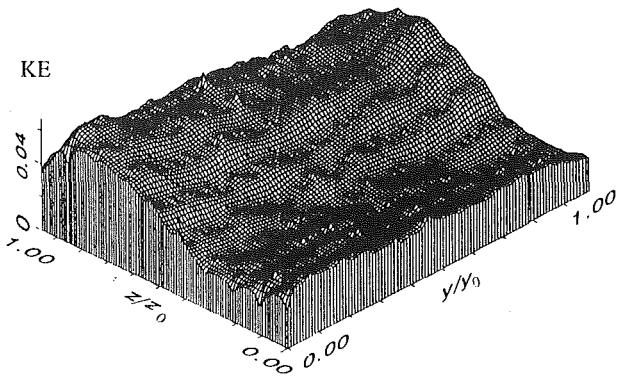

Fig. 22 Turbulent kinetic energy at station 8 ($L/R_o = 0.45$)

wake, which has now largely mixed out. The kinetic energy levels in the passage wake have only decreased a little from station 1 as might be expected as the wake has not significantly decreased in size. As the flow passes through the remaining stations (Figs. 17–22), the kinetic energy level in the passage wake decreases about threefold. The authors believe that this is not due to a significant decrease in the meandering of the wake in the tangential direction, but is due to the rapid decrease in the nonuniformities in this direction. This results in low fluctuating velocities as tangential movement of the passage wake does not result in significant variation in the velocity at any measurement point.

Conclusions

1 The flow entering the diffuser closely resembles that reported previously leaving the impeller. The most prominent features of the flow are a passage wake close to the center of the shroud wall and a strong anticlockwise passage vortex.

2 A strong blade wake is observed at station 1, but mixes out very rapidly because of the shearing effect of the opposed secondary flows either side of the wake. High levels of measured turbulent kinetic energy are associated with this process.

3 The passage wake mixes out only slowly. Although high levels of turbulent kinetic energy are observed within the passage wake, they are believed to result from low-frequency meandering of the wake position rather than high levels of Reynolds stress.

4 The passage vortex, characteristic of backswept centrifugal impeller flows, carries over to the diffuser, but decays fairly rapidly in the absence of the secondary flow mechanisms present in the impeller.

5 As the flow progresses through the impeller, variations in the tangential direction mix out, but variations in the axial direction tend to persist. The flow eventually resembles a Couette flow between the walls of the diffuser.

References

Eckardt, D., 1975, "Instantaneous Measurements in the Jet-Wake Discharge Flow of a Centrifugal Compressor Impeller," ASME *Journal of Engineering for Power*, Vol. 97, pp. 337–346.

Farge, T. Z., and Johnson, M. W., 1990, "The Effect of Backswept Blading on the Flow in a Centrifugal Compressor Impeller," ASME Paper No. 90-GT-231.

Farge, T. Z., and Johnson, M. W., 1992, "Effect of Flow Rate on Loss Mechanisms in a Backswept Centrifugal Impeller," *Int J. Heat Fluid Flow*, Vol. 13, No. 2, pp. 189–196.

Hathaway, M. D., Chriss, R. M., Wood, J. R., and Strazisar, A. J., 1993, "Experimental and Computational Investigation of the NASA Low-Speed Centrifugal Compressor Flow Field," ASME JOURNAL OF TURBOMACHINERY, Vol. 115, pp. 527–542.

Inoue, M., and Cumpsty, N. A., 1984, "Experimental Study of the Centrifugal Impeller Discharge Flow in Vaneless Diffusers," ASME *Journal of Engineering for Gas Turbines and Power*, Vol. 106, pp. 455–467.

Johnson, M. W., and Moore, J., 1980, "The Development of Wake Flow in a Centrifugal Compressor," ASME *Journal of Engineering for Power*, Vol. 102, pp. 383–390.

Johnson, M. W., and Moore, J., 1983a, "Secondary Flow and Mixing Losses in a Centrifugal Compressor Impeller," ASME *Journal of Engineering for Power*, Vol. 105, pp. 24–32.

Johnson, M. W., and Moore, J., 1983b, "Influence of Flow Rate on the Wake in a Centrifugal Impeller," ASME *Journal of Engineering for Power*, Vol. 105, pp. 33–39.

Jøngensen, F. E., 1971, "Directional Sensitivity of Wire and Fiber Film Probes," *DISA Information*, No. 11, pp. 31–37.

Krain, H., 1988, "Swirling Impeller Flow," ASME JOURNAL OF TURBOMACHINERY, Vol. 110, pp. 122–128.

Maksoud, T. M. A., and Johnson, M. W., 1987, "Stress Tensor Measurements Within the Vaneless Diffuser of a Centrifugal Compressor," *Proc. IMech E Conf.*, Paper No. C263/87.

Mounts, J. S., and Brasz, J. J., 1992, "Analysis of the Jet/Wake Mixing in a Vaneless Diffuser," ASME Paper No. 92-GT-418.

Johnson, M. W., and Moore, J., 1983a, "Secondary Flow and Mixing Losses in a Centrifugal Compressor Impeller," ASME *Journal of Engineering for Power*, Vol. 105, pp. 24–32.

Johnson, M. W., and Moore, J., 1983b, "Influence of Flow Rate on the Wake in a Centrifugal Impeller," ASME *Journal of Engineering for Power*, Vol. 105, pp. 33–39.

Jøngensen, F. E., 1971, "Directional Sensitivity of Wire and Fiber Film Probes," *DISA Information*, No. 11, pp. 31–37.

Krain, H., 1988, "Swirling Impeller Flow," ASME JOURNAL OF TURBOMACHINERY, Vol. 110, pp. 122–128.

Maksoud, T. M. A., and Johnson, M. W., 1987, "Stress Tensor Measurements Within the Vaneless Diffuser of a Centrifugal Compressor," *Proc. IMech E Conf.*, Paper No. C263/87.

Mounts, J. S., and Brasz, J. J., 1992, "Analysis of the Jet/Wake Mixing in a Vaneless Diffuser," ASME Paper No. 92-GT-418.

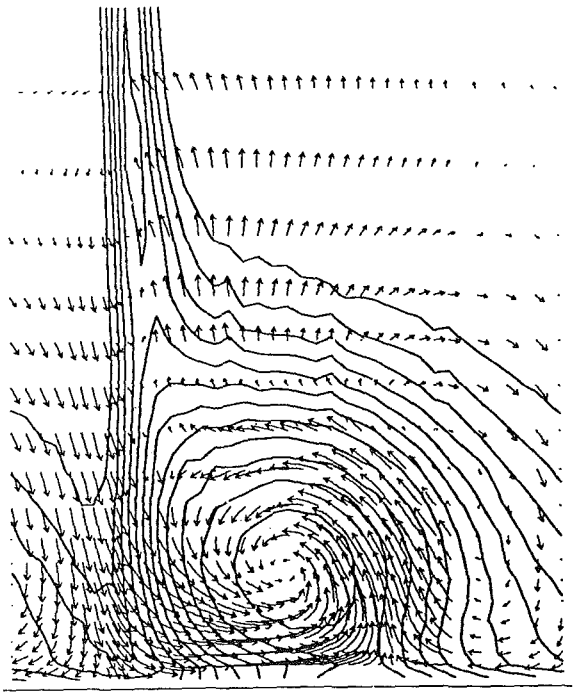

Fig. 23 Contours of stagnation pressure loss and secondary flow vectors downstream of an axial compressor cascade with clearance equal to 2 percent of chord

DISCUSSION

N. A. Cumpsty[1]

The authors are to be thanked for providing detailed measurements in a vaneless diffuser following a backswept impeller, which can be compared with those obtained earlier behind a radial vaned impeller. I would, however, like to raise a few points relating to the interpretation of the results.

In interpreting measurements it seems to be popular to identify and name features, such as the passage vortex in the y–z plane inside or at outlet from a radial impeller. I rather doubt that this is very helpful. Vorticity certainly exists, but that is not the same as a having a feature adequately described as a vortex. For comparison with Fig. 3 of the present paper, what is indisputably a clear vortex is shown here in Fig. 23. This was measured by Storer (1991) and occurred downstream of an axial compressor blade when there was a tip clearance equal to 2 percent of chord; in this case there is no doubt that the term vortex is appropriate and helpful.

A crucial property of a recognizable vortex is its persistence, yet it is pointed out here that the so-called vortex decays rapidly between stations 1 and 2, a radial distance of only 6 percent of impeller outlet radius. This hardly seems consistent with viscous dissipation, to which it is attributed in the text. I would suggest that the axial velocities evident at station 1 are the result of the growth of blockage (i.e., what is referred to in the paper as the passage wake) and movement of the blockage between stations 1 and 2, rather than from a well-formed vortex. Once the amount of blockage has started to change more slowly, as it has from station 2 onward, the axial velocities are less. In other words the principal controlling feature of the flow seen in these y–z planes is the consequence of mass conservation and not the consequence of convection and decay of circulation in this plane.

The rapid decay of the blade wake is explained in the paper in terms of secondary flows; see conclusion 2. I find this implausible. It seems more likely to me that the rapid decay is a result of a process similar to that which Dean and Senoo (1960) addressed, namely the result of very different flow inclinations in the absolute frame of reference for the wake and main flow. The large gradients in flow direction across the blade wake are very evident in Fig. 11.

Finally I wonder if the authors underestimate the inaccuracy

[1]Whittle Laboratory, University of Cambridge, Madingley Road, Cambridge CB3 0DY, United Kingdom.

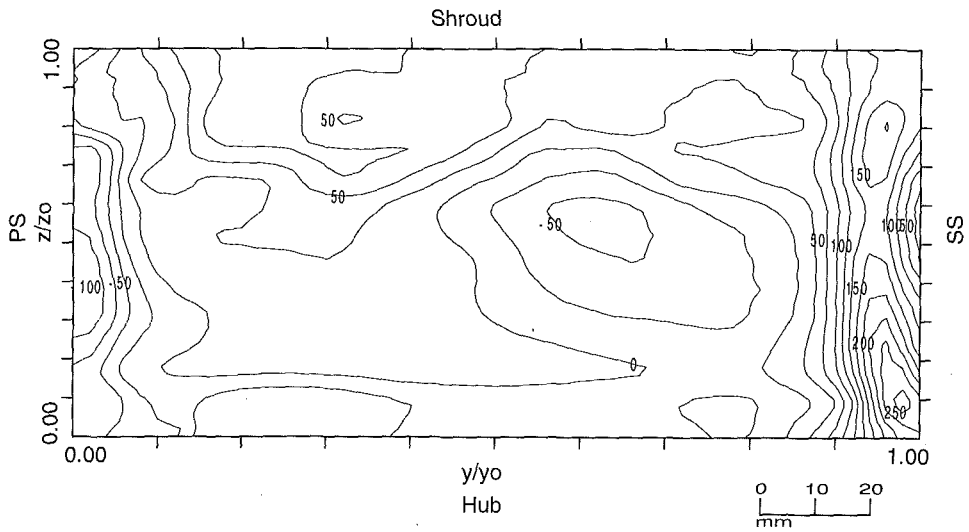

Fig. 24 Radial vorticity at station 1 in s^{-1}

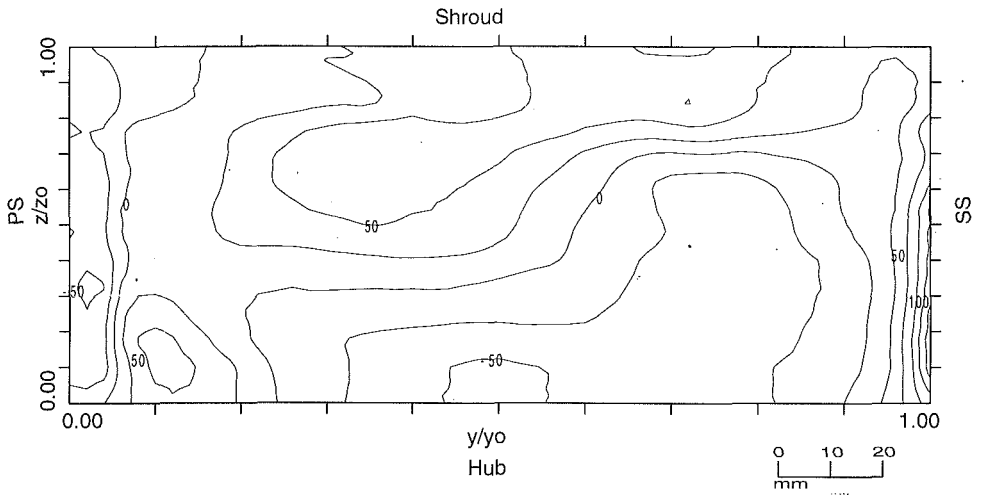

Fig. 25 Radial vorticity at station 2 in s^{-1}

of their measurements. I am particularly struck by the increase in peak radial velocity between stations 6 and 7.

References

Dean, R. C., and Senoo, Y., 1960, "Rotating Wakes in Vaneless Diffusers," ASME *Journal of Basic Engineering*, Vol. 99, pp. 53–63.

Storer, J. A., 1991, "Tip Clearance Flow in Axial Compressors," PhD Dissertation, University of Cambridge, United Kingdom.

Authors' Closure

The authors wish to thank Professor Cumpsty for his useful comments.

Figures 24 and 25 show the radial vorticity at stations 1 and 2, which was computed from the measurements of U_θ and U_z in Figs. 3 and 4. These contours appear to support Professor Cumpsty's view that the vorticity does not decay significantly between stations 1 and 2. It therefore follows that the strong axial velocities at station 1 must be primarily due to the redistribution of the blockage caused by the passage wake in accordance with mass conservation.

The authors would also agree with Professor Cumpsty that the large difference between the blade wake and passage flow angles shown in Fig. 11 is the most probable reason for the rapid mixing out of the blade wake as suggested by Dean and Senoo (1960). However, there is a large difference in flow angles between the passage wake and jet that does not result in rapid mixing out of this wake. This is presumably because the energy transfer required to mix out the passage wake is very much higher than that for the blade wake. Nevertheless the passage wake does mix out more rapidly in the circumferential direction than in the axial direction.

The peak radial velocities for stations 1 to 8 were 18.3, 18.6, 17.8, 18.1, 17.8, 16.7, 18.3, and 17.2 m/s. Thus the change in peak velocity between stations 6 and 7 is within the experimental accuracy of ± 4.8 percent quoted in the paper.

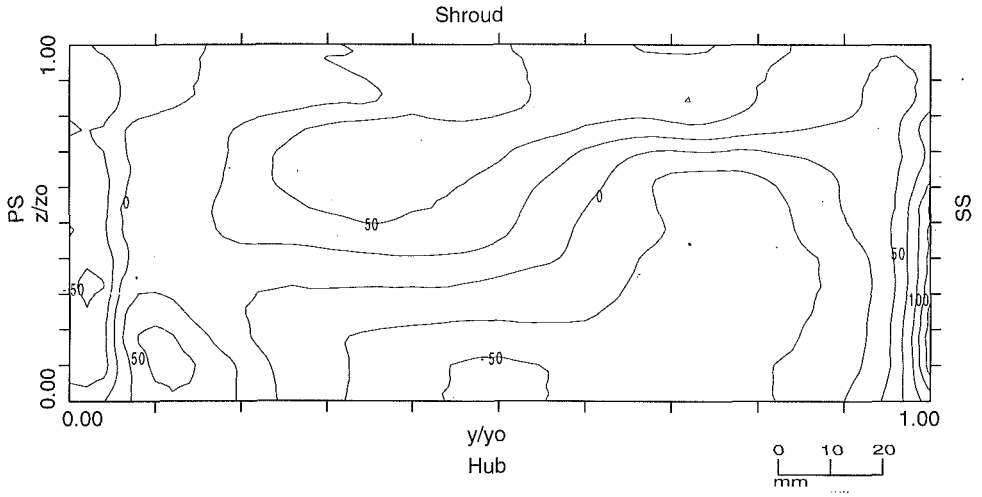

Fig. 25 Radial vorticity at station 2 in s^{-1}

of their measurements. I am particularly struck by the increase in peak radial velocity between stations 6 and 7.

References

Dean, R. C., and Senoo, Y., 1960, "Rotating Wakes in Vaneless Diffusers," ASME *Journal of Basic Engineering*, Vol. 99, pp. 53–63.

Storer, J. A., 1991, "Tip Clearance Flow in Axial Compressors," PhD Dissertation, University of Cambridge, United Kingdom.

Authors' Closure

The authors wish to thank Professor Cumpsty for his useful comments.

Figures 24 and 25 show the radial vorticity at stations 1 and 2, which was computed from the measurements of U_θ and U_z in Figs. 3 and 4. These contours appear to support Professor Cumpsty's view that the vorticity does not decay significantly between stations 1 and 2. It therefore follows that the strong axial velocities at station 1 must be primarily due to the redistribution of the blockage caused by the passage wake in accordance with mass conservation.

The authors would also agree with Professor Cumpsty that the large difference between the blade wake and passage flow angles shown in Fig. 11 is the most probable reason for the rapid mixing out of the blade wake as suggested by Dean and Senoo (1960). However, there is a large difference in flow angles between the passage wake and jet that does not result in rapid mixing out of this wake. This is presumably because the energy transfer required to mix out the passage wake is very much higher than that for the blade wake. Nevertheless the passage wake does mix out more rapidly in the circumferential direction than in the axial direction.

The peak radial velocities for stations 1 to 8 were 18.3, 18.6, 17.8, 18.1, 17.8, 16.7, 18.3, and 17.2 m/s. Thus the change in peak velocity between stations 6 and 7 is within the experimental accuracy of ± 4.8 percent quoted in the paper.

Numerical Analysis of the Three-Dimensional Swirling Flow in Centrifugal Compressor Volutes

E. Ayder

R. Van den Braembussche

von Karman Institute for Fluid Dynamics,
Chaussée de Waterloo 72,
Rhode-Saint-Génèse, Belgium

The improvement of centrifugal compressor performance and the control of the radial forces acting on the impeller due to the circumferential variation of the static pressure caused by the volute require a good understanding of the flow mechanisms and an accurate prediction of the flow pattern inside the volute. A three-dimensional volute calculation method has been developed for this purpose. The volute is discretized by means of hexahedral elements. A cell vertex finite volume approach is used in combination with a time-marching procedure. The numerical procedure makes use of a central space discretization and a four-step Runge-Kutta time-stepping scheme. The artificial dissipation used in the solver is based on the fourth-order differences of the conservative variables. Implicit residual smoothing improves the convergence rate. The loss model implemented in the code accounts for the losses due to internal shear and friction losses on the walls. A comparison of the calculated and measured results inside a volute with elliptical cross section reveals that the modified Euler solver accurately predicts the velocity and pressure distribution inside and upstream of the volute.

Introduction

The large number of parameters influencing the performance of a centrifugal compressor volute prohibits systematic experimental investigation because of the time and cost involved in the manufacturing and testing of the complex three-dimensional geometries. A reliable prediction method is therefore of great help in determining the influence of the different design parameters on the volute flow and losses.

Most prediction methods presented in the literature are based on simplified models assuming one- or two-dimensional flow (Iversen et al., 1960; Kurokawa, 1980; Badie et al., 1992). However, the experimental results of Muller (1973), Van den Braembussche and Hande (1990), and Ayder et al. (1991, 1993) show that the flow inside the volute is highly three dimensional, and that the swirling velocity component has an important influence on the crosswise and circumferential variation of the static pressure and velocity distribution. One- and two-dimensional methods are therefore of limited interest, and are unable to provide a reliable prediction of the circumferential pressure distortion and performance of three-dimensional volutes.

The way the volute flow is built up of layers of nonuniform total pressure and temperature (Van den Braembussche and Hande, 1990), in addition to the high shear forces at the center of the volute, results in a rotational flow. The methods dealing with the solution of the potential flow equations developed to analyze the flow in turbine volutes (Hamed et al., 1983) are of no use here since they start from the irrotational flow equations.

Inviscid analytical methods lead to nonphysical gradients of density, velocity, pressure, and temperature at the center of the vortex (Mayer and Powell, 1990).

The numerical solutions of the Euler equations, however, seem to exhibit no problems in the calculation of vortices. All show regular solutions, with the swirling velocity going to zero at the center of vortices, and with finite values for the pressure, density, and axial velocity (Rizzi and Erikson, 1984; Powell, 1990). The last one concludes that the artificial dissipation required to solve the discretized Euler equations regularizes the solution near the vortex center, where the flow is governed by shear flow.

Numerical Method

Experimental results have shown that the flow in volutes is affected more by the losses in the core than by the wall boundary layer. Increased turbulent mixing on the concave walls (Johnston, 1970) limits the growth of the boundary layers, which are absorbed in any case by the core flow after each rotation. Boundary layer blockage can therefore be neglected, and its influence may be limited to the shear forces on the walls.

Based on these observations, it has been decided to solve the problem by adding second-order dissipation and wall shear forces to an Euler solver, rather than resorting to a more expensive and time-consuming solution of the Navier-Stokes equations.

Contributed by the International Gas Turbine Institute and presented at the 38th International Gas Turbine and Aeroengine Congress and Exposition, Cincinnati, Ohio, May 24–27, 1993. Manuscript received by the ASME Headquarters March 1, 1993. Paper No. 93-GT-122. Associate Technical Editor: H. Lukas.

The method solves the following integral form of the Euler equations:

$$\frac{\partial}{\partial t}\int\int_{\Omega}\int \mathbf{W}d\Omega + \int_{\partial\Omega}\int \mathbf{F}\cdot\mathbf{n}_x dS + \int_{\partial\Omega}\int \mathbf{G}\cdot\mathbf{n}_y dS + \int_{\partial\Omega}\int \mathbf{H}\cdot\mathbf{n}_z dS = 0 \quad (1)$$

applied to a control volume Ω of surface $\partial\Omega$. $\mathbf{n}$ is an outer normal to the surface element dS. The vectors of this equation are defined by:

$$\mathbf{W} = \begin{pmatrix} \rho \\ \rho u \\ \rho v \\ \rho w \\ \rho E \end{pmatrix} \quad \mathbf{F} = \begin{pmatrix} \rho u \\ \rho u^2 + P \\ \rho uv \\ \rho uw \\ \rho u(E + P/\rho) \end{pmatrix}$$

$$\mathbf{G} = \begin{pmatrix} \rho v \\ \rho vu \\ \rho v^2 + P \\ \rho vw \\ \rho v(E + P/\rho) \end{pmatrix} \quad \mathbf{H} = \begin{pmatrix} \rho w \\ \rho wu \\ \rho wv \\ \rho w^2 + P \\ \rho w(E + P/\rho) \end{pmatrix} \quad (2)$$

and the system can be solved by means of the following closure condition:

$$p = (\gamma - 1)\left[\rho E - \frac{1}{2}\rho(u^2 + v^2 + w^2)\right] \quad (3)$$

All quantities in these equations are nondimensionalized by means of l (characteristic length of the channel), R (gas constant), T^0 (total temperature), P^0 (total pressure), ρ^0 (total density) measured at the exit of the compressor.

Discretization. Elementary control volumes are defined by four-sided (quadrilateral) elements on a number of cross sections of the volute and upstream diffuser (Fig. 1). The same number of quadrilateral cells is used for each cross section in order to obtain a structured grid and to enhance the resolution of the flow patterns in small cross sections. Connecting the corresponding elements of each cross section to one another produces hexahedral finite volume cells. The discretization of the flow domain in the tongue region requires special attention. The first discretized cross section of the volute is a line in space coinciding with the tongue. This leads to the triangular prism type of volume between the tongue and first cross section.

The method makes use of a cell-vertex approach in which the unknowns (the components of **W**) are defined at the vertices of the hexahedron. This provides an easy implementation of the solid wall boundary conditions, since discretization points are on the wall.

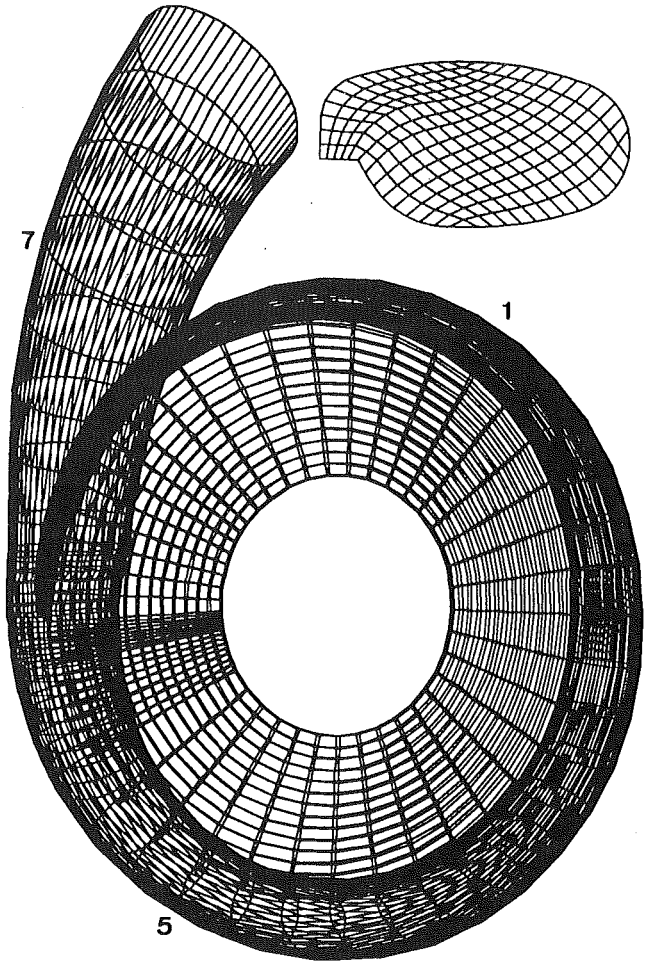

Fig. 1 Three-dimensional view of the discretized flow domain and grid structure over the cross section

A control volume around the point (i, j, k), on which the integral form of the Euler equations will be applied is defined by the eight hexahedrons containing the point under consideration. This leads to overlapping control volumes, which is allowed in the finite volume approach.

Time discretization of the unsteady Euler equations is done by using the well-known four-step Runge–Kutta scheme proposed by Jameson et al. (1981) and Jameson and Baker (1983).

Artificial Dissipation. In order to preserve the conservative form of the scheme, the artificial dissipation terms are intro-

Nomenclature

C_f = friction coefficient
$\mathbf{D}$ = dissipation vector
E = total internal energy
$\mathbf{F}, \mathbf{G}, \mathbf{H}$ = convective flux vectors
$k2$ = diffusion coefficient
l = length
$\mathbf{L}$ = vector of friction losses
$\mathbf{n}$ = unit vector normal to the surface
P = pressure
$\mathbf{Q}$ = vector of residuals
S = area
t = time
T = temperature
u, v, w = Cartesian components of velocity
V = velocity
$\mathbf{W}$ = vector of conservative variables
α = ratio of throughflow velocity to radial velocity
β = ratio of axial velocity to radial velocity
γ = ratio of specific heats
ϵ = implicit residual smooting coefficient
ρ = density
τ = shear stress
Ω = volume

Subscripts

S = swirl component
T = throughflow component
R = radial
Z = axial

Superscripts

$\underline{0}$ = stagnation conditions
= averaged value

duced by adding dissipative fluxes to the integral form of the Euler equations,

$$\Omega_{i,j,k}\left(\frac{d}{dt}\mathbf{W}_{i,j,k}\right)+\mathbf{Q}_{i,j,k}-\mathbf{D}_{i,j,k}=0 \tag{4}$$

Since the volute flow is subsonic, and no shocks are expected, the dissipative flux $\mathbf{D}_{i,j,k}$ will be proportional to the fourth-order differences of the conservative variables in all three index directions and second-order dissipation will not be required to stabilize the equation. The evaluation of the fourth-order differences presents some problems near the boundaries. In the present study, the approach suggested by Kroll and Jain (1987) is used to determine the artificial dissipation at the boundary points. The dissipation term is only calculated in the first step of the Runge–Kutta time integration and is kept constant for the other three steps.

Boundary Conditions. A theoretical analysis of the three-dimensional Euler equations indicates that four physical flow quantities have to be imposed at the inlet of the calculation domain.

In addition to the total pressure and temperature, the third and fourth physical conditions impose the ratio of the through-flow velocity to the radial velocity (α) to determine the through-flow velocity

$$V_{Ti}=\alpha\cdot V_{Ri}$$

and the ratio of the radial velocity to the axial flow velocity (β) to determine the axial velocity

$$V_{Zi}=\beta\cdot V_{Ri}$$

The unknown radial velocity is determined as a function of the internal flow by a numerical boundary condition by which the radial component of the velocity of the first interior point ($i+1$) is extrapolated to the inlet boundary point (i). The following relation is used in the extrapolation procedure to account for the change in area

$$V_{Ri}=V_{Ri+1}\frac{S_{i+1}}{S_i}$$

All other nondimensionalized variables at the inlet can then be calculated by means of the thermodynamic relations.

The downstream static pressure is not uniform because it results from a radial equilibrium with the centrifugal forces, and its definition requires the calculation of the local streamline curvature radius.

A more practical method consists of imposing the static pressure at one point of the outlet plane and calculating the static pressure in all other points by imposing the pressure ratio, calculated between the reference points,

$$\text{Ratio}=\frac{P^*(i_{\text{ref}},\,j_{\text{ref}},\,k_{\max})}{P(i_{\text{ref}},\,j_{\text{ref}},\,k_{\max}-1)}$$

to all corresponding points of the two planes:

$$P(i,\,j,\,k_{\max})=\text{Ratio}\cdot P(i,\,j,\,k_{\max}-1)$$

The three velocity components and density can then be calculated from the Euler equations discretized on the boundary elements. Together with the static pressure, they are used to determine the conservative variables.

The solid wall boundary condition results from imposing the constraint that no mass or other convective flux can penetrate the solid wall:

$$V_n=0$$

As a consequence, all convective flux components through the solid wall vanish and only the pressure contributions at the solid walls remain in the flux vectors **F**, **G**, and **H**. The variables other than the normal velocity are calculated by solving the discretized Euler equations on a one-sided control volume.

Acceleration Technique. The implicit residual averaging provides a better convergence rate compared to the explicit one and is therefore used in the present study (Jameson, 1983). The residual averaging is done at the second and fourth steps of the Runge–Kutta scheme.

Loss Calculation. Determination of the shear stresses on all inner volumes of the volute channel requires a flow-adapted grid where the volume surfaces coincide with the stream surfaces, or are perpendicular to the velocity. This is very difficult to achieve in all volutes of different cross-sectional shapes and varying flow conditions. Shear forces will therefore be calculated only on the walls and applied to the volumes having a surface in common with the wall. The internal friction is approximated by a viscous term.

The additional momentum caused by wall friction is included by adding a term $L_{i,j,k}$ to the momentum equations.

$$\Omega_{i,j,k}\left(\frac{d}{dt}\mathbf{W}_{i,j,k}\right)+\mathbf{Q}_{i,j,k}-\mathbf{D}_{i,j,k}-\mathbf{L}_{i,j,k}=0 \tag{5}$$

Neglecting the displacement thickness of the sublayer and assuming that the surface streamline lies at the edge of the laminar sublayer, the wall shear stress can be defined by the following relation:

$$\tau_{\text{wall}}=C_f\frac{1}{2}\rho V^2 \tag{6}$$

resulting in the following components on each element of the wall:

$$\tau_x=-\frac{u}{V}\tau_{\text{wall}},\ \tau_y=-\frac{v}{V}\tau_{\text{wall}},\ \tau_z=-\frac{w}{V}\tau_{\text{wall}}$$

Due to the nonuniformity of the total temperature at the inlet of the volute, the simplification of the energy equation suggested by Denton (1986) cannot be used and the energy dissipation due to wall friction

$$-\tau V(S_x+S_y+S_z)$$

must be added to the loss vector **L**.

$$\mathbf{L}=\begin{pmatrix}0\\ \tau_x(S_x+S_y+S_z)\\ \tau_y(S_x+S_y+S_z)\\ \tau_z(S_x+S_y+S_z)\\ \tau V(S_x+S_y+S_z)\end{pmatrix}$$

As the loss vector is calculated only on the solid wall surfaces, it influences only the vertices of the volumes adjacent to the solid walls and creates a local velocity gradient perpendicular to the wall.

Viscous energy dissipation, at all regions of nonzero velocity gradient (at the wall and at the vortex center), is achieved by second-order dissipation

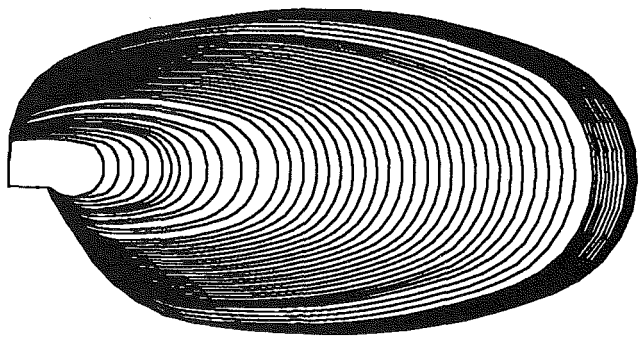

Fig. 2 Circumferential variation of the cross sections of the volute

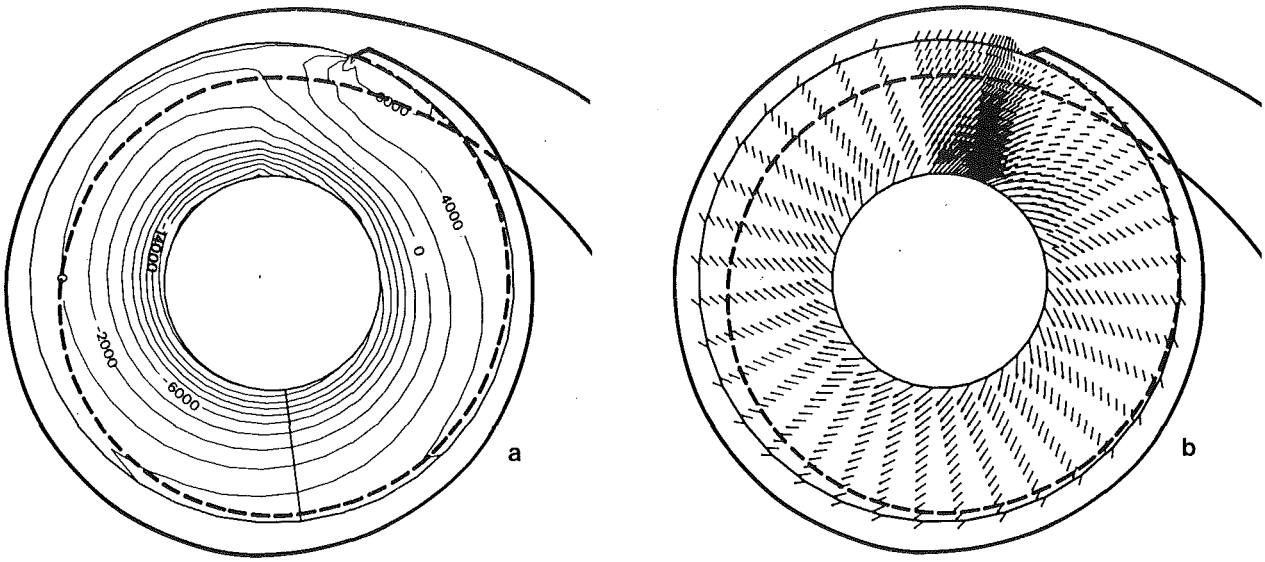

Fig. 3 Calculated static pressure isolines (*a*) and velocity (*b*) over the midplane of the vaneless diffuser at high mass flow

$$k2(\mathbf{W}_{i-1,j,k}+\mathbf{W}_{i+1,j,k}+\mathbf{W}_{i,j-1,k}+\mathbf{W}_{i,j+1,k}+\mathbf{W}_{i,j,k-1}+\mathbf{W}_{i,j,k+1}-6\mathbf{W}_{i,j,k})$$

The coefficient $k2$ is adjusted empirically to simulate the viscous terms in the Navier–Stokes equations. Actual calculations are done with a $k2$ value of 0.002.

Results

The computer program has been validated by calculating the three-dimensional swirling flow inside a volute of elliptic cross section for which detailed experimental data have been obtained by Ayder et al. (1993). The flow field is extended upstream to the impeller outlet in order to be able to study the flow around the tongue, and to minimize the influence of the inlet conditions on the tongue and on the volute flow. However, the inlet boundary conditions (total pressure, total temperature, and the ratios of tangential and axial velocity over the radial velocity) have been measured only at the volute inlet. The values used at the inlet of the calculation domain are derived from the measured ones by correcting for the change in radius between diffuser inlet and volute inlet, taking into account the circumferential shift due to the peripheral velocity in the diffuser. Vaneless diffuser losses and the axial variation of the flow over the diffuser width are neglected.

The static pressure at the outlet equals the atmospheric pressure and is fixed at one point of the solid wall in the last plane of the exit cone.

The vaneless diffuser is discretized by 5 × 15 grid points on each of the 59 cross sections. The volute and exit cone is discretized by 15 × 15 grid points in 74 cross sections. Cross sections are concentrated near the tongue region to obtain a more detailed flow description. A three-dimensional view of the geometry is shown in Fig. 1. Variation of the cross-sectional area along the volute channel, starting from the volute tongue to the volute exit, is shown in Fig. 2.

The calculations have been performed for operating points corresponding to high, medium, and low mass flows. Because of the limited space, detailed results will be shown only for high and low mass flows. Calculation time is 16 hours on a Silicon Graphics IRIS 4D/35 computer.

Diffuser Flow. The variation of velocity and static pressure over the midplane of the diffuser is shown in Fig. 3. As can be expected at high mass flow, the static pressure decreases along the circumference of the diffuser in the direction of the rotation of the impeller up to an abrupt increase in static pressure around the tongue (Fig. 3*a*) resulting in a strong perturbation of the local velocity vectors (Fig. 3*b*). Almost no fluid enters the volute in the region of high pressure. This phenomenon is similar to what has been observed by Elholm et al. (1990).

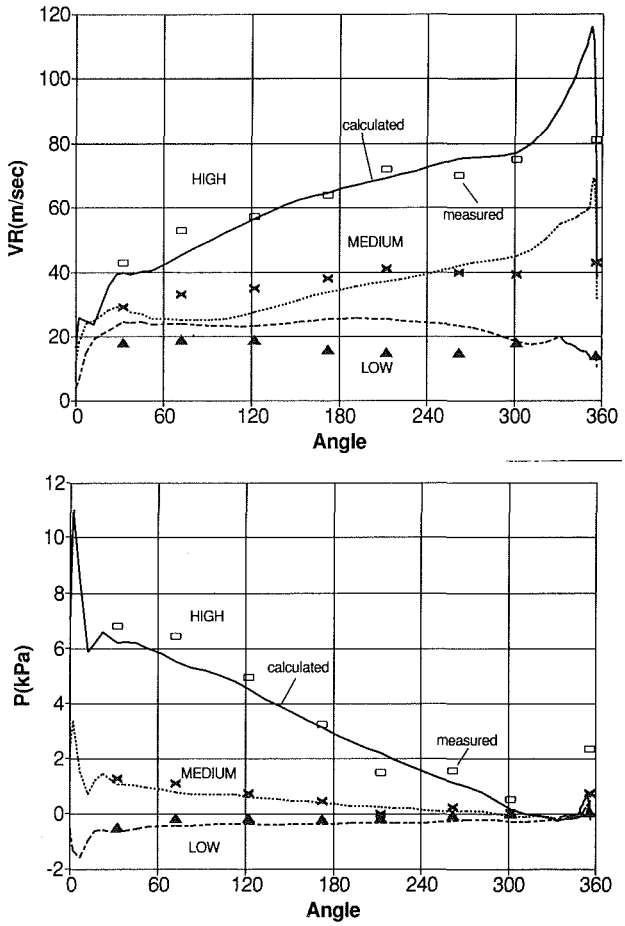

Fig. 4 Comparisons of the calculated and measured spanwise mass-averaged radial velocity (V_R) and static pressure (P) at the volute inlet for high, medium, and low mass flows

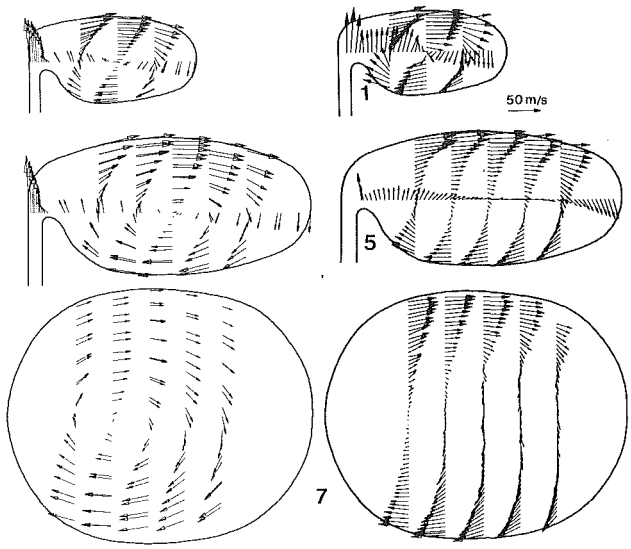

Fig. 5(*a*) Calculated (left) and measured (right) swirl velocities at high mass flow

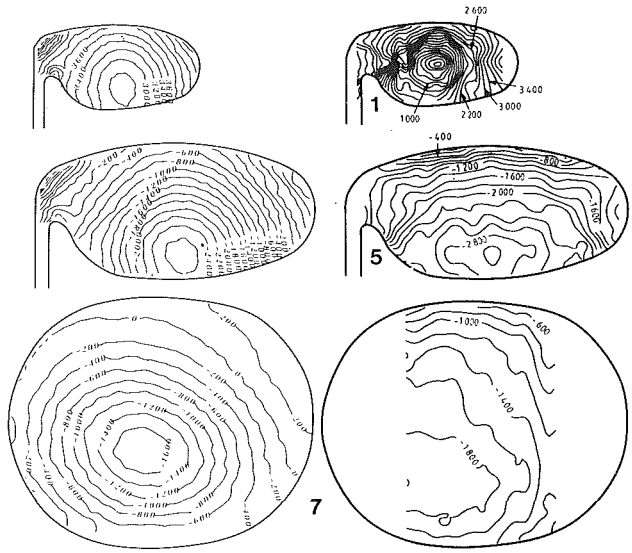

Fig. 5(*c*) Calculated (left) and measured (right) static pressure at high mass flow (Pascal)

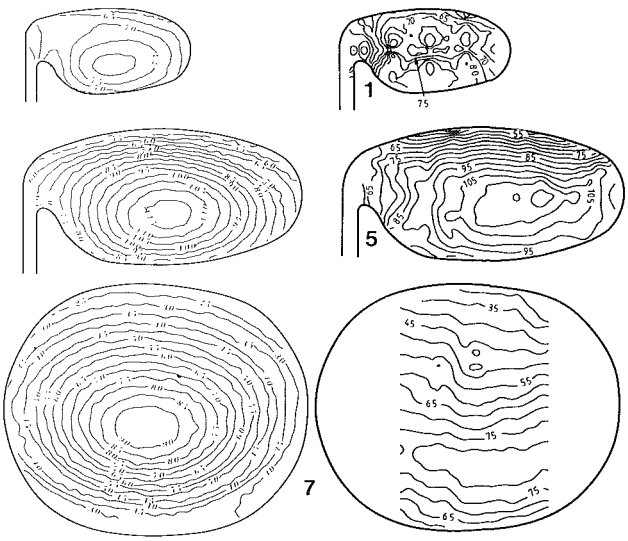

Fig. 5(*b*) Calculated (left) and measured (right) throughflow velocities at high mass flow (m/s)

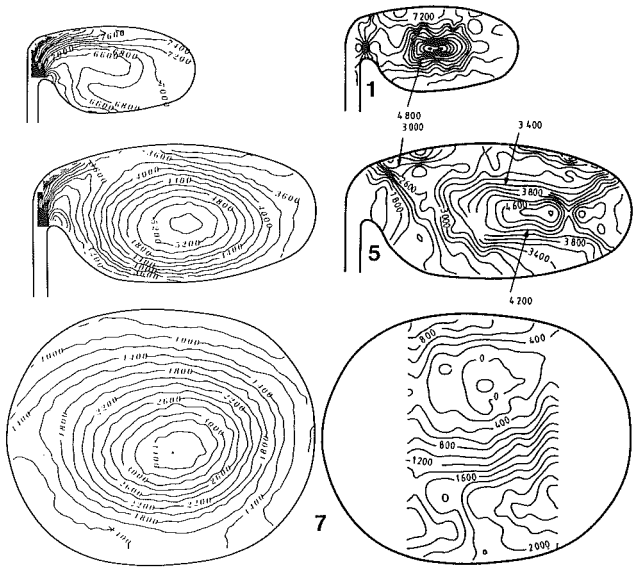

Fig. 5(*d*) Calculated (left) and measured (right) total pressure at high mass flow (Pascal)

The radial velocity (V_R) and static pressure (P) distribution at the diffuser inlet (and as a consequence, also at the volute inlet) are a result of the calculation. Spanwise-averaged calculated values are compared with experimental values in Fig. 4 and show a very good agreement for all flow conditions.

Volute Flow. The variation of the measured and calculated swirl velocity (V_S), throughflow velocity (V_T), total pressure (P^0), and static pressure (P) over the sections corresponding to sections 1, 5, and 7 of the experimental study (indicated in Fig. 1), are shown in Fig. 5 for high mass flow, and in Fig. 6 for low mass flow.

The mechanisms defining the change of flow quantities over the cross section have been explained in detail by Ayder et al. (1993) and will not be repeated.

The circumferential variation of the calculated flow quantities is very similar to the one observed in the experimental study.

The magnitude and variation of the calculated swirl and throughflow velocities over the cross sections and along the volute channel are in agreement with the measurements (Figs. 5*a*, *b* and 6*a*, *b*).

Measured results indicate high total pressure losses at the center of the first cross section (Fig. 5*c*) due to the dissipation of the swirl kinetic energy. The calculations underestimate the concentration of low total pressure at the center of the first cross section. However, the calculated total pressure outside the viscous core is in agreement with the measured one (Fig. 5*c*).

The calculated magnitude of the total pressure and static pressure over the cross section 5 are slightly higher than the measured ones for high mass flow (Fig. 5*c*, *d*). The reason for this is unknown. However, the measured and calculated total and static pressure over cross section 7 are different. It can be seen that the high total pressure losses occurring at high mass flow in the exit cone are underestimated. Measurements at section 7 are restricted to a small portion of the cross section and it is not possible to find out the origin of these high losses. They may be due to separation at the tongue.

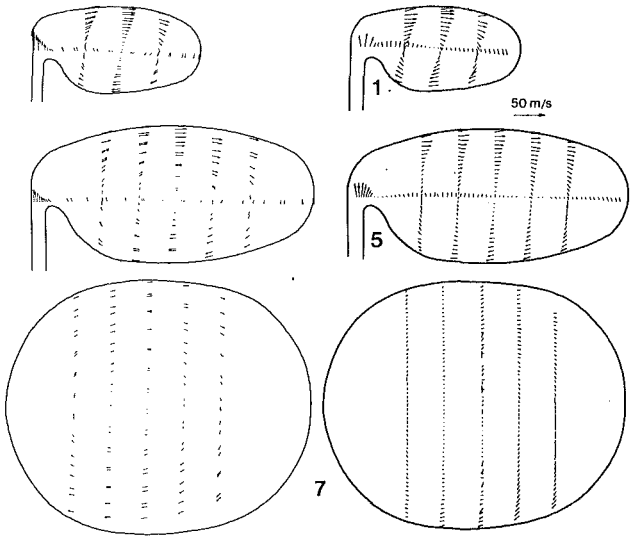

Fig. 6(*a*) Calculated (left) and measured (right) swirl velocities at low mass flow

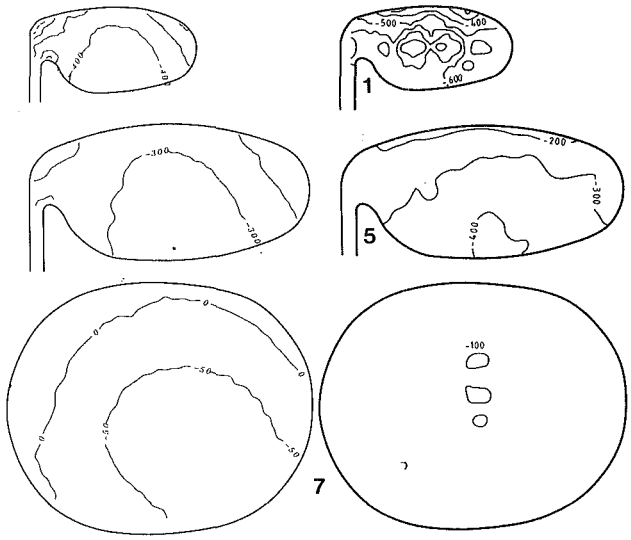

Fig. 6(*c*) Calculated (left) and measured (right) static pressure at low mass flow (Pascal)

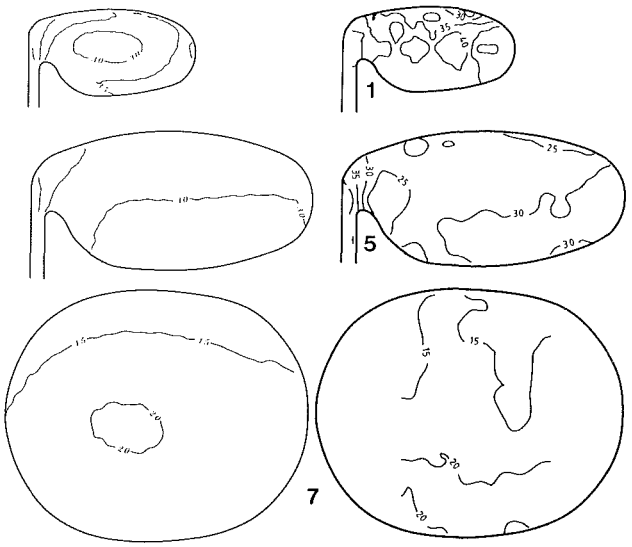

Fig. 6(*b*) Calculated (left) and measured (right) through flow velocities at low mass flow (m/s)

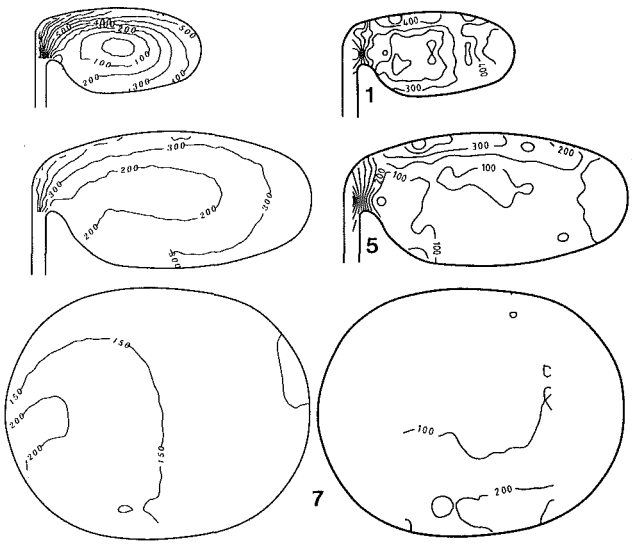

Fig. 6(*d*) Calculated (left) and measured (right) total pressure at low mass flow (Pascal)

In case of the low mass flow, the experimental results do not exhibit large total pressure gradients caused by the viscous effects. The calculated total and static pressures therefore show better agreement with the measured ones (Fig. 6*c*, *d*).

Calculated results are used to trace particles inside the diffuser and volute. The traces start at four circumferential positions at the diffuser inlet. The results obtained at medium mass flow are shown in Fig. 7. One observes that the fluid entering the volute at a position close to the tongue (*A*) remains in the center of the volute until the compressor exit. Fluid entering the volute farther downstream (*B*, *C*, *D*) wraps around the previous one, which confirms the volute flow model suggested by Van den Braembussche and Hande (1990).

Conclusions

To our knowledge, this is the first time that the complex flow in a volute is calculated using a fully three-dimensional method. Taking into account the complexity of the geometry and the uncertainty of the experimental data, results are assumed to be very satisfactory.

Comparisons between the calculated and measured flow fields inside the volute show a good prediction of the cross-sectional variation of the swirl and throughflow velocity. The total and static pressure show a more qualitative agreement, but the internal shear loss mechanism, typical for swirling flows, is correctly captured.

The circumferential distortion of the static pressure and radial velocity at the volute inlet, required for impeller response calculations, is accurately predicted.

The calculated flow patterns around the tongue and leakage flow are in agreement with the flow visualizations.

The calculation of flow patterns by particle tracing also confirm the validity of the volute flow model proposed by Van den Braembussche and Hande (1990).

The proposed combination of an Euler solver with a volute adapted loss model has shown to be an accurate alternative to the solution of the full Navier–Stokes equations of which one can expect that the computational effort will be much larger.

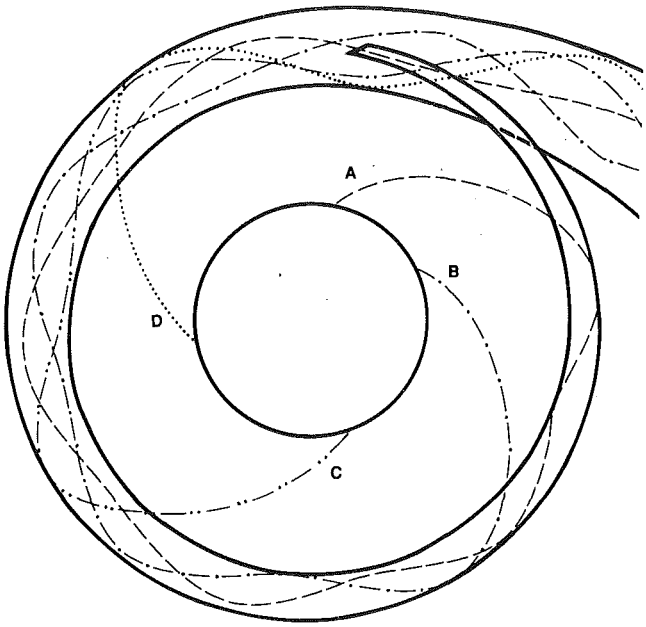

Fig. 7 Particle tracing inside the vaneless diffuser and volute at medium mass flow

References

Ayder, E., and Van den Braembussche, R. A., 1991, "Experimental Study of the Swirling Flow in the Internal Volute of a Centrifugal Compressor," ASME Paper No. 91-GT-7.

Ayder, E., Van den Braembussche, R. A., and Brasz, J. J., 1993, "Experimental and Theoretical Analysis of the Flow in a Centrifugal Compressor Volute," ASME JOURNAL OF TURBOMACHINERY, Vol. 115, pp. 582–589.

Badie, R., Jonker, J. B., and Van Essen, T. G., 1992, "Calculations on the Time-Dependent Potential Flow in a Centrifugal Pump," ASME Paper No. 92-GT-151.

Denton, J. D., 1986, "The Use of a Distributed Body Force to Simulate Viscous Effects in 3D Flow Calculations," ASME Paper No. 86-GT-144.

Elholm, T., Ayder, E., and Van den Braembussche, R., 1990, "Experimental Study of the Swirling Flow in the Volute of a Centrifugal Pump," ASME JOURNAL OF TURBOMACHINERY, Vol. 114, pp. 366–372.

Hamed, A., Tabakoff, W., and Malak, M., 1983, "The Three Dimensional Compressible Flow in a Radial Inflow Turbine Scroll," Paper No. 83-TOKYO-IGTI-66.

Iversen, H., Rolling, R., and Carlson, J., 1960, "Volute Pressure Distribution, Radial Force on the Impeller and Volute Mixing Losses of a Radial Flow Centrifugal Pump," ASME *Journal of Engineering for Power*, Vol. 82, pp. 136–144.

Jameson, A., Schmidt, W., and Turkel, E., 1981, "Numerical Solutions of the Euler Equations by a Finite Volume Method Using Runge-Kutta Time Stepping Schemes," AIAA Paper No. 81-1259.

Jameson, A., and Baker, T. J., 1983, "Solution of the Euler Equations for Complex Configurations," AIAA Paper No. 83-1929.

Johnston, J. P., 1970, "The Effects of Rotation on Boundary Layers in Turbomachine Rotors," NASA SP 304, *Fluid Mechanics, Acoustics and Design of Turbomachinery*, Part 1, 1970, pp. 207–242.

Kroll, N., and Jain, R. K., 1987, "Solutions of Two Dimensional Euler Equations—Experience With a Finite Volume Code," DFVLR-FB 87-41.

Kurokawa, J., 1980, "Theoretical Determinations of the Flow Characteristics in Volutes," IAHR-AIRH Symposium 1980, Tokyo.

Mayer, E. W., and Powell, K. G., 1990, "Similarity Models for Vortex Cores," AIAA Paper No. 90-0592.

Muller, K. J., 1973, "Bemessung und Betriebsverhalten von Spiralgehausen Radialer Stromungsarbeitsmachinen," *VDI-Berichte*, No. 193.

Powell, K. G., 1990, "Computation of Compressible Vortical Flows," VKI Lecture Series 1990-03.

Rizzi, A., and Eriksson, L. E., 1984, "Computation of Flow Around Wings Based on the Euler Equations," *Journal of Fluid Mechanics*, Vol. 148, pp. 45–72.

Van den Braembussche, R. A., and Hande, B. M., 1990, "Experimental and Theoretical Study of the Swirling Flow in Centrifugal Compressor Volutes," ASME JOURNAL OF TURBOMACHINERY, Vol. 112, pp. 38–43.

Three-Dimensional Time-Marching Inviscid and Viscous Solutions for Unsteady Flows Around Vibrating Blades

L. He

J. D. Denton

Whittle Laboratory,
Cambridge University,
Cambridge, United Kingdom

A three-dimensional nonlinear time-marching method of solving the thin-layer Navier–Stokes equations in a simplified form has been developed for blade flutter calculations. The discretization of the equations is made using the cell-vertex finite volume scheme in space and the four-stage Runge–Kutta scheme in time. Calculations are carried out in a single-blade-passage domain and the phase-shifted periodic condition is implemented by using the shape correction method. The three-dimensional unsteady Euler solution is obtained at conditions of zero viscosity, and is validated against a well-established three-dimensional semi-analytical method. For viscous solutions, the time-step limitation on the explicit temporal discretization scheme is effectively relaxed by using a time-consistent two-grid time-marching technique. A transonic rotor blade passage flow (with tip-leakage) is calculated using the present three-dimensional unsteady viscous solution method. Calculated steady flow results agree well with the corresponding experiment and with other calculations. Calculated unsteady loadings due to oscillations of the rotor blades reveal some notable three-dimensional viscous flow features. The feasibility of solving the simplified thin-layer Navier–Stokes solver for oscillating blade flows at practical conditions is demonstrated.

Introduction

Predictions of unsteady flows around vibrating blades are essential for turbomachinery blade flutter predictions. Numerical methods of calculating unsteady flows through vibration blades are currently under active development. Most of the methods available are for a two-dimensional model. Notable examples are the work by Verdon and Caspar (1982) and Whitehead (1982). Under practical turbomachinery working conditions, three-dimensional effects are important and need to be modeled. Calculations of three-dimensional unsteady flows are usually simplified by assuming that a flow field would behave in a two-dimensional fashion at each spanwise section, so the strip method (i.e., performing two-dimensional calculations at each section) can be used. It has been demonstrated that the strip theory can lead to serious errors for blade flutter calculations (e.g., Namba, 1987).

For simple three-dimensional blade geometries (e.g., flat plate cascade) at purely subsonic or supersonic flow conditions, fully three-dimensional inviscid solutions for oscillating blade flows can be efficiently and accurately obtained by using semi-analytical theories. Examples of this kind are those by Namba (1976, 1987) and Chi (1993). These semi-analytical methods can provide some basic insight into three-dimensional effects on blade aeroelastic behaviors, but their capability in predicting blade flutter under practical flow conditions is rather limited.

Recently three-dimensional numerical methods for blade flutter calculations have begun to emerge. Three-dimensional inviscid Euler solutions have been developed by Giles (1991) and Hall and Lorence (1993) using a time-linearized model, and by Gerolymos (1993) using a time-marching method. So far no work on three-dimensional unsteady viscous flow solutions for blade flutter calculations has been reported.

The objective of the present work is to develop a nonlinear time-marching viscous flow solution method for blade flutter calculations. The major effort is focused on enhancing solution efficiency, which is believed to be a very important factor affecting the feasibility of unsteady time-marching solvers for industrial use. For the phase-shifted periodic boundary condition, the "Shape Correction" method developed for the previous two-dimensional Euler solver (He, 1989) is extended to the present three-dimensional solution to save computer storage. Another feature of the present work is that the time-step limitation on the explicit time-marching scheme is effectively relaxed by using a time-consistent two-grid technique.

Basic Governing Equations and Discretization

For convenience of simulating three-dimensional flows in

Contributed by the International Gas Turbine Institute and presented at the 38th International Gas Turbine and Aeroengine Congress and Exposition, Cincinnati, Ohio, May 24–27, 1993. Manuscript received at ASME Headquarters February 19, 1993. Paper No. 93-GT-92. Associate Technical Editor: H. Lukas.

turbomachinery blade passages, in cylindrical coordinate (x, θ, r) in an *absolute* system is adopted. An integral form of the three-dimensional Navier–Stokes equations over a moving finite volume ΔV is:

$$\frac{\partial}{\partial t}\iiint_{\Delta V} U dV + \oiint_A [(F - Uu_{mg})\mathbf{n}_x + (G - Uv_{mg})\mathbf{n}_\theta + (H - Uw_{mg})\mathbf{n}_r]\cdot\mathbf{dA} = \iiint_{\Delta V} (S_i + S_v) dV \quad (1)$$

where:

$$U = \begin{pmatrix} \rho \\ \rho u \\ \rho v r \\ \rho w \\ \rho E \end{pmatrix} \qquad F = \begin{pmatrix} \rho u \\ \rho u u + p \\ \rho u v r \\ \rho u w \\ (\rho E + p(u \end{pmatrix} \qquad G = \begin{pmatrix} \rho v \\ \rho u v \\ (\rho v v + p) r \\ \rho v w \\ (\rho E + p) v \end{pmatrix}$$

and

$$H = \begin{pmatrix} \rho w \\ \rho u w \\ \rho w v r \\ \rho w w + p \\ (\rho E + p) w \end{pmatrix} \qquad S_i = \begin{pmatrix} 0 \\ 0 \\ 0 \\ \rho v^2 / r \\ 0 \end{pmatrix}$$

It should be mentioned that the circumferential moving-grid velocity v_{mg} includes both the blade vibration velocity and the rotation velocity.

The viscous term S_v in a body force form can be modeled at different levels of approximation. In the present work, a simplified form of the thin-layer Navier–Stokes equations as used in Denton's viscous flow solver for steady turbomachinery flows (Denton, 1992) is adopted. Firstly, the viscous terms in the energy equations are neglected. This simplification is introduced in the light that the work done by the viscous shear forces would be roughly canceled by the heat conduction at a Prandtl number near unity. Furthermore, the viscous terms in the three momentum equations are modeled under the thin-layer assumption. So only the viscous shear stress terms in the direction tangential to solid surfaces are included. For laminar flows, if we have the shear stress τ corresponding to a solid surface:

$$\tau = \mu \frac{\partial u_s}{\partial n} \quad (2)$$

where n is the normal distance from the surface, u_s is the absolute velocity. Then the corresponding viscous terms in the body force form are approximated by:

$$\iiint_{\Delta V} S_v dV = \oiint_A T_v dA \quad (3)$$

where

$$T_v = \begin{pmatrix} 0 \\ \tau \cos\alpha \\ \tau r \cos\beta \\ \tau \cos\eta \\ 0 \end{pmatrix}$$

α, β, η are angles between the velocity and the x, θ, and r directions, respectively.

For turbulent flows the shear stress is modeled in an eddy viscosity form:

$$\tau = \rho \epsilon_m \frac{\partial u_s}{\partial n} \quad (4)$$

The eddy viscosity is at the present stage obtained by using a simple mixing-length model:

$$\epsilon_m = (0.41n)^2 \left| \frac{\partial V}{\partial n} \right| \quad (5)$$

This mixing-length model is simpler than most of other turbulence models currently available, but it is felt that the number of mesh grid points likely to be available for a three-dimensional unsteady viscous solution would probably not justify a more sophisticated model. The eddy viscosity ϵ_m is "cut off" when the mesh point is far from the wall.

The spatial discretization for the three-dimensional equations is made by using the cell-vertex finite volume scheme. The temporal integration is performed using the four-stage Runge–Kutta scheme. The discretized form of Eq. (1) is:

$$U^{n+1/4} = U^n \frac{\Delta V^n}{\Delta V^{n+1/4}} - \frac{1}{4}\frac{\Delta t}{\Delta V^{n+1/4}}(R_i^n - R_v^n - D^n) \quad (6a)$$

$$U^{n+1/3} = U^n \frac{\Delta V^n}{\Delta V^{n+1/3}} - \frac{1}{3}\frac{\Delta t}{\Delta V^{n+1/3}}(R_i^{n+1/3} - R_v^n - D^n) \quad (6b)$$

$$U^{n+1/2} = U^n \frac{\Delta V^n}{\Delta V^{n+1/2}} - \frac{1}{2}\frac{\Delta t}{\Delta V^{n+1/2}}(R_i^{n+1/2} - R_v^n - D^n) \quad (6c)$$

$$U^{n+1} = U^n \frac{\Delta V^n}{\Delta V^{n+1}} - \frac{\Delta t}{\Delta V^{n+1}}(R_i^{n+1} - R_v^n - D^n) \quad (6d)$$

where

$$R_i = \Sigma\{[F - Uu_{mg}]\Delta A_x + [G - Uv_{mg}]\Delta A_\theta + [H - Uw_{mg}]\Delta A_r\} + S_i \Delta V$$

$$R_V = \Sigma T_V \Delta A$$

The summation is taken along the finite volume boundary. The numerical damping term D^n is treated in a similar way to that in the previous two-dimensional Euler solution (He, 1989). The second and fourth-order adaptive smoothing (Jameson, 1983) is used in the streamwise direction and a simple second-

Nomenclature

C = chord length
Cp_1 = unsteady pressure coefficient
$\mathbf{dA}$ = differential area element with unit outward normal vector
dV = differential volume element
E = internal energy
f = frequency
$\mathbf{n}_x$ = the unit vectors in x direction
p = static pressure
r = radial coordinate
S = span
S_v = viscous terms in a body force form
U = primitive flow variable
u = velocity in x direction
u_∞ = absolute velocity in inlet
v = velocity in θ direction
w = velocity in radial direction
x = axial coordinate
ϵ_m = turbulence eddy viscosity
θ = circumferential coordinate
μ = laminar viscosity coefficient
ρ = density
σ = inter blade phase angle
τ = shear stress
ω = angular frequency

Superscript

n = index of time step

Subscripts

0 = time-averaged
mg = moving grid
n = order of the Fourier component
w = on walls

order smoothing is used in the pitchwise and the radial directions. Similar to the numerical damping term, the viscous terms are only updated at the first stage.

On solid surfaces (blade surfaces, hub, and casing), a slip condition is used, i.e., only the normal velocity are set to be zero. The wall shear stress is determined by using an approximate form of the log-law (Denton, 1990):

$$\frac{\tau_w}{0.5\ \rho_w u_w^2} = -0.001767 + \frac{0.03177}{\ln(\mathrm{Re}_w)} + \frac{0.25614}{[\ln(\mathrm{Re}_w)]^2} \tag{7}$$

where u_w and ρ_w are velocity and density at mesh points one grid spacing (normal distance Δn) away from the wall and $\mathrm{Re}_w = \rho_w u_w \Delta n/\mu$. For laminar flows the wall shear stress is simply evaluated by $\tau_w = \mu\ u_w/\Delta n$. It has been found from steady flow solutions (e.g., Denton, 1992) that viscous flow behavior can be adequately modeled by this slip condition, which needs fewer mesh points in the near-wall region than does the standard non-slip wall condition.

At the inlet and outlet boundaries, the nonreflecting boundary conditions are preferred to prevent artificial reflections of outgoing waves. The one-dimensional and two-dimensional nonreflecting boundary conditions methods are currently available (e.g., Giles, 1990), while the three-dimensional nonreflecting boundary conditions are still a subject of research. In the present calculations, the one-dimensional nonreflecting condition (Giles, 1990) is adopted for its simplicity of implementation.

Phase-Shifted Periodic Condition

A single-blade-passage computational domain is adopted. It is assumed that the unsteadiness to be dealt with satisfies a temporal and circumferentially spatial periodicity, characterized by a frequency f and an inter-blade-phase angle σ. Thus the phase-shifted periodic condition can be applied at the periodic boundaries. It is recognized that there is a limitation of the phase-shifted periodicity. That is, self-excited periodic vortex shedding phenomena can only be accommodated if they are locked in with the imposed fundamental frequency and its higher order harmonics. The phase-shifted periodic condition can be applied by using the conventional "Direct Store" method, proposed by Erdos et al. (1977). However the large computer storage required by the "Direct Store" method presents a severe limitation for three-dimensional solutions. To avoid using large computer storage, a new method called "Shape Correction" has been developed for the previous two-dimensional Euler solver (He, 1989). Here we extend the Shape Correction method to three-dimensional solutions.

Let us denote that the single-passage computational domain is bounded by the lower (indicated by "L") and the upper (indicated by "U") periodic boundaries upstream and downstream of the blade row. At these periodic boundaries, the flow primitive variables are approximated by an Nth order Fourier series in time:

$$U^U(x, r, t) = U_0(x, r) + \sum_{n=1}^{N} [A_n(x, r)\ \sin\ (n\omega t + \sigma) + B_n(x, r)\ \cos\ (n\omega t + \sigma)] \tag{8a}$$

$$U^L(x, r, t) = U_0(x, r) + \sum_{n=1}^{N} [A_n(x, r)\ \sin\ (n\omega t) + B_n(x, r)\ \cos\ (n\omega t)] \tag{8b}$$

Instead of directly storing the variables for one period of time as in the "Direct Store" method, only the temporal Fourier components are stored. During the time-marching solution process, the flow variables at the periodic boundaries are corrected by the stored temporal variation (i.e., the Fourier components). The new Fourier coefficients are obtained by a straightforward temporal integration of the flow variables over one period (e.g., for the lower boundary):

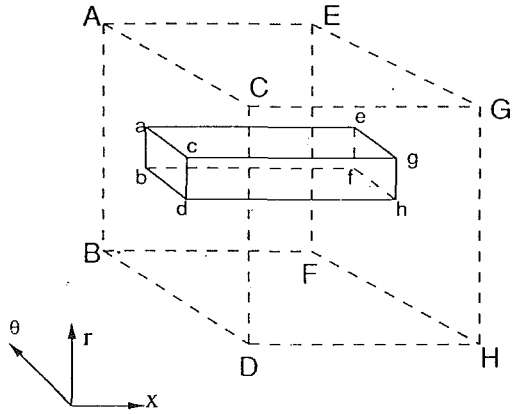

Fig. 1 Two-grid finite volume

$$A_n = \frac{\omega}{\pi} \sum_{1}^{N_p} U^L\ \sin\ (n\omega t)\Delta t \tag{9a}$$

$$B_n = \frac{\omega}{\pi} \sum_{1}^{N_p} U^L\ \cos\ (n\omega t)\Delta t \tag{9b}$$

where N_p is the number of time steps in one period. These new Fourier coefficients will then be used to correct the old ones. In this way, the stored temporal shape and the current solution correct each other until a periodic state is reached. The step by step implementation procedure is given by He (1989). It should be mentioned that another advantage of the "Shape Correction" method, apart from saving computer storage, is that it can be extended to general situations with multiple perturbations at different frequencies and inter-blade phase angles (He, 1992a).

Two-Grid Time Integration

For a typical finite volume, the mesh size in the three directions is comparable in the mainly inviscid part of the flow field. The streamwise mesh grids can usually be more or less uniformly distributed. However, in the radial and circumferential directions highly refined mesh points have to be placed in the near-wall regions in order to resolve thin viscous layers. For time-accurate explicit time-integral schemes like the one adopted in the present method, the time step is limited by the smallest mesh size due to the numerical stability requirement (CFL condition). Thus the corresponding time step for unsteady flow solutions will be very small. It is recognized that a time-step length dictated by the mesh size in the mainly inviscid part of the flow field is sufficiently small to give an adequate temporal resolution. Hence the efficiency of the explicit time-marching method would be enhanced if the usable time-step length in the near-wall fine mesh regions can be increased. For this purpose, we adopt a two-grid time integration method.

The basic fine mesh is the one on which the flow variables are stored and the fluxes are evaluated. The coarse mesh is taken in such a way that each mesh cell contains several pitchwise and radial cells of the fine mesh. As shown in Fig. 1, a small finite volume *abcdefgh* of the fine mesh is contained in a big finite volume *ABCDEFGH* of the coarse mesh. For simplicity we now consider only one stage temporal integration over a fixed computational cell. If evaluated on a cell of the fine mesh as in a direct time-marching solution, the temporal change of flow variables is:

$$(U^{n+1}-U^n)_{\text{fine}}=\frac{\Delta t_{\text{fine}}}{\Delta V_{\text{fine}}}R_{\text{fine}} \tag{10}$$

where R_{fine} is the net flux for the finite volume on the fine mesh. If the temporal change is evaluated on a big cell of the coarse mesh, which contains the small cell on the fine mesh, we have:

$$(U^{n+1}-U^n)_{\text{coarse}}=\frac{\Delta t_{\text{coarse}}}{\Delta V_{\text{coarse}}}R_{\text{coarse}} \tag{11}$$

where $_{\text{coarse}}$ is the net flux for the big cell on the coarse mesh.

The time step Δt_{fine} is the time step allowed on the fine mesh limited by the smallest mesh spacing, while Δt_{coarse} is dictated by the mesh size of the coarse mesh and therefore can be much larger than Δt_{fine}. Suppose we want to run an unsteady solution with a time step Δt. Based on the smallest mesh size of the fine mesh (either in a radial direction or in the circumferential direction), Δt gives a Courant number CFL, much larger than CFL^0, the one dictated by the numerical stability. The idea is that the temporal integration should be formulated in such a way as if the solution were time marched first on the fine mesh up to its stability limit Δt_{fine} and then on the coarse mesh using Δt_{coarse} to make up the desired time step Δt. The time consistence condition is thus:

$$\Delta t=\Delta t_{\text{coarse}}+\Delta t_{\text{fine}}$$

Take

$$\Delta t_{\text{fine}}=\Delta t\,\frac{\text{CFL}^0}{\text{CFL}}$$

The final formulation for evaluating the temporal change on the fine mesh is:

$$(U^{n+1}-U^n)_{\text{fine}}=\frac{R_{\text{fine}}}{\Delta V_{\text{fine}}}\frac{\text{CFL}^0}{\text{CFL}}\Delta t+\frac{R_{\text{coarse}}}{\Delta V_{\text{coarse}}}\left(1-\frac{\text{CFL}^0}{\text{CFL}}\right)\Delta t \tag{12}$$

The implementation of the above formula is very easy, if we recall that the conservation relations give:

$$\Delta V_{\text{coarse}}=\sum_{i=1}^{N_c}\Delta V_{\text{fine}},\quad R_{\text{coarse}}=\sum_{i=1}^{N_c}R_{\text{fine}} \tag{13}$$

where N_c is the number of the small cells contained in the big cell. This two-grid formulation is applied at each stage of the Runge–Kutta integration. In the mainly inviscid flow part where the mesh size in the three directions is comparable, the basic one-grid time-marching formulation is recovered.

It should be pointed out that for a steady flow solution, this two-grid scheme is equivalent to a direct solution on the fine mesh because the residual, which drives the solution, is formed based on the net fluxes on the fine mesh. For an unsteady flow solution, the timewise accuracy on the fine mesh is no longer guaranteed. The loss in the temporal accuracy depends on the local ratio between fine and coarse mesh sizes. The length scale on which the temporal resolution is lost would be the mesh spacing length on the coarse mesh. As long as the coarse mesh spacing is taken to be much smaller than the physical wavelength of interest, this loss in time accuracy should be acceptable. More details and validations of this two-grid method for the two-dimensional full Navier–Stokes calculations have been recently given by He (1992b, 1993).

Validation of Three-Dimensional Euler Solution

For three-dimensional flows, validations of unsteady flow calculation methods become more difficult, because three-dimensional unsteady experimental data are currently hardly available in the published literature. Therefore comparisons between numerical methods and analytical or semi-analytical linear theories for simple cascade geometries at inviscid flow conditions must play an essential part in validations of three-dimensional unsteady solution methods. The present authors have proposed the following test case.

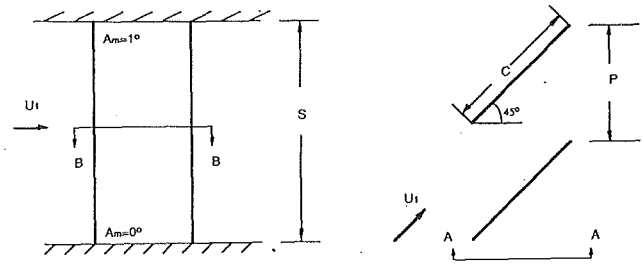

Fig. 2 Three-dimensional flat plate cascade test case geometry

The geometry is of a simple linear flat plate cascade placed between two parallel solid walls as shown in Fig. 2. The geometric parameters are

Chord length:	$C=0.1$ m
Stagger angle:	$\gamma=45$ deg
Pitch/chord ratio:	$P/C=1$
Span/chord ratio:	$S/C=3$

The inlet flow Mach number is 0.7 and the incidence is zero. The blades are oscillated in a three-dimensional mode. Each two-dimensional section is subject to torsion mode around its leading edge. The torsion amplitude is linearly varied along the span. At one end ("hub section"), the amplitude is 0. At the other end ("tip section"), the amplitude is 1 deg. The reduced frequency ($K = \omega C/u_\infty$) is 1. Two inter-blade phase angles, $\sigma = 0$ and 180 deg, are chosen.

For this kind of flat plate cascade geometries at zero incidence flow condition, time-linearized semi-analytical theories should be very accurate and can be practically regarded as "exact" solutions. A well-known three-dimensional semi-analytical lifting-surface method has been developed by Namba (e.g., 1977, 1987), who provided his results for this three-dimensional case (Namba, 1991).

The present calculations were carried out by using the inviscid Euler equations (setting viscous terms S_v to be zero). The mesh density is $81 \times 25 \times 21$ in the streamwise, pitchwise, and radial directions, respectively. Calculated unsteady pressure differences (jump) at each two-dimensional section are presented in the form of

$$\Delta CP_1=\frac{\Delta P_1}{0.5\rho_\infty u_\infty^2 A_m}$$

where ΔP_1 is the first harmonic pressure jump across the blade; A_m is the torsion amplitude at the tip (i.e., 1 deg) in radian. The spanwise position of each two-dimensional section is given by:

$$\Delta R=\frac{R}{S}$$

where R is the distance measured from the hub section.

Figure 3 shows the chordwise distributions of the real and imaginary parts of the unsteady pressure jump at six spanwise sections ($\Delta R = 0.0$; 0.2; 0.4; 0.6; 0.8; 1.0) for the interblade phase angle $\alpha = 0$ deg. The corresponding results for $\sigma = 180$ deg are given in Fig. 4. Also presented in these figures are Namba's semi-analytical results. For both inter-blade phase angles, the present Euler calculations agree very well with Namba's theory.

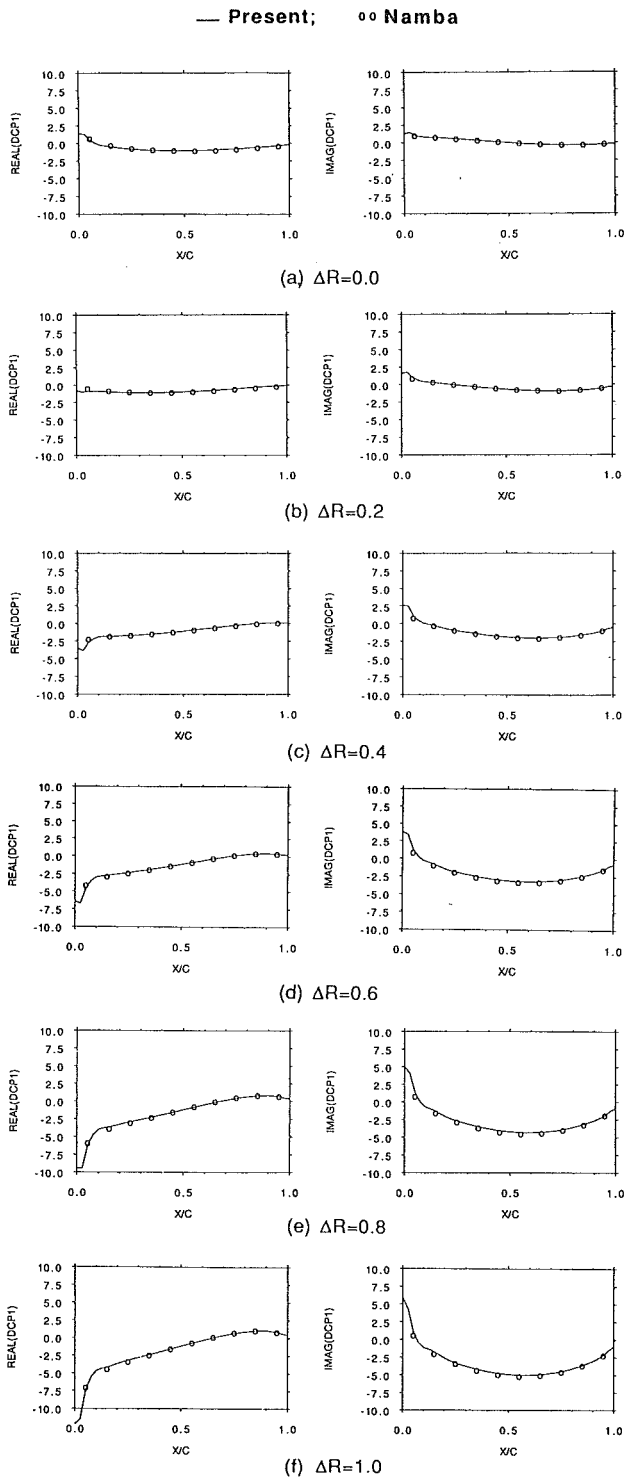

Fig. 3 Real and imaginary parts of unsteady pressure jump coefficient at different spanwise sections (σ = 0 deg)

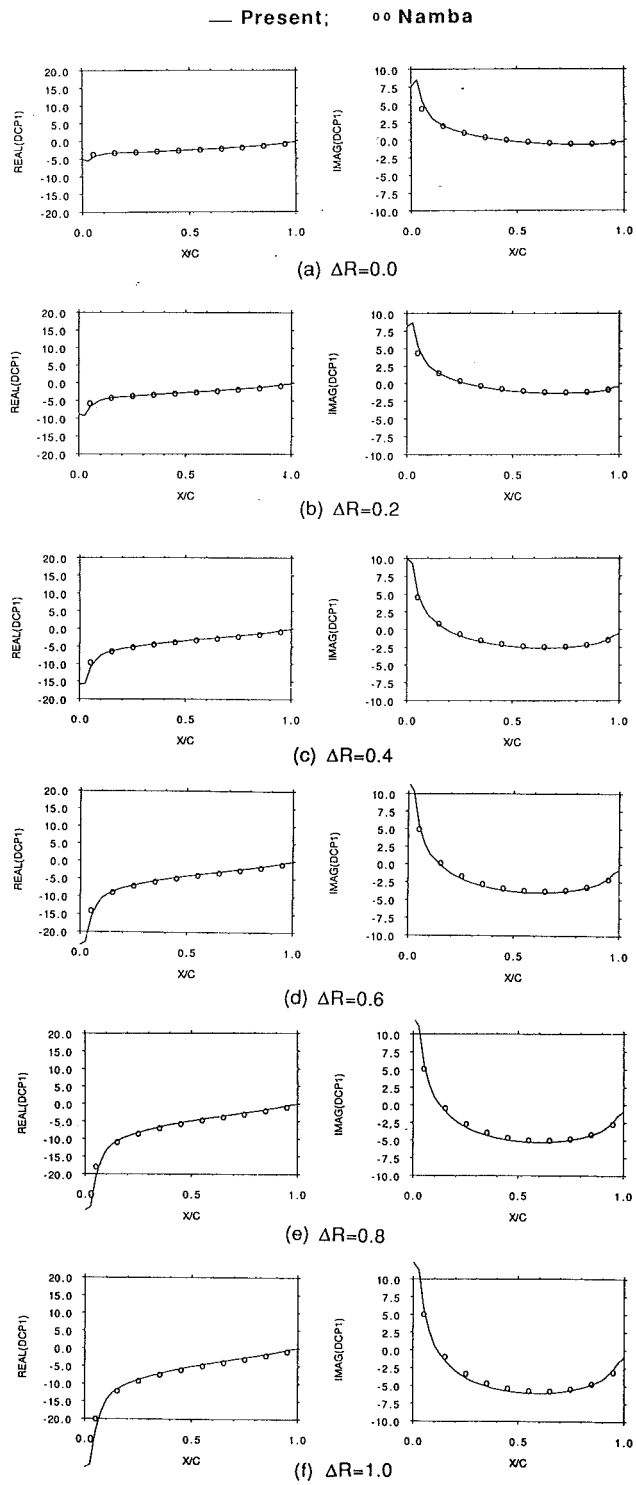

Fig. 4 Real and imaginary parts of unsteady pressure jump coefficient at different spanwise sections (σ = 180 deg)

Steady and Unsteady Viscous Results for a Transonic Fan

A check on the present viscous flow solution has been made by calculating the steady flow through a transonic fan rotor, known as "NASA Rotor 67," of which the steady flow field had been extensively measured at NASA Lewis (Strazisar et al., 1989). A computational domain with mesh points 73 × 25 × 25 was used in the calculation. Figure 5(*a*) shows the meridional view of the mesh. The blade-to-blade view of the mesh at the midspan section is given in Fig. 5(*b*).

For this experimental case, the rotor blades have about 0.8 percent tip clearance. To take this into account, a very simple tip-clearance model is adopted in the present calculation. As shown in Fig. 6, the radial mesh spacing (*a-c* or *b-d*) of the computational cells adjacent to the tip is taken to be the tip gap (i.e., 0.8 percent of the span). For steady flows, the tip-leakage effect is approximately included by equating flow variables at *a* and *b* (*c* and *d*). For unsteady flows, this simple tip-clearance model is implemented by applying the phase-shifted periodic condition for two mesh lines near the tip.

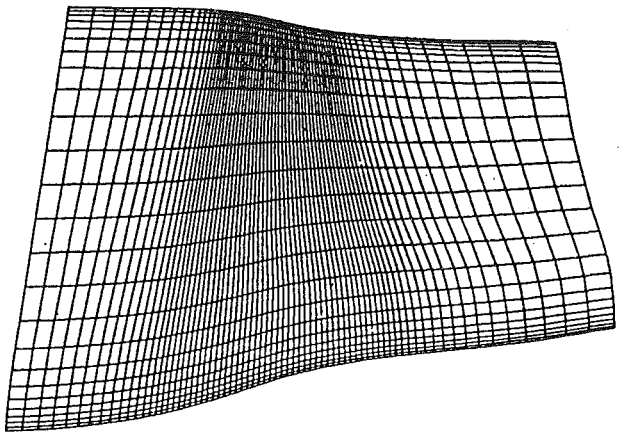

(a). Meridional View at Midpassage

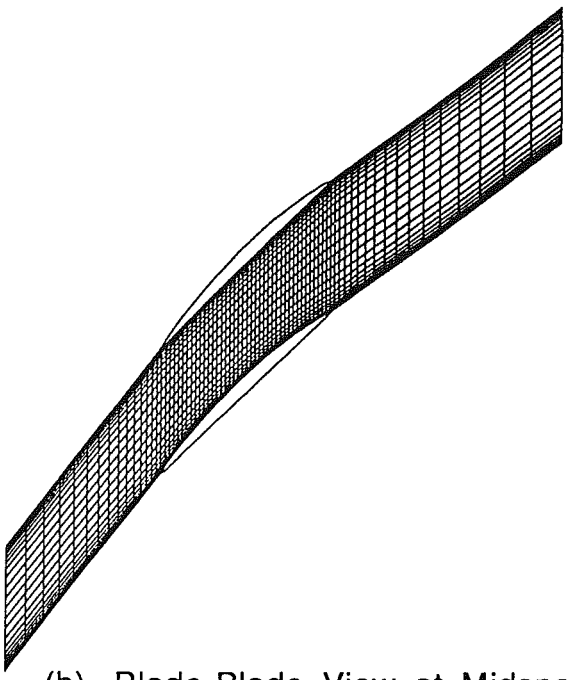

(b). Blade-Blade View at Midspan

Fig. 5 Computational mesh for a transonic rotor

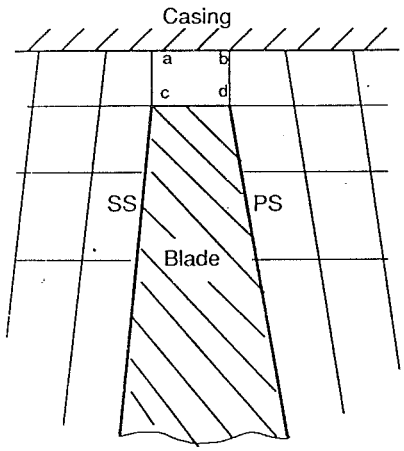

Fig. 6 A tip-leakage model

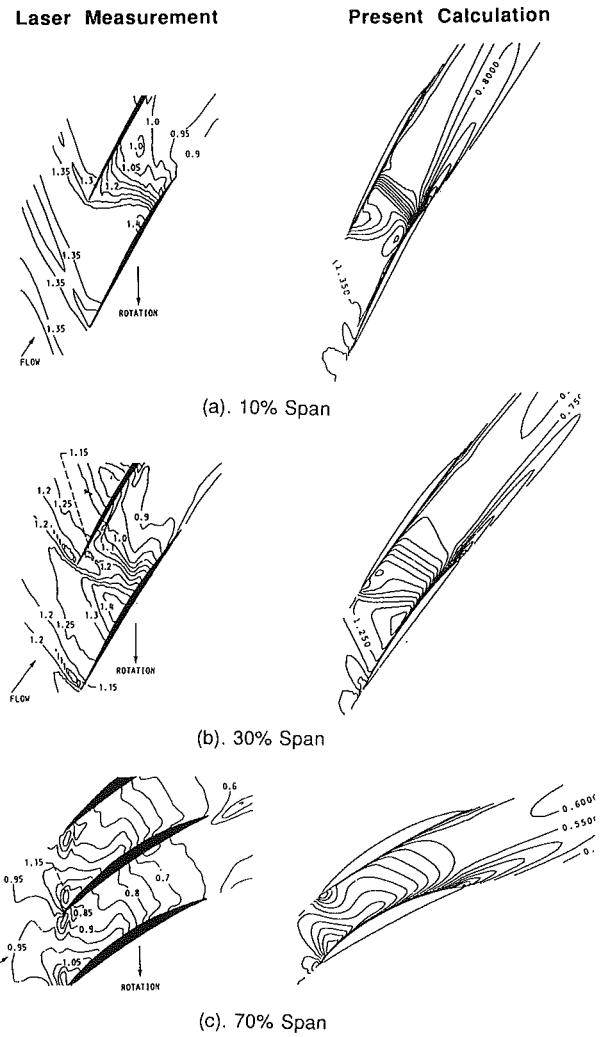

Fig. 7 Mach number contours (interval = 0.05) at three spanwise sections (position measured from the tip)

The flow condition chosen for the present calculation is that at the rotor's peak efficiency. The calculation is performed assuming that the flow is fully turbulent. At the inlet the measured flow angle, stagnation pressure, and stagnation temperature in the absolute system are specified. The measured static pressure at the outlet is specified. Figure 7 shows the calculated steady Mach number contours at the blade-to-blade sections of 10, 30, and 70 percent span measured from the tip. Also shown in Fig. 7 is the corresponding Laser Anemometry measurements result (Strazisar et al., 1989). The results near the hub agree reasonably well with the experiment. At the section near the tip, the present calculated shock position is more rearward than that experimentally observed, indicating that the tip-leakage effect might be underpredicted. This is not unexpected considering the simple tip-clearance treatment adopted in the calculation. It may also be argued that the simple mixing-length turbulence model adopted may be another major reason for the discrepancy. It is, however, noticed that the flow patterns for this case predicted recently by Jennions and Turner (1992) who adopted the full Navier–Stokes equations with the $k \sim \epsilon$ turbulence model, are similar to the present ones.

In order to demonstrate the feasibility of the present three-dimensional unsteady viscous solver for blade flutter calculations under practical conditions, an unsteady calculation was carried out for this transonic fan. After the above-mentioned steady solution is obtained, the blades are oscillated in a torsion mode at each radial section. The torsion axis for all the sections

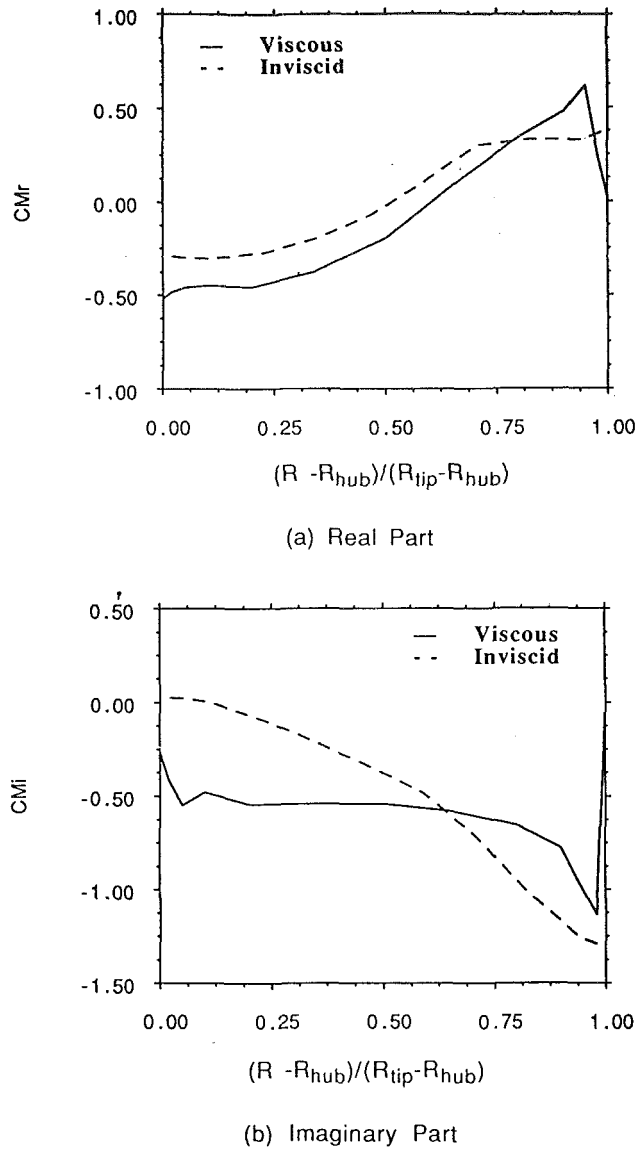

Fig. 8 Calculated spanwise distribution of unsteady moment coefficient

is a radial line, which goes through the midpoint of the chord on the hub section. The amplitude is linearly varied from 0 deg at the hub to 0.5 deg at the tip. The oscillation frequency is taken to be 1000 Hz, which based on parameters at the rotor-tip section gives a reduced frequency of 1.5. The interblade-phase angle is 180 deg. It should be mentioned that for this unsteady viscous solution, the time step by using the two-grid method is increased by a factor of 10 compared to the direct explicit time-marching solution. A periodic solution with 10 periods of oscillation requires a total of 48 CPU hours on a single processor of the Alliant FX-80 computer, which is 40 percent faster than a personal computer PC-486 for the present code.

Figure 8 shows calculated spanwise distributions of real and imaginary parts of the unsteady moment coefficient. The moment coefficient at each spanwise section is defined in the same way as that for a two-dimensional cascade case (Fransson, 1984) except that the blade vibration amplitude for normalization is taken from the tip section. Also presented in Fig. 8 are results from the three-dimensional inviscid Euler solution obtained at the same steady and unsteady conditions. For the inviscid Euler solution, a mesh with the same number of points and a uniform distribution in the circumferential and radial directions is used. It has been well established that for transonic fans, inviscid and viscous steady flow methods predict very different shock structures. So the marked difference in the unsteady results between the inviscid and viscous solutions for the present case is not unexpected. The imaginary part of the moment coefficient is a direct measure of the aerodynamic damping. The negative values (i.e., positive damping) of the imaginary part are predicted along the whole span by the viscous solution and virtually along the whole span by the inviscid solution. Thus both the solutions suggest that the rotor blades under these unsteady conditions would be aeroelastically stable. It should be noted, however, that the maximum differences in terms of magnitude and phase of the unsteady loading between the inviscid and the viscous solution are in the regions near the tip and hub where the flow is dominated by three-dimensional viscous effects. The tip-leakage effect can be clearly seen from the results of the viscous solution. The unsteady loading is diminished at the tip section. In addition, there is a local region of high loading near the tip, probably induced mainly by the variation of the tip leakage flow due to the blade vibration. The three-dimensional inviscid Euler solution, on the other hand, shows a much smoother spanwise loading distribution.

Concluding Remarks

This paper describes the first-known three-dimensional unsteady viscous flow solution method for blade flutter calculations. The simplified thin-layer Navier–Stokes equations are discretized in the cell-vertex finite volume scheme in a single-blade-passage computational domain, and temporally integrated in the four-stage Runge–Kutta scheme.

The phase-shifted periodic condition is implemented by using the Shape Correction method, which greatly reduces the computer storage requirement compared to the conventional "Direct Store" method.

The time-step limitation on the explicit time-marching scheme due to thin-viscous-layer resolution is considerably relaxed by using a time-consistent two-grid time-marching technique.

Two test cases have been used to validate the present method. The first one is a proposed three-dimensional oscillating flat plate cascade. Calculated unsteady pressure distributions using the Euler equations (setting zero viscosity) are in very good agreement with a well-established semi-analytical theory. The second test case is for a transonic fan rotor with tip leakage. Calculated steady viscous flow results agree well with the corresponding experiment and with other calculations. Calculated unsteady loadings due to oscillations of the rotor blades reveal some significant three-dimensional viscous effects. The feasibility of the present simplified thin-layer Navier–Stokes solver for oscillating blade flows at practical conditions has been demonstrated.

Acknowledgments

The authors wish to thank Professor M. Namba for providing his results for the three-dimensional flat plate cascade test case. The present work has been sponsored by Rolls-Royce plc. L. He has been in receipt of a Rolls-Royce Senior Research Fellowship at Girton College, Cambridge University. The technical support provided by Drs. Peter Stow, Alex Cargill, and Arj Suddhoo of Rolls-Royce is gratefully acknowledged.

References

Chi, R. M., 1993, "An Unsteady Lifting Surface Theory for Ducted Fan Blades," ASME JOURNAL OF TURBOMACHINERY, Vol. 115, pp. 175–188.

Denton, J. D., 1992, "The Calculation of Three-Dimensional Viscous Flow Through Multistage Turbomachines," ASME JOURNAL OF TURBOMACHINERY, Vol. 114, pp. 18–26.

Erdos, J. I., Alzner, E., and McNally, W., 1977, "Numerical Solution of Periodic Transonic Flow Through a Fan Stage," *AIAA Journal*, Vol. 15, No. 11.

Fransson, T. H., 1984, "Two-Dimensional and Quasi-Three-Dimensional Experiments of Standard Configuration for Aeroelastic Investigations in Turbomachine-Cascades," *Proc. of the 3rd Symp. on Unsteady Aerodynamics and Aeroelasticity of Turbomachines and Propellers*, Cambridge, United Kingdom.

Giles, M. B., 1990, "Nonreflecting Boundary Conditions for Euler Equation Calculations," *AIAA Journal*, Vol. 28, No. 12, pp. 2050–2058.

Giles, M. B., 1991, Massachusetts Institute of Technology, Private Communication.

Gerolymos, G. A., 1993, "Advances in the Numerical Integration of the Three-Dimensional Euler Equations in Vibrating Cascades," ASME JOURNAL OF TURBOMACHINERY, Vol. 115, pp. 781–790.

Hall, K. C., and Lorence, C. B., 1993, "Calculation of Three-Dimensional Unsteady Flows in Turbomachinery Using the Linearized Harmonic Euler Equations," ASME JOURNAL OF TURBOMACHINERY, Vol. 115, pp. 800–809.

He, L., 1989, "An Euler Solution for Unsteady Flows Around Oscillating Blades," ASME JOURNAL OF TURBOMACHINERY, Vol. 112, pp. 714–722.

He, L., 1992a, "A Method of Simulating Unsteady Turbomachinery Flows With Multiple Perturbations," *AIAA Journal*, Vol. 30, No. 12.

He, L., 1992b, "Numerical Solutions for Unsteady Turbomachinery Flows," Lecture Notes on "Turbomachinery C.F.D.," Advanced Course for Industry, Cambridge, United Kingdom, June.

He, L., 1993, "A New Two-Grid Acceleration Method for Unsteady Navier-Stokes Calculations," *AIAA Journal of Propulsion and Power*, Vol. 9, No. 2.

Jameson, A., 1983, "Numerical Solution of the Euler Solution for Compressible Inviscid Fluids," Report MAE 1643, Princeton University, Princeton, NJ.

Jennions, I. K., and Turner, M. G., 1993, "Three-Dimensional Navier-Stokes Computations of Transonic Fan Flow Using an Explicit Flow Solver and an Implicit k–ϵ Solver," ASME JOURNAL OF TURBOMACHINERY, Vol. 115, pp. 261–272.

Namba, M., 1976, "Lifting Surface Theory for Unsteady Flows in Rotating Annular Cascade," in: *Proceedings of the 1st IUTAM Symposium on Aeroelasticity in Turbomachines*, Paris.

Namba, M., 1987, "Three-Dimensional Methods," in: *Aeroelasticity in Axial-Flow Turbomachines*, AGARD-AG-298, Vol. 1, M. F. Platzer and F. O. Carta, eds.

Namba, M., 1991, Kyushu University, Private Communication.

Strazisar, A. J., Wood, J. R., Hathaway, M. D., and Suder, K. L., 1989, "Laser Anemometer Measurements in a Transonic Axial-Flow Fan Rotor," NASA Technique Report 2879.

Verdon, J. M., and Caspar, J. R., 1982, "Development of a Linear Unsteady Aerodynamics for Finite-Deflection Cascades," *AIAA Journal*, Vol. 20, No. 9.

Whitehead, D. S., 1982, "The Calculations of Steady and Unsteady Transonic Flow in Cascades," Report CUED/A-Turbo/TR118, Cambridge University Engineering Department, United Kingdom.

A Linearized Euler Analysis of Unsteady Transonic Flows in Turbomachinery

K. C. Hall

W. S. Clark

C. B. Lorence

Department of Mechanical Engineering
and Materials Science,
Duke University,
Durham, NC 27708-0300

A computational method for efficiently predicting unsteady transonic flows in two- and three-dimensional cascades is presented. The unsteady flow is modeled using a linearized Euler analysis whereby the unsteady flow field is decomposed into a nonlinear mean flow plus a linear harmonically varying unsteady flow. The equations that govern the perturbation flow, the linearized Euler equations, are linear variable coefficient equations. For transonic flows containing shocks, shock capturing is used to model the shock impulse (the unsteady load due to the harmonic motion of the shock). A conservative Lax-Wendroff scheme is used to obtain a set of linearized finite volume equations that describe the harmonic small disturbance behavior of the flow. Conditions under which such a discretization will correctly predict the shock impulse are investigated. Computational results are presented that demonstrate the accuracy and efficiency of the present method as well as the essential role of unsteady shock impulse loads on the flutter stability of fans.

Introduction

In recent years, a number of linearized flow analyses have been developed to compute unsteady flows in cascades, especially the unsteady flows that produce the aeroelastic phenomena of flutter and forced response. The unsteady aerodynamic loads acting on transonic airfoils in cascades are composed of two parts: the unsteady pressure distribution away from the shock, and a "shock impulse" load that acts where the shock impinges on the airfoil surface. This shock impulse arises from the unsteady motion of the shock. Accurate prediction of the shock impulse is important since the unsteady aerodynamic load due to the shock impulse is of the same order as the unsteady aerodynamic loads due to the unsteady pressure away from the shock. In viscous flows, the shock is smeared near the airfoil surface due to shock/boundary layer interaction and hence, strictly speaking, no shock impulse exists at the surface. Away from the airfoil, however, the shock wave is very thin, typically on the order of a few mean free paths thick, and the concept of a shock impulse is important in connecting the regions of smooth flow on either side of the shock.

Verdon and Caspar (1984), Verdon (1987), and Whitehead (1987, 1990) have developed linearized potential analyses of two-dimensional subsonic and transonic flows in cascades. Both Verdon and Whitehead have used shock capturing to model unsteady shock loads. Verdon has also used shock fitting in his linearized potential analysis to model the shock motion explicitly. Because of the assumption of isentropic and irrotational flow, however, these potential analyses cannot be used to model unsteady flows with strong shocks, flows with shocks that span the blade passage, or general three-dimensional flows. For this reason, investigators have begun to develop linearized Euler analyses of unsteady cascade flows (Hall and Crawley, 1989; Hall and Clark, 1993a; Holmes and Chuang, 1993; Kahl and Klose, 1993; Hall and Lorence, 1993). Hall and Crawley (1989) have shown that shock fitting can be implemented within the framework of a linearized Euler analysis to model accurately the unsteady motion of shocks. However, due to the inherent complexity of shock fitting algorithms, one would prefer to use the simpler shock capturing technique to model the shock impulse.

While shock capturing is favored for its simplicity, it has only recently been shown that the shock impulse load can be modeled properly using shock capturing within a linearized framework. For example, Lindquist (1991) and Lindquist and Giles (1991, 1994) have shown that the unsteady shock load can be accurately modeled using linearized Euler analyses provided that the scheme is conservative and the shock is sufficiently smeared. Their results thus far, however, have been limited to quasi-one-dimensional channel flows.

Two approaches have been suggested for obtaining discretizations of the linearized Euler equations. Using the first approach, referred to in this paper as Method I, one first discretizes the nonlinear unsteady Euler equations and then linearizes the resulting finite difference equations. Using the second approach, Method II, one first linearizes the nonlinear unsteady Euler equations and then discretizes the resulting linearized equations using traditional finite difference or finite volume techniques.

Contributed by the International Gas Turbine Institute and presented at the 38th International Gas Turbine and Aeroengine Congress and Exposition, Cincinnati, Ohio, May 24-27, 1993. Manuscript received by the ASME Headquarters February 19, 1993. Paper No. 93-GT-94. Associate Technical Editor: H. Lukas.

In this paper, we show by numerical experiment that both Method I and Method II linearizations will produce the correct shock impulse provided that the finite difference representation of the linearized Euler equations is consistent and conservative. Having demonstrated the validity of a linearized analysis of transonic flows with shocks, we present a linearized Euler analysis (Method II type) of unsteady two- and three-dimensional flow in cascades. Ni's Lax-Wendroff scheme (Ni, 1982) is used to obtain a finite volume representation of the unsteady linearized Euler equations. Computational results are presented for both two- and three-dimensional unsteady transonic flows in cascades. Some of these calculations are compared to those computed using a nonlinear time-marching shock capturing Euler analysis. It is shown that the present unsteady linearized analysis agrees quite well with the nonlinear analysis. The computed results also demonstrate that the unsteady shock loads can provide a destabilizing influence on the flutter stability of cascades.

Theory

Flow Field Description. In this paper, we assume that the unsteady flow is inviscid and adiabatic, and that the unsteady flow in a cascade may be modeled by the Euler equations. For a three-dimensional rotating Cartesian coordinate system, the Euler equations are given by

$$\frac{\partial \hat{\mathbf{U}}}{\partial t}+\frac{\partial \hat{\mathbf{F}}}{\partial x}+\frac{\partial \hat{\mathbf{G}}}{\partial y}+\frac{\partial \hat{\mathbf{H}}}{\partial z}-\hat{\mathbf{S}}=0 \tag{1}$$

where $\hat{\mathbf{U}}$ is the vector of conservation variables, $\hat{\mathbf{F}}$, $\hat{\mathbf{G}}$, and $\hat{\mathbf{H}}$ are the so-called flux vectors, and $\hat{\mathbf{S}}$ is a vector of source terms arising from centrifugal and Coriolis forces. These vector quantities are given by

$$\hat{\mathbf{U}}=\begin{bmatrix}\hat{\rho}\\ \hat{\rho}\hat{u}\\ \hat{\rho}\hat{v}\\ \hat{\rho}\hat{w}\\ \hat{e}\end{bmatrix},\quad \hat{\mathbf{F}}=\begin{bmatrix}\hat{\rho}\hat{u}\\ \hat{\rho}\hat{u}^2+\hat{p}\\ \hat{\rho}\hat{u}\hat{v}\\ \hat{\rho}\hat{u}\hat{w}\\ \hat{\rho}\hat{u}\hat{I}\end{bmatrix},\quad \hat{\mathbf{G}}=\begin{bmatrix}\hat{\rho}\hat{v}\\ \hat{\rho}\hat{u}\hat{v}\\ \hat{\rho}\hat{v}^2+\hat{p}\\ \hat{\rho}\hat{v}\hat{w}\\ \hat{\rho}\hat{v}\hat{I}\end{bmatrix},$$

$$\hat{\mathbf{H}}=\begin{bmatrix}\hat{\rho}\hat{w}\\ \hat{\rho}\hat{u}\hat{w}\\ \hat{\rho}\hat{v}\hat{w}\\ \hat{\rho}\hat{w}^2+\hat{p}\\ \hat{\rho}\hat{w}\hat{I}\end{bmatrix},\quad \hat{\mathbf{S}}=\begin{bmatrix}0\\ 0\\ \hat{\rho}(\Omega^2 y-2\Omega\hat{w})\\ \hat{\rho}(\Omega^2 z+2\Omega\hat{v})\\ 0\end{bmatrix}$$

where $\hat{\rho}$ is the density, $\hat{p}$ is the pressure, $\hat{u}$, $\hat{v}$, and $\hat{w}$ are the x, y, and z components of velocity, $\hat{e}$ is the internal energy, and $\hat{I}$ is the rothalpy. Here we have assumed that the coordinate system is rotating about the x axis with rotational speed Ω. The pressure, $\hat{p}$, and the rothalpy, $\hat{I}$, are given by

$$\hat{p}=(\gamma-1)\left[\hat{e}-\frac{1}{2}\hat{\rho}(\hat{u}^2+\hat{v}^2+\hat{w}^2)+\frac{1}{2}\hat{\rho}\Omega^2 r^2\right]$$

and

$$\hat{I}=\frac{\hat{e}+\hat{p}}{\hat{\rho}}=\frac{\gamma}{\gamma-1}\frac{\hat{p}}{\hat{\rho}}+\frac{1}{2}(\hat{u}^2+\hat{v}^2+\hat{w}^2)-\frac{1}{2}\Omega^2 r^2$$

where r is the distance from the x axis ($r=\sqrt{y^2+z^2}$).

Next, we would like to determine the small disturbance behavior of Eq. (1) due to, for example, the fluttering motion of the blades of the cascade. To improve the accuracy of these calculations, a number of investigators have proposed the use of a harmonically deforming computational grid (Huff and Reddy, 1989; Hall and Clark, 1993a, 1993b; Holmes and Chuang, 1993; Hall and Lorence, 1993). The motion of the grid is defined by

$$x(\xi,\eta,\zeta,\tau)=\xi+f(\xi,\eta,\zeta)e^{j\omega\tau} \tag{2a}$$

$$y(\xi,\eta,\zeta,\tau)=\eta+g(\xi,\eta,\zeta)e^{j\omega\tau} \tag{2b}$$

$$z(\xi,\eta,\zeta,\tau)=\zeta+h(\xi,\eta,\zeta)e^{j\omega\tau} \tag{2c}$$

$$t(\xi,\eta,\zeta,\tau)=\tau \tag{2d}$$

where ω is the frequency of vibration of the blades, and where f, g, and h are the perturbation amplitudes of the grid motion

Nomenclature

A = channel height
B = model equation source term coefficient
$\mathbf{b}$ = inhomogeneous part of linearized Euler equations
C_m = unsteady pitching moment coefficient
C_p, c_p = mean and unsteady coefficient of pressure $= (P - P_{-\infty})/(\rho V^2/2)$
$\hat{e}$ = internal energy
f, g, h = grid motion perturbation functions
$\hat{\mathbf{F}}$, $\hat{\mathbf{G}}$, $\hat{\mathbf{H}}$ = Euler equation flux vectors
$\mathbf{F}$, $\mathbf{G}$, $\mathbf{H}$ = Euler equation mean flow flux vectors
$\hat{F}$ = model equation flux
F = model equation mean flow flux
G = linear blade-to-blade gap
$g(x, t)$ = test function
$\hat{I}$ = rothalpy
I = impulse
j = $\sqrt{-1}$
M = Mach number
$\hat{P}$ = model equation "pressure"
P = model equation mean flow "pressure"
$\hat{p}$ = static pressure
r = distance from x axis
R = overrelaxation factor
$\hat{\mathbf{S}}$ = Euler equation source term
$\mathbf{S}$ = Euler equation mean flow source term
t = time
$\hat{u}$, $\hat{v}$, $\hat{w}$ = Cartesian components of velocity
$\hat{\mathbf{U}}$ = vector of conservation variables
$\mathbf{U}$, $\mathbf{u}$ = mean, perturbation conservation variables
$\hat{U}$ = model equation conservation variable
U, u = model equation mean and perturbation conservation variable
X_s = mean shock location
x_s = complex amplitude of shock motion
x, y, z = Cartesian coordinates
β = inflow angle measured from axial direction
γ = ratio of specific heats
Θ = stagger angle
ξ, η, ζ = computational coordinates
$\hat{\rho}$ = static density
σ = interblade phase angle
τ = time in computational coordinates
ω, $\bar{\omega}$ = dimensional and reduced frequencies
Ω = shaft rotation rate

Subscripts

i = grid index
p = due to perturbation in pressure
T = total or stagnation quantity
u = due to perturbation in conservation variable
$-\infty, \infty$ = far upstream and downstream regions

Superscripts

n = time index

about the mean positions, ξ, η, and ζ. Having defined the grid motion, the unsteady flow field is represented by the perturbation series

$$\hat{\mathbf{U}}(\xi, \eta, \zeta, \tau) = \mathbf{U}(\xi, \eta, \zeta) + \mathbf{u}(\xi, \eta, \zeta)e^{j\omega\tau} \tag{3}$$

Substitution of Eqs. (2) and (3) into Eq. (1) and collection of the terms that are first order in the perturbations $\mathbf{u}$ and $(f, g, h)^T$ results in the linearized Euler equations,

$$j\omega\mathbf{u} + \frac{\partial}{\partial\xi}\left(\frac{\partial\mathbf{F}}{\partial\mathbf{U}}\mathbf{u}\right) + \frac{\partial}{\partial\eta}\left(\frac{\partial\mathbf{G}}{\partial\mathbf{U}}\mathbf{u}\right) + \frac{\partial}{\partial\zeta}\left(\frac{\partial\mathbf{H}}{\partial\mathbf{U}}\mathbf{u}\right) - \frac{\partial\mathbf{S}}{\partial\mathbf{U}}\mathbf{u} = \mathbf{b} \tag{4}$$

where $\mathbf{b}$ is a fairly complex expression that depends on the mean flow and the prescribed grid motion (see, for example, Hall and Lorence, 1993).

Numerical Modeling of the Shock Impulse. The first question we address in this paper is: What is the proper way to discretize and linearize the Euler equations in such a way that the linearized finite difference or finite volume equations properly predict the shock impulse loads that result from the unsteady shock motion. There are two obvious approaches one can take to obtain a discretization of the linearized Euler equations. One approach (Method I) is first to discretize the nonlinear Euler equations and then linearize the resulting nonlinear finite difference equations. The other approach (Method II) is first to linearize the nonlinear Euler equations then discretize the resulting linearized equations. We claim here that both approaches will produce the correct result provided that the resulting difference equations are conservative.

Due to the complexity of the three-dimensional Euler equations, we consider the simpler one-dimensional model equation given by

$$\frac{\partial\hat{U}}{\partial t} + \frac{\partial\hat{F}}{\partial x} + B\hat{P} = 0 \tag{5}$$

where $\hat{F} = \hat{F}(\hat{U})$, $\hat{P} = \hat{P}(\hat{U})$, and $B = B(x)$. This model equation is very similar in form to the quasi-one-dimensional Euler equations that describe flow in a channel with a spatially varying cross sectional area. Since $\hat{F}$ and $\hat{P}$ are in general nonlinear functions of the conservation variable $\hat{U}$, this model equation is nonlinear.

As before, we model the conservation variable $\hat{U}$ as the sum of a mean part U plus a small harmonic perturbation $ue^{j\omega t}$. The mean solution is governed by

$$\frac{\partial F}{\partial x} + BP = 0 \tag{6}$$

where $F = F(U)$ and $P = P(U)$. The linearized unsteady model equation is given by

$$j\omega u + \frac{\partial}{\partial x}\left(\frac{\partial F}{\partial U}u\right) + B\frac{\partial P}{\partial U}u = 0 \tag{7}$$

where u is the perturbation solution, and $\partial F/\partial U$ and $\partial P/\partial U$ are steady flow Jacobians.

Returning for the moment to the unsteady nonlinear model equation, Eq. (5), it is well known that because the model equation is nonlinear, it will in general admit genuine solutions, that is, solutions with flow discontinuities. In smooth regions of the flow, the genuine solutions satisfy the differential equation, Eq. (5). The *weak* solution is that genuine solution that also satisfies the integral relation

$$\int\int (g_t\hat{U} - g_x\hat{F})dxdt + \int g(x, 0)\hat{U}(x, 0)dx = 0 \tag{8}$$

for every test function $g(x, t)$ that vanishes for large x or t and that has continuous first derivatives (Lax, 1954; Lax and Wendroff, 1960). One can then show that the unsteady Rankine-Hugoniot shock jump conditions at flow discontinuities are given by

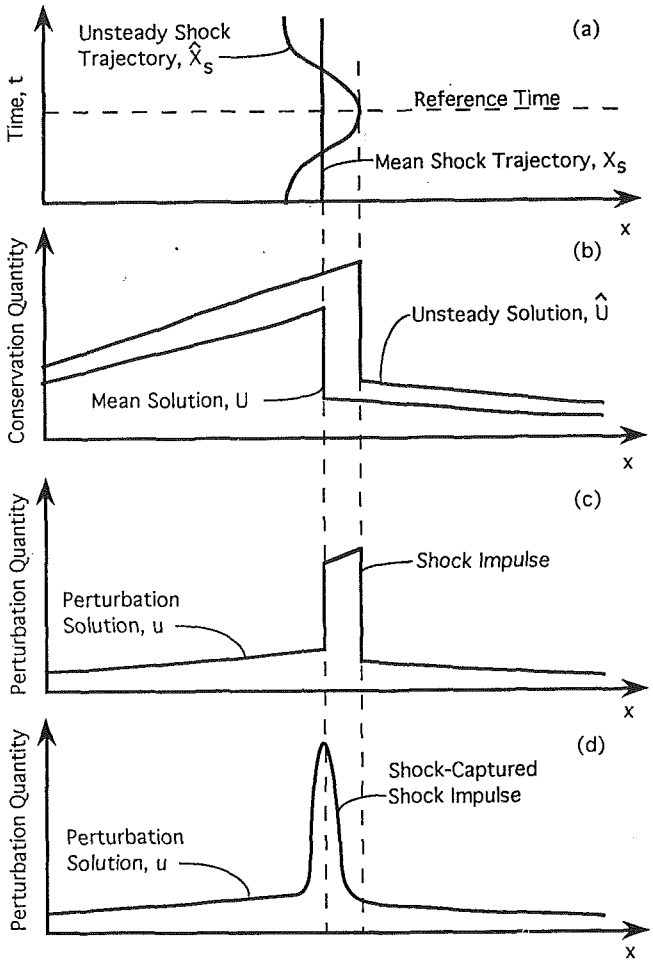

Fig. 1 Top to bottom: (*a*) trajectory of shock in a channel or on an airfoil surface; (*b*) mean and unsteady flow distribution; (*c*) perturbation flow showing shock impulse; (*d*) same as (*c*) with impulse modeled by shock capturing. Note that the area under the impulse is the same as in (*c*).

$$\dot{\hat{X}}_s[\![\hat{U}]\!] - [\![\hat{F}]\!] = 0 \tag{9}$$

where the symbol $[\![\ldots]\!]$ denotes the jump in the enclosed quantity across the shock, and $\hat{X}_s$ is the velocity of the shock.

If one then considers an unsteady flow with small harmonic unsteadiness, one may linearize Eq. (9) to obtain the linearized shock jump conditions (Hall and Crawley, 1989)

$$j\omega x_s[\![U]\!] - \left[\!\left[\frac{\partial F}{\partial U}u\right]\!\right] - x_s\left[\!\left[\frac{\partial F}{\partial x}\right]\!\right] = 0 \tag{10}$$

where u is the small disturbance part of the unsteady flow and x_s is the small complex amplitude of the shock motion. Noting that the steady flow solution is given by $\partial F/\partial x = -BP$, Eq. (10) may be rewritten as

$$j\omega x_s[\![U]\!] - \left[\!\left[\frac{\partial F}{\partial U}u\right]\!\right] + x_sB[\![P]\!] = 0 \tag{11}$$

A graphic interpretation of Eq. (11) is shown in Fig. 1. Shown are the mean and unsteady flow shock trajectories as well as the resulting unsteady flow, $\hat{U}$, the mean flow U, and the perturbation flow, u. Note that u is just the difference between the unsteady and mean flows, $u = \hat{U} - U$. Further note that near the shock, an impulse in u appears due to the motion of the shock. In the limit as the unsteadiness in the flow tends toward zero, the integrated value of this impulse is given by

$$I_u = \int_{X_S-\epsilon}^{X_S+\epsilon} u\,dx = -x_s[\![U]\!] = -x_s(U_2 - U_1) \tag{12}$$

Finally, Eq. (11) may be written as

$$j\omega I_u + \left[\!\left[\frac{\partial F}{\partial U}\,u\right]\!\right] + BI_p = 0 \tag{13}$$

We presently demonstrate that the weak solution of the linearized unsteady model equation, Eq. (7), produces an equivalent shock jump condition. Multiplying Eq. (7) by a test function $g(x)$ and integrating the result over the solution domain $x \in [0, L]$, we obtain

$$\int_0^L g(x)\left[j\omega u + \frac{\partial}{\partial x}\left(\frac{\partial F}{\partial U}\,u\right) + B\,\frac{\partial P}{\partial U}\,u\right]dx = 0 \tag{14}$$

Integration by parts applied to the middle term in Eq. (14) gives

$$\int_0^L \left[j\omega g u - \frac{dg}{dx}\,\frac{\partial F}{\partial U}\,u + gB\,\frac{\partial P}{\partial U}\,u\right]dx + \left(g\,\frac{\partial F}{\partial U}\,u\right)\Bigg|_0^L = 0 \tag{15}$$

Next we let the test function $g(x)$ be given by

$$g(x) = \begin{cases} 1 \text{ if } X_s - \epsilon \le x \le X_s + \epsilon \\ 0 \text{ otherwise} \end{cases} \tag{16}$$

where X_s is the mean shock position and ϵ is a small positive number. Differentiating Eq. (16) with respect to x gives

$$\frac{dg}{dx} = \delta[x - (X_s - \epsilon)] - \delta[x - (X_s + \epsilon)] \tag{17}$$

where $\delta[\ldots]$ is the Dirac delta function. Substitution of Eqs. (16) and (17) into Eq. (15) gives the desired shock jump conditions of the linearized unsteady model equation,

$$j\omega \int_{X_s-\epsilon}^{X_s+\epsilon} u\,dx + \left[\!\left[\frac{\partial F}{\partial U}\,u\right]\!\right] + B\int_{X_s-\epsilon}^{X_s+\epsilon} \frac{\partial P}{\partial U}\,u\,dx = 0 \tag{18}$$

The integrals in Eq. (18) are the areas under the impulse in u and the impulse in p, the perturbations in the conservation variable and pressure, respectively, and are denoted here by I_u and I_p (see Fig. 1).

Finally then, we may write the Rankine-Hugoniot jump condition for the linearized model equation as

$$j\omega I_u + \left[\!\left[\frac{\partial F}{\partial U}\,u\right]\!\right] + BI_p = 0 \tag{19}$$

This expression is identical to Eq. (13), thus demonstrating that the weak solution to the linearized unsteady model equation *may* be equal to the linearized weak solution of the nonlinear model equation. However, the equality of Eqs. (13) and (19) should be regarded as a necessary but not sufficient condition for the linearized model equation to predict the correct shock impulse. As a practical matter, as will be demonstrated shortly, the shock impulse is correctly predicted using the linearized Euler equations provided that the discretization scheme is stable, consistent, and conservative.

Also note the importance of the *area* of the impulse. When capturing the shock impulse, the width and height of the impulse will depend on the amount of smoothing (or artificial viscosity) in the numerical scheme. The area under the impulse, however, should be independent of the smoothing.

Method I and Method II Linearizations. To illustrate the difference between Method I and Method II linearizations, we consider again the model equation given by Eq. (5) with the source term set to zero ($B = 0$).

Method I linearization. Consider the discretization of the nonlinear unsteady model equation, Eq. (5), using the Lax-Wendroff scheme. The one-dimensional computational grid is assumed to have constant cell size Δx and constant time step Δt. The solution at time level $n + 1$ is found by Taylor expanding the solution about time level n to obtain

$$\hat{U}_i^{n+1} = \hat{U}_i^n + \Delta t\,\frac{\partial \hat{U}}{\partial t}\bigg|_i^n + \frac{\Delta t^2}{2}\,\frac{\partial^2 \hat{U}}{\partial t^2}\bigg|_i^n + O(\Delta t^3) \tag{20}$$

where i denotes the ith grid node in the x direction. The time derivatives in Eq. (20) are obtained by manipulation of the original model equation, Eq. (5). Rearranging Eq. (5) gives

$$\frac{\partial \hat{U}}{\partial t} = -\frac{\partial \hat{F}(\hat{U})}{\partial x} \tag{21}$$

Differentiating Eq. (21) with respect to time gives

$$\frac{\partial^2 \hat{U}}{\partial t^2} = -\frac{\partial}{\partial x}\left(\frac{\partial \hat{F}}{\partial \hat{U}}\,\frac{\partial \hat{U}}{\partial t}\right) = \frac{\partial}{\partial x}\left(\frac{\partial \hat{F}}{\partial \hat{U}}\,\frac{\partial \hat{F}}{\partial x}\right) \tag{22}$$

Next, substitution of Eqs. (21) and (22) into Eq. (20) yields

$$\hat{U}_i^{n+1} = \hat{U}_i^n - \Delta t\,\frac{\partial \hat{F}}{\partial x}\bigg|_i^n + \frac{\Delta t^2}{2}\,\frac{\partial}{\partial x}\left(\frac{\partial \hat{F}}{\partial \hat{U}}\,\frac{\partial \hat{F}}{\partial x}\right)\bigg|_i^n + O(\Delta t^3) \tag{23}$$

Finally, using centered finite difference expressions to approximate the spatial derivatives, the familiar Lax-Wendroff finite difference equation is obtained, i.e.,

$$\hat{U}_i^{n+1} = \hat{U}_i^n - \frac{\Delta t}{2\Delta x}\,[\hat{F}_{i+1}^n - \hat{F}_{i-1}^n] + \frac{\Delta t^2}{2\Delta x^2}\left[\frac{\partial \hat{F}}{\partial \hat{U}}\bigg|_{i+1/2}^n (\hat{F}_{i+1}^n - \hat{F}_i^n) - \frac{\partial \hat{F}}{\partial \hat{U}}\bigg|_{i-1/2}^n (\hat{F}_i^n - \hat{F}_{i-1}^n)\right] \tag{24}$$

The Lax-Wendroff scheme above is second-order accurate [i.e., $O(\Delta x^2, \Delta t^2)$] and is conservative (for constant Δx and Δt). A Fourier stability analysis indicates the scheme is stable for CFL numbers less than unity. Lax (1954) and Lax and Wendroff (1960) have shown that if the conservative form of the Euler equations is used, and the discretization of the Euler equations satisfies numerical conservation, and further that the scheme is consistent and stable, then the shock wave speed and strength will be correctly predicted. The Lax-Wendroff scheme above satisfies these conditions and therefore will correctly predict the unsteady shock motion.

Next, we would like to determine the behavior of Eq. (24) when the unsteadiness in the flow is small compared to the mean flow field. Since the resulting equations will be linear, we may without loss of generality assume that the flow field is composed of a nonlinear steady mean flow and a small perturbation harmonic unsteady flow so that

$$\hat{U}(x, t) = U(x) + u(x)e^{j\omega t} \tag{25}$$

where u is much smaller than U. When viewed on our computational grid, Eq. (25) becomes

$$\hat{U}_i^n = U_i + u_i e^{j\omega \Delta t n} \tag{26}$$

Substitution of Eq. (26) into Eq. (24) and collecting terms of first order in the perturbation quantity u gives the desired discrete small disturbance behavior of the nonlinear finite difference equations,

$$(1 - e^{j\omega\Delta t})u_i - \frac{\Delta t}{2\Delta x}\left[\frac{\partial F}{\partial U}\bigg|_{i+1} u_{i+1} - \frac{\partial F}{\partial U}\bigg|_{i-1} u_{i-1}\right] + \frac{\Delta t^2}{2\Delta x^2}\left[\frac{\partial F}{\partial U}\bigg|_{i+1/2}\left(\frac{\partial F}{\partial U}\bigg|_{i+1} u_{i+1} - \frac{\partial F}{\partial U}\bigg|_i u_i\right)\right.$$

$$-\frac{\partial F}{\partial U}\bigg|_{i-1/2}\left(\frac{\partial F}{\partial U}\bigg|_{i} u_i-\frac{\partial F}{\partial U}\bigg|_{i-1} u_{i-1}\right)\Bigg]$$
$$+\frac{\Delta t^2}{2\Delta x^2}\left[\frac{\partial^2 F}{\partial U^2}\bigg|_{i+1/2} u_{i+1/2}(F_{i+1}-F_i)\right.$$
$$\left.-\frac{\partial^2 F}{\partial U^2}\bigg|_{i-1/2} u_{i-1/2}(F_i-F_{i-1})\right]=0 \quad (27)$$

Equation (27) describes the small disturbance behavior of the nonlinear Lax–Wendroff equation. One interesting feature of Eq. (27) is the appearance of the terms involving $\partial^2 F/\partial U^2$. These terms appear because of nonlinearities in the Lax–Wendroff scheme itself rather than nonlinearities of the Euler equations.

For a one-dimensional problem, Eq. (27), along with appropriate inflow and outflow boundary conditions, could be assembled into a tridiagonal matrix equation, which could then be solved quite efficiently using Gaussian elimination (the Thomas algorithm). For two- and three-dimensional problems, however, this approach would be computationally expensive and require large amounts of computer storage. For these reasons, an iterative solution technique is preferred. The following explicit relaxation procedure is proposed:

$$u_i^{n+1}=u_i^n+\delta u_i^n \quad (28)$$

where δu_i is the left-hand side of Eq. (27). As Eq. (28) is marched in time, a steady-state value of u^n will be obtained and the solution to Eq. (27) will be recovered. This procedure is similar to the pseudo-time time-marching technique proposed by Ni and Sisto (1976) for solving the linearized Euler equations. Equation (27) can be shown to be consistent with the linearized model equation, Eq. (7), with truncation errors that are $O(\Delta x^2, \Delta t^2)$. A Fourier analysis of Eq. (28) reveals that the scheme is unconditionally unstable if ω is nonzero. A spectral radius stability analysis, however, that takes into account the stabilizing effect of the far-field boundary conditions shows that the scheme is stable for CFL numbers less than unity (Clark, 1992).

Method II linearization. An alternative approach to Method I is first to linearize the nonlinear unsteady flow equations, and then discretize the resulting linear equations. To illustrate this approach, we return again to the one-dimensional model equation given by Eq. (5) and, introducing the pseudo-time assumption of Ni and Sisto (1976), assume that the unsteady flow $\hat{U}(x, t)$ is composed of a nonlinear mean flow, $\hat{U}(x)$, plus a small unsteady harmonic perturbation flow, $u(x, t)e^{j\omega t}$, so that

$$\hat{U}(x, t)=U(x)+u(x, t)e^{j\omega t} \quad (29)$$

Substitution of Eq. (29) into Eq. (5) and collection of first-order terms results in the pseudo-time linearized model equation

$$\frac{\partial u}{\partial t}+j\omega u+\frac{\partial}{\partial x}\left(\frac{\partial F}{\partial U}u\right)=0 \quad (30)$$

Note that Eq. (30) is now hyperbolic in time so that it can be marched in time. Furthermore, as time advances, u will reach a steady-state value so that the solution to Eq. (7) will be recovered.

The next step is to discretize the linearized equation using the Lax–Wendroff scheme. Manipulation of Eq. (30) gives

$$\frac{\partial u}{\partial t}=-j\omega u-\frac{\partial}{\partial x}\left(\frac{\partial F}{\partial U}u\right) \quad (31)$$

and

$$\frac{\partial^2 u}{\partial t^2}=-\omega^2 u+2j\omega\frac{\partial}{\partial x}\left(\frac{\partial F}{\partial U}u\right)+\frac{\partial}{\partial x}\left[\frac{\partial F}{\partial U}\frac{\partial}{\partial x}\left(\frac{\partial F}{\partial U}u\right)\right] \quad (32)$$

Finally, making use of centered spatial derivatives and substitution into the Taylor expansion, Eq. (20) gives the desired Lax–Wendroff formula,

$$\delta u_i^n=-\frac{j\omega\Delta t}{4}[u_{i+1}^n+2u_i^n+u_{i-1}^n]$$
$$-\frac{\Delta t}{2\Delta x}\left[\frac{\partial F}{\partial U}\bigg|_{i+1}u_{+1}^n-\frac{\partial F}{\partial U}\bigg|_{i-1}u_{i-1}^n\right]$$
$$-\frac{\omega^2\Delta t^2}{8}[u_{i+1}^n+2u_i^n+u_{i-1}^n]$$
$$+\frac{j\omega\Delta t}{4}\frac{\Delta t}{\Delta x}\left[\frac{\partial F}{\partial U}\bigg|_{i+1}u_{i+1}^n-\frac{\partial F}{\partial U}\bigg|_{i-1}u_{i-1}^n\right]$$
$$+\frac{j\omega\Delta t}{2}\frac{\Delta t}{\Delta x}\left[\frac{\partial F}{\partial U}\bigg|_{i+1/2}u_{i+1/2}^n-\frac{\partial F}{\partial U}\bigg|_{i-1/2}u_{i-1/2}^n\right]$$
$$+\frac{\Delta t^2}{2\Delta x^2}\left[\frac{\partial F}{\partial U}\bigg|_{i+1/2}\left(\frac{\partial F}{\partial U}\bigg|_{i+1}u_{i+1}^n-\frac{\partial F}{\partial U}\bigg|_{i}u_i^n\right)\right.$$
$$\left.-\frac{\partial F}{\partial U}\bigg|_{i-1/2}\left(\frac{\partial F}{\partial U}\bigg|_{i}u_i^n-\frac{\partial F}{\partial U}\bigg|_{i-1}u_{i-1}^n\right)\right] \quad (33)$$

As in the Method I discretization [Eq. (27)], the Method II discretization [Eq. (33)] is consistent with the linearized model equation [Eq. (7)] with truncation errors that are $O(\Delta x^2, \Delta t^2)$.

Note that the Method II discretization [Eq. (33)] differs significantly from that obtained using Method I [Eq. (27)]. In particular, the unsteady terms involving ω are somewhat different, and the quasi-steady terms involving $\partial^2 F/\partial U^2$ in Eq. (27) do not appear in Eq. (33). Clearly, the order in which the linearization is performed is important in determining the precise form of the difference equations.

Test for Linearized Conservation. Consider the Method I discretization of the model equation, Eq. (27). The one-dimensional computational grid has M nodes. To test for conservation, Eq. (27) is multiplied by $g_i\Delta x/\Delta t$ (where $g_i = g(x_i)$) and summed over the computational domain. After some manipulation including summation by parts, one can show that this sum is given by

$$\frac{(1-e^{j\omega t})}{\Delta t}\sum_{i=1}^{M}u_i g_i\Delta x+\sum_{i=2}^{M-1}\frac{g_{i+1}-g_{i-1}}{2\Delta x}\frac{\partial F}{\partial U}\bigg|_i u_i\Delta x$$
$$-g_M\frac{\partial F}{\partial U}\bigg|_M u_M+g_1\frac{\partial F}{\partial U}\bigg|_1 u_1+O(\Delta x, \Delta t) \quad (34)$$

In the limit as $\Delta t, \Delta x \to 0$, Eq. (34) approaches Eq. (15). Therefore, this Method I linearization of the Lax–Wendroff scheme is conservative (at least for the case considered here of constant $\Delta t, \Delta x$). A similar analysis of Method II reveals that is also conservative.

Two- and Three-Dimensional Linearized Euler Solvers. The two- and three-dimensional linearized Euler analyses used in these codes have been previously described (Hall and Clark, 1993a; Lorence, 1991; Hall and Lorence, 1993; Clark, 1992). We therefore briefly outline the computational method used to calculate the unsteady flow field and refer the interested reader to the references above for more detail.

The general solution procedure is as follows. First, an **H**-grid is generated for a single blade passage of the cascade. The mean flow field is then computed using a conservative nonlinear steady Euler solver. Then, for each interblade phase angle, vibratory mode shape, and reduced frequency of inter-

est, the unsteady grid motion is prescribed. The mean flow field and prescribed blade motion are then used to form the variable coefficients and the inhomogeneous part of the linearized Euler equations. Finally, the linearized Euler equations are solved in a single computational passage using the pseudo-time technique proposed by Ni and Sisto (1976). Ni's Lax-Wendroff scheme (Ni, 1982; Dannenhoffer, 1987; Ni and Bogoian, 1989) is used to discretize and solve the pseudo-time linearized Euler equations. For the comparisons presented in this paper, we have developed both Method I and Method II versions of the linearized unsteady Euler solver. Both Method I and Method II schemes are second-order accurate [$O(\Delta x^2, \Delta t^2)$]. A combination of second and fourth difference smoothing is used to eliminate sawtooth modes and capture shocks. Ni's multiple grid acceleration technique is used to speed convergence.

In the present analysis, we assume that the blade row is an isolated blade row in an infinitely long duct. The computational domain, however, is finite in extent. At the far-field computational boundaries, nonreflecting boundary conditions are applied to prevent spurious reflections of outgoing pressure, entropy, and vorticity waves back into the computational domain (Hall et al., 1993).

For transonic flow calculations, a conservative discretization is required to model accurately the shock impulse. For Ni's two-dimensional scheme to be conservative, the ratio of the cell time step to the cell area must be a constant throughout the computational domain (in the three-dimensional scheme, the ratio of the time step to the cell volume must be constant). Furthermore, for stability, the CFL restriction must not be violated anywhere in the domain. This means that the time step used in some computational cells may be much smaller than the maximum permissible time step for that cell, greatly slowing the convergence of the scheme, even when using multiple grid acceleration. To overcome this difficulty, we propose the following modification to the linearized scheme. Consider again the finite difference representation of the linearized model problem [Eq. (27)]. We modify this equation such that

$$u_i^{n+1} = u_i^n + R_i \delta u_i^n \tag{35}$$

where δu_i^n is as before and R_i is an overrelaxation factor. In the present analysis we have taken this factor to be roughly equal to the maximum permissible local time step size divided by the actual conservative time step.

A Fourier analysis shows that for overrelaxation factors greater than unity, Eq. (35) produces an unconditionally unstable scheme. It would seem, therefore, that overrelaxation would not be useful. However, for transonic flow calculations, smoothing must be added to the scheme to capture shocks. This smoothing stabilizes the overrelaxation scheme so long as the overrelaxation factor is not too large. Hence, a clamp is also applied so that the maximum overrelaxation factor can be no larger than about five. As we will demonstrate, the overrelaxation scheme is stable and significantly reduces the computational time required to obtain a converged solution.

Results

Transonic Channel Flow. To test the present linearized Euler analyses, we first consider the transonic flow through a diverging channel. This case is presented to demonstrate the ability of the linearized Euler method to model shock motion accurately using shock capturing. We will demonstrate that both Method I and Method II linearizations will produce satisfactory results as long as they are conservative.

The channel considered here has a height, A, given by

$$A(x) = A_{\text{inlet}}\left\{1.10313 + 0.10313\tanh\left[10\left(x - \frac{1}{2}\right)\right]\right\}, \quad 0 \le x \le 1 \tag{36}$$

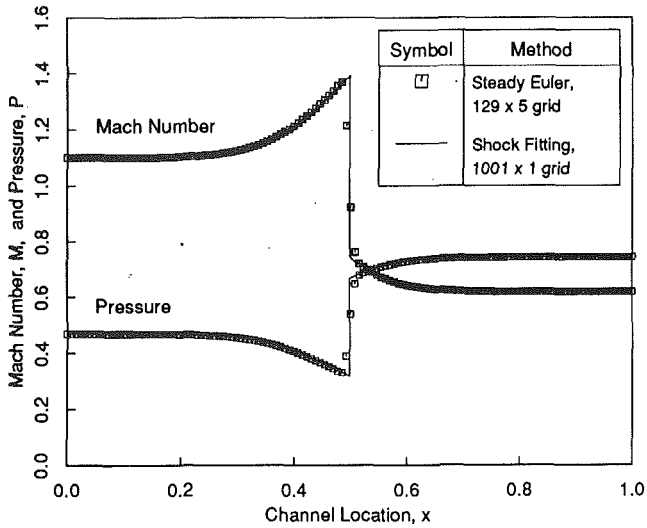

Fig. 2 Steady transonic flow in a diverging channel

(The units may be taken to be any consistent set of units.) So that we may compare the results obtained by the present method to those obtained by a one-dimensional shock-fitting theory, A_{inlet} is taken to be small compared with the channel length ($A_{\text{inlet}} = 0.01$). The inflow total pressure, P_T, total density, ρ_T, and flow velocity, U, are 1.0, 1.364, and 1.0, respectively. The back pressure, P_{exit}, is 0.7422. Shown in Fig. 2 is the Mach number and pressure distribution as computed using the present nonlinear steady Euler solver on a 129 × 5 node computational grid. The grid was generated so that the computational cells all have the same area, ΔA. The time step, Δt, used in these calculations was constant throughout the computational domain unless otherwise noted. Constant Δt and ΔA were chosen because Ni's scheme is only conservative if the ratio $\Delta t/\Delta A$ is constant throughout the computational domain.

Also shown for comparison in Fig. 2 is the solution determined using a steady quasi-one-dimensional, shock-fitting Euler solver using 1001 grid nodes in the x direction. The shock-fitting Euler solution is grid converged and may be taken to be the exact solution. Note the excellent agreement between the two different approaches. The only noticeable differences occur at the shock, where the present nonlinear Euler analysis smears the shock over about five grid nodes.

Next, we consider a quasi-steady perturbation in the back pressure. The perturbation solution was calculated using four different approaches. First, the solution was calculated using a quasi-one-dimensional, shock-fitting, linearized Euler analysis. This solution was computed on an extremely fine grid (1001 nodes in the x direction) and is essentially the exact solution. Next, the present nonlinear steady Euler solver was used to compute two nonlinear solutions at slightly different back pressures. These two solutions were then subtracted one from the other and the result was normalized by the difference in back pressures to obtain the perturbation solution. Finally, the solution was determined using the present linearized Euler analysis (both Methods I and II). It should be noted that for this comparison the usual nonreflecting far-field boundary conditions were replaced with reflecting boundary conditions. Upstream the perturbation in total pressure and density as well as the inflow angle was set to zero. Downstream the perturbation in static pressure was prescribed. These boundary conditions for this model problem were chosen for their simplicity and are not meant to model any real physical system. The results of these various approaches are shown in Fig. 3. The Method I and Method II results are indistinguishable from one

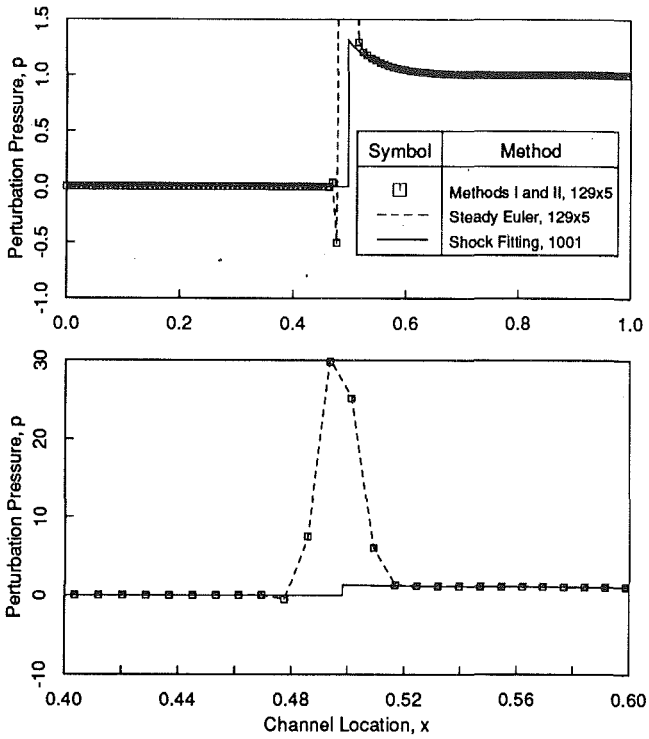

Fig. 3 Top: perturbation pressure in a diverging channel due to a steady perturbation in back pressure; bottom: enlarged view of the shock impulse region

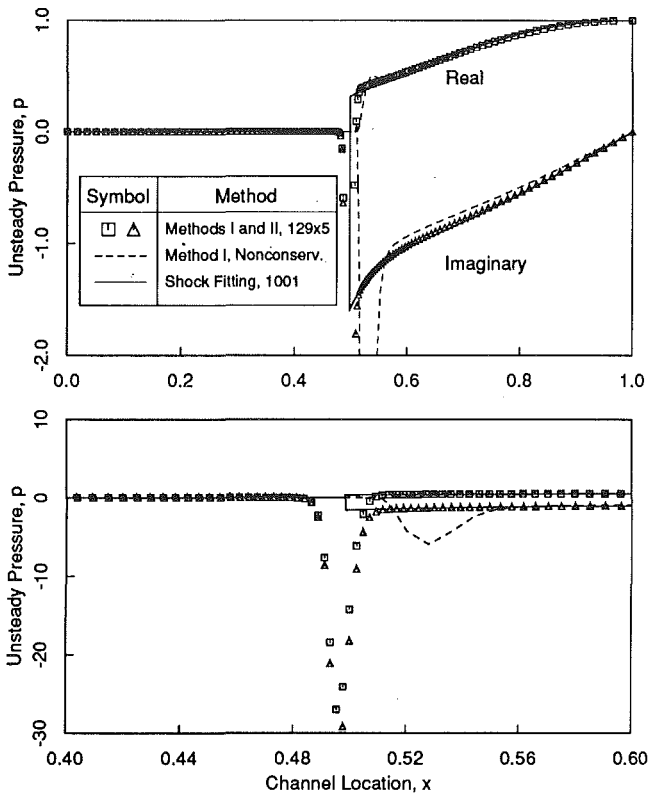

Fig. 4 Top: unsteady pressure in a diverging channel due to an unsteady perturbation in back pressure, $\omega = 1.0$; bottom: enlarged view of the shock impulse region

another and are therefore plotted with a single symbol. As expected, all the solutions are in excellent agreement in regions away from the shock. At the shock, however, the methods using shock-capturing produce an impulse of pressure. The area under the impulse is equal to the product of the shock displacement and the mean pressure jump across the shock. The shock impulse then represents the load exerted on the wall due to the motion of the shock. Also shown in Fig. 3 is an enlarged view of the shock region. Note that the computed results from the Method I and Method II linearizations are virtually identical to the perturbation of the nonlinear Euler analysis.

To validate the linearized shock capturing technique further for unsteady flows, we computed the unsteady pressure distribution due to an unsteady perturbation in back pressure with an excitation frequency, ω, of 1.0. The results are shown in Fig. 4. Also shown are the results of a quasi-one-dimensional, unsteady, shock-fitting, linearized Euler solver. Away from the shock, the results agree quite well with the Method I and II results. At the shock, the present Method I and II solutions show an impulse. This impulse represents the unsteady load acting on the channel wall due to the motion of the shock.

To determine whether the present linearized Euler solver correctly predicts the unsteady loads induced by the shock motion, the pressure was integrated over the lower channel wall to determine the net wall force. The results from this analysis are tabulated in Table 1 for several different frequencies. Also tabulated in Table 1 is the wall force computed using the linearized unsteady shock-fitting code. The conservative forms of the Method I and Method II analyses are seen to be in almost perfect agreement with the shock-fitting scheme for all frequencies, suggesting that the shock impulse found using shock capturing is properly modeled. Even in the higher frequency cases the agreement is quite good, although there is a slight error (about 0.5 deg) in the phase of the wall force.

Table 1 Predicted pressure loads in a transonic diverging channel due to an unsteady perturbation in back pressure using a uniform area computational grid

Frequency	Scheme	Wall Force	
0.0	1D Shock Fitting	1.0305 ∠ 0.0°	
	Nonlinear Euler[a]	1.0346 ∠ 0.0°	
	Method I	1.0273 ∠ 0.0°	
	Method II	1.0273 ∠ 0.0°	
1.0	1D Shock Fitting	0.6390 ∠ −78.7°	
	Method I	0.6353 ∠ −78.8°	
	Method II	0.6354 ∠ −78.8°	
	Method I	0.5397 ∠ −46.6°	Nonconservative [b]
	Method II	0.6229 ∠ −84.9°	Nonconservative [c]
2.0	1D Shock Fitting	0.1974 ∠ −114.1°	
	Method I	0.1983 ∠ −113.6°	
	Method II	0.1984 ∠ −113.6°	

[a]Results from the steady analysis were found for two slightly different back pressures. The two solutions were then differenced and normalized by ΔP_{exit}.
[b]Time accurate time marching steady and unsteady solution on a nonuniform area computational grid.
[c]Local time stepping used in steady and unsteady analyses.

We believe that these differences arise from the dispersion errors in the solution away from the shock rather than from a limitation in shock capturing at high reduced frequencies.

Finally, for the $\omega = 1.0$ case, we deliberately made the Method I and II calculations nonconservative to demonstrate that the shock impulse cannot be properly modeled using a nonconservative algorithm. In the Method I calculation, the

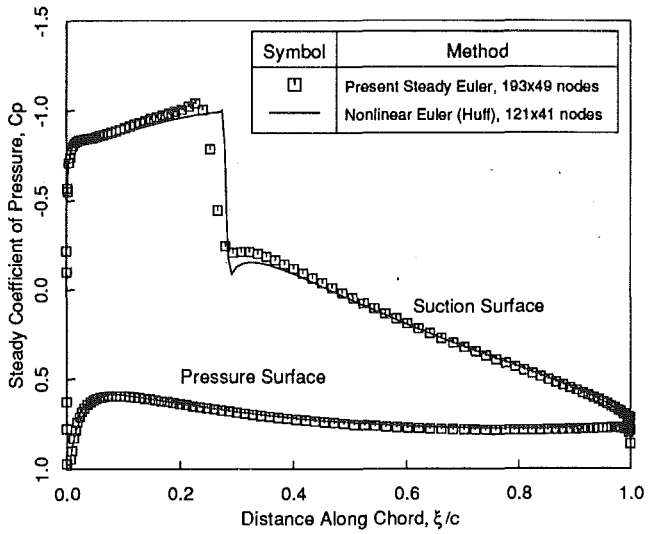

Fig. 5 Coefficient of pressure distribution, Tenth Standard Configuration: $M_{-\infty} = 0.8$, $G = 1.0$, $\Theta = 45$ deg, $\Omega_{-\infty} = 58$ deg

time step Δt was held constant throughout the domain, but a grid with variable cell areas near the shock was used. In the Method II calculations, the cell areas ΔA were constant throughout the computational domain, but the time step used in each computational cell was based on a local CFL number (local time stepping). In both cases, the ratio $\Delta t/\Delta A$ varies over the computational domain making the schemes nonconservative. As shown in Table 1, the incorrect wall force is predicted whenever the scheme is nonconservative. In the Method I case (see also Fig. 4), the phase of the wall force is in error by about 32.1 deg. The phase error in the Method II example is 6.2 deg.

From these numerical results we conclude that both Method I and Method II linearizations will produce satisfactory results if and only if the linearizations are conservative. However, since the Method I linearization is predicated on the assumption that a constant time step is used throughout the computational domain, this precludes the use of Method I for most problems since it would be difficult and undesirable to generate computational grids with constant cell areas throughout the computational domain. With the Method II analysis, we only require that $\Delta t/\Delta A$ be constant for the scheme to be conservative. Therefore, for the remaining examples, we will use a conservative Method II analysis.

Unsteady Compressor and Fan Flows. Having demonstrated the ability of the present method to model transonic channel flow, we next consider the unsteady flow in compressors and fans.

Tenth Standard Configuration. The first cascade considered is the Tenth Standard Configuration (Bölcs and Fransson, 1986; Fransson, 1991). The airfoils of this cascade have a NACA 0006 thickness distribution slightly modified so that the trailing edge is wedged rather than blunt. The camber line is a circular arc with a maximum height of 5 percent of the chord. The flow conditions are such that there is a supersonic patch on the suction surface of the airfoil. The stagger angle, Θ, is 45 deg and the gap-to-chord ratio, G, is 1.0. The mean inflow angle, $\beta_{-\infty}$, is 58 deg and the inflow Mach number, $M_{-\infty}$, is 0.8. Figure 5 shows the computed coefficient of pressure distribution along the airfoil surface calculated using the present nonlinear steady Euler code. The grid used for this calculation was a 193 × 49 node **H**-grid with a total of 193 nodes on the airfoil surface. Note in particular the transonic

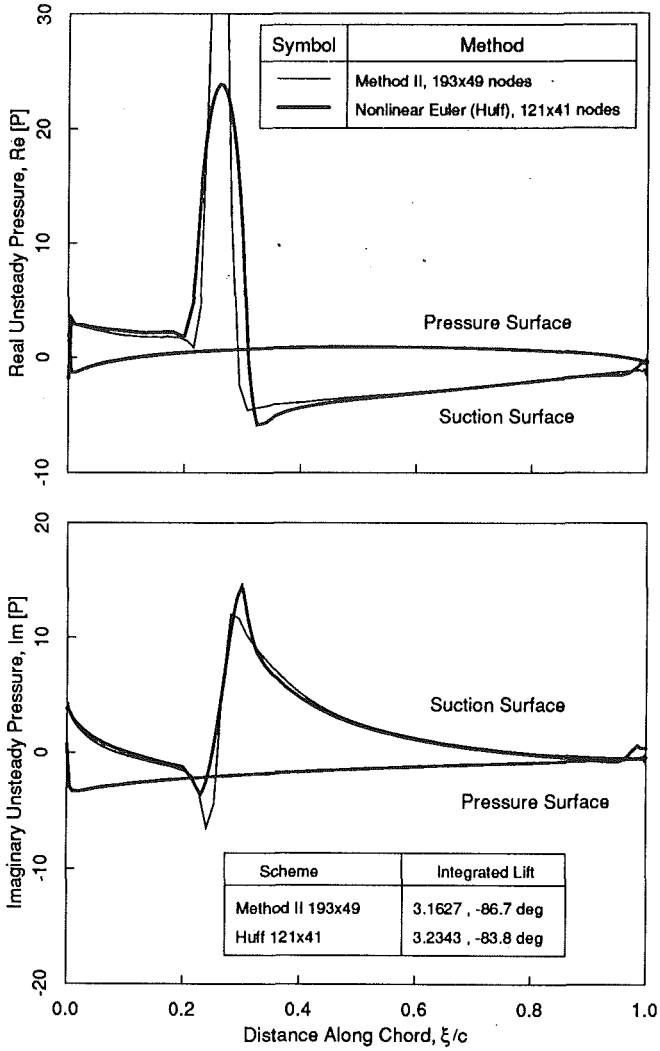

Fig. 6 Real and imaginary unsteady surface pressure, Tenth Standard Configuration, plunging: $\omega = 1.287$, $\sigma = -90$ deg

patch on the suction surface of the airfoil. The present steady Euler solver captures the shock over about five grid points. Also shown is the nonlinear Euler solution provided by Huff based on a flux difference splitting algorithm (Huff and Reddy, 1989; Huff, 1992).

With the steady solution now known, consider the case where the airfoils plunge with an interblade phase angle, σ, of -90 deg and a reduced frequency, $\bar{\omega}$ (based on the upstream velocity and blade chord), of 1.287. Figure 6 shows the computed unsteady pressure distribution on the airfoil surface using Method II linearization. The impulsive shock load is clearly visible on the suction surface. Also shown for comparison is the pressure distribution computed using Huff's nonlinear time-marching algorithm. The agreement between the present linearized analysis and the nonlinear time-marching Euler analysis is excellent away from the shock. Shown in the table insert in Fig. 6 is the magnitude and phase of the resulting unsteady lift. The magnitude of the unsteady lift calculated using the two different approaches agrees within about 2 percent; the phase differs by only about 3 deg. Note that the shock impulse predicted by the present unsteady linearized Euler analysis is somewhat narrower and taller than that predicted by the nonlinear code. The *areas* of the impulses, however, are very nearly equal. Furthermore, the unsteady load due to the impulse is of the same order of magnitude as the unsteady load due to the unsteady pressure distribution away from the shock.

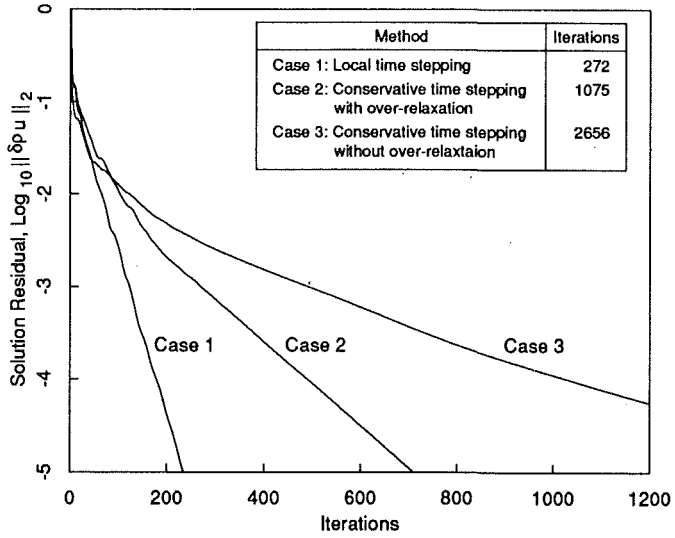

Fig. 7 Convergence histories of unsteady solution for different methods. All cases use multigrid acceleration.

Because conservative Method II linearizations require that the ratio $\Delta t/\Delta A$ be constant throughout the computational domain, the time step taken in a particular computational cell may be considerably smaller than the maximum permitted for stable calculations. The result is that the convergence will be considerably slower than if the local maximum permissible time step had been taken everywhere (local time stepping). To overcome this problem, we use conservative time stepping in conjunction with multiple grid acceleration and overrelaxation. Figure 7 shows the convergence histories for three linearized unsteady flow calculations for the previous example: one using local time stepping with multigrid, one using conservative time stepping with multigrid, and one using conservative time stepping with overrelaxation plus multigrid.

Note that overrelaxation reduces the computational time required by a factor of about 2.5 compared to conservative time stepping without overrelaxation. Finally, we should mention that a comparable nonlinear time marching algorithm would require about 20 to 50 times the computational time required by the global time step calculations with overrelaxation and multigrid.

Next, we consider a three-dimensional linear cascade of Tenth Standard Configuration airfoils. The airfoils have an aspect ratio of 2. The steady flow conditions are the same as in the two-dimensional problem. The solution was computed on a 129 × 33 × 17 node **H**-grid. For the unsteady flow problem, the airfoils are again assumed to vibrate in plunge with an interblade phase angle, σ, of -90 deg and a reduced frequency, $\bar{\omega}$, of 1.287. The mode shape is assumed to be the first bending mode shape of a cantilevered beam. Figure 8 shows the real and imaginary parts of the unsteady pressure distribution at three spanwise stations. Also shown is the two-dimensional "strip theory" result at the tip. Shown in Fig. 9 are contours of unsteady pressure on the pressure and suction surfaces. Note the shock impulse on the suction surface. For comparison, the contours predicted by two-dimensional strip theory are shown in Fig. 10. These results clearly indicate the need to model three-dimensional effects. For example, the unsteady pressures at the tip of the blade are significantly less than would be predicted by strip theory. Furthermore, the unsteady load at the hub is not zero as would be predicted by strip theory.

High-Speed Cascade. The next case considered is a two-dimensional cascade of fan blades with a relative inlet Mach number, $M_{-\infty}$, of 1.2, stagger angle, Θ, of 55 deg, and blade-

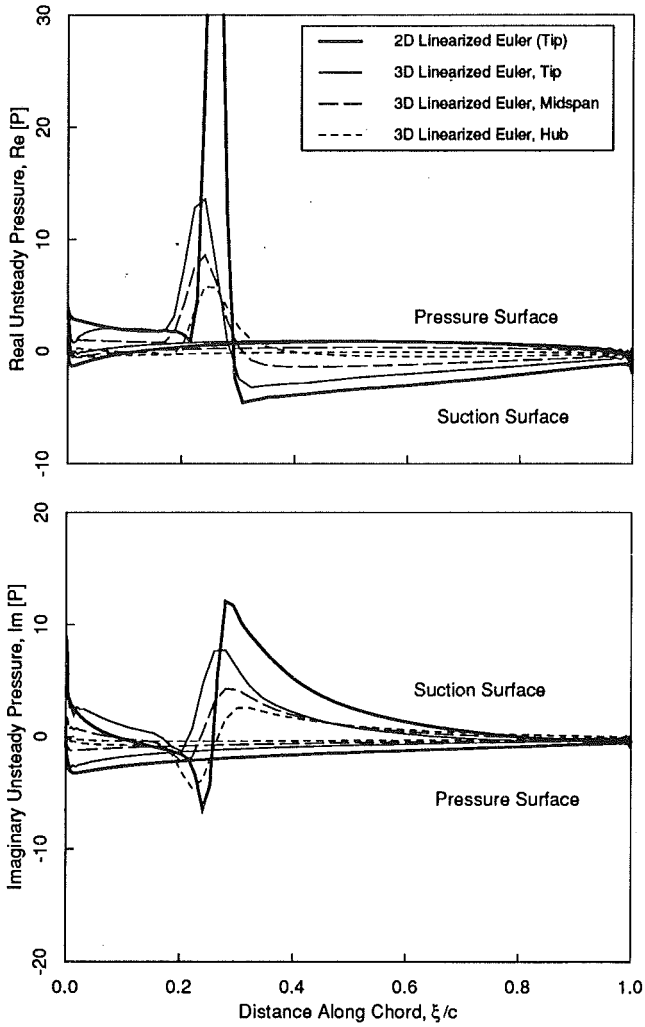

Fig. 8 Real and imaginary unsteady surface pressure, Tenth Standard Configuration, plunging, airfoils vibrating in first bending mode: ω = 1.287, σ = −90 deg

to-blade gap, G, of 1.0. This case is presented to demonstrate the importance of moving shocks on the aeroelastic response of fan blades. Figure 11 shows the steady pressure contours. The solution was computed on a 129 × 33 node grid with a total of 129 nodes on the airfoil surface. Figure 12 shows the computed isentropic Mach number on the airfoil's surface. The pressure rise due to the passage shock can be clearly seen on both the suction and pressure surfaces. The shock is smeared over about four grid nodes.

Next, we computed the unsteady aerodynamic response of the cascade for a range of interblade phase angles. The airfoils pitch about their midchords with a reduced frequency, $\bar{\omega}$, of 0.5. For each interblade phase angle, the computed unsteady surface pressure was integrated to obtain the unsteady pitching moment. Shown in Fig. 13 is the imaginary part of the unsteady pitching moment as a function of interblade phase angle. Positive imaginary pitching moments correspond to negative aerodynamic damping which will produce flutter for tuned cascades. Note that for σ = 120 deg, the cascade is slightly unstable.

Shown in Fig. 14 is the unsteady pressure for the case where the airfoils vibrate in pitch with a reduced frequency, $\bar{\omega}$, of 0.5 and interblade phase angle, σ, of 120 deg. Note that the unsteady aerodynamic load on the airfoil is dominated by the shock impulses. The impulse acting near the trailing edge pro-

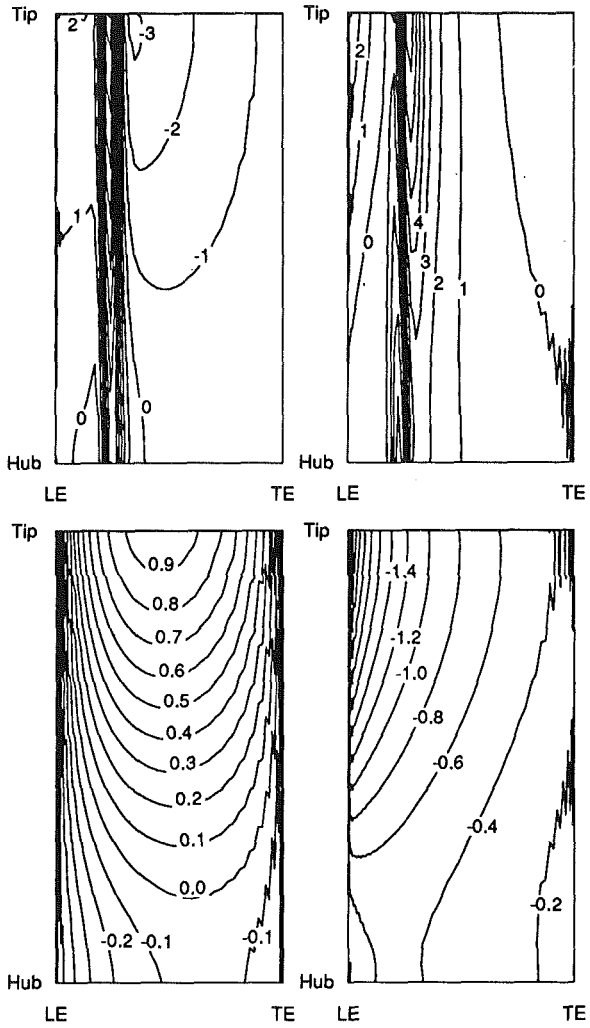

Fig. 9 Unsteady surface pressure contours, Tenth Standard Configuration, plunging, airfoils vibrating in first bending mode: $\omega = 1.287$, $\sigma = -90$ deg; top: real (left) and imaginary (right) parts of unsteady pressure on suction surface; bottom: real (left) and imaginary (right) parts of unsteady pressure on pressure surface

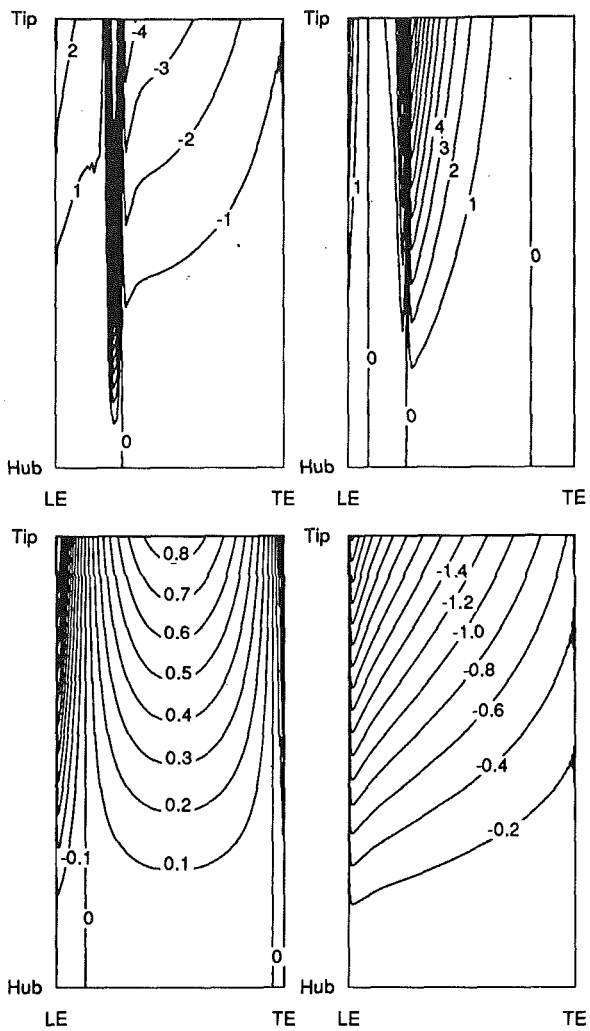

Fig. 10 Unsteady surface pressure contours, Tenth Standard Configuration, plunging, airfoils vibrating in first bending mode, two-dimensional strip theory approximation: $\omega = 1.287$, $\sigma = -90$ deg; top: real (left) and imaginary (right) parts of unsteady pressure on suction surface; bottom: real (left) and imaginary (right) parts of unsteady pressure on pressure surface

vides a positive contribution to the imaginary part and hence is destabilizing. The impulse near the leading edge, on the other hand, is stabilizing. While these results demonstrate the importance of unsteady shock motion on the unsteady aerodynamic behavior of the fan, it should be noted that whenever strong in-passage shocks occur, viscous effects become important due to the large adverse pressure gradient at the shock. These effects are not modeled here.

Concluding Remarks

In this paper, we have presented a linearized Euler analysis of two- and three-dimensional unsteady transonic flows in channels and cascades. Two different types of linearization were examined. Using Method I, the nonlinear Euler equations are first discretized using a conservative, time-accurate Lax–Wendroff scheme. The resulting nonlinear finite volume discretization is then linearized. Using Method II, the Euler equations are first linearized and then discretized using a Lax–Wendroff scheme. It was shown by numerical experiment that both the Method I and Method II linearizations correctly predict the unsteady shock impulse in transonic flows if and only if the scheme is conservative; the order of linearization and discretization appears to be inconsequential. When either the Method I or Method II discretization was made nonconservative by using a nonconstant $\Delta t/\Delta A$, the shock impulse was found to be incorrectly predicted even though the methods are formally second-order accurate and consistent with the linearized Euler equations.

Because a constant $\Delta t/\Delta A$ is required in the steady and unsteady flow calculations to insure conservation, the time step taken at a computational cell may be significantly smaller than the maximum local permissible time step for stability. This small time step in turn slows convergence of the scheme. To overcome this difficulty, an overrelaxation technique was proposed that dramatically improves the convergence rate of the linearized Euler analysis while leaving the method fully conservative. When coupled with Ni's multiple grid acceleration technique, the present linearized Euler solver can compute unsteady transonic flows nearly two orders of magnitude faster than a comparable nonlinear time-accurate time-marching solver.

A number of two- and three-dimensional unsteady transonic flows in cascades were computed using the linearized Euler analyses. Where possible, these results were compared to a nonlinear time-accurate time-marching scheme and found to

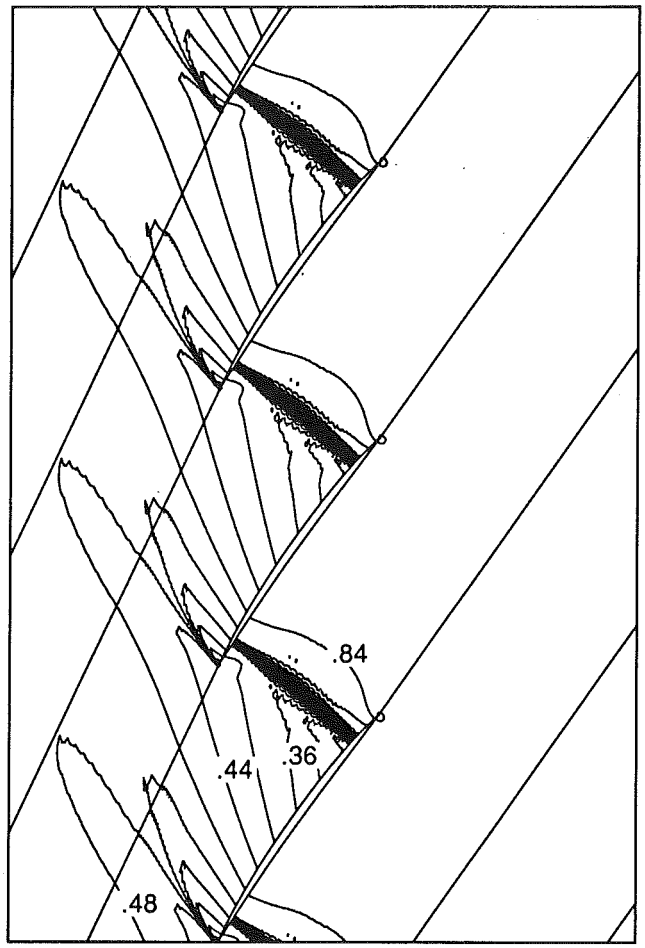

Fig. 11 Steady pressure contours, modified circular arc airfoil: $M_{-\infty}$ = 1.2, G = 1.0, Θ = 55 deg, $\Omega_{-\infty}$ = 60 deg

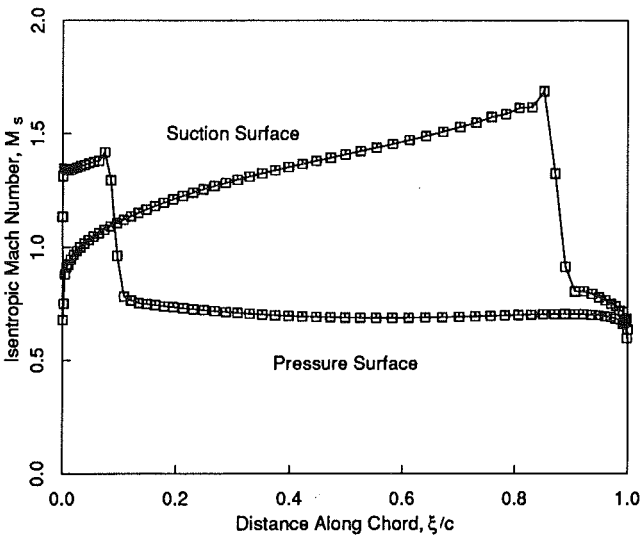

Fig. 12 Isentropic Mach number distribution, modified circular arc airfoil: $M_{-\infty}$ = 1.2, G = 1.0, Θ = 55 deg, $\Omega_{-\infty}$ = 60 deg

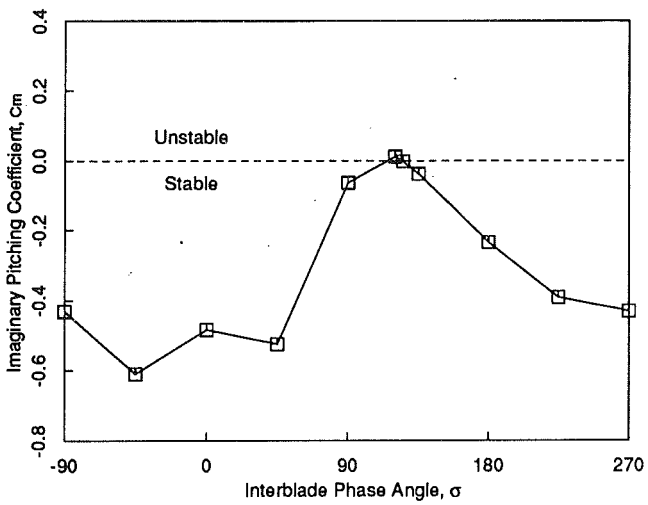

Fig. 13 Imaginary part of moment coefficient for a range of interblade phase angles, modified circular arc airfoil, pitching about midchord, ω = 0.5

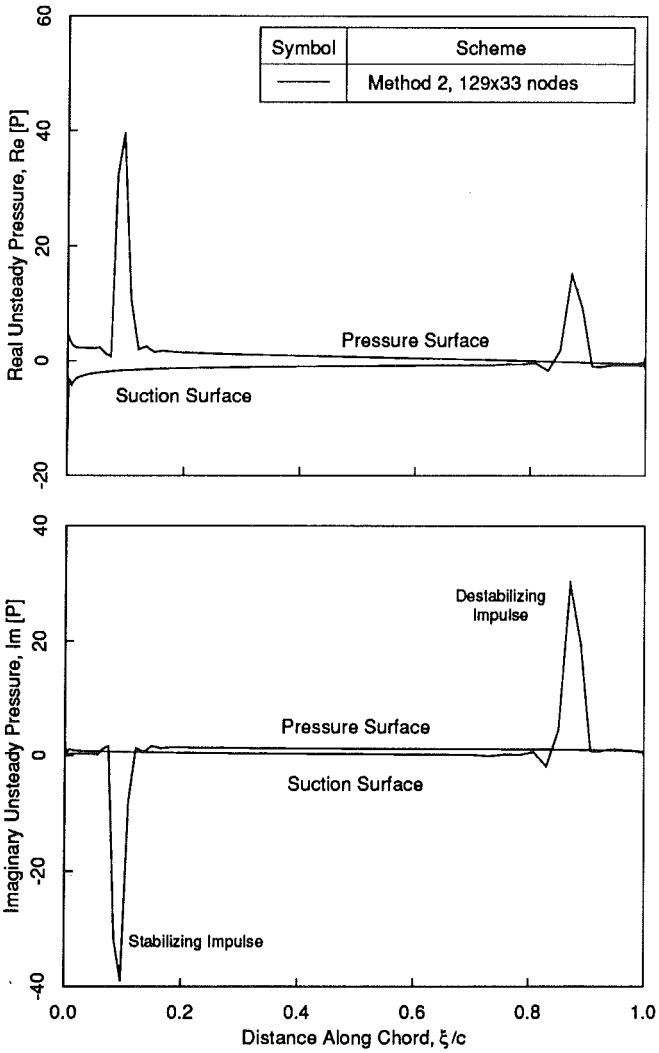

Fig. 14 Real and imaginary unsteady surface pressure, modified circular arc airfoil, pitching about midchord: ω = 0.5, σ = 120 deg

be in excellent agreement. Furthermore, the unsteady shock load was found to be a significant contributor to the unsteady aerodynamic forces acting on the airfoil.

Acknowledgments

This work was supported by NASA Grant No. NAG3-1192 with Dr. Daniel Hoyniak serving as technical monitor, and by a research contract from General Electric Aircraft Engines with Dr. Andrew Chuang serving as technical monitor. Additional

support was provided by the National Science Foundation through a Presidential Young Investigator award to the first author. The authors wish to thank Dr. Dennis Huff of NASA Lewis Research Center for providing computational results, which are presented in this paper. The authors also wish to acknowledge helpful discussions on the topic of shock capturing with Dr. Dana Lindquist and Dr. Michael Giles while they were at M.I.T., and Dr. Graham Holmes of the General Electric Company Research and Development Center.

References

Bölcs, A., and Fransson, T. H., 1986, "Aeroelasticity in Turbomachines: Comparison of Theoretical and Experimental Cascade Results," Air Force Office of Scientific Research, AFOSR-TR-87-0605.

Clark, W. S., 1992, "Prediction of Unsteady Flows in Turbomachinery Using the Linearized Euler Equations on Deforming Grids," M.S. Thesis, Duke University, Durham, NC.

Dannenhoffer, J. F., III, 1987, "Grid Adaptation for Complex Two-Dimensional Transonic Flows," Sc.D. Thesis, Massachusetts Institute of Technology, Cambridge, MA.

Fransson, T. H., 1991, private communication.

Hall, K. C., and Crawley, E. F., 1989, "Calculation of Unsteady Flows in Turbomachinery Using the Linearized Euler Equations," *AIAA Journal*, Vol. 27, No. 6, pp. 777–787.

Hall, K. C., and Clark, W. S., 1993a, "Linearized Euler Predictions of Unsteady Aerodynamic Loads in Cascades," *AIAA Journal*, Vol. 31, No. 3, pp. 540–550.

Hall, K. C., and Clark, W. S., 1993b, "Calculation of Unsteady Linearized Euler Flows in Cascades Using Harmonically Deforming Grids," in: *Unsteady Aerodynamics, Aeroacoustics, and Aeroelasticity of Turbomachines and Propellers*, H. M. Atassi, ed., Springer-Verlag, New York.

Hall, K. C., and Lorence, C. B., 1993, "Calculation of Three-Dimensional Unsteady Flows in Turbomachinery Using the Linearized Harmonic Euler Equations," ASME JOURNAL OF TURBOMACHINERY, Vol. 115, pp. 800–809.

Hall, K. C., Lorence, C. B., and Clark, W. S., 1993, "Nonreflecting Boundary Conditions for Linearized Aerodynamic Calculations," AIAA Paper No. 93-0882.

Holmes, D. G., and Chuang, H. A., 1993, "2D Linearized Harmonic Euler Flow Analysis for Flutter and Forced Response," in: *Unsteady Aerodynamics, Aeroacoustics, and Aeroelasticity of Turbomachines and Propellers*, H. M. Atassi, ed., Springer-Verlag, New York.

Huff, D. L., and Reddy, T. S. R., 1989, "Numerical Analysis of Supersonic Flow Through Oscillating Cascade Sections by Using a Deforming Grid," AIAA Paper No. 89-2805.

Huff, D. L., 1992, private communication.

Kahl, G., and Klose, A., 1993, "Time Linearized Euler Calculations for Unsteady Quasi-3D Cascade Flows," in: *Unsteady Aerodynamics, Aeroacoustics, and Aeroelasticity of Turbomachines and Propellers*, H. M. Atassai, ed., Springer-Verlag, New York.

Lax, P. D., 1954, "Weak Solutions of Nonlinear Hyperbolic Equations and Their Numerical Computation," *Comm. Pure Appl. Math.*, Vol. 7, pp. 159–193.

Lax, P. D., and Wendroff, B., 1960, "Systems of Conservation Laws," *Comm. Pure Appl. Math.*, Vol. 13, pp. 217–237.

Lindquist, D. R., 1991, "Computation of Unsteady Transonic Flowfields Using Shock Capturing and the Linear Perturbation Euler Equations," Ph.D. Thesis, Massachusetts Institute of Technology, Cambridge, MA.

Lindquist, D. R., and Giles, M. B., 1991, private communication.

Lindquist, D. R., and Giles, M. B., 1994, "Validity of Linearized Unsteady Euler Equations With Shock Capturing," *AIAA Journal*, Vol. 32, No. 1, pp. 46–53.

Lorence, C. B., 1991, "An Investigation of Three-Dimensional Unsteady Flows in Turbomachinery Using the Linearized Euler Equations," M.S. Thesis, Duke University, Durham, NC.

Ni, R. H., and Sisto, F., 1976, "Numerical Computation of Nonstationary Aerodynamics of Flat Plate Cascades in Compressible Flow," ASME *Journal of Engineering for Power*, Vol. 98, pp. 165–170.

Ni, R. H., 1982, "A Multiple-Grid Scheme for Solving the Euler Equations," *AIAA Journal*, Vol. 28, No. 12, pp. 2050–2058.

Ni, R. H., and Bogoian, J. C., 1989, "Prediction of Three-Dimensional Multistage Turbine Flow Field Using a Multiple-Grid Euler Solver," AIAA Paper No. 89-0203.

Verdon, J. M., and Caspar, J. R., 1984, "A Linearized Unsteady Aerodynamic Analysis for Transonic Cascades," *Journal of Fluid Mechanics*, Vol. 149, pp. 403–429.

Verdon, J. M., 1987, "Linearized Unsteady Aerodynamic Theory," Chap. 1 in: *AGARD Manual on Aeroelasticity in Axial-Flow Turbomachines, Unsteady Turbomachinery Aerodynamics*, Vol. 1, M. F. Platzer and F. O. Carta, eds., AGARD-AG-298.

Whitehead, D. S., 1987, "Classical Two-Dimensional Methods," Chap. 2 in: *AGARD Manual on Aeroelasticity in Axial-Flow Turbomachines, Unsteady Turbomachinery Aerodynamics*, Vol. 1, M. F. Platzer and F. O. Carta, eds., AGARD-AG-298.

Whitehead, D. S., 1990, "A Finite Element Solution of Unsteady Two-Dimensional Flow in Cascades," *International Journal for Numerical Methods in Fluids*, Vol. 10, pp. 13–34.

Passive Control of Flow-Induced Vibrations by Splitter Blades

H. W. D. Chiang[1]

S. Fleeter

School of Mechanical Engineering,
Purdue University,
West Lafayette, IN 47907

Splitter blades as a passive control technique for flow-induced vibrations are investigated by developing an unsteady aerodynamic model to predict the effect of incorporating splitter blades into the design of an axial flow blade row operating in an incompressible flow field. The splitter blades, positioned circumferentially in the flow passage between two principal blades, introduce aerodynamic and/or combined aerodynamic-structural detuning into the rotor. The unsteady aerodynamic gust response and resulting oscillating cascade unsteady aerodynamics, including steady loading effects, are determined by developing a complete first-order unsteady aerodynamic analysis together with an unsteady aerodynamic influence coefficient technique. The torsion mode flow induced vibrational response of both uniformly spaced tuned rotors and detuned rotors are then predicted by incorporating the unsteady aerodynamic influence coefficients into a single-degree-of-freedom aeroelastic model. This model is then utilized to demonstrate that incorporating splitters into axial flow rotor designs is beneficial with regard to flow induced vibrations.

Introduction

Axial flow blade rows that can achieve higher pressure ratios without flow separation are required for the development of advanced gas turbine engines, which are more compact, lighter weight, and have increased reliability as compared to current technology engines. Thus these engines will feature high-solidity, low aspect ratio blade rows, with the number of airfoils and/or the airfoil chord increased. Unfortunately, these adversely affect aerodynamic efficiency, with the additional airfoils and end wall surface areas resulting in increased losses and the increased blockage reducing the flow capacity. In addition, the effect of flow-induced vibrations of these advanced blade row designs must be considered.

One approach to minimizing these performance penalties is the use of partial chord blades, termed splitters, between principal full chord blades. In particular, the splitters help to control trailing edge flow separation without the aerodynamic penalties associated with high-solidity full chord blade rows, i.e., the splitters enable the aft rotor blade row to have increased flow turning, thereby increasing the work transfer. In addition, the splitters do not affect the blade row flow capacity as it is controlled by the entrance region, with the splitters not affecting the entrance region solidity.

Splitter vanes are routinely incorporated into high pressure ratio centrifugal compressor impellers. However, the incorporation of splitters into the design of axial flow rotors is still a research concept. Wennerstrom and Frost (1974) and Wennerstrom et al. (1975) utilized splitters in the design of a 3:1 single-stage axial flow rotor. The camberline of the splitters was identical to that of the principal blades, with the full span splitters positioned circumferentially at midpassage, although other positions were later considered in cascade experiments (Holtman et al., 1973; Fleeter and Riffel, 1977). Although the lack of an advanced design system for splittered rotors resulted in a rotor that did not meet its efficiency and surge margin goals, the splitters did control the deviation levels, resulting in a significant improvement in flow and pressure rise capacity over a baseline conventional design. To overcome this design system deficiency, Tzuoo et al. (1990) are developing a design methodology for axial compressor rotors that incorporate splitters. Thus, the incorporation of splitters into advanced axial flow blade row designs may enable the performance goals of advanced gas turbine engines to be achieved.

In addition to performance goals, advanced engines must also have improved reliability. Thus, it is necessary to address the effect of incorporating splitters on flow-induced vibrations. In this regard, the incorporation of splitters may not only be beneficial with regard to aerodynamic performance but also serve as a passive control technique for flow-induced vibrations, i.e., from an aeromechanical point of view, the splitters introduce both structural and aerodynamic detuning into the rotor. This is particularly important for advanced blade rows that feature very low mechanical damping.

Structural detuning, defined as designed blade-to-blade differences in the natural frequencies of a blade row, has been proposed for passive aeroelastic control. Studies of the effect of structural detuning of rotors have shown that it is often detrimental to flow-induced vibrations, although beneficial to flutter.

Aerodynamic detuning is a relatively new concept for passive aeroelastic control. It is defined as designed blade-to-blade

[1]Current address: Aeromechanical Engineer, General Electric Aircraft Engines.

Contributed by the International Gas Turbine Institute and presented at the 38th International Gas Turbine and Aeroengine Congress and Exposition, Cincinnati, Ohio, May 24–27, 1993. Manuscript received by the ASME Headquarters March 1, 1993. Paper No. 93-GT-147. Associate Technical Editor: H. Lukas.

differences in the unsteady aerodynamic flow field of a blade row. Thus, aerodynamic detuning creates blade-to-blade differences in the unsteady aerodynamic forces and moments, thereby affecting the fundamental driving force. This results in the blades not responding in a classical traveling wave mode typical of a conventional uniformly spaced aerodynamically tuned rotor. Studies of rotors operating in both incompressible flow fields (Chiang and Fleeter, 1989) and supersonic flow fields with subsonic axial components (Hoyniak and Fleeter, 1986; Fleeter and Hoyniak, 1987), have shown that aerodynamic detuning is beneficial to flutter stability and may be either beneficial or detrimental to flow-induced vibrations, depending on the particular operating condition and geometric configuration.

Splitter blades introduce combined aerodynamic-structural detuning into a rotor. The aerodynamic detuning results from the differences in the principal blade passage unsteady aerodynamics due to the splitters, with the structural detuning achieved through the higher natural frequencies of the splitter blades as compared to the full chord principal rotor blades. Hence, the incorporation of splitters into a rotor may not only result in improved aerodynamic performance, but also in decreased susceptibility to flutter and flow induced vibration problems. This has been shown for rotors operating in supersonic flow fields with subsonic axial components, with the airfoils modeled as flat plates (Topp and Fleeter, 1986; Fleeter et al., 1988).

Thus, the splittered rotor concept for increased performance also offers the potential of being beneficial with regard to blade row flow-induced vibrations. This may have an impact on performance design systems for splittered rotors. That is, splittered rotors may be able to be designed for safe operation in regions of the performance map wherein an unsplittered rotor would encounter severe flow-induced vibration problems, with blade row aerodynamic performance in these parts of the performance map previously unattainable.

In this paper, the effect on flow-induced vibrations of incorporating splitter blades into a subsonic rotor design, including airfoil profile effects, is considered. This involves the investigation of the viability of splitters as a passive torsion mode flow induced vibration control technique of an aerodynamically loaded rotor operating in an incompressible flow field. Thus, this research significantly extends the previous modeling and understanding of the fluid dynamics and aeroelasticity of splittered rotors. This is accomplished by developing a complete first-order unsteady aerodynamic model, i.e., the thin airfoil approximation is not utilized, to analyze the unsteady aerodynamic gust response and the oscillating airfoil motion-induced aerodynamics of both conventional uniformly spaced rotors without splitters and rotors incorporating variably spaced splitters between principal blades, including the effects of steady aerodynamic loading.

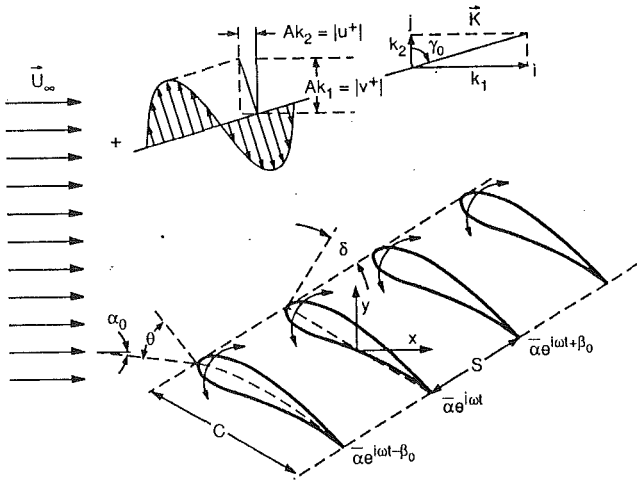

Fig. 1 Cascade and flow geometry

The analysis of the torsion mode flow-induced vibration characteristics of a rotor requires the prediction of the unsteady pressure resulting from an aerodynamic gust and the resulting harmonic torsional motion of the cascade. The steady and unsteady aerodynamics acting on the typical two-dimensional airfoil sections of a blade row are determined by considering: (1) a single principal blade passage with periodic boundary conditions for the conventional tuned uniformly spaced rotor; and (2) two principal blade passages with two passage periodic boundary conditions for the aerodynamically detuned rotor. The flow field is assumed to be linearly comprised of a steady potential mean flow and an harmonic unsteady flow field. The steady and unsteady potential flow fields are individually described by Laplace equations, with both the steady and unsteady potentials further decomposed into circulatory and noncirculatory components. The steady flow field is independent of the unsteady flow. However, the unsteady flow is coupled to the steady flow field through the unsteady boundary conditions on the airfoil surfaces.

A locally analytical solution is developed in which the discrete algebraic equations that represent the flow field equations are obtained from analytical solutions in individual grid elements. A body-fitted computational grid is utilized. General analytical solutions to the transformed Laplace equations are developed by applying these solutions to individual grid elements, with the complete flow field then obtained by assembling these locally analytical solutions.

Mathematical Model—Tuned Cascade. Figure 1 presents a schematic representation of a thick, cambered airfoil cascade at finite mean flow incidence, α_0, to the far-field uniform mean

Nomenclature

$\overline{Cp}$ = steady surface static pressure = $P/1/2\rho U_\infty^2$
$[CG]^n$ = gust influence coefficient of airfoil n
$[CM]^n$ = motion-induced influence coefficient of airfoil n
k_l = reduced frequency = $\omega b/U_\infty$
k_2 = transverse gust wave number
M_{GR} = gust unsteady aerodynamic moment
M_{MR} = motion-induced unsteady aerodynamic moment
P = steady pressure
P' = unsteady pressure
$\mathbf{Q}$ = complete flow field
$\mathbf{Q}_0$ = steady mean flow
$\overline{U}_\infty$ = far-field uniform mean flow
U_0 = steady airfoil surface chordwise velocity
V_0 = steady airfoil surface normal velocity
u^+ = streamwise gust component
v^+ = transverse gust component
W = complex gust amplitude
β_0 = interblade phase angle
β_d = detuned interblade phase angle
γ_0 = gust direction angle
Γ = steady circulation constant
Γ' = unsteady circulation constant
ϵ = level of aerodynamic detuning
Φ = general velocity potential
Φ_0 = steady velocity potential
Φ' = unsteady velocity potential
Φ'_C = circulatory unsteady velocity potential
Φ'_{NC} = noncirculatory unsteady velocity potential
ω_α = natural torsional frequency
ω_0 = reference frequency

flow, $\mathbf{U}_\infty = U_\infty \mathbf{i}$, executing torsion mode oscillations with a superimposed convected two-dimensional harmonic gust. The cascade has a stagger angle of δ, with S the distance between the airfoils along the stagger line and θ the inlet blade angle. The stagger angle is defined as the angle between the leading edge locus line and the line that is perpendicular to the airfoil chord. The inlet blade angle is defined as the angle between the line tangent to the camberline and the line that is perpendicular to the leading edge locus line. The gust amplitude and harmonic frequency are denoted by A and ω, with the interblade phase angle β_0 specified by the ratio of the number of gusts to the number of airfoils in the rotor blade row. The harmonic two-dimensional gust with transverse and streamwise components v^+ and u^+ propagates in the direction $\mathbf{K} = k_1\mathbf{i} + k_2\mathbf{j}$ where $k_1 = \omega b/U_\infty$ is the reduced frequency and k_2 is the transverse gust wave number, i.e., the transverse component of the gust propagation direction vector, with the gust direction angle γ_0 defined as $\tan^{-1}(k_1/k_2) = \tan^{-1}(-v^+/u^+)$.

The complete flow field is assumed to be comprised of a steady mean flow and an harmonic unsteady flow field, Eq. (1). The unsteady flow field corresponds to either the gust unsteady flow field $\mathbf{Q}'_G$ or the motion-induced unsteady flow field $\mathbf{Q}'_M$.

$$\mathbf{Q}(x, y, t) = \mathbf{Q}_0(x, y) + \mathbf{Q}'(x, y)\exp[ik_1 t] \tag{1}$$

Steady Flow Field. A velocity potential function can be defined for the steady flow of an incompressible inviscid fluid. The complete flow field is then described by the Laplace equation:

$$\nabla^2\Phi_0(x, y) = 0 \tag{2}$$

where $\mathbf{Q}_0(x, y) = \nabla\Phi_0(x, y)$.

Since the Laplace equation is linear, the velocity potential can be decomposed into noncirculatory and circulatory components $\Phi_{NC}(x, y)$ and $\Phi_C(x, y)$.

$$\Phi_0(x, y) = \Phi_{NC}(x, y) + \Phi_C(x, y) \tag{3}$$

where $\nabla^2\Phi_{NC} = 0$ and $\nabla^2\Phi_C = 0$.

To complete the steady flow mathematical model, far-field inlet, far-field exit, airfoil surface, wake dividing streamline (positioned at the bisector line form the airfoil trailing edge) and cascade periodic boundary conditions must be specified. The steady far-field inlet flow is uniform, with the mass flow rate specified by the far-field exit boundary conditions. Also, a zero normal velocity is specified on the airfoil surfaces.

The steady velocity potential is discontinuous along the airfoil wake dividing streamline. This discontinuity is satisfied by a continuous noncirculatory velocity potential, with the discontinuity in the circulatory velocity potential equal to the steady circulation, Γ. The Kutta condition is also applied, thereby enabling the steady circulation constant to be determined. It is satisfied by requiring the chordwise velocity components on the upper and lower airfoil surfaces to be equal in magnitude at the airfoil trailing edge. In addition, the cascade periodic steady velocity potential boundary conditions are satisfied by requiring both the normal and chordwise velocity components to be continuous between the upper and lower periodic boundaries. Refer to Chiang and Fleeter (1988) for a complete description of the steady flow boundary conditions.

Unsteady Gust Aerodynamics. The two-dimensional gust unsteady flow field $\mathbf{Q}'_G$ is determined by decomposing the gust-generated unsteady flow field into harmonic rotational $\mathbf{Q}_R$ and potential $\mathbf{Q}_P$ components. The rotational gust component is specified consistent with linearized unsteady Euler equations, determined by linearizing the unsteady flow about the steady flow field. The gust is assumed to be convected with the steady mean flow and therefore does not interact with the airfoil cascade. Thus the following solution for the rotational gust is determined by solving the linearized Euler equations in the far upstream where the steady flow field is uniform:

$$\mathbf{Q}_R = u^+\mathbf{i} + v^+\mathbf{j} \tag{4}$$

where $u^+ = -Ak_2 \exp[ik_1(t - x) - ik_2 y]$ and $v^+ = Ak_1 \exp[ik_1(t - x) - ik_2 y]$.

It should be noted that in this gust solution, the components u^+ and v^+ are coupled with the ratio of their amplitudes being $u^+/v^+ = -k_2/k_1$. Also, the solution corresponds exactly to the Sears (1941) transverse gust, when $k_2 = 0$. However, this gust solution differs from that used in the Horlock (1968) and Naumann and Yeh (1972) models in which the two components are uncoupled, $u^+ = \bar{u}^+ \exp[ik_1(t - x)]$ and $v^+ = \bar{v}^+ \exp[ik_1(t - x)]$, where $\bar{u}^+$ and $\bar{v}^+$ denote the individual amplitudes of the two independent gust components and the gust and resulting unsteady aerodynamics are independent of the transverse component of the gust propagation direction vector $\mathbf{K} = k_1\mathbf{i} + k_2\mathbf{j}$.

The potential gust component Φ'_G is described by a Laplace equation. The solution is determined by decomposing this potential gust component into circulatory and noncirculatory components $\Gamma'_{GC}(x, y)$ and $\Phi'_{GNC}(x, y)$, each of which is individually described by a Laplace equation:

$$\mathbf{Q}_P = \frac{\partial\Phi'_G}{\partial x}\mathbf{i} + \frac{\partial\Phi'_G}{\partial y}\mathbf{j} \tag{5a}$$

$$\Phi'_G = \Gamma'_{GNC} + \Phi'_{GC} \tag{5b}$$

$$\nabla^2\Phi'_{GC} = 0; \quad \nabla^2\Phi'_{GNC} = 0 \tag{5c}$$

Boundary conditions must be specified in the far-field inlet, far-field exit, airfoil surface, wake dividing streamline, and cascade periodic boundary for the gust circulatory and noncirculatory components. The inlet far-field gust velocity potential boundary conditions are obtained by using a Fourier series to satisfy the periodicity condition at the far upstream. The exit far-field gust noncirculatory potential boundary condition is obtained in a manner analogous to that for the inlet. Since the wake does not attenuate in the far field, the gust circulatory potential boundary equation is obtained by solving the Laplace equation at the far-field exit and satisfying the blade-to-blade periodicity condition (Verdon, 1987):

$$\Phi'_{GNC}|_{\text{far-field inlet}} = -\left|\frac{S}{\beta_0}\right| \left.\frac{\partial\Phi'_{GNC}}{\partial n}\right|_{\text{far-field inlet}} \tag{6a}$$

$$\Phi'_{GC}|_{\text{far-field inlet}} = -\left|\frac{S}{\beta_0}\right| \left.\frac{\partial\Phi'_{GC}}{\partial n}\right|_{\text{far-field inlet}} \tag{6b}$$

$$\Phi'_{GNC}|_{\text{far-field exit}} = -\left|\frac{S}{\beta_0}\right| \left.\frac{\partial\Phi'_{GNC}}{\partial n}\right|_{\text{far-field exit}} \tag{6c}$$

$$\Phi'_{GC}|_{\text{far-field exit}} = -\Delta\Phi' e^{-ik_1 x}\left[\frac{e^{k_1 y}}{1 - e^{(k_1 - i\nu)S\cos\delta}} + \frac{e^{-k_1 y}}{1 - e^{-(k_1 + i\nu)S\cos\delta}}\right] \tag{6d}$$

where $\nu = (\beta_0 + k_1 \sin\delta/S)/S \cos\delta$ and $\Delta\Phi'$ is the unsteady velocity potential discontinuity at the far-field exit.

The airfoil surface boundary conditions specify that the normal velocity of the flow field must be equal to that of the airfoil. The gust-generated unsteady rotational and potential flow fields are coupled through the boundary conditions on the noncirculatory gust component. In particular, the airfoil cascade is stationary, with the rotational gust convected with the mean steady flow field. Thus the upwash on the airfoil is determined by requiring the normal component of the unsteady flow field to be zero on the airfoil.

$$\left.\frac{\partial\Phi'_{GC}}{\partial n}\right|_{\text{airfoil}} = 0$$

$$\left.\frac{\partial\Phi'_{GNC}}{\partial n}\right|_{\text{airfoil}} = W'_G(x, y) = -\mathbf{n}\cdot\mathbf{Q}_R$$

or

$$W'_G(x, y) = -A\left(\frac{\partial f}{\partial x}k_2 + k_1\right)\exp[-i(k_1x + k_2y)] \quad (7)$$

where $f(x)$ specifies the airfoil profile.

The unsteady gust velocity potential is discontinuous along the airfoil wake dividing streamline. This discontinuity is satisfied with a continuous noncirculatory velocity potential and a discontinuous circulatory velocity potential. The unsteady circulatory velocity potential discontinuity is specified by requiring the pressure to be continuous across the wake and then utilizing the unsteady Bernoulli equation to relate the unsteady velocity potential and the pressure. Also specified is the continuity of the noncirculatory velocity potential along the wake streamline. The Kutta condition is applied to the unsteady gust flow field thereby enabling the unsteady circulation constant Γ'_G to be determined. It is satisfied by requiring no unsteady pressure difference across the airfoil chord at the trailing edge:

$$\Delta\Phi'_{GC}|_{\text{wake}} = \Gamma'_G \exp[-ik_1(x-1)] \quad (8a)$$

$$\Delta\Phi'_{GNC}|_{\text{wake}} = 0 \quad (8b)$$

The unsteady dependent variable of primary interest is the unsteady pressure P'_G from which the airfoil unsteady aerodynamic lift and moment are calculated. It is determined from the solution for the steady and unsteady gust velocity potentials, the unsteady Bernoulli equation, and the unsteady rotational gust pressure P_R. The unsteady aerodynamic moment on a reference airfoil for the gust unsteady model M_{GR} is then calculated by integrating the gust unsteady surface pressure difference across the airfoil chord:

$$M_{GR} = \int [(P'_G(x - x_0)dx - P'_G y dy]$$

Motion-Induced Unsteady Aerodynamics. The unsteady flow field associated with the harmonic motion of the airfoil cascade $\mathbf{Q}'_M$ is assumed to be potential and is therefore described by a Laplace equation. The solution is again determined by decomposing this velocity potential into circulatory and noncirculatory components $\mathbf{Q}'_{MC}$ and $\mathbf{Q}'_{MNC}$, each of which is individually described by a Laplace equation:

$$\mathbf{Q}'_M = \frac{\partial\Phi'_M}{\partial x}\mathbf{i} + \frac{\partial\Phi'_M}{\partial y}\mathbf{j} \quad (9a)$$

$$\Phi'_M = \Phi'_{MNC} + \Phi'_{MC} \quad (9b)$$

$$\nabla^2\Phi'_{MC} = 0; \quad \nabla^2\Phi'_{MNC} = 0 \quad (9c)$$

The boundary conditions in the far-field inlet, far-field exit, wake dividing streamlines, and cascade periodic boundaries as well as the Kutta condition for the motion-induced circulatory and noncirculatory components are identical to those for the gust potential flow. The only boundary condition that changes is that requiring the normal flow velocity to be equal to the airfoil velocity on the airfoil surface, the upwash condition.

The upwash on the airfoil for the motion-dependent model W'_M is a function of both the position of the airfoil and the steady flow field. Thus, this boundary condition couples the unsteady flow field to the steady aerodynamics. For an airfoil cascade executing harmonic torsion mode oscillations about an elastic axis location at x_0, the upwash on the airfoil is

$$W'_M(x, y) = \bar{\alpha}\left\{\frac{ik_1[(x-x_0) + y\partial f/\partial x] + U_0 + V_0\partial f/\partial x}{[1+(\partial f/\partial x)^2]^{1/2}} + \frac{\partial U_0/\partial y[(x-x_0)\partial f/\partial x + y]}{[1+(\partial f/\partial x)^2]^{1/2}} - \frac{\partial V_0/\partial y[(x-x_0) - y\partial f/\partial x]}{[1+(\partial f/\partial x)^2]^{1/2}}\right\} \quad (10)$$

where $U_0 = U_0(x, y)$ and $V_0 = V_0(x, y)$ are the steady airfoil surface velocity components, $f(x)$ denotes the airfoil profile, and $\bar{\alpha}$ is the amplitude of the torsional oscillations.

The unsteady pressure for the motion-dependent model P'_M is determined from the solution for the steady flow field, the unsteady velocity potential, and the unsteady Bernoulli equation. The unsteady aerodynamic moment on the reference airfoil is calculated by integrating the unsteady surface pressure difference across the chord:

$$M_{MR} = \int [P'_M(x - x_0)dx - P'_M y dy]$$

Locally Analytical Solution. A boundary-fitted computation grid generation technique is utilized for the numerical solution. A Poisson-type grid solver is used to fit a **C**-type grid around a reference airfoil in the cascade. This method permits grid points to be specified along the entire boundary of the computational plane.

Laplace equations describe the complete flow field including the unknown velocity potentials Φ_{NC}, Φ_C, Φ_{NC}, and Φ'_C. In the transformed (ξ, η) coordinate system, the Laplace equation takes on the following nonhomogeneous form:

$$\frac{\partial^2\bar{\Phi}}{\partial\xi^2} + \alpha\frac{\partial^2\bar{\Phi}}{\partial\eta^2} - 2\alpha\beta\frac{\partial\bar{\Phi}}{\partial\eta} - 2\gamma\frac{\partial\bar{\Phi}}{\partial\xi} = F(\xi, \eta) \quad (11)$$

where $\bar{\Phi}$ is a shorthand method of writing these four velocity potentials in the transformed plane, $F(\xi, \eta)$ contains the cross-derivative term $\partial^2\Phi/\partial\xi\partial\eta$, and the coefficients α, β, and γ are functions of the transformed coordinates ξ and η, which are treated as constants in each individual grid element.

To obtain the analytical solution to the transformed Laplace equation, it is first rewritten as a homogeneous equation by defining a new dependent variable $\hat{\phi}(\xi, \eta)$:

$$\frac{\partial^2\hat{\phi}}{\partial\xi^2} + \alpha\frac{\partial^2\hat{\phi}}{\partial\eta^2} - (\gamma^2 + \alpha\beta^2)\hat{\phi} = 0 \quad (12)$$

where $$\bar{\Phi} = \hat{\phi}\exp\{\gamma\xi + \beta\eta\} - \frac{F(\gamma\xi + \beta\eta)}{2(\gamma^2 + \alpha\beta^2)}$$

The following general solution for $\hat{\phi}$ is determined by separation of variables:

$$\hat{\phi}(\xi, \eta) = [A_1\cos(\lambda\xi) + A_2\sin(\lambda\xi)][B_1\cos(\mu\eta) + B_2\sin(\mu\eta)] \quad (13)$$

where $\mu = [(\gamma^2 + \alpha\beta^2 + \lambda^2)/\alpha]^{1/2}$ and λ, A_1, A_2, B_1, and B_2 are constants to be determined from the boundary conditions.

Analytical solutions in individual computation grid elements are determined by applying proper boundary conditions to evaluate the unknown constants in this general velocity potential solution. The solution to the global problem is then determined through the applications of the global boundary conditions and the assembly of the locally analytical solutions. The locally analytical method for steady two-dimensional fluid flow and heat transfer problems was initially developed by Chen et al. (1981). They have shown that the locally analytical method has several advantages over the finite difference and finite element methods.

Aerodynamically Detuned Cascade. For the aerodynamically detuned rotor configuration of interest herein, i.e., variable circumferential spacing and chord length, an analogous cascade unsteady aerodynamic model is developed by considering two passages with two passage periodic boundary conditions.

In this model, the rotor will incorporate splitters (short chord airfoils) between each pair of full chord airfoils. As schematically depicted in Fig. 2, the splitters are not required to have the same airfoil shape as the full chord airfoils, nor are they restricted to particular circumferential or axial positions between each pair of full chord airfoils.

There are two distinct passages: (1) a reduced spacing, or

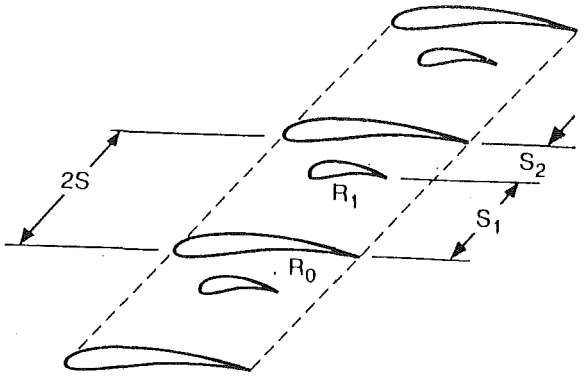

Fig. 2 Aerodynamically detuned cascade with splitters

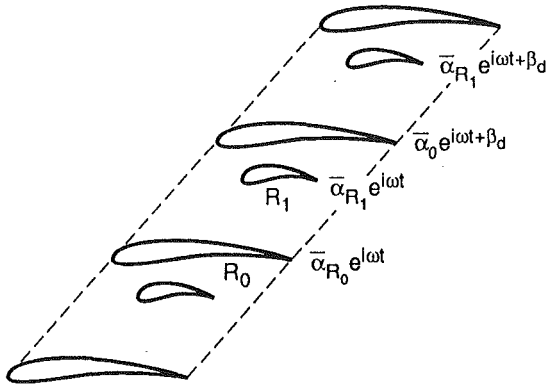

Fig. 3 Reference airfoils and passages of detuned cascade

increased solidity, passage; and (2) an increased spacing, or reduced solidity, passage. There are also two distinct sets of airfoils, with the two reference airfoils denoted by R_0 and R_1. These individual sets of airfoils can be considered as cascades of uniformly spaced airfoils each with twice the spacing of the associated baseline aerodynamically tuned uniformly spaced cascade. The circumferential spacing between these two sets of airfoils, S_1 and S_2, is determined by specifying the level of aerodynamic detuning, ϵ:

$$S_{2,1} = (1 \pm \epsilon)S \tag{14}$$

where S is the spacing of the baseline uniformly spaced cascade, and S_1 and S_2 denote the spacings of the detuned cascade.

An interblade phase angle for this aerodynamically detuned cascade configuration can be defined. In particular, each set of airfoils is individually assumed to be executing harmonic torsional oscillations with a constant aerodynamically detuned interblade phase angle, β_d, between adjacent airfoils of each set, Fig. 3. Thus, this detuned cascade interblade phase angle is two times that for the corresponding baseline tuned cascade:

$$\beta_d = 2\beta_0$$

where β_0 is the tuned baseline cascade interblade phase angle, defined between adjacent airfoils on the rotor.

For a rotor with N uniformly spaced blades, Lane (1956) showed that the values of β_0 must satisfy the following condition:

$$\beta_0 = \frac{2\pi r}{N}, \quad r = 0, \pm 1, \pm 2, \ldots, \pm N - 1 \tag{15}$$

where $\pm$ refers to forward and backward traveling waves, respectively.

Steady Aerodynamics. The steady aerodynamic model developed for the baseline uniformly spaced cascade can be applied directly to the two reference passage model of the detuned cascade with the addition that the steady potential for the detuned cascade, $\Phi_{d0}(x, y)$ is decomposed into one noncirculatory $\Phi_{dNC}(x, y)$ and two circulatory components, one associated with each of the two reference airfoils, $\Phi_{CR_0}(x, y)$ and $\Phi_{CR_1}(x, y)$.

$$\Phi_{d0}(x, y) = \Phi_{dNC}(x, y) + \Phi_{CR_0}(x, y) + \Phi_{CR_1}(x, y) \tag{16}$$

where $\nabla^2\Phi_{dNC} = 0$; $\nabla^2\Phi_{CR_0} = 0$; and $\nabla^2\Phi_{CR_1} = 0$.

The circulatory component $\Phi_{CR_0}(x, y)$ is discontinuous along the wake dividing streamline of the reference airfoil R_0 and is continuous along the wake dividing streamline of the reference airfoil R_1, while $\Phi_{CR_1}(x, y)$ is continuous along the wake of R_1 and continuous along the wake of R_0. The steady potential discontinuity is satisfied by a continuous noncirculatory velocity potential, with the discontinuities in the circulatory components Φ_{CR_0} and Φ_{CR_1} equal to the steady circulation, Φ_{R_0} and Φ_{R_1}, respectively. Also, the steady circulation constants Γ_{R_0} and Γ_{R_1} are determined by simultaneously applying the Kutta condition to the two reference airfoils.

Unsteady Aerodynamics. The unsteady potential for the detuned cascade Φ'_d is also decomposed into one noncirculatory $\Phi'_{dNC}(x, y)$ and two circulatory components, one associated with each of the two reference airfoils $\Phi'_{CR_0}(x, y)$ and $\Phi'_{CR_1}(x, y)$:

$$\Phi'_d(x, y) = \Phi'_{dNC}(x, y) + \Phi'_{CR_0}(x, y) + \Phi'_{CR_1}(x, y) \tag{17}$$

where $\Phi'_{CR_0}(x, y)$, Φ'_{CR_1}, and the unsteady circulation constants Γ'_{R_0}, and Γ'_{R_0} are defined analogous to the corresponding detuned cascade steady aerodynamic quantities.

Influence Coefficient Technique. The unsteady airfoil surface boundary conditions require that the cascaded airfoils oscillate with equal amplitudes. Also, the interblade phase angle between adjacent nonuniformly spaced airfoils must be specified. Neither of these requirements is appropriate for the aerodynamically detuned cascade. To overcome these limitations, an unsteady aerodynamic influence coefficient technique is utilized.

The unsteady aerodynamic moment acting on the two reference airfoils is expressed in terms of influence coefficients:

$$M_{R_0,R_1} = \begin{pmatrix} W_{R_0}[CG]^0_{R_0,R_1} + W_{R_1}[CG]^1_{R_0,R_1} \\ + \\ \bar{\alpha}_{R_0}[CM]^0_{R_0,R_1} + \bar{\alpha}_{R_1}[CM]^1_{R_0,R_1} \end{pmatrix} e^{i\omega t} \tag{18}$$

where $\bar{\alpha}_{R_0}$ and $\bar{\alpha}_{R_1}$ are the unknown complex oscillatory displacements for the reference airfoils R_0 and R_1, respectively, and W_{R_0,R_1} are the complex gust amplitudes, which are related by the detuned interblade phase angle β_d and the level of aerodynamic detuning ϵ:

$$W_{R_0} = W_{R_1} \exp\left[-i(1-\epsilon)\beta_d/2\right] \tag{19}$$

The influence coefficients $[CG]^0_{R_0,R_1}$, $[CG]^1_{R_0,R_1}$, $[CM]^0_{R_0,R_1}$, and $[CM]^1_{R_0,R_1}$ are the unsteady aerodynamic moments acting on the two reference airfoils. They are determined by analyzing the two reference passages with the unsteady cascade model developed herein. $[CG]^0_{R_0,R_1}$ and $[CM]^0_{R_0,R_1}$ are determined by considering a unit amplitude gust acting only on the reference airfoil R_0 and unit amplitude motion of only the reference airfoil R_0, respectively, and reference airfoil R_1 with no gust and stationary. Note that the gust is modeled only through the airfoil surface boundary conditions. Thus, the gust acts either on one or both airfoils. The influence coefficients $[CG]^1_{R_0,R_1}$ and $[CM]^1_{R_0,R_1}$ are obtained in an analogous manner.

Forced Response Model

The equations describing the single-degree-of-freedom tor-

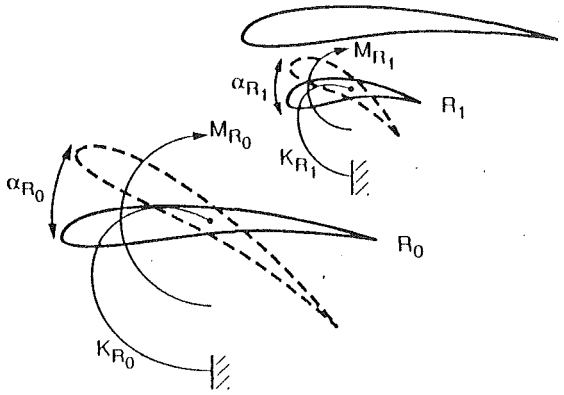

Fig. 4 Single-degree-of-freedom detuned cascade model

sional motion of the two reference airfoils of the aerodynamically detuned cascade are developed by considering the typical airfoils depicted in Fig. 4. The elastic restoring forces are modeled by linear torsional springs at the elastic axis location, with the inertial properties of the airfoils represented by their mass moments of inertia about the elastic axis. The equations of motion, determined by Lagrange's technique, are

$$I_{\alpha R_0}\ddot{\alpha}_{R_0} + (1 + 2ig_{\alpha R_0}) I_{\alpha R_0}\omega^2_{\alpha R_0}\alpha_{R_0} = M_{R_0}$$
$$I_{\alpha R_1}\ddot{\alpha}_{R_1} + (1 + 2ig_{\alpha R_1}) I_{\alpha R_1}\omega^2_{\alpha R_1}\alpha_{R_1} = M_{R_1} \quad (20)$$

where $I_{\alpha R_0,R_1}$ are the mass moments of inertia about the elastic axis, $g_{\alpha R_0}$ and $g_{\alpha R_1}$ denote the structural damping coefficients for the reference airfoils, and the undamped natural frequencies are $\omega^2_{\alpha R_0} = K_{\alpha R_0}/I_{\alpha R_0} = \omega^2_{\alpha R_1} = K_{\alpha R_1}/I_{\alpha R_1}$.

Considering harmonic time dependence of the reference airfoils and utilizing the total unsteady aerodynamic moments and Eq. (19), the equations of motion are written in matrix form:

$$\begin{bmatrix} \mu_0 & [CM]^1_{R_0} \\ [CM]^0_{R_1} & \mu_1 \end{bmatrix} \begin{bmatrix} \bar{\alpha}_{R_0} \\ \bar{\alpha}_{R_1} \end{bmatrix} = -w_{R_0} \begin{bmatrix} [CG]^0_{R_0} + e^{i(1-\epsilon)\beta_d/2}[CG]^1_{R_0} \\ [CG]^0_{R_1} + e^{i(1-\epsilon)\beta_d/2}[CG]^1_{R_1} \end{bmatrix} \quad (21)$$

where $\mu_0 = \mu_{R_0} r^2_{\alpha R_0} + [CM]^0_{R_0} - (1 + 2ig_{\alpha R_0})\mu_{R_0} r^2_{\alpha R_0}\gamma^2_{\alpha R_0}\gamma$

$$\mu_1 = \mu_{R_1} r^2_{\alpha R_1} + [CM]^1_{R_1} - (1 + 2ig_{\alpha R_0})\mu_{R_1} r^2_{\alpha R_0}\gamma^2_{\alpha R_1}\gamma$$

$$\mu_{R_0,R_1} = \frac{m_{R_0,R_1}}{\pi\rho b^2}; \quad r^2_{\alpha R_0,R_1} = \frac{I_{\alpha R_0,R_1}}{m_{R_0,R_1} b^2}$$

$$\gamma^2_{\alpha R_0,R_1} = \frac{\omega_{\alpha R_0,R_1}}{\omega_0}; \quad \gamma = \frac{\omega^2_0}{\omega^2}$$

and ω_0 = reference frequency.

The aerodynamically forced response of a tuned or detuned cascade is determined by solving Eq. (21) for the airfoil displacements using standard matrix techniques. It should be noted that both the motion dependent oscillating airfoil and the gust response unsteady aerodynamic influence coefficients must be determined for each specified interblade phase angle β_d. The resulting airfoil displacement vector solution is

$$\begin{bmatrix} \bar{\alpha}_{R_0} \\ \bar{\alpha}_{R_1} \end{bmatrix} = -w_{R_0} \begin{bmatrix} \mu_0 & [CM]^1_{R_0} \\ [CM]^0_{R_1} & \mu_1 \end{bmatrix}^{-1} \cdot \begin{bmatrix} [CG]^0_{R_0} + e^{i(1-\epsilon)b_d/2}[CG]^1_{R_0} \\ [CG]^0_{R_1} + e^{i(1-\epsilon)b_d/2}[CG]^1_{R_1} \end{bmatrix} \quad (22)$$

The effects of structural detuning are included through the frequency terms $\gamma_{\alpha R_0,R_1}$. These terms represent the ratios of the natural frequency to a specified reference frequency. Defining the reference frequency ω_0 as the torsion mode natural frequency, a structurally tuned cascade would have α_{0R_0,R_1} equal to unity. For the case when the cascade is structurally detuned, the values of α_{0R_0,R_1} are altered.

In this regard, splitters enable combined aerodynamic and structural detuning to be introduced into a rotor. In particular, the natural torsion mode frequency of an airfoil is a function of its chord length, thickness, and span as well as its material properties. As a result, the splitters may have a higher natural frequency than the full chord airfoils.

The vibrational characteristics of the full chord and splitter airfoils are determined by modeling each airfoil as a thin rectangular cross-section cantilevered slender beam. The torsion mode natural frequency ω_α is

$$\omega_\alpha = \sqrt{\frac{G}{2\pi^2\rho_m}}\frac{T}{CL} \quad (23)$$

where G is the material modulus of rigidity, L is the airfoil span, T is the airfoil thickness, C is the chord length, $m = \rho_m LTC$ is the mass of the airfoil, and ρ_m is the material density.

Two types of splitters are of interest: (1) splitters with the same thickness-to-chord ratio as the full chord airfoils, and (2) splitters with the same thickness as the full chord airfoils.

For the first type, the splitters and full chord airfoils have the same natural frequency when their material properties and spans are the same, with the splitters having a higher natural frequency when the material properties are different or the splitter span is smaller than that of the full chord airfoils. Hence, these splitters incorporate either aerodynamic detuning or combined aerodynamic-structural detuning into a rotor design.

For the second case, the splitters have a higher natural frequency than the full chord airfoils as long as the two sets of airfoils have the same material properties and spans, with the possibility of the splitters and full chord airfoils having the same natural frequency if different materials are utilized or the splitters have increased span. Thus, these splitters can also introduce either aerodynamic detuning or combined aerodynamic-structural detuning into the rotor.

Results

To demonstrate the effects of the splitter-generated aerodynamic and structural detuning on flow-induced vibrational response, the single-degree-of-freedom torsional aeroelastic model is applied to a baseline twelve-bladed rotor and to a rotor with alternate blades replaced with splitters.

Baseline Rotor Configurations. The baseline rotor is comprised of twelve uniform circumferentially spaced blades characterized by a Gostelow cascade geometry with a solidity of 0.83, a stagger angle of 40 deg, a mean flow incidence angle of 24 deg, and an airfoil mass ratio μ and radius of gyration r_α of 193.776 and 0.3957, respectively, typical of modern fan blades. The reduced frequency is 1.67, resulting in a stable baseline rotor for all interblade phase angles.

The aerodynamic forcing function considered is a 45 deg two-dimensional gust characterized by interblade phase angles β_0 of -30, 0, and 180 deg, corresponding to detuned interblade phase angles β_d of -60, 0, and 360 deg. These values were selected because they are the gust loads that were found to result in the highest amplitudes of response. In this study, the frequency of the gust ω is nondimensionalized by the undamped natural torsional frequency of the baseline airfoils ω_0. The rotor response generated by this forcing function is presented in the format of the reference airfoil amplitude of response α normalized by the maximum response of the baseline reference airfoil α_0. The amplitudes of response for the three gust in-

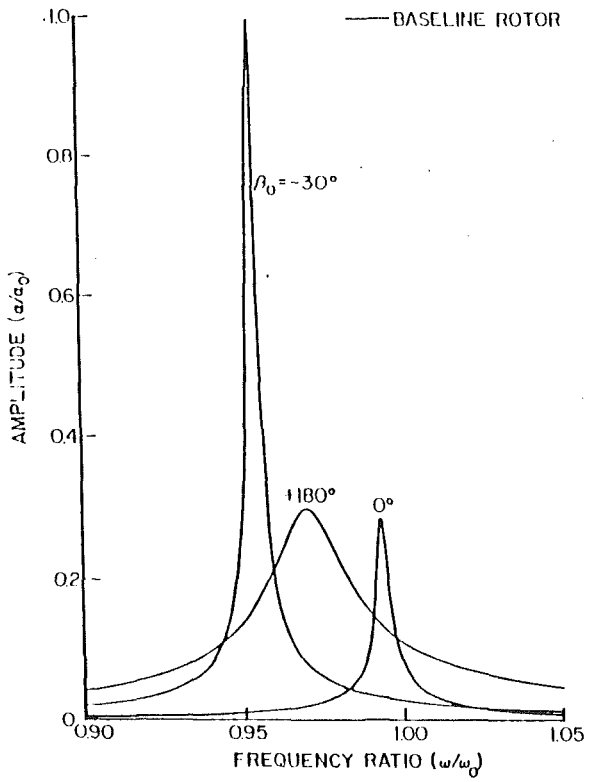

Fig. 5 Baseline airfoil response for gust with $\beta_0 = -30$, 180, and 0 deg

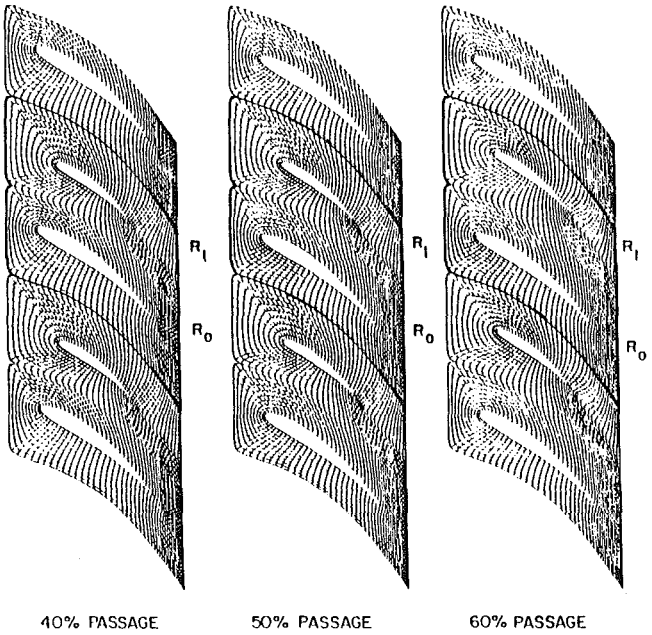

Fig. 6 Aerodynamically detuned twelve-bladed splittered-rotor flow geometries and computational grids

terblade phase angles of the baseline reference airfoil as a function of the nondimensional gust frequency ω/ω_0 are shown in Fig. 5.

Splittered-Rotor Configuration. Splitters are a convenient means of introducing aerodynamic and/or structural detuning into a rotor. Thus, the baseline twelve-bladed rotor is detuned by replacing alternate airfoils with splitters with chords that are two-thirds that of the full chord airfoils, with two splitter designs considered.

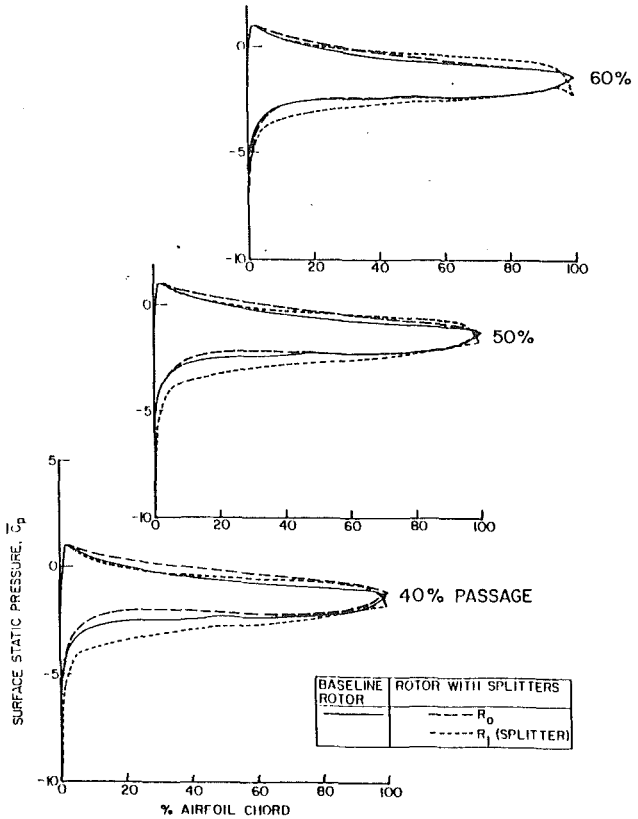

Fig. 7 Steady aerodynamic performance of baseline and splittered rotors

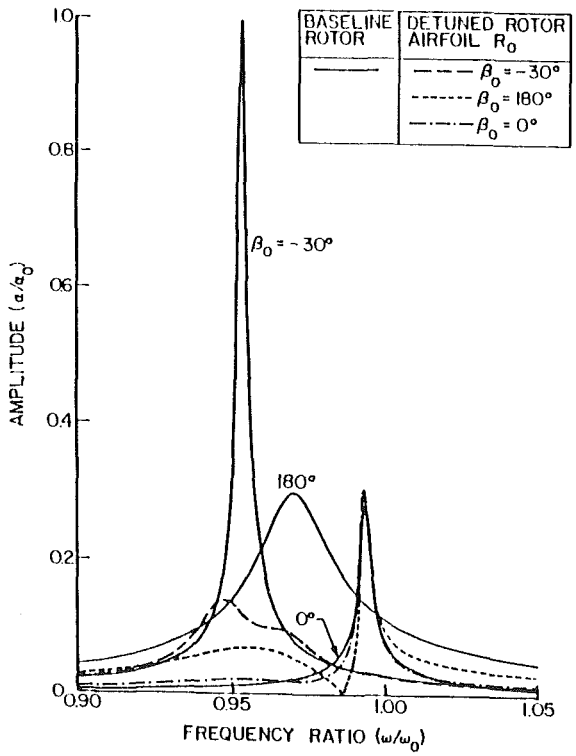

Fig. 8 Aerodynamic detuning effect on airfoil R_0 response with splitters with the same *T/C* as baseline airfoils at 40 percent circumferential spacing

Aerodynamic detuning is introduced into the rotor by means of splitters with the same thickness-to-chord ratio as the fully chord airfoils, and thus the same natural frequencies. The aerodynamic detuning results from both the decreased chord

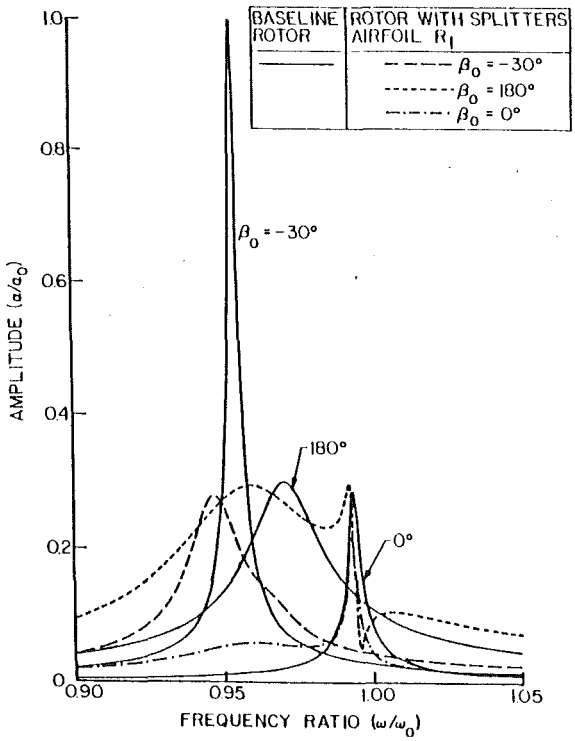

Fig. 9 Aerodynamic detuning effect on airfoil R_1 response with splitters with the same *T/C* as baseline airfoils at 40 percent circumferential spacing

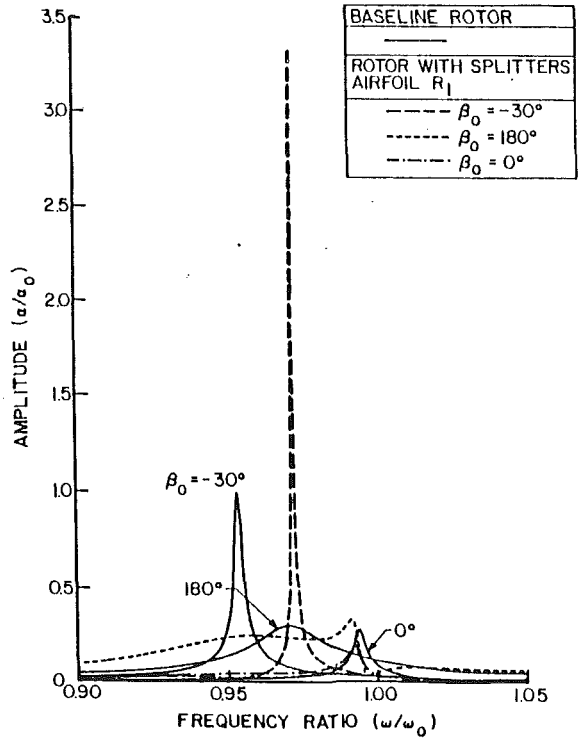

Fig. 11 Aerodynamic detuning effect on airfoil R_1 response with splitters with the same *T/C* as baseline airfoils at 50 percent circumferential spacing

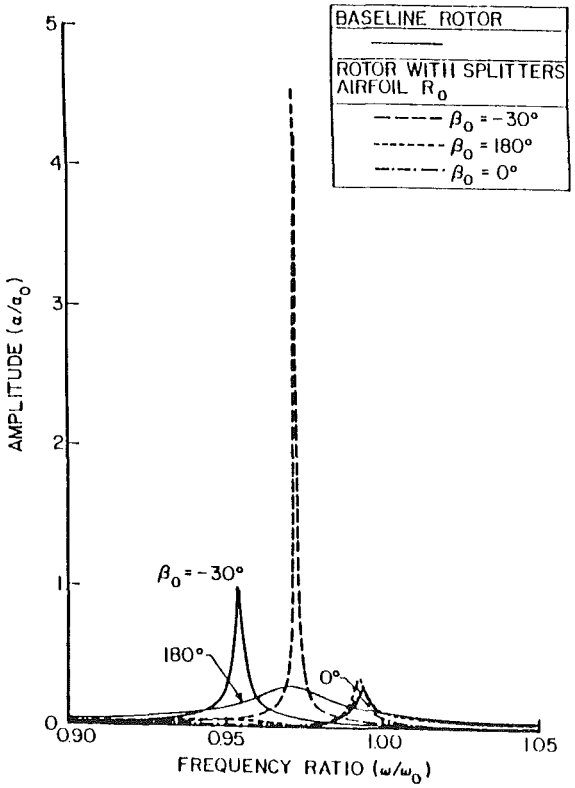

Fig. 10 Aerodynamic detuning effect on airfoil R_0 response with splitters with the same *T/C* as baseline airfoils at 50 percent circumferential spacing

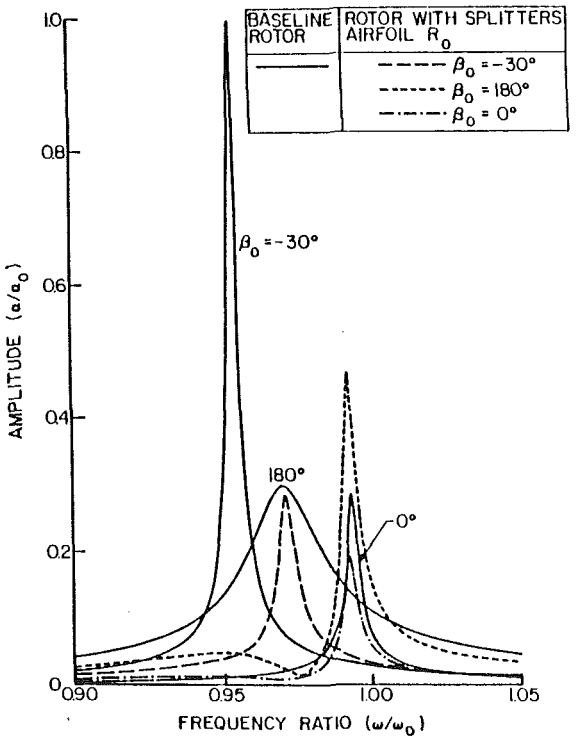

Fig. 12 Aerodynamic detuning effect on airfoil R_0 response with splitters with the same *T/C* as baseline airfoils at 60 percent circumferential spacing

of the splitters and the splitter circumferential position between adjacent full chord airfoils. Three circumferential splitter locations are considered: 40, 50, and 60 percent. Figure 6 shows examples of these splittered-rotor flow geometries and the associated computational grids.

Combined aerodynamic-structural detuning is accomplished with splitters having the same thickness but a different chord length than the full chord airfoils positioned such that the splitter trailing edge is aligned with that of the full chord airfoils.

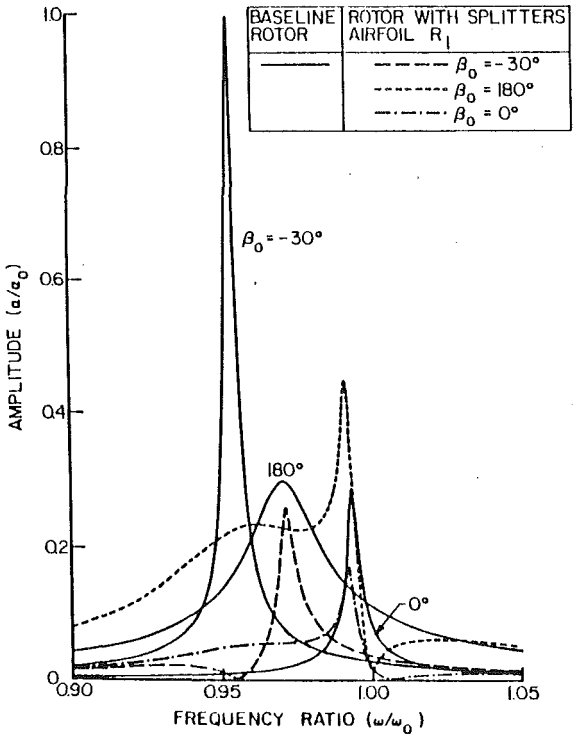

Fig. 13 Aerodynamic detuning effect on airfoil R_1 response with splitters with the same *T/C* as baseline airfoils at 60 percent circumferential spacing

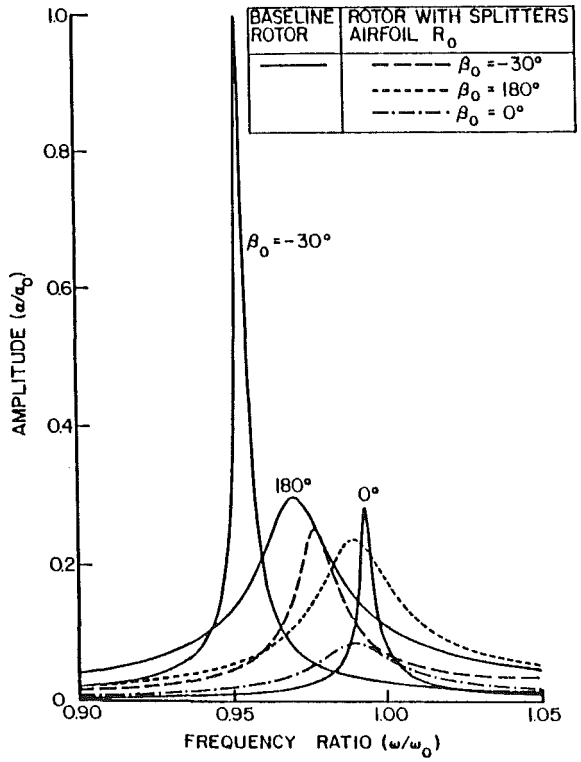

Fig. 14 Aerodynamic-structural detuning effect on airfoil R_0 response with splitters with the same *T/C* as baseline airfoils at 40 percent circumferential spacing

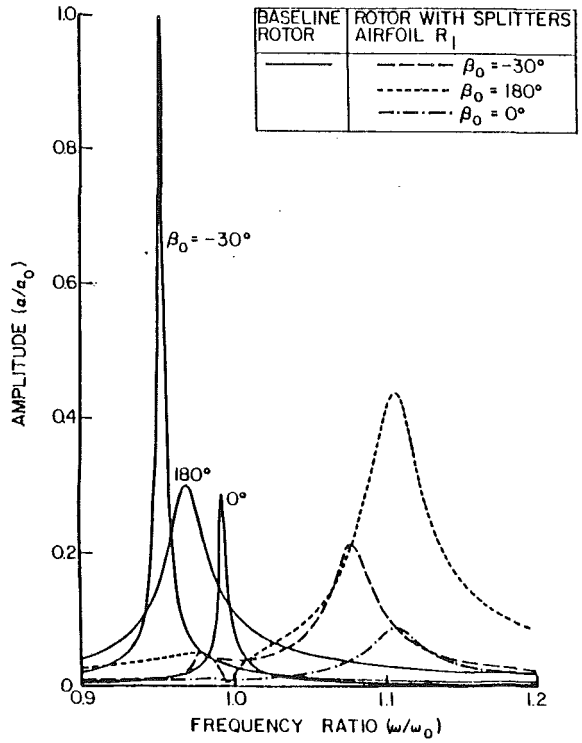

Fig. 15 Aerodynamic-structural detuning effect on airfoil R_1 response with splitters with the same *T/C* as baseline airfoils at 40 percent circumferential spacing

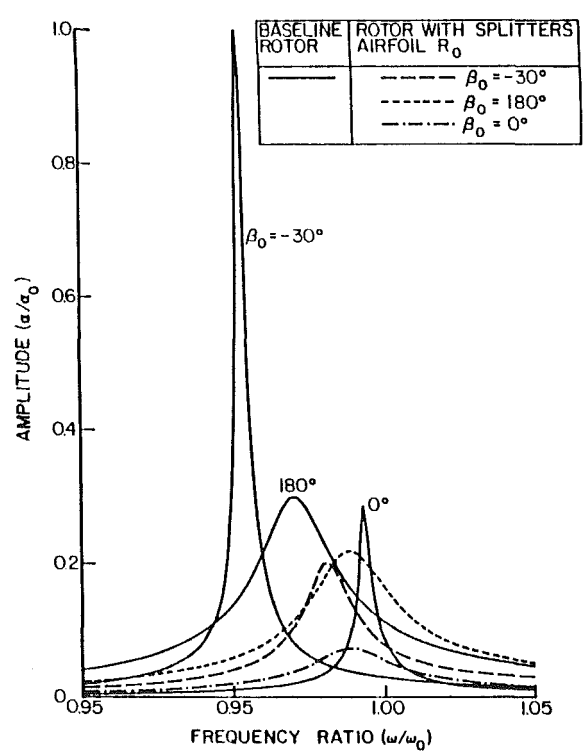

Fig. 16 Aerodynamic-structural detuning effect on airfoil R_0 response with splitters with the same *T/C* as baseline airfoils at 50 percent circumferential spacing

Steady Aerodynamic Performance. Steady rotor performance is defined by the chordwise distributions of the airfoil surface steady static pressure coefficient, presented in Fig. 7 for the baseline and splittered rotors. The introduction of the splitters into the rotor has a noticeable effect on the steady loading distribution of the full chord airfoils, with this effect being a function of the splitter circumferential position.

Forced Vibrational Response. For the rotor with splitters having the same thickness-to-chord ratio as the full chord

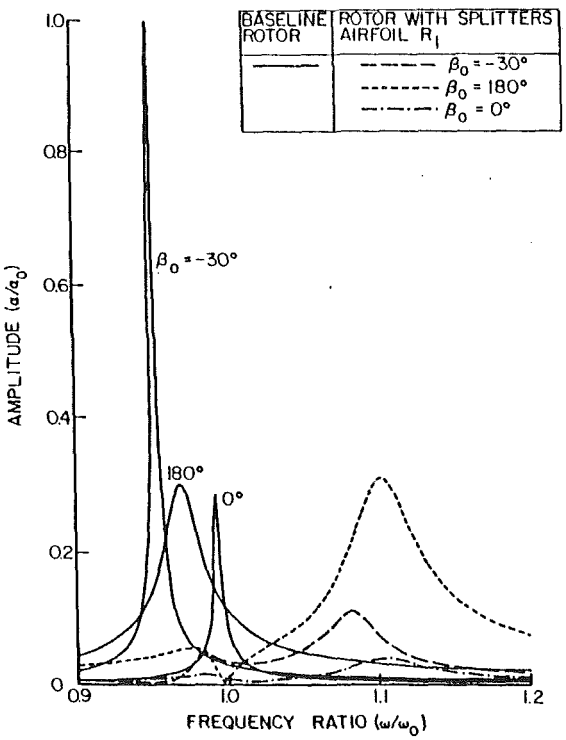

Fig. 17 Aerodynamic-structural detuning effect on airfoil R_1 response with splitters with the same *T/C* as baseline airfoils at 50 percent circumferential spacing

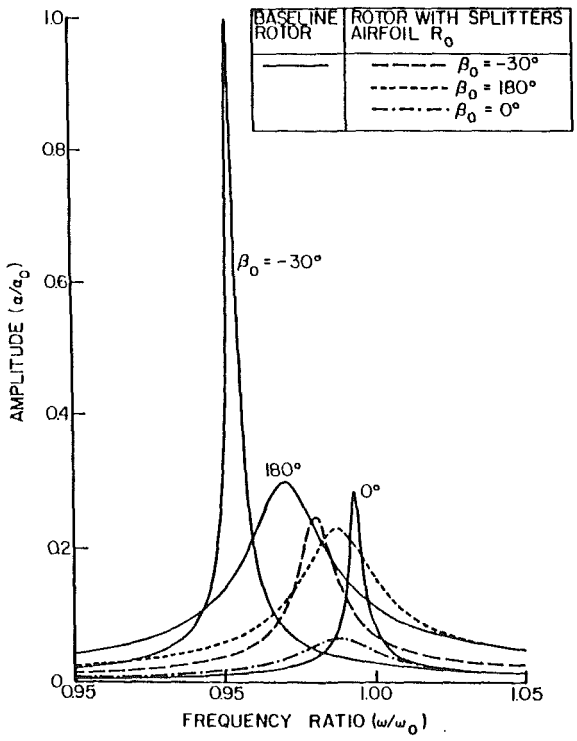

Fig. 18 Aerodynamic-structural detuning effect on airfoil R_0 response with splitters with the same *T/C* as baseline airfoils at 60 percent circumferential spacing

airfoils, the effect of aerodynamic detuning on forced response is shown in Figs. 8–13.

With the splitters at 40 percent passage spacing, the aerodynamic detuning results in a significant decrease in the maximum amplitude of response for the backward traveling wave mode ($\beta_0 = -30$ deg). For the full chord reference airfoil R_0,

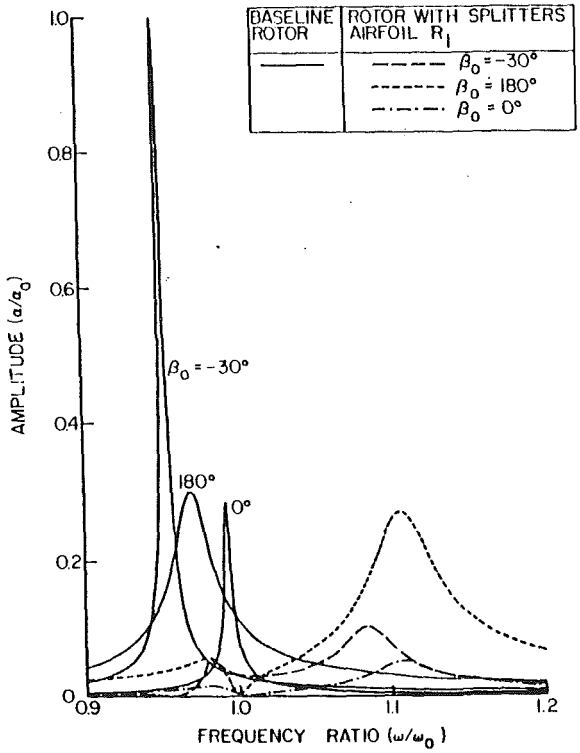

Fig. 19 Aerodynamic-structural detuning effect on airfoil R_1 response with splitters with the same *T/C* as baseline airfoils at 60 percent circumferential spacing

as shown in Fig. 8, the response amplitude for the forward traveling wave mode ($\beta_0 = +180$ deg) is decreased as compared to the baseline around $\omega/\omega_0 = 0.96$ but increased near $\omega/\omega_0 = 1.0$. The response for the in-phase mode is almost unchanged by this detuning. For the splitter reference airfoil R_1, as shown in Fig. 9, the response amplitude is decreased slightly for the in-phase mode and exhibits coupling of the two modes for the forward traveling wave mode ($\beta_0 = +180$ deg).

With these splitters at 50 percent passage spacing, as shown in Figs. 10 and 11, there is a significant increase in the maximum response amplitude of both reference airfoils as compared to the baseline for the backward traveling gust wave mode. For the other two interblade phase angles ($\beta_0 = 0$ and 180 deg), analogous trends as previously seen with the splitter at 40 percent passage spacing are found. Thus, this splitter aerodynamic detuning has an adverse effect on forced response.

Positioning these splitters at 60 percent passage spacing results in a significant decrease in the response amplitude for a gust characterized by $\beta_0 = -30$ deg, as shown in Figs. 12 and 13. However, there is an increase in the response amplitude associated with the forward traveling wave mode and a slightly decreased response amplitude in the in-phase mode. Thus, depending on the gust interblade phase angle, this aerodynamic detuning may be either beneficial or detrimental to the rotor forced response.

The effect on forced response of combined aerodynamic and structural detuning generated by these splitters is also considered, with the splitters considered to have a 15 percent higher natural frequency than the full chord airfoils, Figs. 14–19. This combined alternate blade structural and aerodynamic detuning results in decreased amplitudes of response of the reference full chord airfoils for all modes. Also, there is minimal response of the reference splitter in the range of frequencies near that of the full chord natural frequency. However, for some of the detuned rotor configurations, the splitter response at the higher frequency is greater than or of the same order

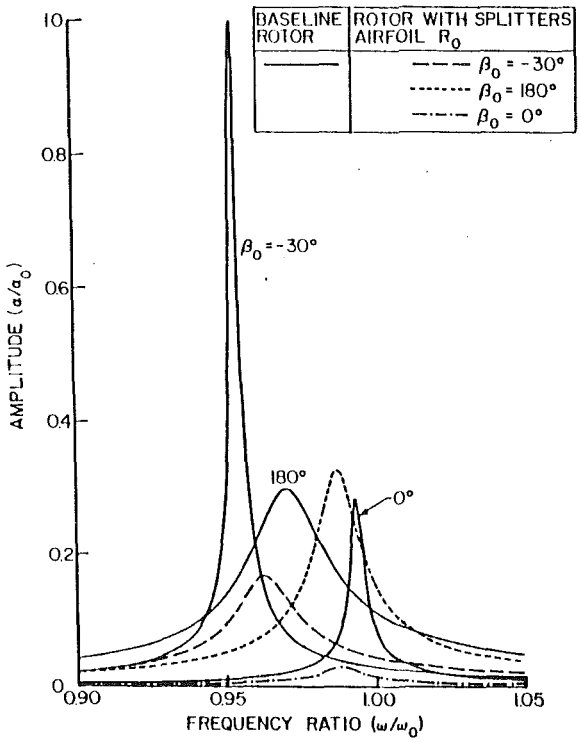

Fig. 20 Aerodynamic-structural detuning effect on airfoil R_0 response with splitters with the same thickness as baseline airfoils at 50 percent circumferential spacing

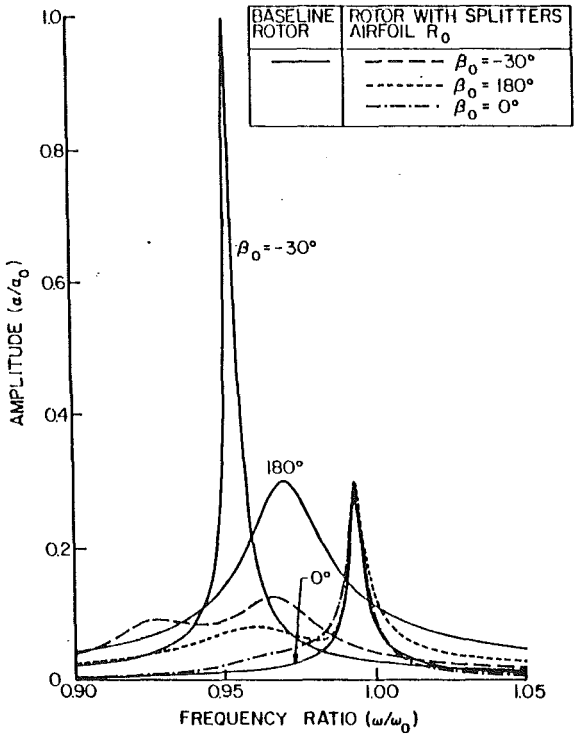

Fig. 22 Aerodynamic detuning effect on airfoil R_0 response with splitters with the same thickness as baseline airfoils at 50 percent circumferential spacing

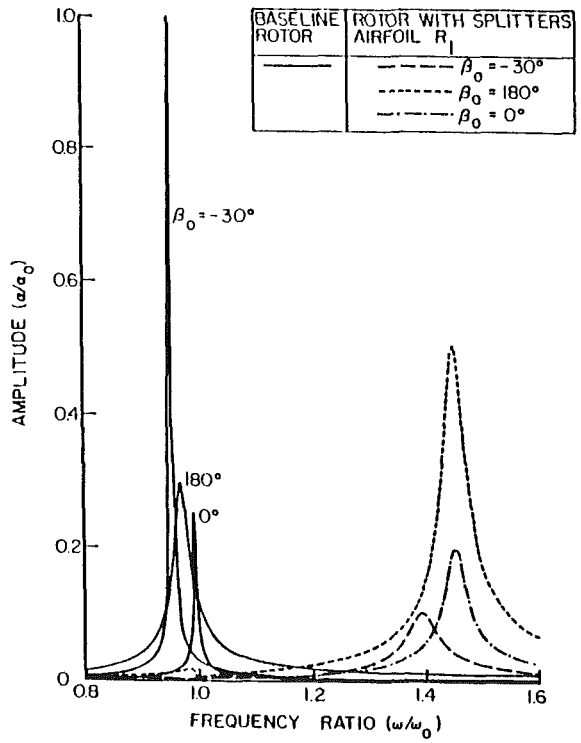

Fig. 21 Aerodynamic-structural detuning effect on airfoil R_1 response with splitters with the same thickness as baseline airfoils at 50 percent circumferential spacing

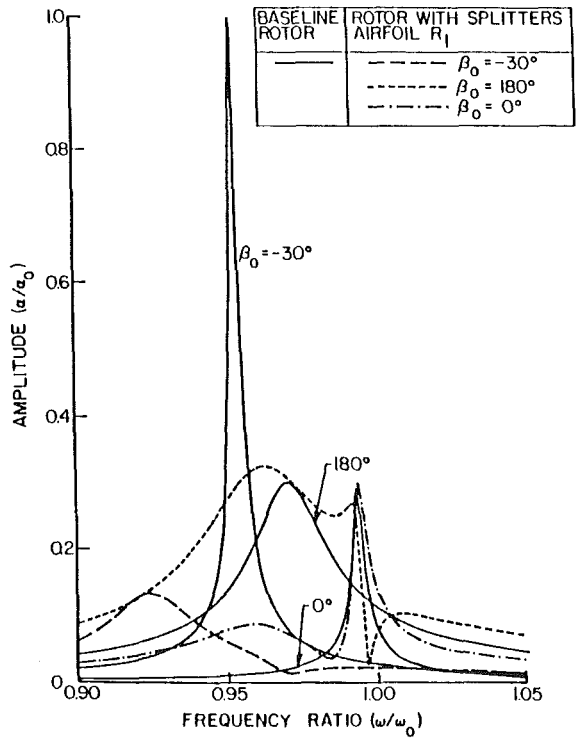

Fig. 21 Aerodynamic detuning effect on airfoil R_1 response with splitters with the same thickness as baseline airfoils at 50 percent circumferential spacing

as the 180 deg mode response of the baseline full chord airfoils at the lower frequency.

For the rotor with splitters having the same thickness as the full chord airfoils, the effect of combined aerodynamic and structural detuning on forced responses is shown in Figs. 20 and 21, with the effect of aerodynamic detuning presented in Figs. 22 and 23. The combined detuning significantly decreases the response for both the backward and in-phase traveling wave gust modes of the full chord reference airfoil R_0. However, it results in a small increase in the response for the 180 deg gust mode. Also, this combined aerodynamic and structural detuning results in minimal response of the splitters in

the range of frequencies near that of the full chord airfoil natural frequency, but an additional response near the splitter natural frequency. This higher frequency splitter response is not small, being somewhat larger for the forward wave mode and smaller for the other two modes than the full chord airfoil response amplitudes. When only the aerodynamic detuning generated by these thick splitters is considered, the response of the full chord airfoils in the backward traveling wave mode is decreased. However, this aerodynamic detuning alone has little effect on the full chord airfoil response for the other two gust modes. Also, with only aerodynamic detuning, the splitter response is decreased as compared to the case with combined aerodynamic and structural detuning. It should be noted that in this case the splitter resonant response frequency is near that of the baseline airfoils.

Summary and Conclusions

A mathematical model has been developed and utilized to predict the effect of incorporating splitter blades on the torsion mode forced response of a rotor operating in an incompressible flow field. The splitter blades, positioned circumferentially in the flow passage between two principal blades, introduce aerodynamic and/or combined aerodynamic-structural detuning into the rotor. The two-dimensional gust response and oscillating cascade unsteady aerodynamics, including steady loading effects, were determined by developing a complete first-order unsteady aerodynamic analysis together with an unsteady aerodynamic influence coefficient technique. The torsion mode forced response of both uniformly spaced tuned rotors and detuned splittered rotors were then predicted by incorporating the unsteady aerodynamic influence coefficients into a single-degree-of-freedom aeroelastic model.

The viability of splitters as a passive torsion mode forced response control technique for an aerodynamically loaded rotor operating in an incompressible flow field was then considered, accomplished by applying this model to a baseline twelve-bladed rotor. This study demonstrated that the aerodynamic detuning associated with the splitters was sometimes beneficial and other times detrimental with regard to forced response. However, the combined aerodynamic and structural detuning due to the splitters was generally beneficial for the full chord airfoils, with minimal splitter response in the frequency range near to that of the full chord airfoils. Thus, aerodynamic detuning and combined aerodynamic-structural detuning associated with the incorporation of splitters into a rotor are viable passive control mechanisms for flow-induced response of rotors.

Acknowledgments

This research was sponsored, in part, by the NASA Lewis Research Center.

References

Chen, C. J., Naseri-Neshat, H., and Ho, K. S., 1981, "Finite Analytic Numerical Solution of Heat Transfer in Two-Dimensional Cavity Flow," *Journal of Numerical Heat Transfer*, Vol. 4, pp. 179–197.

Chiang, H. D., and Fleeter, S., 1988, "Locally Analytical Prediction of the Steady Inviscid Incompressible Flow Through an Airfoil Cascade," *International Journal of Computers & Mathematics With Applications*, Vol. 15, No. 3, pp. 221–233.

Chiang, H., and Fleeter, S., 1989, "Oscillating Aerodynamics and Flutter of an Aerodynamically Detuned Cascade in an Incompressible Flow," AIAA Paper No. 89-0289.

Fleeter, S., and Riffel, R. E., 1977, "The Influence of Circumferential Splitter Location on the Performance of a Transonic Compressor Cascade," Air Force Aero Propulsion Laboratory Report AFAPL-TR-77-20, Feb.

Fleeter, S., and Hoyniak, D., 1987, "Chordwise Spacing Aerodynamic Detuning for Unstalled Supersonic Flutter Stability Enhancement," *Journal of Sound and Vibration*, Vol. 115, No. 3, pp. 483–497.

Fleeter, S., Hoyniak, D., and Topp, D. A., 1988, "Control of Rotor Aerodynamically Forced Vibrations by Splitters," *AIAA Journal of Propulsion and Power*, Sept.–Oct., pp. 445–451.

Holtman, R. L., McClure, R. B., and Sinnet, G. T., 1973, "Test of a Supersonic Compressor Cascade With Splitter Vanes," *ARL 73-0142, ADA774549*, Aerospace Research Laboratories, WPAFB, OH.

Horlock, J. H., 1968, "Fluctuating Lift Forces on Airfoils Moving Through Transverse and Chordwise Gusts," ASME *Journal of Basic Engineering*, Vol. 90, No. 4, pp. 494–500.

Hoyniak, D., and Fleeter, S., 1986, "Aerodynamic Detuning Analysis of an Unstalled Supersonic Turbofan Cascade," ASME *Journal of Engineering for Gas Turbines and Power*, Vol. 108, pp. 60–67.

Lane, F., 1956, "System Mode Shapes in the Flutter of Compressor Blades Rows," *Journal of the Aeronautical Science*, Vol. 23, pp. 54–66.

Naumann, H., and Yeh, H., 1972, "Lift and Pressure Fluctuations of a Cambered Airfoil Under Periodic Gusts and Applications to Turbomachinery," ASME Paper 72-GT-30.

Sears, W. R., 1941, "Some Aspects of Nonstationary Airfoil Theory and Its Practical Applications," *Journal of the Aeronautical Sciences*, Vol. 8, No. 3, pp. 104–108.

Topp, D. A., and Fleeter, S., 1986, "Splitter Blades as an Aeroelastic Detuning Mechanism for Unstalled Supersonic Flutter of Turbomachine Rotors," ASME JOURNAL OF TURBOMACHINERY, Vol. 108, No. 2, pp. 244–252.

Tzuoo, L. L., Hingorani, S. S., and Sehra, A. K., 1990, "Design Methodology for Splittered Axial Compressor Rotors," ASME Paper No. 90-GT-66.

Verdon, J. M., 1987, "The Unsteady Flow in the Far Field of an Isolated Blade Row," United Technologies Research Center Report R87-957333301, Apr.

Wennerstrom, A. J., and Frost, G. R., 1974, "Design of a Rotor Incorporating Splitter Vanes for a High Pressure Ratio Supersonic Axial Compressor Stage," ARL-TR-74-0110.

Wennerstrom, A. J., Buzzell, W. A., and DeRose, R. D., 1975, "Test of a Supersonic Axial Compressor Stage Incorporating Splitter Vanes in the Rotor," ARL-75-0165, ADA014732, Aerospace Research Laboratories, WPAFB, OH, June.

S. H. Chen
Member of Technical Staff.

A. H. Eastland
Manager, Advanced Fluid Dynamics.

E. D. Jackson
Director, Design Technology.

Rocketdyne Division,
Rockwell International Corporation,
Canoga Park, CA 91303

Unsteady Aerodynamic Analysis of Subsonic Oscillating Cascade

This paper describes the development of the source-doublet-based potential paneling method for oscillating cascade unsteady aerodynamic load predictions. By using the integral influence coefficient method and by using the interblade phase angles, the unsteady loads on an oscillating cascade can be accurately predicted at a minimum cost. As the grids are placed only on the blade surfaces, the blades are allowed to vibrate without grid deformation problems. Four notable subsonic oscillating cascade test cases that cover most important parameters, e.g., blade geometry, interblade phase angle, flow coefficient, flow speed, frequency, etc., are studied in this paper. The agreement between the present solutions and other numerical/experimental results demonstrates the robustness of the present model. Applicability of the method for realistic compressible flow cascades is also discussed.

Introduction

Unsteady load predictions on modern turbomachinery blades have been given increasing attention in recent years in search of a better understanding of high cycle fatigue blade failures. The forced response due to rotor–stator interaction and the unsteady loads due to blade oscillatory motion are two major causes of vibratory stress that can result in blade cracks. To be able to predict fatigue life accurately, a reliable aerodynamic forcing function must be provided. A frequency domain source-doublet-based potential paneling method has been developed to predict the forced response in a blade-wake or rotor–stator type of interaction with cost many times less than that of finite difference schemes. The latter are based on rigid blade (non-vibrating) assumptions. The present study extends the former numerical scheme to predict the unsteady aerodynamic loads on oscillating blades.

Notable researchers studying unsteady loads on oscillating cascades are Atassi, Verdon, Carta, Hardin, Fleeter, Chiang, Huff, etc. Atassi (1980) developed a linearized analytical theory for oscillating cascades in uniform incompressible flows. Verdon and Caspar (1979, 1981), Verdon and Usab (1986, 1988), and Verdon (1990) developed a linearized theory for solving oscillating cascade unsteady loads imposed on a steady-state solution. Carta (1983) investigated the effects of interblade phase angles on the loading of an oscillating first standard cascade and showed that the interblade phase angle is the most important parameter affecting the stability of oscillating cascaded airfoils. Thus, the ability to predict the unsteady loading of an oscillating cascade with arbitrarily assigned interblade phase angle is very important. Hardin et al. (1987) studied the oscillating loads of a rotating compressor blade row at low Mach number over a wide range of flow rate. Verdon's linearized solution was used to compare the experimental data. Chiang and Fleeter (1989) studied the stability of a detuned cascade via a locally analytical incompressible solution. Buffum and Fleeter (1989) investigated the unsteady aerodynamics of a biconvex cascade at high subsonic and transonic flow by using an influence coefficient technique and a linearized theory developed by Fleeter (1973). Huff (1989) predicted oscillating cascade loading over a wide range of flow and interblade phase angle by solving Navier–Stokes/Euler equations, and by using a deforming grid technique.

In the previous potential paneling solution for blade-wake interaction analysis, the blades were assumed totally rigid with no vibratory motion. The inflow is nonuniform. In the present study, the blades are vibrating with a uniform inflow. The unsteady load is induced due to unsteady relative motion between blade and fluid. Generally, the blade motion is prescribed. The blades can oscillate at any frequency and with any arbitrary motion. However, solutions with only a single degree of freedom, pitching or plunging, will be shown to verify this methodology.

One of the greatest advantages of using the source-doublet-based integral method is the simplicity of boundary condition treatment. Since the grid is distributed only on the blade surfaces, the blade surface is allowed to deform arbitrarily without any of the difficulties encountered by typical finite difference algorithms in which the mesh must conform to the instantaneous configuration. In the present source-doublet-based integral method, the source term is determined from the nonpenetrating boundary condition. Once the relative motion between the fluid and body is defined for either nonoscillating or oscillating blade motion, the boundary condition is readily determined and thus the source term is decided. Moreover, the solution in the frequency domain avoids the time-marching calculation and greatly saves computational time.

The main purpose of the present report is to show the development of the method and demonstrate the robustness of the present methodology for unsteady aerodynamic prediction

Contributed by the International Gas Turbine Institute for publication in the JOURNAL OF TURBOMACHINERY. Manuscript received by the International Gas Turbine Institute March 1992. Associate Technical Editor: H. L. Julien.

of oscillating cascades. Four test cases with varied flow rate, interblade phase angle, frequency, flow speed, etc., are illustrated. The last of the four cases investigated is for high subsonic Mach number flow. The influence of the compressibility on the unsteady loading of an oscillating cascade is discussed.

Theory

The formulation for the oscillating cascade unsteady loads calculation is based on the author's previous works (Chen and Eastland, 1990; Chen, 1992) in which a two-dimensional frequency-domain source-doublet-based potential paneling method is used to solve incompressible flow.

The velocity potentials on the blade surfaces are expressed as distribution of sources and doublets,

$$\phi = \frac{1}{\pi}\int v_n \ln R ds - \frac{1}{\pi}\int \phi \frac{\partial}{\partial n}(\ln R) ds \tag{1}$$

This can be further written as two sets of simultaneous equations:

$$[\delta_{ij} - \overline{C}_{ij}]\{\overline{\phi}_j\} - [\overline{W}_{iw}]\{\Delta\overline{\phi}_w\} = [\overline{B}_{ij}]\{\overline{v}_{n_j}\} \tag{2}$$

$$[\delta_{ij} - \tilde{c}_{ij}]\{\tilde{\phi}_j\} - [\tilde{w}_{iw}]\{\Delta\tilde{\phi}_w\} = [\tilde{b}_{ij}]\{\tilde{v}_{n_j}\} \tag{3}$$

where

δ_{ij} = Kronecker delta function

$$\overline{C}_{ij} = \frac{-1}{\pi}\sum_l \int \frac{\partial}{\partial n}\ln R ds$$

$$\tilde{c}_{ij} = \frac{-e^{im\omega t}}{\pi}\sum_l (e^{\pm i(l-1)\sigma}) \int \frac{\partial}{\partial n}\ln R ds$$

$$\overline{W}_{iw} = \frac{-1}{\pi}\sum_l \sum_k \int \frac{\partial}{\partial n_w}\ln R ds_w$$

$$\tilde{w}_{iw} = \frac{-e^{im\omega t}}{\pi}\sum_l e^{\pm i(i-1)\sigma}\sum_k e^{-i(NT-k)\Delta\varphi}\int \frac{\partial}{\partial n_w}\ln R ds_w$$

$$\overline{B}_{ij} = \frac{1}{\pi}\sum_l \int \ln R ds$$

$$\tilde{b}_{ij} = \frac{e^{im\omega t}}{\pi}\sum_l e^{\pm i(l-1)\sigma}\int \ln R ds$$

The steady and unsteady potentials $\overline{\phi}$ and $\tilde{\phi}$ are solved separately from Eqs. (2) and (3) with a closure of Kutta condition that the wake doublet strengths, $\Delta\overline{\phi}_w$ and $\Delta\tilde{\phi}_w$, are equal to the velocity potential discontinuity at the trailing edge of the blade. The source terms on the right-hand side are determined from the blade surface nonpenetrating boundary condition.

The influence coefficient calculations include the influences from all the elements on the blades and the wakes with relative interblade phase angles between them. The interblade phase angles can be any assigned values. One advantage of using the frequency domain calculation for oscillating cascade problems is it needs only one calculation at any reference time and greatly saves the computational cost. Moreover, the boundary condition treatment is simple using the present formulation. The source terms can be precisely defined once the oscillating motion is determined.

Blade Motion. In an oscillatory blade motion, the relative velocity between blades and fluid is unsteady. The blade surface normal velocity v_n is composed of two parts, the normal velocity v_{n_o} with no vibrational motion, and the oscillating normal velocity v_n' arising from the blade vibrational motion,

$$v_n = v_{n_o} + v_n' \tag{4}$$

The vibrational part of normal velocity is the difference between the instantaneous unsteady normal velocity and mean normal velocity,

$$v_n' = -\mathbf{U}'\cdot\mathbf{n}' + \mathbf{U}\cdot\mathbf{n}$$
$$= -(U+\Delta u)\cdot n_x' - (V+\Delta v)\cdot n_y' + U\cdot n_x + V\cdot n_y \tag{5}$$

where $\mathbf{U}'$ is the instantaneous relative fluid velocity and $\mathbf{n}'$ is the instantaneous surface outward unit normal. Two types of motion, plunging and pitching, are discussed in the following. More complicated motion can be analyzed with a linear combination of the two single-degree-of-freedom harmonic motions.

Plunge Motion. Assuming the blades in plunging motion, Fig. 1(*a*), are vibrating in a simple harmonic motion with respect to their chord, with a magnitude $\overline{h}$ and frequency ω. The instantaneous amplitude is

$$h = \overline{h}e^{i(\omega t \pm l\sigma)} \tag{6}$$

where σ is the interblade phase angle and l is the blade index counted outward from the reference blade. The interblade phase angle is defined to be negative if the upper blade is lagging the lower blade. The phase angle is referenced to the airfoil at the maximum blade height. The plunging velocity is a derivative of the plunging amplitude,

$$dv = \frac{dh}{dt} = i\omega\overline{h}e^{i(\omega t \pm l\sigma)} \tag{7}$$

The velocity dv has two components, Δu and Δv in the x and y directions, respectively. Since the blade surface unit normal is unchanged through the motion, $\mathbf{n} = \mathbf{n}'$ the surface normal velocity in Eq. (5) is then

Nomenclature

$\overline{B}_{ij}$ = surface steady source influence coefficient
$\tilde{b}_{ij}$ = surface unsteady source influence coefficient
$\overline{C}_{ij}$ = surface steady doublet influence coefficient
$\tilde{c}_{ij}$ = surface unsteady doublet influence coefficient
c = blade chord
C_p = pressure coefficient
$\overline{h}$ = amplitude of plunge motion
k = reduced frequency
l = blade index
M = Mach number
$\mathbf{n}$ = surface outward unit normal
p' = pressure
P_p = pitch motion pivot point
q = inlet dynamic head
R = distance between surface point and field point
s = blade pitch
t = time
U, V = mean inlet velocity
$\Delta u, \Delta v$ = vibrational velocity
v_n = surface normal velocity
$\overline{W}_{iw}$ = wake steady doublet influence coefficient
$\tilde{w}_{iw}$ = wake unsteady doublet influence coefficient
$\overline{\alpha}$ = amplitude of pitch angle
β = phase lag (lead)
β_1 = inflow angle
θ = angle of blade rotation
σ = interblade phase angle
ϕ = velocity potential
φ = flow coefficient
ω = oscillating frequency

Subscripts

I = imaginary part
R = real part
st = steady part
un = unsteady part
upper = upper surface
lower = lower surface
w = wake

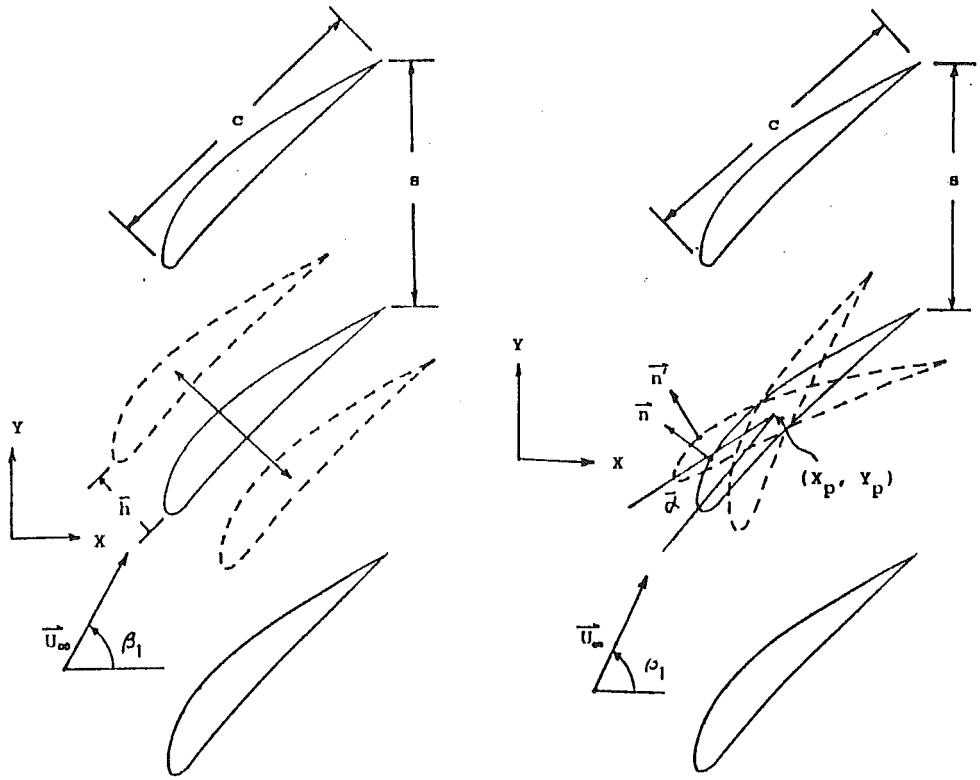

(a) (b)

Fig. 1 Blade motion: (*a*) plunging and (*b*) pitching

$$v_n' = -\Delta u \cdot n_x - \Delta v \cdot n_y \tag{8}$$

Pitch Motion. If the blades are undergoing pitching vibration about their pivot points (x_p, y_p), Fig. 1(*b*), with a magnitude $\bar{\sigma}$ and frequency ω, the instantaneous pitching angle is

$$\alpha = \bar{\alpha} e^{i(\omega t \pm l\sigma)} \tag{9}$$

The blade angle change is followed by a blade orientation change and an associated velocity variation.

The new blade coordinate $\mathbf{P}'$ resulting from the new blade angle is expressed in terms of the original coordinate $\mathbf{P}$ at the reference time, $t = 0$,

$$\mathbf{P}' = J \cdot \mathbf{P} \tag{10}$$

where

$$J = \begin{bmatrix} \cos\theta & \sin\theta \\ -\sin\theta & \cos\theta \end{bmatrix}$$

θ is the angle of rotation relative to the mean coordinate, and $-\bar{\alpha} \le \theta \le \bar{\alpha}$.

The pitching velocity at any point and any instant in time is expressed as

$$dv = ds \cdot \frac{d}{dt}\left(\bar{\alpha} e^{i(\omega t \pm l\sigma)}\right)$$

$$= ds \cdot \bar{\alpha}(i\omega) e^{i(\omega t \pm l\sigma)} \tag{11}$$

where ds is the distance between the new coordinate $\mathbf{P}'$ and the pivot point $\mathbf{P}_p$,

$$ds = |\mathbf{P}' - \mathbf{P}_p| \tag{12}$$

The surface normal velocity in Eq. (4) can now be written as

$$v_n' = -\Delta u n_x' - \Delta v n_y' + (n_x - n_x')U + (n_y - n_y')V \tag{13}$$

Influence Coefficient Matrix. The influence coefficient matrices in Eqs. (2) and (3) are calculated in the same way as the previous rigid blade calculations in which all the blade and wake element influences are included. The only difference is that in the oscillation calculation, each blade is placed at its instantaneous position, and not in the mean position. The influence coefficients for source and doublet are calculated based on the distance between the instantaneous positions. As the elements are distributed only on the blade boundaries and on their wakes, the blades are free to deform without having the grid deformation problems associated with using a finite difference scheme.

Pressure Calculation. Once the influence coefficient matrix and the source term are determined, the doublet (the velocity potential) can be calculated from Eqs. (2) and (3). The pressure is calculated from the unsteady Bernoulli equation,

$$\frac{p'}{\rho} = -\frac{\partial \phi}{\partial t} - \mathbf{U} \cdot \nabla \phi - \frac{1}{2} |\nabla \phi|^2 \tag{14}$$

The pressure difference across the blade surface, Δp, is defined as the pressure on the upper surface subtracted from that on the lower surface,

$$\Delta p = p_{\text{lower}}' - p_{\text{upper}}' \tag{15}$$

The unsteady pressure coefficient is the unsteady part of the pressure $p_{un}'(= p' - p_{st}')$ normalized by the mean inlet dynamic head q and the amplitude of vibration A,

$$C_{p_{un}} = \frac{p_{un}'}{qA} \tag{16}$$

where A could be the magnitude of plunging motion $\bar{h}$ or pitching motion $\bar{\alpha}$.

The magnitude of phase angle with respect to the motion is

$$\beta = \tan^{-1}\left(\frac{C_{p_I}}{C_{p_R}}\right)_{un} \tag{17}$$

where the phase angle $-\pi \le \beta \le \pi$. The phase angle is positive if the pressure is leading the motion, and is negative if the pressure is lagging the motion.

Result and Discussion

Four test cases of cascaded configurations with a combination of different cross section, thickness, camber, stagger angle, flow angle, flow coefficient, interblade phase angle, flow speed, etc., are calculated. They are shown in sequence in the following as (1) flat plate cascade, (2) first standard cascade, (3) UTRC rotor, and (4) NASA transonic cascade.

Test Case 1: Flat Plate. The flat plate case has been shown by many researchers (Whitehead, 1960; Smith, 1971; Fleeter, 1973; Atassi and Akai, 1980; Verdon and Caspar, 1981; Huff, 1989; etc.) as a simple case to test their algorithms. The present method is not valid when the blade thickness is zero. A thin (1 percent) parabolic airfoil is used instead. The operating condition of the flat plate case is shown in Table 1.

The plunging motion case is a flat plate cascade at 45 deg stagger, inflow angle 45 deg, amplitude of plunge $\bar{h} = 1$, out-of-phase oscillation with interblade phase angle $\sigma = 180$ deg, solidity $c/s = 1$, and circular frequency $\omega = 1$. The result is compared with that of Verdon and Caspar (1981) at Mach No. M = 0.3 in Fig. 2(*a*). The pressures across the blade surface, *dCp*, show smaller amplitudes than those of Verdon's calculation for both real and imaginary parts. This difference is believed to be due in small part to the thickness effect, and mostly due to the Mach number effect for this particular case as shown by the trend of the higher Mach number calculations by Verdon.

The result for a pitching motion with an amplitude of $\bar{\alpha} = 1$ deg of the same configuration, pivoted at midblade chord, is shown in Fig. 2(*b*). Again, the trends for the two predictions are similar and the discrepancy is attributed to the Mach number effect.

Test Case 2: First Standard Cascade. The first standard cascade is a NACA65-series cascade with low subsonic inflow. These experimental data were obtained by Carta (1983) and have been used by many researchers for their code validation.

The cascade operating condition is listed in Table 2. The cascade configuration has a NACA65-series airfoil with a 6 percent thickness distribution on a 10 deg circular-arc camber line. It has a 55 deg stagger angle, incidence 6 deg, solidity $c/s = 1.33$, inlet Mach number M = 0.17, reduced frequency $k = 1.22$ based on semichord length, and an amplitude of vibration $\bar{\alpha} = 2$ deg. There has been some uncertainty concerning the inlet flow angle as pointed out by Verdon (1986) and Huff (1989). Verdon and Usab found that an inflow angle of $\beta_1 = 62.23$ deg gave the best agreement with the experimental mean flow pressure distributions using the potential solution; while Huff found $\beta_1 = 64.0$ deg gave the best com-

Table 1 Test case 1: flat plate

Stator (*Flat Plate*)	
Stagger	45 deg
Inflow	45 deg
σ	180 deg
M_1	0.3
Motion	plunge or pitch
Plunge h	1
Pitch α	1 deg
ω	1.0

Table 2 Test case 2: first standard cascade

Stator (*NACA65-series*)	
Stagger	55 deg
β_1	66 deg
σ	$-135 \sim +180$ deg
M_1	0.17
Motion	pitch
$\bar{\alpha}$	0.5 ~ 2 deg
k	0.122 (based on semichord)

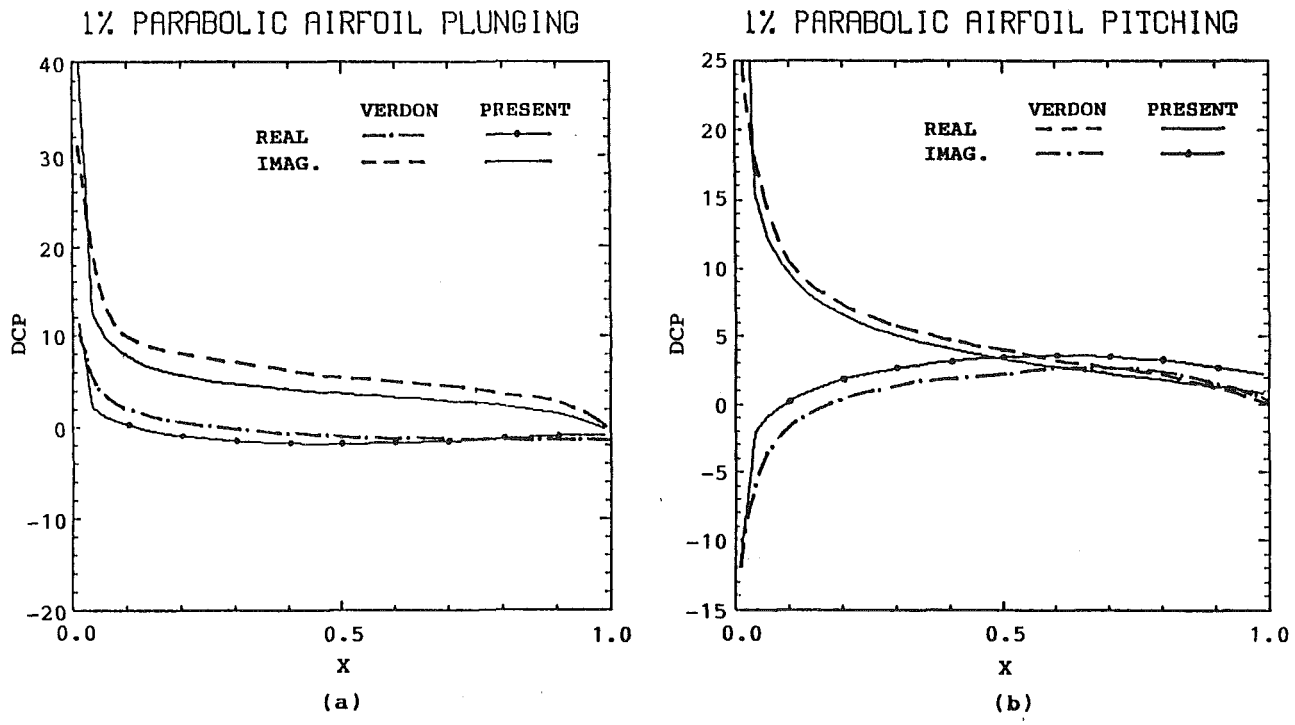

Fig. 2 1 percent parabolic airfoil cascade unsteady pressure: (*a*) plunging motion, (*b*) pitching motion

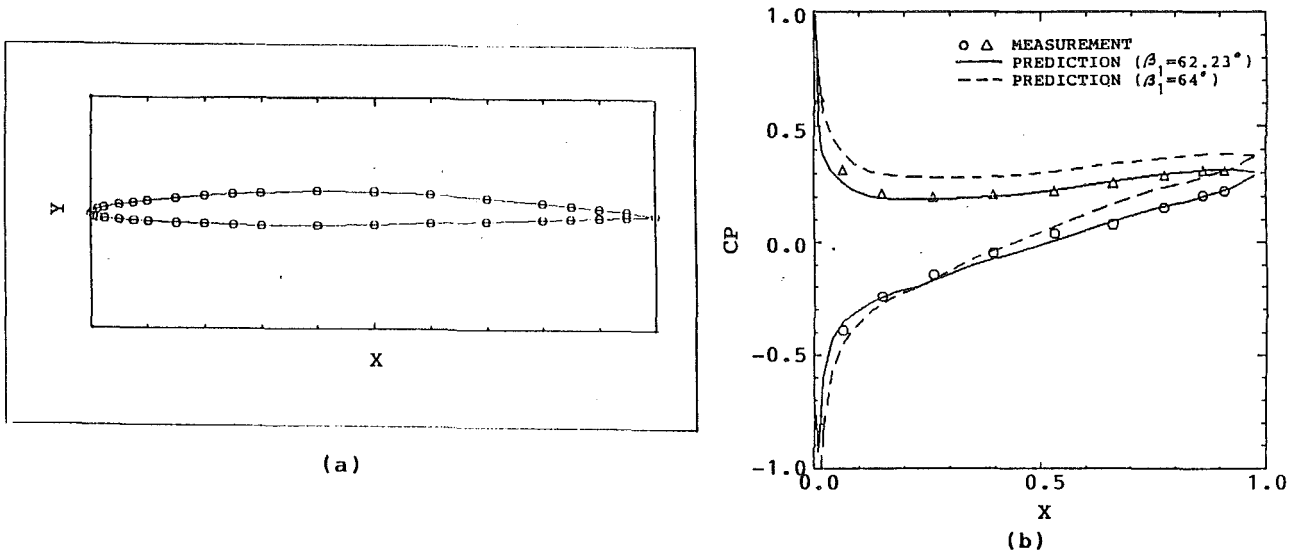

Fig. 3 First standard cascade: (*a*) profile; (*b*) steady loading

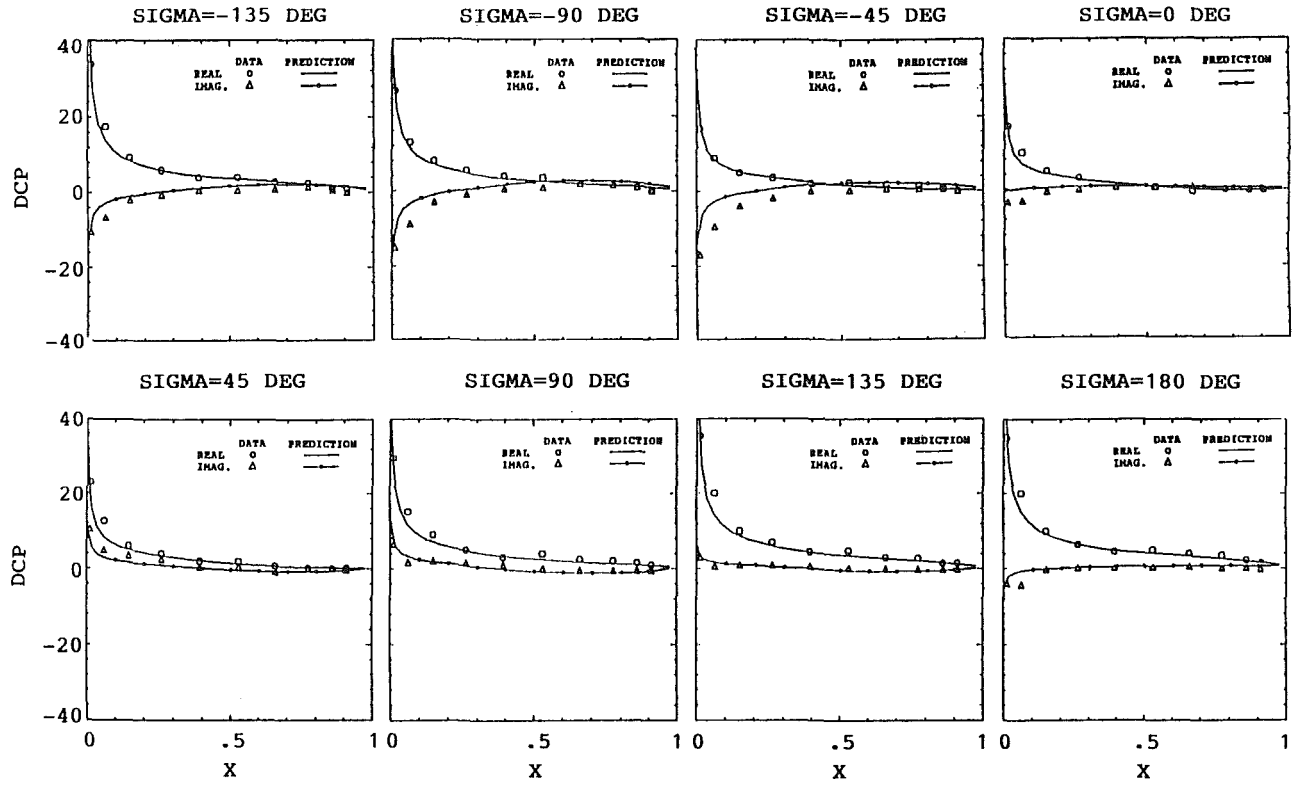

Fig. 4 First standard cascade unsteady loading in pitching motion

parison with the experimental data from his Navier–Stokes solution. The present steady-state solutions for both $\beta_1 = 62.23$ and 64.0 deg are shown in Fig. 3. The $\beta_1 = 62.23$ deg solution gives better agreement with the data and is consistent with that of Carta's steady-state solution. Thus, the following calculations for the first standard cascade geometry are based on the inflow angle of 62.23 deg.

The first standard cascade is used to test the dependency of unsteady load on interblade phase angle. The results are compared with those experimental data obtained by Carta (1983) and the linearized solution by Verdon and Usab (1986). Figure 4 shows the unsteady pressure along the blade surface for eight different interblade phase angles from -135 deg to $+180$ deg at a 45-deg interval. The present calculation agrees excellently with the experimental data for both real and imaginary parts over the entire interblade phase angle range. The suction and pressure surface unsteady pressure amplitudes and phase angles shown in Figs. 5(*a*) and 5(*b*), respectively, for $\sigma = -135$ deg are compared with the calculations by Verdon and Usab (1986). The amplitude of unsteady pressure agrees very well with both the measured data and the solutions from Verdon and Usab. The phase angle of the unsteady pressure agrees better with the data than does Verdon and Usab's on the suction side, but worse than theirs on the pressure side toward the trailing edge.

Test Case 3: UTRC Compressor Rotor. This compressor

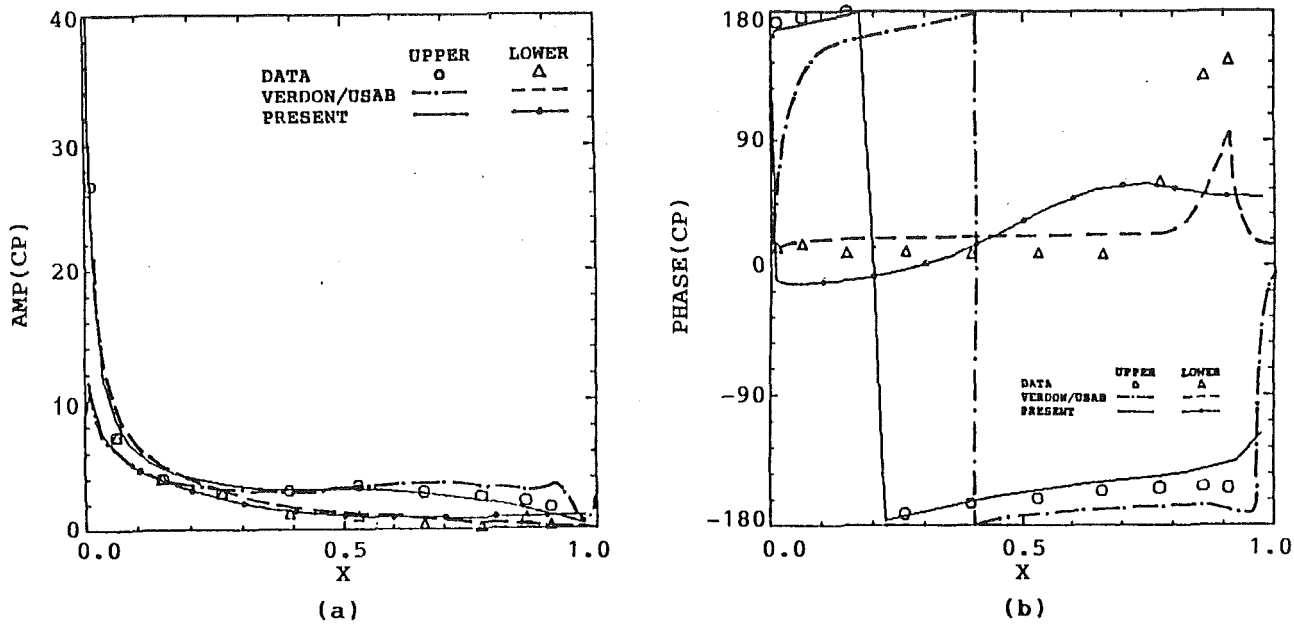

Fig. 5 First standard unsteady pressure (σ = −135 deg): (*a*) amplitude; (*b*) phase angle

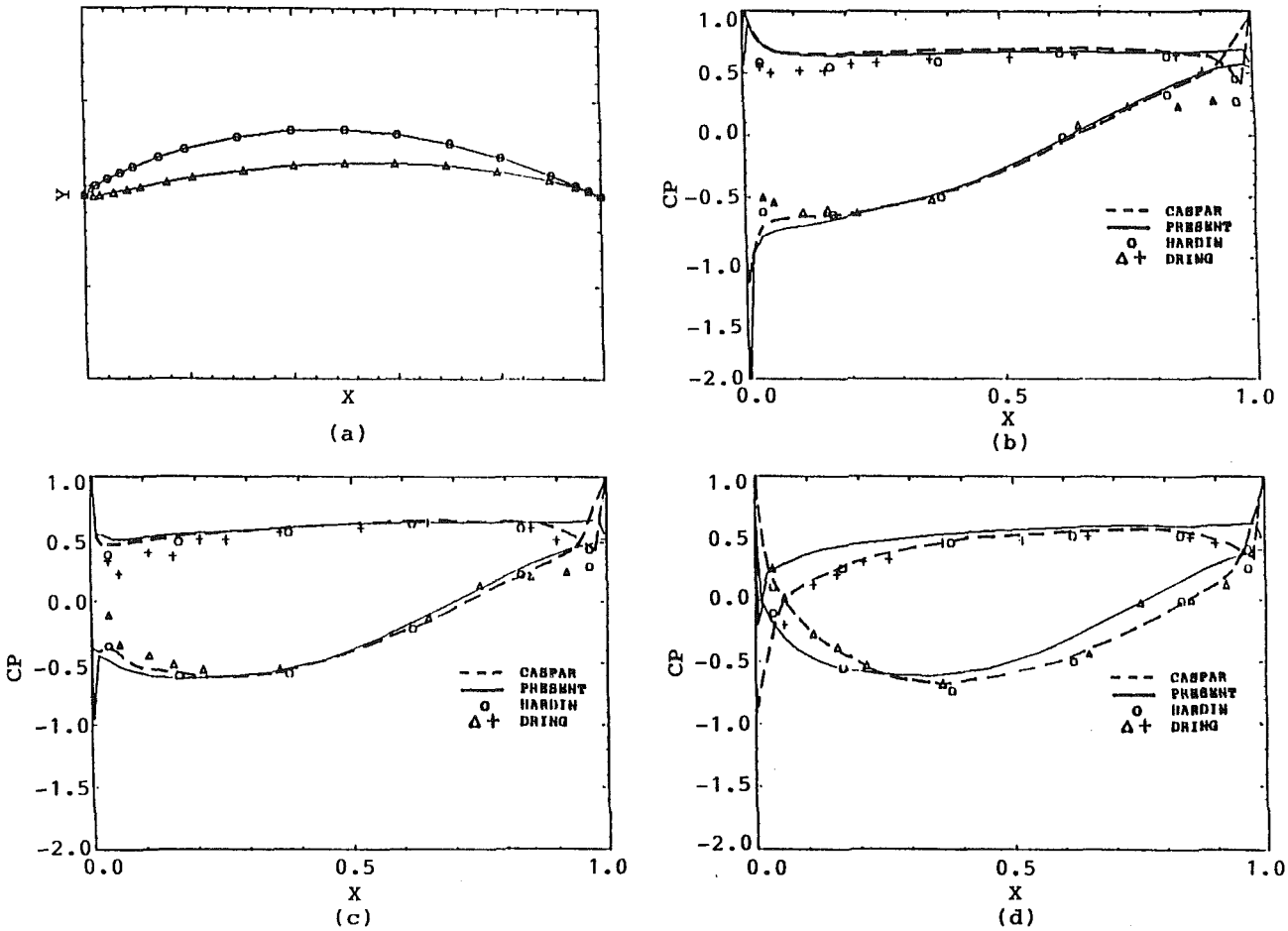

Fig. 6 UTRC rotor steady loading: (*a*) profile; (*b*) φ = 0.65; (*c*) φ = 0.75; (*d*) φ = 0.85

rotor case was experimentally studied by Hardin et al. (1987) at United Technologies Research Center (UTRC). This case is different from the other test cases in that this one is a rotor and the others are linear cascades. The operating condition of this case is shown in Table 3. The airfoil is a NACA65-series thickness distribution superimposed on a nominal circular arc

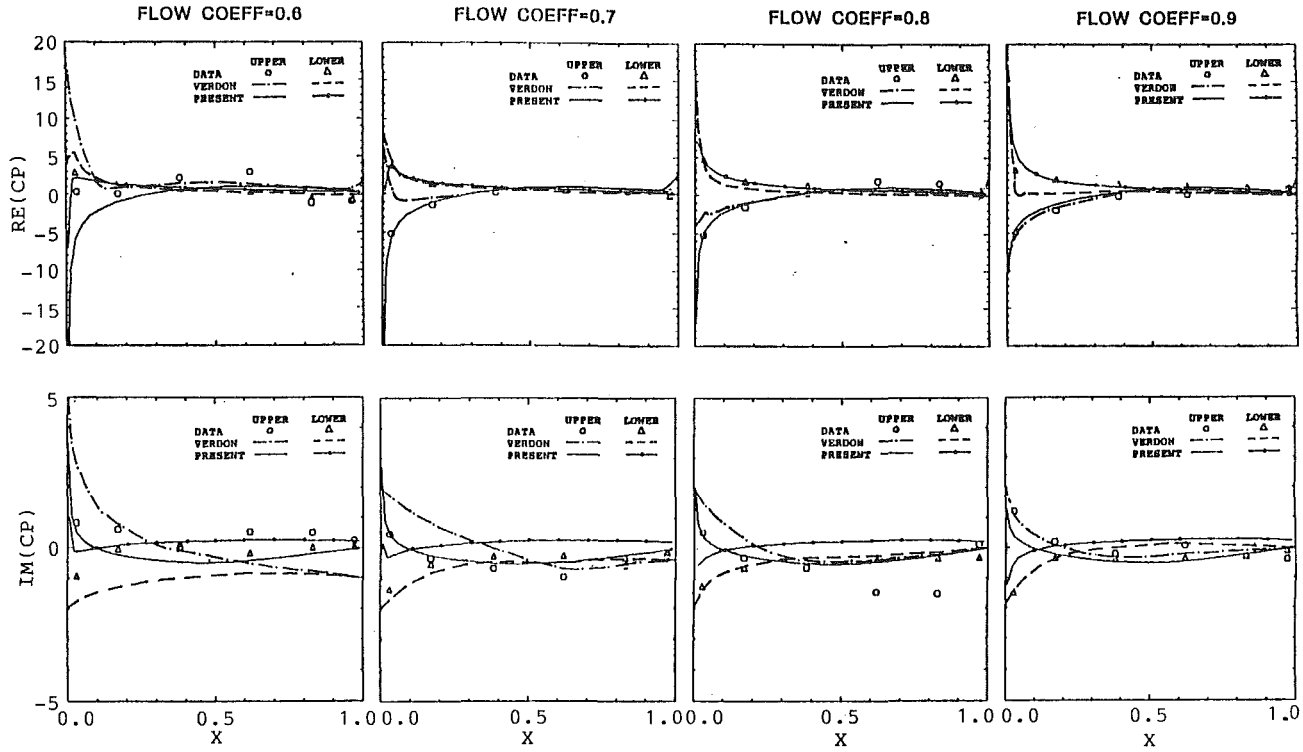

Fig. 7 UTRC rotor unsteady pressure in pitching motion

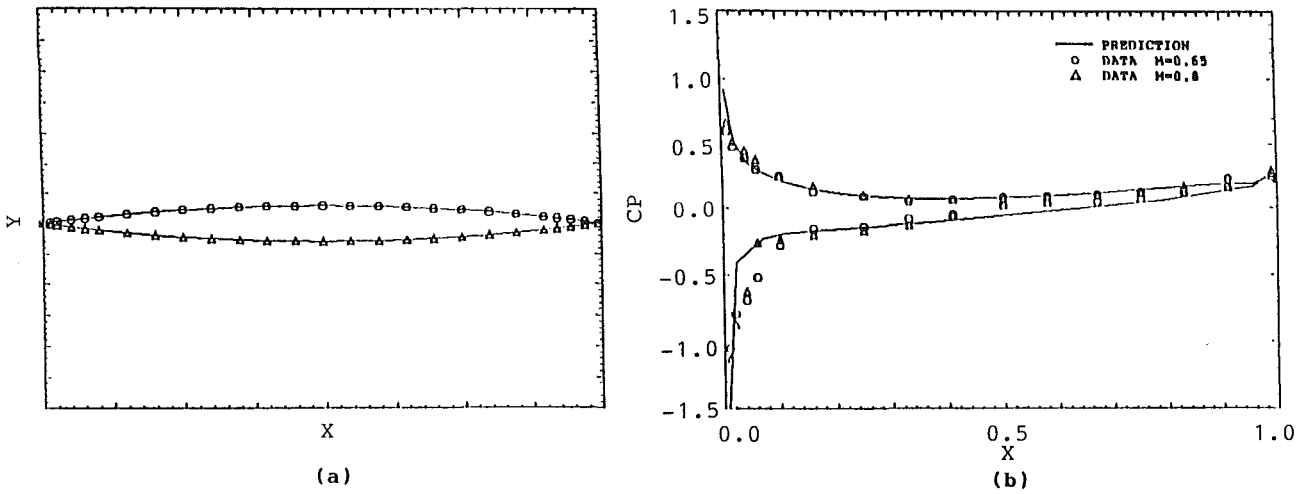

Fig. 8 NASA Lewis binconvex cascade (*a*) profile; (*b*) steady loading

Table 3 Test case 3: UTRC rotor

Rotor (*NACA65-series*)		
	Stagger	35.47 deg
	Flow coefficient φ	0.6 ~ 0.9
	σ	−12.9 deg
	M_1	0.127 ~ 0.147
	Motion	pitch
	$\bar{\alpha}$	2 deg
	Ω	510 rpm
	k	53.4 rad

Table 4 Test case 4: NASA Lewis cascade

Stator (*biconvex*)		
	Stagger	53 deg
	β_1	60 deg
	σ	−90, 0, +90 deg
	M_1	0.65
	Motion	pitch
	$\bar{\alpha}$	1.2 deg
	k	0.221 (based on semichord)
	Solidity c/s	1.3

mean camber line, Fig. 6(*a*). The rotor is 5 ft in diameter, with a hub-to-tip ratio of 0.8, and 28 blades. The dynamic loading at midspan was investigated. At midspan, the stagger angle is 35.47 deg, the interblade phase angle σ is −12.9 deg, and the motion is pitching at midchord with an amplitude of 2 deg at frequency 8.5 Hz. The rotating speed of the rotor is maintained at 510 rpm while varying the flow rate to make the flow coefficient φ vary from 0.6 to 0.9 in 0.1 intervals. This yields a Mach number M = 0.127 ~ 0.147.

The steady-state solutions for flow coefficient 0.65, 0.75,

and 0.85 are shown in Figs. 6(*b*) to 6(*d*) and compared with results shown in the paper of Hardin et al. (1987). The three steady-state pressure distributions agree excellently with Caspar's potential solutions except near the trailing edge. Both inviscid calculations predicted larger leading edge loading than the experimental data. The viscous effects near the leading edge essentially remove the singularity behavior inherent in potential flow approaches in that area. Moreover, both calculations show higher discharge pressures than the data. Again, this is due to the negligence of the viscosity effect, in that the boundary layer produces a higher discharge velocity and lower discharge pressure. Despite the deficiency frequently encountered in using inviscid calculations, it has been shown (Hodson, 1985; Hardin et al., 1987; Verdon and Usab, 1986; etc.) that the viscous boundary layer has little effect on the unsteady pressure calculations unless the boundary layer is thick or separated.

The unsteady pressures for real and imaginary parts are shown in Fig. 7 for flow coefficients ranging from 0.60 to 0.90 in 0.1 intervals. The imaginary part scales are four times larger than the real part to highlight the difference between the present solution and that of Verdon. The present calculation shows excellent agreement with all the experimental data on both suction and pressure surfaces for all the flow range, except near the leading edge on the suction side for flow coefficient equals 0.6. The discrepancy is attributed to a separation bubble formed near the leading edge on the suction surface at this large incidence operating condition. In comparing to Verdon's prediction, the present method essentially correlates better with the data over the entire flow range in this particular case for both the real and imaginary parts.

Test Case 4: NASA Lewis Transonic Cascade. The last test case is the NASA Lewis Transonic Oscillating Cascade. The operating condition is shown in Table 4. The geometry of the airfoil is a symmetric biconvex airfoil with a thickness of 7.6 percent, Fig. 8(*a*), stagger 53 deg, incidence 7 deg, solidity $c/s = 1.3$. The blade is pitching about the midchord with an amplitude of 1.2 deg, and a reduced frequency $k = 0.221$ based on semichord. The measurements were made at high inlet flow Mach numbers 0.65 (subsonic) and 0.8 (transonic) (Shaw et al., 1986; Buffum et al., 1987). Although the present method is developed for incompressible flow, its applicability and the deviation from the measured compressible flow were investigated. The measurement for the subsonic case with M = 0.65 is used here to test the present unsteady calculations. Similar studies have been made by Huff (1989) and Buffum and Fleeter (1989). Their solutions will also be shown in the figures for comparison.

The steady-state calculations for 7 deg incidence angle are shown in Fig. 8(*b*). The pressure distributions are nearly identical for these two Mach numbers, 0.65 and 0.8, except there is a shock formed near the leading edge on the suction surface for M = 0.8. A surprisingly good agreement is achieved between the incompressible flow calculation and the compressible flow measurement. Because the stagger angle is large and the solidity is high, the blade-to-blade interaction is more significant than the streamwise compressibility effect.

The three unsteady operating conditions in this study include out-of-phase oscillations ($\sigma = -90$ deg and $+90$ deg) shown in Figs. 9 and 10, respectively, and in-phase oscillation ($\sigma =$ 0 deg) shown in Fig. 11. For each figure, comparisons are shown for pressure distribution on each surface, pressures across blade surface, amplitude of pressures, and phase angles of pressures.

For the $\sigma = -90$ deg case, Figs. 9(*a*) to 9(*d*), the real part, imaginary part, and amplitude of unsteady loads agree well with the measurement, though the imaginary part on the pressure side predicts higher values than the data. The phase angle deviates more from the measured data on the suction side due to the pressure curve shift. The Navier–Stokes compressible solution (Huff, 1989) seems to predict better imaginary and phase angles in this part. For the pressure across the blade (lower–upper), Figs. 9(*e*) to 9(*h*), the agreement is excellent with the data though deviation is found on the imaginary part. The other two prediction from Huff's N–S solution (1989) and the Buffum and Fleeter classical linearized unsteady theory (1989) together with the present calculation agree quantitatively well with the data in this pressure difference part. The present calculation predicts the magnitude of the unsteady blade loading better than the two compressible methods but does worse in the phase angle.

The case for $\sigma = +90$ deg shown in Fig. 10 has similar characteristics to that of the $\sigma = -90$ deg calculation.

The reason that the incompressible flow method predicts good Δp at a high subsonic flow condition is due to the fact that the unsteady pressure fluctuations for an oscillating cascade are more influenced by the blade-to-blade interaction than by the streamwise compressibility effect. The compressibility influence has a similar effect on both suction and pressure surfaces, and thus the pressure difference across the surface is not significantly affected by the compressibility effect. As a result the present incompressible method does give a reliable solution. Compressibility effects should become less significant for higher solidity cascades.

For the in-phase oscillation ($\sigma = 0$ deg) calculation, Fig. 11, the present method correlated better with the experimental data than for the out of phase calculations. However, there is a significant discrepancy from the N–S solution for the real, imaginary, and thus the phase angles obtained by Huff (1989). He attributes this disagreement to the operating near an acoustic resonant condition. However, it does not seem to affect the Buffum and Fleeter solution (1989) nor the present calculation.

Overall, the present incompressible flow method seems to give quantitatively and qualitatively good solutions for high Mach number subsonic cascaded flow in both steady and unsteady calculations. This should be true particularly when the solidity is high, but should fail in the transonic and supersonic regimes based on the present formulation.

Computational Cost

The computational cost is very low for the present frequency domain calculation. Taking the first standard cascade as an example, using 40 grids (upper + lower), and 50 wake elements for each blade, the CPU time on a APOLLO DN4000 work station is 140 seconds. This is equivalent to about 1.4 seconds of CRAY time. Similar calculations by using a Navier–Stokes time-marching scheme as shown by Huff (1989) use about 13,100 seconds on a CRAY-XMP. Relatively, the present method is nearly 10,000 times faster than the Navier–Stokes solution but with a similar quality of results.

Summary

The frequency domain unsteady aerodynamic solution described in this report has been developed to determine the unsteady loads arising from the relative motion of blades in two-dimensional cascades in subsonic flow. Complex turbomachinery problems including real blade geometry, operating condition, stagger angle, incidence angle, interblade phase angle, etc., are accounted for.

Four notable cascade configurations under oscillating motions were investigated to predict the unsteady loads. The calculated results are compared as much as possible with available experimental data and other numerical/analytical methods shown in the literature.

Generally very good agreement was achieved for real, imaginary, amplitude of individual surface pressures and pressure

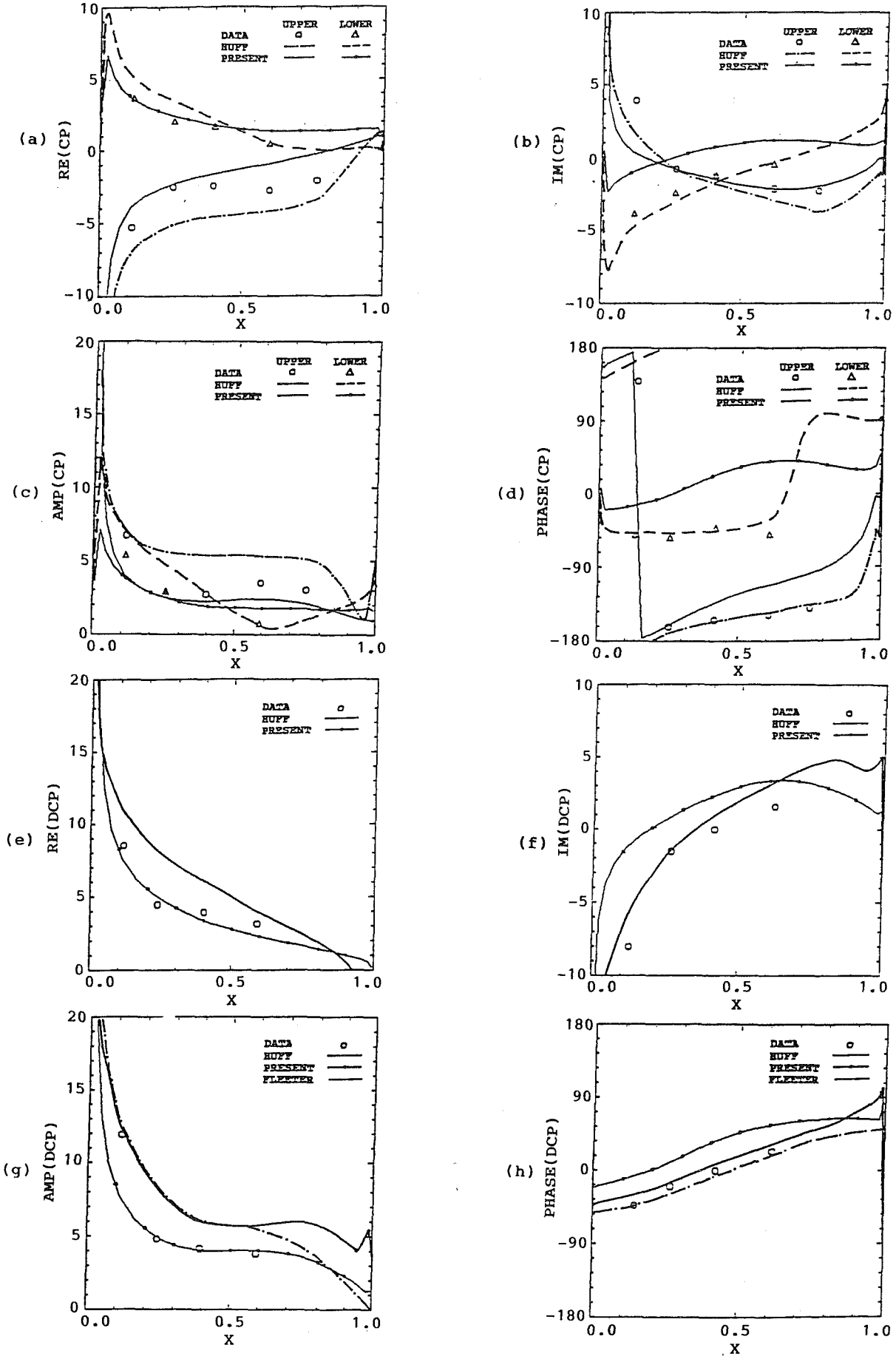

Fig. 9 NASA Lewis cascade unsteady pressure ($\sigma = -90$ deg)

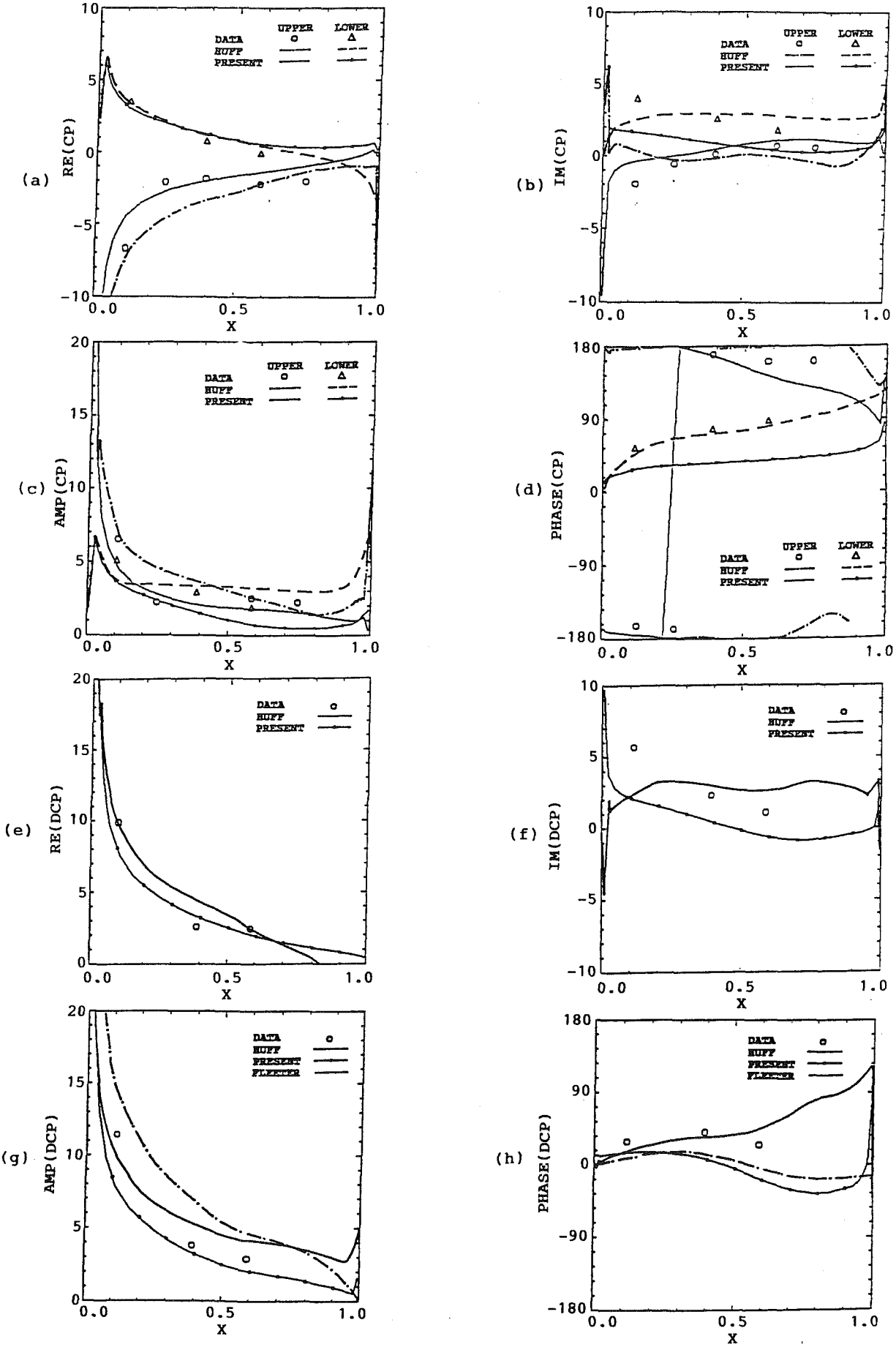

Fig. 10 NASA Lewis cascade unsteady pressure (σ = +90 deg)

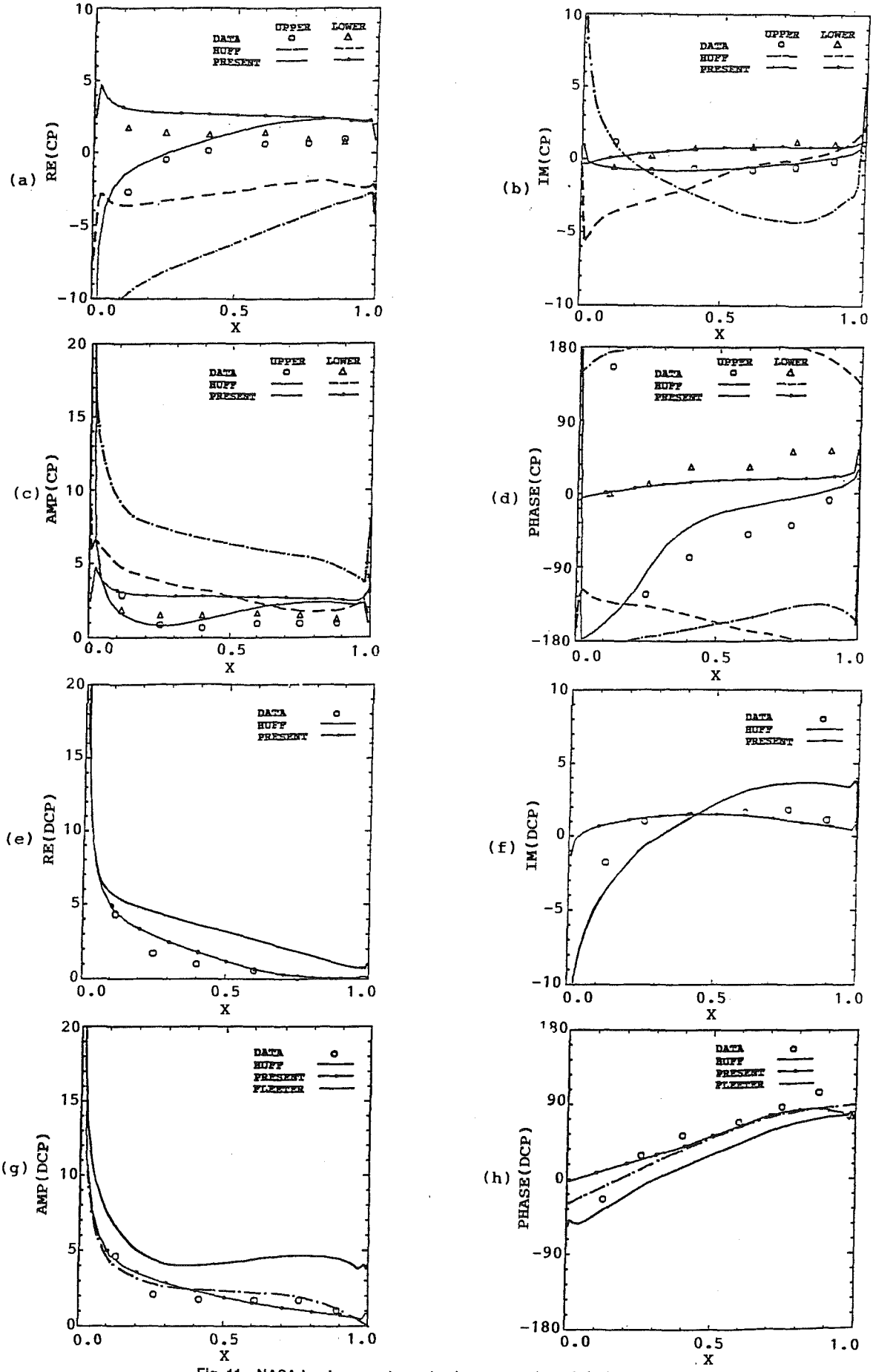

Fig. 11 NASA Lewis cascade unsteady pressure (σ = 0 deg)

difference across the blades when comparing to the experimental data and other numerical methods. In many cases, the present method predicts significantly better than other methods. This is attributed to two factors:

1 The present method is numerically reliable.

2 The boundary condition treatment is simple and can be precisely defined once the oscillating motion is determined. As the grid is distributed only on the blade boundary, the blade can be arbitrarily deformed without any of the grid deformation problems encountered when using finite difference schemes.

The computational cost is small and is about 10,000 times faster than a Navier–Stokes solution with the same quality of solution.

Future development of the present method will be aimed at the force and moment calculation from the predicted unsteady pressures. Flutter boundary and the aerodynamic damping factor associated with the forces will then be compared with the data available.

References

Atassi, H., and Akai, T. J., 1980, "Aerodynamic and Aeroelastic Characteristics of Oscillating Loaded Cascades at Low Mach Number, Parts 1 and 2," ASME *Journal of Engineering for Power*, Vol. 102, pp. 344–356.

Buffum, D. H., Boldman, D. R., and Fleeter, S., 1987, "The Unsteady Aerodynamics of an Oscillating Cascade in a Compressible Flow Field," NASA TM-100219.

Buffum, D. H., and Fleeter, S., 1989, "Experimental Investigation of Transonic Oscillating Cascade Aerodynamics," AIAA Paper No. 89-0321.

Carta, F. O., 1983, "Unsteady Aerodynamics and Gapwise Periodicity of Oscillating Cascaded Airfoils," ASME *Journal of Engineering for Power*, Vol. 105, pp. 565–574.

Chen, S. H., and Eastland, A. H., 1990, "Forced Response on Turbomachinery Blades Due to Passing Wakes," AIAA Paper No. 90-2353.

Chen, S. H., 1992, "Turbomachinery Unsteady Load Predictions With Nonuniform Inflow," *Journal of Propulsion and Power*, Vol. 8, No. 3.

Chiang, H., and Fleeter, S., 1989, "Oscillating Aerodynamics and Flutter of an Aerodynamically Detuned Cascade in an Incompressible Flow," AIAA Paper No. 89-0289.

Fleeter, S., 1973, "Fluctuating Lift and Moment Coefficients for Cascaded Airfoils in a Nonuniform Compressible Flow," *Journal of Aircraft*, Vol. 10, Feb., pp. 93–98.

Hall, K. C., and Crawley, E. F., 1988, "Calculation of Unsteady Flows in Turbomachinery Using the Linearized Euler Equations," *Unsteady Aerodynamics and Aeroelasticity of Turbomachines and Propellers*, Aachen Institute of Technology, Aachen, W. Germany.

Hardin, L. W., Carta, F. O., and Verdon, J. M., 1987, "Unsteady Aerodynamic Measurements on a Rotating Compressor Blade Row at Low Mach Number," ASME JOURNAL OF TURBOMACHINERY, Vol. 109, pp. 499–507.

Hodson, H. P., 1985, "An Inviscid Blade-to-Blade Prediction of a Wake-Generated Unsteady Flow," ASME *Journal of Engineering for Gas Turbines and Power*, Vol. 107, pp. 337–344.

Huff, D. L., 1989, "Numerical Analysis of Flow Through Oscillating Cascade Sections," AIAA Paper No. 89-0437.

Shaw, L. M., Boldman, D. R., Buggele, A. E., and Buffum, D. H., 1986, "Unsteady Pressure Measurements on a Biconvex Airfoil in a Transonic Oscillating Cascade," ASME *Journal of Engineering for Gas Turbines and Power*, Vol. 108, pp. 53–59.

Smith, S. N., 1971, "Discrete Frequency Sound Generation in Axial Flow Turbomachines," British Aeronautical Research Council RM 3709, London.

Verdon, J. M., and Caspar, J. R., 1979, "Subsonic Flow Past an Oscillating Cascade With Finite Mean Flow Deflection," *AIAA Journal*, Vol. 18, No. 5, pp. 540–548.

Verdon, J. M., and Caspar, J. R., 1981, "Development of an Unsteady Aerodynamic Analysis for Finite-Deflection Subsonic Cascades," NASA CR-3455.

Verdon, J. M., and Usab, W. J., Jr., 1986, "Application of a Linearized Unsteady Aerodynamic Analysis to Standard Cascade Configurations," NASA CR-3940.

Verdon, J. M., and Usab, W. J., Jr., 1988, "Advances in the Numerical Analysis of Linearized Unsteady Cascade Flows," AFWAL-TR-88-2055.

Verdon, J. M., 1990, "Linearized Unsteady Aerodynamics for Turbomachinery Aeroelastic Applications," AIAA Paper No. 90-2355.

Whitehead, D. S., 1960, "Force and Moment Coefficients for Vibrating Aerofoils in Cascade," British Aeronautical Research Council RM 3254, London, Feb.

Effect of Wind Tunnel Acoustic Modes on Linear Oscillating Cascade Aerodynamics

D. H. Buffum
NASA Lewis Research Center,
Cleveland, OH 44135

S. Fleeter
Thermal Sciences and Propulsion Center,
School of Mechanical Engineering,
Purdue University,
West Lafayette, IN 47907

The aerodynamics of a biconvex airfoil cascade oscillating in torsion is investigated using the unsteady aerodynamic influence coefficient technique. For subsonic flow and reduced frequencies as large as 0.9, airfoil surface unsteady pressures resulting from oscillation of one of the airfoils are measured using flush-mounted high-frequency-response pressure transducers. The influence coefficient data are examined in detail and then used to predict the unsteady aerodynamics of a cascade oscillating at various interblade phase angles. These results are correlated with experimental data obtained in the traveling-wave mode of oscillation and linearized analysis predictions. It is found that the unsteady pressure disturbances created by an oscillating airfoil excite wind tunnel acoustic modes, which have detrimental effects on the experimental results. Acoustic treatment is proposed to rectify this problem.

Introduction

Aerodynamically induced vibration of the blading in gas turbine engines is an ongoing problem, which affects both the development cost of new engines and the reliability and maintenance costs of existing engines. Accurate analysis tools could reduce these costs significantly, hence the development of advanced aerodynamic analyses for oscillating cascaded airfoils is of current research interest. Oscillating cascade experiments play a key role in the development of these analyses, providing data used both to evaluate existing analyses and to provide direction for advanced modeling efforts.

A review of previous oscillating cascade investigations reveals there are, in general, few data available for cascaded airfoils driven to oscillate simultaneously. Focusing on subsonic and transonic flows for axial compressor geometries, there are several noteworthy publications. Davies and Whitehead (1984) performed experiments in an annular oscillating cascade in subsonic through supersonic flow regimes, but the measurements were limited to unsteady aerodynamic moments. Kobayashi (1990) has made detailed blade surface pressure measurements in an annular oscillating cascade at high subsonic and supersonic inlet conditions. Large pressure fluctuations occurred due to shock wave motion and cascade instability was noted over a wide range of conditions. Unsteady pressure measurements have been made at the NASA Lewis Research Center in a linear cascade oscillating in a traveling-wave mode (Buffum and Fleeter, 1993a). In some instances, it was found that unsteady pressure disturbances reflected by the wind tunnel walls interfered with the cascade unsteady aerodynamics.

The lack of oscillating cascade data is due to the inherent complexity of the experiments. First, oscillating cascades are expensive to build, traditionally requiring a drive system capable of oscillating the airfoils simultaneously in traveling-wave modes for various interblade phase angles at realistic values of the reduced frequency. Second, because the measurements must be obtained not only for each steady flow condition and reduced frequency, but also over a range of interblade phase angles, the experiments can be quite time consuming. As a result, data are typically obtained only for several interblade phase angles.

An alternative to the traveling-wave mode of oscillation is the unsteady aerodynamic influence coefficient technique. Assuming the unsteady disturbances are small, as in a typical flutter stability problem, only one airfoil in the cascade is oscillated, with the resulting unsteady pressures measured on the oscillating airfoil and its stationary neighbor. Through summation of these influence coefficient data, the unsteady aerodynamics of an equivalent cascade with all airfoils oscillating at any specified interblade phase angle may be predicted.

Figure 1 depicts a two-dimensional finite cascade representation of a blade row. For a given mean flow field and reduced frequency of oscillation, and assuming small unsteady disturbances, the cascade unsteady aerodynamics may be expressed as linearly combined influence coefficients that can be determined experimentally or analytically. Consider a finite airfoil cascade with $2N+1$ airfoils executing constant-amplitude harmonic oscillations with a constant interblade phase angle β. The airfoil surface unsteady pressure, expressed as a pressure coefficient $C_p(x, y, \beta)$ acting at a point on the reference airfoil (airfoil 0 in Fig. 1), can be expressed as a Fourier series

$$C_p(x, y, \beta) = \sum_{n=-N}^{N} \hat{C}_p^n(x, y) e^{in\beta} \quad (1)$$

Contributed by the International Gas Turbine Institute and presented at the 38th International Gas Turbine and Aeroengine Congress and Exposition, Cincinnati, Ohio, May 24–27, 1993. Manuscript received at ASME Headquarters March 1, 1993. Paper No. 93-GT-149. Associate Technical Editor: H. Lukas.

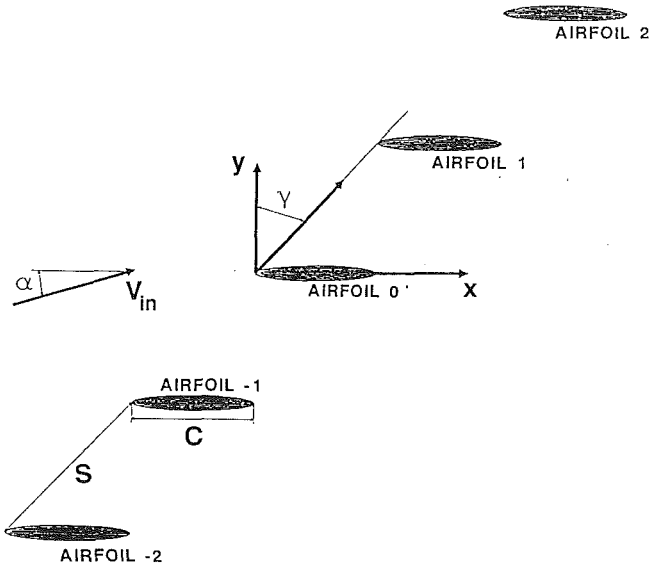

Fig. 1 Cascade geometry

where $\hat{C}_p^n(x, y)$ is the complex-valued unsteady aerodynamic influence coefficient. This influence coefficient defines the unsteady pressure coefficient developed on the reference airfoil at the point (x, y) due to the motion of airfoil n.

Mathematical models for an infinite cascade of airfoils oscillating with a specified interblade phase angle can also be used to determine these unsteady aerodynamic influence coefficients. For this case, the influence coefficients are determined by inversion of Eq. (1):

$$\hat{C}_p^n(x, y) = \frac{1}{2\pi} \int_{-\pi}^{\pi} C_p(x, y, \beta) e^{-in\beta} d\beta. \quad (2)$$

Analytically determined unsteady aerodynamic influence coefficients can thus be found from oscillating cascade analyses by integrating predicted values of C_p over the complete interblade phase angle interval per Eq. (2). Substituting these influence coefficients into Eq. (1) then enables analytical predictions for a finite number of airfoils oscillating in an infinite cascade to be determined.

If this technique is valid, the most important advantage is that the drive system must oscillate only one airfoil, reducing the complexity and cost of the experimental facility. In addition, as already mentioned, the influence coefficients may be used to predict the cascade unsteady aerodynamics for any interblade phase angle, although these predictions are theoretically suspect in the vicinity of acoustic resonances (Buffum and Fleeter, 1990a). An added advantage is the physical insight gained by knowing the values of the various influence coefficients and therefore the impact that the oscillations of airfoil n will have on the stability of the reference airfoil.

Several experimental investigations have been directed at validation of this technique through correlation of unsteady aerodynamic influence coefficient results with corresponding data acquired with all airfoils oscillating at specified interblade phase angles. Hanamura et al. (1980) found good results for flow in a water channel, but this is insufficient to validate the technique for compressible flow. Davies and Whitehead (1984) performed such experiments at high subsonic inlet conditions and reduced frequencies to 0.21, but there was considerable scatter in the traveling-wave mode data. In supersonic inflow experiments, Szechenyi (1985), the summation of influence coefficients has been compared to data for a linear cascade with two airfoils oscillating, but the scope of the experiments was very limited. Bölcs et al. (1989) reported very good results for this technique in an annular turbine cascade with mean exit flow fields ranging from subsonic to supersonic and reduced frequencies as large as 0.42. Buffum and Fleeter (1990a) reported good results using this method, but further analysis now indicates that wind tunnel acoustic modes similar to those discussed in this paper had detrimental effects on the data.

Of the investigations mentioned above, only that of Bölcs et al. was conclusive regarding the influence coefficient technique. However, as those experiments were conducted in an annular cascade, it would be rash to conclude that this technique is also valid for use in a linear cascade. While circumferential pressure disturbances are free to propagate around the annulus of an annular cascade, disturbances will be constrained by the wind tunnel walls in a linear cascade, possibly resulting in detrimental effects on the cascade unsteady aerodynamics. In fact, in traveling-wave mode experiments, Buffum and Fleeter (1993a) found that reflection of unsteady pressure disturbances off the wind tunnel walls interfered with the linear cascade unsteady aerodynamics for some interblade phase angles. Thus it is important to investigate thoroughly the validity of this technique in a linear environment.

In the present study, the unsteady aerodynamic influence coefficient technique is investigated in a low-solidity linear oscillating cascade. The cascade solidity, 0.65, was chosen to be representative of an advanced propeller model, which fluttered during wind tunnel tests (Mehmed et al., 1982). For an inlet Mach number of 0.55, the torsion mode biconvex airfoil oscillating cascade aerodynamics are investigated for reduced frequencies as high as 0.90. To help ascertain the validity of the influence coefficient technique, correlation of the influence coefficient results is made with data obtained for all the airfoils oscillating at various interblade phase angles and the predictions of a linearized oscillating cascade analysis.

Oscillating Cascade Facility

The NASA Lewis Transonic Oscillating Cascade, Fig. 2, combines a linear cascade wind tunnel capable of inlet flow approaching Mach one with a high-speed airfoil drive system, which imparts torsion-mode oscillations to the cascaded airfoils at specified interblade phase angles and realistically high reduced-frequency values.

Nomenclature

C = airfoil chord
C_p = unsteady pressure coefficient $= p_1/(\rho_{in} V_{in}^2 \alpha_1)$
$\hat{C}_p^n$ = unsteady pressure influence coefficient due to oscillation of nth airfoil
$\overline{C}_p$ = steady pressure coefficient $= (p_{in} - p_0)/(\rho_{in} V_{in}^2)$
k = reduced frequency $= \omega C/V_{in}$
M = Mach number
n = relative position of oscillating airfoil
p_j = jth harmonic of airfoil surface static pressure
p_{in} = mean inlet static pressure
S = airfoil spacing
t = time
V_{in} = inlet velocity magnitude
x = airfoil chordwise coordinate
α_j = jth harmonic of incidence angle
β = interblade phase angle
γ = stagger angle
ΔC_p = unsteady pressure difference coefficient
ρ_{in} = inlet density
ϕ = phase of unsteady pressure coefficient
ω = airfoil oscillation frequency, rad/s

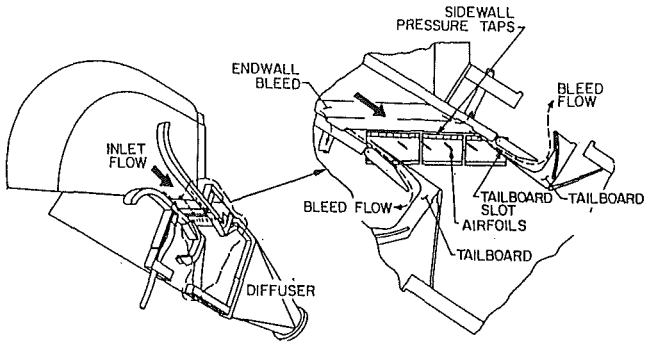

Fig. 2 Oscillating cascade facility

Air drawn from the atmosphere passes through a smooth contraction inlet section into a constant area rectangular test section of 9.78 cm span, which measures 58.6 cm along the stagger line. Upstream of the test section, suction is applied through perforated walls to reduce the boundary layer thickness. Tailboards are used to adjust the cascade exit region static pressure and also form bleed scoops that further reduce upper and lower wall boundary layer effects. Downstream of the test section, the air is expanded through a diffuser into an exhaust header. The exhaust system, part of a central air facility at Lewis, maintains a 30 kPa pressure downstream of the flow control valves. The cascade inlet and the airfoil angles may be adjusted to obtain a wide range of incidence and stagger angle combinations.

The facility features a high-speed mechanism, which may drive any or all of the airfoils in controlled torsional oscillations. Stainless steel barrel cams, each having a six-cycle sinusoidal groove machined into its periphery, are mounted on a common rotating shaft driven by a 74.6 kW electric motor. A cam follower assembly, consisting of a titanium alloy connecting arm with a stainless steel button on one end, is joined on the other end to an airfoil trunnion. The button fits into the cam groove, thus coupling the airfoil to the camshaft. Lubrication of the cam/follower assembly is provided by an oil bath. The amplitude of the torsional airfoil motion is 1.2 deg as dictated by the cam and follower geometry. The drive system is configured for oscillations at a chosen interblade phase angle by fixing the cams at the required relative positions on the shaft. A reduced frequency of 0.90 is achieved at 0.55 inlet Mach number with an oscillation frequency of 350 Hz. For more information on the experimental facility, see Buffum and Fleeter (1990b).

Airfoils and Instrumentation

The airfoil and cascade geometry is summarized in Table 1. Four uncambered, 7.6 percent thick biconvex airfoils were used to create a low-solidity ($C/S = 0.65$) cascade. The stagger angle was 45 deg and the airfoils oscillated about the midchord.

Airfoils instrumented with static pressure taps were used to measure the airfoil surface steady pressure distributions. There were 16 chordwise measurement locations, with a higher density in the leading edge region used to capture the larger gradients there. Rows of sidewall static pressure taps located upstream and downstream of the cascaded airfoils were used to determine the mean inlet and exit pressures.

Flush-mounted high-frequency-response Kulite pressure transducers were used to measure the unsteady surface pressures on the oscillating airfoils. Two airfoils were instrumented, each having six transducers mounted symmetrically about the midchord on one airfoil surface. These transducers, having active sensor diameters of 1.3 percent of the airfoil chord, were epoxied into milled slots and potted in room-temperature-vulcanizing rubber for isolation from airfoil strain.

Table 1 Airfoil and cascade geometry

Airfoil	
Type	biconvex, no camber
Surface radius of curvature	27.4 cm
Leading and trailing edge radii of curvature	0.025 cm
Chord, C	7.62 cm
Maximum thickness / chord	0.076
Elastic axis	midchord
Dynamic pressure transducer locations, % chord	12,25,40,60,75,88
Cascade	
Number of airfoils	4
Airfoil spacing, S	11.72 cm
Solidity, C/S	0.65
Stagger angle, γ	45 degrees
Mean flow incidence angle, α_0	2 degrees
Amplitude of oscillation, α_1	1.2 degrees

A thin coating of rubber was also used to fair the transducer surface into the airfoil contour.

From static and dynamic calibrations, the pressure transducers were found to be highly linear in response over the frequency and pressure ranges of interest. However, the pressure transducers may produce undesirable signals as a consequence of the airfoil motion. This effect was quantified by oscillating the instrumented airfoils under no-flow conditions. The response of each transducer was found to be a linear function of the airfoil acceleration, implying that the acoustic response, which varies with the airfoil velocity magnitude, was dominated by the acceleration response. These calibration data were used to correct the oscillating airfoil pressure data for acceleration effects.

The time-dependent position of the reference oscillating airfoil was determined by a capacitance-type proximity sensor, which produces a voltage proportional to the air gap between it and an adjacent object. This sensor was positioned to face a six-cycle sinusoidally shaped cam mounted on the airfoil drive camshaft so as to be in phase with the reference airfoil motion.

Data Acquisition and Analysis

Conventional instrumentation was used to quantify the steady flow field. An average of the upstream sidewall static pressures along with the atmospheric (total) pressure were used to calculate the inlet Mach number. Steady flow airfoil surface static pressures were calculated from an average of approximately 100 samples in time at each tap. The steady pressure coefficient at a point (x, y) on the airfoil surface is defined as:

$$\overline{C}_p(x, y) = \frac{p_{in} - p_0(x, y)}{\rho_{in} V_{in}^2} \tag{3}$$

p_{in} is the mean inlet static pressure, p_0 is the mean airfoil surface static pressure, and ρ_{in} and V_{in} are the inlet values of density and velocity.

Unsteady signals were recorded on magnetic tape for post-experiment processing. During tape playback the signals were simultaneously digitized at rates sufficient to capture at least three harmonics of the oscillation frequency, with 32,768 samples taken per channel. Each channel of data was divided into contiguous blocks, each block typically with 2048 samples, and then Fourier decomposed to determine the first harmonic of each block of data. The first harmonic pressure of each block was referenced to the airfoil motion by subtracting from it the phase of the first harmonic motion signal of the same block. Once all of the blocks from a channel were decomposed in this manner, the first harmonic block results were averaged and the complex-valued acceleration response was subtracted

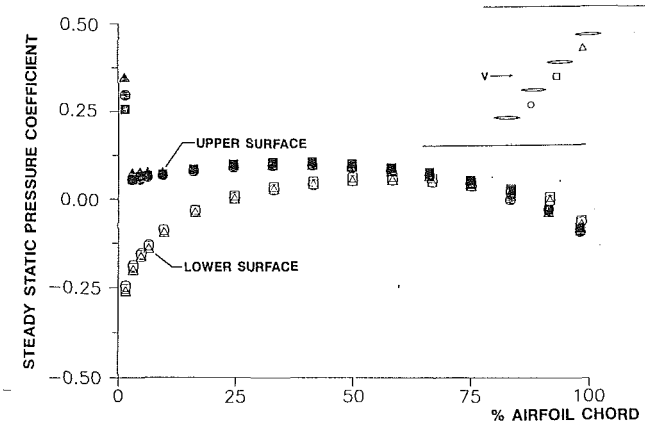

Fig. 3 Airfoil surface steady pressure coefficient distributions, M = 0.55, $\alpha_0 = 2$ deg

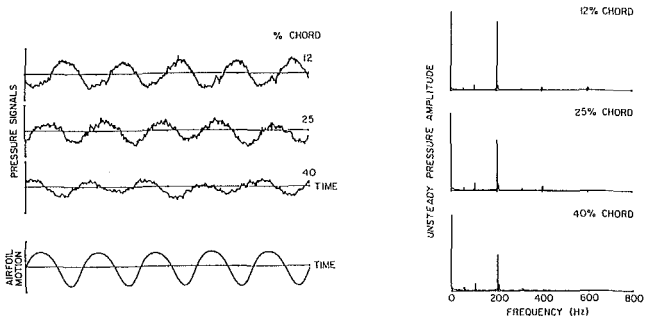

Fig. 4 Time-dependent signals and averaged pressure spectra

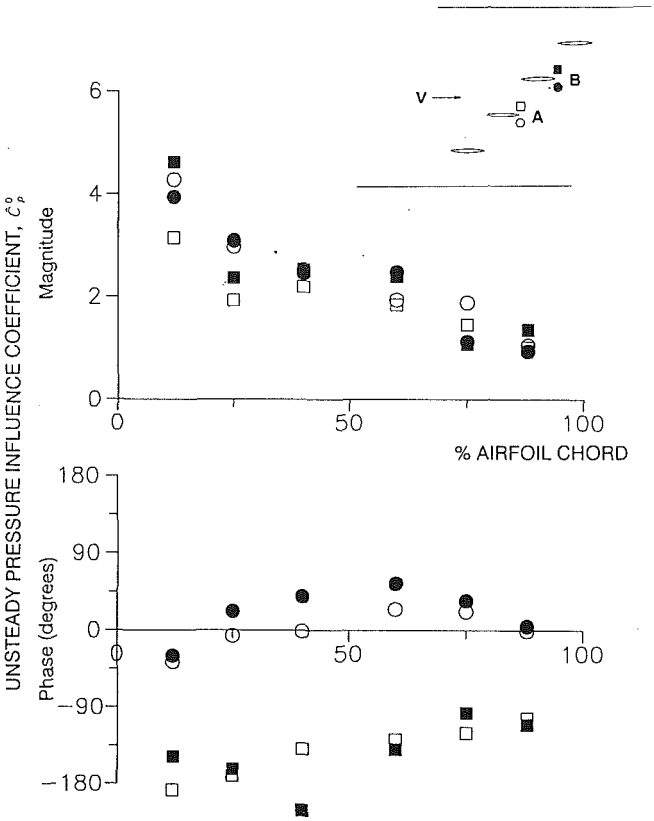

Fig. 5 Cascade dynamic periodicity, oscillating airfoil in relative position 0, $k = 0.90$

vectorally. Statistical analysis of the block results was used to estimate uncertainties for the average first harmonic values.

The motion of an oscillating airfoil is defined by the change in the incidence angle with time: $\alpha(t) = \alpha_0 + \alpha_1 \cos(\omega t)$ where α_0 is the mean incidence angle, α_1 is the torsional oscillation amplitude, and ω is the frequency.

The complex-valued unsteady pressure coefficient is defined as

$$C_p(x, y) = \frac{p_1(x, y)}{\rho_{in} V_{in}^2 \alpha_1}. \tag{4}$$

p_1 is the first harmonic airfoil surface static pressure. The dynamic pressure difference coefficient is the difference between the lower (y^-) and upper (y^+) surface unsteady pressure coefficients:

$$\Delta C_p(x) = C_p(x, y^-) - C_p(x, y^+). \tag{5}$$

Results

The experimental influence coefficient technique is investigated in a linear oscillating cascade. For a mean inlet Mach number of 0.55 and 2 deg mean incidence, the airfoil surface steady pressure coefficient distributions are presented first. Then the unsteady aerodynamic influence coefficients are presented, with special attention given to the effect of the relative position of the oscillating airfoil, the effect of reduced frequency, and convergence of the influence coefficient series. Finally, the influence coefficient predictions are correlated with data for all airfoils oscillating and linearized analysis predictions.

Steady-State Aerodynamics. For a linear cascade to be a valid simulation of a turbomachine blade row, the cascade must exhibit good passage-to-passage periodicity for the steady flow field. In Fig. 3, steady pressure coefficient data are presented for the center cascade passage and the two adjacent passages. Good cascade periodicity is apparent, with the only significant differences found at the leading edge of the airfoil upper surface.

The upper surface pressure coefficient distribution peaks near the leading edge with a corresponding maximum Mach number of 0.74. At the lower surface peak of $\overline{C}_p = -0.25$, the Mach number is 0.39. There is negligible loading beyond 50 percent of chord. Using the method of Kline and McClintock (1953), a 95 percent confidence interval of ± 0.003 is estimated for these pressure coefficients. The exit region mean static pressure divided by the inlet total pressure was 0.8251.

Unsteady Aerodynamics

Influence Coefficient Technique. Chordwise distributions of the first harmonic pressure influence coefficients on the individual surfaces of the position 0 instrumented airfoil are presented for the oscillating airfoil in the five relative positions defined by $n = -2$ through $n = 2$. Sample time-dependent pressure signals are presented along with the resulting pressure spectra in Fig. 4. These results illustrate the typical dominance of the first harmonic that was found in the signals. 95 percent confidence intervals of ± 5 percent in magnitude and ± 4 deg in phase were estimated for the mean value of the first harmonic pressure coefficients.

Dynamic Periodicity. To investigate the dynamic periodicity of the cascade, self-induced unsteady pressure data were obtained for the two airfoil locations surrounding the cascade center passage. That is, an instrumented airfoil was oscillated in position A of Fig. 5 with the other airfoils fixed. Then an instrumented airfoil was oscillated in position B with the other airfoils fixed. The resulting unsteady pressure coefficients $\hat{C}_p^0$ are presented for $k = 0.90$. Ideally, the unsteady pressure data for these two positions would be identical, but this is not

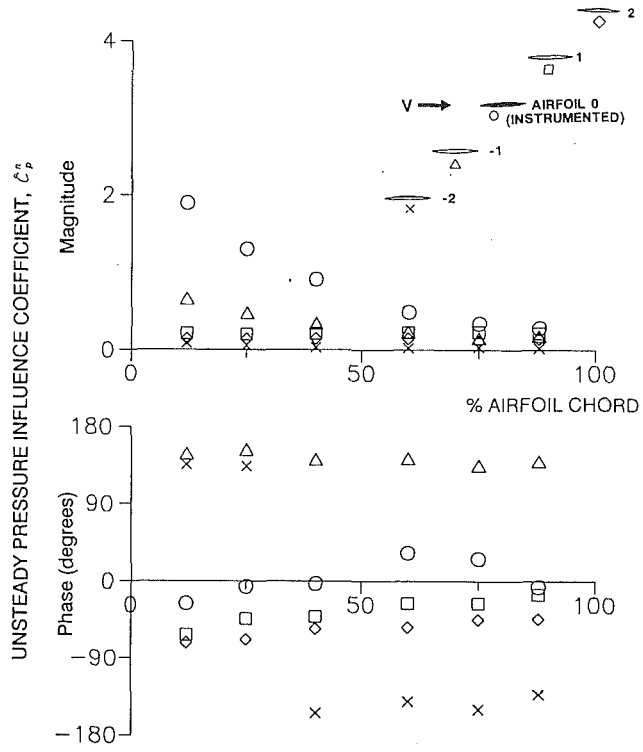

Fig. 6 Airfoil lower surface unsteady pressure influence coefficient distribution as a function of the oscillating airfoil relative position, $k = 0.40$

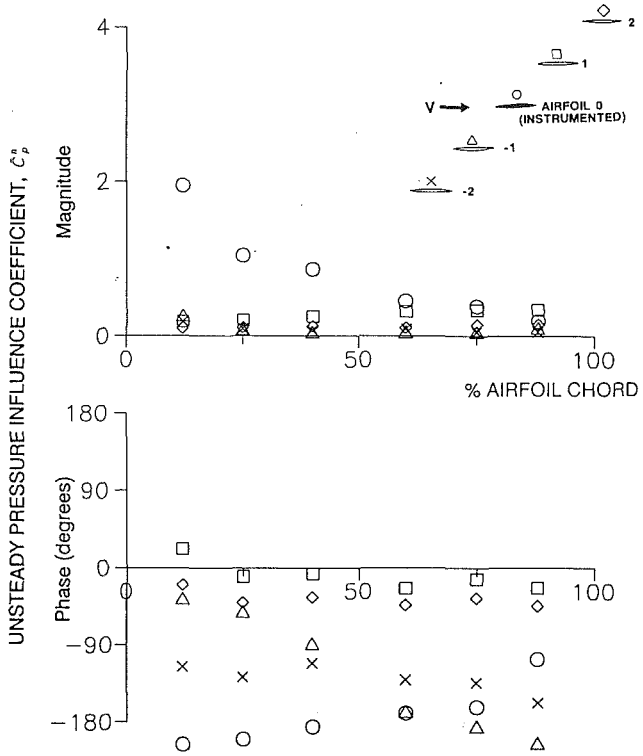

Fig. 7 Airfoil upper surface unsteady pressure influence coefficient distribution as a function of the oscillating airfoil relative position, $k = 0.40$

the case for these data. On the airfoil lower surface, the magnitude periodicity is good except at 60 and 75 percent of chord, and the phase periodicity also varies with position, being good at 12, 75, and 88 percent of chord but having significant differences otherwise. The upper surface magnitude periodicity is not particularly good at any measurement location, although the phase periodicity is good except for the 12 and 40 percent of chord locations. For the rest of this paper, data obtained from the airfoil surfaces defining the center passage of the cascade will be used for $\hat{C}_p^0$.

There are several possible causes of the shortcomings in the cascade dynamic periodicity. One would be a lack of periodicity in the mean flow field coupling with the unsteady perturbations to produce aperiodic behavior in the unsteady flow. Since the steady flow periodicity was found to be very good, this is not a problem.

It is more likely that the lack of dynamic periodicity was caused by acoustic waves created by the oscillating airfoils interacting with the solid boundaries imposed by the wind tunnel walls and the wind tunnel flow field. One form of interaction would be reflection of waves propagating away from the cascade along the axis of the wind tunnel by nonuniformities in the flow, for example, gradients found at the wind tunnel inlet and also at the diffuser section. At the nonuniformities, some fraction of the incident acoustic energy would be reflected back toward the cascade while the rest continues to travel away from the cascade.

Propagating and decaying acoustic waves will be created by an airfoil oscillating in a wind tunnel. Since the decaying waves decay exponentially with distance from the airfoil, only propagating acoustic modes are likely to reach either the inlet or diffuser with significant energy. The modal cutoff frequencies, which determine whether or not a mode will propagate, are given by Buffum and Fleeter (1993b) for a rigid rectangular duct of width A' and height B' with uniform axial flow at Mach number M. For waves propagating either upstream or downstream without attenuation, the requirement for the frequency of oscillation is

$$\omega > \omega_{lm} = a_0 \sqrt{(1-M^2)\left[\left(\frac{l\pi}{A'}\right)^2 + \left(\frac{m\pi}{B'}\right)^2\right]} \qquad (6)$$

for integer values of l and m. Thus the ($l=0$, $m=0$) modes always propagate. For the present wind tunnel geometry ($A' = 9.60$ cm and $B' = 41.4$ cm), the (0, 1) mode has the lowest nontrivial cutoff frequency, 337 Hz. Only for the highest reduced frequency, 0.90 (345 Hz oscillation frequency), will a (0, 1) mode propagate. However, since the (0, 0) mode will propagate at all frequencies, the potential always exists for undesirable reflections at the inlet and diffuser sections.

Only some portion of the acoustic energy created by the oscillating airfoil will feed into the propagating modes, and it remains to be seen whether this portion is significant. The amount of this energy that will be reflected is also unknown. Thus it is difficult to determine whether wave reflections at the inlet and diffuser sections had significant effects on the measurements.

Even if a duct acoustic mode doesn't propagate, it may cause significant unsteady pressure variations in the vicinity of the cascade. For a given geometry, the resulting mode shapes depend upon the location of the excitation source, i.e., the position of the oscillating airfoil. Therefore positions A and B of the oscillating airfoil will excite the various modes differently, and only if the resulting acoustic modes are of negligible amplitude relative to the unsteady pressure on the oscillating airfoil will periodic data be expected. Whether this effect is more or less significant than the previously mentioned effects due to flow field nonuniformities is unknown.

Effect of Relative Position of Oscillating Airfoil. To investigate the effect of the oscillating airfoil relative position on the reference airfoil unsteady pressure distribution, first harmonic pressure influence coefficient data are presented for the five relative positions of the oscillating airfoil. For 0.40 reduced frequency, the influence coefficients $\hat{C}_p^n$ are presented for the

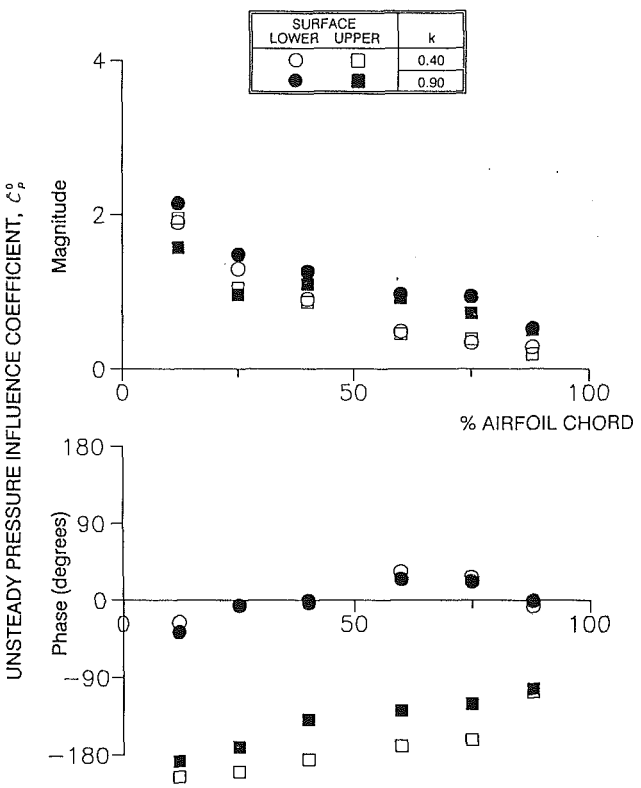

Fig. 8 Effect of reduced frequency on unsteady pressure influence coefficient, oscillating airfoil in relative position 0

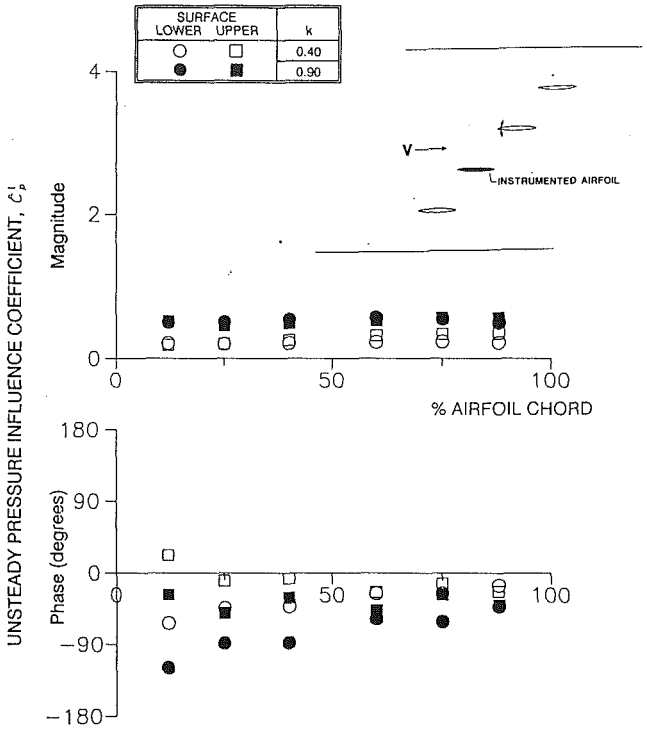

Fig. 9 Effect of reduced frequency on unsteady pressure influence coefficient, oscillating airfoil in relative position 1

airfoil lower surface in Fig. 6. In the accompanying schematic, each symbol corresponds to the effect of oscillation of the indicated airfoil on the reference instrumented airfoil.

For the lower surface data, the self-induced unsteady pressures $|\hat{C}_p^0|$ are dominant, attaining a maximum near the leading edge, then tending toward zero at the trailing edge. The unsteady pressure magnitude distribution due to airfoil -1 oscillations, the airfoil adjacent to the reference airfoil lower surface, also peaks near the leading edge. As expected, airfoil 1 oscillations cause smaller amplitudes along the forward half of the reference airfoil lower surface, but, unexpectedly, $|\hat{C}_p^1|$ is slightly larger than $|\hat{C}_p^{-1}|$ along the aft half. The $n=2$ and $n=-2$ magnitudes are quite small, illustrating the expected decrease in unsteady pressure magnitude with distance from the oscillating airfoil.

Lower surface phase angle data are strong functions of the oscillating airfoil position but, for any one value of n, change little with chordwise position. The $n=0$ phase changes from a small phase lag at 12 percent of chord to a small phase lead at 60 and 75 percent of chord. For $n=-1$ and $n=-2$, the phase data are roughly out-of-phase, while the $n=1$ and $n=2$ phases are closer to being in-phase with the airfoil motion.

For the airfoil upper surface, Fig. 7, the self-induced unsteady pressures are dominant over the first 50 percent of chord. The other unsteady pressures are generally small. Decreasing values of $|\hat{C}_p^n|$ with distance from the oscillating airfoil are apparent when $n=1$ and $n=2$, but when the airfoils upstream of the instrumented airfoil, $n=-1$ and $n=-2$, are oscillating, values of $|\hat{C}_p^{-2}|$, although small, are larger than $|\hat{C}_p^{-1}|$ in the midchord region. The $n=0$ unsteady pressure fluctuations are approximately out-of-phase relative to the airfoil motion while airfoil 1 oscillations result in in-phase unsteady pressures. The rest of the unsteady pressures tend to lag the motion by varying amounts.

Effect of Reduced Frequency. To clarify the effect of reduced frequency, the unsteady pressure influence coefficients $\hat{C}_p^n$ are presented individually for each value of n for two reduced frequencies, $k=0.40$ and $k=0.90$. Starting with the oscillating airfoil unsteady pressure coefficient distribution, Fig. 8, the larger amplitudes generally occur at the larger reduced frequency except near the leading edge on the upper surface. For $k=0.90$, the lower surface amplitudes at a given chordwise location are larger than those for the upper surface. In contrast, for $k=0.40$, the amplitudes for the two surfaces tend to be equal. Reduced frequency affects the phase distribution on the upper surface somewhat but does not affect the lower surface phase.

Unsteady pressures resulting from oscillation of the airfoil in relative position 1 are shown in Fig. 9. A schematic of the cascade as it was configured to obtain these data is also shown; the solid lines above and below the cascade airfoils designate the wind tunnel walls. The unsteady pressure magnitudes at either reduced frequency are nearly constant with chordwise position and equal for each of the two surfaces. The magnitude increases with reduced frequency, $k=0.90$ having nearly twice the magnitude of $k=0.40$. For either value of reduced frequency, the phases of the upper and lower surface unsteady pressure are about the same along the aft half of the airfoil. Forward of there, the phase distributions diverge with the lower surface lagging the upper surface. The lower surface phase variation is roughly linear.

Similar trends occur for $\hat{C}_p^2$, Fig. 10. For either value of k, the unsteady pressure magnitude distributions vary little with chordwise position and are nearly equal for the two surfaces. The higher reduced frequency data have significantly larger magnitudes. For either value of k, the phase distributions are nearly equal beyond the midchord but diverge over the forward half of the airfoil, with the lower surface lagging the upper surface. The lower surface phases vary in approximately a linear manner.

That the magnitudes of $\hat{C}_p^n$ in Figs. 9 and 10 are constant with chordwise position and equal for the two airfoil surfaces suggests that these unsteady pressure distributions are mainly due to planar (mode (0, 0)) acoustic waves. Under ideal con-

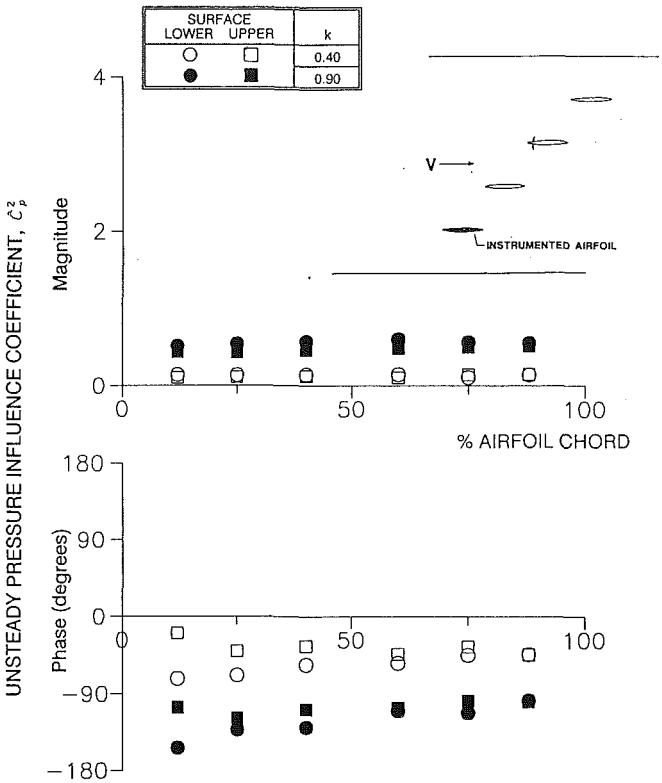

Fig. 10 Effect of reduced frequency on unsteady pressure influence coefficient, oscillating airfoil in relative position 2

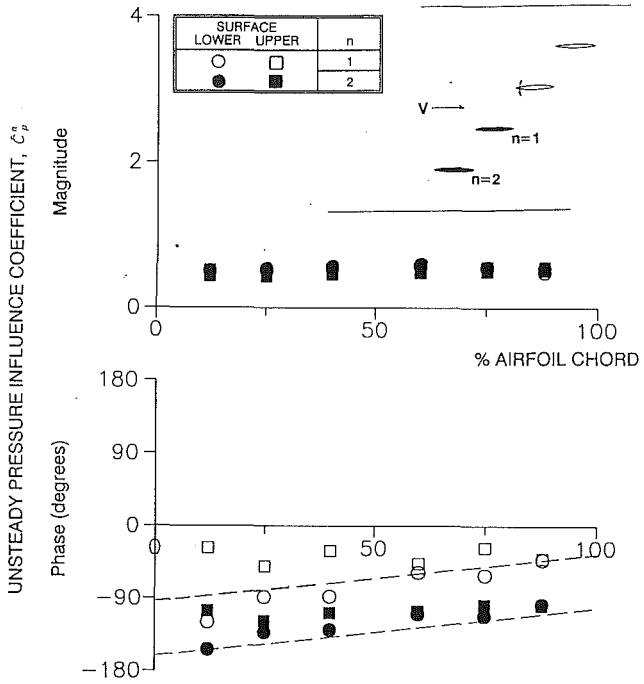

Fig. 11 Effect of oscillating airfoil relative position on unsteady pressure influence coefficient, $k = 0.90$

ditions, such as an acoustic wave propagating upstream past a flat plate aligned with a uniform mean flow, the amplitude of the resulting unsteady pressure on the flat plate would be constant and the phase would vary linearly with chordwise position and have a positive slope. The lower surface phase data approximate this condition, having a fairly linear phase change with chord and positive slope.

There are other characteristics of these data that are consistent with an upstream-traveling acoustic wave. Near the trailing edge, the lower and upper surface phases are equal. The phase distributions for the two surfaces remain approximately equal over the aft half of the airfoil, where steady pressure distributions (and hence Mach number distributions) for the two surfaces are nearly equal. The phase distributions diverge along the airfoil forward half, with the lower surface having larger positive slope, indicating a larger upstream propagation velocity along the lower surface; this is expected because the mean flow velocities are smaller on the lower surface than the upper surface. But the negative slope of the phase distribution found on the upper surface near the leading edge is inconsistent with an upstream-traveling wave. On the whole, however, the upstream-traveling acoustic waves dominate the $\hat{C}_p^1$ and $\hat{C}_p^2$ distributions.

The $k = 0.90$ data from Figs. 9 and 10 are cross-plotted in Fig. 11 to show that, for the same value of k, $|\hat{C}_p^2| = |\hat{C}_p^1|$. This is clearly a wind tunnel effect; without the wind tunnel walls to reflect acoustic waves, $|\hat{C}_p^2|$ would surely be less than $|\hat{C}_p^1|$ as a result of the increased distance from the source of the unsteadiness. For the phase data, dashed lines are included to indicate the theoretical phase variation due to an upstream-traveling acoustic wave, which is assumed to have the same phase as the 88 percent of chord, lower surface data for $n = 1$. The theory is in good agreement with the phase data on the lower surface for both $n = 1$ and $n = 2$.

The main effect of oscillating the airfoil in relative position -1 is a peak in the unsteady pressure magnitude near the leading edge on the adjacent, lower surface of the instrumented

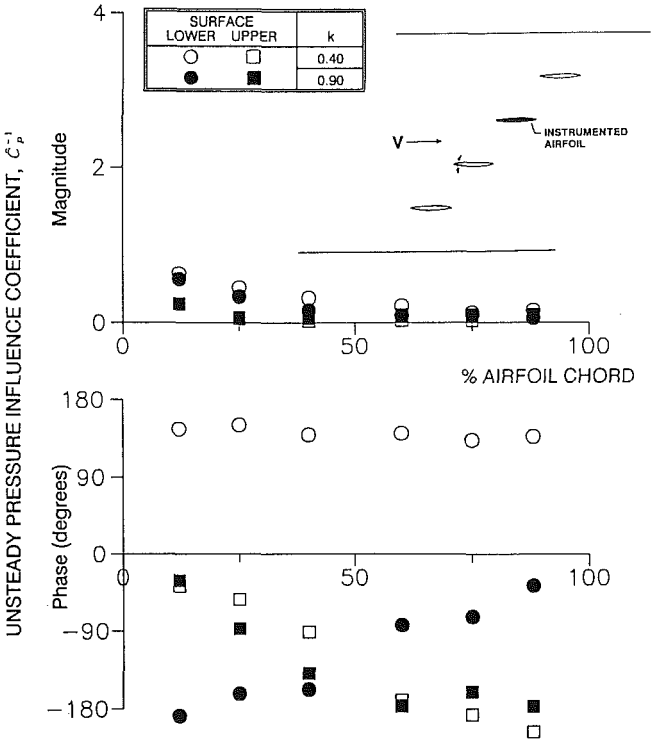

Fig. 12 Effect of reduced frequency on unsteady pressure influence coefficient, oscillating airfoil in relative position -1

airfoil, Fig. 12. Upper surface magnitudes are very small except near the leading edge. Contrary to the trend for $n > 0$ of larger magnitudes for higher reduced frequencies, the magnitudes on the lower surface are slightly larger for the lower reduced frequency. Phase distributions for the upper surface are quite similar for the two reduced frequencies, both with the phase at 12 percent of chord leading the phase at 88 percent of chord by about 150 deg and having reasonably linear variation with chordwise position. There are large differences due to reduced

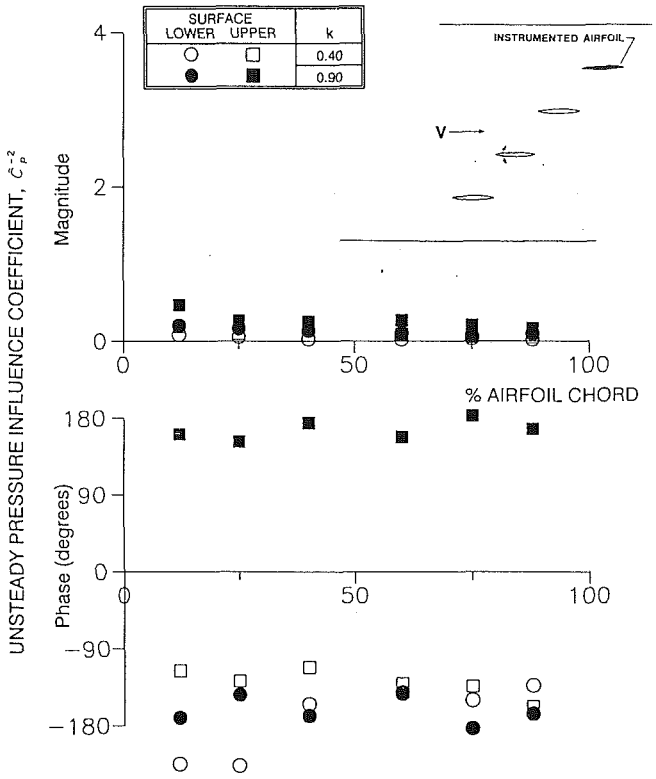

Fig. 13 Effect of reduced frequency on unsteady pressure influence coefficient, oscillating airfoil in relative position −2

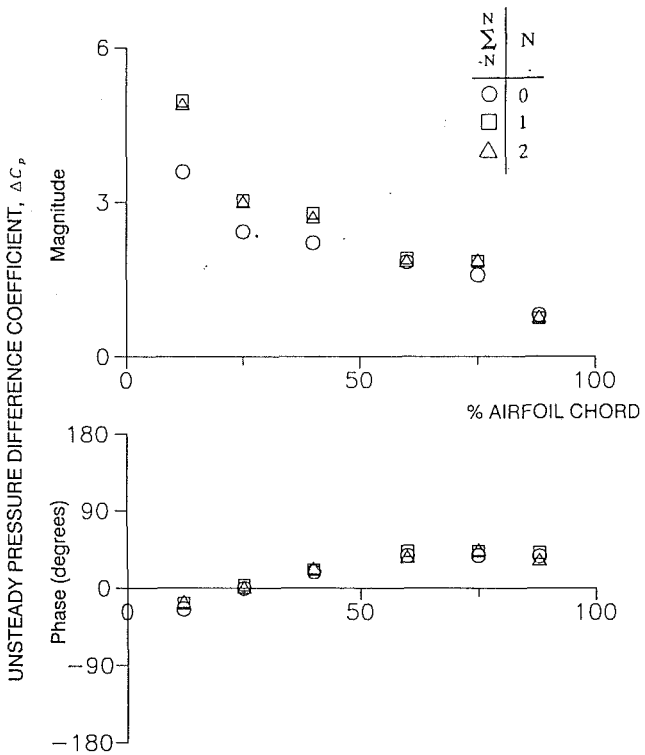

Fig. 15 Summation of unsteady pressure difference influence coefficients, $k = 0.90$, $\beta = 180$ deg

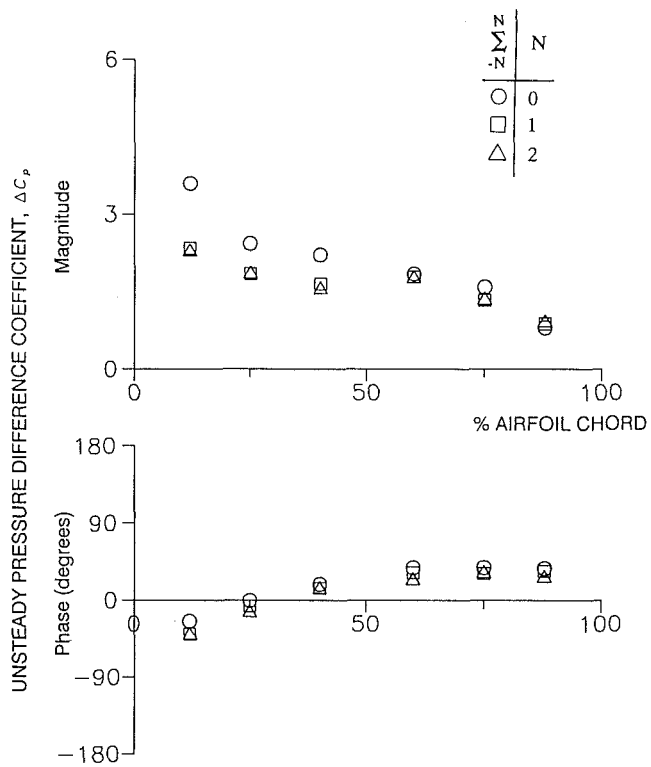

Fig. 14 Summation of unsteady pressure difference influence coefficients, $k = 0.90$, $\beta = 0$ deg

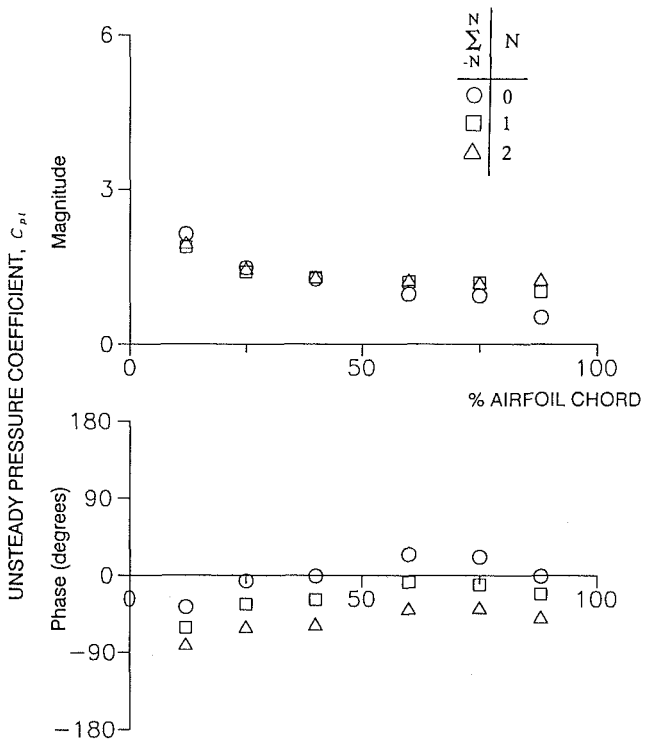

Fig. 16 Summation of airfoil lower surface unsteady pressure influence coefficients, $k = 0.90$, $\beta = 0$ deg

frequency in the phase distributions on the lower surface: The $k = 0.40$ data remain constant with chord while the $k = 0.90$ data vary greatly with position. There is no clear evidence of a downstream-traveling planar acoustic wave in the data.

Figure 13 presents $\hat{C}_p^{-2}$. The larger magnitude data occur at the higher reduced frequency. A more significant finding is that the unsteady pressure magnitudes are larger on the airfoil upper surface. Referring to the accompanying cascade schematic, it is seen that the instrumented airfoil upper surface is adjacent to a wind tunnel wall. Pressure waves that were reflected off the wind tunnel wall toward the instrumented airfoil

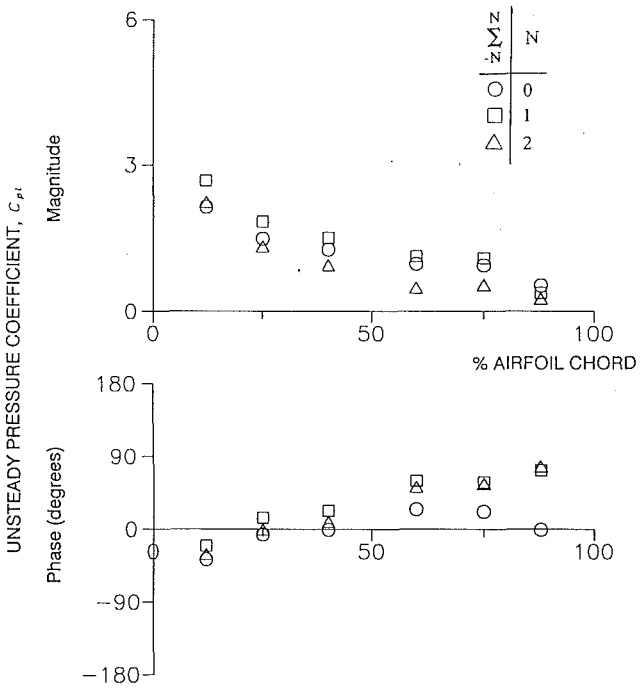

Fig. 17 Summation of airflow lower surface unsteady pressure influence coefficients, $k = 0.90$, $\beta = 180$ deg

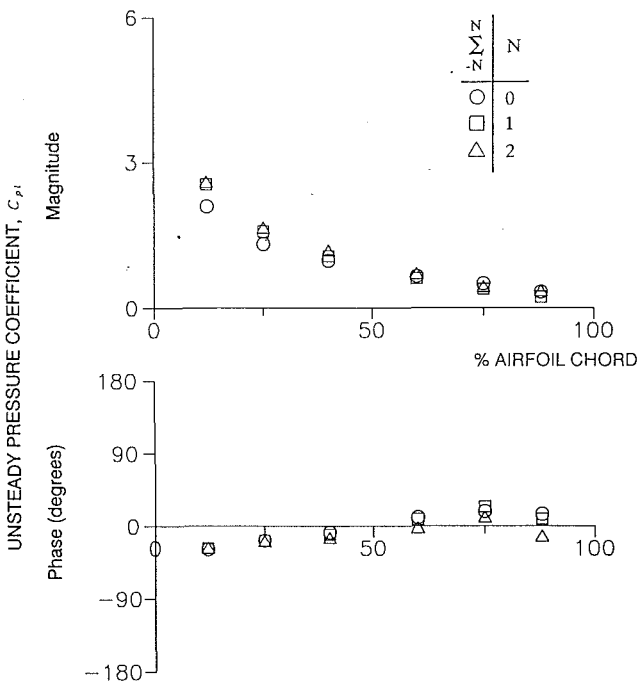

Fig. 19 Summation of airfoil lower surface unsteady pressure influence coefficients, $k = 0.40$, $\beta = 180$ deg

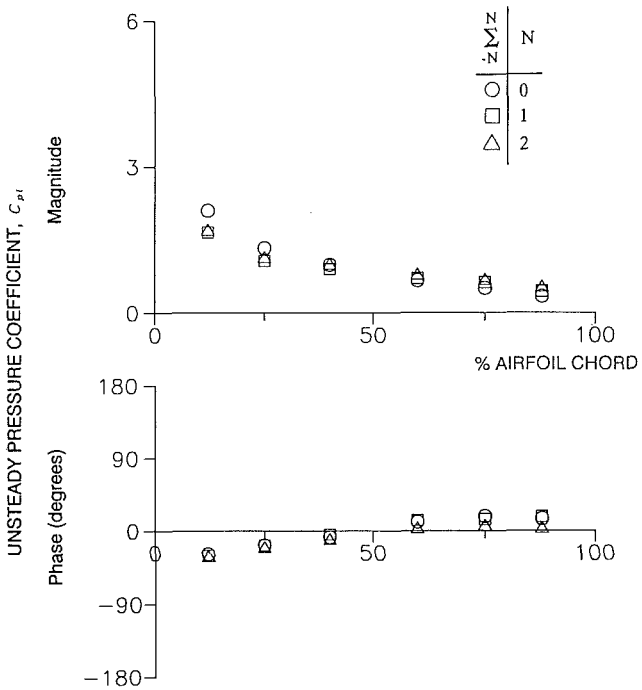

Fig. 18 Summation of airfoil lower surface unsteady pressure influence coefficients, $k = 0.40$, $\beta = 0$ deg

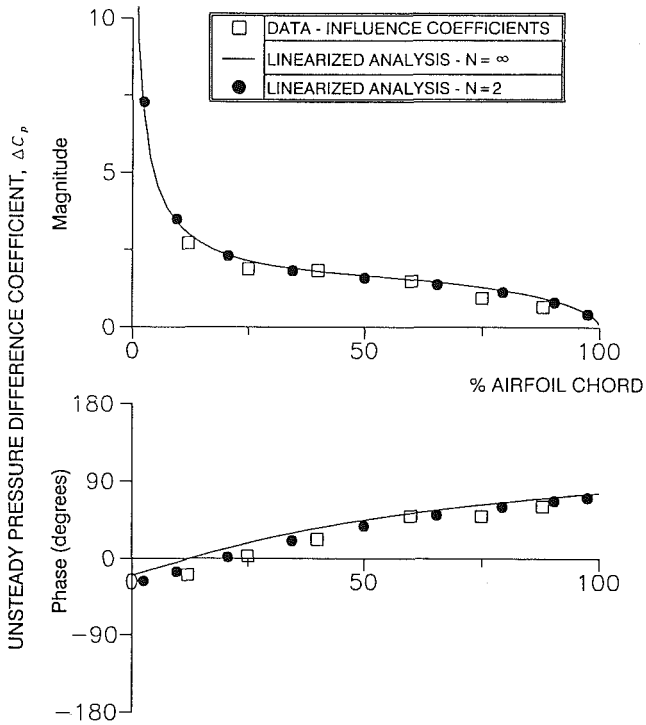

Fig. 20 Unsteady pressure difference coefficient distribution, $k = 0.64$, $\beta = 0$

upper surface probably caused the larger pressures there. The phase distributions generally change little with position and are approximately out-of-phase. As in the $\hat{C}_p^{-1}$ data, a downstream-traveling acoustic wave is not apparent.

Summation of Influence Coefficients. Summation of the experimentally determined influence coefficients to determine the unsteady pressure difference coefficient ΔC_p is depicted in Figs. 14 and 15 for the limit of summation in Eq. (1), N, varying from 0 to 2 and $k = 0.90$. Thus $N = 0$ corresponds to the self-induced unsteady aerodynamic response. For both values of the interblade phase angle, 0 and 180 deg, the ΔC_p series is rapidly convergent. Only the oscillations of the reference airfoil and its two immediate neighbors have a significant effect on the resulting dynamic pressure difference coefficients.

In contrast, the series for the unsteady pressure coefficient C_p is not necessarily convergent. For example, Figs. 16 and 17 demonstrate summation of the lower surface pressure coefficients for the same conditions as Figs. 14 and 15, respectively. In both of these cases, the series are not convergent over the

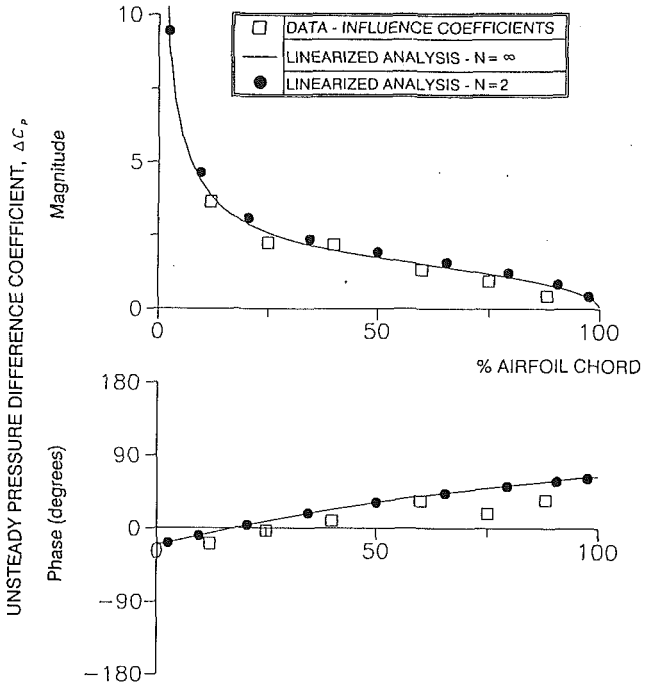

Fig. 21 Unsteady pressure difference coefficient distribution, $k = 0.64$, $\beta = 45$

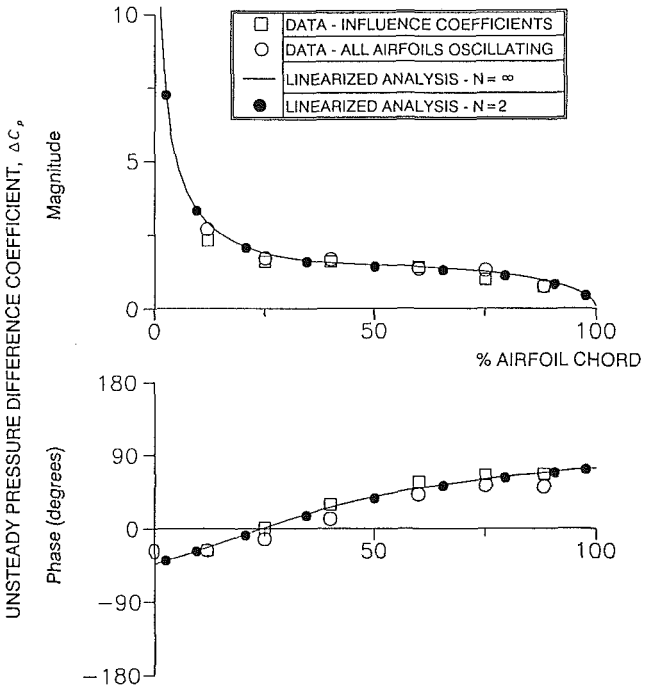

Fig. 22 Unsteady pressure difference coefficient distribution, $k = 0.64$, $\beta = -45$ deg

range for which data are available: the phase is rapidly varying with N for $\beta = 0$ deg while the magnitude is not converging for $\beta = 180$ deg. This is mainly due to the relatively large magnitudes of $\hat{C}_p^n$, which do not diminish for increasing positive values of n. That the series for the unsteady pressure difference coefficient is convergent despite this is because the pressures on the two surfaces largely cancel when the pressure difference is taken. This is evident from the data in Figs. 9 and 10, where the complex individual surface values of $\hat{C}_p^n$ are approximately equal for $n = 1$ or $n = 2$ so that $\Delta \hat{C}_p^1$ and $\Delta \hat{C}_p^2$ are quite small.

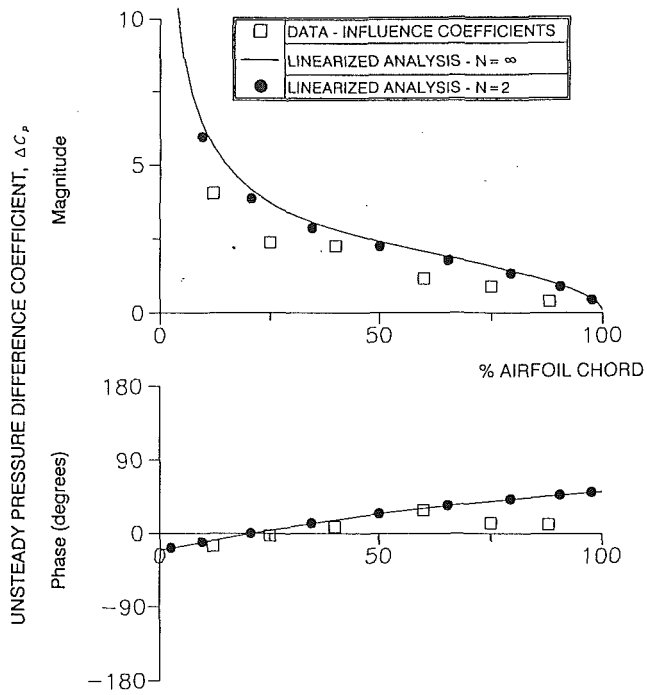

Fig. 23 Unsteady pressure difference coefficient distribution, $k = 0.64$, $\beta = 90$ deg

Since the amplitudes of $\hat{C}_p^1$ and $\hat{C}_p^2$ increase with reduced frequency, lowering the reduced frequency, should result in a C_p series with better convergence properties. This effect is shown in Figs. 18 and 19, where a reduction in k to 0.20 while keeping the same Mach number and interblade phase angle results in good convergence for the airfoil lower surface unsteady pressure coefficient.

Correlation of Data. Unsteady pressure difference coefficients obtained via summation of the experimental influence coefficient are correlated with experimental data obtained when all the airfoils were oscillating simultaneously with a constant interblade phase angle in Figs. 20–25. The reduced frequency is 0.64 and the interblade phase angles range from -90 to 180 deg. Summation of the experimental influence coefficient data makes use of all of the available experimental data, that is, $N = 2$ in Eq. (1). These data are correlated with the predictions of a computer program published by Whitehead (1987), which is based on the analysis of Smith (1972). The assumptions of inviscid, isentropic, subsonic flow through an infinite cascade of flat plate airfoils are made. The analysis also assumes that the airfoils are at zero mean incidence, and that the airfoil oscillations create small unsteady disturbances to the uniform mean flow. Predictions obtained from Smith's analysis via the influence coefficient technique are also presented for $N = 2$.

As mentioned in the introduction, the wind tunnel walls have been found to affect some experiments adversely in which all of the airfoils were oscillating simultaneously (Buffum and Fleeter, 1993a). For the interblade phase angle values 0, 45, 90, and 180 deg, the cascade dynamic periodicity was found to be poor; thus the unsteady pressures obtained at these conditions are not reliable and will not be used for correlation purposes.

As shown in Figs. 20–25, the experimental influence coefficient results and the analytical predictions are generally in good agreement. In addition, where reliable experimental data exist for traveling-wave mode oscillation of the airfoils, $\beta = -45$ deg and $\beta = -90$ deg, these data are in good agreement with the experimental influence coefficient results and the analytical predictions. The only significant differences occur at $\beta = 90$ deg, Fig. 23, where the analytical predictions for the magnitude

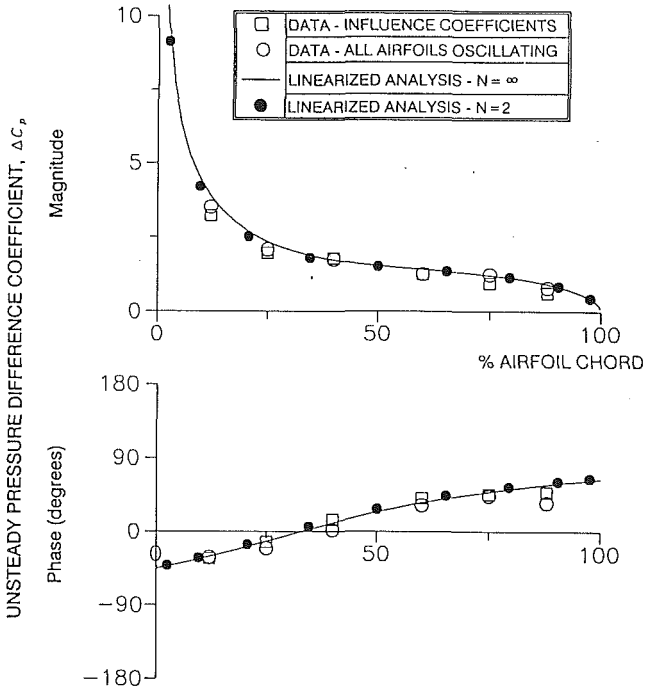

Fig. 24 Unsteady pressure difference coefficient distribution, $k = 0.64$, $\beta = -90$ deg

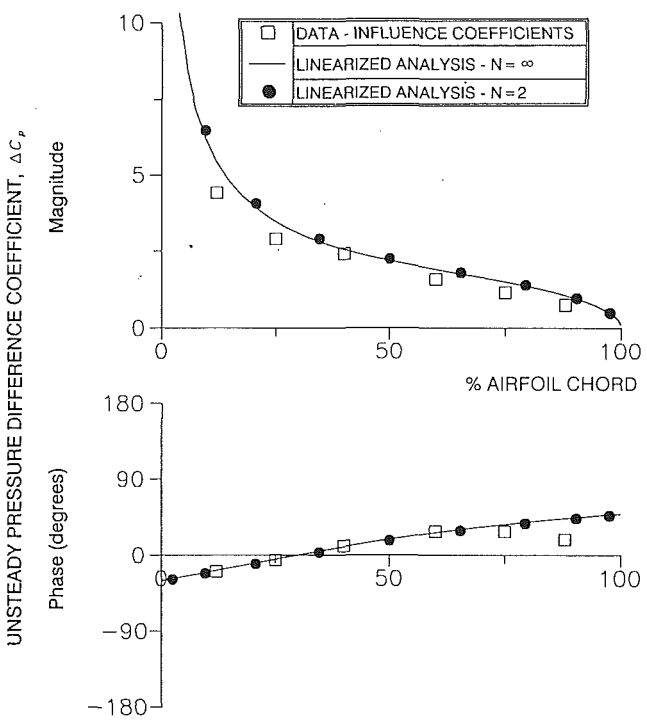

Fig. 25 Unsteady pressure difference coefficient distribution, $k = 0.64$, $\beta = 180$ deg

are offset to larger values than the experimental influence coefficient results. In general, the analyses tend to predict slightly larger magnitudes than the experimental influence coefficient results. For values of β ranging from 0 to 90 deg, the analytical phase predictions tend to lead the experimental influence coefficient results by a small amount. That the infinite and finite cascade analysis predictions are in good agreement indicates that a linear experimental facility with a limited number of airfoils can successfully be used to model an infinite cascade.

Summary and Conclusion

The unsteady aerodynamic influence coefficient technique has been investigated in a linear cascade for torsional airfoil oscillations at reduced frequencies up to 0.90 with 0.55 inlet Mach number. Steady and unsteady airfoil surface pressure distributions were measured, the latter using flush-mounted miniature pressure transducers. Discrete Fourier analysis techniques were used to analyze the unsteady pressure data. Behavior of the unsteady pressure influence coefficients was examined in detail as were the convergence characteristics of the influence coefficient series. Predictions obtained from summation of the experimentally determined influence coefficients were compared with experimental data obtained with all the airfoils oscillating simultaneously and the predictions of linearized unsteady aerodynamic analyses.

If was found that constraints introduced by the wind tunnel had detrimental effects on the experimental results. First, the self-induced unsteady pressure distributions were found to vary with the location of the oscillating airfoil due to excitation of undesirable wind tunnel acoustic modes. Second, a relatively minor effect was found when the instrumented airfoil was located adjacent to the upper wind tunnel wall. In that case, reflection of pressure disturbances off the wall onto the adjacent airfoil surface caused small but undesirable effects. Third, relatively large unsteady pressures were found on the airfoils upstream of the oscillating airfoil. These were shown to result from excitation of a plane wave acoustic mode of the wind tunnel. This effect increased with increasing reduced frequency and caused the influence coefficient series for C_p to be nonconvergent at the largest reduced frequency. However, the ΔC_p series was convergent due to cancellation effects.

Undesirable effects aside, the predicted unsteady pressure difference coefficients obtained by the experimental influence coefficient technique are in good agreement with experimental data for all airfoils oscillating and linearized analysis predictions. This agreement is an indication that the experimentally determined values of ΔC_p are valid. But this is due, in part, to the cancellation of the unsteady pressures due to the plane acoustic waves that occurred when ΔC_p was calculated. Presumably, if the airfoils were highly loaded, differences between the lower and upper surface mean flow gradients might distort the waves to the extent that cancellation would be greatly reduced, and the plane wave mode of the wind tunnel would render even ΔC_p results invalid.

As it stands, the unsteady aerodynamic influence technique is of limited usefulness in this linear cascade. To reduce the effects of the wind tunnel walls, an effort is currently under way to replace the solid walls with porous walls designed to absorb incident acoustic waves using technology developed to reduce aircraft gas turbine engine noise (Groeneweg and Rice, 1987).

Acknowledgments

This investigation was supported by the Turbomachinery Technology Branch, Propulsion Systems Division of the NASA Lewis Research Center. The experiments were performed with the technical assistance of R. Olsey, S. Orahoske, and V. Verhoff. Helpful comments on the contents of this paper were provided by L. Bober, D. Hoyniak, and D. Huff.

References

Bölcs, A., Fransson, T. H., and Schläfli, D., 1989, "Aerodynamic Superposition Principle in Vibrating Turbine Cascades," AGARD-CRP-468/469.

Buffum, D. H., and Fleeter, S., 1990a, "Oscillating Cascade Aerodynamics by an Experimental Influence Coefficient Technique," *Journal of Propulsion*, Vol. 6, No. 5, pp. 612–620.

Buffum, D. H., and Fleeter, S., 1990b, "Aerodynamics of a Linear Oscillating Cascade," NASA Technical Memorandum 103250.

Buffum, D. H., and Fleeter, S., 1993a, "Wind Tunnel Wall Effects in a Linear Oscillating Cascade," NASA Technical Memorandum 103690; ASME JOURNAL OF TURBOMACHINERY, Vol. 45, pp. 147–156.

Buffum, D. H., and Fleeter, S., 1993b, "Effect of Wind Tunnel Acoustic Modes on Linear Oscillating Cascade Aerodynamics." NASA Technical Memorandum 106367.

Davies, M. R. D., and Whitehead, D. S., 1984, "Unsteady Aerodynamics Measurements in a Transonic Annular Cascade," *Unsteady Aerodynamics of Turbomachines and Propellers*, Cambridge University Engineering Department, Cambridge, United Kingdom, pp. 487–502.

Groeneweg, J. F., and Rice, E. J., 1987, "Aircraft Turbofan Noise," ASME JOURNAL OF TURBOMACHINERY, Vol. 109, pp. 130–141.

Hanamura, Y., Tanaka, H., and Yamaguchi, K., 1980, "A Simplified Method to Measure Unsteady Forces Acting on the Vibrating Blades in Cascade," *Bulletin of the JSME*, Vol. 23, No. 180, pp. 880–887.

Kline, S. J., and McClintock, F. A., 1953, "Describing Uncertainties in Single-Sample Experiments," *Mechanical Engineering*, Jan., pp. 3–8.

Kobayashi, H., 1990, "Annular Cascade Study of Low Back-Pressure Supersonic Fan Blade Flutter," ASME JOURNAL OF TURBOMACHINERY, Vol. 112, pp. 768–777.

Mehmed, O., Kaza, K. R. V., Lubomski, J. F., and Kielb, R. E., 1982, "Bending-Torsion Flutter of a Highly Swept Advanced Turboprop," NASA Technical Memorandum 82975.

Smith, S. N., 1972, "Discrete Frequency Sound Generation in Axial Flow Turbomachines," Aeronautical Research Council Reports and Memoranda No. 3709.

Szechenyi, E., 1985, "Fan Blade Flutter—Single Blade Instability or Blade to Blade Coupling?" ASME Paper No. 85-GT-216.

Whitehead, D. S., 1987, "Classical Two-Dimensional Methods," *AGARD Manual on Aeroelasticity in Axial Flow Turbomachines, Vol. 1: Unsteady Turbomachinery Aerodynamics*, AGARDograph No. 298, pp. 3-1–3-30.

Shroud Heat Transfer Measurements From a Rotating Cavity With an Axial Throughflow of Air

C. A. Long

P. G. Tucker[1]

Thermo-Fluid Mechanics Research Centre,
School of Engineering,
University of Sussex,
Brighton, BN1 9QT,
Sussex, United Kingdom

The paper discusses measurements of heat transfer obtained from the inside surface of the peripheral shroud. The experiments were carried out on a rotating cavity, comprising two 0.985-m-dia disks, separated by an axial gap of 0.065 m and bounded at the circumference by a carbon fiber shroud. Tests were conducted with a heated shroud and either unheated or heated disks. When heated, the disks had the same temperature level and surface temperature distribution. Two different temperature distributions were tested; the surface temperature either increased, or decreased with radius. The effects of disk, shroud, and air temperature levels were also studied. Tests were carried out for the range of axial throughflow rates and speeds: $0.0025 \le m \le 0.2$ kg/s and $12.5 \le \Omega \le 125$ rad/s, respectively. Measurements were also made of the temperature of the air inside the cavity. The shroud Nusselt numbers are found to depend on a Grashof number, which is defined using the centripetal acceleration. Providing the correct reference temperature is used, the measured Nusselt numbers also show similarity to those predicted by an established correlation for a horizontal plate in air. The heat transfer from the shroud is only weakly affected by the disk surface temperature distribution and temperature level. The heat transfer from the shroud appears to be affected by the Rossby number. A significant enhancement to the rotationally induced free convection occurs in the regions $2 \le Ro \le 4$ and $Ro \ge 20$. The first of these corresponds to a region where vortex breakdown has been observed. In the second region, the Rossby number may be sufficiently large for the central throughflow to affect the shroud heat transfer directly. Heating the shroud does not appear to affect the heat transfer from the disks significantly.

1 Introduction

In some gas-turbine high-pressure compressors, there is an axial throughflow of turbine cooling air, which is passed between the bores of adjacent compressor disks. Some of this flow enters the cavities formed between adjacent disks, and a parasitic temperature rise occurs as a result of convective heat transfer. The engine designer obviously needs to know the temperature of this turbine cooling air and so needs to estimate the heat transfer that occurs in the compressor cavities. The designer must also know the heat transfer in order to predict the surface temperatures, stress, and thermal growth of the compressor drum structure.

A typical cavity comprises two disks and a peripheral shroud. The flow structure and disk heat transfer for the case when only the disks are heated has been studied by Farthing et al. (1992a, b). They found that rotationally induced buoyancy forces caused the flow to enter the cavity. The heat transfer from the disks was correlated and found to depend on both the Reynolds number of the axial throughflow, Re_z, and the Grashof number, Gr. One particularly significant finding was that the appropriate characteristic length for the Nusselt and Grashof numbers was the distance measured radially inward from the shroud, implying that the boundary layer flow is in this direction. Another finding was that the Nusselt numbers appeared to correlate with the Grashof number raised to the 1/4 power; implying that the heat transfer was in the laminar regime.

The effect of heating the peripheral shroud was not, however, investigated by these authors. In a real engine, the shroud will generally be hotter than the disks and so contribute to the total heat transfer in the cavity.

In most of the work associated with heat transfer in rotating cavities, the relevant nondimensional parameters have been evaluated using the air inlet temperature, T_i, as the reference

[1]Present address: School of Mechanical Engineering, University of Bath, Bath, BA2 7AY, United Kingdom.

Contributed by the International Gas Turbine Institute and presented at the 37th International Gas Turbine and Aeroengine Congress and Exposition, Cologne, Germany, June 1-4, 1992. Manuscript received by the International Gas Turbine Institute February 4, 1992. Paper No. 92-GT-69. Associate Technical Editor: L. S. Langston.

temperature. It has often been acknowledged that this may be inappropriate but it has not been considered necessary to measure the cavity air temperature, T_{cav}. This has mainly occurred for historical reasons; the relatively simple integral model used to predict heat transfer with *superposed radial flows* (Owen et al., 1985), was successfully developed by knowing T_i: T_{cav} could then be predicted.

For a heated rotating cavity with an *axial throughflow* of cooling air, it is not possible to develop a simple integral model to predict the heat transfer from the disks unless T_{cav} is known explicitly. Knowing T_{cav} may also allow the heat transfer from the shroud to be predicted using an existing correlation for a horizontal plate, replacing gravitational acceleration with centripetal acceleration.

This paper discusses the results of experiments conducted to measure the heat transfer from the shroud and also the temperature of the air inside the cavity itself. A brief review of the flow structure in these cavities is given in Section 2, and the apparatus is described in Section 3. The temperature measurements are discussed in Section 4 and the heat transfer results are discussed in Section 5.

2 Flow Structure

The current understanding of the flow structure in a *heated* rotating cavity with an axial throughflow of cooling air is described by Farthing et al. (1992a). A brief description of their work will be given here to aid the discussion in this paper.

The essential features of the flow structure are illustrated in Fig. 1. The cavity comprises two disks of outer radius, b, and a shroud of axial width, s. These rotate with an angular velocity of Ω rad/s. A central throughflow of cooling air enters the cavity axially, via a hole of radius a, in the upstream disk. The flow leaves the cavity via an identical hole in the downstream disk and the bulk average axial velocity of the central throughflow is W. When the disks and shroud are at the same temperature as the incoming air ($T_s = T_{sh} = T_i$), the flow structure is as shown in Fig. 1(a). In this case, the central jet passing through the cavity (the throughflow) generates a toroidal vortex. In the absence of vortex breakdown, the flow is two dimensional and there is virtually no penetration of the throughflow into the cavity itself. When the disks are heated, there is a dramatic change in the flow structure; it becomes three dimensional as a result of buoyancy forces induced by rotation.

A schematic of the heated flow structure, given in the r–ϕ plane as this best illustrates the relevant features, is shown in Fig. 1(b). In the region between the two disks, the heated flow structure comprises a radial arm, two regions of circulation and a dead zone. This entire flow structure rotates at an angular velocity, ω, which varies with the cavity gap ratio, G ($G = s/b$), Rossby number, Ro (Ro $= W/\Omega a$), and thermal conditions, typically $0.9 < \omega/\Omega < 1$. Fluid in the radial arm penetrates the cavity, bifurcates in the vicinity of the shroud, and forms the two regions of circulation. The cyclonic region rotates in the same direction as the disks; the anticyclonic region, in the opposite direction. The regions of circulation do not merge but are separated by another region, referred to as the dead zone. Because the circulations rotate in opposite directions, they are at different pressures; and just as their meteorological equivalents, the cyclonic region has a lower pressure than the anticyclonic region. The consequence of this can be demonstrated by considering the linear tangential momentum equation in a rotating frame of reference. For steady, incompressible, and inviscid flow, this equation simplifies to:

$$2\Omega u = -1/\rho r(\partial p/\partial \phi) \tag{1}$$

where u is the radial velocity.

It is evident from inspection of Eq. (1) that there can only be a radial flow (in this case u) in the inviscid region between the disks if there is also a circumferential variation of pressure, which of course is provided by the two regions of circulation. Inspection of Fig. 1(b) also reveals that pressure decreases in the direction of rotation in the radial arm, $\partial p/\partial \phi < 0$ and from Eq. (1) $u > 0$ so radial outflow occurs.

The way in which the flow penetrates the cavity itself is relatively well understood; the way in which the flow leaves the cavity is not so well understood. It is almost certain that boundary layers form on the disks; they start at the outer radius ($r = b$) and flow radially inward. The disk surface heat transfer measurements carried out by Farthing et al. (1992b) appear to confirm this.

Nomenclature

a = inner radius of cavity
A = acceleration
b = outer radius of cavity
C_o = constant
Cp = specific heat capacity
g = acceleration due to earth's gravity
$G = s/b$ = cavity gap ratio
$\mathrm{Gr} = Al^3\beta\Delta T/\nu^2$ = Grashof number
$H = \mathrm{Nu}_{sh,av}/\mathrm{Gr}_{sh}^{0.25}$ = laminar free convection parameter
k = thermal conductivity
l = characteristic length
m = coolant mass flow rate
n = constant
$\mathrm{Nu} = ql/\Delta Tk$ = Nusselt number
p = pressure
$\mathrm{Pr} = \mu Cp/k$ = Prandtl number
q = heat flux
r = radial coordinate
$\mathrm{Re}_z = 2aW/\nu$ = axial Reynolds number
$\mathrm{Re}_\phi = \Omega b^2/\nu$ = rotational Reynolds number
$\mathrm{Ro} = W/\Omega a$ = Rossby number
s = axial gap between the disks
T = temperature
u = radial velocity
W = bulk average velocity at inlet to cavity
$x = r/b$ = nondimensional radial coordinate
z = axial coordinate
$\beta = 1/T$ = buoyancy parameter
ΔT = temperature difference
θ = temperature ratio
μ = dynamic viscosity
ν = kinematic viscosity
ρ = density
ϕ = tangential coordinate
ω = circumferential average speed of the fluid in the cavity
Ω = angular speed of the disks

Subscripts and Superscripts

av = denotes a radially weighted average
cav = pertaining to conditions inside the cavity
i = inlet value
max = maximum value
min = minimum value
s = pertaining to the disk surface
sh = pertaining to the shroud
* = denotes that T_{cav} is used as a reference temperature

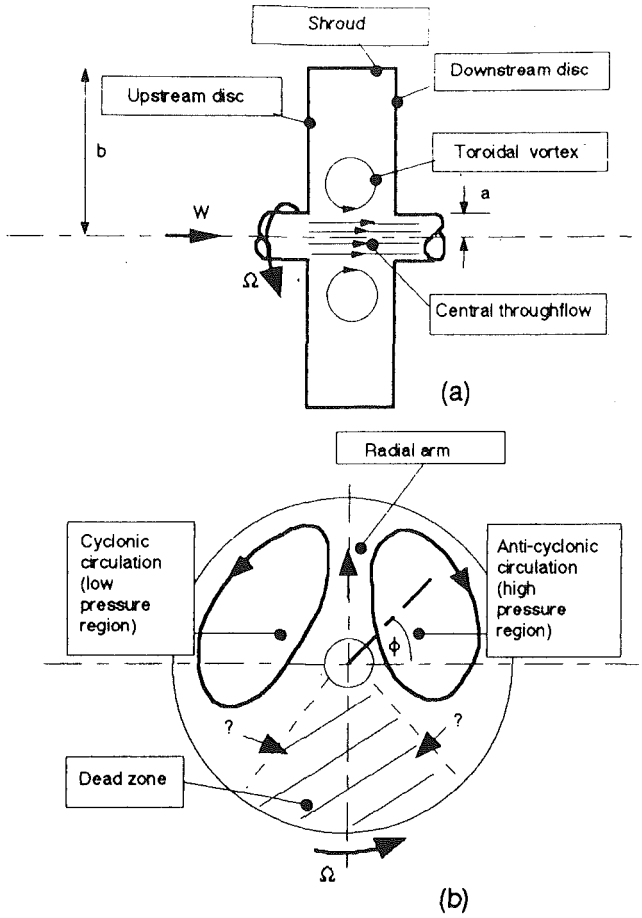

Fig. 1 Schematic diagrams of flow structure in a rotating cavity with an axial throughflow. (*a*) $T_{sh} = T_s = T_i$ (r–z plane); (*b*) T_{sh} and $T_s \geq T_i$ (r–ϕ plane)

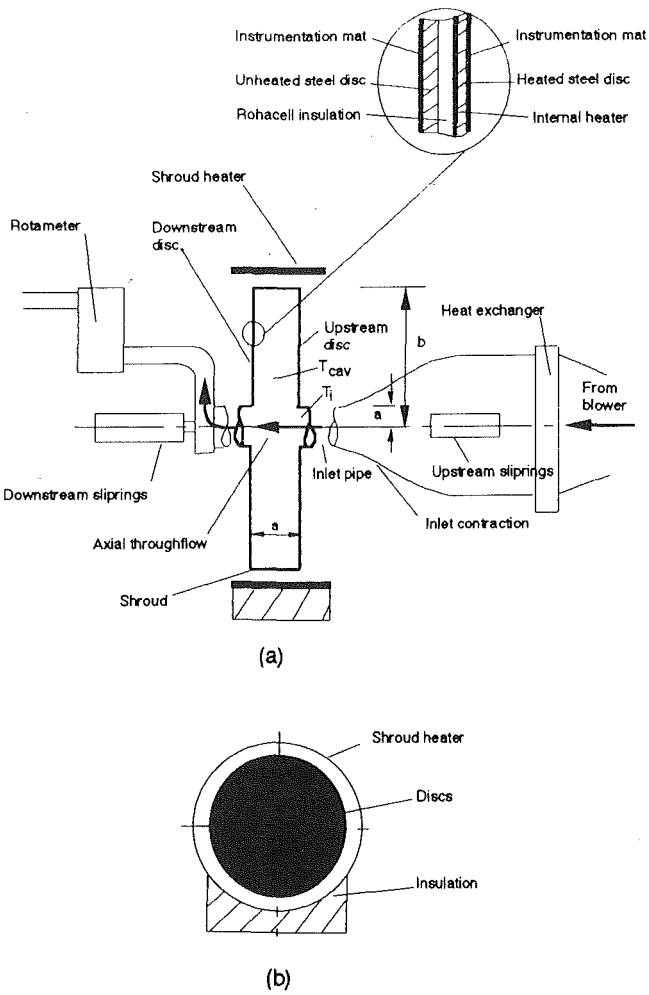

Fig. 2 Schematic diagram of the rotating cavity rig: b = 0.4845 m, a = 0.045 m,and s = 0.065 m: (*a*) side view; (*b*) end view

Fluid has in fact been seen to flow radially inward on the disk surface adjacent to the dead zone, but it is still not known if this flow is confined to the disk surface under just the dead zone, or if it occurs over the entire disk surface. The radial inflow on the disk is assumed to be caused by rotationally induced buoyancy forces. A temperature difference between surface and adjacent air creates a density difference and in an analogous way to free convection from a stationary heated plate, a boundary layer flow occurs in accord with the density gradient.

The description above of the heated flow structure is based on observations carried out with an unheated shroud. Farthing (1988) conducted some flow visualization tests on a cavity with a heated shroud. When only the shroud was heated (the disks remaining unheated), a similar flow structure to that shown in Fig. 1(*b*) was observed, except there were multiple radial arms and multiple dead zones. Heating the disks *and* the shroud did not appear to change this. To revert back to a single radial arm (associated with heat heated disk case) required the disk temperature to be approximately 40°C greater than the shroud temperature.

3 Apparatus

The design of the rotating cavity rig and the methods used to analyze the data can be found from Farthing et al. (1992b).

A schematic diagram of the experimental rig is shown in Fig. 2. Frame (*a*) shows a side-view of the rig and (*b*) an end-view illustrating the shroud heater. The cavity has an outer radius of b = 0.4845 m and the disks are separated by an axial distance s = 0.065 m. The disks are heated by internal electrical heaters; there are five annular 5 kW heaters inside each disk. This allows the disk surface temperature distribution to be controlled by the operator. For the tests discussed this either increased with radius, which will be referred to as an increasing temperature distribution, or it was allowed to decrease with radius (a decreasing temperature distribution). The shroud is heated by an external heater comprising thirty 0.75 kW "Firebar" heater elements. The centerlines of the elements lie parallel to the axis of rotation of the cavity, their active lengths are roughly the width of the outer surface of the shroud, and the elements are located in a ring with a 15 mm radial clearance from the outer surface of the shroud.

An axial throughflow of air is supplied to the cavity through a hole of radius a = 0.045 m in the upstream disk. The temperature of this air measured at the cavity inlet (1.65 m upstream of the cavity) is T_i. For the tests reported here, T_i was in the range 20 to 35°C. The air leaves the cavity via an identical hole in the downstream disk. The flow rate is measured by one of a number of devices (depending on the magnitude). For low flow rates ($2 \times 10^3 \leq \mathrm{Re}_z \leq 2 \times 10^4$ one of the two Rotameter flowmeters on the exit pipe is used. There is some leakage of air into the rig, mainly from the upstream slipring cooling air. Although the leakage flow is small, it is a significant fraction of the total flow at the lower flow rates. The rotameters are on the downstream side of the leaks and so will give an accurate reading of the flow rate entering the cavity. For higher flow rates ($\mathrm{Re}_z > 2 \times 10^4$), where the leakage is considered not to be as significant, either a "one-inch" Annubar or the pressure

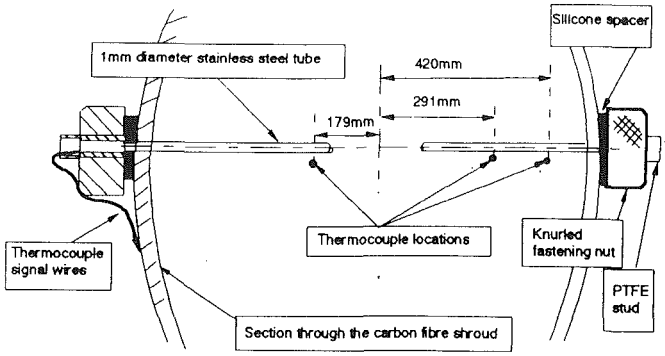

Fig. 3 Schematic diagram of the cavity air temperature probe

drop across the inlet contraction itself is used to measure the flow.

The surface temperature of the disks is measured using copper-constantan thermocouples located in an instrumentation mat (see the inset of Fig. 2). There are 13 thermocouples on outside face of each disk: 23 on the inside face of the upstream disk and 18 on the inside face of the downstream disk.

The shroud itself is a carbon fiber composite ring of 2.5 mm radial thickness, 969 mm internal diameter ($=2b$) and 127 mm overall axial width. The shroud is located on the outer radius of the disks using a layer of silicone foam. Two RdF fluxmeters are installed on the shroud and their sensor elements are positioned at $z = s/3$ (measured from the downstream disk) and $z = s/2$. In addition to measuring the heat flux by a thermopile gage, each fluxmeter also contains a thermocouple. The calibration of these fluxmeters is discussed by Long (1991) and the interested reader is referred to that paper for further information. The overall accuracy of the fluxmeters is estimated to be within 10 W/m^2; that of the thermocouples is 0.2°C.

The temperature of the air inside the cavity, T_{cav}, is measured using the probe illustrated in Fig. 3. A 1-mm-dia stainless steel tube is located at $z = s/2$ and spans the inside of the cavity on a diameter. The tube carries three thermocouples positioned at nondimensional radial coordinates $x\,(x=r/b) = 0.369, 0.600$, and 0.867. The innermost thermocouple (at $x = 0.369$) is located on one radius of the tube; the other two are located on the diametrically opposing radius. Each thermocouple is constructed from 0.1-mm-dia copper and constantan wires. The beads protrude from the surface of the tube by approximately 3 mm and are isolated from it using epoxy resin adhesive. These precautions ensure that the local air temperature, and not that of the tube, is being measured. Errors associated with conduction along the length of the tube are reduced by using PTFE studs to fix the temperature probe to the shroud. The thermal response time of the thermocouple beads can be estimated using the so-called lumped capacitance equation. Taking a value of heat transfer coefficient for cylinders and wires in crossflow (see Schlichting, 1979), shows that the bead will respond to 87 percent of an imposed temperature change in time, $t = C_o\sqrt{[1/r(\Omega-\omega)]}$ seconds (where $C_o = 0.9$ m$^{1/2}$ s$^{1/2}$). For most tests, this is approximately the time period of the flow relative to the disks.

4 Temperature Measurements

4.1 Disk and Shroud Temperature Distributions. Examples of disk surface temperature distributions are shown in Fig. 4. The temperatures shown here were recorded from tests with $Re_z = 8\times10^4$ and $Re_\phi = 2\times10^6$, and with the shroud heated to approximately 110°C. Although obtained for this particular test condition, they illustrate typical features of the temperature distributions for all of the heat transfer tests. Each frame shows the variation of nondimensional temperature θ,

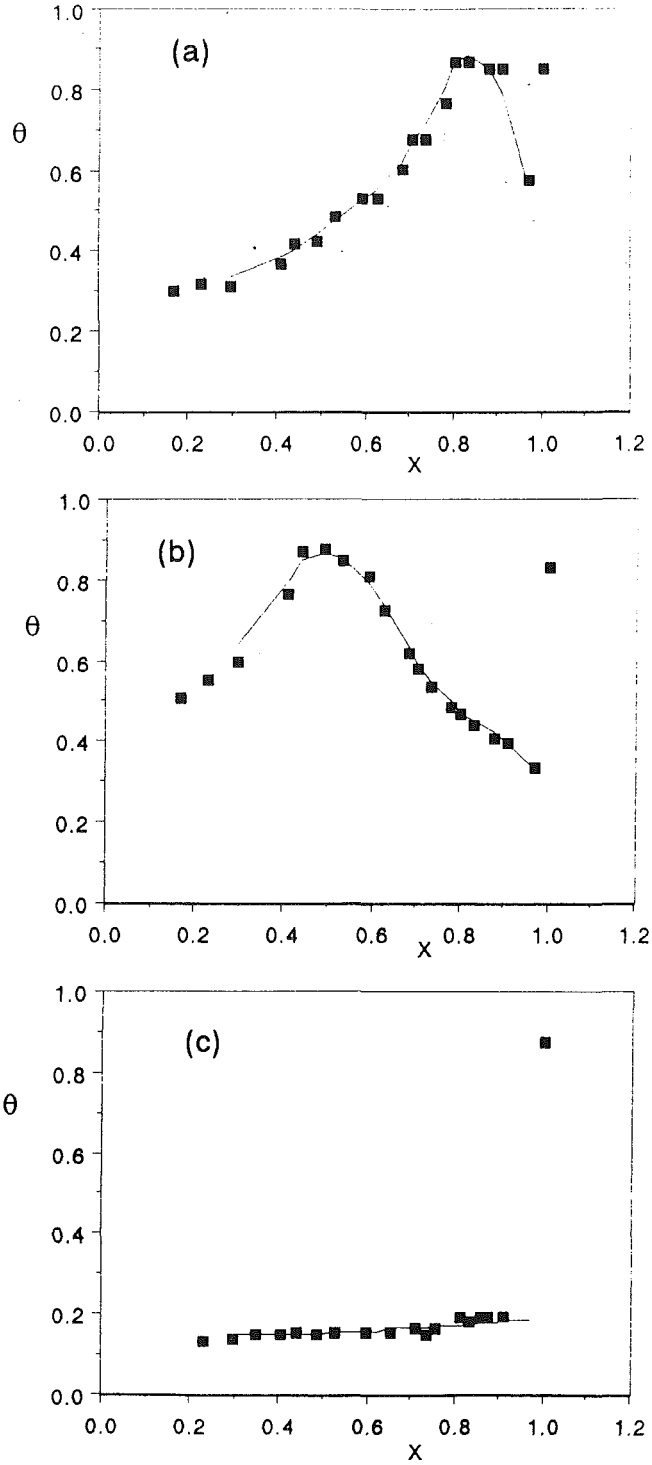

Fig. 4 Dimensionless surface temperature distributions for tests at $Re_\phi = 2 \times 10^6$ and $Re_z = 8 \times 10^4$ with the shroud heated to approximately 100°C: (*a*) downstream disk: heated with a surface temperature distribution that increases with radius ($T_{s,max} = 114$°C, $T_i = 18$°C); (*b*) downstream disk: heated with a surface temperature distribution that decreases with radius ($T_{s,max} = 115$°C, $T_i = 19$°C); (*c*) upstream disk unheated ($T_{sh} = 108$°C, $T_i = 19$°C)

$\theta = (T_s - T_i)/(T_{s,max} - T_i)$, with nondimensional radius $x(x=r/b)$. In frame (*a*), the results are shown for just the downstream disk, but both disks of the cavity are heated with an increasing temperature distribution (a symmetrically heated cavity). In frame (*b*) the results shown are for the downstream disk of a symmetrically heated cavity with a decreasing temperature distribution. In frame (*c*), the disks are unheated, but as is also

the case in frames (*a*) and (*b*), the shroud is heated. The temperature of the shroud itself is indicated by the symbols at $x = 1$. These temperature distributions are chosen as they are typical of those found in real engines. For structural reasons the bore of the disk is usually more massive than the rim, and consequently has greater thermal inertia. Frame (*a*), the increasing surface temperature distribution, is characteristic of that following an acceleration of an engine. Conversely, frame (*b*), the decreasing temperature distribution, is similar to that found after an engine deceleration.

For the increasing temperature distribution, the maximum surface temperature of 114°C ($\beta\Delta T_{max} = 0.32$) occurs at $x \approx 0.85$; for the decreasing temperature distribution, at $x \approx 0.55$. Frictional heat conducted from the bearings and radiation from other parts of the cavity maintains the minimum disk temperature above the air entering the cavity (in this case $\beta\Delta T_{min} \approx 0.14$). So, in frame (*c*), where the discs are *unheated*, their surface temperature is also greater than that of the inlet air and for this case $\beta\Delta T = 0.06$

It is convenient here to draw the reader's attention to some terms that are used in this paper to describe the surface temperatures of the disks and shroud and also the air temperature. "Cold" is taken as ambient conditions: 20°C. "Warm" and "Hot" are taken to mean within the ranges 60 to 70°C and 100 to 120°C, respectively. "Unheated" refers to a surface that is not heated directly, but as for the unheated disks shown in Fig. 4(*c*), indirectly through conduction and radiation. In most cases unheated disks were at 30–40°C. For future reference, the buoyancy parameters corresponding to these different conditions ($\beta\Delta T_{max}$) are tabulated below. The use of this buoyancy parameter is considered both appropriate and informative, since the flow itself is generated by buoyancy forces. In this table, β is evaluated at the air inlet temperature T_i and ΔT_{max} is based on the maximum disk or shroud surface to air inlet temperature difference.

Table 1 Buoyancy parameters for the different thermal conditions

Surface	Air	Buoyancy parameter
Warm	Cold	$0.133 \le \beta\Delta T_{max} \le 0.167$
Hot	Cold	$0.267 \le \beta\Delta T_{max} \le 0.333$
Unheated	Cold	$\beta\Delta T_{max} \le 0.08$
Hot	Warm	$0.014 \le \beta\Delta T_{max} \le 0.163$

(4.2) Cavity Air Temperature Measurements. Temperatures were measured inside the cavity at three radial locations and for $2 \times 10^5 \le Re_\phi \le 8 \times 10^5$ and $2 \times 10^3 \le Re_z \le 4 \times 10^4$. Tests were conducted with an unheated shroud and heated disks and also for a heated shroud and unheated disks. Both disks had the same radial temperature distribution and two different temperature distributions were tested: the surface temperature either increased or decreased with radius.

A typical set of measurements is shown in Fig. 5 where the results are from tests at $Re_\phi = 4 \times 10^5$ and $Re_z = 2 \times 10^4$. Frame (*a*) shows the results for the increasing temperature distribution, (*b*) for the decreasing temperature distribution, and (*c*) for the unheated disks with a heated shroud. The symbols indicate the measured disk and shroud temperatures, and also the values of air temperature measured inside the cavity T_{cav}. The air inlet temperature T_i is included for reference, and is shown by the dashed line. For the results shown in frame (*c*) the thermocouple at $x = 0.6$ failed and consequently this symbol is omitted from the graph.

For the increasing temperature distribution, Fig. 5(*a*), the radially weighted average and maximum disk temperatures (T_{av} and T_{max}) are approximately 100 and 114°C, respectively. The shroud temperature $T_{sh} = 45$°C and the air inlet temperature T_i is 38°C. There is some radial variation of the temperature inside the cavity: from 80°C at the innermost location to 72°C at the outermost near the shroud. But the most significant effect is the difference between T_{cav} and T_i: 30 to 40°C.

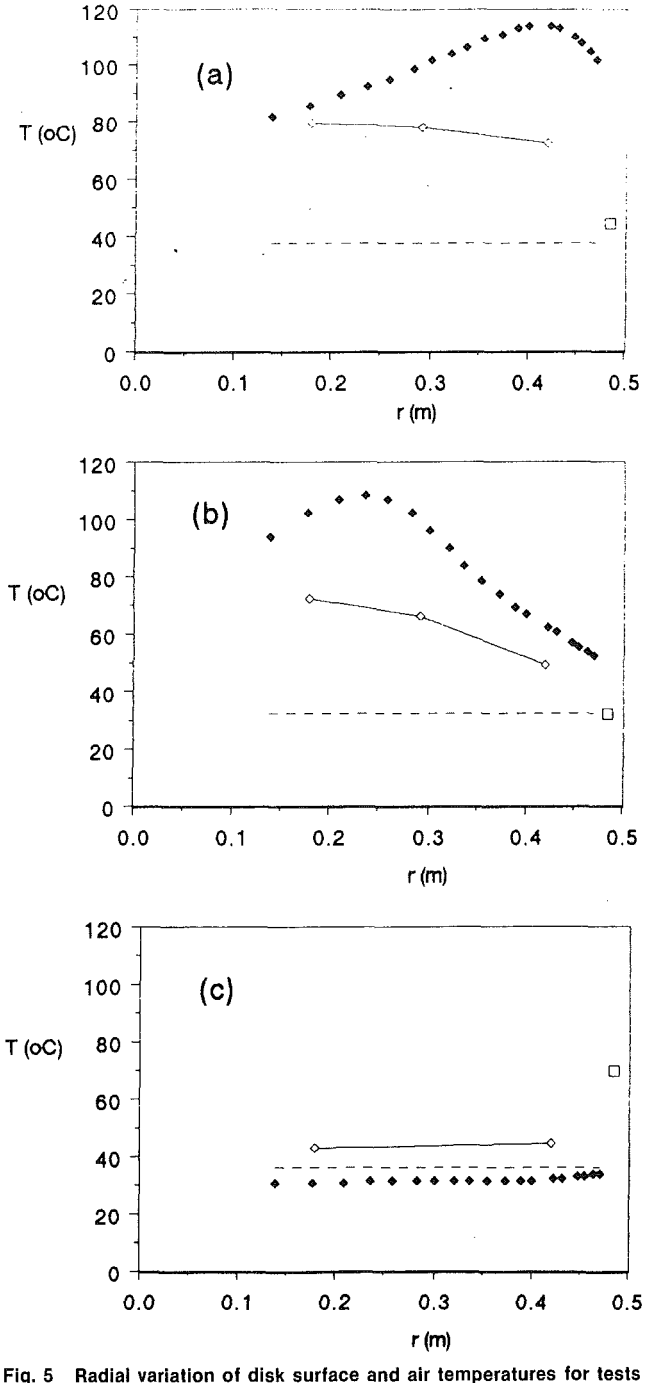

Fig. 5 Radial variation of disk surface and air temperatures for tests at $Re_\phi = 4 \times 10^5$ and $Re_z = 2 \times 10^4$: (*a*) a disk surface temperature distribution that increases with radius and an unheated shroud; (*b*) a disk surface temperature distribution that decreases with radius and an unheated shroud; (*c*) unheated disks and a heated shroud;
◆ disk surface
□ *shroud*
··· cavity inlet air, T_i
— ◆ — cavity air, T_{cav}

The corresponding measurements when there is a decreasing surface temperature distribution on each disk are shown in Fig. 5(*b*). Compared with the increasing disk temperature distribution, there is now a larger radial variation of air temperature inside the cavity. The air near the shroud is also significantly cooler than measured for the test with an increas-

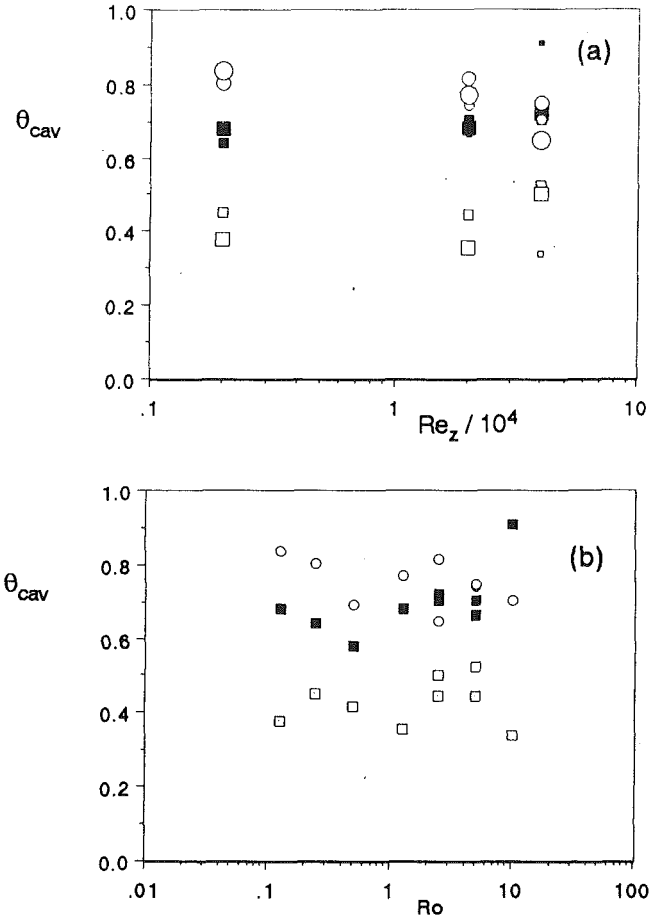

Fig. 6 Variations of θ_{cav} with: (*a*) axial Reynolds number Re_z and (*b*) Rossby number, Ro; legend for frame (*a*): □ □ □: T_s increasing with radius, Re_ϕ = 0.2, 0.4, and 0.8 × 10^6, respectively; $\theta_{cav} = (T_{s,av} - T_{cav})/(T_{s,av} - T_i)$; ■ ■ ■: T_s decreasing with radius, Re_ϕ = 0.2, 0.4, and 0.8 × 10^6, respectively; $\theta_{cav} = (T_{s,av} - T_{cav})/(T_{s,av} - T_i)$; ○ ○ ○: unheated disks and a heated shroud, Re_ϕ = 0.2, 0.4, and 0.8 × 10^6, respectively; $\theta_{cav} = (T_{sh} - T_{cav})/(T_{sh} - T_i)$; legend for frame (*b*): □: T_s increasing with radius; ■: T_s decreasing with radius; ○: unheated disks and a heated shroud

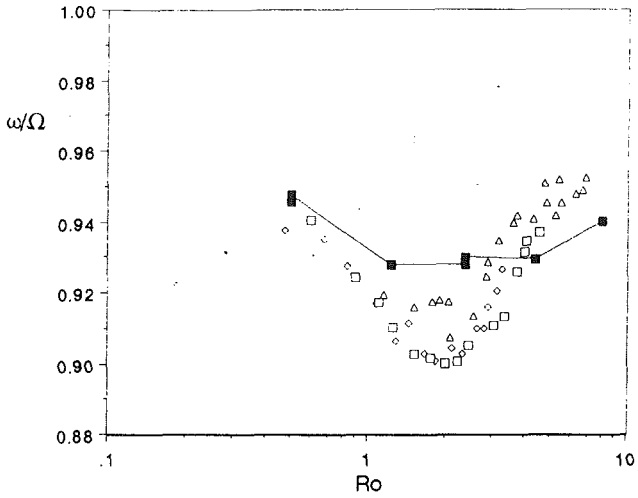

Fig. 7 Variation of tangential velocity ratio, ω/Ω, with Rossby number, Ro. Tests conducted with an unheated shroud and heated disks having a surface temperature distribution that increases with radius. ■: measurements from the temperature probe; LDA results from Farthing et al. (1992a):
◇ $Re_\phi = 0.4 \times 10^6$
□ $Re_\phi = 0.6 \times 10^6$
△ $Re_\phi = 0.8 \times 10^6$

ing temperature distribution. When only the shroud is heated, T_{cav} is still significantly greater than T_i.

This is shown in Fig. 5(*c*) for the same values of Re_ϕ and Re_z; when T_{sh} = 70°C and T_{av} = 32°C, the measured value of T_{cav} is approximately 45°C. Note that for this test the rotational speed is relatively low and there is little frictional heat conducted from the bearings, consequently the air inlet temperature is actually greater (by about 5°C) than the disk surface temperature.

As seen in Figs. 5(*a*, *b*, *c*) the temperatures inside the cavity are strongly affected by the disk surface temperature distribution; the flow rate and rotational speed have less of an effect. This is summarized in Fig. 6, which shows the variation of nondimensional cavity air temperature, θ_{cav}, with both rotational Reynolds number and axial Reynolds number. Note that $\theta_{cav} = (T_s - T_{cav})/(T_s - T_i)$; for heated disks, $T_s = T_{av}$ and for a heated shroud $T_s = T_{sh}$. The cavity air temperature measurement is taken from the outermost thermocouple bead, since this will be the air temperature outside the shroud boundary layer. The tests were conducted at three different axial Reynolds numbers Re_z = 0.2, 2, and 4×10^4, and three different values of Re_ϕ (Re_ϕ = 0.2, 0.4, and 0.8 × 10^6); these and the different disk surface temperature distributions are indicated on the graph. There does not appear to be any *systematic* variation of θ_{cav} with Re_z and Re_ϕ. Also as shown in Fig. 6(*b*), there does not appear to be any systematic variation of the temperature parameter with the Rossby number Ro (Ro = $W/\Omega a = 0.5(b/a)^2\ Re_z/Re_\phi$). It is possible that more experimental data would reveal the dependence of the cavity air temperature on Re_z and Re_ϕ. But for the range of Re_z and Re_ϕ considered, the cavity air temperature is found to depend primarily on the disk surface temperature *distribution*. Since θ_{cav} must also depend on the fraction of the central throughflow that actually penetrates the cavity, this too will be significantly affected by the surface temperature distribution.

The cavity temperatures discussed above were obtained from signals averaged over a number of rotations of the cavity. It is also possible to measure the circumferential variation of temperature in the cavity: recording the signals using a chart recorder. As noted in Section 3, the thermocouple bead response time is of the order of the period of the flow inside the cavity relative to the disks.

Noting this, it was found that the three thermocouples recorded similar values of the circumferential variation of cavity air temperature. This was usually in the range 5 to 10°C, which is considered to be sufficiently small to justify use of the circumferentially averaged value. It is also worth noting that the magnitude is reduced when the disks have a temperature distribution that decreases with radius. When only the shroud is heated, and there are multiple radial arms (Farthing, 1988), the thermocouple beads are not expected to have a sufficiently rapid response time. So it was not possible to obtain accurate measurements of the circumferential variation of air temperature inside the cavity for this case.

Measurements of the circumferential variation of air temperature taken on the chart recorder were also used to estimate the relative rotation of the fluid in the cavity. The results of these tests are shown in Fig. 7 as the variation of the ratio of fluid to disk velocities, ω/Ω, against the Rossby number, Ro. The tests were conducted with an unheated shroud and disk temperature distributions that increased with radius on both disks. Considering the simple method used to obtain these measurements, the results are in reasonable agreement with the LDA measurements of Farthing et al. (1992a) with G = 0.24. As reported by those authors, at a given value of Ro the effect of increasing the gap ratio is to reduce the value of ω/Ω. Where the current measurements are above those obtained from LDA, the difference is consistent with the differ-

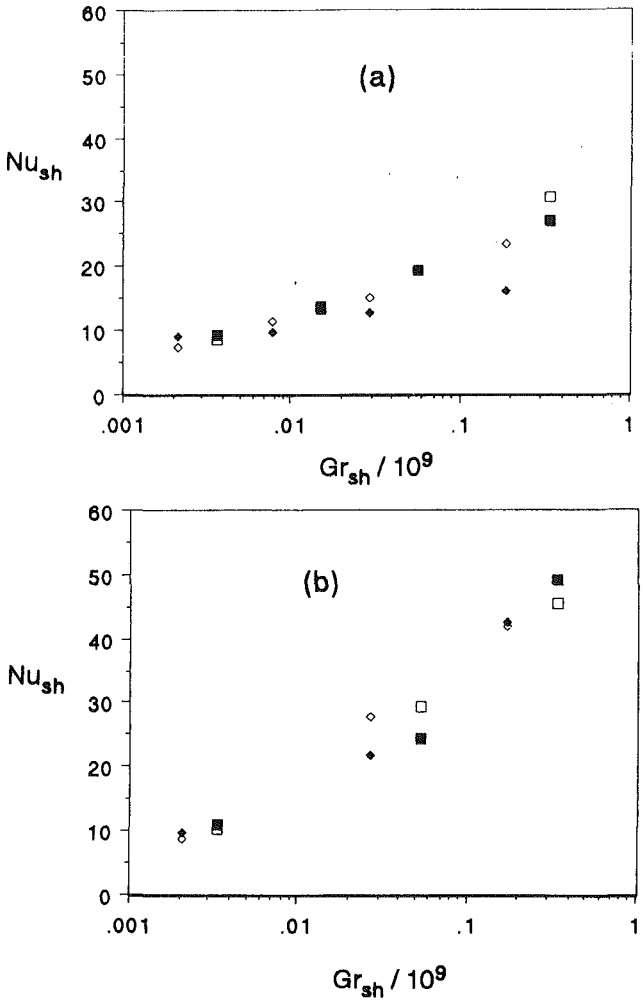

Fig. 8 Measurements of shroud Nusselt number and variation with Grashof number for tests with unheated disks and a heated shroud: (*a*) $Re_z = 0.2 \times 10^4$; (*b*) $Re_z = 8 \times 10^4$:
◇ measurements at $z = s/2$ and with $\beta\Delta T = 0.13$
♦ measurements at $z = s/3$ and with $\beta\Delta T = 0.13$
□ measurements at $z = s/2$ and with $\beta\Delta T = 0.3$
■ measurements at $z = s/3$ and with $\beta\Delta T = 0.3$

ence in gap ratios. It is of some interest to note that the LDA measurements show a decrease in the ratio ω/Ω at a Rossby number of 2. Flow visualization tests have revealed that vortex breakdown occurs at $Ro \approx 2$ and the decrease in measured values of ω/Ω may occur as a result of this.

5 Heat Transfer Measurements

To avoid disturbing the flow structure and therefore disturbing the heat transfer measurements from the shroud, heat transfer tests were not conducted at the same time as measurements of the cavity air temperature. In the heat transfer tests the air inlet temperature was kept constant at approximately 20°C. As mentioned in Section 3, two fluxmeters were installed in the shroud: one on the shroud centerline ($z = s/2$) and the other adjacent to the downstream disk ($z = s/3$). The shroud temperature was also measured at these locations, and for all tests, the temperatures were equal to within ±3°C. Results from these two different fluxmeters are shown in Fig. 8, for tests conducted out at constant axial Reynolds numbers of $Re_z = 0.2 \times 10^4$ and 8×10^4 in frames (*a*) and (*b*), respectively. The tests were conducted at a number of different rotational speeds corresponding to the range $2 \times 10^5 \le Re_\phi \le 2 \times 10^6$. Tests were also carried out for two different values of buoyancy parameter: $\beta\Delta T \approx 0.13$ and $\beta\Delta T \approx 0.3$, where $\Delta T = T_{sh} - T_i$ and $\beta = 1/T_i$. The inlet temperature T_i is also used as the reference temperature in the definition of the Grashof and Nusselt numbers. In this and subsequent figures, the Nusselt number for the shroud, Nu_{sh}, and the Grashof number, Gr_{sh}, are defined using the ratio of shroud-area to perimeter for the characteristic length, l. This choice of characteristic length for free convection from horizontal surfaces is recommended by Goldstein et al. (1973) and so $l = s/2$. The centripetal acceleration, $\Omega^2 b$, also replaces the gravitational acceleration, g, in the conventional Grashof number. The two shroud fluxmeters give similar results. But at the lower flow rate and for $Gr_{sh} > 0.01 \times 10^9$, the results from the fluxmeter adjacent to the downstream disk ($z = s/3$) are below those on the shroud centerline. This difference is also greatest at the lower value of $\beta\Delta T$ and so is consistent with the effect of using T_i rather than T_{cav} as the air reference temperature. The difference in the two measurements on the shroud could also be consistent with an axial variation of the local Nusselt numbers, i.e., they occur as a result of a developing thermal boundary layer on the shroud. There is currently insufficient data to make this a firm conclusion, and so in subsequent graphs, the average of the two fluxmeter readings is used (denoted by the subscript "av").

Figure 9 shows the variation of the average shroud Nusselt number $Nu_{sh,av}$ with Grashof number, Gr_{sh}. These results were obtained for unheated disks and for a constant flow rate of $Re_z = 8 \times 10^4$; the different symbols indicate the various thermal conditions imposed on the shroud and incoming air. In Fig. 9(*a*), the two parameters use in their definition the temperature difference $\Delta T = T_{sh} - T_i$. In Fig. 9(*b*), the estimated cavity air temperature is used and $\Delta T^* = T_{sh} - T_{cav}$, where T_{cav} is the local air temperature adjacent to the shroud. These cavity-air values are denoted by using the superscript '*', and

$$Nu^*_{sh,av} = Nu_{sh,av}/\theta_{cav}$$

$$\beta\Delta T^* = \beta\Delta T\theta_{cav},$$

and so (2)

$$Gr^*_{sh} = Gr_{sh}\theta_{cav}$$

As illustrated in Fig. 6, the precise behavior of θ_{cav} with Re_z and Re_ϕ is not yet established. Also, the measurements of heat transfer and cavity air temperature were not carried out for exactly the same range of flows and speeds. It is therefore considered appropriate, for the purpose of illustrating a point, to assume the following average values of θ_{cav}: heated disks (temperature increasing with radius) $\theta_{cav} = 0.43$; heated disks (temperature decreasing with radius) $\theta_{cav} = 0.70$; unheated disks and a heated shroud $\theta_{cav} = 0.75$.

Also shown on each figure are correlations for free convection from a *horizontal* surface, heated with a constant surface temperature, facing upward and in a gravitational field. These are as suggested by Gebhart et al. (1988) and in the current nomenclature are given by:

$$Nu_{sh,av} = qs/[2(T_{sh} - T_i)k]$$

$$= 2^{(1-3n)} C_o Pr^n Gr^n_{sh} \quad (3)$$

As previously noted, the recommended characteristic length scale is the ratio of the shroud area to perimeter, i.e., $s/2$. For the laminar regime, $2.2 \times 10^4 \le Gr_{sh}Pr \le 8 \times 10^6$, $C_o = 0.54$, and $n = 1/4$; for the turbulent regime, $8 \times 10^6 \le Gr_{sh}Pr \le 1.6 \times 10^9$, $C_o = 0.15$, and $n = 1/3$.

Inspection of Fig. 9(*a*) shows that the measured values of $Nu_{sh,av}$ are either in relatively good agreement with Eq. (3) or they lie below it; the difference depends on the air inlet temperature. For tests where the incoming air is "warm" and the

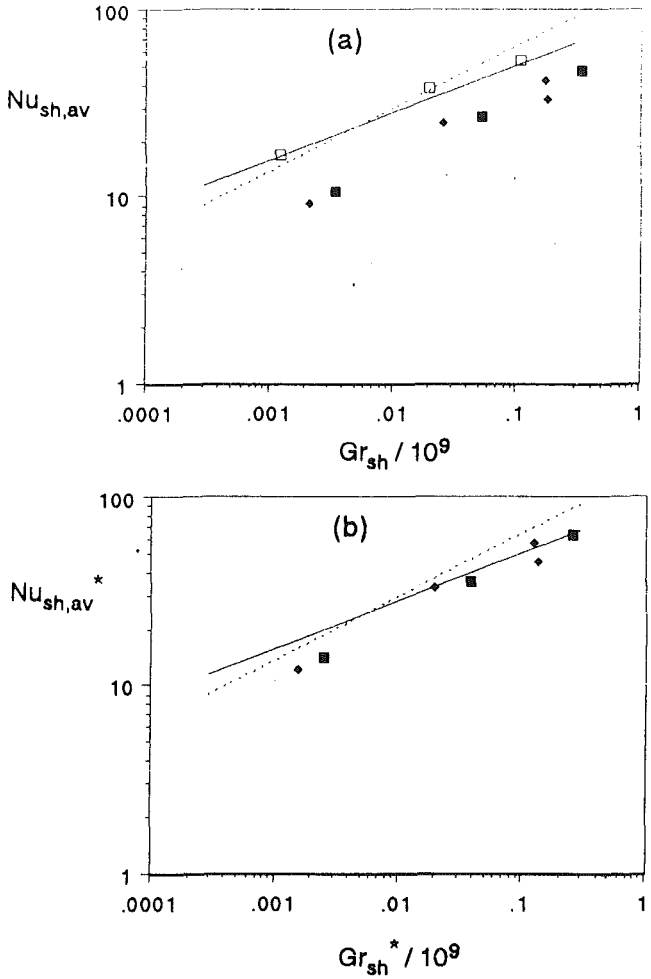

Fig. 9 Variation of shroud average Nusselt number with Grashof number for tests with unheated disks and a heated shroud at $Re_z = 8 \times 10^4$: (*a*) using air inlet temperature, T_i, for the reference temperature; (*b*) using cavity temperature, T_{cav}, for the reference temperature:
- □ hot shroud, warm air
- ♦ warm shroud, cold air
- ■ hot shroud, cold air
- — Eq. (3), laminar n = 1/4
- . . . . Eq. (3), turbulent n = 1/3

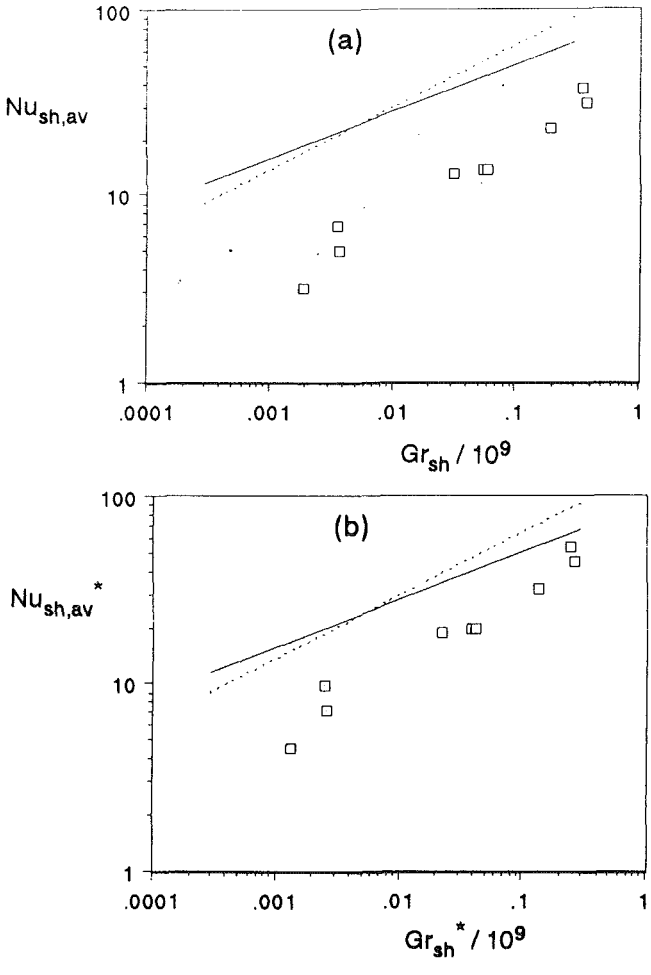

Fig. 10 Variation of shroud average Nusselt number with Grashof number for tests with heated disks having a surface temperature distribution that decreases with radius and a heated shroud at $Re_z = 8 \times 10^4$: (*a*) using air inlet temperature, T_i, for the reference temperature; (*b*) using cavity temperature, T_{cav}, for the reference temperature:
- □ experimental results
- — Eq. (3), laminar n = 1/4
- . . . . Eq. (3), turbulent n = 1/3

disks are unheated, only the shroud transfers heat to the surrounding air. Therefore T_{cav} and T_i are expected to be similar, as can be seen from Fig. 9(*a*) the Nusselt numbers lie close to either of the horizontal plate correlations.

When the incoming air is "cold" it is below the disk temperature (see Table 1), and heat transfer from the disks *and* shroud both contribute to increase the air temperature inside the cavity. The air near the shroud is warmer than at the inlet to the cavity; as a consequence this reduces the apparent value of $Nu_{sh,av}$. It is not possible to comment on the occurrence of transition from laminar to turbulent free convection for the shroud, because the range of Gr_{sh} tested is not large enough, and the curves for the two horizontal plate correlations are similar.

The data also lie in the expected transition range of Gr_{sh}. As shown in Fig. 9(*b*), when these values are defined using T_{cav}, then the results are in much better agreement with the horizontal plate correlations. Again, it is not possible to comment whether they are in better agreement with the laminar or turbulent correlation as there are insufficient data points; and over the range of Grashof numbers tested the two correlations give fairly similar results.

Figures 10 and 11 show the corresponding results for the case of when the disks are also heated. In Fig. 10, the disks have a temperature distribution that decreases with radius; in Fig. 11 the temperature distribution increases with radius. These tests were conducted at $Re_z = 8 \times 10^4$ and for the range of rotational Reynolds numbers $2 \times 10^5 \leq Re_\phi \leq 2 \times 10^6$. At a given value of Re_ϕ, tests were carried out with a constant air inlet temperature of 20°C and with different shroud and disk temperatures: T_{sh} = 60 and $T_{s,max}$ = 100°C; T_{sh} = 100 and $T_{s,max}$ = 60°C and T_{sh} = 100 and $T_{s,max}$ 100°C. The data points are clustered into groups of three, indicating the results from tests carried out at constant Re_ϕ but with these different shroud and disk temperatures. The scatter in the Nusselt numbers within each cluster is consistent with the effect expected from imposing the different shroud and disc temperatures. Comparing these (Figs. 10 and 11) figures with Fig. 9 clearly shows that heating the disks above the air inlet temperature reduces the value of $Nu_{sh,av}$. However, using the cavity air temperature can eliminate this reduction. Note that the assumed values of θ_{cav} are based on measurements taken with an *unheated* shroud, and disks heated to a maximum surface temperature of 100°C. Heating the shroud will certainly decrease θ_{cav} below that used to obtain these results. For the decreasing temperature distribution the contribution to the total (disks and shroud) cavity

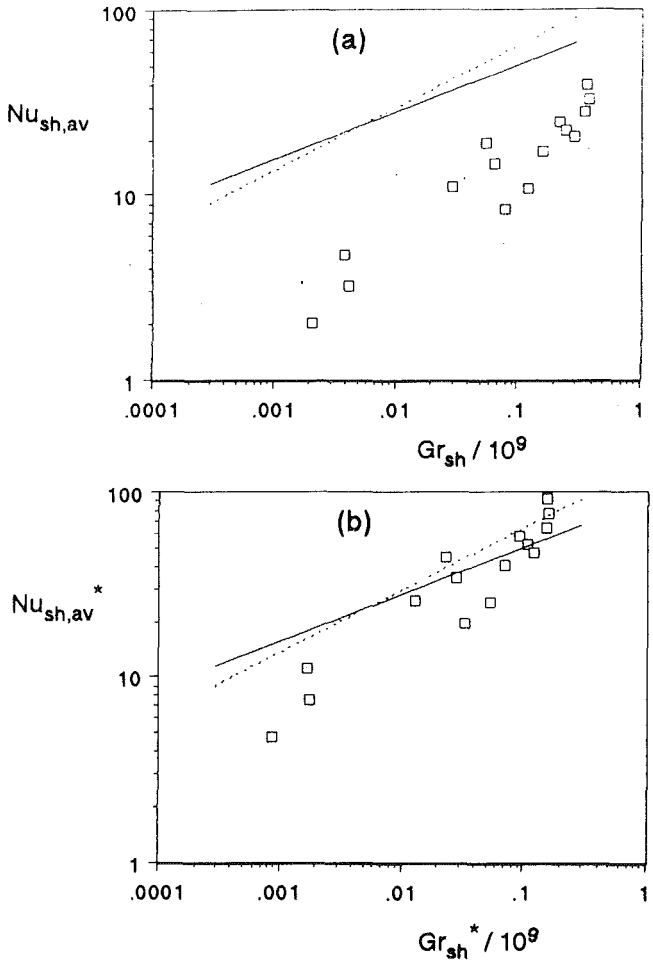

Fig. 11 Variation of shroud average Nusselt number with Grashof number for tests with heated disks having a surface temperature distribution that increases with radius and a heated shroud at $Re_z = 8 \times 10^4$: (*a*) using air inlet temperature, T_i, for the reference temperature; (*b*) using cavity temperature, T_{cav}, for the reference temperature:
□ experimental results
— Eq. (3), laminar $n = 1/4$
· · · · Eq. (3), turbulent $n = 1/3$

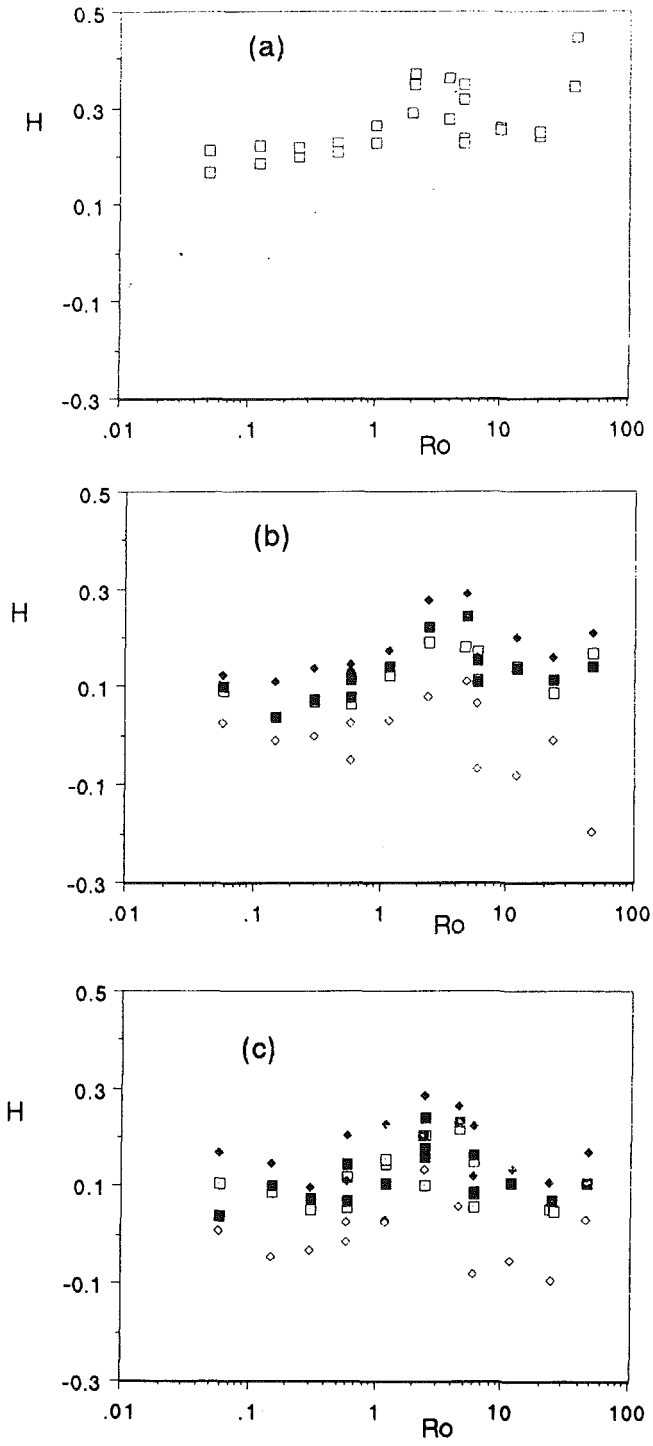

Fig. 12 Variation of free convection parameter, $H(H = Nu_{sh,av}/Gr_{sh}^{0.25})$, with Rossby number, Ro: (*a*) unheated disks and a heated shroud; (*b*) heated disks, decreasing temperature distribution, heated shroud; (*c*) heated discs increasing temperature distribution, heated shroud; legend for frames (*b*) and (*c*):

Symbol	$T_{s,max}$(°C)	T_{sh}(°C)
□	60	60
◆	60	100
■	100	100
◇	100	60

heat transfer is less than the increasing temperature distribution (see Farthing et al., 1992b), so the decrease in θ_{cav} will be even greater.

The effect of the Rossby number on the heat transfer from the shroud is shown in Fig. 12. The results shown here were obtained from tests conducted in the range $2 \times 10^3 \leq Re_z \leq 16 \times 10^4$ and $2 \times 10^5 \leq Re_\phi \leq 2 \times 10^6$. The laminar free convection parameter, H, is defined as $Nu_{sh,av}/Gr_{sh}^{0.25}$. A constant value of this parameter is consistent with the heat transfer being caused by laminar free convection. A significant increase is presumably an enhancement due to forced convection. For the tests with a heated shroud and unheated disks, Fig. 12(*a*) shows there is a significant increase in H in the regions $2 \leq Ro \leq 4$ and $Ro \geq 20$. The first of these corresponds to a region where vortex breakdown has been observed. In the second region, the Rossby number may be sufficiently large for the central throughflow to directly affect the shroud heat transfer. This increase in H is also seen in the same regions of Rossby number when the disks are heated: Fig. 12(*b*) for the decreasing temperature distribution and Fig. 12(*c*) for the temperature distribution that increases with radius.

The effect of heating the disks on the heat transfer from the shroud is also shown in Fig. 12. In general, the larger the numerical value of $(T_{s,max} - T_{sh})$ the smaller the value of $Nu_{sh,av}$ (defined here using T_i and not T_{cav}). Since increasing this parameter also affects the total (disks and shroud) heat transfer in the cavity it will also affect T_{cav}. As shown, when $T_{s,max} \gg T_{sh}$, H can be negative and heat is actually transferred *into* the

shroud. Conversely, when $(T_{s,\max} - T_{sh})$ is negative, heat is always transferred *from* the shroud. Although no measurements of T_{cav} were made for all these tests, it is expected that this apparent variation of Nu_{sh} will vanish and the variation of Nu^*_{sh} with Gr^*_{sh} would then be consistent with the horizontal plate correlations.

Although not explicitly reported on in this paper, measurements were also made of the heat transfer from the disk surfaces. It is expected that these will be discussed along with other aspects of the work in a future paper. But it is considered appropriate to note here that heating the shroud does not appear significantly to affect the heat transfer from the disks.

6 Conclusions

Tests were carried out on a rotating cavity comprising two disks of radius $b = 0.4845$ m bounded at the circumference by a carbon fiber shroud. Experiments were conducted for the range of parameters: $\beta\Delta T \le 0.3$; $2 \times 10^3 \le Re_z \le 16 \times 10^4$ and $2 \times 10^5 \le Re_\phi \le 2 \times 10^6$; the cavity gap ratio, $G = s/b$, and inlet radius ratio, a/b, remained constant ($G = 0.13$ and $a/b = 0.1$). Different thermal conditions were investigated: heated disks and shroud or unheated disks and a heated shroud. For heated disks, two different disk surface temperature distributions were tested: The temperature either increased or decreased with increasing radius.

Measurements were made of the air temperature inside the cavity by three thermocouple probes located on a diameter halfway between the two disks (at $z = s/2$).

The shroud heat transfer was measured using two thermopile fluxmeters located on the inside surface of the peripheral shroud at $z = s/2$ and $z = s/3$.

The temperatures inside the cavity are strongly affected by the disk surface temperature distribution. For the air adjacent to the shroud, there appears to be no systematic variation of nondimensional cavity air temperature, θ_{cav} with Re_z or Re_ϕ. There also does not appear to be any *systematic* variation of the temperature parameter with the Rossby number, Ro.

The following average values of θ_{cav} are taken as being representative: heated disks (temperature increasing with radius) $\theta_{cav} = 0.43$; heated disks (temperature decreasing with radius) $\theta_{cav} = 0.70$; unheated disks and a heated shroud $\theta_{cav} = 0.75$.

For heated disks with an increasing surface temperature distribution, the three thermocouples recorded similar values of the circumferential variation of cavity air temperature. The circumferential variation is usually in the range 5 to 10°C, which is significantly less than the temperature difference between cavity air and inlet air. The magnitude is reduced when the disks have a temperature distribution that decreases with radius. Accurate measurements were not obtained for the case of unheated disks and a heated shroud.

The circumferential variations of air temperature were also used to estimate the tangential velocity of the fluid inside the cavity. Considering the simple method used to obtain these measurements, the results are in good agreement with previously published LDA measurements.

Although there are some differences, the two shroud fluxmeters give broadly similar results. The disk surface temperature distribution appears to have little affect on the shroud heat transfer, providing the cavity air temperature is used as a reference temperature to define the Nusselt and Grashof numbers. The shroud heat transfer is then in reasonable accord with an established correlation for free convection from a horizontal surface: $Nu_{sh} = 2^{(1-3n)}\, C_o Pr^n Gr^n_{sh}$. The recommended characteristic length scale is the ratio of the shroud area to perimeter, i.e., $s/2$. For the laminar regime $C_o = 0.54$ and $n = 1/4$; for the turbulent regime $C_o = 0.15$ and $n = 1/3$. It is not possible to comment on the occurrence of transition from laminar to turbulent free convection for the shroud, because the range of Gr_{sh} tested is not large enough, and the curves for the two horizontal plate correlations are similar. The data also lie in the expected transition range of Gr_{sh}.

There appears to be an effect of the Rossby number on the heat transfer from the shroud. A significant enhancement to the rotationally induced free convection occurs in the regions $2 \le Ro \le 4$ and $Ro \ge 20$. The first of these corresponds to a region where vortex breakdown has been observed. In the second region, the Rossby number may be sufficiently large for the central throughflow to affect the shroud heat transfer directly.

The disk temperature can appear to affect the shroud heat transfer; the larger the value of $T_{s,\max} - T_{sh}$, the smaller the value of Nu_{sh}; attributed to using T_i, rather than T_{cav} for the reference temperature. It is also noted that heating the shroud does not appear significantly to affect the heat transfer from the disks.

The results presented in this paper for $G = 0.13$ suggest that an established correlation for free convection from horizontal surfaces can be used to predict the shroud heat transfer in a rotating cavity with an axial throughflow of cooling air. Further work with a larger gap ratio is currently being carried out to investigate the validity of this conclusion and it is hoped to report on this at a future date.

References

Farthing, P. R., 1988, "The Effect of Geometry on Flow and Heat Transfer in a Rotating Cavity," D. Phil. Thesis, School of Engineering and Applied Sciences, University of Sussex, United Kingdom.

Farthing, P. R., Long, C. A., Owen, J. M., and Pincombe, J. R., 1992a, "Rotating Cavity With Axial Throughflow of Cooling Air: Flow Structure," ASME Journal of Turbomachinery, Vol. 114, pp. 237–246.

Farthing, P. R., Long, C. A., Owen, J. M., and Pincombe, J. R., 1992b, "Rotating Cavity With Axial Throughflow of Cooling Air: Heat Transfer," ASME Journal of Turbomachinery, Vol. 114, pp. 229–236.

Gebhart, D., Jaluria, Y., Mahajan, R. L., and Sammakia, B., 1988, *Buoyancy-Induced Flows and Transport*, Hemisphere Publishing Corporation, New York, p. 227.

Goldstein, R. J., Sparrow, E. M., and Jones, D. C., 1973, "Natural Convection Mass Transfer Adjacent to Horizontal Plates," *Int. J. Heat Mass Transfer*, Vol. 16, p. 1025.

Long, C. A., 1991, "A Calibration Technique for Thermopile Heat-Flux Gauges," *Proceedings of Sensor 91 Conference*, Nuremberg, Germany, Vol. IV, Paper No. B12.2, pp. 247–262.

Owen, J. M., Pincombe, J. R., and Rogers, R. H., 1985, "Source-Sink Flow in a Rotating Cylindrical Cavity," *J. Fluid Mech.*, Vol. 155, pp. 233–265.

Schlichting, H., 1979, *Boundary-Layer Theory*, 7th ed., McGraw-Hill, New York, Fig. 12.18.

Measurement of Compressible Flow Pressure Losses in Wye-Junctions

N. I. Abou-Haidar[1]
Department of Engineering,
University of Leicester,
Leicester, United Kingdom

S. L. Dixon
Department of Mechanical Engineering,
The University of Liverpool,
Liverpool, United Kingdom

This paper considers the compressible flow pressure losses in sharp-cornered wye-junctions with symmetric branches under dividing and combining flow conditions. Determination of the additional total pressure losses occurring in flow through several three-leg junctions, using dry air as the working fluid, has been made experimentally. Results covering a wide speed range up to choking are presented for 30, 60, and 90 deg wye-junctions. Separate flow visualization schlieren tests detected the presence of normal shock waves, located at up to one duct diameter downstream of the junction, and therefore confirmed the choking of the flow at the vena contracta. The highest attainable Mach number (M_3) of the averaged whole flow was 0.9 for one of the dividing flow geometries and 0.65 for several of the combining flow cases. These values of M_3 were the maximum possible and hence represent a limiting condition dictated by choking. In general, the compressible flow loss coefficients, caused by the presence of the wye-junctions, can be expected to be higher for dividing flows and lower for combining flows than would be the case for incompressible flows because of the influence of Mach number, M_3.

Introduction

The data currently available on total pressure losses resulting from dividing or combining of flows in wye-junctions are mainly confined to low-speed incompressible flows. The amount of information available relating to high-speed, compressible flows ($M_3 \geq 0.2$) is restricted to few basic geometries such as the tee-junction and for a limited range of Mach numbers. Recent developments in the design of internal air systems of large turbo-jet engines such as the Rolls-Royce RB211, require accurate data for the junction losses at high-speed flows, in order to allow the network losses to be determined confidently. Without these data, engine designers have had to rely on extrapolations based upon incompressible junction loss data. Rolls-Royce (1986) and Jeal (1988) state that up to 20 percent of the total engine core mass air flow may pass into the internal air system for various purposes and some account of the overall total pressure losses (i.e., additional to those arising from simple skin friction in a straight duct) is of importance in determining the overall engine efficiency.

Previous investigations of symmetric wye-junction losses have been carried out by Oki et al. (1951), Marchetti and Noseda (1960), Gardel and Rechsteiner (1970), and Ito and Imai (1973). Probably the most comprehensive and recognized data are those of Miller (1971, 1978) and the compilation of data by ESDU (1973). All of these data relate to incompressible flow losses only. No significant data on the additional total pressure losses could be found for compressible flow.

The present investigation is part of an experimental program initiated by Rolls-Royce Plc, Derby. This paper deals primarily with the determination of the additional total pressure losses of dividing and combining flows in sharp-cornered wye-junctions over a wide range of subsonic Mach numbers. Comparison between measured results and other experimental data obtained by earlier researchers, for incompressible flow ($M_3 \leq 0.2$ and $10^5 \leq Re_3 \leq 2 \times 10^5$) tests, are presented. The findings of separate flow visualization schlieren tests, used to detect the presence of normal shock waves and to indicate the extent of any separation regions at high-speed flows, are also included. Previous papers by the same authors, Abou-Haidar and Dixon (1988, 1992), reported the results of an experimental, analytical, and flow visualization study of other junction geometries. A comprehensive summary of the complete research program is available from Abou-Haidar (1989).

Flow Modeling

The BIHARMCC code, developed by Johnson (1988), was used by the authors to model the flow at a tee-junction. In Figs. 1 and 2, the streamline patterns and velocity field of a two-dimensional flow model for one type of dividing flow geometry, $q = 0.75$, are shown. The code employs the stream function vorticity method but is suitable only for modeling two-dimensional, viscid, steady, incompressible flows. Upstream of the junction the flow is assumed to be fully developed but downstream of the junction the flow is characterized by two large separation regions, which are the main source of the additional total pressure losses. It is, of course, the momentum

[1]Present address: Senior Lecturer, Department of Mechanical and Manufacturing Engineering, University of Brighton, Brighton BN2 4GJ, United Kingdom.

Contributed by the International Gas Turbine Institute and presented at the 37th International Gas Turbine and Aeroengine Congress and Exposition, Cologne, Germany, June 1-4, 1992. Manuscript received by the International Gas Turbine Institute February 14, 1992. Paper No. 92-GT-71. Associate Technical Editor: L. S. Langston.

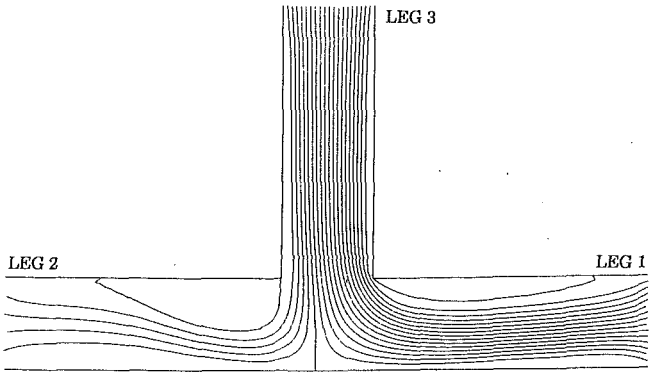

Fig. 1 Streamline contours for a dividing flow geometry at $q = 0.75$

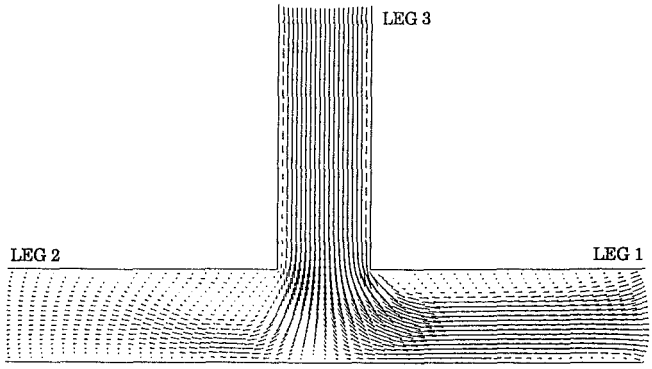

Fig. 2 Velocity field for a dividing flow geometry at $q = 0.75$

of the flow in the upstream duct that causes the fluid to separate as it enters the downstream branches, thus leaving behind two separated regions of lower "stagnation" pressure and recirculating flows within them, as illustrated in Fig. 2. The size of these regions appears to be dependent on the geometry of the junction, sharpness of the duct intersections, mass flow ratio (q), and magnitude of M_3.

The total pressure losses in the flow through any junction are composed of frictional losses and "additional" losses. Whereas the former loss is usually considered to be uniformly distributed along each leg, the latter appears as a result of flow separation and mixing processes. The frictional losses, in the leg upstream of the junction, can be easily determined from the pressure gradient. In this paper the main causes of the additional total pressure losses are attributed to the effects of the contraction and following sudden expansion caused by the presence of the adjacent separation region. The flow mixing downstream of the junction must produce eddies and therefore a loss in total pressure. Additionally, in high-speed flow the

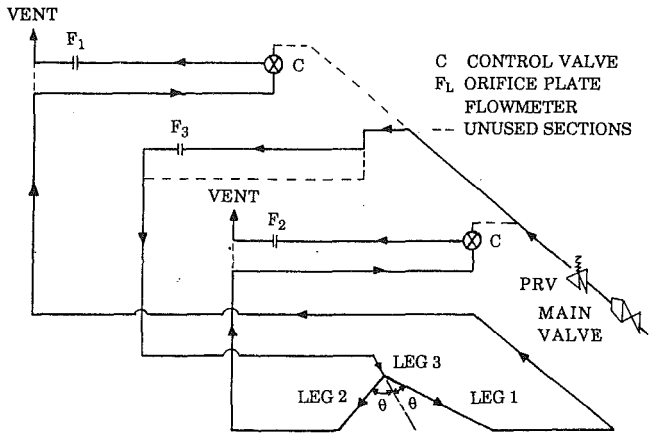

Fig. 3 Test plant layout for dividing flows

presence of secondary flow motion, shock waves, flow entrainment, and expulsion across the boundary of the separation region and skin friction stresses due to localized flow disturbances are likely to contribute to the additional losses.

Test Plant and Instrumentation

In Fig. 3, a simple schematic diagram of the test plant is depicted. Compressed air was supplied via the main pressure reducing valve (PRV) at about 0.8 MPa. The required test conditions were for steady dividing and combining flows of dry air up to $0.2 \leq M_3 \leq 1.0$ and $Re_3 \geq 2 \times 10^5$ and based on a duct diameter of 4.04 cm. As shown in Fig. 3, control valves in each section enabled any appropriate combination of flow geometries and mass flow ratios to be achieved. Specially manufactured orifice plate flowmeters conforming to British Standard 1042 (1987) were used to measure the mass flow rate in each leg. Calibrated shielded thermocouple probes were installed within the test sections in order to measure the local air temperatures. Further details regarding the air supply equipment manufacture, etc., are available from Abou-Haidar (1989).

The junctions examined were all circular in cross section, and covered a selection of straight-through duct with wye branches. The semi-angle between the main duct axis and the wye-branch ranged between 30 to 90 deg, in 30 deg increments, as shown in Fig. 3. All ducts were of equal diameter with coplanar axes and sharp intersections. A flow straightener followed by an area reducing duct well upstream of the junction ensured that the flow entering the test section was fairly uniform. A straight length of $15D$ separated the reducer and the first pressure measurement point on each leg. The pressure drop along each test section was monitored at six different static pressure locations, evenly distributed along each leg up

Nomenclature

A_R = aspect ratio = d/D
d = depth of branch
D = pipe diameter or breadth of branch
g = gravitational acceleration
h = potential head
K = additional overall total pressure loss coefficient
K_{13} = additional total pressure loss coefficient between legs 1 and 3 for combining flows
K_{23} = additional total pressure loss coefficient between legs 2 and 3 for combining flows
K_{31} = additional total pressure loss coefficient between legs 3 and 1 for dividing flows
K_{32} = additional total pressure loss coefficient between legs 3 and 2 for dividing flows
m = mass flow rate
M = Mach number
p = static pressure
P = total pressure
q = mass flow ratio = m_1/m_3
Re = Reynolds number
$\bar{V}$ = average velocity
θ = semi-angle between the main duct axis and the wye branch
ρ = mass density of the fluid

Subscripts

e = extrapolated value of pressure at the geometric center of the junction
L = referring to leg L (1, 2, or 3)
1 = leg carrying the branch flow
2 = leg carrying the branch flow
3 = leg carrying the whole flow

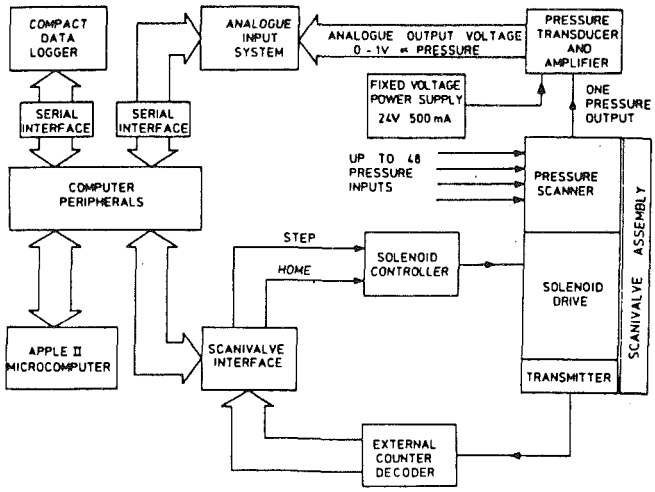

Fig. 4 Instrumentation layout

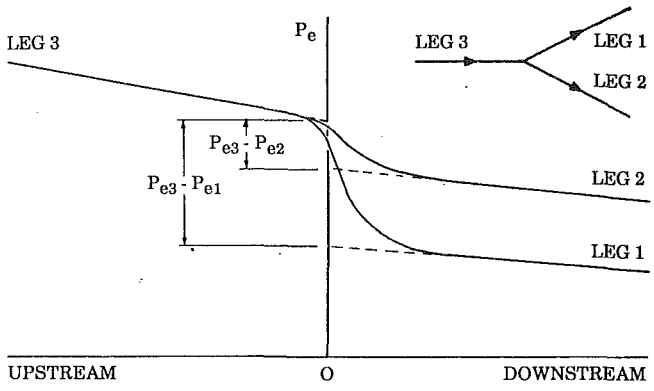

Fig. 5 Extrapolated additional total pressure junction loss between legs 3 and 1 and legs 3 and 2 for a dividing flow geometry

to 65 cm from the junction center. Each location measured the average static pressure by means of a piezometer ring connected to four evenly displaced pressure tappings around the duct.

The instrumentation system used, shown schematically in Fig. 4, comprises of the following: a 48-port high-speed scanivalve, a pressure transducer, an AI13 analogue to digital device, a compact (temperature) data logger, and an Apple II computer. The system enabled fast and accurate readings of the flowmeters and test sections to be made. Each test lasted for about one minute and was comprised of 30 different pressure and temperature measurements. A computer program controlled the sequence of operation of various testing equipment and performed the required calculations in order to reduce the data to the required form.

Test Results

The "traditional" method used to evaluate the junction flow loss coefficients K_{31} and K_{32} for uniformly dividing steady flows (Fig. 2), is by the use of simple flow loss terms in the energy equation, namely:

Incompressible Flow

$$\frac{p_{e3}}{\rho g}+\frac{(\overline{V}_3)^2}{2g}+h_3=\frac{p_{e1}}{\rho g}+\frac{(\overline{V}_1)^2}{2g}+h_1+K_{31}\frac{(\overline{V}_3)^2}{2g} \tag{1}$$

and

$$\frac{p_{e3}}{\rho g}+\frac{(\overline{V}_3)^2}{2g}+h_3=\frac{p_{e2}}{\rho g}+\frac{(\overline{V}_2)^2}{2g}+h_2+K_{32}\frac{(\overline{V}_3)^2}{2g} \tag{2}$$

Equations (1) and (2) refer to the additional losses caused by the presence of the junction only, i.e., no friction losses are included. The first term on both sides of the two previous equations is the static pressure head, the second term is the velocity head, and the third term is the potential head. The further terms on the right-hand sides are the losses due to the junction, K_{31} for the flow dividing into branch 1 and K_{32} for the flow dividing into branch 2. Both loss terms are based upon the approach bulk velocity $\overline{V}_3$.

The third term (h_L) on both sides of Eqs. (1) and (2) can be eliminated since the wye-junction layout is horizontal. Furthermore, multiplying both sides of Eqs. (1) and (2) by ρg, simplifying, and solving for K_{31} and K_{32} gives:

$$K_{31}=\frac{P_{e3}-P_{e1}}{\frac{1}{2}\rho(\overline{V}_3)^2} \tag{3}$$

and

$$K_{32}=\frac{P_{e3}-P_{e2}}{\frac{1}{2}\rho(\overline{V}_3)^2} \tag{4}$$

Compressible Flow. P_{eL}, which is determined from the knowledge of p_{eL} (for air) is given by:

$$P_{eL}=p_{eL}(1+0.2\mathrm{M}_L^2)^{3.5} \tag{5}$$

The dynamic pressure is defined as the difference between total (stagnation) and static pressure and hence is given as:

$$\frac{1}{2}\rho(\overline{V}_3)^2=P_{e3}-p_{e3} \tag{6}$$

Eliminating the term $\frac{1}{2}\rho(\overline{V}_3)^2$ from Eqs. (3) and (6) gives:

$$K_{31}=\frac{P_{e3}-P_{e1}}{P_{e3}-p_{e3}} \tag{7}$$

and

$$K_{32}=\frac{P_{e3}-P_{e2}}{P_{e3}-p_{e3}} \tag{8}$$

The overall loss coefficient K is defined as:

$$K=qK_{31}+(1-q)K_{32} \tag{9}$$

The extrapolated additional total pressure losses for one type of dividing flow geometry are sketched in Fig. 5. The same procedure as above is applied in order to determine the combining flow loss coefficients, K_{13} and K_{23}.

The results reported in this paper cover wye-junctions with θ = 30, 60, and 90 deg. The additional total pressure coefficients K_{31} for dividing flow geometries and K_{13} for combining flow geometries are represented as functions of Mach number, M_3, for mass flow ratios, q = 0, 0.25, 0.50, 0.75, and 1.0. Results for K_{32} and K_{23} were omitted since they are identical to K_{31} and K_{13}, respectively. The compressible flow results are presented in graphic form, as performance charts, in Figs. 6–11.

Discussion of Results

Compressible Flow ($M_3 \geq 0.2$ and $Re_3 \geq 2 \times 10^5$). The results for flows dividing into 30, 60, and 90 deg wye branches are shown in Figs. 6–8. The results show a fairly slow growth in K_{31} for the majority of the mass flow ratios considered. For θ = 30 and 60 deg, the increase in the loss coefficient K_{31} was more noticeable for values of Mach number higher than 0.6. The highest value of Mach number reached was 0.9 for θ = 30 deg at q = 0.50. The range of variation was appreciable. For θ = 30, 60, and 90 deg at q = 1 and M_3 = 0.2, K_{31} = 0.17, 0.57, and 1.36, respectively. The sharpest K_{31} increase

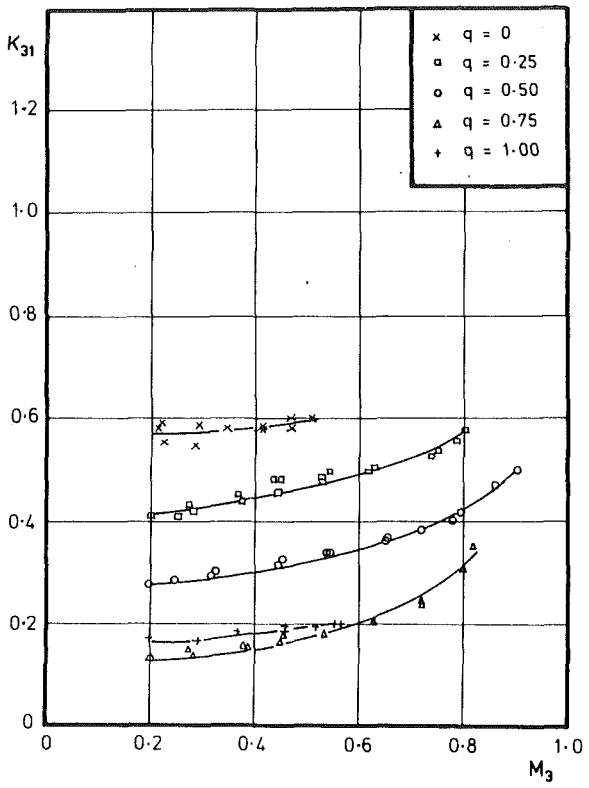

Fig. 6 Compressible flow loss coefficient K_{31} for dividing flow geometry $\theta = 30$ deg (uncertainty in $K_{31} = \pm 0.041$, in $M_3 = \pm 0.012$, in $q = 0.025$)

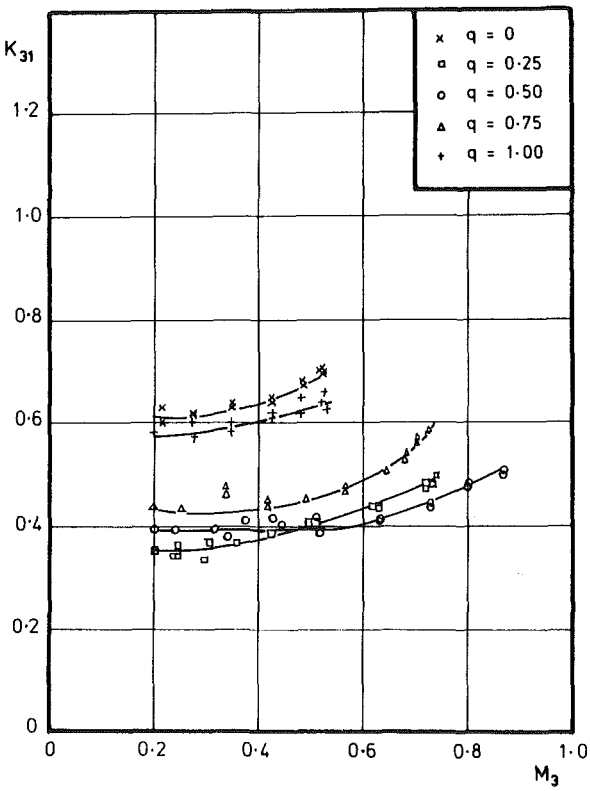

Fig. 7 Compressible flow loss coefficient K_{31} for dividing flow geometry $\theta = 60$ deg (uncertainty in $K_{31} = \pm 0.041$, in $M_3 = \pm 0.012$, in $q = 0.025$)

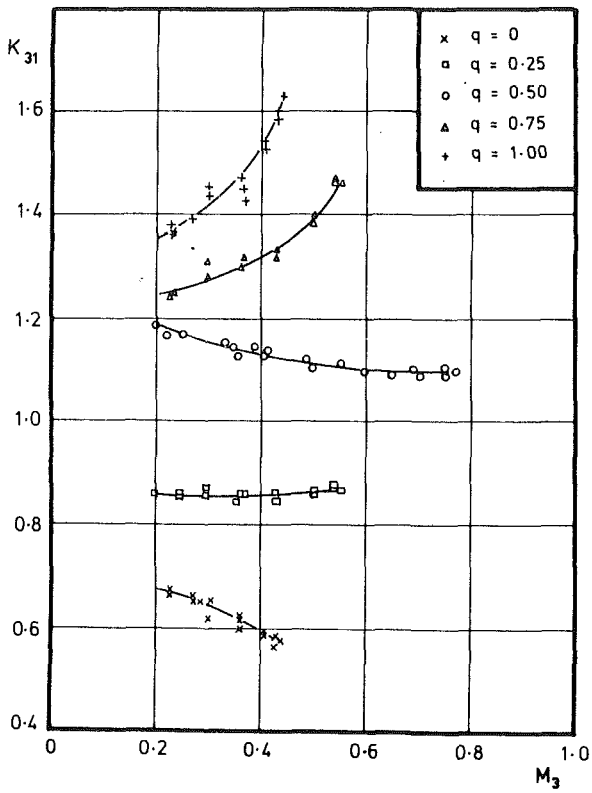

Fig. 8 Compressible flow loss coefficient K_{31} for dividing flow geometry $\theta = 90$ deg (uncertainty in $K_{31} = \pm 0.041$, in $M_3 = \pm 0.012$, in $q = 0.025$)

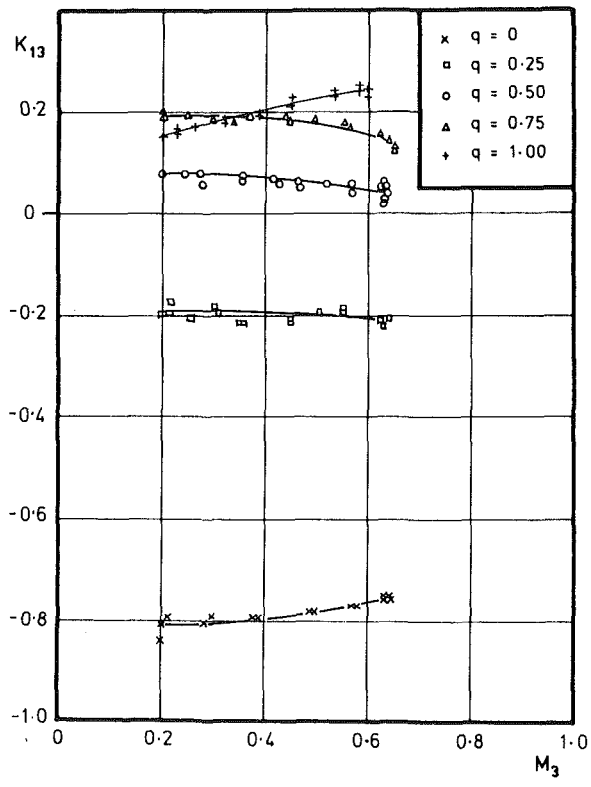

Fig. 9 Compressible flow loss coefficient K_{13} for combining flow geometry $\theta = 30$ deg (uncertainty in $K_{13} = \pm 0.031$, in $M_3 = \pm 0.012$, in $q = 0.025$)

of 20 percent occurred in the 90 deg wye-junction flow configuration at $q \geq 0.75$. For $M_3 = 0.2$, the overall loss coefficient (K) results for $\theta = 90$ deg can be about 8 times higher in value than those for $\theta = 30$ deg at $q = 1$, i.e., $K = K_{31}$.

The loss coefficient K_{13} results for flows combining from 30, 60, and 90 deg wye-branches are shown in Figs. 9–11. While the decline in the loss coefficient was fairly slow over most of the range of K_{13} for $\theta = 30$ and 60 deg, it was more

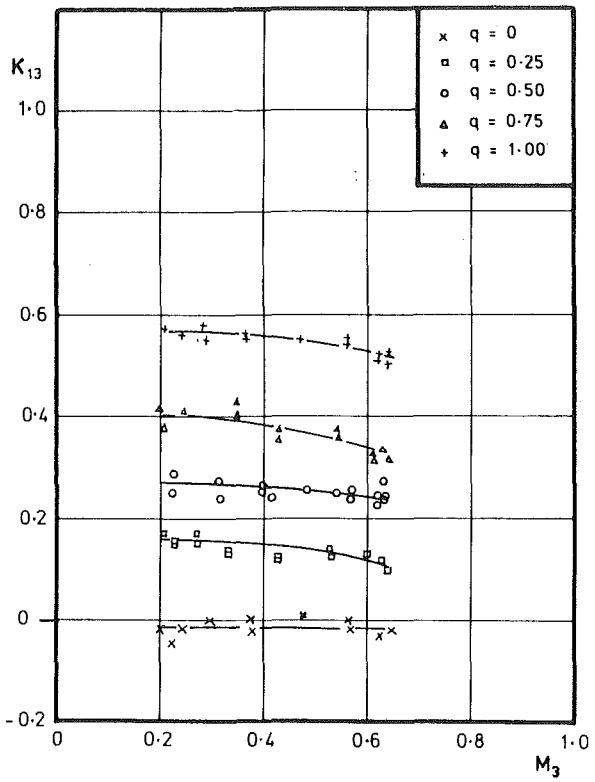

Fig. 10 Compressible flow loss coefficient K_{13} for combining flow geometry θ = 60 deg (uncertainty in K_{13} = ±0.031, in M_3 = ±0.012, in q = 0.025)

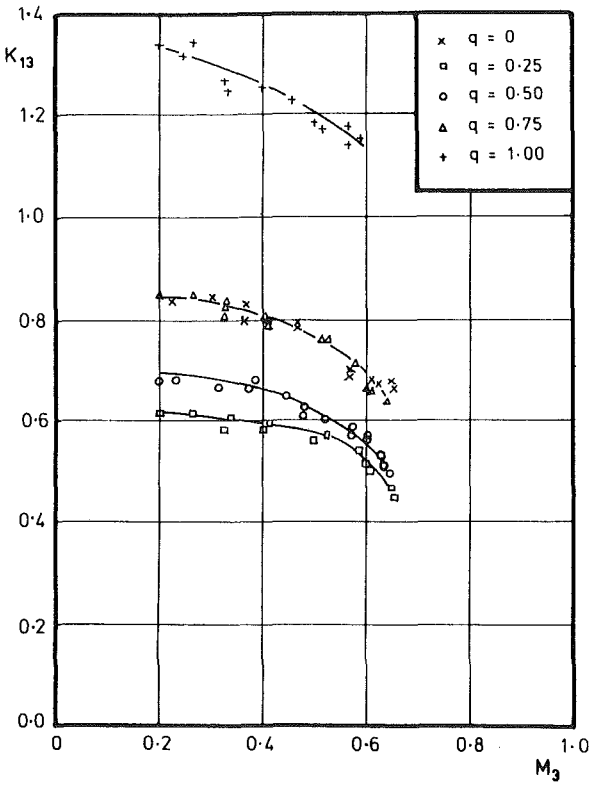

Fig. 11 Compressible flow loss coefficient K_{13} for combining flow geometry θ = 90 deg (uncertainty in K_{13} = ±0.031, in M_3 = ±0.012, in q = 0.025)

significant for θ = 90 deg over the range of Mach number, M_3. The range of variation was noticeable. For θ = 30, 60, and 90 deg at q = 1 and M_3 = 0.2, K_{13} = 0.16, 0.57, and

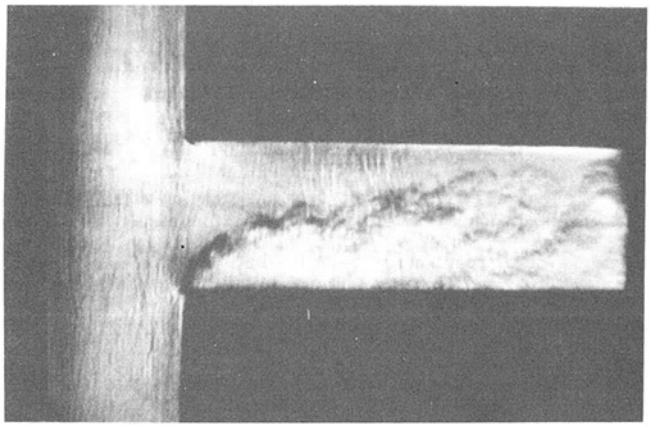

Fig. 12 Schlieren photograph showing successive normal shock waves at about one duct width downstream of the junction. M_3 = 0.61, q = 1, A_R = 2, and flow is combining from left to right.

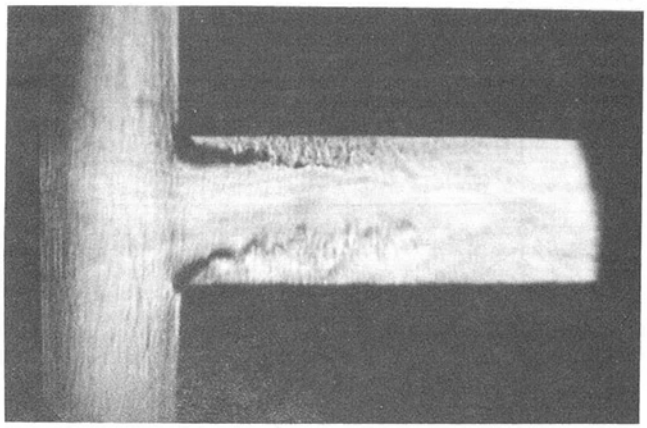

Fig. 13 Schlieren photograph showing two faint normal shock waves at about 0.5 duct width downstream of the junction and two approximately symmetric acoustic cell patterns with either source located in the vicinity of the two opposite corners. M_3 = 0.66, q = 0.5, A_R = 2, and flow is combining from left to right.

1.33, respectively, almost identical to the same dividing flow cases. The largest drop in K_{13} of about 0.2 occurred in 90 deg wye-junction flow configuration at all mass flow ratios (q) considered. For M_3 = 0.2, the overall loss coefficient (K) results for θ = 90 deg can be about 8 times higher in value than those for θ = 30 deg at q = 1, i.e., $K = K_{13}$.

In Figs. 6–11, it is evident that loss coefficients for $M_3 > 0.9$ could not be obtained despite adequate pressure being available upstream. The results for K_{31} were determined over the range $0.2 \leq M_3 \leq 0.9$, while the results for K_{13} were determined over the range $0.2 \leq M_3 \leq 0.65$. In both cases, the upper limit of M_3 effectively represented the choking limit. Furthermore, by increasing the upstream pressure still further, the loss coefficients increased rapidly at almost constant M_3 for all geometries considered, i.e., typical of choking. All experimentally determined values for loss coefficients (Figs. 6–11) were in every case limited by the last data obtained before a sharp increase occurred at constant Mach number, M_3. In other words, once the sonic velocity is approached at the vena contracta of the downstream branch, every additional increase in the extrapolated total pressure ratio would be accompanied by an increase in the loss coefficients and with no increase in M_3.

Separate flow visualization schlieren tests, carried out on a 90 deg wye-junction, confirmed that sonic conditions were reached in the duct at high-speed flows. Figures 12 and 13 show schlieren pictures of the "combined" flow in the down-

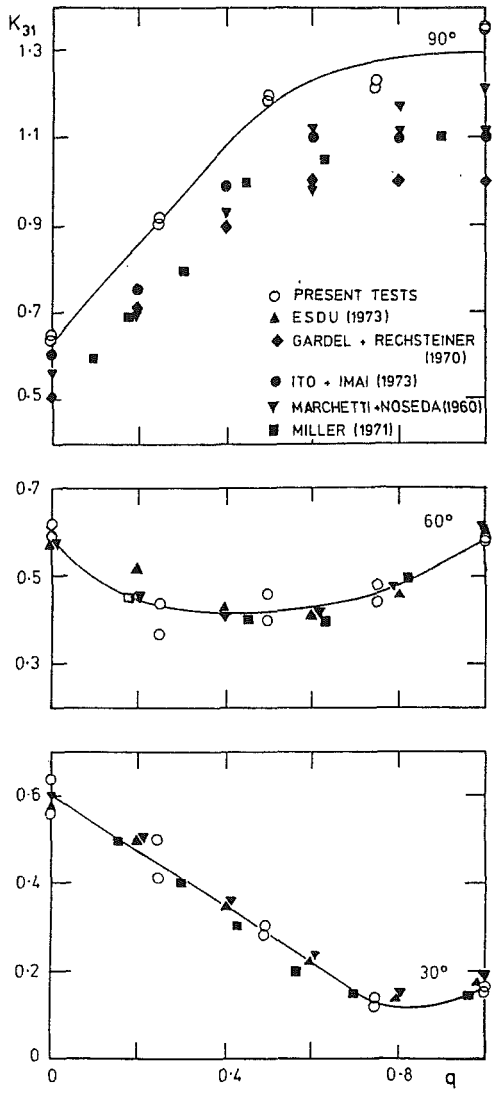

Fig. 14 Incompressible flow loss coefficient K_{31} for dividing flow geometries θ = 30, 60, and 90 deg compared with data obtained from various sources (uncertainty in K_{31} = ±0.031, in q = 0.025)

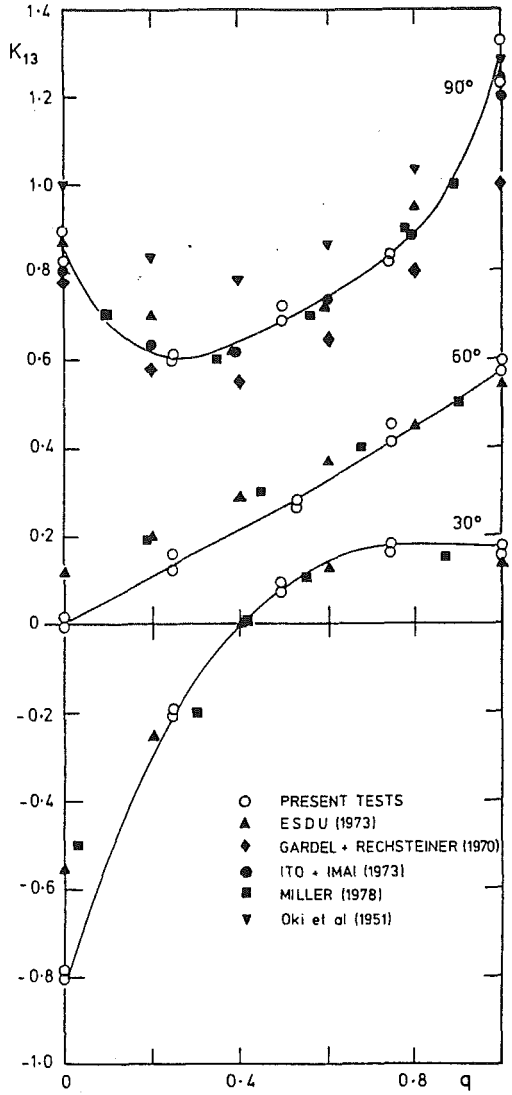

Fig. 15 Incompressible flow loss coefficient K_{13} for combining flow geometries θ = 30, 60, and 90 deg compared with data obtained from various sources (uncertainty in K_{13} = ±0.029, in q = 0.025)

stream (main) duct of the wye-junction for $M_3 = 0.61$ at $q = 1$ and $M_3 = 0.66$ at $q = 0.5$, respectively. In both photographs the distinct thick dark curve commencing at the duct intersections corresponds to the boundary between the two flow regions. After about one duct width downstream this dark line has broadened into a region of flow mixing. Careful examination of Fig. 12 reveals the presence of successive weak shock waves. These would appear as lines of increased illumination, located at about one duct width downstream of the main duct entrance. Also, Fig. 13 reveals the presence of two "faint" shock waves, located at about half a duct width downstream of the main duct entrance. Moreover, the formations of two approximately symmetric acoustic cell patterns with their sources located in the vicinity of the two opposite corners are noticeable in Fig. 13. This phenomenon has been thoroughly detailed in the work of Davies and Oldfield (1962) and Davies (1964).

Incompressible Flow ($M_3 \leq 0.2$ and $10^5 \leq Re_3 \leq 2 \times 10^5$). In Figs. 14 and 15 the results measured at $M_3 = 0.2$ are compared with experimental data obtained by other researchers for dividing and combining flow geometries in wye-junctions with symmetric branches at semi-angles θ = 30, 60, and 90 deg with respect to the main duct. In Fig. 14, the dividing flow results for K_{31} at 30 and 60 deg show excellent agreement with those of Marchetti and Noseda (1960), Miller (1971), and ESDU (1973). At θ = 90 deg, the results for K_{31} are generally higher than the rest over the range $0 \leq q \leq 1$, but still show the same trend. The maximum difference between the present results and the average scatter of those obtained by other investigators is about 22 percent at $q > 0.75$.

In Fig. 15, the combining flow results for K_{13} at θ = 30 deg show excellent agreement with those of ESDU (1973) and Miller (1978), especially at $q > 0.25$. At θ = 60 deg, the results for K_{13} are generally lower than the rest over the range of $0 \leq q \leq 0.7$, but in close agreement at $q > 0.7$. The K_{13} results for θ = 90 deg are in excellent agreement with those of Gardel and Rechsteiner (1970), ESDU (1973), Ito and Imai (1973), and Miller (1978).

Conclusions

The important conclusions regarding the additional total pressure loss coefficients and flow characteristics in 30, 60, and 90 deg sharp-cornered wye-junctions reported here are summarized as follows:

1 The maximum Mach numbers M_3 of the whole flow for the dividing and combining flow geometries were 0.9 and 0.65, respectively, at a limit dictated by a combination of choking and flow separation in the downstream branch(es) of the junction.
2 Separate flow visualization schlieren tests detected the presence of normal shock waves, located at about 0.5 to 1.0 duct width downstream of the junction at high speed flows, and therefore confirmed the choking of the flow at the vena contracta.
3 In general, the compressible flow loss coefficients, caused by the presence of a wye-junction, can be expected to be higher for dividing flow geometries and lower for combining flow geometries than would be the case for incompressible flows because of the influence of Mach number, M_3.
4 Loss coefficients K_{31} and K_{13} diminish with decreasing angle of bifurcation (2θ) for both dividing and combining flow geometries.
5 For $\theta = 30$, 60, and 90 deg, at $q = 1$ and $M_3 = 0.2$, K_{31} for dividing flows and K_{13} for combining flows have almost identical values.
6 The results obtained at low Mach number were in good agreement with the experimental results of other researchers.
7 For both dividing and combining flows the overall loss coefficient (K) results for $\theta = 90$ deg can be about 8 times higher in value than those for $\theta = 30$ deg at $q = 1$.

Acknowledgments

The manuscript has been prepared with appreciated care by Ms. G. Hammersley.

References

Abou-Haidar, N. I., and Dixon, S. L., 1988, "Compressible Flow Losses in Branched Ducts," *Collected Papers in Heat Transfer*, The Winter Annual Meeting of the American Society of Mechanical Engineers, Chicago, IL, ASME HTD-Vol. 104, No. 2, pp. 17–23.

Abou-Haidar, N. I., 1989, "Compressible Flow Pressure Losses in Branched Ducts," Ph.D. Thesis, The University of Liverpool, Department of Mechanical Engineering, Liverpool, United Kingdom.

Abou-Haidar, N. I., and Dixon, S. L., 1992, "Pressure Losses in Combining Subsonic Flows Through Branched Ducts," ASME JOURNAL OF TURBOMACHINERY, Vol. 114, pp. 264–270.

B. S. 1042, 1987, "Measurement of Fluid Flow in Closed Conduits," British Standard Institution.

Davies, M. G., and Oldfield, D. E. S., 1962, "Tones From a Choked Axisymmetric Jet. I. Cell Structure, Eddy Velocity and Source Locations," *Acoustica*, Vol. 12, No. 4, pp. 257–267.

Davies, M. G., 1964, "A Note on the Radiation and Cell Pattern of Choked Jets," *Journal of Sound and Vibration*, Vol. I, No. 3, pp. 298–301.

ESDU, 1973, "Pressure Losses in Three-Leg Pipe Junctions: Dividing Flows and Combining Flows," Engineering Science Data Unit Nos. 73022 and 73023.

Gardel, A., and Rechsteiner, G. F., 1970, "Les Pertes de Charge dans les Branchements en Té des Conduites de Section Circulaire," Bulletin Technique de la Suisse Romade, Vol. 96, No. 25, pp. 363–391.

Ito, H., and Imai, K., 1973, "Energy Losses at 90° Pipe Junctions," *Proceedings of the American Society of Civil Engineers, Journal of the Hydraulics Division*, Vol. 99, No. HY9, pp. 1353–1368.

Jeal, B., 1988, "Moving Towards the Non-metallic Aero Engine," *The Rolls-Royce Magazine*, No. 36, pp. 23–27.

Johnson, M. W., 1988, "Introduction to Computational Fluid Dynamics (Short Course Notes)," The University of Liverpool, Department of Mechanical Engineering, Liverpool, United Kingdom.

Marchetti, M., and Noseda, G., 1960, "Heat Losses in Symmetrical Constant Diameter Bifurcations," *L'Energia Elettrica*, Vol. 37, No. 4, pp. 289–301.

Miller, D. S., 1971, "Internal Flow. A Guide to Losses in Pipe and Duct Systems," The British Hydrodynamics Researchg Association, United Kingdom.

Miller, D. S., 1978, "Internal Flow Systems," The British Hydrodynamic Research Association, United Kingdom.

Oki, I., et al., 1951, "Some Computations of Flow Distributions in Simple Systems of Pipe Line Nets (2nd Report)," *Transactions of the Japanese Society of Mechanical Engineers*, Vol. 17, pp. 88–92.

Rolls-Royce, 1986, "The Jet Engine," The Technical Publications Department, Rolls-Royce plc, United Kingdom.

Flow Pattern and Heat Transfer in a Closed Rotating Annulus

D. Bohn

G. H. Dibelius

E. Deuker

R. Emunds

Institute of Steam and Gas Turbines,
Technical University Aachen,
Aachen, Federal Republic of Germany

The prediction of the temperature distribution in a gas turbine rotor containing gas-filled closed cavities, for example between two disks, has to account for the heat transfer conditions encountered inside these cavities. In an entirely closed annulus no forced convection is present, but a strong natural convection flow occurs induced by a nonuniform density distribution in the centrifugal force field. A computer code has been developed and applied to a rotating annulus with square cross section as a base case. The co-axial heat flux from one side wall to the other was modeled assuming constant temperature distribution at each wall but at different temperature levels. Additionally the inner and outer walls were assumed to be adiabatic. The code was first verified for the annulus approaching the plane square cavity in the gravitational field, i.e., the ratio of the radius r over the distance h between outer and inner cylindrical wall was set very large. The results obtained agree with De Vahl Davis' benchmark solution. By reducing the inner radius to zero, the results could be compared with Chew's computation of a closed rotating cylinder, and again good agreement was found. Parametric studies were carried out varying the Grashof number Gr, the rotational Reynolds number Re, and the r/h ratio, i.e., the curvature of the annulus. A decrease of this ratio at constant Gr and Re number results in a decrease of heat transfer due to the Coriolis forces attenuating the relative gas velocity. The same effect can be obtained by increasing the Re number with the h/r ratio and the Gr number being constant. By inserting radial walls into the cavity the influence of the Coriolis forces is reduced, resulting in an increase of heat transfer.

Introduction

For the development of gas turbines toward higher gas inlet temperatures not only the blade cooling but also the rotor cooling is equally important. Gas-filled cavities resulting from rotor design can reduce the heat transfer in the rotor region. Though, due to the centrifugal acceleration, a flow induced by the buoyancy force corresponding to temperature differences of the cavity walls will appear. Such a flow considerably increases the heat transfer throughout the cavities. Therefore, an understanding of the heat flow mechanisms in the rotor cavities is of great importance for an improved design of a gas turbine rotor.

A lot of experimental and theoretical work has been done in the past to investigate the heat transfer in rotor cavities with a throughflow of cooling fluid; see, for example, Ong and Owen (1991), Farthing et al. (1992a, b), Owen et al. (1985), and Chew (1985). Chew also studied the flow and heat transfer mechanism in a closed rotating cylinder. But there seems to be a lack of knowledge about rotating sealed cavities bounded by outer and inner cylindrical walls and operating under conditions valid for gas turbines. In such a geometry an additional parameter, the r/h ratio, appears and not only an axial but also a radial heat flux component may occur. As a first step in better understanding such a complex flow and heat transfer we want to discuss the basic behavior of the buoyancy-induced flow within such cavities, considering a simplified test geometry with an axial heat transfer from one side wall to the other.

The Computational Model

Basic Modeling Assumptions. A closed rotating annulus with square cross section was chosen (Fig. 1). The essential co-axial heat flux was modeled assuming the temperatures at the side walls being different but uniformly distributed, while all other walls (the outer and inner cylindrical surfaces and, in the case of a sectored annulus, the walls in radial direction) were assumed to be adiabatic.

When the annulus is divided into sections by inserting radial walls (Fig. 2), the flow becomes three dimensional. Without this subdivision no gradients in circumferential direction occur and the flow is essentially two dimensional.

The computer code solves the steady-state conservation equations for mass, momentum, and energy. All computations were carried out for air, the density is calculated by the ideal gas law, and all other properties are treated as functions of the temperature. Some common assumptions for natural convection flows are made: In the viscous terms of the momentum equations the compressibility is neglected because the velocities at this type of flow are very small. In the energy equation the influence of the dissipation and the pressure changes is assumed to be negligible too due to very small Eckert numbers ($Ec < 0.1$

Contributed by the International Gas Turbine Institute and presented at the 37th International Gas Turbine and Aeroengine Congress and Exposition, Cologne, Germany, June 1-4, 1992. Manuscript received by the International Gas Turbine Institute February 4, 1992. Paper No. 92-GT-67. Associate Technical Editor: L. S. Langston.

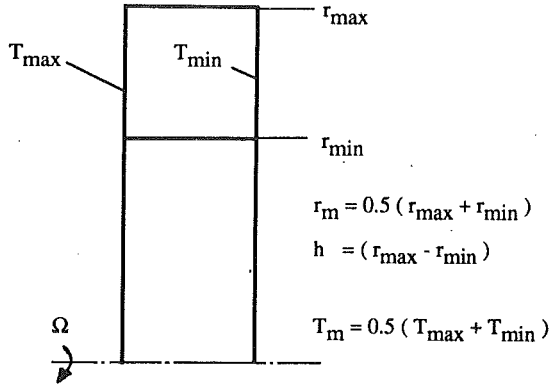

Fig. 1 Model of rotating cavity

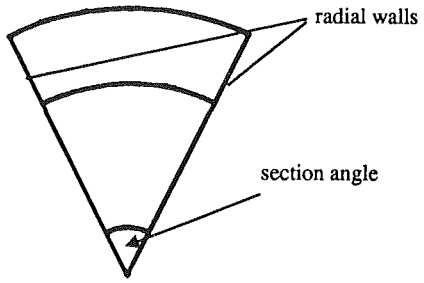

Fig. 2 Sectored rotating cavity

except for some cases with very small temperature differences and Nu numbers smaller than 1.1). The flow is assumed to be laminar in the range of the Gr numbers considered, which are not larger than 10^9. Even for greater Gr numbers no significant turbulent motion is to be expected. This will be discussed in more detail below.

The Governing Equations. Making use of the radial momentum equation for a rotating solid body at constant temperature:

$$-\frac{\partial p_{SB}}{\partial r} + \rho_{SB}\cdot\Omega^2\cdot r = 0 \quad \rho_{SB} = \frac{p_{SB}}{R\cdot T_m} \tag{1}$$

a reduced pressure can be introduced:

$$p_{red} = p - p_{SB}$$

Thus, the governing equations can be written in a rotating coordinate system as follows:

$$\frac{1}{r}\cdot\left(\frac{\partial \rho u r}{\partial x} + \frac{\partial \rho v r}{\partial r} + \frac{\partial \rho w}{\partial \varphi}\right) = 0 \tag{2}$$

$$\frac{1}{r}\frac{\partial}{\partial x}\left(\rho r u u - \mu r\frac{\partial u}{\partial x}\right) + \frac{1}{r}\frac{\partial}{\partial r}\left(\rho r v u - \mu r\frac{\partial u}{\partial r}\right) + \frac{1}{r}\frac{\partial}{\partial \varphi}\left(\rho w u - \frac{\mu}{r}\frac{\partial u}{\partial \varphi}\right) = -\frac{\partial p_{red}}{\partial x} \tag{3}$$

$$\frac{1}{r}\frac{\partial}{\partial x}\left(\rho r u v - \mu r\frac{\partial v}{\partial x}\right) + \frac{1}{r}\frac{\partial}{\partial r}\left(\rho r v v - \mu r\frac{\partial v}{\partial r}\right) + \frac{1}{r}\frac{\partial}{\partial \varphi}\left(\rho w v - \frac{\mu}{r}\frac{\partial v}{\partial \varphi}\right) = -\frac{\partial p_{red}}{\partial r} - \frac{\mu}{r^2}\left[v + 2\cdot\frac{\partial w}{\partial \varphi}\right] + \rho\cdot\left[\frac{w^2}{r} + 2\Omega w\right] + (\rho - \rho_{SB})\cdot\Omega^2 r \tag{4}$$

$$\frac{1}{r}\frac{\partial}{\partial x}\left(\rho r u w - \mu r\frac{\partial w}{\partial x}\right) + \frac{1}{r}\frac{\partial}{\partial r}\left(\rho r v w - \mu r\frac{\partial w}{\partial r}\right) + \frac{1}{r}\frac{\partial}{\partial \varphi}\left(\rho w w - \frac{\mu}{r}\frac{\partial w}{\partial \varphi}\right) = -\frac{1}{r}\frac{\partial p_{red}}{\partial \varphi} - \frac{\mu}{r^2}\left[w - 2\cdot\frac{\partial v}{\partial \varphi}\right] - \rho\cdot\left[\frac{w v}{r} + 2\Omega v\right] \tag{5}$$

$$\frac{1}{r}\frac{\partial}{\partial x}\left(\rho r u T - \frac{\lambda r}{c_p}\frac{\partial T}{\partial x}\right) + \frac{1}{r}\frac{\partial}{\partial r}\left(\rho r v T - \frac{\lambda r}{c_p}\frac{\partial T}{\partial r}\right) + \frac{1}{r}\frac{\partial}{\partial \varphi}\left(\rho w T - \frac{\lambda}{r c_p}\frac{\partial T}{\partial \varphi}\right) = 0 \tag{6}$$

In Eq. (4) the term $(\rho - \rho_{SB})\,\Omega^2 r$ represents the buoyancy force, while $2\rho\Omega w$ and in Eq. (5) $2\rho\Omega v$ represent the Coriolis forces.

The Numerical Procedure. The system of coupled partial differential equations is solved numerically with a finite volume scheme using the SIMPLE pressure correction method defined by Patankar and Spalding (1972). A nonuniform staggered grid is defined, with T and p being calculated at the main grid points and u, v, w being calculated at locations that are midway between the main grid points. In the employed "hybrid" differencing method upwind differencing is used for the convective terms when the cell Peclet number is greater than 2, otherwise central differencing is used for these terms.

Nomenclature

a = thermal diffusivity
c_p = specific heat at constant pressure
d = diameter
h = distance between outer and inner cylindrical wall
L = distance between hot and cold side wall
p = pressure
$\dot{q}$ = heat flux transferred to or from the side wall
$\dot{q}_c$ = heat flux throughout the cavity generated by conduction, when no fluid motion is present
R = gas constant
T = temperature
ΔT = temperature difference between hot and cold side wall
(x, r, φ) = axial, radial, circumferential coordinate
(u, v, w) = relative velocity components in (x, r, φ) directions
λ = thermal conductivity
μ = dynamic viscosity
ρ = density
Ω = angular velocity of the cavity
Gr = $\rho_0^2\cdot\Delta T\cdot\Omega^2\cdot r_m\cdot L^3/T_m\cdot\mu_0^2$ = Grashof number
Pr = $\mu_0\cdot c_{p0}/\lambda_0$ = Prandtl number
Ra = Gr·Pr = Rayleigh number
Re = $\rho_0\cdot L\cdot\Omega\cdot r_m/\mu_0$ = Reynolds number
Ec = $(\Omega\cdot r_m)^2/2c_p\Delta T$ = Eckert number
Nu = $\dot{q}/\dot{q}_c$ = Nusselt number

Subscripts

min = minimum
max = maximum
m = arithmetic mean
red = reduced
sb = solid body
0 = reference

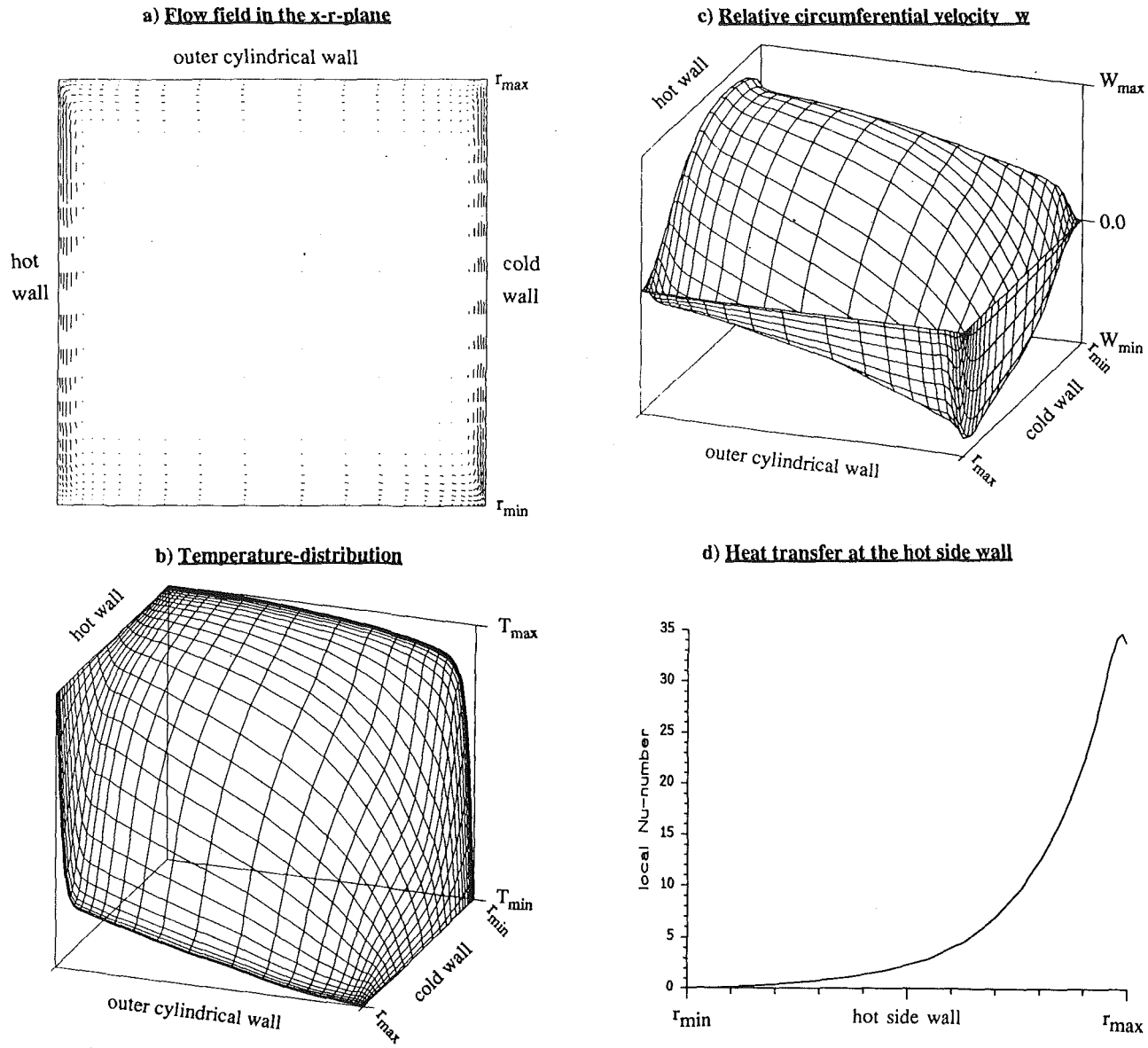

Fig. 3 Flow pattern, temperature distribution, and heat transfer in a rotating cavity at Re = 10^4, Gr = 10^7, $r_m/h = 4$

The results obtained are computed for the three-dimensional calculations on a Siemens VP 400 computer and for the two-dimensional calculations on an IBM 3090. A typical CPU time for a 45 deg segment with a (30, 30, 40) grid is less than one minute. For the two-dimensional calculation on a (30, 30) grid shown in Fig. 3 a CPU time about 50 seconds is needed.

Dimensionless Equations. To show the typical dimensionless groups for this flow type, Eqs. (2) to (6) can be made dimensionless with the following transformations, which are common at natural convective flows (dimensionless variables marked with an overbar):

$$u = \bar{u} \cdot \frac{a_0}{L}; \quad p = \bar{p} \cdot \frac{\rho_0 \cdot a_0^2}{L^2}; \quad \rho = \bar{\rho} \cdot \rho_0;$$

$$T = \bar{T} \cdot \Delta T + T_m; \quad \lambda = \bar{\lambda} \cdot \lambda_0; \quad \mu = \bar{\mu} \cdot \mu_0;$$

$$c_p = \bar{c}_p \cdot c_{p0}; \quad x = \bar{x} \cdot L; \quad r = \bar{r} \cdot L$$

The fluid properties λ_0, a_0, ρ_0, μ_0, c_{p0} are evaluated for T_m as the reference temperature (see Fig. 1). The changes of pressure are very small compared to its absolute value:

$$p_{red} \ll p.$$

Hence, the density difference in the buoyancy term can be written as

$$\rho = \frac{p}{R \cdot T} \approx \frac{p_{SB}}{R \cdot T} = \rho_{SB} \cdot \frac{T_m}{T}$$

$$\Rightarrow (\rho - \rho_{SB}) \approx \rho_{SB} \cdot \frac{1}{T} \cdot (T_m - T) \tag{7}$$

The dimensionless equations are then:

$$\frac{1}{r} \cdot \left(\frac{\partial \overline{\rho} \overline{u} \overline{r}}{\partial \bar{x}} + \frac{\partial \overline{\rho} \overline{v} \overline{r}}{\partial \bar{r}} + \frac{\partial \overline{\rho} \overline{w}}{\partial \varphi} \right) = 0 \tag{8}$$

$$\frac{1}{\bar{r}} \left(\frac{\partial}{\partial \bar{x}} \overline{\rho} \overline{r} \overline{u} \overline{u} + \frac{\partial}{\partial \bar{r}} \overline{\rho} \overline{r} \overline{v} \overline{u} + \frac{\partial}{\partial \varphi} \overline{\rho} \overline{w} \overline{u} \right) - \frac{\mathrm{Pr}}{\bar{r}}$$

$$\cdot \left(\frac{\partial}{\partial \bar{x}} \left(\overline{\mu r} \frac{\partial \bar{u}}{\partial \bar{x}} \right) + \frac{\partial}{d\bar{r}} \left(\overline{\mu r} \frac{\partial \bar{u}}{\partial \bar{r}} \right) + \frac{\partial}{\partial \varphi} \left(\frac{\bar{\mu}}{\bar{r}} \frac{\partial \bar{u}}{\partial \varphi} \right) \right) = - \frac{\partial \bar{p}_{red}}{\partial \bar{x}} \tag{9}$$

$$\frac{1}{\bar{r}}\left(\frac{\partial}{\partial\bar{x}}\bar{\rho}\bar{r}\bar{u}\bar{v}+\frac{\partial}{\partial\bar{r}}\bar{\rho}\bar{r}\bar{v}\bar{v}+\frac{\partial}{\partial\varphi}\bar{\rho}\bar{w}\bar{v}\right)-\mathrm{Pr}\cdot\left(\frac{\partial}{\partial\bar{x}}\left(\bar{\mu}\bar{r}\frac{\partial\bar{v}}{\partial\bar{x}}\right)+\frac{\partial}{\partial\bar{r}}\left(\bar{\mu}\bar{r}\frac{\partial\bar{v}}{\partial\bar{r}}\right)+\frac{\partial}{\partial\varphi}\left(\frac{\bar{\mu}}{\bar{r}}\frac{\partial\bar{v}}{\partial\varphi}\right)\right)=-\frac{\partial\bar{p}_{\mathrm{red}}}{\partial\bar{r}}-\mathrm{Pr}\frac{\bar{\mu}}{\bar{r}^2}\left(\bar{v}+2\frac{\partial\bar{w}}{\partial\varphi}\right)+\bar{\rho}\frac{\bar{w}^2}{\bar{r}}+2\bar{\rho}\bar{w}\frac{L}{r_m}\mathrm{Re}\cdot\mathrm{Pr}-\bar{\rho}_{SB}\bar{r}\frac{T_m}{\bar{T}}\frac{L}{r_m}\mathrm{Gr}\cdot\mathrm{Pr}^2\cdot\bar{T}\quad(10)$$

$$\frac{1}{\bar{r}}\left(\frac{\partial}{\partial\bar{x}}\bar{\rho}\bar{r}\bar{u}\bar{w}+\frac{\partial}{\partial\bar{r}}\bar{\rho}\bar{r}\bar{v}\bar{w}+\frac{\partial}{\partial\varphi}\bar{\rho}\bar{w}\bar{w}\right)-\mathrm{Pr}\left(\frac{\partial}{\partial\bar{x}}\left(\bar{\mu}\bar{r}\frac{\partial\bar{w}}{\partial\bar{x}}\right)+\frac{\partial}{\partial\varphi}\left(\frac{\bar{\mu}}{\bar{r}}\frac{\partial\bar{w}}{\partial\varphi}\right)+\frac{\partial}{\partial\bar{r}}\left(\bar{\mu}\bar{r}\frac{\partial\bar{w}}{\partial\bar{r}}\right)\right)=-\frac{1}{\bar{r}}\frac{\partial\bar{p}_{\mathrm{red}}}{\partial\varphi}-\mathrm{Pr}\frac{\bar{\mu}}{\bar{r}^2}\left(\bar{w}-2\frac{\partial\bar{v}}{\partial\varphi}\right)-\bar{\rho}\frac{\bar{v}\bar{w}}{\bar{r}}-2\bar{\rho}\bar{v}\frac{L}{r_m}\mathrm{Re}\cdot\mathrm{Pr}\quad(11)$$

$$\frac{1}{\bar{r}}\frac{\partial}{\partial\bar{x}}\left(\bar{\rho}\bar{r}\bar{u}\bar{T}-\frac{\bar{\lambda}\bar{r}}{\bar{c}_p}\frac{\partial\bar{T}}{\partial\bar{x}}\right)+\frac{1}{\bar{r}}\frac{\partial}{\partial\bar{r}}\left(\bar{\rho}\bar{r}\bar{v}\bar{T}-\frac{\bar{\lambda}\bar{r}}{\bar{c}_p}\frac{\partial\bar{T}}{\partial\bar{r}}\right)+\frac{1}{\bar{r}}\frac{\partial}{\partial\varphi}\left(\bar{\rho}\bar{w}\bar{T}-\frac{\bar{\lambda}}{\bar{r}\bar{c}_p}\frac{\partial\bar{T}}{\partial\varphi}\right)=0\quad(12)$$

Herein the Re number occurs within the Coriolis terms, while the Gr number is related to the buoyancy term. The Prandtl number occurring in the momentum equations does not change very much due to temperature variations. It was reported by several investigators (e.g., Bohn et al., 1984), that even a greater variation of the Pr number, e.g., by changing the fluid, has only a weak influence on the heat transfer.

Results and Discussion

Comparison With Previous Work. As no appropriate experimental and numerical data are available, the computer code could only be verified by simulating some extreme situations. Results from other authors are available for these cases.

Increasing the r_m/h ratio to infinity leads to a plane square cavity, which is a well-known test case for codes dealing with natural convection problems. Good agreement was found with De Vahl Davis' benchmark solution (1983); see Table 1. The average Nu numbers are never more than 1.5 percent different. To conform with De Vahl Davis' solution the results in Table 1 have been computed with the Boussinesq approximation, i.e., all properties are constant except for the density in the buoyancy term. It was found that this assumption has only a small effect; the Nu numbers change within less than 1 percent in all cases.

By reducing the inner radius to zero, the flow inside a closed rotating cylinder is simulated. This configuration was computed by Chew (1985), and his results could be confirmed (Table 2). In accordance with his computations a linear temperature distribution at the outer cylindrical wall has been established.

Results for the Rotating Cavity. In Figs. 3–6 results are presented for the closed rotating annulus. All computations were carried out for air at $T_m = 750$ K, which gives a Pr number of 0.66. Temperature differences up to 300 K between the hot and the cold side wall have been used. A typical example of the flow and the heat transfer is shown in Fig. 3. The fluid circulates around the walls in boundary layers, and nearly no motion occurs in the core region (Fig. 3*a*). Near the hot wall

Table 1 Benchmark test: comparison of the presented method and the De Vahl Davis method for plane square cavity

Correlation parameter	Ra = 10^4 (1)	Ra = 10^4 (2)	Ra = 10^5 (1)	Ra = 10^5 (2)	Ra = 10^6 (1)	Ra = 10^6 (2)
$\bar{v}_{\max}$	19.5	19.6	69.2	68.6	221.8	219.4
$(\bar{x}, \bar{y}=0.5)$	0.102	0.119	0.063	0.066	0.031	0.038
$\mathrm{Nu}_{\max}$	3.60	3.53	7.75	7.72	17.4	17.9
$(\bar{x}=0, \bar{y})$	0.140	0.143	0.081	0.081	0.035	0.038
Nu (average value)	2.27	2.24	4.51	4.52	8.68	8.80

(1) Current solution; (2) De Vahl Davis benchmark solution.

Table 2 Rotating cylinder: comparison of the presented method and Chew's method

Nu (average value)	Chew (1985)	Current solution
Hot side wall	3.0	3.08
Cold side wall	1.3	1.28

$\rho\Omega\, r^2_{\max}/\mu = 2\cdot10^4$
$\Delta T / T_{\max} = 0.391$
Reference temperature = $T_{\min}$ = 288 K
Linear temperature distribution at the cylindrical wall

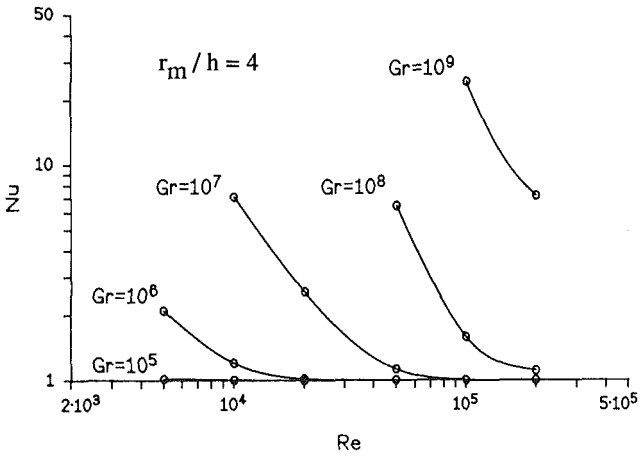

Fig. 4 Heat transfer in a rotating cavity ($r_m/h = 4$) for various Reynolds and Grashof numbers

the fluid has a lower density than its environment, causing a motion in opposite direction to the centrifugal acceleration. The cold and heavy fluid on the other side wall is moving in the same direction as the centrifugal acceleration, i.e., radially outward. While moving from the cold to the hot wall along the outer cylindrical surface, the fluid remains relatively cold (Fig. 3b). Thus, a large temperature gradient occurs, when the fluid reaches the hot wall at the outer edge. At the inner edge on the cold side an analogous but opposite situation occurs. In the core itself heat is conducted in the axial direction from the hot to the cold side, but also in the radial direction due to the temperature difference between the hot flow at the inner radius and the cold flow at the outer radius (Figs. 3*a*, 3*b*).

Figure 4 shows the influence of Re and Gr number variation on the Nu number. As expected, the heat transfer grows with increasing Gr number at a constant Re value. An increase of the Re number at a constant Gr value attenuates the heat transfer, which can be understood by taking the Coriolis forces into account.

The buoyancy force (represented by $(\rho - \rho_{SB})\Omega^2 r$ in the radial momentum equation (Eq. (4)) actually causes the flow. Thus, without density differences no motion will occur. But the Coriolis force ($2\rho\Omega w$ in Eq. (4)) always works against the buoyancy force: Near the hot wall the fluid is light, resulting in a *negative buoyancy force*. The fluid, which comes from the outer cylindrical wall with a great absolute circumferential speed, must move radially inward along the hot side wall. The absolute

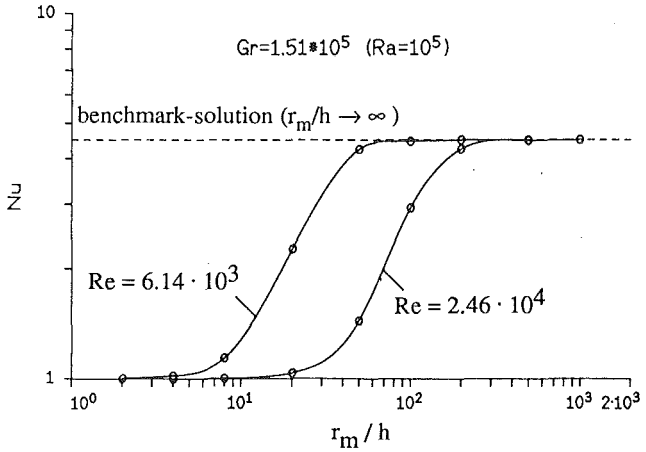

Fig. 5 Heat transfer in a rotating cavity ($Ra = 10^5$) with respect to the r_m/h ratio for various Reynolds numbers

circumferential speed of the fluid is reduced by viscous effects, but it is greater than the wall speed, so that a positive relative circumferential velocity remains in the region near the hot wall (Fig. 3*c*), giving a *positive Coriolis force*. On the cold wall the situation is analogous but opposite. Thus, fluid motion is driven by buoyancy force and damped by the Coriolis force.

Increasing the Re number at constant Gr number (Fig. 4) strengthens the Coriolis forces compared to the buoyancy force, which leads to a reduction of the flow circulating between the hot and the cold wall and therefore to a reduction of the heat transfer by convection.

To study the influence of the curvature of the cavity, the r_m/h ratio was varied at constant Re and Gr number (Fig. 5). For great r_m/h ratios the difference is small between the absolute circumferential speed at the outer and the inner radius compared to the reference velocity Ωr_m. Thus, only a small Coriolis effect is present and heat transfer is better than in case of a smaller r_m/h ratio. This effect can be understood discussing the Coriolis and buoyancy terms in the dimensionless form of the radial momentum equation (Eq. (10)): While Re and Gr are constant and L/r_m occurs in both the Coriolis and the buoyancy term, the latter, however, includes $\bar{r}$, which increases the buoyancy term compared to the Coriolis term, when the r_m/h ratio is increased.

Increasing the r_m/h ratio to infinity leads to the plane square cavity, where no Coriolis forces are present. Thus, the Nu number for the plane cavity gives the limit, which must be approached by increasing the r_m/h ratio. With a smaller Re number this limit is reached earlier (see Fig. 5). The results in Fig. 5 have been computed with the Boussinesq approximation to be comparable with De Vahl Davis' benchmark solution.

In Fig. 3(*d*) the distribution of the local Nu number at the hot side wall of the rotating annulus is plotted. Most of the heat is transferred in the outer region, where the cold fluid reaches the hot wall. For greater Gr numbers the flow in the hot side wall boundary layer will possibly become turbulent near the inner cylindrical wall. This may result in a local increase of the heat transfer in this region, but probably will not significantly change the overall heat transfer.

Some useful information about the onset of turbulence can be achieved by looking again at the square cavity in the gravitational field. Bohn et al. (1984) found in their experiments boundary layer waviness (transition to turbulence) in the upper 1/3 of the hot side wall for $Ra > 3 \times 10^{10}$. Several investigators computed the heat transfer numerically for great Ra numbers using different turbulence models (see Silva and Emery (1989) for discussion). In Table 3 experimental and theoretical results for Ra numbers up to 10^{11} are listed. Bohn's experimental results are within 10 to 25 percent smaller than Wan Hassan's

Table 3 Comparison of the average Nu number for the plane square cavity at high Ra numbers

	$Ra = 10^9$	$Ra = 10^{10}$	$Ra = 10^{11}$
Bohn et al.[1] (experimental, Pr = 3.5)	55	98	174
Wan Hassan (numerical, ACM turbulence model)	61	129	239
Current solution (laminar code)	54	97	173

[1]Results taken from his correlation equation

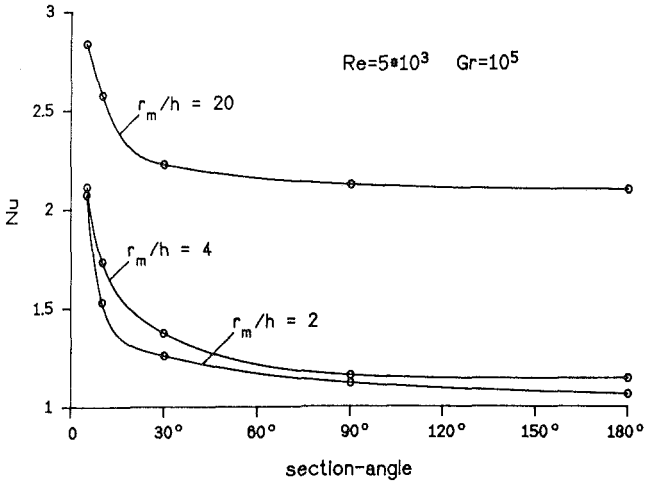

Fig. 6 Heat transfer in a sectored rotating cavity ($Re = 5 \times 10^3$, $Gr = 10^5$) with respect to the section angle for various values of the r_m/h ratio

results, which have been computed with an algebraic stress model. (According to Silva and Emery this turbulence model seems to give the best results for this flow type.) On the other hand our laminar computations are in surprisingly good agreement with Bohn's experimental results. This may indicate that the influence of turbulence on the overall heat transfer is smaller than predicted with the ASM model.

For the rotating cavity the damping effect of the Coriolis forces has to be taken into account additionally, which might suppress the turbulent motion completely. Nevertheless, it seems to be sure that the heat transfer is strongly dominated by laminar boundary layer convection even for Gr numbers much greater than considered here.

It is of interest to see what happens when the annulus is sectored by radial walls (see Fig. 2). The flow and heat transfer become three dimensional, and mainly the motion in the circumferential direction, especially near the radial walls, will be attenuated. In Fig. 6 the average Nu number versus the section angle is shown for different r_m/h ratios at constant Re and Gr number. The attenuation of the circumferential velocity with decreasing section angle leads to a decrease of the Coriolis forces, while the buoyancy force is not affected directly. So the heat transfer increases for smaller sections. In all three cases a significant increase occurs foremost for section angles less than 30 deg.

For very small section angles the boundary layers at the two radial walls will grow together, and it is to be expected that viscous action will become dominant in the entire annulus slowing down the whole motion and in turn decreasing the heat transfer. In the computations the section angle was varied down to 5 deg, and no decrease was found so far. Calculations were then stopped, for it is of no practical interest to consider an essentially axial heat flux in a cavity with the isotherm side walls being very small due to the small section angle but large adiabatic walls in the radial direction.

Conclusions

A rotating closed annulus with square cross section and isothermal sidewalls of different temperature has been investigated as a simplified test geometry approaching gas filled cavities inside a gas turbine rotor. Due to buoyancy effects in the centrifugal force field flow is induced causing convective heat transfer from the hot to the cold side wall.

It was found that fluid motion and heat transfer are attenuated by the Coriolis forces. Thus, a decrease of heat transfer can be obtained by strengthening the Coriolis forces compared to the buoyancy force. This can be done in several ways: increasing the Re number at constant Gr number and decreasing the r_m/h ratio at constant Re and Gr number.

Dividing the annulus into sections by inserting radial walls attenuates the circumferential velocity, giving a decrease of the Coriolis forces. So the heat transfer increases.

The calculations provide a data base for the design of a test rig within the institute where experiments proving the theoretical work will be carried out.

Acknowledgments

We wish to thank the Arbeitsgemeinschaft Hochtemperatur-Gasturbine funded by German Gas Turbine Industry Companies and the BMFT for sponsoring the work described in the paper.

References

Bohn, M. S., Kirkpatrick, A. T., and Olson, D. A., 1984, "Experimental Study of Three-Dimensional Natural Convection High-Rayleigh Number," ASME *Journal of Heat Transfer*, Vol. 106, pp. 339–345.

Chew, J. W., 1985, "Computation of Convective Laminar Flow in Rotating Cavities," *J. Fluid Mech.*, Vol. 153, pp. 339–360.

De Vahl Davis, G., 1983, "Natural Convection of Air in a Square Cavity: a Benchmark Numerical Solution," *Int. J. Num. Methods Fluids*, Vol. 3, pp. 249–264.

Farthing, P. R., Long, C. A., Owen, J. M., and Pincombe, J. R., 1992a, "Rotating Cavity With Axial Throughflow of Cooling Air: Heat Transfer," ASME JOURNAL OF TURBOMACHINERY, Vol. 114, pp. 229–236.

Farthing, P. R., Long, C. A., Owen, J. M., and Pincombe, J. R., 1992b, "Rotating Cavity With Axial Throughflow of Cooling Air: Flow Structure," ASME JOURNAL OF TURBOMACHINERY, Vol. 114, pp. 237–246.

Ong, C. L., and Owen, J. M., 1991, "Prediction of Heat Transfer in a Rotating Cavity With a Radial Outflow," ASME JOURNAL OF TURBOMACHINERY, Vol. 113, pp. 115–122.

Owen, J. M., Pincombe, J. R., and Rogers, R. H., 1985, "Source-Sink Flow Inside a Rotating Cylindrical Cavity," *J. Fluid Mech.*, Vol. 155, pp. 233–265.

Patankar, S. V., and Spalding, D. B., 1972, "A Calculation Procedure for Heat, Mass and Momentum Transfer in Three-Dimensional Parabolic Flows," *Int. J. Heat Mass Transfer*, Vol. 15, pp. 1787–1806.

Silva, D. J., and Emery, A. F., 1989, "A Preliminary Comparison of the k–ϵ and Algebraic Stress Models for Turbulent Heat Transfer in a Square Enclosure," *National Heat Transfer Conference*, ASME HTD-Vol. 110, pp. 193–200.

Wan Hassan, M. N., 1986, "The National Convection in a Cavity at High Rayleigh Numbers," Ph.D. Thesis, University of Washington, Seattle, WA.

N. E. May
Aircraft Research Association Ltd.,
Manton Lane,
Bedford MK41 7PF United Kingdom

J. W. Chew
Rolls-Royce Ltd.,
PO Box 31,
Derby DE2 8BJ United Kingdom

P. W. James
Polytechnic South West,
Drake Circus,
Plymouth PL4 8AA United Kingdom

Calculation of Turbulent Flow for an Enclosed Rotating Cone

Prediction of the flow in the cavity between a rotating cone and an outer stationary cone with and without throughflow is considered. A momentum-integral method and a finite difference method for solution of the Reynolds-averaged Navier–Stokes equations with a mixing-length model of turbulence are applied. These two methods have previously been validated for flow between corotating and rotor–stator disk systems, but have not been properly tested for conical systems. Both methods have been evaluated by comparing predictions with the experimental measurements of other workers. There is good agreement for cone half-angles greater than or equal to 60 deg but discrepancies are evident for smaller angles. "Taylor-type" vortices, the existence of which has been postulated by other workers and which are not captured by the present steady, axisymmetric models, may contribute to these discrepancies.

1 Introduction

The need to improve design methods for turbomachinery has led to considerable effort being put into the development of predictive techniques for the flow in turbine and compressor disk cavities. Despite the variety of geometries of this type that occur in gas turbine engines, most predictive methods have been validated only for relatively simple plane disk geometries. In the present paper two predictive techniques that have been previously validated using data for turbulent flow in rotating disk cavities are evaluated using data for a shrouded rotating cone. The objective of this work is to clarify the range of validity of current methods and identify any particular problems associated with the conical geometry.

For a review of predictive methods for rotating disk flows the interested reader is referred to Chew (1990). However, to put the present contributions in context it is appropriate to mention some of the previous work on predictive methods. The earliest relevant publication is perhaps that of von Karman (1921). Von Karman derived a momentum-integral solution for turbulent flow induced by a disk rotating in a quiescent environment (the "free disk" problem). Many workers have subsequently used similar momentum-integral methods for a variety of rotating disk flows and the technique remains popular because of its computational efficiency and convenience in analysis. Relatively recent applications of the momentum-integral method include radial outflow and inflow between corotating disks (Owen et al., 1985; Chew and Rogers, 1988; Farthing et al., 1991) and flow in rotor–stator disk systems with or without an imposed throughflow (Owen and Rogers, 1989; Chew, 1991).

Over the last decade or so use of finite difference methods to solve the Reynolds-averaged Navier–Stokes equations for rotating disk flows has become increasingly popular. Some difficulties have been encountered both with turbulence modeling and with numerical algorithms, but it has now been demonstrated that a variety of turbulence models and numerical schemes can be successfully applied to rotating disk flows. Examples for corotating disk systems are given by Chew (1985) and Morse (1988), and for rotor–stator disk systems by Chew and Vaughan (1988), Roscoe et al. (1988), and Morse (1991).

In contrast to the disk problem, the rotating cone has received little attention. Tien (1960) showed that under laminar boundary layer assumptions the laminar free disk solution can be applied to the free cone problem. Kreith (1966) applied von Karman's momentum-integral method to the turbulent free cone problem and, as shown below, with appropriate nondimensionalization, the momentum-integral equations become identical to those for the free disk. Koosinlin et al. (1974) applied boundary layer finite difference methods, with a mixing-length turbulence model, to flow on a spinning cone with and without an imposed axial flow. The authors are not aware of any previous attempts to predict the flow for the problem considered here, namely the enclosed rotating cone with throughflow.

The two predictive methods that have been adopted here for the rotating cone problem are a von Karman-type momentum-integral method and the finite difference method of Vaughan et al. (1989), which uses a mixing-length model of turbulence. The momentum-integral method is developed from that applied previously to rotor–stator disk cavities and the turbulence model, which has been validated against data for free disks and cones, corotating disk cavities, and rotor–stator disk systems, is based on that of Koosinlin et al. These two methods are described in Sections 2 and 3 below. Comparison of theoretical predictions with the experimental results for moment coefficient of Yamada and Ito (1975, 1979) are then given in

Contributed by the International Gas Turbine Institute and presented at the 37th International Gas Turbine and Aeroengine Congress and Exposition, Cologne, Germany, June 1–4, 1992. Manuscript received by the International Gas Turbine Institute February 4, 1992. Paper No. 92-GT-70. Associate Technical Editor: L. S. Langston.

Section 4. Also included in Section 4 is a comparison of the finite difference predictions with the measurements of Bilgen and Boulous (1973) for an enclosed rotating cylinder, as this flow configuration could be considered a limiting case of the cone problem. The conclusions from the present study are summarized in Section 5.

2 The Momentum-Integral Method

2.1 Assumptions. The geometry of the rotor–stator cone system considered and the assumed flow structure are shown in Fig. 1. The outer and inner radii of the cones are b and a, respectively. The perpendicular distance between the rotor and stator is denoted by d. The rotor is rotating about an axis at $r = 0$ with constant angular velocity Ω and the orthogonal coordinate system (s, θ, n), shown in Fig. 1, is used. The cone half-angle is denoted by λ and the nondimensional mass throughflow rate (which may be zero) is denoted by Cq. Throughout this paper, the flow is assumed to be turbulent and flow variables are assumed to have been averaged over a suitably large time scale, so that they denote turbulent mean quantities. The components of velocity are denoted by (u, v, w), the pressure by p, and the density by ρ.

The flow pattern shown in Fig. 1 is postulated assuming that the flow develops in a similar way to that in rotor–stator disk systems. The pattern occurring in rotor–stator disk systems has been confirmed by experimental work (see, for example, Daily and Nece, 1960; Daily et al., 1964) and by finite difference results (see, for example, Chew and Vaughan, 1988). In the "source" region, fluid is entrained into a boundary layer on the rotor; any flow on the stator up to this point is neglected. Outside the source region fluid is "centrifuged" radially outward in a boundary layer on the rotor and radially inward along the stator. Flow is channeled into the stator boundary layer through a boundary layer on the shroud. Between these boundary layers there is a core where there is a weak axial velocity toward the rotor and negligible radial velocity. The

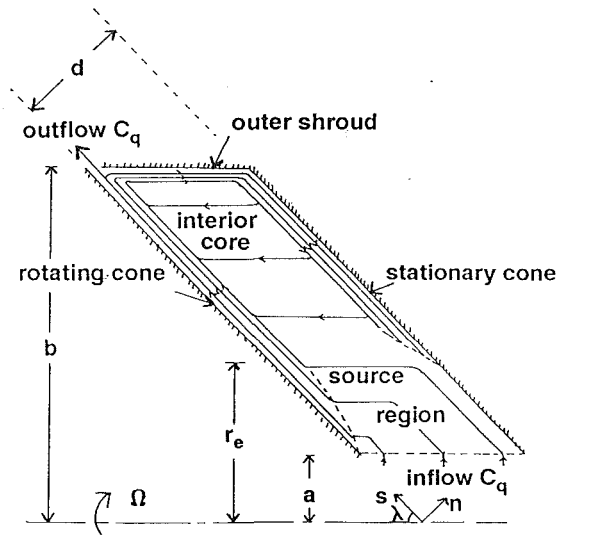

Fig. 1 Postulated flow pattern in rotor–stator cone system (⟶ typical streamline, · · · · · boundary layer edge)

Nomenclature

a = inner radius
b = outer radius
Cm = moment coefficient = $2M \sin \lambda/\rho\Omega^2 b^5$
Cm' = moment coefficient = $2M/\pi\rho\Omega^2 b^4 t$
Cq = nondimensional mass throughflow rate = $\dot{m}/\mu b$
d = perpendicular distance between rotor and stator
F = friction factor
$F_i(\overline{V})$ = see Eqs. (16) and (17)
I_1, I_2, I_3, I_4, I_5 = constants obtained by integrating velocity profiles across the boundary layer (see Section 2.2)
l = mixing length
$\dot{m}$ = mass flow rate
$\dot{m}_b$ = mass flow rate in shroud boundary layer
M = moment exerted on rotor
n = normal coordinate direction in "tilted" cylindrical polar coordinate system
$p(s, n)$ = static pressure
r = radial coordinate direction in cylindrical polar coordinate system
r_e = radial location of end of source region
Re = Reynolds number used by Yamada and Ito = $\Omega b^2/\nu$
Re_θ = Reynolds number used in integral method = $\Omega b^2/\nu \sin \lambda$
s = coordinate direction parallel to cone in "tilted" cylindrical polar system
t = length of cylinder
$u(s, n)$ = s-velocity component
$\hat{u}(s)$ = s-dependent component of $u(s, n)$
$u_1(x)$ = nondimensionalized $u(s) = u/\Omega r_o$
$v(s, n)$ = tangential velocity component
$\overline{V}(x)$ = nondimensionalized boundary layer edge tangential velocity = $\overline{v}/\Omega r_o$
$V_b(z)$ = bulk tangential velocity in shroud boundary layer
$V_o(x)$ = nondimensionalized surface tangential velocity = $v_o/\Omega r_o$
$w(s, n)$ = n-velocity component
x = nondimensional distance = r_o/b
x_n = normal distance from surface
Y_1 = dependent variable used in integral method = $u_1\delta_1 x^3$
Y_2 = dependent variable used in integral method = $\delta_1 x$
z = coordinate direction in cylindrical polar coordinate system
$\delta(s)$ = boundary layer thickness
$\delta_1(x)$ = nondimensional boundary layer thickness = $\mathrm{Re}_\theta^{1/5} \sin \lambda\, \delta/r_o$
θ = tangential coordinate in cylindrical and "tilted" cylindrical polar coordinate systems
λ = cone half angle
μ = laminar dynamic viscosity
$\mu_e(s, n)$ = effective dynamic viscosity = $\mu + \mu_t$
$\mu_t(s, n)$ = turbulent dynamic viscosity
ν = laminar kinematic viscosity = μ/ρ
ρ = density
$\tau_{ij}(s, n)$ = stress components, where i and j represent s, θ, or n
$\tau_W(s)$ = resultant wall shear stress
ω = under-relaxation factor (Eq. (18))
Ω = angular velocity of rotor

Subscripts

o = value on rotor or stator surface

Superscripts

s = stator variable
$\overline{\ }$ = values at the boundary layer edge

flow throughout the cavity is assumed to be incompressible, steady, and axisymmetric and the flow external to the boundary layers in both the source region and the core region will be treated as inviscid.

The application of boundary layer assumptions to the Navier-Stokes equations for the conical geometry is similar to that for disk systems but requires the additional assumption

$$s \sin \lambda \gg n \cos \lambda. \tag{1}$$

The physical interpretation of this assumption is that the change in radius across the boundary layer is small compared with the local radius. May (1990) has confirmed numerically that this assumption is appropriate for the conditions considered here.

Applying the usual boundary layer assumptions, along with the above assumption, to the Reynolds-averaged Navier-Stokes equations, the following boundary layer equations are obtained:

$$\frac{1}{r}\frac{\partial}{\partial s}(\rho r u) + \frac{1}{r}\frac{\partial}{\partial n}(\rho r w) = 0, \tag{2}$$

$$\frac{1}{r}\frac{\partial}{\partial s}(\rho r u^2) + \frac{1}{r}\frac{\partial}{\partial n}(\rho r u w) - \frac{\rho v^2}{r}\sin\lambda + \frac{\partial p}{\partial s} = \frac{1}{r}\frac{\partial}{\partial n}(r\tau_{sn}), \tag{3}$$

$$\frac{1}{r^2}\frac{\partial}{\partial s}(\rho r^2 u v) + \frac{1}{r}\frac{\partial}{\partial n}(\rho r w v) = \frac{1}{r^2}\frac{\partial}{\partial n}(r^2\tau_{\theta n}), \tag{4}$$

$$\frac{\partial p}{\partial n} = 0. \tag{5}$$

The shear stresses τ_{sn} and $\tau_{\theta n}$ in these equations represent the sum of the laminar and Reynolds stresses.

2.2 Rotor Boundary Layer. The velocity profiles and surface shear stress formulae used for the rotor boundary layer at $n = 0$ are the following generalizations of those used by von Karman:

$$v(s, n) = \bar{v}(s) - (\bar{v}(s) - v_0(s))[1 - (n/\delta)^{1/7}], \tag{6}$$

$$u(s, n) = \tilde{u}(s)\,(n/\delta)^{1/7}(1 - n/\delta), \tag{7}$$

$$\tau_{\theta n,o} = -0.0225\rho(\nu/\delta)^{1/4}(v_0 - \bar{v})[\tilde{u}^2 + (v_0 - \bar{v})^2]^{3/8}, \tag{8}$$

$$\tau_{sn,o} = -\frac{\tilde{u}}{v_0 - \bar{v}}\,\tau_{\theta n,o}. \tag{9}$$

In Eqs. (6)-(9), δ is the boundary layer thickness, ν is the kinematic viscosity, the subscript 0 denotes wall value, and the overbar represents values at the boundary layer edge.

Using Eqs. (6)-(9), Eqs. (2)-(5) may be integrated from $n = 0$ to $n = \delta$ and the resulting equations combined to give two momentum integral equations. These two equations, when nondimensionalized by the substitutions

$$x = \frac{r_0}{b}, \quad u_1 = \frac{\tilde{u}}{\Omega r_0}, \quad \bar{V} = \frac{\bar{v}}{\Omega r_0},$$

$$V_0 = \frac{v_0}{\Omega r_0}, \quad \delta_1 = \frac{\delta}{r_0}\,\mathrm{Re}_\theta^{1/5}\sin\lambda, \quad \mathrm{Re}_\theta = \frac{\Omega b^2}{\nu \sin\lambda}, \tag{10}$$

are

$$2I_4 Y_1 Y_2 \frac{dY_1}{dx} - I_4 Y_1^2 \frac{dY_2}{dx} =$$

$$-0.0225\,Y_1 x^{7/4}\left[\left(\frac{Y_1}{x^2}\right)^2 + Y_2^2(V_0 - \bar{v})^2\right]^{3/8}$$

$$+\frac{Y_1^2 Y_2}{x} I_4 - (Y_2 x)^3[2\bar{V}(\bar{V} - V_0)I_2 - (\bar{V} - V_0)^2 I_5], \tag{11}$$

$$I_3 Y_2 \frac{dY_1}{dx} = 0.0225 x^{7/4}\left[\left(\frac{Y_1}{x_2}\right)^2 + Y_2^2(V_0 - \bar{V})^2\right]^{3/8}$$

$$-\frac{(I_1 - I_3)}{(V_0 - \bar{V})} Y_1 Y_2 \frac{d\bar{V}}{dx} - \frac{2Y_1 Y_2}{x(V_0 - \bar{V})}[I_1\bar{V} + I_3(V_0 - \bar{V})]. \tag{12}$$

Here $Y_1 = u_1\delta_1 x^3$ and $Y_2 = \delta_1 x$. The constants I_1 to I_5 in Eqs. (11) and (12) arise from the integration of the power law velocity profiles and are given by $I_1 = 49/120$, $I_2 = 1/8$, $I_3 = 49/720$, $I_4 = 343/1656$, and $I_5 = 1/36$. It may be noted that Eqs. (11) and (12), and their initial conditions (see Section 2.5), are independent of λ, and so their solutions are also independent of cone half angle. However, as will be seen from results presented in Section 4, the validity of the assumptions underlying the equations may well depend on cone half-angle λ.

2.3 Stator Boundary Layer. The equations describing the flow in the stator boundary layer are the same as those derived by Chew (1991) for rotor-stator disk systems. This model is based on finite difference predictions for a disk system, which show that the tangential velocity profile (Eq. (6) with $v_0 = 0$) gives a reasonable representation of the flow on the stator, whereas the s-velocity profile (Eq. (7)) gives a poor representation. In a further finite difference study (May, 1990) it was shown that the conclusions for the disk system also applied to rotor-stator cone systems with λ as small as 15 deg. As in the disk flow work the following equations are used for the stator boundary layer:

$$u_1^s = -0.364\bar{V}^s, \tag{13}$$

$$\frac{dY_2^s}{dx} = \frac{Y_2^s}{x} - \frac{0.0648}{I_3^s(\bar{V}^s Y_2^s x)^{1/4}} + \frac{Y_2^s}{x}\frac{(2I_1^s - 5I_3^s)}{I_3^s}$$

$$-\frac{d\bar{V}^s}{dx}\frac{Y_2^s}{\bar{V}^s}\left(\frac{2I_3^s - I_1^s}{I_3^s}\right), \tag{14}$$

where $I_1^s = I_1$, $I_3^s = I_3/2$ and the superscript s denotes evaluation for the stator boundary layer. Equation (14) expresses conservation of angular momentum. Equation (13) is based on an examination of finite difference predictions, which showed that the velocity vector of the flow close to the stator surface is at an angle of about 20 deg to the tangential direction. However, as described by May (1990), the value of the limiting flow angle becomes more erratic for cases with throughflow and the assumption that it is always 20 deg becomes questionable. In an attempt to avoid the use of the limiting flow angle, momentum integral equations were derived by May (1990) using radial and tangential velocity profiles that more closely match the finite difference results. However, the equations were more complex than Eq. (14) and the results obtained did not show sufficient improvement to justify their use.

2.4 Shroud Treatment. The shroud channels fluid from the rotor boundary layer into the stator boundary layer, as shown in Fig. 1. Constant mass flow rate ($\dot{m}_b$) and friction factor, F, are assumed in this thin layer, as in the disk flow model. Conservation of angular momentum in the shroud layer then gives the equation

$$\dot{m}_b \frac{dV_b}{dz} = 2\pi b \frac{F}{2}\rho V_b^2, \tag{15}$$

where V_b is the bulk tangential velocity and $z = n \sin\lambda - s\cos\lambda$. Equation (15) may be integrated directly to obtain $\bar{V}^s$ at $x = 1$ from the rotor boundary layer solution at $x = 1$.

2.5 Solution Method. The solutions of the boundary layer equations for the rotor and stator are coupled through the shroud boundary layer and the inviscid flow region. The ordinary differential Eqs. (11), (12), and (14) were solved using

a variable order, variable step-length Numerical Algorithms Group (NAG) library routine for the solution of a stiff system of ordinary differential equations.

In the source region, between $r = a$ and $r = r_e$, (see Fig. 1), $\overline{V}(x)$ is given by the free vortex relation $r\overline{V} = \text{const}$, which expresses conservation of angular momentum external to the rotor boundary layer. Equations (11) and (12) are then integrated from $x = a/b$ to find Y_1 and Y_2. The initial conditions for Y_1 and Y_2 are $Y_1 = Y_2 = 0$ at $x = a/b$, corresponding to zero mass flow rate and zero boundary layer thickness. In practice, to avoid singularities in Eqs. (11) and (12), Y_1 and Y_2 were given initial values of 10^{-10}. The end of the source region is defined as the point at which all the inlet throughflow has been entrained into the rotor boundary layer. Any boundary layer flow on the stator in the source region is neglected.

In the core region, it is assumed that both the radial velocity component and the axial gradient of tangential velocity are zero (i.e., $\overline{V}(x) = \overline{V}^s(x)$) in the inviscid region between the boundary layers. An iterative solution procedure is used to find solutions to Eqs. (11), (12), and (14), which satisfy conservation of mass within the cavity. The velocity $\overline{V}(x)$ is specified at N points x_i ($i = 1, \ldots, N$), equally spaced (radially) in the core region with $x_1 = r_e/b$ and $x_N = 1$. A cubic spline curve fit is then used to interpolate $\overline{V}(x)$ between these points. Using a specified $\overline{V}$ distribution, the rotor equations may be solved from $x = r_e/b$ to $x = 1$, using the solutions from the end of the source region as initial conditions. From a mass balance at $x = 1$, initial conditions may be obtained for the stator equation, which is then solved from $x = 1$ to $x = r_e/b$. The solutions thus obtained are then fed into mass balance equations at each radial location, giving rise to a set of $(N - 1)$ nonlinear simultaneous equations of the form

$$F_i(\overline{V}) = \frac{Y_1 - Y_1^s - Cq/(2\pi I_1 \,\mathrm{Re}_\theta^{4/5})}{Y_1} = 0, \quad i = 1, \ldots, (N-1). \tag{16}$$

A final equation at $x = 1$ is obtained from the shroud condition:

$$F_N(\overline{V}) = \frac{\overline{V}^s(1) - \overline{V}(1)}{\overline{V}(1)} = 0. \tag{17}$$

The $\overline{V}$ distribution is updated iteratively as described below and the solution procedure is repeated until $\max |F_i(\overline{V})| < T$, where T is a tolerance which, from numerical experiments, was given a value of 0.01.

Several schemes were tried to update the $\overline{V}$ distribution. The best scheme in terms of speed and robustness was found to be one where the values of $\overline{V}(x_i)$ for the jth iteration are calculated from

$$\overline{V}^j(x_i) = \overline{V}^{j-1}(x_i) + \omega \overline{V}^{j-1}(x_i) F_i(\overline{V}). \tag{18}$$

In Eq. (18) ω is an underrelaxation factor, which is normally taken to be 0.5.

A typical run took about 30 iterations to converge and used about 30 seconds processing time on a Prime 6350 computer. Numerical experiments showed that a value of $N = 10$ was sufficient to give grid-independent solutions. This solution scheme is significantly faster than that used by Chew (1991), in which a linear variation of $\overline{V}$ between radial stations was assumed and the resulting equations were solved using a library routine for simultaneous nonlinear equations.

3 The Finite Difference Method

The finite difference code used in this work is a modified version of that written by Vaughan et al. (1989) to investigate flows in rotating disk systems. The modifications involved "tilting" the original plane disk cavity through an arbitrary angle, λ, to produce the computational domain shown in Fig. 2.

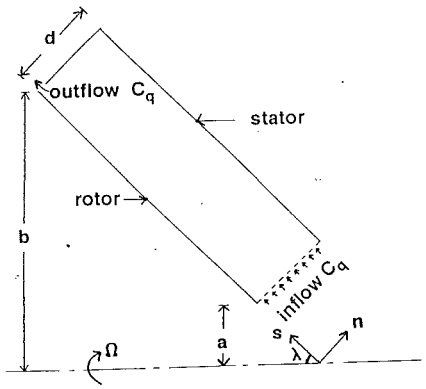

Fig. 2 Solution domain for the tilted rotating cavity

3.1 Governing Equations and Turbulence Model. For steady, axisymmetric flow, the Reynolds-averaged continuity and momentum equations may be written in terms of the (s, θ, n) coordinate system as

$$\frac{\partial}{\partial s}(\rho r u) + \frac{\partial}{\partial n}(\rho r w) = 0, \tag{19}$$

$$\frac{1}{r}\frac{\partial}{\partial s}(\rho r u \phi) + \frac{1}{r}\frac{\partial}{\partial n}(\rho r w \phi) = \frac{1}{r}\frac{\partial}{\partial s}\left[\mu_e \frac{\partial \phi}{\partial s}\right] + \frac{1}{r}\frac{\partial}{\partial n}\left[\mu_e \frac{\partial \phi}{\partial n}\right] + S_\phi, \tag{20}$$

where $\Phi = u$, v, or w. The density is assumed to be constant for the present studies. The source terms S_Φ for the u, v, and w momentum equations are given by

$$S_u = \rho \frac{v^2}{r} \sin\lambda - \frac{\partial p}{\partial s} + \frac{1}{r}\frac{\partial}{\partial s}\left[\mu_e r \frac{\partial u}{\partial s}\right] + \frac{1}{r}\frac{\partial}{\partial n}\left[\mu_e r \frac{\partial w}{\partial s}\right] - 2\frac{\mu_e}{r^2}\sin\lambda(u \sin\lambda + w \cos\lambda), \tag{21}$$

$$S_v = -\rho \frac{wv}{r}\cos\lambda - \rho \frac{uw}{r}\sin\lambda + v\frac{\cos\lambda}{r^2}\frac{\partial}{\partial n}(\mu_e r) - v\frac{\sin\lambda}{r^2}\frac{\partial}{\partial s}(\mu_e r), \tag{22}$$

and

$$S_w = +\rho \frac{v^2}{r}\cos\lambda - \frac{\partial p}{\partial n} + \frac{1}{r}\frac{\partial}{\partial n}\left[\mu_e r \frac{\partial w}{\partial n}\right] + \frac{1}{r}\frac{\partial}{\partial s}\left[\mu_e r \frac{\partial u}{\partial n}\right] - 2\frac{\mu_\theta}{r^2}\cos\lambda(u \sin\lambda + w \cos\lambda). \tag{23}$$

The system of Eqs. (19)–(23) is closed using a mixing-length turbulence model as described by Chew and Vaughan (1988). Briefly, μ_e is calculated as the sum of the laminar viscosity, μ, and a turbulent viscosity, μ_t. The turbulent viscosity is calculated from

$$\mu_t = \rho l^2 \left[\left(\frac{\partial u_p}{\partial x_n}\right)^2 + \left\{r\frac{\partial}{\partial x_n}\left(\frac{v}{r}\right)\right\}^2\right]^{1/2}, \tag{24}$$

where l is the mixing length, u_p is the velocity component parallel to the boundary surface in the s, n plane, and x_h is the direction normal to the surface. Close to the wall,

$$l = 0.42 x_n [1 - \exp\{-x_n(\rho\tau_w)^{1/2}/(26\mu)\}],$$

where τ_w is the wall shear stress, and elsewhere $l = 0.085\delta$. The influence of rotation on mixing length is accounted for by use of a Richardson number correction, as described by Koosinlin et al. (1974) and Chew and Vaughan (1988).

3.2 Numerical Method. The derivation of the finite difference equations from Eqs. (19)–(24) follows the finite volume approach of Patankar (1980) using "hybrid" differencing for the convective terms. An iterative, nonlinear, multigrid method is used to solve the equations on a staggered nonuniform rectangular mesh. The continuity Eq. (19) is used to derive a pressure correction equation following the SIMPLEC formulation of van Doormal and Raithby (1984). Due to the nonlinearity of the equations, underrelaxation factors are used for the three velocity components, pressure, turbulent viscosity, and multigrid corrections.

An additional damping term was included in the radial momentum equation for disk flows by Vaughan et al. (1989). This approach was extended here to both the u and w momentum equations. For further details of the numerical scheme, see Vaughan et al.

A typical run performed on a 65 × 65 grid took about three hours processing time on a Prime 6350.

4 Results

In this section, the moment coefficients Cm, predicted by the integral method of Section 2 and by the finite difference method of Section 3, will be compared with experimental data. The experimental data are those of Yamada and Ito (1975, 1979) who considered the effects of gap width, d/b, Reynolds number, Re (where $\mathrm{Re} = \mathrm{Re}_\theta \sin\lambda$) and throughflow rate, Cq, on Cm for rotor-stator cone systems with $\lambda = 15, 30, 45, 60, 75$, and 90 deg. In addition the data of Bilgen and Boulos (1973) are used to compare the moment coefficient predicted by the finite difference program for a rotor-stator cylinder system (i.e., $\lambda = 0$ deg).

The effect of cone half-angle on moment coefficient is shown in Figs. 3(*a–f*), for $C_q = 0$, where d/b decreases from 0.24 in Fig. 3(*a*) to 0.008 in Fig. 3(*f*). Figures 3(*a–e*) show excellent agreement between the predictions of the integral method and experiment for $\lambda \geq 60$ deg, the relative error always being less than 5 percent. From the same figures it can be seen that the agreement between the integral method predictions and experiment is poor for $\lambda \leq 45$ deg, where it is clear that the integral method is not reproducing the experimental trend. In Fig. 3(*f*), the agreement is poor for all λ, which can be explained by the experimentally observed fact that for such a small gap width the rotor and stator boundary layers are merged. The finite difference predictions shown in Figs. 3(*a–b*) do not show any overall improvement over those of the integral method, the dependence of Cm on λ being similar to that predicted by the integral method. (The differences between the finite difference and integral method results for $\lambda \geq 60$ deg may, in part, be attributed to the influence of the different solution domains near the outer shroud.)

It is clear from Figs. 3(*a–f*) that the experimental trend of the Cm versus λ curves is not well predicted over part of the range of λ considered. This may be due to a change in secondary

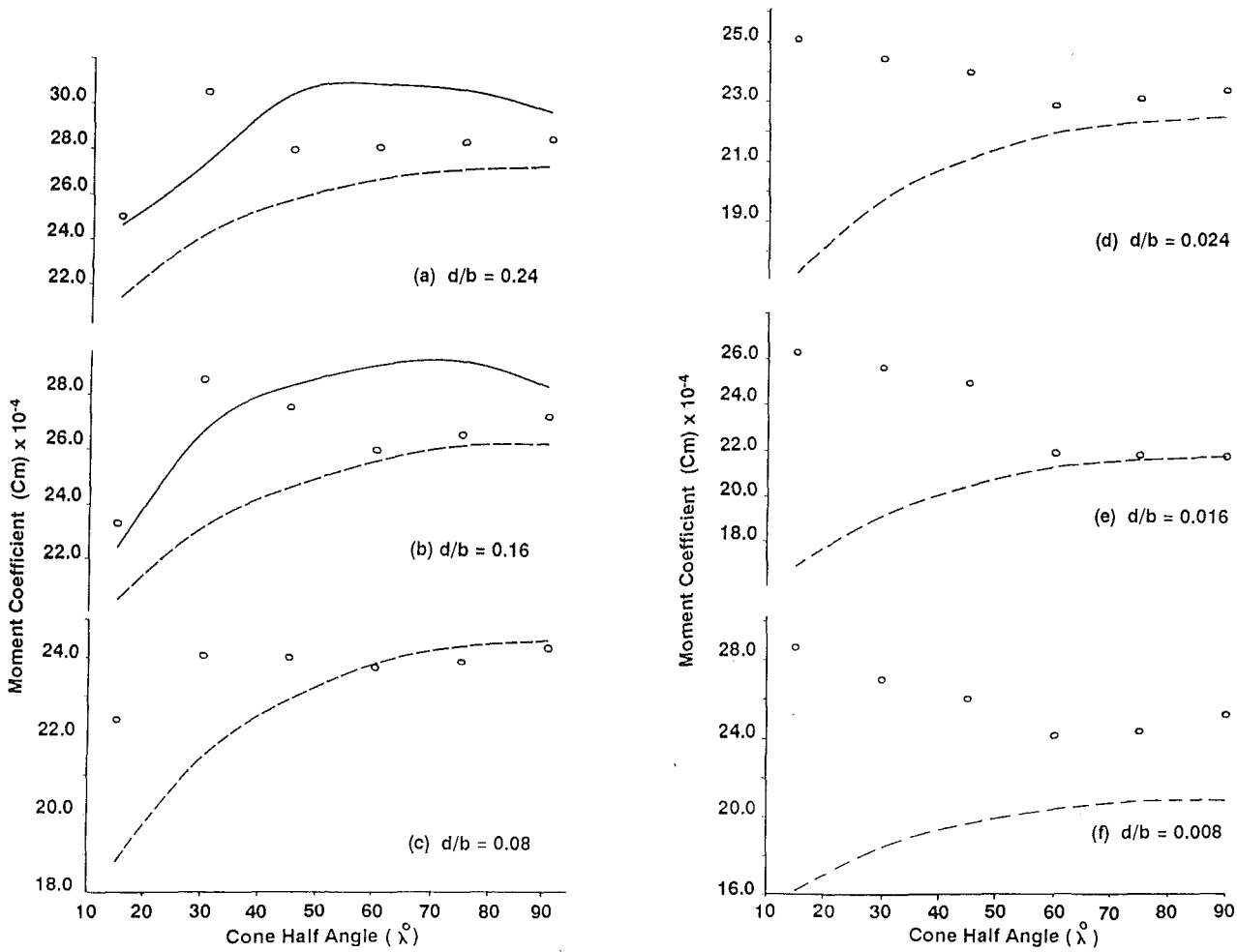

Fig. 3 Comparison of predicted moment coefficients with the data of Yamada and Ito (1975): $C_q = 0$, $a/b = 0$, $\mathrm{Re} = 10^6$ (0 data, —— finite difference, · · · · integral method)

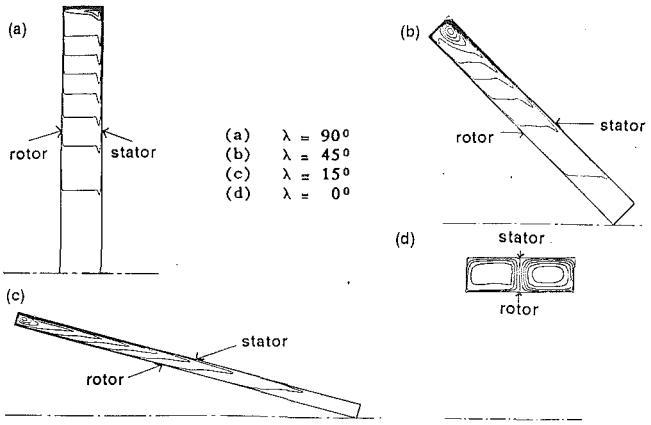

Fig. 4 Streamline predictions for zero throughflow: (*a*)-(*c*): *d*/*b* = 0.16, *a*/*b* = 0, Re = 10^6; (*d*): *d*/*b* = 0.208, *t*/*b* = 0.59, Re = 6.6 × 10^6 (—·—·— axis of rotation)

flow pattern, which is not predicted by the theoretical methods used in this work, occurring at smaller cone half angles. From visual flow studies, Yamada and Ito (1975) report that when $\lambda \geq 60$ deg, any secondary flow will always be of the large-scale "disk-type" as assumed in the integral method. However, for $\lambda \leq 45$ deg, these authors observe that the secondary flow may consist of both the disk-type flow and "Taylor-type" vortices similar to those known to occur in rotor–stator cylinder systems. According to Yamada and Ito, the presence of these vortices, which may be nonaxisymmetric and unsteady, causes an increase in *Cm*, which would explain the experimental trends shown in Figs. 3(*a–f*). While it is clear that the theoretical models cannot be expected to capture large-scale three-dimensional and unsteady effects, it should be noted that there are other assumptions underlying the two models, which might be questioned at low values of λ. These are, first, the assumed forms of the velocity profiles and shear stress laws for the integral method and, second, the mixing-length turbulence model for the finite difference method.

Typical predicted streamline plots obtained from the finite difference method, for cases in which there is no throughflow, are shown in Figs. 4(*a–d*). Figures 4(*a–c*) show that the predicted secondary flow is similar to that assumed in the integral method (Fig. 1) and that the Taylor-type vortices reported in experiments are not predicted. However, Fig. 4(*d*) shows that for a rotor–stator cylinder case ($\lambda = 0$ deg, $Re_\theta = 6.6 \times 10^6$, $d/b = 0.208$, $t/b = 0.59$), the finite difference method predicts two distinct vortices in the secondary flow. For this case the predicted moment coefficient (Cm') of 2.50×10^{-3} compares well with the value of 2.59×10^{-3} given by the empirical correlation of Bilgen and Boulos (1973). Of course, it should not be assumed that the finite difference method predicts the correct velocity field for $\lambda = 0$, but the level of agreement between the moment coefficients is certainly encouraging.

The effect of Reynolds number on *Cm* is shown in Figs. 5(*a–c*). As is to be expected from the above discussion, the agreement between prediction and measurement for $\lambda = 30$ deg shown in Fig. 5(*c*) is generally poor. Figures 5(*a*) and 5(*b*) show good agreement between the integral method predictions and measurement for $Re \geq 2 \times 10^5$. While the results of the integral method and finite difference method agree closely at high Reynolds numbers there is some discrepancy as the Reynolds number decreases. A slight overprediction of moment coefficient at low Reynolds numbers using the present mixing-length turbulence model is consistent with earlier disk cavity studies.

The effect of throughflow rate, *Cq*, on *Cm* is shown in Figs. 6(*a–c*). The figures show that the agreement between theory and experiment generally improves a little as the throughflow

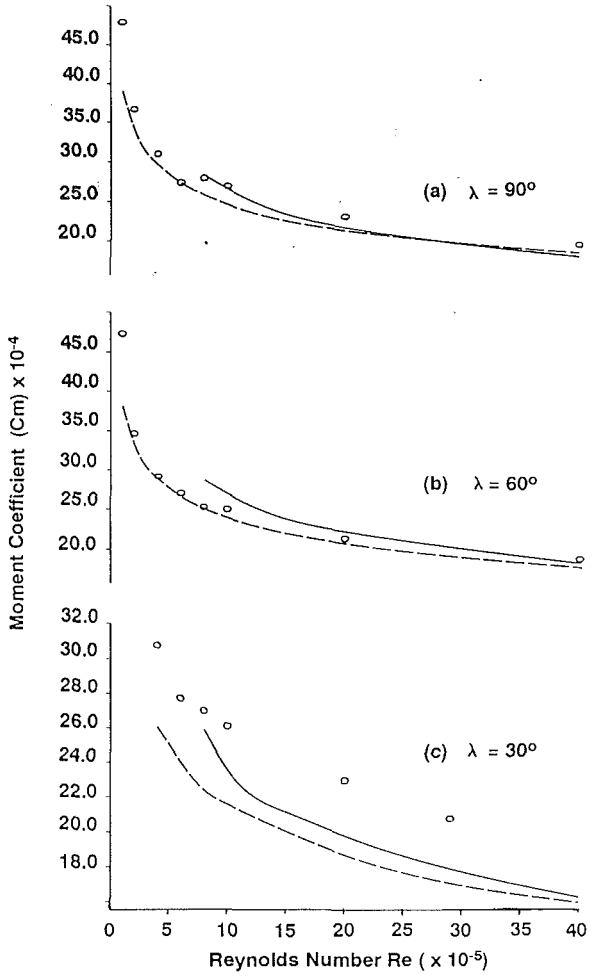

Fig. 5 A comparison of predicted moment coefficients with the data of Yamada and Ito (1975): *Cq* = 0, *a*/*b* = 0, *d*/*p* = 0.8 (○ data; —— finite difference; ···· integral method)

rate is increased. This is, perhaps, to be expected from the results of Yamada and Ito (1979) who found that if, for a particular case with no throughflow, Taylor-type vortices were expected in the secondary flow, then the application of throughflow suppresses their formation.

5 Conclusions

The following conclusions may be drawn from the present study of rotor–stator cone systems:

(*i*) For systems where $\lambda \geq 60$ deg, the integral method moment coefficient predictions are in excellent agreement with experiment. The finite difference predictions are in good agreement and discrepancies for $\lambda = 60$ deg and $\lambda = 75$ deg may be attributable to differences between the geometry of the experimental apparatus and the numerical solution domain.

(*ii*) The experimentally measured increase in moment coefficient as λ decreases is not reproduced by either predictive method. This discrepancy may be due to Taylor-type vortices being present in the flow, which are not predicted by the finite difference method because they are nonaxisymmetric and/or unsteady. For 15 deg $\leq \lambda \leq 45$ the finite difference predictions for moment coefficient are closer to the measured values than those of the integral method but, over the full range of values of λ considered, the performance of both methods is similar.

(*iii*) The finite difference method predicts the same secondary flow pattern as assumed in the integral method for conical systems where $\lambda \geq 15$ deg. The finite difference results also indicate that the assumptions made in the stator model,

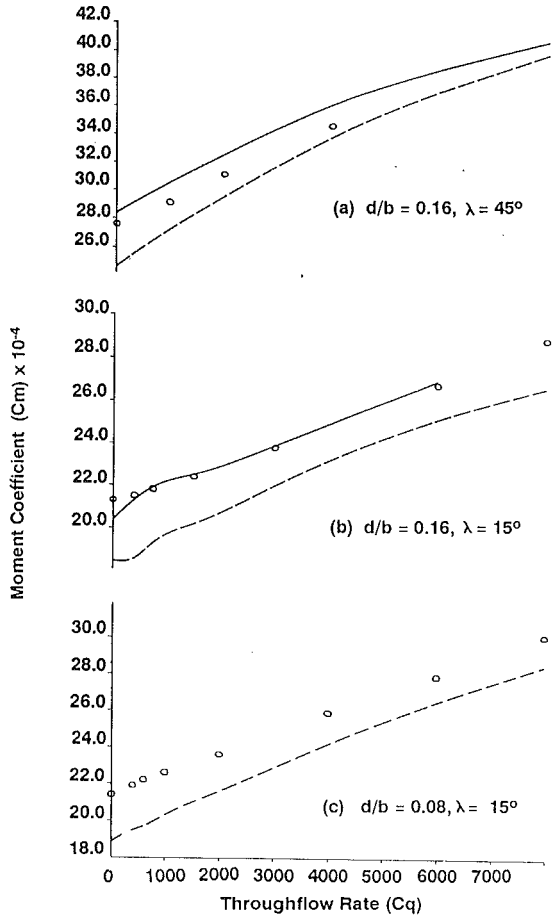

Fig. 6 A comparison of predicted moment coefficients with data of Yamada and Ito (1979): a/b = 0, Re = 10^6 (○ data; —— finite difference; · · · · integral method)

originally for rotor–stator disk systems, may be generalized to conical systems. For the limiting case of a rotating cylinder (λ = 0 deg) the flow structure is quite different. For this case, moment coefficient predictions from the finite difference method are in good agreement with experiment.

(iv) In addition to providing accurate predictions for $\lambda \geq$ 60 deg, the speed of the integral method should be stressed. Comparing a typical computer processing time of tens of seconds with the several hours taken by the finite difference method shows that the integral method does provide an attractive design aid.

Acknowledgments

The authors would like to thank Dr. Craig Vaughan for his assistance with the finite difference coding. The financial support of the Science and Engineering Research Council (UK), and Rolls-Royce plc, via a CASE Studentship, is also gratefully acknowledged.

References

Bilgen, E., and Boulos, R., 1973, "Functional Dependence of Torque Coefficient of Coaxial Cylinders on Gap Width and Reynolds Number," ASME *Journal of Fluids Engineering*, Vol. 95, p. 122.

Chew, J. W., 1985, "Prediction of Flow in a Rotating Cavity With Radial Outflow Using a Mixing-Length Turbulence Model," *Proc. Int. Conf. Lam. and Turb. Flow*, Pineridge, Swansea, United Kingdom.

Chew, J. W., and Rogers, R. H., 1988, "An Integral Method for the Calculation of Turbulent Forced Convection in a Rotating Cavity With Radial Outflow," *Int. J. Heat Fluid Flow*, Vol. 9, p. 37.

Chew, J. W., and Vaughan, C. M., 1988, "Numerical Predictions for the Flow Induced by an Enclosed Rotating Disc," ASME Paper No. 88-GT-127.

Chew, J. W., 1990, "Prediction of Rotating Disc Flow and Heat Transfer in Gas Turbine Engines," *Proc. 3rd Int. Symposium of Transport Phenomena and Dynamics of Rotating Machinery*, Honolulu, HI.

Chew, J. W., 1991, "A Theoretical Study of Ingress for Shrouded Rotating Disk Systems With Radial Outflow," ASME JOURNAL OF TURBOMACHINERY, Vol. 113, pp. 91–97.

Daily, J. W., and Nece, R. E., 1960, "Chamber Dimension Effects on Induced Flow and Frictional Resistance of Enclosed Rotating Discs," ASME *Journal of Basic Engineering*, Vol. 82, p. 217.

Daily, J. W., Ernst, W. D., and Asbedian, V. V., 1964, "Enclosed Rotating Discs With Superposed Throughflow," Report No. 64, Hydrodynamics Lab., Massachusetts Inst. Tech., Cambridge, MA.

Farthing, P. R., Chew, J. W., and Owen, J. M., 1991, "The Use of Deswirl Nozzles to Reduce the Pressure Drop in a Rotating Cavity With a Radial Inflow," ASME JOURNAL OF TURBOMACHINERY, Vol. 113, pp. 106–114.

Kreith, F., 1966, "Frictional Drag and Convective Heat Transfer of Rotating Cones in Mixed and Turbulent Flow," *Proc. Heat Trans. and Fluid Mech. Inst.*, Stanford University Press, p. 29.

Koosinlin, M. L., Launder, B. E., and Sharma, B. I., 1974, "Prediction of Momentum, Heat and Mass Transfer in Swirling Turbulent Boundary Layers," ASME *Journal of Heat Transfer*, Vol. 96, p. 204.

May, N. E., 1990, "Prediction of the Flow and Heat Transfer Between a Rotating and a Stationary Cone," Ph.D. Thesis, Polytechnic South West, Plymouth, United Kingdom.

Morse, A. P., 1988, "Numerical Prediction of Turbulent Flow in Rotating Cavities," ASME JOURNAL OF TURBOMACHINERY, Vol. 110, p. 202.

Morse, A. P., 1991, "Application of a Low Reynolds Number k–ϵ Turbulence Model to High-Speed Rotating Cavity Flows," ASME JOURNAL OF TURBOMACHINERY, Vol. 113, pp. 98–104.

Owen, J. M., Pincombe, J. R., and Rogers, R. H., 1985, "Source-Sink Flow Inside a Rotating Cylindrical Cavity," *J. Fluid Mech.*, Vol. 155, p. 233.

Owen, J. M., and Rogers, R. H., 1989, *Fluid Flow and Heat Transfer in Rotating Disc Systems, Vol. 1; Rotor-Stator Systems*, Research Studies Press, Taunton, United Kingdom.

Patankar, S. V., 1980, *Numerical Heat Transfer and Fluid Flow*, McGraw-Hill, London, United Kingdom.

Roscoe, D. V., Buggeln, R. C., Foster, J. A., and McDonald, H., 1988, "A Numerical Investigation of Fluid Flow for Disc Pumping Applications," ASME Paper No. 88-GT-299.

Tien, C. L., 1960, "Heat Transfer by Laminar Flow From a Rotating Cone," ASME *Journal of Heat Transfer*, Vol. 82, p. 252.

Van Doormal, J. P., and Raithby, G. D., 1984, "Enhancements of the SIMPLE Method for Predicting Incompressible Fluid Flows," *Num. Heat Trans.*, Vol. 7, p. 147.

Vaughan, C. M., Gilham, S., and Chew, J. W., 1989, "Numerical Solutions of Rotating Disc Flows Using a Non-linear Multigrid Algorithm," *Proc. 6th Int. Conf. Num. Meth. Lam. and Turb. Flow.*, Pineridge Press, Swansea, p. 63.

von Karman, T., 1921, "Uber laminare und turbulente Reibung," *Z. angeur. Math. Mech.*, Vol. 1, p. 233.

Yamada, Y., and Ito, M., 1975, "On the Frictional Resistance of Enclosed Rotating Cones," *Bulletin of the JSME*, Vol. 18, No. 123, p. 1026.

Yamada, Y., and Ito, M., 1979, "Frictional Resistance of Enclosed Rotating Cones With Superposed Throughflow," ASME *Journal of Fluids Engineering*, Vol. 101, p. 259.